64TH ELECTRONIC MATERIALS CONFERENCE

June 29-July 1, 2022 // The Ohio State University // Columbus, Ohio

PROGRAM & EXHIBIT GUIDE

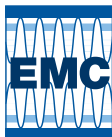

64TH ELECTRONIC MATERIALS CONFERENCE

June 29-July 1, 2022 // The Ohio State University // Columbus, Ohio

WELCOME TO THE CONFERENCE!

It is with great pleasure that we welcome you to the 64th Electronic Materials Conference (EMC 2022) at The Ohio State University. We expect this Conference to follow in EMC's long tradition of offering premier research on the preparation, characterization and use of electronic materials. Below, we have outlined highlights we believe will be of interest to you.

Conference Chair
Lisa Porter
Carnegie Mellon University

Program Chair
Daniel Wasserman
The University of Texas at Austin

CONFERENCE HIGHLIGHTS

The 64th EMC Program

Features over 300 oral/poster presentations and 36 technical sessions focused on Electronic Materials Science and Technology; Energy Storage and Conversion Materials; Nanoscale Science and Technology; Organic Materials, Thin Films and Devices; Oxide Semiconductors and Dielectrics; and Wide Bandgap Semiconductors.

EMC Awards Ceremony & Plenary Session

The 64th EMC kicks off Wednesday morning with the Awards Ceremony & Plenary Session. First, the 2021 Best Student Presentation Award winners and the 2021 NIST Uncertainty Analysis Student Award winner will be announced and honored. The Plenary Lecture follows, where **Susan Trolier-McKinstry** of The Pennsylvania State University will give her presentation, *New Materials for Three-Dimensional Ferroelectric Microelectronics.*

Welcome Reception/Poster Session

Join us for a Welcome Reception on Wednesday evening from 6:00 pm – 8:00 pm in the Performance Hall located in the Ohio Union. During this time, poster authors will be available for in-depth discussions at the Poster Session, also located in the Performance Hall in the Ohio Union. Both of these events are great for meeting with longtime colleagues, making new connections and sharing information. Light snacks and refreshments will be served.

Exhibit

Be sure to visit the EMC exhibitors Wednesday and Thursday in the Performance Hall located on the first floor of the Ohio Union. Learn more about the latest products and services in the rapidly evolving world of electronic materials. See page 18 for exhibit hours.

Conference Dinner Reception

Don't miss this year's Conference Dinner Reception, Thursday evening from 6:00 pm – 8:30 pm, in the Archie M. Griffin East Ballroom of the Ohio Union. Full Conference registration includes one Dinner Reception ticket. You can purchase additional Dinner Reception tickets at the EMC Registration Desk for $90 per person, subject to availability.

Save the Date

The 65th Electronic Materials Conference (EMC 2023) will be June 28 – 30, 2023, at the University of California, Santa Barbara. Mark your calendar today!

EMC is being coordinated with the Device Research Conference (DRC 2022), held at the Ohio Union from June 26 – 29. Badges will be accepted for admittance to both Conferences on Wednesday, June 26.

DRC attendees who wish to attend EMC sessions must sign the EMC Code of Conduct prior to admittance.

EMC respectfully requests that attendees wear masks while in the technical session rooms.

The 64th EMC has been managed by

CONFERENCE SERVICES
Because the Experience Matters
mrs.org/conference-services

SPECIAL THANKS!

CONFERENCE SUPPORT

https://pubs.acs.org/journal/aaembp

www.nsf.gov

THE OHIO STATE UNIVERSITY
INSTITUTE FOR MATERIALS RESEARCH

www.imr.osu.edu

www.umccorp.com

STUDENT SUPPORT

www.tms.org/foundation

www.nist.gov

TABLE OF CONTENTS

Committees 2
Maps 4
EMC Awards Ceremony & Plenary Session 5
Daily Schedule of Events 6
Travel Resources 6
Program At-A-Glance 7
Poster Session 10
Exhibit 18
Wednesday Oral Presentations 20
Poster Presentations 59
Thursday Oral Presentations 77
Friday Oral Presentations 122
EMC Index 144

COMMITTEES

Executive Committee

Chair — **Lisa Porter**, Carnegie Mellon University

Vice-Chair — **Daniel Wasserman**, The University of Texas at Austin

Secretary — **Adrienne Stiff-Roberts**, Duke University

Treasurer — **William Wong**, University of Waterloo

ELECTRONIC MATERIALS SCIENCE AND TECHNOLOGY

Contacts to Semiconductor Epilayers, Nanostructures and Organic Films

Leonard Brillson, The Ohio State University
Shadi Dayeh, University of California, San Diego
Suzanne Mohney, The Pennsylvania State University
Lisa Porter, Carnegie Mellon University
Tae-Yeon Seong, Korea University
Jerry Woodall, University of California, Davis

Epitaxial Materials and Devices

Seth Bank, The University of Texas at Austin
Kurt Eyink, Air Force Research Laboratory
Archie Holmes, The University of Texas at Austin
Sriram Krishnamoorthy, University of California, Santa Barbara
Charles Lutz, Lumentum Operations LLC
Nadeemullah Mahadik, U.S. Naval Research Laboratory
Kyle McNicholas, Lincoln Laboratory, Massachusetts Institute of Technology
Siddharth Rajan, The Ohio State University
Shadi Shahedipour-Sandvik, State University of New York Polytechnic Institute
Stephanie Tomasulo, U.S. Naval Research Laboratory
Christine Wang, **Lincoln Laboratory**, Massachusetts Institute of Technology
Dan Wasserman, The University of Texas at Austin
Kin-Man Yu, City University of Hong Kong

Hetero-Integration, Interconnects and Packaging

Guohai Chen, National Institute of Advanced Industrial Science and Technology
Mona Ebrish, U.S. Naval Research Laboratory
Daniel Ewing, Department of Energy's Kansas City National Security Campus
Michael Hamilton, Auburn University
Jamie Phillips, University of Delaware

Materials Discovery

Anderson Janotti, University of Delaware
Sriram Krishnamoorthy, University of California, Santa Barbara
Patrick Shea, Northrop Grumman Corporation
Angel Yanguas-Gil, Argonne National Laboratory

Materials for Memory and Computation

Alan Doolittle, Georgia Institute of Technology
Susan Fullerton, University of Pittsburgh
Feng Xiong, University of Pittsburgh
Ke Xu, Rochester Institute of Technology
Angel Yanguas-Gil, Argonne National Laboratory

Materials Processing and Integration

Daniel Ewing, Department of Energy's Kansas City National Security Campus
Mark Goorsky, University of California, Los Angeles
Doug Hall, University of Notre Dame
Karl Hobart, U.S. Naval Research Laboratory
Becky (R.L.) Peterson, University of Michigan
Nate Quitoriano, McGill University
Steve Ringel, The Ohio State University
Patrick Shea, Northrop Grumman Corporation
Jerry Woodall, University of California, Davis

Metamaterials and Materials for THz, Plasmonics and Polaritons

Joshua Caldwell, Vanderbilt University
Kurt Eyink, Air Force Research Laboratory
Rachel Goldman, University of Michigan
Anthony Hoffman, University of Notre Dame
Stephanie Law, University of Delaware
Thomas Searles, University of Illinois at Chicago
Berardi Sensale Rodriguez, The University of Utah
Jason Valentine, Vanderbilt University
Daniel Wasserman, The University of Texas at Austin
Huili Grace Xing, Cornell University

Micro-LEDs and -Displays—Materials, Fabrication and Characterization

Steven DenBaars, University of California, Santa Barbara
Zetian Mi, University of Michigan
Tae-Yeon Seong, Korea University
Jerry Woodall, University of California, Davis

Nanofabrication and Processing

Bruno Azeredo, Arizona State University
Kris Bertness, National Institute of Standards and Technology
Mona Ebrish, U.S. Naval Research Laboratory
Munho Kim, Nanyang Technological University, Singapore
Xiuling Li, The University of Texas at Austin
Parsian Mohseni, Rochester Institute of Technology
Angel Yanguas-Gil, Argonne National Laboratory

Nano-Magnetic, Magnetic Memory and Spintronic Materials

Hemant Dixit, Wolfspeed
Michael Flatté, The University of Iowa
Cheng Gong, University of Maryland
Jean Anne Incorvia, The University of Texas at Austin
Roland Kawakami, The Ohio State University
Xinyu Liu, University of Notre Dame
Pawan Tyagi, University of the District of Columbia
Angel Yanguas-Gil, Argonne National Laboratory

Narrow Bandgap Materials and Devices

Ganesh Balakrishnan, The University of New Mexico
Suprem Das, Kansas State University
Shanti Iyer, North Carolina Agricultural and Technical State University
Sanjay Krishna, The Ohio State University
Andrej Lenert, University of Michigan
Kyle McNicholas, Lincoln Laboratory, Massachusetts Institute of Technology
Kunal Mukherjee, Stanford University
Jamie Phillips, University of Delaware
Gregory Triplett, Virginia Commonwealth University
Christine Wang, Lincoln Laboratory, Massachusetts Institute of Technology
Daniel Wasserman, The University of Texas at Austin
Joshua Zide, University of Delaware

Point Defects, Doping and Extended Defects

Andrew Armstrong, Sandia National Laboratories
Ramon Collazo, North Carolina State University
Rachel Goldman, University of Michigan
Lincoln Lauhon, Northwestern University
Kunal Mukherjee, Stanford University
Steve Ringel, The Ohio State University
Shadi Shahedipour-Sandvik, State University of New York Polytechnic Institute
Jun Suda, Kyoto University and Nagoya University
Christian Wetzel, Rensselaer Polytechnic Institute
Jerry Woodall, University of California, Davis

Quantum, Strongly Correlated and Topological Materials

Matthew Doty, University of Delaware
Rachel Goldman, University of Michigan
Anthony Hoffman, University of Notre Dame
Stephanie Law, University of Delaware
Connie Li, U.S. Naval Research Laboratory
Jeremy Robinson, U.S. Naval Research Laboratory
Thomas Searles, University of Illinois at Chicago
Chakrakpani Varanasi, U.S. Army Research Office—Materials Science Division

ENERGY STORAGE AND CONVERSION MATERIALS

Electrochemical Energy Storage and Conversion

Susan Fullerton, University of Pittsburgh
David Gundlach, National Institute of Standards and Technology
Jung-Hyun Kim, The Ohio State University
Zetian Mi, University of Michigan
Edward Yu, The University of Texas at Austin

Energy Harvesting

Alan Doolittle, Georgia Institute of Technology
Deidra Hodges, Florida International University
Ken Jones, U.S. Army Research Laboratory
Suzanne Mohney, The Pennsylvania State University
Jamie Phillips, University of Delaware
Shadi Shahedipour-Sandvik, State University of New York Polytechnic Institute

Solar Cell Materials and Devices

Geoffrey Bradshaw, Air Force Research Laboratory
Rachel Goldman, University of Michigan
Mark Goorsky, University of California, Los Angeles
Andrej Lenert, University of Michigan
Steve Ringel, The Ohio State University
Oleg Rubel, McMaster University
Jae-Hyun Ryou, University of Houston
Mike Scarpulla, The University of Utah
Christian Wetzel, Rensselaer Polytechnic Institute
Mark Wistey, Texas State University
Jerry Woodall, University of California, Davis

Thermoelectrics and Thermal Transport

Kris Bertness, National Institute of Standards and Technology
Samuel Graham, Georgia Institute of Technology
Ferdinand Poudeu, University of Michigan
Xiaojia Wang, University of Minnesota
Yaguo Wang, The University of Texas at Austin
Joshua Zide, University of Delaware

NANOSCALE SCIENCE AND TECHNOLOGY

Graphene, BN, MoS_2 and Other 2D Materials and Devices

Thomas Beechem, Sandia National Laboratories
Kevin Daniels, University of Maryland
Mona Ebrish, U.S. Naval Research Laboratory
James Edgar, Kansas State University
Randall Feenstra, Carnegie Mellon University
Susan Fullerton, University of Pittsburgh
Jyoti Katoch, Carnegie Mellon University
Roland Kawakami, The Ohio State University
Manos Kioupakis, University of Michigan
Rachel Koltun, Guardian Industries
Lincoln Lauhon, Northwestern University
Suzanne Mohney, The Pennsylvania State University
Siddharth Rajan, The Ohio State University
Joan Redwing, The Pennsylvania State University
Joshua Robinson, The Pennsylvania State University
Michael Snure, Air Force Research Laboratory
Michael Spencer, Morgan State University
Christine Wang, Lincoln Laboratory, Massachusetts Institute of Technology
Huili Grace Xing, Cornell University

Low-Dimensional Structures—Quantum Dots, Wires and Wells

Ganesh Balakrishnan, The University of New Mexico
Matthew Doty, University of Delaware
Kurt Eyink, Air Force Research Laboratory
Rachel Goldman, University of Michigan
Lincoln Lauhon, Northwestern University
Minjoo (Larry) Lee, University of Illinois at Urbana-Champaign
Zetian Mi, University of Michigan
Jamie Phillips, University of Delaware
Paul Simmonds, Boise State University
Daniel Wasserman, The University of Texas at Austin

Nanoscale Characterization—Scanning Probes, Electron Microscopy and Other Techniques

Thomas Beechem, Sandia National Laboratories
Rachel Goldman, University of Michigan
Lincoln Lauhon, Northwestern University
James LeBeau, Massachusetts Institute of Technology
Anders Mikkelsen, Lund University
Jay Mody, Intel Corporation
Volker Rose, Argonne National Laboratory
Rainer Timm, Lund University
Heayoung Yoon, The University of Utah
Edward Yu, The University of Texas at Austin

Nanostructured Materials

Kris Bertness, National Institute of Standards and Technology
Matt Brubaker, National Institute of Standards and Technology
Xiuling Li, The University of Texas at Austin
Zetian Mi, University of Michigan
Anders Mikkelsen, Lund University
Parsian Mohseni, Rochester Institute of Technology
Roberto Myers, The Ohio State University
Nate Quitoriano, McGill University
Rainer Timm, Lund University
George Wang, Sandia National Laboratories
William Wong, University of Waterloo

ORGANIC MATERIALS, THIN FILMS AND DEVICES

Flexible, Printed and/or Dissolvable Thin Films or Nanomembranes

Suprem Das, Kansas State University
Daniel Ewing, Department of Energy's Kansas City National Security Campus
Gerd Grau, York University
Thomas Jackson, The Pennsylvania State University
Thomas Kuech, University of Wisconsin–Madison
Becky (R.L.) Peterson, University of Michigan
Jae-Hyun Ryou, University of Houston
William Scheideler, Dartmouth College
Jung-Hun Seo, University at Buffalo, The State University of New York
Sarah Swisher, University of Minnesota
William Wong, University of Waterloo

Organic and Hybrid Optoelectronic Devices

Alexander Ayzner, University of California, Santa Cruz
David Gundlach, National Institute of Standards and Technology
Diedra Hodges, Florida International University
Tina Ng, University of California, San Diego
Oleg Rubel, McMaster University
Adrienne Stiff-Roberts, Duke University
Wei You, University of North Carolina at Chapel Hill

Organic Devices and Molecular Electronics

Gerd Grau, York University
David Gundlach, National Institute of Standards and Technology
Thomas Jackson, The Pennsylvania State University
David Janes, Purdue University
Ioannis Kymissis, Columbia University
Takhee Lee, Seoul National University
Tina Ng, University of California, San Diego
Curt Richter, National Institute of Standards and Technology
Adrienne Stiff-Roberts, Duke University
William Wong, University of Waterloo

Wearable Electronics and Biosensors

Francesca Cavallo, The University of New Mexico
Buddhadev Paul Chaudhuri, Biolinq Inc.
Tzahi Cohen-Karni, Carnegie Mellon University
Shadi Dayeh, University of California, San Diego
David Estrada, Boise State University
David Gundlach, National Institute of Standards and Technology
Thomas Jackson, The Pennsylvania State University
David Janes, Purdue University
Shayla Sawyer, Rensselaer Polytechnic Institute

OXIDE SEMICONDUCTORS AND DIELECTRICS

Dielectrics and Multifunctional Oxides

Alan Doolittle, Georgia Institute of Technology
Doug Hall, University of Notre Dame
Anderson Janotti, University of Delaware
David Lederman, University of California, Santa Cruz
Patrick Lenahan, The Pennsylvania State University
Joseph Ngai, The University of Texas at Arlington
Angel Yanguas-Gil, Argonne National Laboratory

Gallium Oxide and Other Ultra-Wide Bandgap Oxides

Elaheh Ahmadi, University of Michigan
Shizuo Fujita, Kyoto University
Masataka Higashiwaki, National Institute of Information and Communications Technology
Sriram Krishnamoorthy, University of California, Santa Barbara
Shin Mou, Air Force Research Laboratory
Becky (R.L.) Peterson, University of Michigan
Lisa Porter, Carnegie Mellon University
Siddharth Rajan, The Ohio State University
Chintalapalle Ramana, The University of Texas at El Paso
Marko Tadjer, U.S. Naval Research Laboratory
Huili Grace Xing, Cornell University
Hongping Zhao, The Ohio State University

Oxide Semiconductors—Growth, Doping, Defects, Nanostructures and Devices

Leonard Brillson, The Ohio State University
Steve Durbin, Western Michigan University
Thomas Jackson, The Pennsylvania State University
Anderson Janotti, University of Delaware
Mark Losego, Georgia Institute of Technology
Becky (R.L.) Peterson, University of Michigan
Shayla Sawyer, Rensselaer Polytechnic Institute
Sarah Swisher, University of Minnesota

WIDE BANDGAP SEMICONDUCTORS

Diamond and Related Materials

Mark Goorsky, University of California, Los Angeles
Andrew Koehler, U.S. Naval Research Laboratory
Jung-Hun Seo, University at Buffalo, The State University of New York
Patrick Shea, Northrop Grumman Corporation

Group III-Nitrides—Growth, Processing, Characterization, Theory and Devices

Zakaria Y. Al Balushi, University of California, Berkeley
Andrew Allerman, Sandia National Laboratories
Srabanti Chowdhury, Stanford University
Theeradetch Detchprohm, Georgia Institute of Technology
Alan Doolittle, Georgia Institute of Technology
Russell Dupuis, Georgia Institute of Technology
Daniel Ewing, Department of Energy's Kansas City National Security Campus
Qhalid Fareed, Texas Instruments
Daniel Feezell, The University of New Mexico
Hiroshi Fujioka, The University of Tokyo
Jennifer Hite, U.S. Naval Research Laboratory
Andrew Koehler, U.S. Naval Research Laboratory
Xiaohang Li, King Abdullah University of Science and Technology
Siddharth Rajan, The Ohio State University
Shadi Shahedipour-Sandvik, State University of New York Polytechnic Institute
Andrei Vescan, RWTH Aachen University
Christian Wetzel, Rensselaer Polytechnic Institute
Jonathan Wierer, North Carolina State University
Huili Grace Xing, Cornell University

Silicon Carbide—Growth, Processing, Characterization, Theory and Devices

Joshua Caldwell, Vanderbilt University
MVS Chandrashekhar, University of South Carolina
Sarit Dhar, Auburn University
Michael Dudley, Stony Brook University, The State University of New York
Daniel Ewing, Department of Energy's Kansas City National Security Campus
Nadeemullah Mahadik, U.S. Naval Research Laboratory
Michael Spencer, Morgan State University
Jun Suda, Kyoto University and Nagoya University

THE OHIO STATE UNIVERSITY MAPS

The Ohio Union at The Ohio State University

First Floor

Registration .... Great Hall Foyer
Exhibit .... Performance Hall
Welcome Reception .... Performance Hall
Posters .... Performance Hall
Refreshment Breaks .... Performance Hall
Technical Session .... U.S. Bank Conference Theater
Technical Session .... Great Hall Meeting Room 1 & 2
Technical Session .... Great Hall Meeting Room 3

Second Floor

EMC Awards Ceremony & Plenary Session .... Archie M. Griffin West Ballroom
Technical Session .... Archie M. Griffin West Ballroom
Conference Dinner Reception .... Archie M. Griffin East Ballroom
Technical Session .... Ohio Staters Inc. Traditions Room
Technical Session .... Ohio Staters Inc. Founders Room
Technical Session .... Senate Chamber

Third Floor

Technical Session .... Cartoon Room 1
Technical Session .... Rosa M. Ailabouni Room

EMC AWARDS CEREMONY & PLENARY SESSION

Wednesday, 8:20 am – 9:20 am
Archie M. Griffin West Ballroom

PLENARY SPEAKER

Susan Trolier-McKinstry
The Pennsylvania State University

New Materials for Three Dimensional Ferroelectric Microelectronics

Susan Trolier-McKinstry is an Evan Pugh University Professor and Steward S. Flaschen Professor of Ceramic Science and Engineering and professor of electrical engineering. Her main research interests include thin films for dielectric and piezoelectric applications. She directs both the Center for Dielectrics and Piezoelectrics and the Center for Three-Dimensional Ferroelectric Microelectronics. She is a member of the National Academy of Engineering, a fellow of the American Ceramic Society, IEEE and the Materials Research Society, and an academician of the World Academy of Ceramics. She currently serves as an associate editor for *Applied Physics Letters.* She was 2017 President of the Materials Research Society; previously she served as president of the IEEE Ultrasonics, Ferroelectrics and Frequency Control Society, as well as Keramos.

2021 BEST STUDENT PRESENTATION AWARDS

ORAL PRESENTATIONS

A F M Anhar Uddin Bhuiyan
The Ohio State University
Orientation-Dependent Band Offsets at MOCVD Grown β-$(Al_xGa_{1-x})_2O_3$/β-Ga_2O_3 Heterointerfaces
Advisor – Hongping Zhao

Angela Cleri
The Pennsylvania State University
Mid-Wave to Near-IR Optoelectronic Properties and Epsilon-Near-Zero Behavior in In-Doped CdO
Advisor – Jon-Paul Maria

Zhe (Ashley) Jian
University of Michigan
Electrical Properties of MOCVD-Grown AlSiO Gate Dielectric on (001) β-Ga_2O_3
Advisor – Elaheh Ahmadi

Jonathan McCandless
Cornell University
Stabilizing α-Ga_2O_3 and α-$(Al,Ga)_2O_3$ up to 900°C
Advisor – Debdeep Jena

Student participation in this Conference is partially supported by a grant from the TMS Foundation

2021 BEST STUDENT PRESENTATION AWARDS

POSTER PRESENTATION

Bosun Abbas Roy-Layinde
University of Michigan
Temperature Dependence of Thermophotovoltaic Conversion Using InGaAs Air-Bridge Cells
Advisor – Andrej Lenert

2021 NIST UNCERTAINTY ANALYSIS STUDENT AWARD

Annatoma Arif
The University of Texas at El Paso
Inkjet Printed 3D Metal Electrodes on Shape Memory Polymer towards Improved Electrochemical Bio-Sensing Performance
Advisor – Robert Roberts

Sponsored by NIST

DAILY SCHEDULE OF EVENTS

TUESDAY

Event	Time	Location
Registration	3:00 pm – 5:00 pm	First Floor, Great Hall Foyer

WEDNESDAY

Event	Time	Location
Registration	7:30 am – 5:00 pm	First Floor, Great Hall Foyer
EMC Awards Ceremony and Plenary Session	8:20 am – 9:20 am	Second Floor, Archie M. Griffin West Ballroom
Exhibit	9:00 am – 12:00 pm	First Floor, Performance Hall
BREAK	9:20 am – 10:00 am	First Floor, Performance Hall
Poster Set-up	9:30 am – 3:00 pm	First Floor, Performance Hall
A: Group III-Nitrides—Power Diodes	10:00 am – 12:00 pm	First Floor, Great Hall Meeting Room 3
B: Silicon Carbide—Devices and Reliability	10:00 am – 12:00 pm	Second Floor, Archie M. Griffin West Ballroom
C: Wearable Electronics and Biosensors	10:00 am – 12:00 pm	Second Floor, Ohio Staters Inc. Founders Room
D: Gallium Oxide Devices	10:00 am – 12:00 pm	Second Floor, Ohio Staters Inc. Traditions Room
E: Dielectrics and Multifunctional Oxides	10:00 am – 12:00 pm	Second Floor, Senate Chamber
F: Point Defects, Doping and Extended Defects	10:00 am – 12:00 pm	Third Floor, Rosa M. Ailabouni Room
DRC Session 11: Heterogeneous Integration	10:00 am – 12:00 pm	First Floor, U.S. Bank Conference Theater
Lunch	12:00 pm – 1:30 pm	(Not provided by Conference)
DRC Session 12: Wide Bandgap III - III N HEMTs	1:20 pm – 3:00 pm	First Floor, U.S. Bank Conference Theater
G: 2D Material Devices and Sensors	1:30 pm – 5:10 pm	First Floor, Great Hall Meeting Room 1 & 2
H: Group III-Nitrides—Power Diodes and HEMTs	1:50 pm – 5:10 pm	First Floor, Great Hall Meeting Room 3
I: Silicon Carbide Materials and Characterization	1:30 pm – 3:10 pm	Second Floor, Archie M. Griffin West Ballroom
K: Metasurfaces and Structured Photonics	1:30 pm – 2:50 pm	Second Floor, Ohio Staters Inc. Founders Room
L: Gallium Oxide Growth	1:30 pm – 5:10 pm	Second Floor, Ohio Staters Inc. Traditions Room
M: Solar Cell Materials and Devices	1:30 pm – 4:30 pm	Second Floor, Senate Chamber
Exhibit	1:30 pm – 4:00 pm	First Floor, Performance Hall
BREAK	3:10 pm – 3:30 pm	First Floor, Performance Hall
Poster Viewing	3:10 pm – 3:30 pm	First Floor, Performance Hall
J: Nanoscale Characterization	3:30 pm – 5:10 pm	Second Floor, Archie M. Griffin West Ballroom
Exhibit	6:00 pm – 8:00 pm	First Floor, Performance Hall
Welcome Reception/Poster Session	6:00 pm – 8:00 pm	First Floor, Performance Hall

THURSDAY

Event	Time	Location
Registration	8:00 am – 5:00 pm	First Floor, Great Hall Foyer
N: 2D Materials Growth and Surfaces	8:20 am – 11:40 am	First Floor, Great Hall Meeting Room 1 & 2
O: Group III-Nitrides—MOCVD Growth	8:20 am – 12:00 pm	First Floor, Great Hall Meeting Room 3

THURSDAY (CONT.)

Event	Time	Location
P: Quantum, Strongly Correlated and Topological Materials	8:20 am – 12:00 pm	First Floor, U.S. Bank Conference Theater
Q: Oxide Semiconductor Devices, Defects and Transport	8:20 am – 11:40 am	Second Floor, Ohio Staters Inc. Traditions Room
R: Detectors and Narrow Bandgap Materials	8:20 am – 12:00 pm	Second Floor, Senate Chamber
S: Emerging Epitaxial Materials	8:20 am – 10:00 am	Third Floor, Cartoon Room 1
Exhibit	9:00 am – 12:00 pm	First Floor, Performance Hall
BREAK	10:00 am – 10:20 am	First Floor, Performance Hall
Poster Viewing	10:00 am – 10:20 am	First Floor, Performance Hall
T: Epitaxial Growth of Highly Mismatched Alloys	10:20 am – 12:00 pm	Third Floor, Cartoon Room 1
Lunch	12:00 pm – 1:30 pm	(Not provided by Conference)
U: Nano-Magnetic, Magnetic Memory and Spintronic Materials	1:30 pm – 5:10 pm	First Floor, Great Hall Meeting Room 1 & 2
V: Group III-Nitrides—Light Emitting Diodes	1:30 pm – 2:50 pm	First Floor, Great Hall Meeting Room 3
X: Low-Dimensional Materials and Nanofabrication	1:30 pm – 4:50 pm	First Floor, U.S. Bank Conference Theater
Y: Materials Processing and Integration	1:30 pm – 3:10 pm	Second Floor, Ohio Staters Inc. Traditions Room
AA: Plasmon and Surface Phonon Polaritons	1:30 pm – 5:10 pm	Second Floor, Senate Chamber
BB: Electrochemical Energy Storage and Conversion	1:30 pm – 5:30 pm	Third Floor, Cartoon Room 1
BREAK	3:10 pm – 3:30 pm	First Floor, Performance Hall
Exhibit	1:30 pm – 4:00 pm	First Floor, Performance Hall
Poster Viewing	3:10 pm – 3:30 pm	First Floor, Performance Hall
W: Group III Nitrides—MBE, CVD and Sputtering	3:30 pm – 5:10 pm	First Floor, Great Hall Meeting Room 3
Z: Heterogeneous Integration Technologies	3:30 pm – 5:10 pm	Second Floor, Ohio Staters Inc. Traditions Room
Poster Tear-down Deadline	5:30 pm	First Floor, Performance Hall
Conference Dinner Reception	6:00 pm – 8:30 pm	Second Floor, Archie M. Griffin East Ballroom

FRIDAY

Event	Time	Location
Registration	8:00 am – 12:00 pm	First Floor, Great Hall Foyer
CC: Neuromorphic + Late News	8:20 am – 12:00 pm	First Floor, Great Hall Meeting Room 1 & 2
DD: Group III-Nitrides—Contacts and Novel Devices	8:20 am – 11:20 am	First Floor, Great Hall Meeting Room 3
EE: Flexible, Printed and Organic Electronic Materials and Devices	8:20 am – 12:00 pm	First Floor, U.S. Bank Conference Theater
FF: Gallium Oxide—Material Processing, Characterization and Defects	8:20 am – 12:00 pm	Second Floor, Ohio Staters Inc. Traditions Room
GG: Epitaxial Growth on Patterned Substrates	8:20 am – 10:00 am	Third Floor, Cartoon Room 1
BREAK	10:00 am – 10:20 am	First Floor, Performance Hall
HH: Lattice Mismatched Epitaxial Growth	10:20 am – 12:00 pm	Third Floor, Cartoon Room 1

TRAVEL RESOURCES

The Conference does not endorse or sponsor any of the listings below. Information is provided as a courtesy to attendees.

PARKING

Visitors and guests to The Ohio State University are **required to purchase parking any time they park on campus.**

The closest parking available to the Conference is the **Ohio Union South Parking Garage.**

Located near the eastern corridor of the academic campus, the Ohio Union South Garage offers visitor and limited permit parking.

Visitors can park in this garage anytime. All garage fees are due upon exit. Pay-on-foot machines accept cash, credit, and validations.

For more information on CampusParc, visit osu.campusparc.com.

INTERNET ACCESS

The Ohio Union offers **free wireless internet.** Connect to **Wifi@OSU and open your browser to accept the terms of service.**
No password is required.

Wireless internet service is typically available in the residence halls, but due to maintenance schedules, is not always guaranteed.

OHIO STATE UNIVERSITY SMOKE-FREE AND TOBACCO-FREE POLICY

Ohio State has adopted a tobacco-free policy that supports a healthy environment for all. Effective January 1, 2014, **the use of all types of tobacco products is prohibited** in all university buildings and on all university-owned properties, including parking lots, garages, and all outside areas.

DINING OPTIONS

Inside the Ohio Union you'll find the **Union Market,** a fast, casual option offering a variety of grab-and-go food choices; **Woody's Tavern,** a pub-style restaurant serving wood-fired pizza and Ohio's finest beer and wine; and **Espress-OH**, a coffee shop serving specialty drinks, breakfast items, and gelato. In addition, there are many dining options within walking distance.

Summer hours for dining options inside the Ohio Union are as follows:

- o Express-OH is open Monday - Friday 8:00 am-4:00 pm; Weekends 10:00 am-4:00 pm
- o Union Market is open Monday - Thursday 10:30am-7:00 pm; Friday 10:30am-5:00 pm; Closed Saturday and Sunday
- o Woody's Tavern is open Monday – Friday 4:00 pm-7:00 pm; Closed Saturday/Sunday

Time	Speaker	Code	Title
EMC Awards Ceremony and Plenary Session			**Archie M. Griffin West Ballroom**
8:20 am			Awards Ceremony
8:30 am	Susan Trolier-McKinstry	PL01*	New Materials for Three Dimensional Ferroelectric Microelectronics
9:20 am			BREAK
A: Group III-Nitrides—Power Diodes			**Great Hall Meeting Room 3**
10:00 am	Lincoln Lauhon	A01	Correlated Nanoscale Imaging of Doping, Conductivity, and Cathodoluminence in GaN p-n Junctions Prepared by Selected Area Regrowth
10:20 am	Russell Dupuis	A02	1.3 kV Vertical GaN p-i-n Rectifier with Nitrogen-Implanted Field Guard Ring Edge Termination
10:40 am	Andrew M. Armstrong	A03	1.6 kV Etched-and-Regrown GaN pn-Diodes Realized by Mitigation of Plasma Etch-Enhanced Deep Level Defects
11:00 am	Matthew Alexander Porter	A04	(Student) Design, Manufacturability and Optimization of Hybrid Guard Ring-JTE Edge Terminations via Nitrogen Implantation in Epitaxial GaN PN Power Diodes
11:20 am	Christopher M. Matthews	A05	(Student) AlN Homojunction PN Diodes—The Highest Bandgap Semiconductor Diodes Ever Demonstrated
11:40 am	Vincent E. Meyers	A06	(Student) Defect Microstructural and Diffusion Studies of Implant-Gyrotron Microwave Annealed GaN:Mg—Effect of Sequential High- and Moderate-Temperature Annealing
B: Silicon Carbide—Devices and Reliability			**Archie M. Griffin West Ballroom**
10:00 am	Sami El Hageali	B01	(Student, Late News) Structural and Optical Characterization of Trapezoidal Defects in 4H-SiC Epilayers and Their Effect on MOSFETs Reliability
10:20 am	Shengnan Zhu	B02	(Student) JFET Region Design for 650 V 4H-SiC Planar Power MOSFETs
10:40 am	Suman Das	B03	(Student) Channel Hole Scattering Processes in 4H-SiC MOSFETs
11:00 am	Suvendu Nayak	B04	(Student) Process-Induced Variability of SiC DMOSFET Short Circuit Capability
11:20 am	Hema Lata Rao Maddi	B05	Characterization of SiC-SiO_2 Interface States in Commercial 4H-SiC Power MOSFETs from Cryogenic to High Temperature
11:40 am	Ashton Purcell	B06	(Student) Recombination Centers in 4H-SiC pin Diodes Observed by Electrically Detected Magnetic Resistance and Near-Zero Field Magnetoresistance
C: Wearable Electronics and Biosensors			**Ohio Staters Inc. Founders Room**
10:00 am	Nam-In Kim	C01	(Student) Stress Hormone Detection by Single-Crystalline III-N Piezoelectric Thin-Film-Based Sensor
10:20 am	Dongseop Lee	C02	(Student) Recessed AlGaN/GaN HEMT Biosensors with High Sensitivity and Linearity for Detection of Microcystin-LR
10:40 am	Nam-In Kim	C03	(Student) Pressure Monitoring at Extremely High-Temperature Range Using Highly Flexible Piezoelectric Sensor Made of Ultrawide-Bandgap III-N Thin Film
11:00 am	Julia Isidora Salas Toledo	C04	(Student) Flexible Modified Carbon Nanotube/Nanofiber-Based Triboelectric Nanogenerator
11:20 am	Lauren Brady	C05	(Student) Detection of the Nitrogen Cycle Using the Metabolic Activity of Shewanella Oneidensis MR-1
11:40 am	Nam-In Kim	C06	(Student) Wearable Eye Movement Sensors Using Flexible and Biocompatible III-N Thin Films for Personal Safety, Healthcare Monitoring and Abnormality Diagnosis
D: Gallium Oxide Devices			**Ohio Staters Inc. Traditions Room**
10:00 am	Nidhin Kurian Kalarickal	D01	(Student) Demonstration of Self-Aligned Delta Doped MISFETs with Current Density > 550 mA/mm
10:20 am	Marko Tadjer	D02	Growth and Electrothermal Characterization of β-$(Al_xGa_{1-x})_2O_3/Ga_2O_3$ Heterostructure Field-Effect Transistors
10:40 am	Ashok Vedantum Dheenan	D03	(Student) β-Ga_2O_3 MESFETs with Insulating Mg-Doped Buffer Grown by MBE
11:00 am	Zhenwei Wang	D04	Electrical Characteristics and Band Alignment of n-Si/n-Ga_2O_3 Heterojunction Fabricated by Surface-Activated Bonding
11:20 am	Joseph Spencer	D05	(Student) Beta-Gallium Oxide Junction Barrier Schottky Diodes with Sputtered P-Type Nickel Oxide
11:40 am	Zhe Ashley Jian	D06	(Student, Late News) Heterogeneous Integration of Single-Crystal -Ga2O3 and N-Polar GaN Substrates with ZnO Interlayer Deposited by Atomic Layer Deposition
E: Dielectrics and Multifunctional Oxides			**Senate Chamber**
10:00 am	Aminat Oyiza Suleiman	E01	The Role of Thermal Vibrational Disorder in the Structural Phase Transition of VO2 Probed by Raman Spectroscopy
10:20 am	Samuel Marks	E02	High Transparent Conductor Figure-of-Merit for $SrVO_3$ Grown by Solid-Phase Epitaxy
10:40 am	Kamila J Thompson	E03	(Student) Correlation of Native Point Defects with Piezoelectric Voltage in Strained ZnO Microwires
11:00 am	Brenton A Noesges	E04	(Student) Controlling Charge Distributions Near Complex Oxide Interfaces via Defect Engineering
11:20 am	Lyndon E Smith	E05	(Student, Late News) Mechanothermal Synthesis and Characterization of Ti-Doped Bismuth Ferrite Using Nano-Agitator Milling Process
11:40 am	Tetyana V. Torchynska	E06	On the Impact of Impurities' Nature and Annealing Conditions on Structural and Optical Properties of Hafnia-Based Thin Films
F: Point Defects, Doping, and Extended Defects			**Rosa M. Ailabouni Room**
10:00 am	Rafael Jaramillo	F01	Small Defects, Big Deal—Using Point Defects to Control Giant Opto-Mechanical Effects and to Engineer New Resistive Switches
10:20 am	Eamonn T Hughes	F02	(Student) Dislocations Altering the Microstructure and Luminescence of InAs Quantum Dots on Silicon
10:40 am	Yekan Wang	F03	(Student) Defects with Mg Segregation in Mg-Implanted GaN After Ultra-High-Pressure Annealing
11:00 am	Fatih Furkan Ince	F04	(Student) Growth of High Indium Percentage InGaSb on InP Substrates Using the Interfacial Misfit Dislocation Array Growth Mode.
11:20 am	Chunyi Huang	F05	(Student) Remote Si Doping of InGaAs Nanowires for Topological Quantum Computing
11:40 am	Joshua Ferrigno	F06	Irradiation Effects on Phonon Mediated Thermal Transport and Defect Evolution in GaAs

*Plenary Talk

PROGRAM AT-A-GLANCE

WEDNESDAY PM

G: 2D Material Devices and Sensors			Great Hall Meeting Room 1 & 2
1:30 pm	Sarbashis Das	G01	(Student) Multifunctional $MoTe_2$ Transistors for Analog, Digital, Neuromorphic and Modulation Primitives
1:50 pm	Akhil Dodda	G02	(Student) Near Sensor Security Based on Multifunctional Monolayer MoS_2 FETs
2:10 pm	Zhihui Cheng	G03	Are Two-Dimensional Interfaces Really Flat?
2:30 pm	Rafael Jaramillo	G04	The (Mostly) Unwelcome Guest in Transition Metal Chalcogenides—Native Oxidation and the Effects of Oxygen During Processing MoS_2, TiS_2 and $Zr(S,Se)_2$
2:50 pm	Yuanyue Liu	G05	(Late News) What Limits Electronic Transport in 2D Transition Metal Dichalcogenides—Phonons or Defects?
3:10 pm			BREAK
3:30 pm	Jenifer R Hajzus	G06	Comparison of Epitaxial Graphene Electrodes for Electrochemical Detection and Identification of Heavy Metals in Seawater
3:50 pm	Soaram Kim	G07	Lattice Strain Induced Biosensing of SARS-CoV-2 Enabled by Quasi-Freestanding Epitaxial Graphene
4:10 pm	Hirandeep Reddy Kuchoor	G08	Improved Density of GaAsSb Nanowires on Monolayer Graphene/SiO_2/Si for Near-Infrared Photodetector Application
4:30 pm	Elisabeth Mansfield	G09	Degradation of CVD-Grown MoS_2 Subjected to DC Electrical Stress
4:50 pm	Emanuel Ber	G10	(Student, Late News) Reducing Schottky Barrier Height vs Width—Which is Most Effective in Improving Contact Resistance to Atomically Thin Semiconductors?

H: Group III-Nitrides—Power Diodes and HEMTs			Great Hall Meeting Room 3
1:50 pm	Yekan Wang	H01	(Student) Defect Characteristics Under Devices and Reverse Leakage Current Investigated Using X-Ray Topography
2:10 pm	Yafei Liu	H02	(Student) Investigation of the Nature and Origins of Area Defects in Gallium Nitride Substrate Wafers
2:30 pm	James C Gallagher	H03	Effects of Surface Defects on Vertical GaN Diode Performance
2:50 pm	Yuxuan Zhang	H04	(Student) Correlating Optical Characteristics and Electrical Performance of Vertical GaN-on-GaN PN Diodes
3:10 pm			BREAK
3:30 pm	Caleb Glaser	H05	(Student) Interface Trap Density Characterization of ALD Gate Dielectrics for GaN Power MOSFETs
3:50 pm	Mahlet Molla	H06	(Student) Thermodynamic and Band Structure Study of $Sc_xAl_{1-x}N$
4:10 pm	Md Didarul Alam	H07	(Student) Fabrication of Flexible AlGaN/GaN HEMTs Using Laser Liftoff
4:30 pm	Alan G Jacobs	H08	Efficient N-Type Ion Implantation Activation in GaN with High Mobility
4:50 pm	Zexuan Zhang	H09	(Student) N-Polar GaN/AlGaN High Electron Mobility Transistor Structures on Single-Crystal AlN Substrates

I: Silicon Carbide Materials and Characterization			Archie M. Griffin West Ballroom
1:30 pm	Daniel J Pennachio	I01	Exploring SiC CVD Growth Parameters Compatible with Remote Epitaxy on Epitaxial Graphene Substrates
1:50 pm	Nadeemullah Mahadik	I02	Expansion of BPDs from Star-Shaped Defects in 4H-SiC
2:10 pm	Zeyu Chen	I03	(Student) Analysis of Strain Gradient in High Energy Implanted 4H-SiC Epi Wafer by Synchrotron X-Ray Rocking Curve Topography
2:30 pm	Hongyu Peng	I04	Analysis of Dislocations in 4H-SiC Wafers Using Synchrotron X-Ray Topography
2:50 pm	Qianyu Cheng	I05	(Student) Determination of Effective Penetration Depths on Synchrotron X-Ray Topographic Images of Dislocations Lying on the Basal Plane in 4H-SiC Crystals
3:10 pm			BREAK

J: Nanoscale Characterization			Archie M. Griffin West Ballroom
3:30 pm	Luis Miaja Avila	J01	EUV Pulsed Atom Probe Tomography of β-Ga_2O_3 Semiconductor Materials
3:50 pm	Moritz Hansemann	J02	(Student) STM Simulation of High Aspect Ratio Tunneling Behavior on the Example of *in situ* Harvested GaAs Nanowire
4:10 pm	Seth Shields	J03	(Student) Atomic Resolution Scanning Tunneling Microscopy Studies of Oxidized Cu(100) Surfaces
4:30 pm	Dorothee Sophie Rosenzweig	J04	(Student) GaAs(110) Surface Modifications by Adsorption Hydrogen at Room Temperature and Above
4:50 pm	Fedor V Sharov	J05	(Student) A Near-Adiabatic Rapid-Sweep (NARS) Approach to Electrically Detected Magnetic Resonance (EDMR) and Near-Zero-Field Magnetoresistance (NZFMR)

CONFERENCE BADGE

Badges must be worn at all times within the Conference venue, including all receptions.

RECORDING/PHOTO POLICY

Recording or photographing Conference presentations, posters or displays is strictly prohibited without prior permission of the presenter.

Americans with Disabilities Act (ADA) Compliance

The Materials Research Society (MRS), its meeting partners and event venues, are responsible for complying with the Americans with Disabilities Act ("ADA") including the "readily achievable" removal of physical barriers to access meeting rooms, sleeping rooms and common areas. This may also include reasonable provisions for auxiliary aids and services when necessary and where achievable without undue burden. MRS will make every attempt to ensure that disabled individuals are accommodated so that they can receive the full benefit of participation in our events, and will modify, where possible, the policies, practices and procedures as necessary to provide goods and services to disabled individuals. On-site needs will be met to the extent possible.

K: Metasurfaces and Structured Photonics			Ohio Staters Inc. Founders Room
1:30 pm	Hanyu Zheng	K02	(Student) Meta-Optic Accelerators for Object Classifiers
1:50 pm	Milan Palei	K03	Probing Long-Range Coupling in Plasmonic Metasurfaces via Far-Field Diffraction
2:10 pm	Raymond C Rumpf	K04	Electromagnetics and Photonics in the Age of Digital Manufacturing
2:30 pm	Anjali Chaudhary	K05	Electroplated Helical Slow-Wave Structures for Millimeter-Through-THz Vacuum Electronic Devices
L: Gallium Oxide Growth			**Ohio Staters Inc. Traditions Room**
1:30 pm	Takeki Itoh	L01	(Student) Epitaxial Growth on β-Ga_2O_3 (110) Substrate by Plasma-Assisted Molecular Beam Epitaxy
1:50 pm	Thaddeus J Asel	L02	Source Material Oxidation Challenges in Ge-Doped β-Ga_2O_3 Grown via Plasma-Assisted Molecular Beam Epitaxy
2:10 pm	Tianchen Yang	L03	(Student) Characterization of β-Phase MgGaO Thin Films Grown by Molecular Beam Epitaxy
2:30 pm	A F M Anhar Uddin Bhuiyan	L04	(Student) MOCVD growth of Si Doped (010) β-$(Al_xGa_{1-x})_2O_3$ Films—Structural and Electrical Properties
2:50 pm	Lingyu Meng	L05	(Student) MOCVD Epitaxy of β-Ga_2O_3 Thin Films on (100) β-Ga_2O_3 Substrate
3:10 pm			BREAK
3:30 pm	Kunyao Jiang	L06	(Student) Phase Composition and Microstructure of κ-Ga_2O_3 Heteroepitaxial Films Grown by MOCVD
3:50 pm	Kenny Huynh	L07	(Student) Inhomogeneous Aluminum Incorporation in (-201) β-$(Al_xGa_{1-x})_2O_3$ Films Grown on c-Plane and Miscut Sapphire Substrates
4:10 pm	A F M Anhar Uddin Bhuiyan	L08	(Student) MOCVD Development and Bandoffsets of ε-Ga_2O_3 on GaN, AlN, YSZ and c-Sapphire Substrates
4:30 pm	Jani Jesenovec	L09	(Student) Electronic and Optical Properties of Rare-Earth Doped β-Ga_2O_3 Crystals
4:50 pm	Jonathan McCandless	L10	(Student, Late News) Si-Doping in MBE-Grown Beta-Ga2O3 with Room Temperature Mobility > 125 cm2/Vs
M: Solar Cell Materials and Devices			**Senate Chamber**
1:30 pm	Bora Kim	M01	(Student, Late News) GaAs Laser Power Converters for Cryogenic Applications
1:50 pm	Kevin Ye	M02	(Student) Time-Resolved Photoluminescence Studies of Perovskite Chalcogenides
2:10 pm	Mohammed Alaani	M03	(Student) An Optical Response Analysis of Cadmium Telluride-Based Solar Cell Structures Incorporating High Resistivity Transparent Layers of Magnesium-Zinc Oxide
2:30 pm	Intuon Chatratin	M04	(Student) Group-V Acceptors and Their AX Centers in CdTe
2:50 pm	Marzieh Savadkoohi	M05	(Student) Investigation of Spin-Based Photovoltaic Effect in a Magnetic Tunnel Junction-Based Molecular Spintronic Devices (MTJMSDs)
3:10 pm			BREAK
3:30 pm	Alexander A Milder	M06	(Student) A New Family of Hybrid Thiocyanate-Halide Compounds: A2Cd(SCN)2X2
3:50 pm	Soubantika Palchoudhury	M07	Designing New Sustainable Semiconductor Materials with Cu-Chalcogenide Nanocrystals
4:10 pm	Samba Gaye	M08	(Student, Late News) Solar Cell Effect with Magnetic Metamaterials Produced by Combining Magnetic Tunnel Junction and Magnetic Molecules
DRC Session 11: Heterogeneous Integration			**U.S. Bank Conference Theater**
10:00 am	Mario Lanza	11.1	Hybrid 2D/CMOS Microchips
10:40 am	Marko Radosavljevic	11.2	Large-Scale Heterogeneous Device Integration
11:20 am	Rahul Pendurthi	11.3	Monolithic and Heterogeneous Integration of Atomically Thin Semiconductors for non-von Neumann CMOS
11:40 am		11.4	LATE NEWS
DRC Session 12: Wide Bandgap III - III-N HEMTs			**U.S. Bank Conference Theater**
1:20 pm	Siddharth Rajan	12.1	Ultra-Wide Bandgap Semiconductor Transistors for mm-wave Applications
2:00 pm	Bohao Wu	12.2	Modeling of the Charge-Voltage Characteristics of AlScN/AlN/GaN Heterostructures
2:20 pm	Tuofu Zhama	12.3	Improved On/Off Current Ratio of TiO2/AlGaN/GaN MIS-HEMTs with N2O Surface Treatment on TiO2 Layer
2:40 pm	Eungkyun Kim	12.4	First demonstration of N-polar GaN/AlGaN/AlN HEMT on Single Crystal AlN Substrates

POSTER SESSION

WEDNESDAY PM | PERFORMANCE HALL, 1ST FLOOR

General Viewing

Wednesday
3:10 pm – 3:30 pm

Poster Session
6:00 pm – 8:00 pm

Thursday
10:00 am – 10:20 am
3:10 pm – 3:30 pm

Poster Set-up

Wednesday, 9:30 am – 3:00 pm

Poster Tear Down

Thursday, no later than 5:30 pm

Remaining posters will be discarded.

Poster presenters should be standing with their poster.
Student poster presenters must attend from 6:00 pm to 8:00 pm to present poster and answer questions to be eligible for the Best Student Poster Presentation award.

Presenter	Paper #	Title
Majid Aalizadeh	PS01	(Student) Growth and Characterization of High-Temperature Nitrogen-Polar InAlN Films and HEMTs Using Plasma Assisted Molecular Beam Epitaxy
Elizabeth Favela	PS02	(Student) Ni/Au and Co/Au Schottky Contacts on β-Ga_2O_3 and Effects of Annealing
Farnood Mirkhosravi	PS03	(Student) Comparison of Electrical Behavior in Ga-Polar and N-Polar GaN n-Type Schottky Diodes After Fast and Thermal Neutron Irradiation
Kenneth McAfee	PS04	(Student) Leveraging Thermoelectric Anisotropy in Single Crystal Antimony for Novel Heat Flux Sensing Devices
Ryan Schalip	PS05	Growth of Iron Selenide Thin Films on c-Al_2O_3(0001) via Molecular Beam Epitaxy
Akshay Wali	PS06	(Student) A Machine Learning Attack Resilient True Random Number Generator Based on Stochastic Programmability in Two-Dimensional Transistors
Harish Kumarasubramanian	PS07	(Student) *In situ* Chemical Analysis of Complex Oxide Interfaces via Auger Electron Spectroscopy
Vikrant Kumar	PS08	(Student) Design and Fabrication of ITO Based Transparent and Flexible Electrode Array for Simultaneous 2-Photon Imaging and Electrophysiology
Hayden Brown	PS09	(Student) Impact of Biquadratic Exchange Coupling via Molecule on Magnetic Tunnel Junction Based Molecular Spintronics Devices with Competing Molecule Induced Inter-Electrode Coupling
Andrew Christopher Grizzle	PS10	(Student) Spin Fluctuations in Molecule-Electrode Magnetic Tunnel Junction-Based Spintronics Devices
Andoniaina Mariah Randriambololona	PS11	(Student) A Comparison Between Heisenberg and Biquadratic Exchange Coupling Effects on Magnetic Tunnel Junction Molecular Spintronics Devices (MTJMSDs)
Pranshu Tyagi	PS12	(Student) A Monte Carlo Study of Paramagnetic Nanostructure Coupled with Two Ferromagnetic Electrodes of a Cross-Junction Shaped Spintronics Device At Different Thermal Energies
Katja Sofia Diaz-Granados	PS13	(Student) Influence of Crystallographic Orientation on the Asymmetric Emission of Calcite
Bishnu R Dahal	PS14	Magnetic Anisotropy Effect on the Magnetic Tunnel Junction-Based Molecular Spintronics Devices
Summayya Kouser	PS15	Control of the Color Centers in Diamond Through Surface Encapsulation
Rodneycia Taylor	PS16	(Student) Spatial and Thermal Properties of Magnetic Tunnel Junction Based Molecular Spintronics Device (MTJMSD) Due to Magnetic Anisotropy
Joseph T. Race	PS17	(Student) The Design and Synthesis of Lead-Free Layered Hybrid Perovskites as Room-Temperature Ferroelectrics
Annatoma Arif	PS18	(Student) Characterization of Aqueous Lead Sensing Performance of Bismuth Functionalized 3D Inkjet Printed Electrochemical Electrodes
Arush Guliani	PS19	(Student) Spin Fluctuation Effect on Magnetic Tunnel Junction-Based Molecular Spintronics Devices (MTJMSD)
Yao Li	PS20	(Student) Phase Equilibria in the Metal-Sc-N Systems and Their Relevance for Contacts to ScN, ScGaN and ScAlN
A B M Hamidul Islam	PS21	Effect of Distributed Bragg Reflectors on the Optical Crosstalk in InGaN-Based Flip-Chip Micro-LED Arrays
Terje Gunnar Finstad	PS22	Zinc Multi-Pnictogens Semiconductors—Cu Doping and Thermoelectric Characteristics
Rabin Pokharel	PS23	Epitaxial GaAs/GaAsSb Separate Absorption Multiplication (SAM) Avalanche Nanowire Photodetector
Rebekah De Penning	PS24	(Student) Flexible Electrochemically Reduced Graphene Oxide Sensors for Lead and Cadmium Detection
Ghanshyam Das Varma	PS25	Superconducting Properties of Fe (Te, Se) Thin Film on YSZ Substrate Using Pulsed Laser Deposition (PLD) Technique
Paul Gaurav G. Nalam	PS26	(Student) Phase-Control Enabled Tunable Optical Properties of Nanostructured GeO_2 Wide Band Gap Semiconductor Thin Films
Kendall Deon Dawkins	PS27	(Student) Optimized Light Absorption in GaAsSb(N) Nanowires for Photodetector Application
Tetyana V. Torchynska	PS28	Impact of Double Donor In and Ga Doping on Self-Compensating Process in ZnO Nanocrystal Films
Brahim El Filali	PS29	(Student) Structure, Emission and Resistivity Variation with AL and In Co-Doping of ZnO Films Grown by Spray Pyrolysis
Benjamin L Dutton	PS30	(Student) Growth and Characterization of $(Ba_xCa_{1-x})TiO_3$ Single Crystals in Ir, Pt, and Mo Crucibles
Sang Hoon Lee	PS31	Fabrication of a Roll-to-Roll Printed Cantilever Type Touch Sensing and Actuating Device
M. Jasim Uddin	PS32	Force Spun PVDF-TPU/Au Nanofiber Based TENG for Flexible Energy Harvesting and Bio Mechanical Motion Sensor
Bhoj Gautam	PS33	Effect of Radical on Morphology and Charge Generation in Polymer Non-Fullerene Solar Cells
Jian Liu	PS34	(Student) Micro-Sized Si-Based Anodes Characterization and Optimization Using *in situ* Atomic Force Microscopy

Presenter	Paper #	Title
Adesewa Oluwaseun Maselugbo	PS35	(Student) Magnetic Modification of Boron Nitride Nanotubes for Alignment in Thermal Interface Composite
Andres Vercik	PS36	A Universal Expression for Transport in Nanostructured Materials and Devices
Pius Suh	PS37	(Student) Intra-Molecular Coupling on the Magnetic Properties of Magnetic Tunnel Junction-Based Molecular Spintronics Devices
Sk Md Ali Zaker Shawon	PS38	Modified $ZnSnO_3$ Structure in the Smart Helmet as a Promising Human Motion Sensor
Debabrata Das	PS39	Tunable Optical Response by Anion Engineering in Crystalline Gallium Oxynitride Thin Film
Mahir Abrar	PS40	(Student) A Numerical Study of Perovskite Solar Cells by Bandgap Tuning of Active Materials and Operating Temperature Variances
Mauro Caballero Victorio	PS41	(Student) Towards a High-Modulation Reconfigurable Filter for Photodetectors via an Electrochromic Device
Luis F Hernandez Camas	PS42	Simulation and Modeling of Perovskite Solar Cells for Renewable Energy Application
Mohammed Mohammed Abdullah Al-Ghorbani	PS43	2D Material Based Ag-ZnO-CeO_2 Heterostructure for Solar-Driven CO_2 Reduction
Xavier Mathew	PS44	(Late News) Depth-Dependent Photoluminescence Analysis of the Inhomogeneities in Perovskite Solar Cell
Irina Buyanova	PS45	(Late News) Wurtzite Crystalline Structure Enhances Second-Harmonic Generation in GaAs Nanowires
Rahayana Ruth Bautista	PS46	(Student, Late News) Revealing the Electronic Heterogeneity and Inhomogeneity in Perovskite CsPbBr3 Nanowires Using Contactless Dielectric Force Microscopy
Narges Masoumi	PS47	(Late News) Thickness Dependence of Electronic Properties of GaN Slabs: A Density Functional Study
Nini Rose Mathews	PS48	(Late News) Effects of Ge doping on the properties of Cu2ZnSnS4 thin film solar cells
Narin Sunthornpan	PS49	(Student, Late News) Realizing an atomically flat surface of Ge (111) thin film at low temperature (220°C) by gold-induced layer exchange
Sanjee Lamsal	PS50	(Student, Late News) Aerosol Printed Asymmetric Coupled Stripline (ACS) fed Microstrip Antenna for Biomedical Applications
Wondwosen Fekadu Demisse	PS51	(Student, Late News) Design and development of additively manufacture passive heat sink for electronics cooling
Nabil AlZaqri	PS52	(Late News) Rhodium Nanoparticles Incorporated Mesoporous Silica as an Active Catalyst for Cyclohexene Hydrogenation under Ambient Conditions

Journal of Electronic Materials

A special issue of the *Journal of Electronic Materials (JEM)** will be published with peer-reviewed papers from the 64th Electronic Materials Conference.

- Article submission date is **August, 31, 2022**.
- Contact the 2022 Special Issue Editors listed below.

The *Journal of Electronic Materials* reports monthly on the science and technology of electronic materials, while examining new applications for semiconductors, magnetic alloys, dielectrics, nanoscale materials and photonic materials. The Journal welcomes articles on methods for preparing and evaluating the chemical, physical, electronic and optical properties of these materials. Specific areas of interest are materials for state-of-the-art transistors, nanotechnology, electronic packaging, detectors, emitters, metallization, superconductivity and energy applications. Review papers on current topics enable individuals in the field of electronics to keep abreast of activities in areas peripheral to their own.

Manuscripts for the EMC 2022 collection will be evaluated according to the same high standards as would be applied to any article submitted to the Journal. Authors are encouraged to read carefully and comply with the "Instructions for Authors" on the springer.com/journal/11664. Submission of a manuscript implies that the work described has not been previously published and is not under consideration for publication elsewhere.

2022 Special Issue Editors

Joshua Caldwell
josh.caldwell@vanderbilt.edu

Jennifer Hite
Jennifer.hite@nrl.navy.mil

Nadeem Mahadik
nadeem.mahadik@nrl.navy.mil

Parsian Mohseni
pkmohseni@rit.edu

Jamie Phillips
jphilli@udel.edu

Shadi Shahedipour-Sandvik
sshahedipour-sandvik@sunypoly.edu

Randy Tompkins
randy.p.tompkins.civ@mail.mil

TMS

** A journal of The Minerals, Metals & Materials Society (TMS).*
Editor-in-Chief—Shadi Shahedipour-Sandvik

PROGRAM AT-A-GLANCE

THURSDAY AM

N: 2D Materials Growth and Surfaces			Great Hall Meeting Room 1 & 2
8:20 am	Cooper Augustus Voigt	N01	(Student) Molecular Beam Epitaxy Synthesis of In_2Se_3 Thin-Films on Graphite in the Temperature Range 150°C – 250°C and 500°C – 700°C
8:40 am	Yuan Li	N02	(Student) Molecular Beam Epitaxy Growth of Monolayer Hexagonal Boron Nitride on Nickel Substrates Incorporated with Oxygen Atoms
9:00 am	Nicholas Trainor	N03	Kinetics of Wafer-Scale Epitaxial Growth of MoS_2 on Sapphire
9:20 am	Shanchuan Liang	N04	(Student, Late News) Facile Integration of Giant Exchange Bias in 2D Magnet/Oxide Heterostructures
9:40 am	Wouter Mortelmans	N05	Fast and Easy Optical Imaging and Epitaxial Growth Control of Rotational Domains in SnSe Thin Films
10:00 am			BREAK
10:20 am	Daniel Lewis	N06	(Student) Electron Emission Sources from Quasi-Freestanding Epitaxial Graphene Planar Devices
10:40 am	Subrata Das	N07	(Student) Hot Electron Laser Assisted Cathode Using Electronically Tunable Negative Electron Affinity Silicon Surface
11:00 am	Tony Varghese	N08	Additive Manufacturing of Interface Engineered Colloidal 2D-Crystals for Flexible Thermoelectric Energy Harvesting
11:20 am	William Henry Koll	N09	Scanning Tunneling Microscopy of Monolayer Hexagonal Boron Nitride Monolayer Nanoribbons on Graphene

O: Group III-Nitrides—MOCVD Growth			Great Hall Meeting Room 3
8:20 am	Jack Almeter	O01	(Student) Facet Control by Supersaturation in III-Nitrides
8:40 am	Bingjun Li	O02	Growth Evolution in Non-Planar GaN Selective Area Epitaxy
9:00 am	Yuto Ando	O03	Crack Suppression in High Al-Mole-Fraction AlGaN Beyond the Critical Layer Thickness via Non-Planar Growth Approach on Patterned GaN Platforms
9:20 am	Benjamin McEwen	O04	(Student) Effect of Growth Parameters on Be Incorporation Efficiency in MOCVD GaN:Be
9:40 am	Shashwat Rathkanthiwar	O05	Chemical Potential Control in p-Type N-Polar GaN
10:00 am			BREAK
10:20 am	Wenbo Li	O06	(Student) Characterization of Traps in High-Growth-Rate MOCVD GaN
10:40 am	Bingjun Li	O07	High-Speed MOCVD Growth of GaN Assisted by TBCl
11:00 am	Vineeta R Muthuraj	O08	(Student) High to Ultrahigh Si-Doped GaN Grown by Metalorganic Chemical Vapor Deposition at 550°C for Heterogeneous Integration
11:20 am	Tianhai Wu	O09	(Student) Demonstration of Single Crystal InN and GaN/InN Heterostructures by MOCVD
11:40 am	Tim Mirabito	O10	(Student) Effects of Pre-Metallization on the MOCVD Growth and Properties of Ge-Doped AlGaN on AlN Templates

P: Quantum, Strongly Correlated and Topological Materials			U.S. Bank Conference Theater
8:40 am	Jennifer E DeMell	P01	(Student) Nonlocal Measurement as a Probe of the Spin Hall Effect in Topological Insulators
9:00 am	Denis R Candido	P02	Magnon-Mediated Entanglement of Solid-State Spin Qubit
9:20 am	Ian C Nodurft	P03	Entanglement of Circularly Polarized Light with the Quantum Zeno Effect
9:40 am	Mahnaz Islam	P04	(Student) Visible Light Emission During Electrical Threshold Switching of NbO_2 Mott Switches
10:00 am			BREAK
10:20 am	Patrick Taylor	P05	MBE Growth of Bi_2Se_3 with Reduced Twin Defect Density
10:40 am	Shuyu Cheng	P06	(Student) Epitaxial Growth of Kagome Ferromagnet Fe_3Sn_2 and Sn-Modulated Heterostructures
11:00 am	Logan Riney	P07	(Student) Fermi Level Tuning and Band Alignment in Mn Doped InAs/GaSb
11:20 am	Quoc Dai Ho	P08	(Student) Confinement-Induced Topological Phase Transition in Thin-Film Rare-Earth Pnictides
11:40 am	Dhruv Chimanbhai Desai	P09	(Student) Charge Transport in a Dirac Semimetal, Na_3Bi

Q: Oxide Semiconductor Devices, Defects and Transport			Ohio Staters Inc. Traditions Room
8:20 am	Sarah L Swisher	Q01	Large-Area Photonic Lift-off Process for Flexible Thin-Film Transistors
8:40 am	Dong Hun Lee	Q02	(Student) Facile Processing and Properties of P-Type SnO_x and Oxide-Based p-n Heterojunction Application with n-InGaZnO
9:00 am	Eli Powell	Q03	(Student) Separation of Defect States and Intrinsic Channel Mobility on the Electrical Operation of IGZO TFTs
9:20 am	Kishwar Mashooq	Q04	(Student) Investigation of p-Type SnO Sub-Bandgap Defects by Comparing Experimental Transistor Data to Numerical Device Simulations
9:40 am	Rajashree Bhattacharya	Q05	(Student) Materials Characterization of $LaCoO_3$ Grown by Optimized Reactive DC Magnetron Sputtering and Evaluation of Contact Metal Resistivities by Transmission Line Measurement Technique
10:00 am			BREAK
10:20 am	Kingsley Egbo	Q06	Controlling the p-Type Conductivity of SnO (001) Films by Group-III Doping During Molecular Beam Epitaxy
10:40 am	Jade Cowsky	Q07	(Student) Defects, Doping and Electronic Structure Correlations of Indium Tin Oxide (ITO) Thin Films
11:00 am	Jaesung Jo	Q08	(Student) Study of Hole Scattering Mechanisms in P-Type Cu_2O
11:20 am	Yaoqiao Hu	Q09	(Student) Electron Transport Mechanism and Mobility Prediction in Amorphous In_2O_3 for BEOL Transistors
R: Detectors and Narrow Bandgap Materials			**Senate Chamber**
8:20 am	Mark Wistey	R01	Undoing Band Anticrossing in Highly Mismatched Alloys
8:40 am	Ellie Yilien Wang	R02	(Student) Growth and Characterization of $Al_xIn_{1-x}As_ySb_{1-y}$ Digital Alloys Grown on InP
9:00 am	Jarod Meyer	R03	(Student) Exploring the Impact of Sn Alloying on Structure and Luminescence in PbSnSe Epitaxial Films on GaAs
9:20 am	Rachel Corey White	R04	(Student) Growth of InAsSbBi on InSb Towards Lattice-Matched Longwave-Infrared Optoelectronics
9:40 am	Amberly Ricks	R05	(Student) Growth and Characterization of AlInSbBi for Wide-Bandgap Barriers on InSb
10:00 am			BREAK
10:20 am	Leland Joseph Nordin	R06	Low Growth Temperature Epitaxial PbSe for Heterogeneous Mid-Infrared Emitters
10:40 am	Mariah Lauren Schwartz	R07	(Student) Investigation of Polarity of Unintentionally Doped AlGaAsSb and AlInAsSb Avalanche Photodiodes on InP Substrates
11:00 am	Alexander Timothy Newell	R08	(Student) Majority Carrier Concentration and Minority Carrier Lifetime in Mid-wave Infrared InGaAs/InAsSb and InAs/InAsSb Superlattice nBn Detectors
11:20 am	Abhilasha Kamboj	R09	(Student) Guided-Mode Resonance Enhanced Room-Temperature Infrared Detectors
11:40 am	Yinan Wang	R10	(Student) High-Speed Long-Wave Infrared Ultrathin nBn T2SL Detectors
S: Emerging Epitaxial Materials			**Cartoon Room 1**
8:20 am	Ke Zou	S01	Wafer-Scale Ferromagnetic Fe_3GeTe_2 Thin Films by Molecular Beam Epitaxy
8:40 am	Yuxing Ren	S02	(Student) MBE Growth of $Cr:Bi_xSb_{1-x}Te$ for Enhancing Spin-Orbital-Torque Switching and Stabilizing Quantum Anomalous Hall Effect
9:00 am	Mythili Surendran	S03	(Student) Epitaxial Thin Films of Chalcogenide Perovskites and Related Phases
9:20 am	Yongchen Liu	S04	(Student) High-Quality van der Waals Material on a Semiconductor Substrate
9:40 am	Rafael Jaramillo	S05	Making Chalcogenide Perovskite Semiconductor Thin Films by Gas-Source Molecular Beam Epitaxy
10:00 am			BREAK
T: Epitaxial Growth of Highly Mismatched Alloys			**Cartoon Room 1**
10:20 am	Narges Masoumi	T01	Critical Evaluation of Thermal and Compositional Dependences in a Finite Strain Model of Ge-Si-Sn Alloys on Ge(100) and GeSn Buffer Layers from DFT
10:40 am	Tuhin Dey	T02	(Student) Molecular Beam Epitaxy Growth of Highly Tensile Strained GeSnC Alloys up to 4% Sn and 3% C
11:00 am	Augustus Arbogast	T03	(Student) MBE Growth and Characterization of GeSnC/Ge Multiple Quantum Well Structure
11:20 am	Qian Meng	T04	(Student) Mechanical and Electronic Effect of B on the Band Structure of BGaAs Alloys
11:40 am	Harry Lewis	T05	(Student, Late News) Impact Ionization Coefficients and Excess Noise in $Al_{0.85}Ga_{0.15}As_{0.56}Sb_{0.44}$ Avalanche Photodiodes

PROGRAM AT-A-GLANCE

THURSDAY PM

U: Nano-Magnetic, Magnetic Memory and Spintronic Materials			Great Hall Meeting Room 1 & 2
1:30 pm	Alexander J Bishop	U01	Spin-Polarized Scanning Tunneling Microscopy of Epitaxial Fe_3GeTe_2
1:50 pm	Wenyi Zhou	U02	(Student) Kinetically-Controlled Epitaxial Growth of vdW Fe_3GeTe_2 Ferromagnets and Their Heterostructures with Topological Insulators
2:10 pm	Brad Goff	U03	(Student) Spin Polarized STM Imaging of Magnetic Skyrmions in Metallic Thin-Film Heterostructures
2:30 pm	Shuyu Cheng	U04	(Student) Tuning Magnetic Properties of [Pt/Co/Cu] Multilayers
2:50 pm	Richard Harry	U05	(Student, Late News) Electromagnetic Interference (EMI) Shielding Techniques for Simulated PVDF-TrFE/Fe3O4 Multiferroic Monopolar Antenna
3:10 pm			BREAK
3:30 pm	Marzieh Savadkoohi	U06	(Student) The Effect of Spin Fluctuations on Temporal and Spatial Evolution of Magnetic Moment in A Magnetic Tunnel Junction-Based Molecular Spintronic Device (MTJMSD)
3:50 pm	Eva Mutunga	U07	Design of Experiment Approach for Harnessing Robust Molecular Spintronic Devices
4:10 pm	Igor Lyalin	U08	(Student) Spin–Orbit Torque in Bilayers of Kagome Ferromagnet Fe_3Sn_2 and Pt
4:30 pm	Yueguang Shi	U09	(Student) Magnetic Properties of Doped and Undoped Organic Magnetic Semiconductors—$V(TCNE)_2$, $Cr(TCNE)_2$ and $Nb(TCNE)_2$
4:50 pm	Weimin Chen	U10	(Late News) Generating Room-Temperature Electron Spin Polarization Exceeding 90% in an Opto-Spintronic Semiconductor Nanostructure
V: Group III-Nitrides—Light Emitting Diodes			**Great Hall Meeting Room 3**
1:30 pm	Jeong-Hwan Park	V01	(Student) Enhancing the External Quantum Efficiency of Micro-LEDs via Optimized Dry Etching Condition
1:50 pm	Mohammad Awwad	V02	(Student) Impact of Photon Recycling on Absorption Losses in Tunnel Junction-Based III-Nitride LEDs
2:10 pm	Wentao Cai	V03	(Student) High In-Content InGaN Platelets as Underlayer for Light-Emitting Diodes Toward Long Wavelength Application
2:30 pm	Miad Yarali	V04	(Student) Significant Improvement in Quantum Efficiencies and Wall-Plug Efficiency of Flexible AlGaN-Based Deep-Ultraviolet Light-Emitting Diodes
W: Group III Nitrides—MBE, CVD and Sputtering			**Great Hall Meeting Room 3**
3:30 pm	Keisuke Motoki	W01	(Student) Observation of Compositional Modulation in AlGaN Self-Assembled Superlattices by Transmission Electron Microscopy
3:50 pm	Qihua Zhang	W02	(Student) Molecular Beam Epitaxial Growth of AlGaN Epilayers on Si Using a Nanowire Template
4:10 pm	Mina Moradnia	W03	(Student) Transition-Metal-Alloyed Group-III-Nitride Piezoelectric Thin Films Grown by Hybrid Chemical Vapor Deposition and Sputtering Deposition Techniques
4:30 pm	Morton Greenslit	W04	(Student) Use of a TiN Seed Layer to Enhance (0002) Epitaxy and Piezoelectric Coupling of AlN Thin Films
4:50 pm	Joshua Nordlander	W05	(Student) Sputter Deposition of III-N Thin Films
X: Low-Dimensional Materials and Nanofabrication			**U.S. Bank Conference Theater**
1:30 pm	Ruiqi Hu	X01	(Student) Density Functional Theory Calculations of Rare-Earth Mono-Pnictides Embedded in III-Vs
1:50 pm	Sadhvikas Addamane	X02	Ga(As)Sb Nanostructures Formed by Arsenic-Induced Etching of III-Sb Surfaces
2:10 pm	Takafumi Moriyama	X03	(Student) Structural Analysis of Highly Luminescent and Narrow Bandwidth Cl-Doped InP/ZnSe/ZnS Quantum Dot Heterostructures
2:30 pm	Priyanka Ramaswamy	X04	Study of Al_2O_3 Dielectric on Ga-Assisted MBE Grown $GaAs_{1-x}Sb_x$ Nanowires
2:50 pm	Alireza Abrand	X05	(Student) Tuning Selective Narrowband Infrared Absorption Using Coaxial InAs-$GaAs_{0.1}Sb_{0.9}$ Nanowires with Partial Shell Segment Coverage
3:10 pm			BREAK
3:30 pm	Michael Pedowitz	X06	(Student) Growth and Transformation of Mixed Valence Manganese Oxide Nanostructures on Epitaxial Graphene-Silicon Carbide Heterostructures
3:50 pm	Kyle G Tezanos	X07	(Student) Enhancement of Visible Photoluminescence Through Atomic Layer Deposition Surface Passivation of Porous Silicon Nanowire Arrays Fabricated by Metal-Assisted Chemical Etching
4:10 pm	Benjamin Diroll	X08	Intraband Optical Gain in Colloidal Nanoplates
4:30 pm	Laura Biedermann	X09	Development of Granular Metals for High Voltage Applications
Y: Materials Processing and Integration			**Ohio Staters Inc. Traditions Room**
1:30 pm	Glenn Packard	Y01	(Student) Chromium Segregation in Silicon Thin Films During Wide Area Sub-Millisecond Melting and Recrystallization
1:50 pm	Michael Evan Liao	Y02	(Student) Interfacial Thermal Transport of Thinned and Chemical Mechanical Polished (-201) β-Ga_2O_3 Direct Wafer Bonded to (001) Si
2:10 pm	Martin Gregorio Reyes-Banda	Y03	Ionic Exchange in Perovskite Thin Films Using Solid-State Reactions
2:30 pm	Leunam Fernandez-Izquierdo	Y04	Planar and 3D Microstructured $CsPbBr_3$ Perovskite Devices for Neutron Detection
2:50 pm	Cagri Aydinkarahaliloglu	Y05	(Student) Predicting Premature Failure of Quantum Cascade Lasers Using Supervised Machine Learning
3:10 pm			BREAK

Z: Heterogeneous Integration Technologies			Ohio Staters Inc. Traditions Room
3:30 pm	Chenziyi Mi	Z01	(Student) Heterogeneous Integration of Blue GaN Laser Diode Using Electrochemical Etching
3:50 pm	Sherman Peek	Z02	(Student) Electronic Packaging and Interconnect Technologies for Cryogenic and Superconducting Applications
4:10 pm	Rebecca A Wheeling	Z03	Indium Microbump Interface Evolution with Varying Underbump Metallurgy Stack-Ups
4:30 pm	Yuri Piro	Z04	(Student) UV Curable Ink Composition for Novel Direct Ink Writing Processes
4:50 pm	Bhushan Lohani	Z05	(Student) Additive Microfabrication of System in Package for Heterogenous Integration with Semiconductor Dies

AA: Plasmon and Surface Phonon Polaritons			Senate Chamber
1:30 pm	Angela Cleri	AA01	(Student) Lateral Permittivity Patterning by Ion Irradiation in CdO Thin Films for Mid-IR Plasmonics
1:50 pm	Kurt Eyink	AA02	MBE Growth of Delta Doped Si:InAsSb/GaSb HMM and Their Hyperbolic Response
2:10 pm	Seyedeh Maryam Vaghefi Esfidani	AA03	(Student) Understanding Organ Pipe Resonances in SPhP Trenches for Spectroscopic Sensing
2:30 pm	Ryan Spangler	AA04	(Student) Physical Vapor Transport Growth of α-MoO_3 Sheets for Hypersonic Thermal Transport via Hyperbolic Phonon Polaritons
2:50 pm	Sean McSherry	AA05	(Student) Control of Thermal Transport at Ultrahigh Temperatures by Immiscible Oxide Heterostructures
3:10 am			BREAK
3:30 pm	Aaron J. Muhowski	AA06	Plasmon-Enhanced Distributed Bragg Reflectors
3:50 pm	Morgan Bergthold	AA07	(Student) All-Epitaxial Ultra-Thin Long-Wave Infrared Plasmonic Detectors
4:10 pm	Wilder Acuna	AA08	(Student) ErAs:InGaAlBiAs for 1.55 µm-pumped Terahertz Photoconductive Switches
4:30 pm	Quang To	AA09	Plasmon-Phonon-Intersubband Transition Interactions at THz Frequency in Bi_2Se_3-GaAs Heterostructures
4:50 pm	Saadia Nasir	AA10	(Student) In-Plane Plasmon Coupling in Topological Insulator Bi_2Se_3 Thin Films

BB: Electrochemical Energy Storage and Conversion			Cartoon Room 1
1:30 pm	Soonil Lee	BB01	(Student) High Performance Wafer-Scale Metal-Insulator-Semiconductor Photoanodes for Solar-Driven Water Splitting
1:50 pm	Amjad Hussain	BB02	Highly Robust Solid Oxide Fuel Cells—Prevention of Chemical Inter-Diffusion by Introducing a Buffer Layer
2:10 pm	Song Xu	BB03	PiFM (Photo Induced Force Microscopy) Based Nanoscale IR Spectroscopy and Imaging in Energy Research
2:30 pm	Michael Lee	BB04	(Student) Porous Current Collector Network Materials for High-Loading Li-Ion Battery Cathodes
2:50 pm	Lalith Rao	BB05	(Student) Strategy to Passivate High-Voltage Spinel Cathode-Electrolyte Interfaces (CEI)
3:10 pm			BREAK
3:30 pm	Pablo Rosas Martinez	BB06	(Student) Study of V_2O_5/LiPON Interface Using Depth-Resolved Cathodoluminescence Spectroscopy
3:50 pm	Jun Wei Yap	BB07	(Student) Comparing Performance Enhancement by Different Carbon Additives for Si Anodes in Lithium-Ion Batteries
4:10 pm	Yuxuan Zhang	BB08	(Student) Enabling High-Rate Long-Lifespan Lithium-Sulfur Batteries via Stereolithography Technique and Oxidative Chemical Vapor Deposition
4:30 pm	Zhenghuan Tang	BB09	(Student) Optimization of Li_3BO_3 Interlayer for Garnet-Based All-Solid-State Lithium Metal Batteries
4:50 pm	Edward Gillan	BB10	(Late News) Rapid Thermochemical Solvent-Free Synthesis of Crystalline Metal Borides and Their Investigation as Water Splitting Electrocatalysts
5:10 pm	Yuanyue Liu	BB11	(Late News) Atomistic Simulations of Reaction Kinetics at Electrochemical Interface

FRIDAY AM

CC: Neuromorphic + Late News			Great Hall Meeting Room 1 & 2
8:20 am	Yiyang Li	CC01	Nonvolatile Analog Electrochemical Random Access Memory for In-Memory Computing
8:40 am	Colton Duprey	CC02	(Student, Late News) Effects of Small Molecule Dopants in Piezoresistive Sensing PAAMPSA/PANI/PA Polymer Complex
9:00 am	Fei Qin	CC03	(Student) Influence of Oxygen Vacancy and Top Electrode on Switching Behavior of InGaZnO Based Resistive Random Access Memory
9:20 am	Sanghyeon Choi	CC04	(Student) SiOx Nanorod Memristive Neuron for Probabilistic Inference Applications
9:40 am	Joshua Gabriel	CC05	(Late News) Silicon Carbide Growth Reaction Engineering for Quantum Sensing—Impact of Thermodynamic Model Uncertainty on Product Distributions
10:00 am			BREAK
10:20 am	Akhil Dodda	CC06	(Student) A Low-Power, Bio-inspired, Adaptive Machine Vision Based on Atomically Thin Memtransistors
10:40 am	Dipanjan Sen	CC07	(Student) Spike-Timing Based Adaptive Photo Encoder Considering Monolayer MoS_2 Based Memtransistors
11:00 am	Ragib Ahsan	CC08	(Student) Ultralow-Power Photoactivated Spiking Silicon Neurons
11:20 am	James C Carter	CC09	Atomic Layer Deposition of Antimony(III) Telluride
11:40 am	Wondwosen Demisse	CC10	(Student, Late News) Electrochemical Additive Manufacturing Producing Composite Materials for Electronics
DD: Group III-Nitrides—Contacts and Novel Devices			**Great Hall Meeting Room 3**
8:20 am	Cristyan E Quiñones García	DD01	(Student) Role of Point Defects and Compensation in the Formation of Ohmic Contacts to Mg-Doped GaN
8:40 am	Amit P Shah	DD02	Effect of Rhenium Layer Thickness and Annealing Temperature on the Surface Microstructure of Re-Al-Ni-Au Based Ohmic Contacts on n-Type GaN
9:00 am	Taoufik Slimani Tlemcani	DD03	Development of Low Resistance Ohmic Contacts with Bilayer Ni/Al-Doped ZnO Thin Films to p-Type GaN
9:20 am	Nathaniel O'Neal	DD04	(Student, Late News) HTOL Reliability of Novel Re-GaN Schottky Diodes
9:40 am	Subhajit Mohanty	DD05	(Student, Late News) N-Polar GaN HEMTs with ALD HfO_2 as Gate Dielectric
10:00 am			BREAK
10:20 am	Emma Rocco	DD06	(Student) N-Polar GaN Photocathodes Stabilized with h-BN
10:40 am	Kaitian Zhang	DD07	(Student) Pulsed-Mode MOCVD Growth of $ZnSn(Ga)N_2$ and Determination of the Valence Band Offset with GaN
11:00 am	Elaheh Kheirandish	DD08	Novel Treatment of Raman and Photoluminescence Spectroscopy Analysis for Assessment of Electrical Characteristics of Mg Implanted-Annealed GaN
EE: Flexible, Printed, and Organic Electronic Materials and Devices			**U.S. Bank Conference Theater**
8:20 am	William J Scheideler	EE01	Liquid Metal Printing of High Mobility 2D In_2O_3 for Flexible Electronics
8:40 am	Hyunwoo Choi	EE02	(Student) Surface Morphology Effects of Inkjet-Printed Silver Electrodes on the Contact Resistance of Printed Organic Thin-Film Transistors
9:00 am	Emma J. Renteria	EE03	Semiconductor Nanomembranes for Electromagnetic Interference Shielding Applications
9:20 am	Pushpa Raj Paudel	EE04	(Student) Substrate-Free Organic Electrochemical Transistors Based on Ionic Liquid Crystal Elastomer
9:40 am	Sheida Faraji	EE05	Exploration of New Classes of Solution-Processed High-K Dielectric Materials for Low-Power Electronics
10:00 am			BREAK
10:20 am	Benjamin K. Chang	EE06	(Student) Bandlike and Polaronic Charge Transport in Organic Crystals from First-Principles
10:40 am	Song Xu	EE07	PiFM—Nanoscale Chemical Mapping and Spectroscopy via AFM-IR for Ultrathin Organic Films
11:00 am	Tyler James Wiegand	EE08	(Student) Assessing the Contribution to OPV Efficiency of Energy Transfer in Charge Transfer Coupled H-Aggregates
11:20 am	Buang Zhang	EE09	(Student) Impact of Surfactant Choice on Polymer Emulsions, Thin-Film Morphology and LED Performance
11:40 am	Lucas Beagle	EE10	(Late News) Microwave-Facilitated Few-Layer COF/Monolayer TMD Heterostructures

FF: Gallium Oxide—Material Processing, Characterization and Defects			Ohio Staters Inc. Traditions Room
8:20 am	Sushovan Dhara	FF01	(Student) High Breakdown Field Strength in Molecular Beam Epitaxy-Grown Al_2O_3/β-Ga_2O_3 Structures
8:40 am	Ming-Hsun Lee	FF02	Ion Implantation Doping for β-$Al_xGa_{2-x}O_3$ and the Application for Ohmic Contact Formation
9:00 am	Joseph Spencer	FF03	(Student) Activation of Si, Sn, and Ge Donors in High-Resistivity Halide Vapor Phase Epitaxial β-Ga_2O_3:N
9:20 am	Hemant Jagannath Ghadi	FF04	Formation of Deep Acceptors by Nitrogen Implantation in HVPE Grown β-Ga_2O_3
9:40 am	Michael Evan Liao	FF05	(Student) Chemical Mechanical Polishing of (010) β-Ga_2O_3 Substrates
10:00 am			BREAK
10:20 am	Giulia Carini	FF06	(Student) Observation of Hyperbolic Shear Polaritons in Monoclinic Crystals
10:40 am	Alan G Jacobs	FF07	High Temperature Annealing Effects and Defect Populations of β-Ga_2O_3
11:00 am	Jacqueline Cooke	FF08	(Student) Effect of Extended Defects on Photoluminescence of Gallium Oxide and Aluminum Gallium Oxide Epitaxial Films
11:20 am	Daram N Ramdin	FF09	(Student) Ultrafast Laser Induced Deep Level Defects and Correlations with Crystallinity in β-Ga_2O_3
11:40 am	Cassandra Remple	FF10	(Student) Photoluminescence Spectroscopy of Cr^{3+} in β-Ga_2O_3 and $(Al_{0.1}Ga_{0.9})_2O_3$

GG: Epitaxial Growth on Patterned Substrates			Cartoon Room 1
8:20 am	Alec Mason Skipper	GG01	(Student) Selective Area Epitaxy by MBE for Self-Aligned III-V Devices
8:40 am	Subhashree Seth	GG02	(Student) Molecular Beam Epitaxy for Photonic Crystal Surface Emitting Lasers (PCSELs)
9:00 am	Jun Tao	GG03	(Student) Orientation-Aligned InP on Si by Templated Liquid Phase Growth
9:20 am	Ashlee Garcia	GG04	(Student) Molecular Beam Epitaxy Selective Area Regrowth of High Aspect Ratio Microstructures
9:40 am	Yiteng Wang	GG05	(Student) Monolithic Integration of III-Vs with Silicon Nitride Integrated Photonics by MBE
10:00 am			BREAK

HH: Lattice Mismatched Epitaxial Growth			Cartoon Room 1
10:20 am	Mijung Kim	HH01	(Student) Growth of GaP on Silicon-on-Insulator
10:40 am	Hyun Uk Chae	HH02	(Student) Monolithic III-V Growth Directly on Metal for Device Application
11:00 am	Trent Garrett	HH03	(Student) Integrating GaSb-Based Infrared Detectors with Si Substrates via Interfacial Misfit Arrays
11:20 am	Madison D Drake	HH04	(Student) Heteroepitaxy of GaSb on GaAs (111)A Substrates for Electron Transport Studies
11:40 am	Fatih Furkan Ince	HH05	(Student) High Mobility n and p Pseudomorphic Channels Grown on Interfacial Misfit Dislocation Assisted Growth on GaSb/GaAs

EXHIBITOR PROFILES

PERFORMANCE HALL

Wednesday	Thursday
9:00 am – 12:00 pm	9:00 am – 12:00 pm
1:30 pm – 4:00 pm	1:30 pm – 4:00 pm
6:00 pm – 8:00 pm	

Gatan EDAX
www.gatan.com
www.edax.com

Gatan is the world's leading manufacturer of instrumentation and software used to enhance and extend the operation and performance of electron microscopes. EDAX is a leading provider of innovative materials characterization systems encompassing Energy Dispersive Spectroscopy, Wavelength Dispersive Spectrometry, Electron Backscatter Diffraction, and X-ray Fluorescence. Gatan and EDAX are members of AMETEK's Materials Analysis business unit.

Klar Scientific, Inc.
www.klarscientific.com

Key Products: Point-and-shoot confocal spectroscopic microscopes; scanning, autofocus microscopes for mapping photoluminescence and Raman emissions; wavelength kits for 266nm through 975nm illumination; test and measurement services

Klar Scientific develops compact, affordable instruments designed for scientists who need spectral information with high spatial resolution. Klar microscopes provide photoluminescence (PL) and Raman mapping for excitation wavelengths from the deep-UV to near-IR. Klar also offers measurement services to provide clients with spectral maps of their samples.

Lake Shore Cryotronics
www.lakeshore.com

Key Products: source measurement systems; cryogenic probe stations; hall effect measurement systems & instruments; modular characteristic systems; electromagnets; superconducting magnet systems; AC/DC current & voltage sources

A leading innovator of solutions for electronic material research, Lake Shore Cryotronics offers modular multichannel lock-in measurement systems for highly synchronized DC, 100 kHz AC and mixed DC + AC sourcing and measuring; cryogenic probe stations; systems and instruments for fast, highly precise Hall measurements; and modular characterization systems for electronic/electro-transport measurements.

Nextron Corporation
www.microprobesystem.com

Key Products: Micro Probe System; Micro Optical Chamber; Humidity Control System; MFC Gas Control Stage; Pressure Control System; External XYZ Micropositioner.

Nextron has developed researcher-centered equipment, which is highly valuable. Micro Probe System is suitable to measure and analyze the electrical and optical properties of the materials under various environmental conditions; temperature, vacuum, humidity, gas flow, and irradiation of light.

United Mineral and Chemical Corp.
www.umccorp.com

Key Products: MBE Source Materials; MBE Equipment; Dopants; PLD systems

United Mineral and Chemical Corporation is a leading supplier of ultra high purity, MBE grade ingots and metal sources including Arsenic, Red Phosphorus, Indium, Gallium, Aluminum, Antimony, Magnesium, Selenium, Silicon and Tellurium. Compounds of III-V materials are offered as well. UMC also represents Dr. Eberl MBE-Komponenten for MBE effusion cells, crackers, doping and sublimation sources as well as ancillary equipment and components. In additional, UMC also represents TSST for PLD systems and components used for thin film research.

Vacuum One (Veeco, Edwards, and MDC)
www.vacuumone.com

Key Products: MBE Equipment and Sources; Vacuum Pumps and Gauges; Vacuum Components; Cryostats

Renishaw is a recognized leader in Raman spectroscopy, producing high performance Raman systems for a range of applications. We have decades of experience developing flexible Raman systems that give reliable results, even for the most challenging measurements. Whatever your Raman analysis requirements, Renishaw's teams of scientists and engineers are here to provide you with expert advice, as well as product, technical, and applications support.

Wafer Technology
www.wafertech.co.uk

Key Products: III-V Materials; GaAs; InAs; GaSb; InSb; InP; Polycrystal

Wafer Technology Ltd. is a U.K.-based producer of III-V materials and epitaxy-ready substrates, offering the widest product range in Europe. Wafer Technology's unrivalled choice of material types and forms enables it to support almost any customer application.

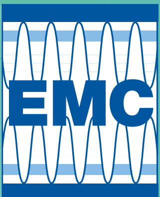

64TH ELECTRONIC MATERIALS CONFERENCE

June 29-July 1, 2022 // The Ohio State University // Columbus, Ohio

WEDNESDAY ORAL PRESENTATIONS

64th Electronic Materials Conference

* Plenary

EMC Awards Ceremony and Plenary Session

Session Chairs: Lisa Porter and Daniel Wasserman
Wednesday Morning, June 29, 2022
Archie M. Griffin West Ballroom

8:20 AM EMC Awards Ceremony

8:30 AM *PL01
New Materials for Three-Dimensional Ferroelectric Microelectronics Susan Trolier-McKinstry; The Pennsylvania State University, United States

In the last decade, there have been major changes in the families of ferroelectric materials available for integration with CMOS electronics. These new materials, including $Hf_{1-x}Zr_xO_2$, $Al_{1-x}Sc_xN$, $Al_{1-x}B_xN$ and $Zn_{1-x}Mg_xO$, offer the possibility of new functionalities. This talk will discuss the possibility of exploiting the 3rd dimension in microelectronics for functions beyond interconnects, enabling 3D ***non-von Neumann*** *computer architectures exploiting ferroelectrics for local memory, logic in memory, digital/analog computation, and neuromorphic functionality*. This approach circumvents the end of Moore's law in 2D scaling, while simultaneously overcoming the "von Neumann bottleneck" in moving instructions and data between separate logic and memory circuits. Computing accounts for 5 – 15% of worldwide energy consumption. In the U.S., data centers alone are projected to consume approximately 73 billion kWh in 2020. While recent efficiency gains in hardware have partially mitigated the rising energy consumption of computing, major gains are achievable in a paradigm shift to 3D computing systems, especially those that closely couple memory and logic. The talk will cover the relevant materials, their deposition conditions, and what is known about the wake-up, fatigue, and retention processes.

9:20 AM Refreshment Break

SESSION A: Group III-Nitrides—Power Diodes

Session Chairs: Theeradetch Detchprohm and Russell Dupuis
Wednesday Morning, June 29, 2022
Great Hall Meeting Room 3

10:00 AM A01
Correlated Nanoscale Imaging of Doping, Conductivity and Cathodoluminence in GaN p-n Junctions Prepared by Selected Area Regrowth Alexander Chang[1], Bingjun Li[2], Sizhen Wang[2], Sam Frisone[3], Rachel S. Goldman[3], Jung Hahn[2] and Lincoln Lauhon[1]; [1]Northwestern University, United States; [2]Yale University, United States; [3]University of Michigan, United States

GaN is an excellent platform for high-power high-frequency electronics due to its intrinsic properties, but device geometry plays crucial role in optimizing performance metrics tailored to specific applications. High theoretical breakdown voltages in power diodes have been predicted for non-planar junction geometries that can be fabricated using selected area regrowth. At present, the main challenge to achieving expected performance limits is the quality of the regrowth interface, which is a significant source of current leakage in regrown diodes. Prior studies have shown that unintentional donors, defects, and Mg depletion in the p-n junction each contribute to non-ideal behaviors of regrown p-n diodes, particularly excessive leakage current. However, a complete understanding of their relative impacts in distinct regions within the junction cannot be achieved without correlated, spatially-resolved analysis of composition and properties.

We report correlated nanoscale-resolution imaging of doping and conductivity in Mg-doped p-GaN regrowth that reveals how position-dependent non-idealities of the non-planar regrowth interface impact local electronic properties and ultimately the performance of devices. p-GaN was selectively regrown in n-GaN trenches formed by inductively coupled plasma etching with SiO_2 masks of variable mask-to-trench-width ratio. Atom probe tomography (APT) was used to analyze intentional and unintentional impurity distributions as a function of growth time and location by reconstructing the evolving shape of the growth surface with Al marker layers, and cross-sectional scanning spreading resistance microscopy (SSRM) was used to generate a two-dimensional map of conductance with nanometer resolution. Cathodoluminesence (CL) mapping and spectroscopy provide further insights into the nature of Mg donors and the distribution of unintentional dopants. Uniquely, our marker-layer approach enables the direct comparison of the laterally and vertically grown regions of non-planar junctions at a given point in time. In the lateral junctions that form at the edges of the c-plane trenches, reduced Mg doping and unintentional oxygen doping create a compensation region that further broadens the junction and may contribute to increased tunneling current under reverse bias. The spatial and temporal dependence of the oxygen concentration revealed by APT point to the SiO_2 mask as the source of the unintentional doping, confirming that alternative mask materials or maskless approaches are needed. We also conclude that residual sub-surface etching damage below the regrowth interface induces both n-type and p-type conductivity through carrier tunneling, broadening the p-n junction and establishing leakage pathways at the regrowth interface. The unprecedented integration of spatially resolved mapping of dopants, impurities, conductivity, and carrier type is a powerful approach to discriminating distinct factors that limit the performance of regrown diodes, enabling the rational optimization of process and device design.

10:20 AM A02
1.3 kV Vertical GaN p-i-n Rectifier with Nitrogen-Implanted Field Guard Ring Edge Termination Minkyu Cho, Marzieh Bakhtiary-Noodeh, Zhiyu Xu, Theeradetch Detchprohm, Russell Dupuis and Shyh-Chiang Shen; Georgia Institute of Technology, United States

Vertical GaN p-i-n diodes with 1.3 kV breakdown voltage are presented. An AIXTRON 6 x 2" closely-coupled showerhead (CCS) metalorganic chemical vapor deposition (MOCVD) reactor was used for the epitaxial growth. The epitaxial structure was grown on a bulk GaN substrate with a low-dislocation density < 10^6 cm^{-2}. The growth structure consists of 0.5 µm of n-GaN:Si ([n] = 6×10^{18} cm^{-3}), 8.5 µm of GaN:uid drift layer, 0.45 µm of p-GaN:Mg ([p] = $1\times10^{18}cm^{-3}$), and 20 nm of p+-GaN:Mg ([Mg] = $1\times10^{18}cm^{-3}$). Floating guard ring (FGR) structures were implemented in the study to prevent premature device breakdown under reverse bias. Both FGR widths and gaps were designed based on TCAD simulation to achieve a smooth potential profile on the device surface. The device fabrication was started with three-step ion implantations with nitrogen species for the electrical device isolation as well as the FGR formation. After the ion implantations, Ni/Ag/Ni/Au metal stacks were formed for the p-GaN ohmic contact. After the p-ohmic contact metal formation, Ti/Al/Ti/Au metal stacks were deposited at the backside for the n-GaN ohmic contact. To evaluate the free carrier concentration in the drift layer, capacitance-voltage measurement was performed with the cathode voltage sweep from 0 to -40 V. The calculated free carrier concentration profile in the drift layer was plotted

along the perpendicular direction to the device surface, and the depth was defined as a relative position from the p-n interface in the drift layer. The free carrier concentration in the drift layer increased as the position was located away from the p-n interface varying from 6×10^{15} cm^{-3} at 0.78 µm to 9×10^{15} cm^{3} at 2.46 µm. The forward bias I-V characteristics showed a 3.3 V turn-on voltage at 100 A/cm^2 and a specific-on resistance of 0.25 mΩ cm^2 . The minimum ideality factor was 1.24 at 2.74 V. The breakdown voltage is 1360 V as evaluated at the reverse current density of 0.01 A/cm^2. The Baliga Figure of Merit (BFOM) of the device is 7.4 GW/cm^2. More detailed statistical breakdown voltage distribution of the devices and analysis will be presented at the conference.

10:40 AM A03

1.6 kV Etched-and-Regrown GaN pn-Diodes Realized by Mitigation of Plasma Etch-Enhanced Deep Level Defects

Andrew M. Armstrong, Andrew Allerman, Mary H. Crawford, Greg Pickrell, Vincent Abate, Caleb Glaser and Trevor Smith; Sandia National Laboratories, United States

GaN offers increased power density for power electronics due to its larger band gap energy compared to Si. However, difficulties in selective area doping limit the development of GaN vertical power devices. Ion implantation of Mg to form selective regions of p-type GaN has been demonstrated, but kV operation with low leakage remains elusive. Selective-area epitaxy can also form p-regions in n-GaN by using inductively coupled plasma (ICP) etching followed by p-GaN regrowth, but etch-induced defects cause severe leakage.

Here, we show that ICP etching increases reverse leakage by increasing the concentration of a deep level defect, however, a slow reactive ion etching (RIE) following ICP etch can achieve low leakage and high voltage performance for etched-and regrown GaN diodes by removing ICP-enhanced defects. Steady-state photocapacitance (SSPC) measured an increased concentration of a defect state with an energy level at 1.9 eV below the conduction band for ICP etched-and-regrown pn-diodes compared to continuously-grown diodes. Increased defectivity correlated with increased reverse leakage. When the ICP etch was followed by the RIE etch, both the concentration of the 1.9 eV deep level and the reverse leakage in etched-and-regrown diodes were reduced to levels observed for continuously-grown diodes. Upon demonstrating improved performance with the RIE treatment, we fabricated etched-and-regrown diodes with a multi-step junction termination extension (JTE) to demonstrate high breakdown voltage (1610 V), excellent forward characteristics (ideality factor ~ 1.5), and low specific on-resistance (1.1 mohm.cm^2)

GaN pn-diodes were grown by metal-organic chemical vapor deposition on free-standing n-GaN. The n-GaN drift region was 10 microns thick with a net donor density 3×10^{16} cm^{-3}. Following n-GaN growth, the surface was etched using $Cl_2/BCl_3/Ar$ ICP. For one sample, termed ICP, a 0.4 micron thick p-GaN epilayer with a Mg concentration of 3×10^{19} cm^{-3} was regrown without any post-ICP treatment. Another sample, termed ICP+RIE+KOH, had nominally the same n-GaN drift growth, ICP etch, and p-GaN regrowth conditions, except that a slow RIE etch and subsequent KOH surface treatment was applied prior to p-GaN regrowth. The RIE etch depth was 270 nm using 45 sccm CF_4 + 5 sccm O_2 with 25 W RF power, resulting in a 0.3 Å/s etch rate. The surface was then treated with KOH at 80 °C for 10 minutes. A continuously-grown pn-diode, termed CT, was also grown as a control sample. Mesa diodes were studied using SSPC to correlate ICP-enhanced deep level defects and increased reverse leakage. An ICP etch was used to form a mesa extending into the n-GaN drift with Pd/Au p-contacts on the p-GaN and a Ti/Al n-contact on the wafer backside. Comparing the SSPC deep level spectra of the CT and ICP diodes revealed a >20x increase in concentration of the 1.9 eV deep level for the former. The reverse leakage for the ICP diode at 500 V also increased >100x vs. CT. We attribute the increase in reverse leakage with ICP etch to recombination-generation current mediated by the ICP-enhanced 1.9 eV deep level. For the ICP+RIE sample, the 1.9 eV deep level concentration was 20x lower than for ICP, i.e., it recovered to the level in the as-grown CT sample. Further, the reverse leakage at 500 V for the ICP+RIE device was almost the same as the CT device. We conclude that the ICP-enhanced 1.9 eV deep level is the primary contributor to increased reverse leakage in etched-and-regrown GaN pn-diodes, and this deep level can be mitigated by post-ICP etch by RIE to recover epilayer quality and reverse leakage equivalent to that of continuously-grown diodes.

Finally, a multi-step JTE was included for another ICP+RIE sample, termed ICP+RIE(JTE), to maximize electrical performance, yielding the forward and reverse characteristics reported above.

SNL is managed and operated by NTESS under DOE NNSA contract DE-NA0003525.

11:00 AM A04

(Student) Design, Manufacturability and Optimization of Hybrid Guard Ring-JTE Edge Terminations via Nitrogen Implantation in Epitaxial GaN PN Power Diodes Matthew A. Porter[1], Mona Ebrish[2], Alan G. Jacobs[2], James C. Gallagher[2], Karl Hobart[2] and Travis Anderson[2]; [1]Naval Postgraduate School, United States; [2]U.S. Naval Research Laboratory, United States

Recent advances in bulk GaN substrate growth have enabled the wafer-scale fabrication of high current, high voltage vertical power devices with performance competitive with similar devices fabricated from SiC. However, significant work remains on optimization of vertical GaN power devices, specifically in the design and implementation of edge terminations which enable high voltage operation. As it is difficult to implement successfully activated p-type implants in GaN, vertical GaN power devices are typically fabricated after epitaxial growth of junctions. Wafer-level variations in doping and junction characteristics have been observed via long range optical techniques, which can greatly impact the performance and design of edge terminations. This work examines the design, manufacturability and optimization, using parametric TCAD simulation, of a novel hybrid bilayer junction termination extension with guard ring extensions, henceforth termed the hybrid GR-JTE in a 1.2 kV GaN PN power diode design. The termination structure is formed via nitrogen implantation into the edge region of the junction. An exploration into the manufacturability of the hybrid GR-JTE was carried out with a focus upon the sensitivity of the breakdown voltage of the device as a function of the effective JTE dose remaining after nitrogen implant through variation of the effective anode thickness with a fixed doping of 1×10^{18} cm^{-3}. Realistic implant damage profiles were derived from SRIM simulations of nitrogen implantation into GaN and modelled in TCAD as mid-gap states. A similar study of dose variation was also carried out through variation of anode doping at a fixed anode thickness of 500 nm. As a basis for comparison, both studies were repeated with a single implant bilayer JTE design. It was found that the hybrid GR-JTE decreased the sensitivity of the breakdown voltage to dose variation by 24% at a 1000 V threshold in comparison to the bilayer JTE design, using an experimental maskset as a basis for guard ring placement. The addition of guard-ring extensions to the JTE structure specifically decreases the dose sensitivity of the edge termination when the dose falls below the optimum for the JTE structure, due to the excess charge available within the guard ring structures. Further study of the influence of interface charge at the device surface demonstrates that breakdown voltage sensitivity is reduced in the hybrid GR-JTE structure due to screening effects of depletion at the top of guard ring structures. A comparison between experimental data on fabricated devices with either bilayer JTE or hybrid GR-JTE terminations is carried out to compare the predicted yield variation between the two designs. Additionally, a study of the optimization of the placement of

guard-ring extensions in the hybrid GR-JTE is examined, exploring the number of guard rings and guard ring spacing distribution (linear and parabolic) as optimization variables at fixed JTE dose. These results demonstrate an edge termination design with increased tolerance for wafer-scale variance of epitaxial layer characteristics.

11:20 AM A05

(Student) AlN Homojunction PN Diodes—The Highest Bandgap Semiconductor Diodes Ever Demonstrated

Christopher M. Matthews, Habib Ahmad, Zachary Engel, Keisuke Motoki, Sangho Lee and W. Alan Doolittle; Georgia Institute of Technology, United States

At 6.1 eV, aluminum nitride (AlN) boasts one of the widest known band gaps, which gives this material the unique potential to address needs in the fields of deep ultraviolet optoelectronics, high performance power conversion devices, radio frequency devices, and extreme environment semiconductor devices. Compared to other commonly used semiconductors (i.e., Si, SiC, GaN, and β-Ga_2O_3), AlN has the highest critical electric field and theoretical breakdown voltage, which lead to the highest Baliga's and Johnson's figures-of-merit (BFOM & JFOM). AlN also has the second highest saturation velocity and thermal conductivity. However, AlN is an insulator and has shown little promise to be converted to a semiconductor via doping during the long history of its study. Prior to this work, the main obstacle preventing the realization of many of AlN's potential applications was the difficulty doping this material. N-type AlN has been reported in near surface regions and with bulk electron concentrations up to 10^{15} cm^{-3}, and p-type conductivity of AlN has been a major challenge with the only success being reports of surface conductivity via carbon doping, but no substantial bulk experimental conductivity had been demonstrated[1].

Using new dopant elements and crystal synthesis methods that produce fewer compensating impurities and reduce metastable defect reconfiguration, we have demonstrated: 1) substantial bulk p-type AlN (p=3.1×10^{18} cm^{-3}), 2) the highest ever reported bulk Si-doped n-type AlN (n=6×10^{18} cm^{-3}, a nearly 6000 times improvement over previous state-of-the-art), and 3) the first AlN homojunction PN diode, with a nearly ideal turn-on voltage of ~6 V.

Recently, we achieved Be-doped p-type AlN films with bulk hole concentrations up to 3.1×10^{18} cm^{-3} via the improved growth kinetics of metal modulated epitaxy (MME) demonstrating high quality films at low substrate temperatures, replicating our successes with p-type doping of GaN[2]. Be is better suited for AlN due to the similar size of Al and Be and thus, reduced strain when substituting on a cation site. MME utilizes low substrate temperatures during growth to lower contamination normally resulting from outgassing of structural components in the growth chamber and controls the surface chemistry and kinetics to facilitate proper incorporation of the dopants on the cation site. Additionally, we have demonstrated Si-doped n-type AlN films with bulk electron concentrations up to 6×10^{18} cm^{-3}, completing the set of essential components needed for homojunction AlN diodes. Presently, low temperatures are believed to play a vital role in Si doping in that it may inhibit the formation of the Si-DX center, and similarly to the p-type case, the use of MME uniquely enables the realization of these highly doped n-type films with reduced compensation of Si.

Highly crystalline material is a pre-requisite for the growth of semiconducting AlN films and devices, but the well-known formation of surface oxides on AlN can result in a dense layer of stacking faults that create dislocations at the growth interface. We additionally report an eradication of these stacking faults by Al-assisted surface cleaning[3], which should further improve the electrical characteristics of the AlN films and devices. While excellent ohmic contacts have been developed to as-grown films, early PN diodes show high sheet resistance due to contact to plasma etched surfaces. Nevertheless, the PN diodes show ~6 decades of rectification and turn on voltages of ~6V as expected for a 6.1 eV semiconductor. The potential role of interface defects will also be detailed.

References

[1] K. Kishimoto, M. Funato, and Y. Kawakami, *Appl. Phys. Exp.* **13**, 015512 (2020).
[2] H. Ahmad, J. Lindemuth, Z. Engel, C.M. Matthews, T.M. McCrone, and W.A. Doolittle, *Adv. Mater.* **33**, 2104497 (2021).
[3] Y.J. Cho, C.S. Chang, K. Lee, M. Gong, K. Nomoto, M. Toita, L.J. Showalter, D.A. Muller, D. Jena, and H.G. Xing, *Appl. Phys. Lett.* **116**, 172106 (2020).

11:40 AM A06

(Student) Defect Microstructural and Diffusion Studies of Implant-Gyrotron Microwave Annealed GaN:Mg—Effect of Sequential High- and Moderate-Temperature Annealing

Vincent E. Meyers[1], Emma Rocco[1], Benjamin McEwen[1], Mike Shevelev[2], Vlad Sklyar[2] and Fatemeh (Shadi) Shahedipour-Sandvik[1]; [1]State University of New York Polytechnic Institute, United States; [2]Gyrotron Technology, Inc., United States

The material properties of the (Al)GaN system, including its high breakdown electric field and high electron mobility, make it a powerful candidate for next-generation high-power and high-frequency electronic devices. The success of this technology is dependent on the ability to form selective-area p-type regions, which ideally may be accomplished by a combination of straightforward, low-cost ion implantation with the prevailing p-type dopant, Mg, and post-implant annealing. Ion implantation induces lattice damage and creates point defects, including V_N and Mg_i, which require high temperatures (1300–1500 °C) to remove or agglomerate into clusters [1]. However, GaN is unstable at these temperatures under near-atmospheric N_2 overpressure [2]. Co-implantation with N can enhance p-type activity by providing a source of implant-region N_i to migrate to V_N sites during the annealing process [3]. To meet the conditions of activation while suppressing defects and restoring bulk crystalline quality, annealing must be performed with either heating on a timescale shorter than that of degradation onset [4] or at ultra-high N_2 overpressure [5]. Obtaining reliable, spatially uniform, high-conductivity p-type material, and activation of Mg-implanted material remains an area of active research.

In this study, we report on the micro-structural changes and diffusion behavior in the implanted region of Mg/N-implanted GaN material after activation-annealing by pulsed gyrotron microwave. MOCVD-grown unintentionally doped (UID) GaN is grown on n^+-HVPE GaN, co-implanted with Mg/N to a depth of 250 nm, capped with AlN, and annealed using a gyrotron under an N_2 overpressure of 3 MPa. Annealing is performed by gyrotron in pulses of 8 sec duration at 1450 °C, either with or without a conventional pre-anneal at 1000 °C for 30 min. Detailed transmission electron microscopy (TEM) studies show that high-temperature annealing under these conditions induce creation of circular defects within the implanted region, comparable to those frequently observed in *in-situ* doped GaN:Mg where [Mg]~10^{19} cm^{-3}. Moreover, a region of AlGaON few-monolayers thick is also observed at the AlN/GaN interface after annealing, indicating that enhanced etching techniques must be developed to remove protective AlN caps after ultra-high temperature annealing. Implanted-annealed dopant profile, as measured by secondary ion mass spectrometry (SIMS), show that the in-diffusion of Mg in material gyrotron annealed with a lower-temperature pre-anneal (D=7.5×10^{-13} cm^2/s) is moderate compared to material annealed by gyrotron only (D=3.5×10^{-12} cm^2/s). This may suggest that a suppression of the Mg_i migration energy occurs with removal of implant-induced point defects during the low temperature thermal pre-anneal, leading to a reduction in the ultra-high-temperature diffusion coefficient during gyrotron annealing.

This work was funded by the Advanced Research Projects

Agency-Energy (ARPA-E), U.S. Department of Energy under the PNDIODES programs directed by Dr. Isik Kizilyalli.
[1] Y. Wang, *et al., physica status solidi (b),* **257(4),** 1900705 (2020)
[2] G. Alfieri, *et al. J. Appl. Phys.*, **123**, 205303 (2018)
[3] R. Tanaka *et al. Japan. J. Appl. Phys.*, **59**, SGGD02 (2020)
[4] J. D. Greenlee, *et al,* ECS J. Solid State Sci Technol., **4(9)** (2015)
[5] Sierakowski, K., *et al., Electronics*, **9(9),** 1380 (2020)
[6] Meyers, V., *et al. J. Appl. Phys.,* **130(8),** 085704 (2021)

SESSION B: Silicon Carbide—Devices and Reliability

Session Chairs: Daniel Ewing and Nadeemullah Mahadik
Wednesday Morning, June 29, 2022
Archie M. Griffin West Ballroom

10:00 AM B01
(Student, Late News) Structural and Optical Characterization of Trapezoidal Defects in 4H-SiC Epilayers and Their Effect on MOSFETs Reliability Sami A. El Hageali[1,2], Harvey Guthrey[2], Steven Johnston[2], Andrew Norman[2], Jake Soto[3], Bruce Odekirk[3], Robert E. Stahlbush[4], Nadeemullah Mahadik[4], Mowafak Al-Jassim[2] and Brian Gorman[1]; [1]Colorado School of Mines, United States; [2]National Renewable Energy Laboratory, United States; [3]Microchip Technology Inc., United States; [4]U.S. Naval Research Laboratory, United States

Presently, 4H-SiC is generally preferred in practical power device manufacturing and the market is expanding rapidly. SiC devices, such as Schottky diodes and FET/MOSFET transistors, include converters, inverters, power supplies, battery chargers and motor control systems for 5G infrastructures, EV/HEVs, renewable energy generation and data centers. The SiC market is rapidly expanding and will soon occupy a large percentage of power microelectronics in the world with a high penetration rate serving as direct replacements for Si-based MOSFETs and IGBTs.

Even though single-crystal 4H-SiC wafers of 8 inches in diameter are now being commercialized, a variety of issues make SiC difficult to mass produce in a consistent way. The progress in SiC device development relies on epitaxial growth technology on SiC substrates. Indeed, material defects in SiC are the root cause of many technological challenges faced by SiC manufacturers. Defects such as stacking faults, basal plane dislocations and threading dislocations in SiC epilayers as well as substrates can affect the performance and reliability of SiC devices and have extensively been investigated in the past. However, trapezoidal defects were reported but have not been fully understood.

In this study, trapezoidal defects in 4H-SiC epitaxial layers were investigated by photoluminescence (PL) imaging, cathodoluminescence spectrum imaging (CLSI), electron beam induced current (EBIC) imaging and by transmission electron microscopy (TEM) observation. The bar-shaped stacking faults were identified by the PL and CL measurements with peak emission wavelengths of ~420 nm and ~450 nm (Figs. 1, 2). The nature of the stacking faults is discussed using the luminescence results combined with movies showing expanding dislocations via the recombination enhanced dislocation glide mechanism. The expanding dislocations show that these towers of defects are made of a combination of Shockley-type and Frank-type stacking faults. The TEM analysis combined with movies of expanding stacking faults showed that trapezoidal defects come from the substrate and are present on multiple basal layers. The origin of this defect in the substrate is speculated based on our results and previous reports. The stacking sequences of some of the faults was determined as (...2, 3, 2, 3...) and (...2, 3 ,2...) in the Zhdanov's notation by high-resolution TEM (Fig. 3). EBIC imaging (Fig. 3) showed that the high density of SFs in these towers act as strong sites of carrier recombination which is likely to have an impact on the on-state transfer characteristics of SiC devices. Furthermore, device electrical measurements have shown that this type of defect impacts the electrical performance of MOSFETs via an increase in the on-state resistance and a reduction of the breakdown voltage depending on the coverage percentage of the tower of defects in the active area of the device.

This study uses a multi-scale luminescence characterization approach coupled to a structural and electrical analysis to provide a detailed understanding of the optoelectronic properties, structural nature of this defect, and its adverse impact on 4H-SiC MOSFETs. The complete understanding of this defect is necessary to develop mitigation strategies and fulfill the potential advantages that 4H-SiC has to offer.

10:20 AM B02
(Student) JFET Region Design for 650 V 4H-SiC Planar Power MOSFETs Shengnan Zhu[1], Tianshi Liu[1], Arash Salemi[2], David Sheridan[2], Marvin H. White[1] and Anant K. Agarwal[1]; [1]The Ohio State University, United States; [2]Alpha and Omega Semiconductor, United States

Summary
Silicon Carbide (SiC) MOSFETs, especially the 600 V class, are gaining increasing attention in the electric vehicles (EVs) market. The design of the JFET region is critical for the static and dynamic performances of the SiC power MOSFET. This work studies the impact of JFET region designs on the I-V and C-V performance of 650 V planar SiC Power MOSFETs. The ON-resistance, breakdown voltage, the gate to drain capacitance (C_{gd}), and oxide electric field during the off-state of the 650 V MOSFETs are studied through device characterization and TCAD simulation. The results suggest that the shortest possible JFET region and the smallest possible cell pitch combined with improved JFET doping leads to the lowest ON-resistance and C_{gd}.

Device Fabrication
The MOSFETs are fabricated on two 6-inch SiC wafers by a state-of-the-art commercial SiC foundry. A 7 µm, 2×10^{16} cm^{-3} doped n-type epitaxial layer on a 2×10^{18} cm^{-3} doped n^+ substrate is used as the starting material. The substrate has been thinned to 170 µm after the front-side fabrication. The body of the MOSFET is defined by ion implantation. The n^+ and p^+ implanted doping concentrations are 1×10^{19} cm^{-3}. The channel length is 0.5 µm for both wafers, while the active area is 6.3×10^{-3} cm^2. Process splits are implemented for the gate oxide thickness and JFET doping concentration for the two wafers. Thinner gate oxide (35 nm) and higher JFET doping (5.5×10^{16} cm^{-3}) are used for wafer II to have a lower $R_{on,sp}$.

Experimental and Simulation Results
The 650 V MOSFETs are designed with JFET width of 0.8 µm, 1.0 µm, 1.2 µm, 1.5 µm, which are named as A1 to A4 for devices on wafer I and B1 to B4 for devices on wafer II. For JFET width equals 1.2 µm, a tight design (A5 and B5) is applied by shrinking the ohmic contact width. The purpose of using the tight design is to reduce the cell pitch of the MOSFET, increase the channel density and reduce the ON-resistance of the devices. The orthogonal P^+ layout topology is used for all devices. On-wafer measurements have been conducted on all devices. The transfer, output, and blocking characterizations are measured using the Keysight 1506A at room temperature. The threshold voltages are extracted using the linear extrapolation method. The measurement results show that the threshold variation is less than 1V for devices on both wafers. The $R_{on,sp}$ is extracted at V_G=20 V, V_D=1 V. Results show that the $R_{on,sp}$ decreases with the increasing JFET width. With a specific JFET width, MOSFET on wafer I has higher $R_{on,sp}$ compared with

the MOSFET on wafer II. It's demonstrated that increasing the JFET doping can reduce the $R_{on,sp}$ of the device. The tight design has a smaller $R_{on,sp}$ compared with the relaxed design with the same JFET width. Therefore, reducing the cell pitch also decreases the $R_{on,sp}$. The blocking characterization results reflect that the devices on wafer II have lower breakdown voltage (~650 V) compared to the MOSFETs on wafer I (~740 V), which is caused by the higher JFET doping. We simulated the oxide electric field of the MOSFETs with different JFET widths and doping through TCAD simulation. A higher JFET width generates a higher oxide field. The thinner oxide on wafer II produces higher oxide fields compared to those on wafer I, which implies potentially oxide reliability issues. The C_{gd} reduces when decreasing JFET width, which indicates better switching performance of the MOSFET with narrower JFET.

Acknowledgment
This work is supported in part by the Block Gift Grant from II-VI Foundation.

10:40 AM B03

(Student) Channel Hole Scattering Processes in 4H-SiC MOSFETs Suman Das, Ayayi Ahyi, Marcelo Kuroda and Sarit Dhar; Auburn University, United States

Silicon Carbide (4H-SiC) has become the principal semiconductor of power electronics and extreme environment applications because of its physical properties such as wide bandgap, high breakdown electric field, and high thermal conductivity[1]. 4H-SiC discrete devices such as diodes and metal-oxide semiconductor-field-effect transistors (MOSFETs) are currently very popular in high voltage power conversion in hybrid/electric vehicles and in various high-temperature sensor applications. On the other hand, the development of an integrated circuit (IC) technology based on 4H-SiC is relatively immature. 4H-SiC IC technology that demands n- and p- channel MOSFETs is very appealing as its potential to operate efficiently at temperatures greater than 300 °C[2] would enable various functions that are not accessible to conventional silicon-based technology.[3] It has been established that, on n-channel 4H-SiC MOSFETs, nitridation of the SiO_2/4H-SiC interface results in a reduction of near-interface trap density, improvement of channel conductivity, and device stability.[4,5] Their p-channel counterparts, in contrast, have been reported to have lower mobilities. But studies on such devices are scarce and more comprehensive investigations are needed[6].

In this study, Hall measurements are used to determine the primary scattering processes for inversion layer holes in nitrided p-channel 4H-SiC MOSFETs produced on a moderately doped (6.2×10^{15} cm^{-3}) substrate. Specifically, analysis of the Hall mobility (μ_{Hall}) by varying the body (substrate) bias and temperature was employed to determine the effective field (E_{eff}) dependence of μ_{Hall} for holes. Under strong inversion, mobility is characterized at a constant carrier concentration in order to keep the screening effect constant, yielding a surface roughness limited mobility with a power-law dependence on E_{eff} as -2.4, comparable to that of holes in silicon p-channel MOSFETs. At very low E_{eff} attained at a low negative body bias, i.e., near the onset of inversion, phonon scattering is observed to limit mobility, as evidenced by a temperature-dependent study. These new findings emphasize the relevance of improved interface state density and fixed positive charge passivation in p-channel FETs, which would result in a lower threshold voltage for strong inversion, resulting in better channel conduction due to reduced E_{eff}.

Acknowledgment: The authors gratefully acknowledge the support from the National Renewable Energy Laboratory/ US Department of Energy sub-contract NREL-AHL-9-92362-01.

References:

[1] B.J. Baliga, *Fundamentals of Power Semiconductor Devices* (2010).
[2] A. Rahman et al., Emerg. Sel. Top. Power Electron. **4**, 935 (2016).
[3] J.M. Homberger et al. *37th IEEE Power Electron. Spec. Conf.* (2006), pp. 1–7.
[4] K. Tachiki and T. Kimoto, IEEE Trans. Electron Devices **68**, 638 (2021).
[5] K. Tachiki et al., Appl. Phys. Express **14**, 031001 (2021).
[6] S. Das et al., J. Appl. Phys. **130**, 225701 (2021).

11:00 AM B04

(Student) Process-Induced Variability of SiC DMOSFET Short Circuit Capability Suvendu Nayak[1,2], Hema Lata Rao Maddi[2], Swaroop Ganguly[1] and Anant K. Agarwal[2]; [1]IIT BOMBAY, India; [2]The Ohio State University, United States

Summary
Among compound semiconductors, Silicon Carbide (SiC) is useful especially in the high voltage, fast switching applications. Like with all technology areas, as SiC DMOSFET technology matures in terms of performance, questions of reliability and failure take on a more central role [1]. The short circuit (SC) capability addresses a key failure mechanism in these devices. The current and the lattice temperature of the device increase tremendously with the voltage stress leading to the device burning out. Among various reasons reported for this, the conducting paths created due to the melting of contacts (Aluminum) may be considered the most important factor [1]. In this work, we investigate the effect of possible process-induced variability on SC capability by 2-D simulation.

Device and Simulation Setup

A generic 1200 V vertical SiC DMOSFET structure, shown in Fig. 1, is simulated in a non-isothermal environment of the TCAD platform to study the short circuit capability of the device. Thus, we have used the thermodynamic model in addition to the usual drift-diffusion for electrons and holes. The parameters for bulk and interface mobility, its degradation with temperature, and thermal parameters such as thermal conductivity and specific heat capacity have been taken from the experimental literature. The acceptor type interface trap ($Q_A = 1.5\times10^{12}$ cm^{-2} at E_C-E_F = 0.18 eV) and oxide fixed charge density 2×10^{11} cm^{-2} are defined at SiC/SiO_2 for the simulation. The device is normally off type, and the important parameters are tabulated in Table 1.

Results

We consider the variability arising from two possible processes for self-aligned channel formation. The first, illustrated in Fig. 2.a, arises from the dry etch process used to form an oxide spacer which follows the p-well implant defined by the oxide hard mask. The spacer then acts as a hard mask during the n^+ source region implant so as to define the channel (additive). The distance between the two p-well, in this case, is fixed. Thus, channel length variability, in this case, is towards the n^+-source side ('1'). The second, illustrated in Fig. 3.a, arises from a wet etch process to move back the oxide hard mask, which is used for the n^+-source implant. The shortened oxide now constitutes a hard mask for the p-well implant, and thereby defines the channel (subtractive). The distance between the two n^+-source implants, in this case, is fixed. The channel length variability, in this case, is therefore from the JFET region side ('2'). The total cell pitch remains constant in both cases. We consider both a decrease and an increase of channel length from each side. Fig. 2.b shows the variability of type '1', while Fig. 3.b shows the variability of type '2'. The effect of these variability types on the SC capability is different and depends on the effective channel length, which here ranges from 0.3 to 0.7 µm. For type '1', the effective channel length increases and decreases with n^+-source, and most of the other device parameters are not affected as shown in Table 1. For type '2', the varied channel length is effectively changing the JFET dimensions. The combined effect is more pronounced which can be observed from the resulting SC curves. The SC capability of the device worsens with a decrease in channel length since that leads to higher currents. The results indicate that the additive method of fabrication is preferable for the SiC-based DMOSFET for reproducible SC performance.

Acknowledgement
This work was supported by the IIT Bombay-Ohio State Frontier Science and Engineering Research Center under "Towards the rugged SiC technology for electric transportation" project.

Reference

1. Hema Lata Rao Maddi, Susanna Yu, Shengnan Zhu, Tian-shi Liu, Limeng Shi, Minseok Kang, Diang Xing, Suvendu Nayak, Marvin H. White, and Anant K. Agarwal, "The road to a robust and affordable SiC power MOSFET technology, "Energies, vol. 14, no. 24, pp. 8283, Dec 2021.

11:20 AM B05

Characterization of SiC-SiO$_2$ Interface States in Commercial 4H-SiC Power MOSFETs from Cryogenic to High Temperature Hema Lata Rao Maddi, Suvendu Nayak, Jiashu Qian, Vishank Talesara, Yibo Xu, Marvin H. White, Wu Lu and Anant K. Agarwal; The Ohio State University, United States

Summary
High-power Silicon Carbide (SiC) metal-oxide-semiconductor field-effect transistors (MOSFETs) have created considerable interest due to their high-speed switching capabilities, avalanche capability, and low on-resistance. In previous research [1], it was shown that a high density of SiC/SiO$_2$ interface states (D_{it}) which increases exponentially towards the conduction band edge (E_C) was primarily responsible for poor inversion layer electron mobility. D_{it} closer to the conduction band edge (E_C) can be determined at low temperatures by monitoring the deterioration of the subthreshold slope in the drain current versus gate voltage (I_D-V_{GS}) characteristics of MOSFETs. Alternatively, it may also be assessed from the change in threshold voltage (V_{th}) caused by temperature changes. The governing characteristics of planar gate MOSFETs at room and high temperatures have been studied in a number of studies, but few have looked at their performance at cryogenic temperatures. In this work, D_{it} near the E_C (E_C-E_T =0.01eV) is measured for two different commercially available 1.2 kV MOSFETs using the threshold voltage change ($\triangle V_{th}$) caused by temperature variation. The temperature is varied from 80 K-500 K using liquid nitrogen cryostat. The experimental setup includes a cryogenic probe station, a liquid nitrogen dewar, and B1506A parametric analyzer. The static characteristics (I_D-V_{GS}) were measured, and the threshold voltage is extracted using the linear extrapolation method. The vendors with their respective voltage and current ratings are tabulated in Table.1.

Results and Discussion

Interface traps per unit area,$\triangle N_{it}$, can be calculated by the following equation,

$\triangle N_{it} = {}_{a1}\int^{a2} D_{it}(\Phi_F)\, d\Phi_F = (\triangle V_{th} C_{ox})/q$, ($a1=\Phi_{F,HT}$ and $a2=\Phi_{F,LT}$)

where the threshold voltage is determined at $\Phi_s=2\Phi_F$. The energy band diagram for low temperature ($\Phi_{F,LT}$) and room temperature ($\Phi_{F,RT}$) in Fig. 1, represents the Fermi potential change ($\triangle\Phi_F$) for the corresponding temperatures.

At low temperature, the Fermi level (E_F) moves closer to the valence band (E_V) in the p-type bulk. Consequently, at $\Phi_s=2\Phi_F$ more band bending is necessary to induce sufficient carrier density at the surface. Conversely, at high temperatures, E_F moves away from the valence band and therefore the required band banding is less. As the temperature increases, electron concentration in the conduction band increases due to the detrapping of the carriers from the interface states above E_F. This results in fewer negative charges at the interface, leading to a decrease in threshold voltage. The I_D-V_{GS} and V_{th} variation within a temperature range of 80 K to 500 K for vendors "C" and "E" is shown in Fig.2, Fig.3, and Fig.4 respectively. D_{it} distributions of devices from vendors "C" and "E" are shown in Fig.5. Lowering the temperature leads to an increase in V_{th}, as expected. The exponential increase in D_{it} towards the conduction band edge is visible as the temperature is lowered to 80 K. The Fermi level enters the conduction band around 100K based on the electrostatic calculations. In our study, due to the lack of process information from vendors, our estimation of the gate oxide thickness was based on the ramp-to-breakdown measurement and an assumption of 2 x 10^{17}/ cm^3 for P-base doping. As observed, the D_{it} value for vendor "C" is higher than vendor "E" which can also be predicted from a higher threshold voltage variation ($\triangle V_{th}$=5.8 V) in vendor "C" as compared to 3.64 V in vendor "E" for the entire range of measured temperatures, attributing to the process of gate oxide formation and annealing.

References:

Yoshioka H, Hirata K. Characterization of SiO$_2$/SiC interface states and channel mobility from MOSFET characteristics including variable-range hopping at cryogenic temperature. AIP Advances. 2018, Vol.8, pp.045217.

Acknowledgment: The funding from the Vehicle Technology Office at the US Department of Energy, Washington DC is gratefully acknowledged.

11:40 AM B06

(Student) Recombination Centers in 4H-SiC pin Diodes Observed by Electrically Detected Magnetic Resistance and Near-Zero Field Magnetoresistance Ashton Purcell[1], Fedor V. Sharov[1], Patrick M. Lenahan[1] and Jacob Biju[2]; [1]The Pennsylvania State University, United States; [2]GE Global Research, United States

Over the last two decades there has been a growing interest in the implementation of 4H-SiC in high power and high temperature applications. This is primarily due to its relatively large bandgap of 3.26 eV. A device of particular interest in high field applications is the pin diode. Although recombination centers play an important role in these devices, relatively little is known about their chemical and physical nature. We report on the observation of recombination centers in 4H-SiC based pin diodes using electrically detected magnetic resonance (EDMR) and near-zero field magnetoresistance (NZFMR). Our results show the presence of at least two physically distinct recombination centers. Our EDMR measurements utilize spin dependent recombination induced changes in device current associated with electron-hole recombination in these devices. EDMR spectra have significant analytical power because they closely match that of well understood conventional EPR spectra. In these magnetic resonance measurements, defect identification is possible due to perturbations to the environment of unpaired electrons in point defects, such as deep level recombination centers. An unpaired electron which is otherwise unaffected by its environment would have a magnetic resonance condition described by a microwave frequency expressed by $hv = g\mu B$. Here, g is a constant called the Lande g factor, h is Planck's constant, and μ is the Bohr magneton. For a defect in a semiconductor this simple expression is altered by the local environment. For the situation of interest in our study, the two main perturbations to the isolated electron case come from spin-orbit coupling and electron-nuclear hyperfine interactions.

In our study, we report on EDMR associated with recombination events caused by magnetic resonance at deep level defects involved in electron -hole recombination; this type of EDMR is called spin dependent recombination (SDR). In SDR the rate of electron-hole recombination events is increased by the magnetic resonance induced "flipping" of unpaired electrons at deep level sites [1]. This electron spin flipping results in measurable changes in device current. We report X-band (9.5GHz) EDMR as well as on the physically related NZFMR response of 4H-SiC pin diodes. The EDMR spectra exhibit a nearly isotropic () spectrum which is almost certainly due to silicon vacancies [2]. We observe an additional strong EDMR spectrum which has a magnetic field orientation dependent which has somewhat higher values which extend to at least . We tentatively ascribe this spectrum to an intrinsic defect but cannot yet provide a more specific identification. In addition, we report on NZFMR results which

provide information about the bias-dependent kinetics of the SDR process within the intrinsic region of the diodes. The results may be of particular use for the fields of deep-space and quantum magnetometry.

[1] D. Kaplan, I. Solomon and N. Mott, "Explanation of the large spin-dependent recombination effect in semiconductors", *J. Phys. Lett.*, vol. 39, no. 4, pp. 51-54, Feb. 1978.
[2] T. Wimbauer, B. Meyer, A. Hofstaetter, and A. Scharmann, "Negatively charged Si vacancy in SiC: A comparison between theory and experiment," Phys. Rev. B - Condens.

SESSION C: Wearable Electronics and Biosensors

Session Chairs: Suprem Das and Shayla Sawyer
Wednesday Morning, June 29, 2022
Ohio Staters Inc. Founders Room

10:00 AM C01
(Student) Stress Hormone Detection by Single-Crystalline III-N Piezoelectric Thin-Film-Based Sensor Nam-In Kim, Jie Chen, Martha Villagran, Jarek Wosik and Jae-Hyun Ryou; University of Houston, United States

Wearable and skin-attachable electronics, especially sensors, are becoming more and more important in biomedical fields including personal healthcare monitoring of physical and physiological signals. Stress plays a crucial role in the overall health of humans. The adrenal gland in a human, who is under stress, emits cortisol and adrenaline into the bloodstream and released hormones are discharged by several body fluids, including sweat, saliva, and tear. Long-lasting stress can decline the homeostasis, which is erupted in the whole body containing cardiovascular, immune, renal, skeletal, and endocrine systems. Furthermore, the ruined homeostasis could be developed to chronic diseases. Therefore, monitoring cortisol levels in body fluids is highly important in sustaining healthy conditions. Most of the current stress sensors in the literature show limitations because they are based on physical sensing of skin perspiration, conduction, pulse rate, and body temperature. These stimuli can be derived from not only stress but the external environment.
Recently, field-effect transistor-based cortisol sensor with cortisol antibody embedding technique to fabricate the sensing layer and organic electrochemical transistors type cortisol sensing were designed and studied. However, both exhibit inherent disadvantages such as vulnerability to interference from other ions present in target body fluids. Also, applied voltage at the gate and drain electrodes can accelerate the absorption of non-target analytes (e.g. serotonin and dopamine) on the sensing area, which occurs malfunction of those sensors. In addition, the transistor-based sensors require an external electric source to monitor cortisol, which is another barrier to commercialization.
The piezoelectric-based quartz crystal microbalance (QCM)-type sensors have a specific resonant frequency and they can be easily functionalized by cortisol monoclonal antibody to fabricate the sensing layer. When the target material (cortisol) interacts with the sensing layer, the force is applied by its mass, then the initial resonant frequency is shifted to the negative direction by the Sauerbrey equation. Furthermore, QCM-type piezoelectric sensors show excellent response time owing to the rapid antigen-antibody interaction process. The sensitivity is influenced by the position of the initial resonant frequency, which means a higher initial frequency can detect a low concentration of cortisol. The selectivity of the QCM-type sensor is quite guaranteed because the driving force of interaction is the only attraction of bonding energy between analyte and antibody. Thus, other chemicals or hormones are not available to react except for an extremely small amount of them.
Among various piezoelectric materials, III-N thin films with single-crystalline characteristics are very promising to be utilized as QCM-type sensors for cortisol detection. III-N materials have a relatively high initial resonant frequency of several GHz, which enables excellent detection capability.
In this study, we developed and demonstrated a III-N thin film-based QCM-type sensor for the detection of cortisol with various conditions. III-N thin-film sensors were designed by the layer transfer method. They were analyzed by X-ray diffraction to reveal their single-crystalline quality without second phase or defects. The controlled cortisol solutions were applied to the sensor and the resonant frequency was shifted as concentration. Then, several hormones were diluted and used to verify the selectivity of our sensor. The artificial body fluid and real sweat collected from a volunteer experiencing exercise and sauna were utilized for comparison.

10:20 AM C02
(Student) Recessed AlGaN/GaN HEMT Biosensors with High Sensitivity and Linearity for Detection of Microcystin-LR
Dongseop Lee, Paul Bertani, Seungjun Lee, Yuehan Ai, Jiyoung Lee and Wu Lu; The Ohio State University, United States

Cyanobacterial blooms, also known as harmful algal blooms (HABs), occur in water systems around the world and have been observed in every region of the United States, causing damage to ecosystems, fisheries, sources for agriculture, recreation, and drinking water. These HABs can produce a variety of harmful toxins (cyanotoxins), including microcystins, saxitoxins, anatoxin-a, and cylindrospermopsins, which can result in illness or death in both human and wildlife populations. In this work, we demonstrate AlGaN/GaN high electron mobility transistors (HEMTs) biosensors for the detection of microcystin -LR (MC-LR). For high sensitivity, the sensing area (gate) is recessed to adjust the threshold voltage to near zero volts. After plasma oxidation, the sensing area is functionalized through a self-assembly process. The peaks of C-C, aluminum carbonate, and CHO (aldehyde) at 284.8, 288.6, and 87.8 eV, respectively, are observed from X-ray photoelectron spectroscopy (XPS) spectra suggesting a silane layer before antibodies were linked. Fluorescence images from the sample with a silane-functionalized surface without antibodies (control) and the sample with MC-LR antibodies and dyed-secondary antibodies confirm that MC-LR antibodies linked on the functionalized surface effectively. A PEG-NH_2 layer is applied as a super-blocking layer to prevent non-specific binding. The devices demonstrate a limit of detection (LOD) of 0.71 pg/L and a linear response range from 1 pg/L to 50 μg/L, respectively. The demonstrated sensor response range covers the concentrations from 6 orders lower to 50 times higher than the MC-LR guideline (1 μg/L) recommended by World Health Organization (WHO). To our knowledge, the sensors demonstrated from this work have the lowest LOD and largest linear response range in comparison with reported devices for MCLR detection based on a variety of technologies.

10:40 AM C03
(Student) Pressure Monitoring at Extremely High-Temperature Range Using Highly Flexible Piezoelectric Sensor Made of Ultrawide-Bandgap III-N Thin Film Nam-In Kim[1], Jie Chen[1], Muhammad Aqib[1], Che-Hao Liao[2], Mongtao Nong[2], Feras Alqatari[2], Xiaohang Li[2] and Jae-Hyun Ryou[1]; [1]University of Houston, United States; [2]King Abdullah University of Science and Technology, Saudi Arabia

Piezoelectric sensors are very promising for various industrial fields including automobile, plant, and biomedical areas due to their advantages of high sensitivity, rapid response time, simplicity for fabrication, reliable operation, lightweight, and low power

consumption. Flexibility is one of the key properties for expanded applications. For example, in gas pressure sensing, the closed-loop in gas inlet or outlet network can be utilized using a flexible sensor located on the diaphragm. The flexible piezoelectric sensors have been reported with several materials for normal condition utilization. However, for extremely high-temperature regions, above 500 °C, sensing materials are limited. Although lead zirconate titanate (PZT) is the most dominant piezoelectric material by its high piezoelectric coefficients, which enable to generate higher output voltages, it is not available for high-temperature operation due to its low Curie temperature (T_c). Zinc oxide (ZnO) and polyvinylidene fluoride (PVDF)-based piezoelectric materials have another barrier for sensing at high temperatures. ZnO is reported to increase oxygen vacancies as the temperature rises and PVDF has low melting (~200 °C) and boiling point (375 °C).
III-N thin films offer the potential for high-temperature operations thanks to their wide bandgap energy, permanent spontaneous polarization, and low electrical conductivity. Especially, single-crystalline gallium nitride (GaN) piezoelectric thin film has been reported to show excellent output voltage up to 400 °C, indicating outstanding sensitivity, rapid response time by a high electromechanical coupling factor, chemical and mechanical long-term stability, high thermal resistance, and excellent biocompatibility. With wider bandgap III-N materials, the benefit is expected to be further extended to higher temperatures.
In this study, we developed and demonstrated piezoelectric AlN thin-film sensors with high flexibility for the detection of gas pressures at extremely high temperatures. Crack-free AlN epitaxial layer was grown by metalorganic chemical vapor deposition. Flexible III-N thin films were fabricated by a layer transfer method from the rigid silicon to flexible copper foil substrate. They were analyzed by X-ray diffraction to reveal their crystalline quality without second phase or defects. The single sensor was attached to the diaphragm of the fitting tool and located in the furnace. The operating condition of the sensor was controlled from low to high temperature with various gas pressures. The long-term stability of the sensor was evaluated using fixed temperature and pressure levels. The simulation was conducted by software to support the results at each temperature and pressure. The flexible III-N piezoelectric sensors with high endurance at extreme conditions can be further applied in several applications such as aerospace and defense fields.

11:00 AM C04
(Student) Flexible Modified Carbon Nanotube/Nanofiber-Based Triboelectric Nanogenerator Julia I. Salas Toledo, Karen Lozano and M. Jasim Uddin; The University of Texas Rio Grande Valley, United States

Flexible triboelectric nanogenerators (TENGs) are the next generation of devices for energy harvesting on wearable and portable electronics. This study presents how the properties of carbon nanotubes (CNT) can enhance the performance of flexible and stretchable triboelectric nanogenerators (TENGs), when it is incorporated into one of the nanofiber layers. These nanofiber layer consisted in Polyvinylidene fluoride (PVDF), which was consider as the negative triboelectric layer, and Thermoplastic Polyurethane (TPU) as the positive, and in which the CNT was incorporated. Both nanofiber layers used were prepared using the Forcespinning® technique. The morphology and structure were characterized through SEM, EDX and XRD and triboelectric properties were characterized, and produce a maximum of 164V in an open circuit at 180 bpm, in contact area of 2.0 x 2.0 in square. PVDF/TPU-CNT, shows potential and versatility in the application of everyday energy harvesting from its flexibility and stretchability.

11:20 AM C05
(Student) Detection of the Nitrogen Cycle Using the Metabolic Activity of Shewanella Oneidensis MR-1 Lauren Brady, James Dylan Rees and Shayla Sawyer; Rensselaer Polytechnic Institute, United States

The presence of excess nutrients in freshwater and marine ecosystems can have significant detrimental effects including altering the dynamics of microbial communities and food-webs, and promoting the formation of harmful algal blooms which can produce toxins that are harmful for fish, wildlife, and humans.

Scientists in diverse fields including chemistry, microbiology, and engineering have noted the capacity to detect the presence and concentration of many of these nutrients, or other chemicals of environmental concern, by electrochemically interfacing with microbes that metabolize these chemicals. The dissimilatory metal-reducing bacterium *Shewanella oneidensis* MR-1 is a particularly versatile model organism capable of both aerobic and anaerobic respiration, dissimilatory metal reduction, participation in the microbial nitrogen cycle, and direct electron transfer to or from a biased electrode. In this study, a porous carbon fiber electrode capable of supporting 3D biofilm growth is combined with several correlated electrochemical techniques to detect nitrogen cycle activity via the metabolic activity of *Shewanella*.

Shewanella oneidensis MR-1 was grown in 800mL batch culture jars each containing a working, reference, and counter electrode. Batches containing *Shewanella* inoculum were compared to a sterile control. The jars were left at room temperature for 24 days, with no clear indication of a biocurrent observed. Next, a -0.2V bias voltage was applied in accordance with prior studies indicating that this bias voltage would activate *Shewanella* cytochrome gene expression [1][2]. Cyclic Voltammetry (CV) was used to electrochemically investigate the electron transfer processes within the system.

A DC biocurrent appeared in the inoculated batches that did not occur in the sterile batches. It is believed that the increase in biocurrent was based on reduction by Shewanella’s nitrate and nitrite reductases. Results also showed evidence of a CV peak at +180mV vs. Ag/AgCl Electrode which can also be represented as +790 mV vs. Standard Hydrogen Electrode that occurred in batches inoculated with Shewanella but not in sterile batches. This peak matches the reduction potential of denitrification (NO_3 reduction to N_2) and concurs with earlier studies indicating the capacity for *Shewanella* to engage in denitrification [3][4].

Thus, the preliminary results indicate that a DC biocurrent is created in the presence of *Shewanella* and the nitrogen cycle processes can be identified using electrochemical measurement techniques such as cyclic voltammetry to verify the reduction of nitrates. Ultimately this work may lead to more cost-effective and versatile chemical sensors for detecting various environmental pollutants in-situ.

References:
[1] D. Baron, E. LaBelle, D. Coursolle, J. A. Gralnick, and D. R. Bond, “Electrochemical measurement of electron transfer kinetics by Shewanella oneidensis MR-1,” *J. Biol. Chem.*, vol. 284, no. 42, pp. 28865–28873, Oct. 2009.
[2] A. A. Carmona-Martínez, F. Harnisch, U. Kuhlicke, T. R. Neu, and U. Schröder, “Electron transfer and biofilm formation of Shewanella putrefaciens as function of anode potential,” *Bioelectrochemistry*, vol. 93, pp. 23–29, Oct. 2013.
[3] M. Jiang, X. Zheng, and Y. Chen, “Enhancement of denitrification performance with reduction of nitrite accumulation and N2O emission by Shewanella oneidensis MR-1 in microbial denitrifying process,” *Water Res.*, vol. 169, p. 115242, Feb. 2020.
[4] L. Sigg, “Redox Potential Measurements in Natural Waters:

Significance, Concepts and Problems," in *Redox: Fundamentals, Processes and Applications*, J. Schüring, H. D. Schulz, W. R. Fischer, J. Böttcher, and W. H. M. Duijnisveld, Eds. Berlin, Heidelberg: Springer Berlin Heidelberg, 2000, pp. 1–12.

11:40 AM C06

(Student) Wearable Eye Movement Sensors Using Flexible and Biocompatible III-N Thin Films for Personal Safety, Healthcare Monitoring and Abnormality Diagnosis Nam-In Kim, Jie Chen, Mina Moradnia, Sara Pouladi and Jae-Hyun Ryou; University of Houston, United States

Personal healthcare is increasingly important in the medical field to detect the symptoms from specific diseases for the diagnosis of early-stage disorders. Abnormal physiological signals including pulse rate, blood pressure, body temperature, muscle movement, and respiration can be the source for symptoms. For example, real-time pulse monitoring is a possible technique for people with a high risk of cardiovascular diseases. Likewise, among the signals, abnormal eye movement and blinking are related to several brain-related disorders, such as attention deficit hyperactivity disorder (ADHD), stroke, autism, Alzheimer's disease (AD), and Parkinson's disease (PD). Thus, monitoring of eye-related motions and movements opens a way to diagnose at an early stage from the symptoms of the slow eye movement, sluggish blinking from external stimulus. Current eye-tracking systems (ETSs) for sensing eye motions and blinking demand complex devices such as helmets, headgear, or goggles, high-resolution cameras, and image processing software. These requirements are the main limitation for monitoring eye-related motion at home with a user-friendly system.

Flexible epidermic sensors can address the shortcomings of present ETS. Specifically, piezoelectric sensors with skin-attachability and wearability have inherent merits in size, weight, power, and cost. Thin-film-based piezoelectric skin-attachable sensors using lead zirconate titanate (PZT) and zinc oxide (ZnO) are inappropriate due to their disadvantages. The toxic lead element is one of the components for PZT crystal and lead can be absorbed in human skin, which is poisoning. Sensors attached to the skin have to contain non-toxic elements. ZnO-based sensors exhibit relatively low output value, sensitivity, and resolution, which requires post-processing steps. As an alternative material, group III-N thin films are very promising to detect physical motion. Furthermore, a single piezoelectric sensor with single-crystalline gallium nitride (GaN) was reported with attachment on the temple area to monitor the eye blinking and lateral eyeball movement. In this study, our skin-attachable and wearable sensors were fabricated as array format developing the single sensor. Arrayable sensors were attached to 3 different temple areas (upper, middle, and lower temple) to monitor the several types of eyeball movements including lateral, vertical, diagonal, and rotational direction. All the results from each sensor are distinguishable, which indicates that the sensors generated different values of output signals from each position with varied stimulates.

SESSION D: Gallium Oxide Devices

Session Chairs: Sriram Krishnamoorthy and Siddharth Rajan
Wednesday Morning, June 29, 2022
Ohio Staters Inc. Traditions Room

10:00 AM D01

(Student) Demonstration of Self-Aligned Delta Doped MISFETs with Current Density > 550 mA/mm Nidhin Kurian Kalarickal, Ashok V. Dheenan, Joe F. McGlone, Andreas Fiedler, Sushovan Dhara, Mark Brenner, Steven A. Ringel and Siddharth Rajan; The Ohio State University, United States

We report on the design and demonstration of β-Ga_2O_3 self aligned delta doped MISFETs with current density exceeding 550 mA/mm using plasma assisted MBE growth. Self aligned devices were fabricated using gate recess of heavily doped β-Ga_2O_3 access regions using in-situ Ga etching, followed by formation of spacer layers using ALD Al_2O_3.

With a high theoretical breakdown field of 8 MV/cm, β-Ga_2O_3 is highly promising for applications in power switching and high power RF electronics. High-performance devices require high current density and low on-resistance, but previously reported β-Ga_2O_3 based transistors fabricated on native substrates were limited to ~ 300 mA/mm drain current [*Applied Physics Express* 10.5 (2017): 051102] and higher current densities were obtained only in β-Ga_2O_3 nano membrane transistors exfoliated onto non-native substrates [*Appl. Phys. Lett.* 111.9 (2017): 092102]. In this report we demonstrate the use of self-aligned gate structure to enable state-of-art current densities exceeding 550 mA/mm.

The growth was carried out in a Riber M7 MBE system equipped with a Veeco O_2 plasma source. The epitaxial structure consits of 30 nm Mg doped β-Ga_2O_3 layer, 500 nm UID β-Ga_2O_3 layer, 2 Si delta doped channels separated by 5 nm, 45 nm UID β-Ga_2O_3 cap layer and 45 nm n++ β-Ga_2O_3 layer. The device fabrication was initiated by ohmic contact formation to the n++ β-Ga_2O_3 layer using Ti/Au (30/100 nm) followed by annealing at 470 under N_2 for 1 min. Device isolation was later carried out by using BCl_3/Ar based dry etch. 200 nm PECVD SiNx was then deposited to form the hard mask for the gate recess etch. The recess etch of 60 nm was carried out using Ga etching using atomic Ga flux in an MBE chamber [*Applied Physics Letters* 119.12 (2021): 123503] at a T_{sub} of 550 ºC . Following the recess etch, T_{sub} was lowered to 400 ºC and 10 nm of Al_2O_3 was deposited as the gate dielectric. To form the sidewall dielectric spacers, 60 nm ALD Al_2O_3 was deposited followed by RIE etching and wet etching (1:10 BOE) to remove it from the gate region, leaving 50 nm of Al_2O_3 on the gate-sidewalls. Gates were then defined using 150 nm Ni to partially cover the source and drain access regions.

Transfer length measurements showed a contact resistance of 0.2 Ω.mm for metal to n++ access region and low sheet resistance of 122 Ω/sq for the n++ access region. In addition, contact resistance of ~ 1 Ω.mm is estimated as the contact resistance between the delta doped channel and n++ access region. The channel sheet resistance post gate recess etch is measured to be 3170 Ω/sq indicating complete removal of the access region above the channel. Capacitance-voltage measurements (100 kHz) indicate a distance of ~52 nm from the gate electrode to the 1st delta doped channel. Transistors I_D-V_D characteristics show high current density of 560 mA/mm for devices with gate length of 0.6 μm and source-drain spacing of 2 μm, similar to the two-terminal (ungated) current density. This is the highest reported current density obtained in lateral β-Ga_2O_3 transistors on native substrates. Significant self heating effects causing drop in current density is also observed above 5 V of drain voltage. Due to the high channel charge density, low on/off ratio between 2 and 3 orders is obtained in the present study, suggesting that further engineering of the channel and dielectric layers is necessary to improve this.

In summary we demonstrated β-Ga_2O_3 self aligned delta doped MISFETs using a novel low-damage atomic Ga-flux etching

method. The record high DC current density of 560 mA/mm on native β-Ga_2O_3 substrates shows the promise of self-aligned device structures in enabling high current density, low on-resistance transistors based on β-Ga_2O_3. This work was supported by funding from Department of Energy / National Nuclear Security Administration under Award Number(s) DE-NA000392, and AFOSR GAME MURI (Award No. FA9550-18-1-0479, project manager Dr. Ali Sayir).

10:20 AM D02

Growth and Electrothermal Characterization of β-$(Al_xGa_{1-x})_2O_3/Ga_2O_3$ Heterostructure Field-Effect Transistors Marko Tadjer[1], Kohei Sasaki[2], Michael Mastro[1], Joseph Spencer[1,3], Alan G. Jacobs[1], Karl Hobart[1], Travis Anderson[1], Georges Pavlidis[4], Andrea Centrone[4], Lei Chen[4], Keita Konishi[2] and Akito Kuramata[2]; [1]Naval Research Laboratory, United States; [2]Novel Crystal Technology, Japan; [3]Virginia Tech, United States; [4]National Institute of Standards and Technology, United States

The promise of Ga_2O_3 to deliver high power, high efficiency, low cost power electronics has advanced significantly in recent years after several breakthroughs were demonstrated [1, 2]. In addition, Ga_2O_3 can form ternary alloys with Al to form pseudomorphic β-$(Al_xGa_{1-x})_2O_3/Ga_2O_3$ (AlGaO/GO) heterostructures suitable for device applications. Despite the ultra-wide energy gap of Ga_2O_3 alloys, shallow donors (e.g. Si) have enabled n-type doping of these films. Furthermore, a two-dimensional electron gas (2DEG) can be formed via the delta doping approach, similar to early AlGaAs/GaAs heterostructures. Thus, Ga_2O_3-based delta-doped heterojunction field-effect transistors (HFETs) hold exceptional promise for high performance power switches with high breakdown, fast switching, and high output power.
Following our demonstration of delta-doped $(Al_xGa_{1-x})_2O_3/Ga_2O_3$ heterojunction field-effect transistors (HFET) grown via the ozone-assisted molecular beam epitaxy technique (O_3-MBE) [3], in this follow-up work we have performed the following experiments. We have performed O_3-MBE growth of β-$(Al_xGa_{1-x})_2O_3$ on (010) and (100) β-Ga_2O_3 simultaneously in order to evaluate critical thickness limits for β-$(Al_xGa_{1-x})_2O_3$ as a function of substrate orientation, Al mole fraction (5-20% Al), and β-$(Al_xGa_{1-x})_2O_3$ film thickness (50-400 nm). Above a certain thickness, epitaxial AlGaO suffered from cracks whose density increased as the AlGaO film grew thicker. Films grown on (010) Ga_2O_3 exhibited cracking at much lower thickness than films grown on (100) Ga_2O_3. This observation agreed with the work of Mu et al. [4, 5], who applied the Griffith criterion in order to provide a critical thickness h_c lower bound for β-AlGaO/GO based on crystal fracture strength Γ, elastic constants C_{xy}, and strain components ε.
For HFET device fabrication, samples of β-$(Al_xGa_{1-x})_2O_3/Ga_2O_3$ with $(Al_xGa_{1-x})_2O_3$ barrier layer thickness of 21 nm and Al mole fraction x of 18.6-18.8 percent were grown via O_3-MBE [6]. Electrochemical capacitance-voltage measurements, performed on calibration samples grown on conductive substrate, showed a single carrier peak with concentration of $2x10^{19}$ cm^{-3}. Room temperature Hall measurements performed on HFET structures grown on Fe-doped substrate resulted in sheet resistance R_{SH} = 10763 Ω/sq., sheet carrier concentration n_s of $9.55x10^{12}$ cm^{-2}, with mobility of 61 cm^2/Vs. Ohmic contacts with specific contact resistivity of $4.6x10^{-4}$ Ω/cm^2 were formed via Si ion implantation and activation annealing at 925 °C for 30 min in N_2, followed by Ti/Au lift-off and contact anneal at 470 °C for 1 min in N_2. Our prior $(Al_xGa_{1-x})_2O_3/Ga_2O_3$ HFET devices did not utilize ion implantation and were observed to have severely degraded over the course of several months, likely due to interfacial TiO_2 formation as reported by Lee and Peterson for the case of Ga_2O_3 [7]. Lateral HFETs were processed with a 20 nm thick ALD Al_2O_3 gate dielectric layer and a 20/200 nm thick Pt/Au gate metal stack. Figure 3 presents the DC I-V characteristics, and Fig. 4 shows open-gated average channel temperature as a function of drain bias (V_{GS} = 0 V) measured via scanning thermal microscopy. [1] S.J. Pearton et al., Appl. Phys. Rev. 5, 011301 (2018). [2] M. Higashiwaki, G. Jessen, Appl. Phys. Lett. 112, 060401 (2018). [3] M.J. Tadjer et al., J. Vac. Sci. Technol. A 39, 033402 (2021). [4] A. A. Griffith, Philos. Trans. R. Soc. London, Ser. A 221, 163 (1921). [5] S. Mu et al., APL Mater. 8, 091105 (2020). [6] Y. Oshima et al., Appl. Phys. Expr. 9, 061102 (2016). [7] M.H. Lee, R.L. Peterson, ACS Appl. Mater. Interfaces 2020, 12, 41, 46277–46287.

10:40 AM D03

(Student) β-Ga2O3 MESFETs with Insulating Mg-Doped Buffer Grown by MBE Ashok V. Dheenan, Joe F. McGlone, Nidhin Kurian Kalarickal, Hsien-Lien Huang, Mark Brenner, Steven A. Ringel, Jinwoo Hwang and Siddharth Rajan; The Ohio State University, United States

Beta phase Ga_2O_3 is an ultrawide bandgap (4.6-4.9 eV) semiconductor that has recently garnered interest as a material for high-power electronics due to its high theoretical electric breakdown field of 8 MV/cm, availability of native melt-grown substrates and ease of n-type doping across a wide range of concentrations [*Appl. Phys. Lett.* 112.6 (2018): 060401]. Although p-type conductivity is unfeasible due to a large hole effective mass, doping with deep acceptor-like impurities such as Magnesium, which forms an energy level 1.1 eV above the valence band [*Appl. Phys. Lett.* 113.6 (2018): 062101], can provide a way to engineer device electrostatics and make highly resistive material.
While Mg doping was used previously to realize semi-insulating layers in MOCVD [*Appl. Phys. Lett.* 117.22 (2020): 222106], this has not been demonstrated by molecular beam epitaxy (MBE) before. In this work, we report on the epitaxial growth and electronic properties of MBE-grown Mg-doped β-Ga_2O_3. Both abrupt and uniform Mg doping profiles were achieved by altering the Mg effusion cell shutter opening times. A relationship between Mg concentration and effusion cell temperature was established by secondary ion mass spectroscopy (SIMS). The doping techniques developed were used to solve the well-reported issue of buffer leakage caused by Si dopants at the substrate-growth interface, suggesting that Mg doping could be a promising way to achieve insulating buffer layers for MBE-grown β-Ga_2O_3 lateral transistors.
Two different epitaxial structures for calibration of abrupt and uniform Mg doping profiles were grown on semi-insulating Fe doped (010) substrates using a Riber M7 MBE system at a substrate temperature of 725 °C. SIMS profiles confirmed the deltas in Mg concentration as a result of a pulsed shuttering scheme (10 s open/30 s closed/10 s open). Sharp peaks in Mg concentrations ranging from 10^{17} – 10^{21} cm^{-3} were attained in the delta-doped sample by varying the effusion cell temperature from 360 °C to 450 °C. The Mg concentration from the uniformly doped SIMS stack was found to drop off faster with temperature than estimates from the delta-doped SIMS stack. Following calibration of the Mg doping, Si and Mg co-doped layers were grown on an Sn-doped (010) substrate and compared to an Si doped control sample. Capacitance-voltage measurements on Schottky diodes were used to extract the estimated doping concentrations. The Mg co-doped sample showed a significant reduction in the donor concentration when compared to the UID sample, confirming the compensating behavior of the Mg dopants.
To understand the effect of doping the buffer with Mg on lateral device performance, three samples with a Si delta-doped channel and varying buffer thicknesses were grown. Mg delta-doping corresponding to a SIMS concentration of $1x10^{20}$ cm^{-3} was introduced at the start of the growth to compensate any Si dopants accumulated on the substrate surface. Processing started with selective area regrowth of n+ source/drain regions. Ti/Au ohmic contacts were deposited and annealed in N_2 ambient. Devices were mesa isolated using BCl_3/Ar based dry etching. Deposition of Ni/Au gates completed the fabrication of the delta-doped MESFETs. Transistor output characteristics on the sample with a 400 nm buffer showed current density above 80 mA/mm and a

pinch-off voltage of -5 V. On/off ratio was 10^6 and limited by the gate leakage, indicating that the Mg delta-doping at the substrate-growth interface was successful in suppressing the source leakage. In summary, we have demonstrated well-controlled Mg doping over a range of concentrations in β-Ga_2O_3 grown by MBE. Mg doping was also shown to compensate unintentional donors and form insulating buffer layers for lateral FETs.
This work was funded by Department of Energy / National Nuclear Security Administration under Award Number(s) DE-NA000392 and the AFOSR GAME MURI (Award No. FA9550-18-1-0479, program manager Dr. Ali Sayir).

11:00 AM D04
Electrical Characteristics and Band Alignment of *n*-Si/*n*-Ga_2O_3 Heterojunction Fabricated by Surface-Activated Bonding
Zhenwei Wang[1], Daiki Takatsuki[2], Jianbo Liang[2], Takahiro Kitada[1], Naoteru Shigekawa[2] and Masataka Higashiwaki[1]; [1]National Institute of Information and Communications Technology, Japan; [2]Osaka City University, Japan

β-Ga_2O_3-based power devices have been studied intensively in recent years, owing to its wide bandgap of 4.5 eV and the availability of single-crystal wafers produced from melt-grown bulks. On the other hand, the lack of *p*-type conductivity is one of the serious technical challenges in terms of its physical properties in developing a variety of Ga_2O_3 devices. Utilization of other *p*-type semiconductors as components of the Ga_2O_3 device structures would be one of the possible solutions for this fundamental issue. Fabrication of high-quality heterostructures between Ga_2O_3 and dissimilar material by epitaxial growth, however, is often hindered by large mismatches in lattice constant and thermal expansion coefficient. In this work, for the first time, we fabricated *n*-Si/*n*-Ga_2O_3 heterostructures by using room-temperature surface-activated bonding (SAB) process instead of epitaxial growth and studied their electrical characteristics to investigate the quality and band alignment of the heterojunction. It is expected that in the case of two semiconductors with fully different lattice parameters, the SAB can provide better-quality heterojunctions compared with epitaxial growth, because it is free from limitations of the mismatches. Note that this is the first step to explore the possibility of using *n*- and/or *p*-Si as components of Ga_2O_3 device structures.

The *n*-Si/*n*-Ga_2O_3 heterostructures were fabricated by SAB using an *n*-Ga_2O_3 (001) substrate and an *n*-Si (100)-on-insulator substrate. For characterization of electrical properties, the bonded substrate was processed into test structures with *n*-Si pillars on the *n*-Ga_2O_3 substrate. Ohmic electrodes were fabricated on top *n*-Si and bottom *n*-Ga_2O_3 sides. Cross-sectional transmission electron microscopy observation revealed that an intermediate amorphous layer with a thickness of about 2 nm was formed at the bonding interface. Rectifying current density–voltage (J–V) characteristics were obtained, suggesting that there was an energy barrier in the electron transport path due to negative charges existing at the interface. Furthermore, depletion regions were formed in both *n*-Si and *n*-Ga_2O_3 layers due to the negative interface charges to maintain the local charge neutrality. The energy barrier heights ($q\varphi_b$) for various reverse applied voltages (V_{rev}) were extracted from J–V characteristics measured at temperatures from 23°C to 200°C. The $q\varphi_b$ initially decreased with decreasing V_{rev} and saturated at around 0.25 eV for $V_{rev} < -9$ V. The decrease in $q\varphi_b$ was attributed to a reduction in the built-in potential at the *n*-Si side. The $q\varphi_b$ saturation, which corresponded to the flat-band condition in the *n*-Si layer, provided an estimate of the conduction band offset of 0.18 eV at the bonding interface.

This study proposes that SAB can be an alternative technique to epitaxial growth for fabricating Ga_2O_3-based heterostructures with dissimilar material having major differences in lattice parameters, and that the SAB heterostructures would expand the design possibility of Ga_2O_3 device structures.

This work was supported in part by JSPS KAKENHI Grant Number 19H02182.

11:20 AM D05
(Student) Beta-Gallium Oxide Junction Barrier Schottky Diodes with Sputtered P-Type Nickel Oxide
Joseph Spencer[1,2], Boyan Wang[1], Ming Xiao[1], Alan G. Jacobs[2], Alyssa Mock[3], James C. Gallagher[2], Karl Hobart[2], Kohei Sasaki[4], Akito Kuramata[4], Yuhao Zhang[1] and Marko Tadjer[2]; [1]Virginia Tech, United States; [2]U.S. Naval Research Laboratory, United States; [3]Weber State University, United States; [4]Novel Crystal Technology, Japan

Gallium oxide (GO) has become a widely researched ultra-wide bandgap semiconductor in both the material and electronic power device fields. The popularity of GO is due in part to its ability for melt growth, growth of high quality homoepitaxial drift layers on native substrates, and the prospect of higher breakdown strength than other wide band gap materials such as gallium nitride (GaN) and silicon carbide (SiC). However, one key disadvantage of GO is the inability to achieve p-type doping due to its flat valence band structure and self-trapping of holes [1]. This fundamental limitation of GO technology precludes the development of PN junctions for this material. Recently, p-type nickel oxide (NiO) heterojunctions with GO have been reported for both PN and JBS diodes [2-4]. Here we report the development of p-type NiO via sputtering and demonstrate GO/NiO Junction Barrier Schottky (JBS) diodes with high forward current density and a breakdown voltage of around 600V.

Prior to device fabrication, NiO thin films were RF-sputtered on silicon substrates and modeled using spectroscopic ellipsometry to confirm bandgap, optical constants, and film thickness. NiO thin films were sputtered on p-type Si to characterize carrier type and free carrier concentration using the capacitance-voltage technique and a Hg probe instrument. Hall effect measurements were employed for resistivity characterization using evaporated Ni/Au Ohmic contacts. However, determining carrier concentration and mobility using Hall effect technique was found to be unreliable due to low mobility and very low Hall voltage values.

JBS diodes were fabricated on ~10 µm thick halide vapor phase homoepitaxial (001) GO layers doped around 2.1e16 cm^{-3}. The GO was etched using inductively-coupled BCl_3 plasma to produce 400 nm deep trenches before NiO deposition by RF sputtering at room temperature and lifted off. NiO-filled GO trenches were 2 µm wide; GO trench pitch was 2, 4, and 6 µm. In addition, NiO was deposited for edge termination around the annular devices. Schottky and PiN diodes were fabricated alongside the JBS diodes as control devices used to confirm proper JBS diode operation.

Initial I-V testing of devices under forward bias showed a JBS diode with a turn-on voltage nearly identical to the Schottky diodes. PiN diodes displayed a higher turn-on voltage than both the Schottky and JBS diodes, as expected. All three types of diodes reached a current density of 100 A/cm^2 before either series resistance or testing compliance limited forward current density. Reverse bias testing was carried out in Fluorinert, where the best performing JBS diodes reached a reverse bias in excess of -600V at which point the set compliance of 10 µA was reached. Catastrophic breakdown was not reached for the best performing device. PiN diodes reached breakdown voltages up to -650V before breaking down or reaching compliance. However, these PiN diodes exhibited substantial reverse leakage with increasing reverse bias and need to be investigated further. The best performing Schottky diodes achieved V_{BR} -500V before compliance was reached.

Further device testing and analysis of both the PiN and Schottky diodes is needed in order to better characterize the JBS diodes. An immediate area of concern is the quality of the sputtered NiO as

well as the NiO/GO interface which could be responsible for a large defect density and large reverse current. Further testing will be used to compare various NiO films deposited under different sputtering conditions, as well as the effect of post etch acid cleaning of the GO sidewalls. Further goals include annealing of diodes to improve breakdown voltage and attempt to improve the quality of the NiO/GO interface.

[1] Varley, J.B., et al. *Phys. Rev. B* 85, 081109 (2012).
[2] K. Sasaki et al., Int. Conf. SiC and Relat. Mater., 2017.
[3] Hao, W., et al. *Appl. Phys. Lett.* 118, 043501 (2021).
[4] Lv, Yuanjie, et al. *IEEE Trans. Power Electronics, vol* 36, pp. 6179 (2020).

11:40 AM D06
(Student, Late News) Heterogeneous Integration of Single-Crystal β-Ga_2O_3 and N-Polar GaN Substrates with ZnO Interlayer Deposited by Atomic Layer Deposition Zhe Ashley Jian[1], Christopher Clymore[2], Daphne Agapiou[1], Umesh Mishra[2] and Elaheh Ahmadi[1]; [1]University of Michigan–Ann Arbor, United States; [2]University of California, Santa Barbara, United States

Recently, β-Ga_2O_3 has attracted great attention as a promising candidate for high power switching applications. However, two main challenges of β-Ga_2O_3 are its relatively low electron mobility (180 $cm^2V^{-1}s^{-1}$) and low thermal conductivity (10-30 W/m-K) [1], [2]. Additionally, p-type doping does not seem feasible currently for this material system. On the other hand, GaN, a well-known wide bandgap semiconductor, has a high electron mobility (2050 $cm^2V^{-1}s^{-1}$), high 2D charge (2DEG) density, moderate thermal conductivity (253 W/m-K), and the availability of p-type doping [3]. Therefore, the integration of β-Ga_2O_3 with GaN can potentially enable the fabrication of novel GaN/Ga_2O_3 high-frequency and high-power devices combining the merits of both GaN and Ga_2O_3 in addition to novel optoelectronic devices.
This work integrated single-crystal (0001) N-polar GaN and (-201) UID β-Ga_2O_3 substrates via wafer bonding using ZnO interlayer deposited by atomic layer deposition (ALD). Both 5×5 mm^2 GaN and 10×10 mm^2 Ga_2O_3 substrates were cleaned in acetone, isopropyl alcohol, and de-ionized water with ultra-sonication, followed by soaking in buffered hydrofluoric acid (BHF) for 30 seconds. The samples were then loaded immediately into the ALD chamber to minimize any surface contamination. The 10 nm-thick ZnO was deposited on both N-polar GaN and (-201) Ga_2O_3 samples via thermal-ALD at 200 °C. Next, the Ga_2O_3 and GaN samples were placed into contact with each other and transferred to an EVG 510 bonding chamber. The bonding was conducted at 400 °C under the pressure of 4 MPa in vacuum for 3 hours. The surfaces were 100% fully bonded. After bonding, both the front and back sides of the sample were evaporated by Ti/Au 20/200 nm. To investigate the impact of post-annealing temperature on the quality of bonding interfaces, the N-polar GaN/ZnO/Ga_2O_3 test structure was annealed in N_2 for 30 minutes at various temperatures of 600 °C and 900 °C with ramping up and down rates of 2 °C/min.
Temperature dependent I-V measurements were performed on the GaN/ZnO/Ga_2O_3 test structure at temperatures from 300 K to 650 K with step increment of 25 K. As-bonded sample without annealing demonstrated Schottky behavior, indicating a conduction band barrier between Ga_2O_3 and ZnO. As measurement temperature increased, the turn-on voltage decreased because the number of electrons with the required energy to pass over the Schottky barrier increases at higher temperatures. The Schottky barrier of around 0.56 eV was extracted from a linear fit to the Richardson plot. The test structure showed a deviation of I-V curves before and after temperature dependent measurement (up to 650 K) and the I-V characteristics recovered after 48 hrs. This could be explained by the existence of slow traps at the bonded interfaces. After annealing at 600 °C, the I-V curves showed almost linear behaviors, indicating that the test structure could be modeled by a series resistor. The maximum current density of 0.02 A/cm^2 at V_{bias} = 6 V and the resistance of 1714 Ω were measured at room temperature. Additionally, increasing the annealing temperature to 900 °C caused a substantial change in the I-V-T characteristics, exhibiting a significant conduction band barrier occurring at the GaN/ZnO interface. This is probably associated with the recrystallization of amorphous ZnO interlayer during high temperature annealing [4]. This work reported the heterogeneous integration of single-crystal GaN and β-Ga_2O_3 substrates with ALD ZnO interlayer which shows promises for the development of novel GaN/Ga_2O_3 high-frequency and high-power devices beyond 5G applications.

[1] Z. Guo *et al.*, *Appl. Phys. Lett.*, vol. 106, no. 11, p. 111909, Mar. 2015. [2] Z. Feng *et al.*, *Appl. Phys. Lett.*, vol. 114, no. 25, p. 250601, Jun. 2019. [3] H. Shibata *et al.*, *Mater. Trans.*, vol. 48, no. 10, pp. 2782–2786, Oct. 2007. [4] J. Bruncko *et al.*, *Thin Solid Films*, vol. 520, no. 2, pp. 866–870, Nov. 2011.

SESSION E: Dielectrics and Multifunctional Oxides

Session Chairs: Doug Hall and Patrick Lenahan
Wednesday Morning, June 29, 2022
Senate Chamber

10:00 AM E01
The Role of Thermal Vibrational Disorder in the Structural Phase Transition of VO_2 Probed by Raman Spectroscopy
Aminat Oyiza Suleiman[1], Sabeur Mansouri[1], Nicolas Émond[2], Théophile Bégin[3], Boris Le Drogoff[1], Joëlle Margot[3] and Mohamed Chaker[1]; [1]Institut National de la Recherche Scientifique, Canada; [2]Massachusetts Institute of Technology, United States; [3]Université de Montréal, Canada

Vanadium dioxide (VO_2) is a typical correlated electron material which exhibits a first-order metal–insulator transition (MIT) at a near-room temperature of about 340 K. Upon heating, VO_2 switches from an insulating monoclinic phase (M1 or M2) to a metallic tetragonal rutile phase (R). The mechanism behind the MIT in VO_2 is still controversial: Is it a structure driven Peierls transition mechanism or a Mott transition where strong electron-electron correlations drive charge localization and collapse the lattice symmetry? By directly comparing the electrical and lattice–dynamic properties of VO_2, useful information about the MIT/SPT in VO_2 can be obtained.

Herein, we therefore present a detailed Raman study of undoped (M1) and Cr-doped (M2) VO_2 thin films as a function of temperature. The studied VO_2 films with different thicknesses are deposited on c- and r-sapphire substrates. While their structural properties and morphology are examined by XRD and AFM techniques, respectively, Raman measurements are correlated to four-point probe resistivity measurements, giving an insight into the coupling between VO_2 structural phase (SP) and MI transitions. By distinctively combining the Raman data with information from reported EXAFS data, a relationship between the Raman intensities and the mean Debye-Waller factors (σ^2 the mean-square relative displacements) is established. The temperature dependence of the vanadium dimers Waller factor (σ^2_R(V-V)), as calculated from the Raman intensity, was found to follow the temperature profile of the σ^2_{EXAFS}(V-V) obtained from the reported EXAFS data. These findings provide an evidence on the critical role of the thermal vibrational disorder in VO_2 phase transitions, demonstrating that by correlating Raman data with EXAFS analysis, both lattice and electronic structural dynamics can be probed.

10:20 AM E02

High Transparent Conductor Figure-of-Merit for $SrVO_3$ Grown by Solid-Phase Epitaxy Samuel Marks[1], Lin Lin[1], Peng Zuo[1], Patrick Strohbeen[1], Dongxue Du[1], Jason Waldvogel[1], Ryan Jacobs[1], Donald Savage[1], Susan Babcock[1], John Booske[2], Jason Kawasaki[1] and Paul Evans[1]; [1]University of Wisconsin–Madison, United States; [2]University of Wisconsin, United States

Transparent conducting oxides (TCO) are critical components in display and photovoltaic technologies requiring simultaneously high visible light transmission and low electrical resistance. $SrVO_3$ has recently emerged as a promising TCO material that can be incorporated into heterostructures as an epitaxial thin film with high optical transparency and electrical conductivity. Epitaxial $SrVO_3$ films were formed by crystallizing amorphous layers deposited on $SrTiO_3$ (001) using solid-phase epitaxy (SPE). Thermodynamic calculations predicting the temperature and oxygen partial pressure conditions required to produce the $SrVO_3$ phase match the experimental conditions. The lattice parameters and mosaic angular width of x-ray reflections from crystallized films exhibit a strain that depends on the film thickness, with 16 and 60 nm films being fully and partially strained, respectively. $SrVO_3$ layers with 16 nm thickness exhibited a room temperature resistivity of 5.2×10^{-5} Ω cm and visible light transmission of 89%. Increasing the film thickness resulted in lower room temperature resistivity and a significant reduction in optical transparency. Temperature-dependent resistivity measurements between 5 K and 300 K reveal residual resistivity ratios of 3.8 and 2 for 16 and 60 nm $SrVO_3$ layers, respectively, suggesting that defect scattering dominates low temperature transport but has a limited effect on room temperature transport properties.

10:40 AM E03

(Student) Correlation of Native Point Defects with Piezoelectric Voltage in Strained ZnO Microwires Kamila J. Thompson, Micah Haseman and Leonard J. Brillson; The Ohio State University, United States

ZnO microwires are biocompatible semiconductors that are piezoelectric and can turn mechanical strain into an electric potential. This is due to the lack of central symmetry in the ZnO hexagonal wurtzite crystal structure. These microstructures have been used to create bio-nanogenerators that can harvest the body's natural movement into power for implanted biomedical devices [1,2]. Nanogenerators can replace lithium-ion batteries in implanted devices which are relatively large, have a limited lifetime requiring multiple replacement surgeries, and can be dangerous for the patient should the battery fail [3]. However, ZnO microwire based devices have an electric potential output that is not always efficient enough to replace lithium-ion batteries. Electrically - active native point defects can have a significant role in macroscale electrical properties. These defects can be electrically charged and have electric fields that can interact with the piezo- electric fields, causing them to redistribute, but this effect has yet to be investigated as a possible solution to improving the device efficiency. This study aims to correlate defects with changes in piezoelectric potential, enabling researchers fabricating ZnO microwire-based nanogenerators to understand the impact of defects on device output and suggest growth and processing treatments to control these defects.

ZnO microwires were grown using a vapor-liquid-solid method via carbothermal reduction in a quartz tube furnace. Wires were then cast on a Si substrate with a native oxide layer and then grounded to the substrate using conductive silver paste. Results presented here for these preliminary experiments involved a wire with a 2.36 µm diameter and ~700 µm length. Cathodoluminescence spectroscopy (CLS) and Kelvin Probe Force Microscopy (KPFM) were used to characterize the defects and surface potential difference of the wire, respectively, for the strained and unstrained wire case. Besides the 2nd order band gap peak at ~1.64 eV, CLS emissions of the unstrained wire appeared at ~2.37 eV, attributed to a Zn interstitial- Zn vacancy Frenkel pair, and the ~3.24 eV bandgap. Emissions also appear at ~1.98 eV and ~3.20 eV, possibly due to Zn vacancy clusters and oxygen vacancy-hydrogen complexes [4]. Defects at position 1 (towards the silver paste) seem to be of lower intensity than defects towards position 7 (at the tip). KPFM potential maps of the tip indicate a maximum potential difference between the wire and substrate of 1.19 V in the unstrained case. The ZnO microwire was strained using micromanipulators on a probe station in air which applied a strain of 0.08%. The KPFM potenital maps in the strained case show a maximum potential difference of 593.3 mV. The defects still showed the same trend of increasing intensity the closer they were measured to the mircowire tip, but in the strained case, the defect intensity is nearly 2X lower relative to the bandgap emission. The unstrained case showed a maximum defect intensity ratio of 2.2 while the strained case displayed a maximum ratio of 1.1. These preliminary results indicate a correlation between piezoelectric tip voltage and defect density such that increasing point defect density decreases tip voltage. These results suggest that controlled nano- and microwire defect removal or passivation can significantly increase bio-nanogenerator device effiency.

The authors gratefully acknowledge support from NSF grant DMR-18-00130.

[1] S. Bagga *et al.*, AIP Conf. Proc. **1989**, 020004 (2018).
[2] D. C. Look, Mat. Sci. and Eng.: B **80**, 383 (2001).
[3] M. A. Hannan *et al.*, BioMed. Eng. Online **13**, 79 (2014).
[4] Y. Dong *et al.*, Phys. Rev. **81**, 081201 (2010).

11:00 AM E04

(Student) Controlling Charge Distributions near Complex Oxide Interfaces via Defect Engineering Brenton A. Noesges[1], Daesu Lee[2], Hongwei Wang[3], Thaddeus J. Asel[1], Jinbo Pan[3], Jung-woo Lee[2], Qimin Yan[3], Xifan Wu[3], Chang-Beom Eom[2] and Leonard J. Brillson[1,1]; [1]The Ohio State University, United States; [2]University of Wisconsin–Madison, United States; [3]Temple University, United States

Complex oxide electronics are attractive for next generation devices because high mobility conducting interfaces can be achieved between ultrathin layers of otherwise insulating materials. $SrTiO_3$ is at the center of these applications but defects impacting the properties of $SrTiO_3$ films can also play a significant role at heterointerfaces involving $SrTiO_3$ or even at junctions between $SrTiO_3$ and non-stoichiometric $SrTiO_3$. Defect formation impacts electron performance at interfaces and within ultra-thin layers. The conducting interface between $LaAlO_3$ & $SrTiO_3$ is one key example of the impact of defects where the interfacial 2D hole gas (2DHG) wasn't observed until O vacancies (V_O) were sufficiently decreased near the interface. V_O donate at least one e^- per site which compensate free holes near the interface. In principle, the interplay of cation defects can be used to control the balance of acceptor-type defects alongside V_O which tune n-type carrier density. Using depth-resolved cathodoluminescence spectroscopy (DRCLS), we determined how reducing Sr content in Sr_xTiO_3 ($0.98 \leq x \leq 1.00$) films grown on $SrTiO_3$ impacted defects and electronic structure extending from the Sr-deficient epilayer to tens of nanometers below the interface. DRCLS allowed us to simultaneously measure multiple defect states with optical transitions corresponding to V_O, Sr vacancies (V_{Sr}), Ti on Sr anti-sites (Ti_{Sr}) and Ti^{3+}. As expected, [V_{Sr}] increased with decreasing Sr content. At the same time, [Ti_{Sr}] also increased with increasing [V_{Sr}] indicating Ti filled in Sr vacancy sites. The increase in the acceptor-type [V_{Sr}] anticorrelates with [Ti^{3+}] as excess electrons which could reduce Ti^{4+} to Ti^{3+} are instead compensated by extra holes from V_{Sr}. The anti-correlation suggests $V_{Sr,}$ and other acceptor-type defects could balance V_O and improve control over free carrier densities. Differential DRCLS (DDRCLS) showed how

the interplay of defects within the epilayer created depth- & Sr-dependent changes in defect densities extending tens of nanometers beneath the interface. DDRCLS is an extension of DRCLS that removes the luminescence contribution of epilayers when studying buried regions. Increasing accumulation of V_{Sr} in the Sr-deficient epilayers suppressed Ti^{3+} within the epilayer but also impacted the distribution of Ti^{3+} extending into the substrate. Control over nanoscale defect-induced charge distributions can advance new device features such as 2DHGs and the performance of existing devices such as ferroelectric tunnel junctions. This study shows how DRCLS directly measures the relative densities and spatial distributions of multiple native defects within and extending away from nanoscale $Sr_xTiO_3/SrTiO_3$ junctions and how their interplay varies with controlled epitaxial growth. These growth-dependent defect variations can help guide $SrTiO_3$ epitaxial growth with other complex oxides. Controlling the interplay of these defects can improve mobility at 2D electron gases (2DEGs) formed between $LaAlO_3$ & SrTiO. Ti_{Sr} sites can be created by increasing the inlet pressure of metal-organic Ti precursor gas which suppresses the amount of V_{Sr} & V_O, in turn leading to mobility improvements at the interface. Controlled growth to directly observe, introduce, and manipulate both cation and anion-related native point defects on a nanometer scale provides a new avenue to improve the interfaces of $SrTiO_3$ with other complex oxides. This control extends to the defects themselves acting as scattering centers that degrade conductivity or alternatively, wave function overlaps between, *e.g.*, lattice sites for quantum communication. The authors gratefully acknowledge support from NSF grant DMR-18-00130.

11:20 AM E05

(Student, Late News) Mechanothermal Synthesis and Characterization of Ti-Doped Bismuth Ferrite Using Nano-Agitator Milling Process Lyndon E. Smith, Vijaya Rangari and Shaik Jeelani; Tuskegee University, United States

Using a novel milling process, Ti-doped bismuth ferrite was synthesized with a nominal composition of $BiFe_{0.95}Ti_{0.05}O_3$. Precursor powders were milled for different durations and analyzed using X-ray diffraction and SEM/EDAX before and after calcination. XRD revealed the formation of $Bi_5(Ti_3Fe)O_{15}$ during milling. The powders were calcined at temperatures ranging from 650°C-850°C in 50°C increments. After heating the sillenite phase ($Bi_{25}FeO_{40}$) was predominant below 800°C. The rhombohedral phase ($BiFeO_3$) only became the primary phase at 800°C. Using the Debye-Scherrer equation, an average grain size of ~20-25 nm for $BiFeO_3$ and ~35-45 nm for $Bi_{25}FeO_{40}$ was estimated from the XRD patterns. The 800°C sample, having the greatest phase purity, underwent electrical characterization, and the leakage current density was found to be lower than undoped $BiFeO_3$ using synthesized using the same method.

11:40 AM E06

On the Impact of Impurities' Nature and Annealing Conditions on Structural and Optical Properties of Hafnia-Based Thin Films Tetyana V. Torchynska[1], Leonardo Vega Macotela[1], Georgiy Polupan[1], Manuel Alejandro Garcia Andrade[1], Nadiia Korsunska[2], Xavier Portier[3], Fabrice Gourbilleau[3] and Larysa Khomenkova[2,4]; [1]Instituto Politécnico Nacional, Mexico; [2]V. Lashkaryov Institute of Semiconductor Physics (Kyiv, Ukraine), Ukraine; [3]CIMAP/ENSICAEN, France; [4]National University "Kyiv-Mohyla academy", Ukraine

Among transition metal oxides, hafnia (HfO_2) is mainly considered as the dielectric alternative to silicon oxide owing to their high dielectric constant. However, HfO_2 based materials offer a high refractive index and a high transparency in UV-NIR spectral range that are promising for photonic applications. For this purpose, the stabilization of the amorphous HfO_2 structure is required to minimize the optical losses in the HfO_2 based optical components. Since HfO_2 is an ionic material, for the stabilization of its amorphous structure the use of silicon is preferable due to the flexibility of covalent Si-O bonds. Earlier, we have reported on the effect of Si content on the formation of Hf silicate host. It turned out that increase of Si content from about 3 at% to 6 at.% favours the formation of amorphous HfO_2 phase stable upon annealing at ~800 ºC, whereas the further increase of Si content up to 12 at % stimulates the formation of Hf silicate with amorphous structure stable up to 900 ºC.

It is known that the tetragonal and cubic structure of HfO_2 can be stabilized by the introduction of trivalent elements. In this case, electrical neutrality is achieved via the formation of oxygen vacancies, i.e. one vacancy for two dopant atoms. At the same time, the interaction between different ions and their redistribution upon high-temperature annealing were not well addressed.

In this report structural transformation of HfO_2 thin films codoped with silicon and lanthanides (RE) is considered in terms of the evolution of optical and light-emitting properties of these materials. The films were grown on Si substrates by radio frequency magnetron sputtering in argon plasma and annealed at T_A=800-1100ºC for t_A=15-60 min in an inert atmosphere. The transformation of film properties was studied by means of SEM, EDX, XRD, XPS, TEM and photoluminescence (PL) techniques. For HfO_2 films doped with RE ions, the stabilization of the tetragonal HfO_2 phase in annealed films was observed contrary to the monoclinic structure of pure HfO_2 films. The main reason responsible for this phenomenon is the formation of oxygen vacancies. For RE-doped HfSiOx films, phase separation between SiOx and HfO_2 occurs upon annealing. For Nd or Er-doped films, the presence of RE ions was detected in SiOx and HfO_2 phases. Contrary to this, the Pr ions appeared in the HfO_2 phase only. This latter was transformed into cubic one upon annealing at 1050°C, while at higher annealing temperature, the formation of monoclinic HfO_2 phase was detected. The shape of RE-related PL spectra followed the structural transformation. Narrow RE-related PL peaks were detected in the samples annealed at 1000-1100°C that confirms the location of RE ions in the phase with a high crystal field. The peculiarities of PL spectra and the mechanism of phase separation for different films are discussed.

SESSION F: Point Defects, Doping, and Extended Defects

Session Chairs: Mark Goorsky and Kunal Mukherjee
Wednesday Morning, June 29, 2022
Rosa Ailabouni Room

10:00 AM F01

Small Defects, Big Deal—Using Point Defects to Control Giant Opto-Mechanical Effects and to Engineer New Resistive Switches Rafael Jaramillo; Massachusetts Institute of Technology, United States

Semiconductor point defects that create deep charge traps are often to be avoided, because they speed up bad things (non-radiative recombination) and slow down good things (photodetector response). Nevertheless, deep traps often feature large charge-lattice coupling phenomena that are fundamentally interesting and could be put to good use. We will discuss two studies and several potential applications of charge-lattice coupling at deep traps in II-VI semiconductors.

We find that deep traps are correlated with giant opto-mechanical effects, such as changes in hardness and elastic modulus greater than 50% under relatively mild illumination (*e.g.* blue light at 1.5 mW/cm^2) during nanoindentation, and that these giant effects can be tuned by materials processing. We present experimental results on three wide-band gap II-VI compounds: CdS, ZnS, and ZnO.

Giant photo-plasticity has been understood for decades, but giant photo-elasticity has remained a mystery. We find that the giant photo-elastic effects arise from strong charge-lattice coupling at point defects. Our results are supported by density functional theory (DFT) and finite element analysis (FEA) simulations.
We also find that deep traps can be engineered as functional elements for two-terminal resistive switches. Point defects that feature giant Stark effects exhibit bistable behavior, and can switch between deep and shallow configurations (DX centers are a well-known example), a phenomenon we call defect level switching (DLS). We demonstrate a DLS device based on CdS that switches from high- to low-conductivity at a small forward bias of <0.5 V; this normally-on behavior is qualitatively unlike most resistive switches, but does resemble negative differential resistance (NDR) devices such as Gunn diodes. We further show how bistable, DLS behavior can be incorporated into a semiconductor device simulation to enable predictive design of nonlinear, hysteretic devices with qualitatively new behavior.
We will conclude with discussions of how these opto-mechanical and resistive switching effects may be useful for applications.

10:20 AM F02
(Student) Dislocations Altering the Microstructure and Luminescence of InAs Quantum Dots on Silicon Eamonn T. Hughes[1], Gunnar Kusch[2], Jennifer Selvidge[1], Bastien Bonef[1], Justin Norman[1], John Bowers[1,1], Rachel A. Oliver[2] and Kunal Mukherjee[3]; [1]University of California, Santa Barbara, United States; [2]University of Cambridge, United Kingdom; [3]Stanford University, United States

Dislocations strongly impact the degradation behavior of direct epitaxial III-V on silicon lasers. While much attention has been on reducing the density of threading dislocations to improve performance and reliability, there has been less focus on how dislocations can alter the structure of the active region itself to negatively impact parameters such as carrier confinement, gain, and linewidth enhancement factor. Here, we study the impact of dislocations on luminescence in a model system consisting of a GaAs buffer on silicon with a single InAs quantum dot (QD) layer near the surface, looking particularly at how dislocations, both local and distant alter the emission intensity and wavelength both by their immediate physical presence but also through secondary effects like structural alterations induced during growth.
In this model structure, we observe the presence and growth of local misfit dislocations (MDs) just below the QD layer *in situ* by cathodoluminescence (CL). These MDs are not the result of relaxation of the QD layer during growth; instead, they form during cooldown after growth as the structure develops tensile strain due to a mismatch in thermal expansion between the silicon substrate and GaAs-based film. This enables existing threading dislocations (TDs) to glide, aided by energy injected by the scanning electron beam, but the TD segment passing through the QD layer is pinned, so only the lower segment can glide, forming a MD at the base of the QD layer. Continuous-wave (CW) CL shows these MDs as dark line defects. With time-resolved cathodoluminescence (TRCL) mapping using a pulsed electron source, we measure the carrier lifetime across this same region and find that reduced lifetimes associated with non-radiative recombination at MDs are closely correlated with reduced emission intensity.
Looking more broadly at CW CL intensity maps, we see that in addition to the sharp dark lines caused by MDs next to the QD layer, there is an additional diffuse crosshatch pattern of dimmed emission. A map of the peak emission wavelength shows that the crosshatch is blue shifted 15-30 meV. Importantly however, the sharper dark lines caused by local MDs are not measurably blue shifted. We hypothesize that these crosshatch alterations are caused by extended strain fields from the MD network at a defect filter layer that lies about 700 nm below the QD layer. This strain does not directly impact the emission wavelength but rather alters the growth of the QDs, perhaps making them smaller or modifying their composition. The local MDs, by contrast, form after growth during cooldown and therefore do not impact QD growth.
In addition to growth alterations due to the strain from distant misfit dislocation networks, clusters of sessile threading dislocations with a screw component form hillocks during growth that also impact emission properties. These hillocks are associated with strongly reduced CW CL emission and also a blue-shift in emission wavelength, which may be explained by an increased surface step density surrounding the hillock providing additional nucleation sites for QDs, leading to a higher density of smaller QDs forming here. We further examine these regions by atom probe tomography (APT), but due to the small volume analyzed, we do not capture any QDs and therefore cannot comment on changes in QD size or composition. We do find, however, that the encasing QW is about 25% wider in the hillock region, although the hillock and defect-free regions have similar composition profiles. The ground state energy level of this thicker QW should be lower and therefore closer to the QD energy states, which could allow for easier thermalization of carriers out of the QDs, thus dimming the region. By combining multiple characterization techniques, we reveal multiple understudied impacts of dislocations on QD emission properties and, in doing so, identify potential avenues to enhancing device performance and reliability.

10:40 AM F03
(Student) Defects with Mg Segregation in Mg-Implanted GaN After Ultra-High-Pressure Annealing Yekan Wang[1], Kenny Huynh[1], Michael E. Liao[1], James Tweedie[2], Pramod Reddy[2], Mathew H. Breckenridge[3], Ramón Collazo[3], Zlatko Sitar[3], Michael Bockowski[4] and Mark Goorsky[1]; [1]University of California, Los Angeles, United States; [2]Adroit Materials, United States; [3]North Carolina State University, United States; [4]Institute of High Pressure Physics of the Polish Academy of Sciences, Poland

In this work, high resolution x-ray scattering and transmission electron microscopy are used to understand the implant-induced strain recovery process and to mitigate the formation of extended defects that cause a degradation in dopant activation efficiency in Mg implanted GaN. Magnesium ions with a box profile at a total dose level of 1 x 10^{15} cm^{-2} were implanted in homoepitaxial GaN grown on high quality ammonothermal GaN substrates. Post-implantation annealing was performed at 1300 °C, 1400 °C, and 1500 °C for a duration of either 10 minutes or 100 minutes. An ultra-high N_2 pressure of 1 GPa was applied to prevent GaN from decomposition without using a dielectric cap. Ongoing electrical measurements show that annealing at 1400 °C leads to higher dopant activation (~3% at room temperature, ~70% at 500 °C) compared to annealing at 1300 °C (~0.1% at room temperature, ~10% at 500 °C).
The triple axis x-ray ω:2θ scans near GaN (0004) peak shows that the implant-induced strain is fully relieved after annealing at 1300 °C for 10 min. Annealing at higher temperatures and longer time, however, does not have any further impact on the strain state. Two beam condition STEM bright field images show residual defects, after annealing at 1300 °C for 10 min, which consist of inversion domains. The inversion domains appear in two morphologies, pyramidal and trapezoidal. High resolution TEM images show that the pyramidal inversion domains (PID) have their base along GaN (0001) plane with facets along on the $\{11\underline{2}3\}$ planes. Energy Dispersive X-Ray Spectroscopy maps and line scans at the PID show an increase in Mg signal close to the base of the PID, where an extra layer of atoms is located, with a decrease in the Ga signal at the same position. The trapezoidal inversion domains (TID) also show base and facets that are similar to the PID. EDX maps and line scans at the TID also revealed Mg segregation near the base. The center part of a TID consists of a series of small aligned pyramids. We speculate that the TIDs are the initial stages of development and will eventually evolve into the PIDs. Thus, both the PIDs and TIDs trap and make inactive Mg atoms and cause a

degradation in Mg activation efficiency. Similar defects have been observed in highly Mg-doped epitaxial layers [1-3]. However, in those structures, it is difficult to remove or suppress the formation of the PIDs unless low growth temperatures are used, such as for metal-modulated epitaxy [4].
However, the PIDs and TIDs are not observed in any of the samples annealed at and above 1400 °C. This suggests that the PIDs and TIDs are thermodynamically unstable and are formed at lower temperatures or would not form at such high temperatures (≥ 1400 °C). This provides insight for improving dopant activation efficiency with annealing temperature ≥ 1400 °C. The prominent residue defects after annealing at and above 1400 °C are dislocation loops. EDX at the dislocation loops shows no sign of Mg segregation. Meanwhile, an overall decreasing trend in the dislocation loop density is observed after annealing at a higher temperature or for a longer time. The loop density measured decreased from 3.8×10^9 cm^{-2} for 1400 °C 10 min, to 1.5×10^9 cm^{-2} for the 1400 °C 100 min, and further to 1.1×10^9 cm^{-2} for 1500 °C 10 min. Results from this work are expected to help understand the key steps to achieve high activation efficiency p-type doping for planar, vertical device structures in a scalable framework.
This research was supported through the ARPA-E PNDIODES program under contract DE-AR0001116 at UCLA.
Reference
1. P. Vennegues et al. PHYSICAL REVIEW B 68, 235214 (2003).
2. P. Vennegues et al. Appl. Phys. Lett, 77, 6, 7 (2000).
3. K. Iwata et al. Appl. Phys. Express 12, 031004 (2019).
4. B.P Gunning et al. J. Appl. Phys. 117, 045710 (2015).

11:00 AM F04
(Student) Growth of High Indium Percentage InGaSb on InP Substrates Using the Interfacial Misfit Dislocation Array Growth Mode Fatih F. Ince[1], Alexander T. Newell[1,2], Kevin J. Reilly[1], Subhashree Seth[1], Thomas J. Rotter[1], Ahmad Mansoori[1], Sadhvikas Addamane[3], Darryl Shima[1], Leonid Miroshnik[1], Brian Rummel[1], Andrew Li[4], Talid Sinno[4], Sang M. Han[1] and Ganesh Balakrishnan[1]; [1]The University of New Mexico, United States; [2]Air Force Research Laboratory, United States; [3]Sandia National Laboratories, United States; [4]University of Pennsylvania, United States

The ability to access lattice constants around 6.3 Å using antimonide alloys such as $InAs_xSb_{1-x}$ can result in MWIR and LWIR detectors, which can be used for remote sensing, medical devices or material sciences.[1] Fully relaxed lattice constants between 6.09 Å and 6.47 Å cannot be achieved due to the lack of substrates with these lattice parameters. An approach that has been used in the past is to grow metamorphic buffers, such as those based on InGaSb or AlInSb, through single-step or step-graded approaches to realize lattice constants around 6.17 Å. In this presentation, we make use of the interfacial misfit (IMF) dislocation array-based growth mode to grow $In_{0.53}Ga_{0.47}Sb$ directly on $In_{0.53}Ga_{0.47}As$/InP. The IMF growth mode is based on the replacement of the As layer with Sb under highly controlled growth conditions. In the case of other systems, such as GaSb on GaAs, this growth mode results in ~10^8 dislocations/cm_2 with instantaneous relaxation, and reduces to 10^7 dislocations/cm^2 by using defect filter layers. This is achieved by the formation of a highly periodic misfit dislocation array between the GaSb and GaAs layers that almost fully accommodates the mismatch.[2] Several publications by various authors have shown cross-section transmission electron micrograph (X-TEM) analysis and selective area diffraction analysis of the growth, showing complete and spontaneous relaxation of the GaSb epilayer.[2,3] Similar to GaSb/GaAs, our objective in this work is to realize high-quality $In_{0.53}Ga_{0.47}Sb$ directly on $In_{0.53}Ga_{0.47}As$/InP. Successful validation of such a growth mode facilitates the growth of detectors and lasers at this lattice constant.
The MBE growth on undoped InP substrates starts with thermal oxide removal at 540 ºC and subsequent growth of a 500 nm thick lattice-matched $In_{0.53}Ga_{0.47}As$ layer on which the $In_{0.53}Ga_{0.47}Sb$ layer is grown. The antimony for arsenic exchange happens similarly to the growth of GaSb on GaAs. Once the InGaAs layer is completed, the arsenic supply is closed for 30 seconds, and the wafer is maintained at 490 ºC to allow for the complete desorption of excess arsenic. In the case of GaSb on GaAs, after the introduction of antimony, RHEED characterization shows a distinct 2x8 reconstruction, which is an excellent visual guide to indicate that the IMF has been formed. In the case of $In_{0.53}Ga_{0.47}Sb/In_{0.53}Ga_{0.47}As$, the lower growth temperatures result in an unclear 2x8 transition, therefore, we cannot rely on RHEED to guide this process. This could mean arsenic is not completely desorbing, such that the interfacial layer is some composition of InGaAsSb.
We present the analysis of such samples grown at various growth temperatures. The baseline structure is grown with the InGaSb at 400 ºC, followed by two subsequent growths at 360 ºC and 460 ºC. In all of these samples, surface morphology, cross-section TEM, HR-XRD, and photoluminescence studies are performed. The presence of the IMF layers is seen very clearly in several samples; however, the expected spacing of 6.2 nm cannot be verified. This could be due to the non-ideal desorption of the arsenic layer in these structures. The XRD analysis of all three samples indicates a fully relaxed $In_{0.53}Ga_{0.47}Sb$ layer; however, there is significant peak broadening. TEM analysis of the 400 ºC growth shows a periodic misfit dislocation array along the interface. However, for higher atomic-resolution TEM images, we see several different crystal orientations, which indicates the possibility of compositional segregation driven by miscibility gap issues. This presentation provides an in-depth analysis of TEM and photoluminescence characterization of IMF-mode-grown InGaSb/InGaAs alloy structures. In addition, we show how phase segregation due to miscibility gap issues associated with high-indium content impacts crystallographic morphology. We will also present results from our recent efforts to suppress segregation due to miscibility gaps.

11:20 AM F05
(Student) Remote Si Doping of InGaAs Nanowires for Topological Quantum Computing Chunyi Huang[1], Didem Dede[2], Martin Friedl[2], Anna Fontcuberta i Morral[2] and Lincoln Lauhon[1]; [1]Northwestern University, United States; [2]EPFL, Switzerland

The manipulation of Majorana zero modes in networks of semiconductor nanowires is a promising route to quantum computing. We have previously demonstrated wafer-scale growth of branched InGaAs nanowires supported on GaAs nanomembranes by molecular beam epitaxy (MBE).[1] Atom probe tomography (APT) analysis found that Si doping during nanowire formation leads to Si segregation on the (111) growth surface, pushing dopants to the top of the nanowire. In follow-up work, enhanced carrier mobilities were realized in nanowires by remote doping of the supporting GaAs nanomembranes.[2] However, Si dopants segregated at the nanowire/membrane interface, which contributes to alloy scattering. Moreover, the nanowire morphology was not well controlled. In the present work, we addressed the challenge of simultaneously controlling nanowire morphology and dopant distribution and developed a process to precisely position dopants *beneath* a well-defined InGaAs channel. InGaAs nanowires were again grown on GaAs membranes, but Al marker layers were used to visualize the growth interface post-growth and inform the growth process. Prior to Si doping, the growth temperature was lowered to suppress Si diffusion, and then a dilute AlGaAs layer was grown immediately after doping to trap excess Si on the growth interface. Following growth of a GaAs spacer to separate the dopants from the channel, the temperature was increased to grow the InGaAs nanowire. To facilitate atom probe analysis, the sample was capped with crystalline GaAs with an additional embedded Al marker layer. The atom probe reconstruction shows that Si was incorporated at the onset of the

AlGaAs trapping layer as intended, forming a narrow doping band several nanometers below the nanowire. By assuming that the Si incorporation rate increases linearly with Al concentration, an empirical model was able to reproduce the Si doping profile, validating the principle of dopant trapping for controlled modulation doping of nanowires grown on faceted supports. Intriguingly, dilute indium bands were observed beneath the nanowire in the atom probe reconstruction, motivating additional structural and chemical analysis. ABF-STEM cross-sectional imaging revealed a region with planar defects in the same region as the indium bands. The disordered region contains twin boundaries and stacking faults confirmed by high-resolution HAADF-STEM imaging. The planar defects nucleated at the intersection between (111) facet and the oblique facets, presumably when Si was introduced. These defects led to a lateral diffusion of indium during the growth of InGaAs NWs. The relative influence of low growth temperature and Si doping on stacking fault generation is under investigation.

References:
[1] Friedl, M., *et al.* Template-assisted scalable nanowire networks. *Nano Letters* **2018**, *18*, 2666.
[2] Friedl, M., Cerveny, K., *et al*. Remote doping of scalable nanowire branches. *Nano Letters* **2020**, *20*, 3577.

11:40 AM F06
Irradiation Effects on Phonon Mediated Thermal Transport and Defect Evolution in GaAs Joshua Ferrigno and Marat Khafizov; The Ohio State University, United States

Gallium Arsenide (GaAs) is a common semiconducting material found in many integrated circuits and possess a modest thermal conductivity at room temperature. Thermal management of electronic devices is critical to their optimal performance and therefore understanding heat transport has been an active are of research. GaAs thermal conductivity is susceptible to reduction in radiation environments as defects decrease phonon scattering times. For successful space exploration, it is critical to quantify change in thermal conductivity of the semiconductor material. As fast, highly ionizing radiation leads to displacement damage characterized by Frenkel pairs (one interstitial and vacancy). Defect evolution under irradiation governed by production and diffusion of self-interstitials and vacancies within the lattice of solid crystalline material can be conveniently modeled using Rate Theory (RT) equations. Defect concentrations found from RT can be coupled to the Klemens-Callaway model to determine lattice conductivity reduction under irradiation. This coupled model allows for the calculation of the impact of radiation defect accumulation and degradation of GaAs properties, including thermal conductivity.

SESSION G: 2D Material Devices and Sensors

Session Chairs: Kevin Daniels and Daniel Pennachio
Wednesday Afternoon, June 29, 2022
Great Hall Meeting Room 1 & 2

1:30 PM G01
(Student) Multifunctional $MoTe_2$ Transistors for Analog, Digital, Neuromorphic and Modulation Primitives Sarbashis Das and Saptarshi Das; The Pennsylvania State University, United States

Stagnation in the thickness scaling of silicon (Si) for the complementary metal oxide semiconductor (CMOS) technology has invoked interest in atomically thin two-dimensional (2D) semiconducting materials for next generations of ultra-short-channel devices. However, the vast majority of emerging 2D materials exhibit unipolar transport with either dominant electron or hole currents making their adoption difficult in CMOS technology. Furthermore, Si replacement must be accompanied by a change in traditional von Neumann architecture that keeps the compute and memory separated. In this work, we accomplish both by integrating ambipolar molybdenum ditelluride ($MoTe_2$) based field effect transistors (FETs) with a floating-gate stack, which can program the threshold voltage of the device in an arbitrary and non-volatile manner. Using this property, a pair of $MoTe_2$ FETs have been used to exhibit reconfigurable CMOS inverters, neuromorphic computing primitives such as sigmoid, hyperbolic tangent, and Gaussian neurons and synapses, and multi-bit analog encoding and modulation primitives such as frequency doubler, frequency quadrupler, frequency shift keying, and phase shift keying. While some of these computing primitives have been demonstrated in the past, they all use heterostructures with separate p- and n-type materials, and none integrates programmable and non-volatile memory. This is the first demonstration where a single semiconducting material has been used to achieve in-memory 2D CMOS capabilities for a wide range of computing paradigms.

1:50 PM G02
(Student) Near Sensor Security Based on Multifunctional Monolayer MoS_2 FETs Akhil Dodda, Nicholas Trainor, Joan M. Redwing and Saptarshi Das; The Pennsylvania State University, United States

With the emergence of the internet of things (IoT) and its critical role in our day-to-day lives, the risk of information loss or security threats has become a raging concern than ever before. Although conventional software crypto modules are powerful, they consume an enormous amount of energy in ciphering the information, necessitating the need for novel hardware cryptographic primitive. While hardware-based cryptographic modules exist, with the aging silicon technology and von Neumann bottleneck, innovation in materials, devices, and architectures is required in designing next-generation secure electronics. Acknowledging this need and deriving inspiration from nature, we here propose and experimentally demonstrate a low-power, bioinspired, crypto engine based on atomically thin and multifunctional MoS_2 field-effect transistors (FETs). We have fabricated an 8×8 crossbar array of a fully integrated crypto engine to encode 8×8-pixel images where each crypto engine comprises five monolithically integrated MoS_2 FETs (5T cell). Each transistor cell is locally back-gated using a gate-dielectric stack comprising of atomic layer deposition (ALD) grown 50 nm Al_2O_3 on sputter-deposited 50/20 nm Pt/TiN to accomplish sensing and encoding functionalities. All the back-gate islands were placed on a commercially purchased SiO_2/p^{++}-si substrate. Our entire hardware platform utilizes a total of 320 MoS_2 FETs to encode the 8×8-pixel images. We exploit the unique optoelectronic properties such as the photogating effect to sense the information from an external light source and combine it with a non-volatile programmable gate dielectric stack to encode

or encrypt the sensed information by adding different amounts of noise. The number of brute force trials required to decrypt the information was found to be significantly high of the order ~10^{33}. We further test the strength of the encryption by performing advanced machine learning attacks on the MNIST dataset by training deep neural networks with different hidden layers and have observed the inference accuracy to be ~20%, indicating the robustness and resilience of our proposed encryption scheme. Also, the amount of energy consumed in encrypting the information was found to be minuscule, in the range of a few hundreds of picojoules. Finally, to decipher the encrypted information we adopt a population voting-based algorithm, a phenomenon widely observed in biological species.

2:10 PM G03

Are Two-Dimensional Interfaces Really Flat? Zhihui Cheng[1,2], Huairuo Zhang[2], Son T. Le[2], Hattan Abuzaid[3], Guoqing Li[4], Linyou Cao[4], Albert Davydov[2], Aaron D. Franklin[3,3] and Curt A. Richter[2]; [1]Purdue University, United States; [2]National Institute of Standards and Technology, United States; [3]Duke University, United States; [4]North Carolina State University, United States

Two-dimensional (2D) van der Waals materials are subject to mechanical deformation and thus forming bubbles and wrinkles during exfoliation and transfer. A lack of interfacial "flatness" has implications for interface properties, such as those formed by metal contacts or insulating layers. Therefore, an understanding of the detailed properties of 2D interfaces, especially their flatness under different conditions, is of high importance. Here we use cross-sectional scanning transmission electron microscopy (STEM) to investigate various 2D interfaces (2D-2D and 3D-2D), and we characterize and compare the flatness of the hBN-2D and metal-2D interfaces down to angstrom resolution. It is observed that the dry transfer of hexagonal boron nitride (hBN) can dramatically alter the interface structure. When characterizing 3D metal-2D interfaces, we found that Ni-MoS_2 interfaces are more uneven and have larger nanocavities compared to other metal-2D interfaces. The electrical properties of an MoS_2-based field-effect transistor are correlated directly with the interfacial transformation in the contact and channel regions. The device transconductance is improved by 40% after the hBN encapsulation, likely due to the interface interactions at both the channel and contacts. Overall, these observations reveal the intricacy of 2D interfaces and their significant dependence on the processes used in their fabrication.

2:30 PM G04

The (Mostly) Unwelcome Guest in Transition Metal Chalcogenides—Native Oxidation and the Effects of Oxygen During Processing MoS_2, TiS_2 and Zr(S,Se)$_2$ Rafael Jaramillo; Massachusetts Institute of Technology, United States

Being a very hard anion, oxygen bonds very differently to transition metals than do the chalcogens. Trace oxygen in a transition metal dichalcogenide (TMD) has a substantial impact on material processing and properties, much more so than for instance trace selenium in a sulfide. Since oxygen is all around us, even in our high-vacuum chambers, it is essential to understand and control the effects of oxygen on processing 2D materials.

We report the results of several studies of the effect of oxygen on synthesizing TMDs. We find that lowering trace oxygen concentration in the reactor makes it possible to lower the processing temperature for large-area TiS_2 films, made by reacting Ti thin films with H_2S gas [1]. We quantify how lowering oxygen concentration enables faster metal sulfurization at lower temperatures (down to 500 °C), leading to thin films that are smooth and homogeneous. In contrast, we find the opposite trend for MoS_2: *adding* trace oxygen enables lower processing temperatures (down to 375 °C) for large-area MoS_2 films, made by sulfurizing Mo thin films [2]. We understand these contrasting effects in the light of particulars of Ti-O and Mo-O bonds, including molecular dynamics (MD) simulations that suggest that oxygen is a catalyst for Mo-S bond formation.

We also report studies of oxidation rates and mechanisms on freshly-cleaved surfaces of MoS_2 and Zr(S,Se)$_2$ [3]. MoS_2 surfaces remain pristine for over a year in laboratory ambient conditions, without a trace of oxide formation. Thermal oxidation of MoS_2 results in the formation of crystalline blocks of MoO_3, due to the high volatility of Mo oxides. We find that non-thermal methods of O_2 plasma processing are required to produce a conformal, amorphous native oxide on MoS_2. We report on advanced characterization of MoS_2 native oxides formed by thermal and plasma oxidation, including transmission electron microscopy (TEM) studies of structure and composition, and electrical properties measured by atomic force microscopy (AFM). In contrast to MoS_2, Zr(S,Se)$_2$ alloys oxidize rapidly, with the native oxide growing at a rate up to 0.5 Å/min in ambient conditions. MD simulations reveal the kinetic mechanisms that limit native oxide growth for MoS_2 and promote it for Zr(S,Se)$_2$, despite oxide formation in ambient conditions being thermodynamically-favorable in all cases.

[1] Y. Li, A. Singh, K. Reidy, S. S. Jo, F. M. Ross, and R. Jaramillo, *Making Large-Area Titanium Disulfide Films at Reduced Temperature by Balancing the Kinetics of Sulfurization and Roughening*, Advanced Functional Materials **30**, 2003617 (2020).

[2] S. S. Jo, Y. Li, A. Singh, A. Kumar, S. Frisone, J. M. LeBeau, and R. Jaramillo, *Formation of Large-Area MoS2 Thin Films by Oxygen-Catalyzed Sulfurization of Mo Thin Films*, Journal of Vacuum Science & Technology A **38**, 013405 (2019).

[3] S. S. Jo, A. Singh, L. Yang, S. C. Tiwari, S. Hong, A. Krishnamoorthy, M. G. Sales, S. M. Oliver, J. Fox, R. L. Cavalero, D. W. Snyder, P. M. Vora, S. J. McDonnell, P. Vashishta, R. K. Kalia, A. Nakano, and R. Jaramillo, *Growth Kinetics and Atomistic Mechanisms of Native Oxidation of ZrSxSe2–x and MoS2 Crystals*, Nano Lett. **20**, 8592 (2020).

2:50 PM G05

(Late News) What Limits Electronic Transport in 2D Transition Metal Dichalcogenides—Phonons or Defects? Yuanyue Liu; University of Texas at Austin, United States

2D transition metal dichalcogenides (MX2) have a low electron mobility at room temperature, while the origin is not clear. Phonons are defects are two major scattering sources, but their individual effects on the mobility are difficult to experimentally isolate and quantify, as they co-exist in samples.

First-principles methods are powerful tools to study materials under idealized conditions, and thus allow one to isolate and quantify the effects of phonons and defects. I will present our progresses in developing first-principles methods to more accurately and efficiently calculate the carrier mobility in 2D materials, and using them to understand the transport bottlenecks [1-3]. I will show the theoretical mobilities in the presence of phonons, and neutral/charged vacancies, and analyze their trends across different materials. I will also present some new 2D semiconductors with very high mobility, which may simulate experimental realization.

[1] Long Cheng, Chenmu Zhang, Yuanyue Liu*, "Why two-dimensional semiconductors generally have low electron mobility", Phys. Rev. Lett. 2020, DOI: 10.1103/PhysRevLett.125.177701

[2] L. Cheng, C. Zhang, Y. Liu*, "The Optimal Electronic Structure for High-Mobility 2D Semiconductors: Exceptionally High Hole Mobility in 2D Antimony", J. Am. Chem. Soc., 2019, DOI: 10.1021/jacs.9b05923

[3] L. Cheng, Y. Liu*, "What Limits the Intrinsic Mobility of Electrons and Holes in Two Dimensional Metal Dichalcogenides?", J. Am. Chem. Soc., 2018, 140, 17895-17900

3:10 PM Refreshment Break

3:30 PM G06

Comparison of Epitaxial Graphene Electrodes for Electrochemical Detection and Identification of Heavy Metals in Seawater

Jenifer R. Hajzus[1,2], Lisa C. Shriver-Lake[1], Scott N. Dean[1], Jeffrey S. Erickson[1], Daniel Zabetakis[1], Joel P. Golden[1], Daniel J. Pennachio[1,3], Scott A. Trammell[1] and Rachael L. Myers-Ward[1]; [1]U.S. Naval Research Laboratory, United States; [2]American Society for Engineering Education Postdoctoral Fellow, United States; [3]National Research Council Postdoctoral Fellow, United States

Underwater contaminants such as heavy metals, industrial compounds, herbicides, and pesticides can pose health risks to humans including toxic and carcinogenic effects. Electrochemical techniques using miniaturized, portable instrumentation can allow for inexpensive, real-time, on-site detection and monitoring of hazardous materials and environmental pollutants in water. The high electrical conductivity, high mechanical strength, low electronic noise, and high surface-to-volume ratio of graphene has motivated its use as a working electrode for such electroanalytical applications. Epitaxial graphene (EG) formed by sublimation of Si from SiC(0001) is particularly attractive because it can be produced as a continuous layer with low defect density over wafer-scale areas, does not require transfer to another substrate, and is compatible with semiconductor processing methods. In this study, EG electrodes with different properties are grown, processed, characterized and then evaluated as working electrodes in an electrochemical sensor for the detection and identification of heavy metals in seawater. Growth temperature and time were varied to produce nominally monolayer EG on on-axis 6H-SiC(0001), hydrogen-intercalated quasi-freestanding (QFS) bilayer EG on on-axis 6H-SiC(0001), and multilayer EG on 4° offcut 4H-SiC(0001). Atomic force microscopy (AFM) revealed differences in surface morphologies dependent upon SiC offcut angle. EG was characterized using Raman spectroscopy, x-ray photoelectron spectroscopy (XPS), and Hall measurements before and after exposure to short durations of 100 W microwave oxygen plasma. After oxygen plasma modification, Raman spectra exhibit D, D' and D+D' peaks associated with defects such as vacancies and sp^3 hybridization. Additionally, XPS shows an increase in intensity of peaks corresponding to C-O and C=O suggesting the formation of oxygen functional groups. The different EG working electrodes, with and without oxygen plasma modification, were mounted in an electrochemical cell and exposed to seawater samples spiked with Cd, Cu, Hg, or Pb. Machine learning models were used to identify the type of heavy metal based on cyclic square wave voltammograms.[1] It was found that hydrogen-intercalated, oxygen plasma-modified QFS bilayer EG performed best for correctly identifying heavy metals in seawater.

[1] Dean, S. N.; Shriver-Lake, L. C.; Stenger, D. A.; Erickson, J. S.; Golden, J. P.; Trammell, S. A. *Sensors (Basel)* **2019**, 19(10), 2392.

3:50 PM G07

Lattice Strain Induced Biosensing of SARS-CoV-2 Enabled by Quasi-Freestanding Epitaxial Graphene

Soaram Kim[1], Heeju Ryu[2], Sheldon Tai[3], Michael Pedowitz[1], John Robertson[4], Daniel J. Pennachio[5], Jenifer R. Hajzus[5], Donald Milton[3], Rachael L. Myers-Ward[5] and Kevin Daniels[1]; [1]University of Maryland, United States; [2]Vaccine and Infectious Diseases Division, Fred Hutchinson Cancer Research Center, United States; [3]Maryland Institute for Applied Environmental Health, University of Maryland School of Public Health, United States; [4]Fischell Department of Bioengineering, University of Maryland, United States; [5]US Naval Research Laboratory, United States

Severe acute respiratory syndrome coronavirus 2 (SARS-CoV-2), the virus responsible for Coronavirus disease 2019 (COVID-19), was classified as a pandemic in March 2020 by the World Health Organization (WHO), with over 300 million cases and 5.5 million deaths worldwide as of January 2022 [1]. The total deaths in the USA are expected to reach over 1,000,000 by May 2022 [2]. The current primary diagnosis of COVID-19 is real-time reverse transcription-polymerase chain reaction (RT-PCR), which is the fastest and most reliable method, for detection and pandemic containment. However, RT-PCR needs an RNA preparation process, which decreases the accuracy and sensitivity of the test, and takes over three hours to confirm the diagnosis. Thus, the direct detection of viral antigens from human to environmental conditions without the RNA sample preparation process is required for future ultra-fast and highly accurate immunological diagnostic methods.

Two-dimensional materials such as graphene are promising for the next generation of electronics, i.e., biological and chemical sensors in environmental and safety monitoring and medical health care systems [3]. In addition, atomically thin 2D graphene has an extremely high surface-to-volume ratio, the most vital parameter for sensing applications. Here we fabricated a heterostructure of SARS-CoV-2 S1 spike antibodies and epitaxial graphene (EG) on 6H silicon carbide (SiC) substrate for SARS-CoV-2 detection. We have combined the advantages of high sensitivity and fast response time of graphene with the high selectivity of antibodies to develop an ultrasensitive SARS-CoV-2 screening platform. A diagram of the fabrication procedure is shown in Fig. 1. Bilayer EG is grown by the thermal sublimation of silicon from silicon carbide, and subsequent hydrogen intercalation as previously demonstrated [4]. Reactive ion etching (CF_4) was used to pattern the EG, and by e-beam evaporation, metal electrodes (Ti/Au = 30/220 nm) were deposited. To functionalize the EG for the selective detection of SARS-CoV-2, a crosslinker (Poly-L-lysine) and SARS-CoV-2 S1 spike antibodies were immobilized on the EG surface. Samples were characterized by atomic force microscopy (AFM), X-ray photoelectron spectroscopy (XPS), and Raman spectroscopy to confirm EG substrate and heterostructure integrity. The electrical response of the sensor was measured using the Gamry 3000 Source/Measure Unit to investigate the sensor performance with SASR-CoV-2 samples.

AFM images of the heterostructure on SiC are shown in Fig. 2. The heterostructure was found to immobilize well onto the EG/SiC and withstand repeated cycles of characterization measurements. Figure 3 presents the (a-c) XPS and (d) Raman results of the heterostructure immobilized EG/SiC. These results indicate that the synthesized structures are indeed EG-based heterostructure with antibody/crosslinker. Furthermore, we investigated the sensor with Raman spectroscopy to see a shift in the graphene G-peak position in the heterostructure with antigen (1 ag/mL) as shown in Fig. 4. The G-peak was redshifted after binding of antigen-antibody in the heterostructure, which resulted from strain induced on the EG, leading to a large reduction in carrier concentration in graphene. The prepared sensor was tested with SARS-CoV-2 S1 spike protein and clinical samples and clearly distinguished between blank and SARS-CoV-2 at room temperature as shown in Fig 5. The sensor detected the SARS-CoV-2 spike protein antigen in a concentration as low as 1 ag/mL and infected patients' samples (exhaled breath aerosol) in concentrations as low as 60 copies/mL in seconds. In addition, the sensor demonstrated as a practical application of the portable sensor to detect the SARS-CoV-2 B.1.1.7 variant as shown in Fig. 6. The portable unit clearly distinguished variant positive saliva samples in 0.6 s at room temperature. Hence, this sensor has great potential as an ultrasensitive SARS-CoV-2 screening platform.

4:10 PM G08
Improved Density of GaAsSb Nanowires On Monolayer Graphene/SiO_2/Si for Near-Infrared Photodetector Application
Hirandeep Reddy Kuchoor, Surya Ratna Kiran Nalamati, Jia Li and Shanthi Iyer; North Carolina Agricultural and Technical State University, United States

In this study, we report the heterogeneous integration of GaAsSb nanowires (NWs) on graphene by utilizing the advantages of bandgap tunability of GaAsSb NWs and flexibility of graphene substrate for next-generation flexible near-infrared optoelectronic devices. We demonstrate the successful growth of high-quality, good density, and vertical $GaAs_{1-x}Sb_x$ NWs on monolayer-graphene/SiO_2/p-Si (111) using molecular beam epitaxy. The surface-functionalized graphene using mild O_2 plasma treatment improves the reactivity of semiconductor adatoms on the graphene surface. The increase in defect peak of the Raman mode, reduced surface conductivity, and formation of additional O_2 groups of surface-treated graphene compared to pristine graphene confirms the functionalization of graphene. The vertical yield of NWs on the graphene surface was enhanced by using the optimized plasma power and duration to increase the nucleation centers. In addition, the growth of higher Sb composition GaAsSb (x=0.4) stem helps to improve the vertical density further by shaping the Ga droplet on the graphene surface via the surfactant effect of Sb and provides a better lattice matching. An ensemble photodetector device in the near-infrared region has been demonstrated exhibiting an optical responsivity of 110 A/W with detectivity of $1.1*10^{14}$ Jones. These findings highlight the potential of GaAsSb NWs growth on graphene for flexible NIR PD devices that operate at room temperature, along with the performance metrics required for next-generation optoelectronic device applications.

4:30 PM G09
Degradation of CVD-Grown MoS_2 Subjected to DC Electrical Stress David M. Goggin, Elisabeth Mansfield and Robert Keller; National Institute of Standards and Technology, United States

Advancements in synthesis techniques allow for electronic-grade 2D materials to be produced at the wafer scale, enabling the fabrication of hundreds of 2D material-based devices in a single batch. Successful incorporation of new materials into large-scale manufacturing environments demands an understanding of the material structure and defects that can lead to device degradation, and sometimes failure, during operation. Device reliability is rooted in material reliability, which fundamentally refers to the stability of the atoms making up a material. Factors affecting material reliability include geometry, microstructure, chemistry, dimensional scale, proximity to other materials, and exposure to external stressors. In this talk, we show how defects in chemical vapor deposited (CVD) MoS_2 flakes can be precursors to material damage sustained during subsequent electrical stressing. Here, monolayer MoS_2 flakes were transferred to pre-patterned electrodes and subjected to a constant DC voltage for defined times. We observed that pre-existing defects oriented normal to the current flow were susceptible to growth in the direction of current flow, increasing in size with stressing time and magnitude of the electric field. Certain conditions yielded complete material failure in the form of open circuits. Our results demonstrate the importance of understanding how synthesis and processing can lead to material defects, and how such defects can compromise the performance and reliability of 2D material-based electronic devices.

4:50 PM G10
(Student, Late News) Reducing Schottky Barrier Height vs Width—Which is Most Effective in Improving Contact Resistance to Atomically Thin Semiconductors? Emanuel Ber[1], Ryan Grady[2], Eric Pop[2,2] and Eilam Yalon[1]; [1]Technion–Israel Institute of Technology, Israel; [2]Stanford University, United States
As atomically thin two-dimensional (2D) materials gain more attention due to their outstanding properties and extreme thinness it becomes apparent that high contact resistance (R_C) is one of their major drawbacks. The two parameters which determine R_C between metals and 2D semiconductors are the Schottky barrier height (Φ_B) and width (λ) [1]. Generally, decreasing λ by increasing the carrier concentration (n) [2] or decreasing Φ_B by Fermi level de-pinning [3] result in lower R_C. However, which approach reduces R_C more dramatically remains an open question. Moreover, the extent of R_C reduction and the relative effect of manipulating Φ_B and n is not widely understood. Here, we study R_C of monolayer MoS_2 by performing experimental analysis and Schottky barrier (SB) current modeling. We patterned test structures by e-beam lithography and used e-gun evaporated Ni as contacts to MoS_2 grown by chemical vapor deposition on SiO_2(90 nm)/Si(p++) substrates [4], where the Si serves as a back-gate. Temperature-dependent electrical characterizations such as I_D-V_{GS} and four-point probe measurements were used to determine the SB height of our devices. We explored the relative R_C contribution of Φ_B and λ by modifying an analytical metal-oxide-semiconductor field-effect transistor (MOSFET) model based on the Landauer-Büttiker formalism [5,6]. Namely, we calculate the transmission coefficient and number of transport modes with the following adjustments: the consideration of the van der Waals (vdW) gap between the metal and semiconductor, the derivation of the gate-dependent λ, and incorporation of the gate-induced band bending. This model was previously used only to analyze the subthreshold current, while our modifications allow its use in the on-state as well. We used the experimentally extracted Φ_B and n as the key parameters for comparison with our measurement data. Note that n affects not only λ, but also the number of transport modes.
Our modeled R_C and *I-V* characteristics exhibit good agreement with the measurements, and the well-known gate dependency, validating the model modifications. In the mid-range of R_C (~1 kΩ×μm) we observe a dependency on both Φ_B and n as there is no clear factor limiting the current. However, to reach desirably low R_C (< 200 Ω×μm) high carrier concentrations (low SB width) are required even for low SB heights, suggesting that high n is crucial in reducing R_C to 2D semiconductors. Interestingly, when n is increased beyond 3×10^{13} cm^{-2}, the R_C dependency on Φ_B weakens as the transmission coefficient becomes close to unity. This stems from the strong dielectric screening that dramatically reduces the SB width, which greatly increases the tunneling probability and makes the SB height a lesser determining aspect of the transmission coefficient. We thus see that the number of transport modes limit the current at low or near-zero Φ_B. We note that this could also limit edge contacts which potentially shunt the vdW gap. In conclusion, our work shows that although both the SB height and width generally determine R_C, the increase of carrier concentration is more consequential in reducing R_C. We found that for low R_C, the major current injection limiting factor is the number of transport modes (determined by n), while the transmission coefficient (and by extent Φ_B) has a lesser effect. Our results suggest that increasing the carrier concentration is a prerequisite for aggressively lowering R_C, for example $n > 5\times10^{13}$ cm^{-2} is needed to reduce R_C below 100 Ω×μm even for near-zero Φ_B. These findings provide a guideline for future contact engineering to atomically thin 2D semiconductors.
Refs: [1] C. Chang *et al*., *Solid State Elec*. 14, 541 (1971). [2] C. McClellan *et al.*, *ACS Nano* 15, 1587 (2021). [3] P. Shen *et al.*, *Nature* 593, 211 (2021). [4] K. Smithe *et al.*, *ACS Nano*. 11, 8456 (2017). [5] A. Penumatcha *et al*., *Nat. Comm*. 6, 8948 (2015). [6] S. Datta, Cambridge Univ. press, (1997).

SESSION H: Group III-Nitrides—Power Diodes and HEMTs

Session Chair: Andrew Armstrong
Wednesday Afternoon, June 29, 2022
Great Hall Meeting Room 3

1:50 PM H01

(Student) Defect Characteristics Under Devices and Reverse Leakage Current Investigated Using X-Ray Topography Yekan Wang[1], Michael E. Liao[1], Kenny Huynh[1], William Olsen[1], James C. Gallagher[2], Travis Anderson[2], Xianrong Huang[3], Michael Wojcik[3] and Mark Goorsky[1]; [1]University of California, Los Angeles, United States; [2]U.S. Naval Research Laboratory, United States; [3]Argonne National Laboratory, United States

In this work, we investigate defect characteristics, such as defect density and distribution in the substrate and epi-layer directly underneath vertical GaN Schottky diodes using x-ray topography and show their impact on the reverse leakage current. GaN Schottky diodes are fabricated using homoepitaxial GaN on HVPE substrate with dot-cores. The core positions, with a spacing of approximately 1 mm, are fixed by intentionally growing periodically patterned inversion domains prior to the bulk growth [1]. During HVPE growth, threading dislocations congregate at the cores and concentrate at the centers of cores while reducing dislocations in regions between the cores. The unique non-uniform but predictable defect distribution makes the dot-core wafer ideal for studying the impact of defects density on the performance of devices with otherwise identical structures.

Our method involves imaging the whole wafer after device fabrication by exposing separate pieces of film to different points along the X-ray rocking curve for the $(11\underline{2}4)$ GaN reflection ("single exposure images" [2]). Globally, the radius of curvature of the wafer is determined to be 34 m. Locally, periodic non-diffracting regions were observed around the core centers, where the defect density is high (up to 10^8 cm^{-2}). These highly tilted regions are misoriented more than 72 arcsecs away from the diffracting regions. Both the global radius of curvature and the amount of local lattice distortion are consistent with what we observed earlier in bare dot-core substrates [3]. In comparison, the regions in between cores, where the defect density is low (as low as 10^4 cm^{-2}), show uniform contrast with no lattice distortion. On the other hand, topography images show distinctive contrast from the metallization pattern and capture the outline of each individual device. Therefore, the distance of each device from the nearest core-center can be determined. Current-voltage (I-V) measurements performed on devices at different distances from the core-centers show that devices located far away (> 300 μm) from the core-centers have low leakage current, on the order of 10^{-7} A/cm^2 at a reverse bias of -10 V. However, as the device gets closer to the core-centers (< 150 μm), an increase in the reverse bias leakage by 2-4 orders of magnitude at -10 V is observed. The results from this study show that the substrate defect density and distribution directly affect the device leakage current and x-ray topography is an effective method for studying defect characteristics in the substrate and epi-layer underneath individual vertical GaN devices. If necessary, the non-destructive nature of x-ray would make it possible to screen the wafer prior to device fabrication and guide devices to regions with low defect density to achieve high performance.

This research was supported through the ARPA-E PNDIODES program under contract DE-AR0001116 at UCLA.

References

1. K. Motoki, SEI Tech. Rev., **70**, 28 (2010).
2. M. E. Liao, et al., ECS Trans., **98**(6), 15 (2020).
3. Y. Wang, et al., ECS J. Solid State Sci. and Technol., **10**, 045010 (2021).

2:10 PM H02

(Student) Investigation of the Nature and Origins of Area Defects in Gallium Nitride Substrate Wafers Yafei Liu, Hongyu Peng, Qianyu Cheng, Shanshan Hu, Zeyu Chen, Balaji Raghothamachar and Michael Dudley; Stony Brook University, The State University of New York, United States

Gallium Nitride (GaN) is one of the most promising wide band gap semiconductor materials that are replacing silicon (Si) in power electronic applications. However, the quality of the material is limiting its application in high performance power electronic materials. Apart from the threading dislocations reported in our previous studies [1-3], some area defects are observed in both ammonothermal GaN substrates and patterned hydride vapor phase epitaxy (HVPE) GaN substrate by synchrotron X-ray topography (XRT) (Figure 1). Information on the nature of these defects is important to prevent the formation of such defects and improve the crystal quality. Since the growth process of patterned HVPE GaN material involves the use of patterns of inverted GaN polarity on the growth template [4], the area defects are likely to be related to the formation of inversion domains. Ammonothermal GaN substrate wafers also show similar area contrast in XRT images. Therefore, it is possible that inversion domain likely formed during the ammonothermal growth process of GaN.

In this study, Nomarski optical microscopy (NOM), scanning electron microscopy (SEM), and high-resolution transmission electron microscopy (HRTEM) are adopted to investigate the nature of the area defects. Apart from XRT images, these domain features are visible in the NOM images (Figure 2). SEM images (Figure 3) show that the area defects are observed as a diffraction contrast instead of the orientation contrast. To investigate the atomic configuration of these domains, HRTEM of specimens sliced from the domains are being compared with those from outside the domains. The characterization results from TEM analysis in conjunction with observations from other techniques will be used to determine the nature of the area defects and their formation mechanisms will be deduced.

[1] B. Raghothamachar, Y. Liu, H. Peng, T. Ailihumaer, M. Dudley, F.S. Shahedipour-Sandvik, K.A. Jones, A. Armstrong, A.A. Allerman, J. Han, H. Fu, K. Fu, Y. Zhao, Journal of Crystal Growth 544 (2020) 125709.
[2] Y. Liu, B. Raghothamachar, H. Peng, T. Ailihumaer, M. Dudley, R. Collazo, J. Tweedie, Z. Sitar, F.S. Shahedipour-Sandvik, K.A. Jones, Journal of Crystal Growth 551 (2020) 125903.
[3] Y. Liu, H. Peng, T. Ailihumaer, B. Raghothamachar, M. Dudley, Journal of Electronic Materials 50 (2021) 2981-2989.
[4] T. Nakamura, K. Motoki, GaN substrate technologies for optical devices, IEEE, vol 101, 2013, p. 2221.

2:30 PM H03

Effects of Surface Defects on Vertical GaN Diode Performance James C. Gallagher[1], Michael Mastro[1], Mona Ebrish[2], Alan G. Jacobs[1], Brendan Gunning[3], Robert Kaplar[3], Karl Hobart[1] and Travis Anderson[1]; [1]U.S. Naval Research Laboratory, United States; [2]National Research Council, United States; [3]Sandia National Laboratories, United States

GaN is one of the most promising wide bandgap semiconductors for high power applications due to its wide bandgap, critical electric field and electron mobility giving it the potential to surpass Si and SiC technology. However, to unlock the full potential of GaN would require perfecting its manufacturing process. Such a process would require a quick, non-destructive technique capable of full wafer mapping.

Since GaN wafer and epitaxial growth technology has not been perfected, most wafers come with localized defects that alter the electrical properties. Many of them can be detected using surface topography techniques such as a wafer scale optical profilometry

measurement. An advantage of this technique is that it can be performed at micron resolution across full wafers in less than a few hours. However, the presence of benign defects with minimal effect on the diode properties presents a significant challenge. This talk will focus on using data analysis techniques for estimating the yield of vertical GaN diodes with comparison to experimental results.

Though qualitative results can be used to predict which surface defects cause failure (for example, pits in the samples that are several microns deep), it is difficult to develop a computer algorithm which accurately evaluates the whole sample. One method involves identifying defects using a generalized extreme studentized deviate test for outliers. The yield can be estimated by calculating the probability of a randomly placed devices being on a defect, and has shown to be 70% accurate at predicting the failure rate. Another method involves intentionally avoiding the defective areas by using lithography to isolate the defects from the rest of the sample, which has been found to make wafer scale diodes. The third method involves training a machine learning model using the optical profilometry as the input data and the current-voltage sweep of the diodes as the output parameter. This method was found to be 91% accurate at predicting forward bias behavior, though a larger training set is needed to predict reverse bias behavior accurately.

This work is supported by the Office of Naval Research.

2:50 PM H04

(Student) Correlating Optical Characteristics and Electrical Performance of Vertical GaN-on-GaN PN Diodes Yuxuan Zhang[1], Vishank Talesara[1], Matthias A. Daeumer[2], Zhaoying Chen[1], Jae Hyuck Yoo[2], Qinghui Shao[2], Andrew Lange[2], Ted Laurence[2], Wu Lu[1] and Hongping Zhao[1,1]; [1]The Ohio State University, United States; [2]Lawrence Livermore National Laboratory, United States

GaN is advantageous for high power electronic applications because of its large bandgap (3.4 eV), high critical electric field (3.4 MV/cm) and high electron mobility (~1200 cm^2/Vs). Vertical GaN PN diode with 5kV breakdown voltage has been demonstrated [1]. The material quality and doping of the thick n^--GaN drift layer represent the key parameters that determine the device performance. Therefore, it is critical to probe and understand the fundamental correlation between material properties and device performance including on-resistance (R_{on}), reverse leakage current (I_R) and breakdown voltage (V_{BR}).
In this work, systematic studies were performed on free-standing HVPE GaN substrates, MOCVD GaN epifilms, and vertical GaN PN diodes, to correlate material properties with device performance. The cathodoluminescence (CL) imaging on GaN substrate revealed three representative regions: (i) dislocation cores originated from the HVPE lateral overgrowth; (ii) coalescent regions; and (iii) inadequate coalescent regions (voids). The threading dislocation densities (TDD) in adequate coalescent regions are estimated as 2×10^6 cm^{-2} while that of the dislocation cores can be higher than 10^8 cm^{-2}.
Room temperature CL spectra showed the highest near band-edge emission (NBE) at the coalescent regions (P1), and much lower NBE with a prominent 520 nm defect peak at the dislocation cores (P3). CL imaging performed on the MOCVD n-GaN epifilm showed that most threading dislocations propagate from the substrate into the epilayer. The dislocation density in the dislocations cores reduces after n-GaN epitaxy. Moreover, new defects with extended dimension were generated after n-GaN epitaxy. Room temperature photoluminescence (PL) with 405 nm laser excitation was utilized to perform the wafer-scale PL mapping. The region in dislocation cores showed low PL intensity, indicating the dominant non-radiative recombination. High PL intensities were observed around the voids regions and the coalescent boundaries, indicating strong radiative recombination in these regions.
To correlate the GaN material properties with vertical PN diodes device performance, a diode structure was grown on a 2” HVPE GaN substrate with 8 µm n-drift layer (Si: $2x10^{16}$ cm^{-3}), 500 nm p-GaN layer and 20 nm p^+-GaN layer. Forward and reverse bias measurements indicate that devices located in the coalescent regions have relatively lower leakage currents and higher breakdown voltages. Specifically, devices with 500 µm diameter located in the coalescent regions have an average V_{BR} of 1194 ± 165 V and I_R of (8.1±0.8) × 10^{-8} A/cm^2, while the V_{BR} and I_R of devices on dislocation clusters are 1014 ± 120 V and (2±0.4) × 10^{-7} A/cm^2. Devices with diameter of 100 µm exhibit more prominent location dependence: V_{BR} of 1282 ± 40 V and I_R of (1.13±0.1) × 10^{-6} A/cm^2 (coalescent region); 1037 ± 27 V and (1.49 ± 0.4) × 10^{-6} A/cm^2 (dislocation clusters).
In summary, systematic studies were performed to correlate the fundamental GaN-on-GaN material properties with the vertical GaN PN diodes device performance. Optical characterization (PL and CL) and electrical measurements (I-V) reveal higher reverse leakage current and lower breakdown voltage for devices fabricated on dislocation clusters.
Acknowledgment: This work was performed under the auspices of the U.S. Department of Energy by Lawrence Livermore National Laboratory under Contract DE-AC52-07NA27344, and DOE ARPA-E (DE-AR0001036).
References:
[1] H. Ohta, et al, Jpn. J. Appl. Phys. 58, SCCD03 (2019).

3:10 PM Refreshment Break

3:30 PM H05

(Student) Interface Trap Density Characterization of ALD Gate Dielectrics for GaN Power MOSFETs Caleb Glaser[1,2], Andrew Binder[1], Luke Yates[1], Andrew Allerman[1], Daniel Feezell[2] and Robert Kaplar[1]; [1]Sandia National Laboratories, United States; [2]The University of New Mexico, United States

This study analyzes the changes in the density of interface traps (DIT) for various atomic layer deposition (ALD) gate dielectric films on gallium nitride (GaN) devices fabricated on bulk GaN substrates. Each film type has been chosen with an optimized insulator/semiconductor interface obtained through chemical cleans or post deposition annealing (PDA). Reduction in dielectric leakage and interface traps in MOSCAP devices may be used in order to understand how these mechanisms affect more complex devices such as vertical GaN MOSFETs.
GaN MOSFET and MOSCAP devices are often investigated and implemented in power systems with applications ranging from electric vehicles (EVs) to smart power grids. The unique material properties of GaN such as wide bandgap, high breakdown voltage, and high electron mobility create unique advantages over traditional silicon FETs. Vertical GaN MOSFETs are better suited for higher voltage applications due to current flow and voltage drop perpendicular to the surface while also reducing required chip area for high operating voltages. Although there are many advantages of vertical GaN devices, such an architecture presents unique challenges that must be addressed before such devices may be implemented in high power applications, such as the requirement for a native substrate and the need to improve the gate dielectric interface. The interface between the gate dielectric and the semiconductor is crucial in order to reduce threshold voltage drift, leakage current, and the density charge traps. Previous work has shown the importance of DIT reduction with chemical cleans and PDAs. Accurate calculations of the density of interface traps (DIT) are vital to fully realize device operation and reliability. The choice between surface cleans and dielectric annealing as a leakage reduction technique is dependent on the material and available processing capabilities. While PDAs may reduce the dielectric breakdown strength, they have been found to reduce gate leakage

current and improve device performance for most gate dielectrics. Several methods have been proposed for DIT characterization, including the voltage dependencies of low- and high-frequency capacitance (CV), conductance (GV), and surface potential (Ψ_sV). DIT may be calculated from the surface potential of the dielectric using the quasi-static capacitance and the capacitance of the chosen gate dielectric. This work uses quasi-static CV and surface potential electrical characterization of GAN MOSCAPs to determine DIT of various gate dielectric materials treated with PDAs and chemical cleans. Optimization of such films on MOSCAPs will allow for implementation into vertical GaN MOSFET architectures. Interface trap density may be reduced by decreasing the capacitance associated with defects and surface contamination or by selection of a dielectric material with a lower dielectric constant. Fixed charges at the dielectric/semiconductor interface are manifested in hysteresis between forward and reverse voltage sweeps and may be the result of contamination prior to ALD or point defects in the material. Al_2O_3 is an attractive gate dielectric material due to its dielectric constant, which may improve breakdown strength (Fig. 1), but it may suffer from higher memory charge between continuous bias sweeps. SiO_2 ALD films have lower breakdown and significantly lower leakage currents but show the lowest density of remaining fixed charges between sweeps, suggestive of the lowest DIT of the tested dielectrics (Fig. 2) with the addition of PDA. Results were verified by altering bias conditions during testing in order to accumulate and deplete interface charges. Minor plateaus in capacitance in forward bias indicate the presence of negative fixed interface charges. Additional characterization may be necessary to determine the optimal conditions for DIT reduction for HfO_2 films, including reduction in PDA temperatures in combination with improved substrate chemical cleans.

3:50 PM H06

(Student) Thermodynamic and Band Structure Study of ScxAl1-xN Mahlet Molla and Emmanouil Kioupakis; University of Michigan–Ann Arbor, United States

III-nitrides like AlN have light-emitting and charge carrying abilities that have led to applications in short-wavelength light emitters and high electron mobility transistors (HEMTs). Issues with lattice constant as well as polarization mismatch between III-nitride heterostructures however, have led to the need to alloy AlN with ScN[1], [2]. Recent work has found that $Sc_xAl_{1-x}N$ alloys at certain compositions have enhanced piezoelectric response which allows the coercive electric field for ferroelectric polarization switching to be below its dielectric breakdown limit [3], [4]. Therefore, the strain and polarization tunability of $Sc_xAl_{1-x}N$ would grant further applications in electronic and optoelectronic devices that would not be possible with AlN.

ScN exists in the rocksalt structure while AlN exists in the wurtzite structure, so the $Sc_xAl_{1-x}N$ alloy has shown to be stabilized in several crystal structures depending on the Sc composition. Understanding the phase and thermodynamic stability of $Sc_xAl_{1-x}N$ alloy is critical to obtain a good baseline for studying its electronic and multiferroic properties. In this work, we performed first-principles calculations based on hybrid density functional theory (DFT) and special quasi-random structure (SQS) methodology to study the ground-state thermodynamic and electronic properties of $Sc_xAl_{1-x}N$ as a function of Sc composition. We utilized DFT calculations to obtain the formation energy of $Sc_xAl_{1-x}N$ alloy in cubic, hexagonal, and wurtzite structures for multiple different Sc compositions. The most stable crystal structure for each composition was determined and the corresponding electronic band structure was calculated. This work provides a holistic view of the thermodynamic stability of $Sc_xAl_{1-x}N$ alloys, an insight into the ferroelectric polarization switching mechanism, and the impact of Sc on the electronic band structure.

1. A. Khan, K. Balakrishnan, and T. Katona, Nat. Photonics 2, 77 (2008).
2. S. Zhang, D. Holec, W. Y. Fu, C. J. Humphreys, and M. A. Moram, J. Appl. Phys. 114, 133510 (2013).
3. P. Wang, D. Wang, N. M. Vu, T. Chiang, J. T. Heron, and Z. Mi, Appl. Phys. Lett. 118, 223504 (2021).
4. S. Fichtner, N. Wolff, F. Lofink, L. Kienle, and B. Wagner, J. Appl. Phys. **125**, 114103 (2019).

4:10 PM H07

(Student) Fabrication of Flexible AlGaN/GaN HEMTs Using Laser Liftoff Md Didarul Alam, Kamal Hussain, Grigory Simin, MVS Chandrashekhar and Asif Khan; University of South Carolina, United States

We report on the first demonstration of flexible AlGaN/GaN high electron mobility transistors (HEMTs) by successful transfer from sapphire substrate to copper tape on flexible polyethylene terephthalate (PET) using excimer laser-based liftoff (LLO). The structural integrity of the heterojunction was preserved during LLO as supported by the marginal decrease in electron mobility (μ_n) from 1670 to 1630 cm^2/Vs as well as the unchanged sheet carrier concentration (n_s) of ~9.8×10^{12} cm^{-2} before and after transfer. The devices exhibit maximum drain current density ($I_{DS,max}$) of 422 and 332 mA/mm before and after transfer, respectively. This ~21% degradation in maximum current density after transfer, primarily due to the thermal effect because of the large difference in thermal conductivities between sapphire (34.6 W/mK) and adhesive on copper tape (0.2 W/mK), is lower than that of other reported transfer techniques on similar substrates without heat spreaders. Under external applied strain, the piezotronics effect of the flexible HEMTs was also investigated. $I_{DS,max}$ of flexible HEMT increased from 332 to 384 mA/mm under tensile stress with a radius of curvature 0.5 cm, and the threshold voltage (V_{th}) shifted negatively by ~0.2 V. This new transfer technique demonstrates the capability of large-scale, low-damage flexible GaN HEMT. This proposed approach is also expected to pave the way for the realization of ultrawide bandgap (UWBG) AlGaN-channel flexible HEMT for electronics needing high-temperature, high-frequency, and high-power applications.

The AlGaN/GaN heterostructures used in this study were grown on a c-plane double side polished (DSP) sapphire substrate by metal-organic chemical vapor deposition (MOCVD). The epitaxial structure consists of a 30 nm GaN nucleation layer, a 1.8 µm unintentionally doped GaN buffer layer, a 1 nm AlN spacer, and a 20 nm $Al_{0.24}Ga_{0.76}N$ barrier layer. This buffer layer also serves as the channel layer for the device epilayers. After fabrication, the epitaxial side of the sample was bonded to a UV tape and a 193 nm excimer laser was used to remove the DSP sapphire followed by the cleaning of the exposed GaN surface with 1:1 dilute HCl. The GaN surface was bonded to a copper tape on PET substrate and the UV tape was removed after curing it in a UV chamber. Involvement of any harsh chemicals or processing is not needed in this technique resulting in intact and low-damage transfer.

Material and electrical characterizations were done before and after transfer onto copper tape. The full width at half maximum (FWHM) values on sapphire and copper tape are 302 and 345 arcsec, respectively suggesting low-damage transfer process. The n_s were measured from frequency-dependent capacitance-voltage (C-V) characteristics. From the transmission line model (TLM) measurements before and after transfer, the contact resistances (R_c) are found to be 0.59 and 0.64 Ω-mm, respectively while the sheet resistance (R_{sh}) increased slightly from 380 to 390 Ω/sq. The μ_n was extracted from the values of R_{sh} and R_c before and after transfer. After transfer, the V_{th} shifted negatively from -3.5 to -3.6V. The maximum transconductance ($g_{m,max}$) values for devices on sapphire and copper tape are 0.11 and 0.08 S/mm, respectively. Moreover, the change in 2DEG density under bending based on the

change in current density in the saturation region is in good agreement with the measurement results.

In this paper, we will present the details of our LLO process and characterization of the fabricated flexible AlGaN/GaN HEMT structures.

4:30 PM H08

Efficient N-Type Ion Implantation Activation in GaN with High Mobility Alan G. Jacobs[1], Boris N. Feigelson[1], Jennifer K. Hite[1], Joseph Spencer[1,2], Marko Tadjer[1], Karl Hobart[1] and Travis Anderson[1]; [1]US Naval Research Lab, United States; [2]Virginia Tech, United States

Gallium nitride (GaN) is the leading material for next generation high power devices owing to its superior figures of merit over current state of the art materials as well as increasing market share in RF applications generating economies of scale. Among the challenges persisting for ease of commercialization include the efficient ion implant activation for n-type, p-type, and durable semi-insulating materials while maintaining the quality and low unintentional doping of unimplanted material. This remains difficult due to instability of GaN at ambient pressures for temperatures high enough to remove ion implant damage and activate dopants, often leading to material degradation and excess unintentional carriers. Here we demonstrate efficient activation of ion implanted silicon in GaN while maintaining film quality and low carrier density of unimplanted material.

Unintentionally doped Ga-polar GaN templates were grown on sapphire 2.2 microns thick by MOCVD. Ion implants were made approximating a 300nm deep, ~1e19 cm^{-3} box profile, with a localized surface concentration of 5e19cm^{-3} to facilitate contacts, for a total dose of 5e14cm^{-2}. Implants were performed at ambient and high temperature (500°C) as well as with an additional matching nitrogen implant to maintain stoichiometry and reduce vacancy formation. Annealing was done via Symmetrical Multicycle Rapid Thermal Annealing (SMRTA) at temperatures up to 1550°C at moderate pressures (~30 bar) where GaN is thermodynamically stabilized to ~1000°C. Successful stabilization of the metastable GaN material up to 1550°C was achieved with a combination of the moderate pressure, a protective PECVD SiNx cap, and rapid heating and cooling at rates up to 300 K/s during SMRTA. Contacts were made using typical Ti/Al/Ni/Au and measured as deposited with a typical measured specific contact resistance of order 10^{-5} ohm-cm^2 by TLM.

Contrary to initial expectations, high temperature silicon implants did not prove advantageous and produced poor mobility with a greater sheet carrier concentration than the implanted dose indicating significant damage generation and retention after annealing. Compensation with room temperature co-implanted nitrogen after the high temperature silicon proved beneficial but still inferior to the ambient temperature silicon implant alone. Implantation of silicon at room temperature yielded a maximum mobility of 160 cm^2/Vs, beyond 90% activation efficiency, while maintaining the unimplanted UID material quality with consistent mobility to the as-grown material and electron concentrations from 10^{16} to 10^{17} cm^{-3}. Sequential co-implantation with both silicon and nitrogen at room temperature exhibited slightly reduced mobility compared to silicon alone while the activation efficiency was comparable indicating that the additional defects generated from the nitrogen implant proved equally or more deleterious than any benefit from maintaining material stoichiometry. The high mobility achieved and low UID carrier concentrations show both the ability to maintain undoped crystal quality and produce low compensation, high quality implanted and doped films for high power devices enabling new device topologies and freeing device designers from the difficulties and drawbacks of regrowth.

4:50 PM H09

(Student) N-Polar GaN/AlGaN High Electron Mobility Transistor Structures on Single-Crystal AlN Substrates Zexuan Zhang[1], Jimy Encomendero[1], YongJin Cho[1], Jashan Singhal[1], Kazuki Nomoto[1], Masato Toita[2], Huili Grace Xing[1] and Debdeep Jena[1]; [1]Cornell University, United States; [2]Asahi Kasei Corporation, Japan

High electron mobility transistors (HEMTs) built on wide-bandgap semiconductor platforms are leading contenders in high-power mm-wave electronics [1-3] with current state-of-the-art performance achieved using N-polar GaN/AlGaN HEMTs with output powers above 8 W/mm at up to 94 GHz.[2] The performance of N-polar III-N HEMTs could be further improved by increasing the Al content in AlGaN barrier. Because of the large bandgap (6 eV) and high thermal conductivity (~ 340 W/mK) of AlN, incorporating Al-rich AlGaN buffer layer has the advantages of enhanced thermal management and a maximized conduction band offset to reduce buffer leakage and short channel effects.[1] Due to smaller lattice mismatch to Al-rich AlGaN compared with GaN substrates, single-crystal AlN substrates are ideal platform for the realization of GaN/AlGaN HEMTs with Al-rich AlGaN barriers thanks to the low dislocation densities ($<10^4$ /cm^2) and the absence of undesired thermal boundary resistance (TBR) unlike AlN templates.
We report the epitaxy of undoped pseudomorphic N-polar GaN/AlGaN heterostructures on single-crystal N-polar AlN substrates by plasma-assisted molecular beam epitaxy (MBE). A schematic layer structure is shown in Fig. 1(a). Three samples with GaN channel thickness varied from 5 nm to 10 nm are studied. A band-diagram simulation suggests the presence of a high-density two-dimensional electron gas (2DEG) at GaN/AlGaN interface [Fig. 1(b)]. Another parallel channel with lower electron density could also exist at the bottom AlGaN/AlN interface (not shown). Fig. 1(c-d) shows the 10×10 and 2×2 um^2 atomic force microscopy (AFM) images on the as-grown surface of the sample with 8 nm GaN. The presence of atomic steps suggests the step-flow growth mode. Similar surface morphology is observed for the other two samples. Fig. 1(e) shows the measured X-ray diffraction (XRD) pattern. The clearly visible interference fringes suggest the abrupt hetero-interface. The reciprocal space maps (RSM) further suggest that the GaN and AlGaN layers are fully strained to the underlying AlN (not shown).
Temperature dependent Hall-effect measurements were conducted in van der Pauw geometry on as-grown heterostructures with indium dots as the contacts. The red circles in Fig. 2 (a) show the 300 K electron density as a function of GaN channel thickness. The electron densities show almost no change while cooling down to 77 K, as expected for polarization-induced 2DEG. The measured electron densities match well with the calculated values at GaN/AlGaN interface [gray dashed line in Fig. 2 (a)] with the surface Fermi level at ~ 0.4 eV below GaN conduction band.[4] Fig. 2 (b) shows the dependence of 300 (red circles) and 77 K (blue circles) electron mobility on channel thickness. A sharp drop (~ 50%) in electron mobility is observed when the GaN channel thickness decreases to 5 nm. Similar behavior reported in N-polar GaN/AlGaN HEMTs on GaN platform [5-6] is attributed to a stronger interface scattering when channel thickness scales down. The measured electron densities with AlN buffer layers in this work (red triangles) are higher than those with GaN buffer layers [5-10] (blue circles) due to a higher Al-content in the AlGaN barrier [Fig. 2(c)]. Meanwhile, comparable sheet resistances of ~ 400-600 Ω/sq at room temperature are achieved. We believe this is the first experimental demonstration of high mobility 2DEG in N-polar GaN/AlGaN structures on AlN platform.

1. A. Hickman, *Semicond. Sci. Technol.* **36**, 044001 (2021)
2. B. Romanczyk, *IEEE Electron Device Lett.* **41**, 349 (2020)
3. K. H. Hamza, *Int. J. Electron. Commun.* **116**, 153040 (2020)
4. L. Janicki, *Sens. Actuators B Chem.* **281**, 561 (2019)
5. H. Li, *Appl. Phys. Lett.* **112**, 073501 (2018)

6. U. Singisetti, *Appl. Phys. Lett.* **101**, 012101 (2012)
7. S. Diez, *Appl. Phys. Lett.* **117**, 042102 (2020)
8. S. Keller, *J. Appl. Phys.* **104**, 093510 (2008)
9. M. H. Wong, *Phys. Stat. Sol. (a)* **204**, 2049 (2007)
10. S. Rajan, *J. Appl. Phys.* **102**, 044501 (2007)

SESSION I: Silicon Carbide Materials and Characterization

Session Chairs: Daniel Ewing and Nadeemullah Mahadik
Wednesday Afternoon, June 29, 2022
Archie M. Griffin West Ballroom

1:30 PM I01
Exploring SiC CVD Growth Parameters Compatible with Remote Epitaxy on Epitaxial Graphene Substrates Daniel J. Pennachio[1], Jenifer R. Hajzus[2], Andrew C. Lang[3], Rhonda M. Stroud[3] and Rachael L. Myers-Ward[3]; [1]NRC Research Associate at the U.S. Naval Research Laboratory, United States; [2]ASEE Research Associate at the US Naval Research Lab, United States; [3]U.S. Naval Research Laboratory, United States

Remote epitaxy is a promising new technique for epitaxial film removal and substrate reuse that utilizes monolayer graphene as a release layer [1]. Epitaxial graphene (EG) natively grown on SiC(0001) substrates through Si sublimation is an ideal platform for remote epitaxy of wide bandgap (WBG) semiconductors due to its compatibility with commercially-viable WBG semiconductor growth and processing, negating the requirement of transferring the EG to another substrate. In addition, EG has reduced defect density compared to CVD-grown graphene, providing a clearer system for investigating remote epitaxy without influence of direct epitaxy through breaks in the graphene layer. However, the SiC CVD process is typically conducted with conditions that would damage or remove graphene. This study investigates the effect of CVD growth conditions on SiC/EG/SiC(0001) remote epitaxy and optimizes CVD parameters to produce high-quality SiC epilayers while reducing damage to the EG barrier. In addition, since the effect of EG features such as SiC macrostep morphology and associated layer inhomogeneity on the RE process is currently unknown, EG/SiC substrate preparation and associated morphology is varied to explore its effect on SiC epilayer formation.
Semi-insulating nominally on-axis 6H-SiC(0001) and n-type 4° off-axis 4H-SiC(0001) substrates were used to produce different SiC surface morphologies and EG layer numbers. Ar:H_2 process gas flow ratio, growth precursor C/Si ratio, and growth temperature were optimized during hot-wall CVD remote epitaxy to promote smooth film morphology. Nomarski optical microscopy, scanning electron microscopy, and atomic force microscopy found growths at 1620°C with Ar/H_2 ratios <20/5 slm, and C/Si ratios <1.55 to have the smoothest surface morphology and fewest polytype inclusions. Substrates with offcuts <0.5° from SiC(0001) exhibited lower epilayer macrostep density, but showed evidence of polytype impurities and 3D growth at C/Si ratios > 1.0. Point defect density in RE SiC epilayers was able to be reduced by using graphene grown in the same run as the SiC epilayer rather than using graphene substrates grown in a separate growth chamber. Cross-sectional TEM was utilized to assess the growth interface and EG layer integrity after CVD growth. Through this study, optimal SiC RE growth conditions are suggested for a balance of EG survivability and SiC film morphology.
[1] Kim, Y., Cruz, S., Lee, K. *et al. Nature* **544,** 340–343 (2017).
Distribution A: Approved for public release; Distribution unlimited

1:50 PM I02
Expansion of BPDs from Star-Shaped Defects in 4H-SiC
Nadeemullah Mahadik[1], Robert E. Stahlbush[1], Jake Soto[2] and Bruce Odekirk[2]; [1]Naval Research Laboratory, United States; [2]Microchip Technology Inc., United States

Silicon Carbide (SiC) power devices are being widely used for electric vehicles, traction control and other high power applications due to its superior breakdown field and thermal conductivity compared to silicon, which results in lower losses, compact system, and low system cost. For wider SiC adoption, long term device reliability must be addressed and related issues need to be investigated. Basal plane dislocations (BPDs) in SiC generate stacking faults (SF), which leads to forward voltage degradation in bipolar devices. SFs also cause increased reverse bias leakage and higher on-state resistance in all SiC devices. Recently a star-shaped defect was reported to cause device degradation in SiC gate turn-off thyristors (GTO) [1]. This defect was reported by Lee et. al. [2] to originate from a core region with high threading dislocations and extending with six arms of dislocation arrays (DA) along the *'a'* directions. The six DAs are consistent with a prismatic slip: a/3 <11-20>{1-100}. Such prismatic slip was also observed to generate BPDs and SFs along *'a'* directions originating from micropipes [3]. Since the defect has a smaller highly defective core, its influence on devices was mostly observed in a limited region. However, expansion of defects from the core and the six spoked DAs have not been investigated. This could cause reliability issues over a significantly larger region of the wafer. In this work, we investigate the expansion of SFs emanating from the star-shaped defect and its six DAs as well as secondary DAs using ultraviolet photoluminescence (UVPL) and x-ray topography (XRT).
For this work, 150 mm diameter SiC wafers with 10 mm thick n-type epitaxial layers were commercially obtained. Whole wafer UVPL imaging was performed to observe extended defects using a custom system equipped with a 355 nm quasi-continuous excitation laser, automated XYZ sample stage, and a LN_2 cooled camera connected to microscope setup with 660 nm long pass filter. XRT imaging was performed using Rigaku XRTMicron system with 70 mm microfocus Cu/Mo rotating anode, collimating mirror, reflection/transmission sample stage and a high resolution x-ray camera. High resolution UVPL imaging with higher UV excitation was performed at the star-defect to expand SFs from BPDs in both the substrate as well as epitaxial layer.
Five star defects were observed in UVPL wafer map. As previously reported [1], they appear as having a center core of dislocations and six DAs emanating from it. However, we also observed secondary DAs from some of the primary DAs, which also lie in one of the *'a'* directions making an angle of 60º with the primary DA. Some of the core regions appeared bright and some were dark. Upon further UV excitation, the bright core star defects generated SFs which expanded throughout the epitaxial layer. The dark core star defects did not generate SFs until a higher intensity UV power of ~1000 W/cm^2 was used. This indicates that the bright core star defects had generated BPDs inside the epitaxial layer, whereas the dark core ones had BPDs inside the substrate only. The high intensity UV causes faulting of BPDs inside the substrate and the SFs enter the epitaxial layer and expand up to the surface. Furthermore, high intensity UV excitation also resulted in SF generation at the intersection of primary and secondary DAs. Details of the expansion behavior as well as depth resolved section x-ray topography will be presented.

[1] Y. Cui et. al., Materials, 12 (2019) 4042
[2] Lee et. al., Mater. Sci. Forum, 527-529 (2006) 403
[3] Wang et. al.J. Cryst. Growth, 401 (2014) 423

2:10 PM I03

(Student) Analysis of Strain Gradient in High Energy Implanted 4H-SiC Epi Wafer by Synchrotron X-Ray Rocking Curve Topography Zeyu Chen[1], Yafei Liu[1], Hongyu Peng[1], Qianyu Cheng[1], Shanshan Hu[1], Balaji Raghothamachar[1], Michael Dudley[1], Reza Ghandi[2], Stacey Kennerly[2] and Peter Thieberger[3]; [1]Stony Brook University, The State University of New York, United States; [2]Ge Research, United States; [3]Brookhaven National Laboratory, United States

Silicon Carbide (SiC) is a wide bandgap semiconductor, which has been widely applied to power electronics due to its excellent properties of wide band gap, high break down voltage and thermal stability. High voltage superjunction devices are necessary for realization of hybrid aircraft and intelligent power systems. Ghandi and coworkers have demonstrated 2 kV superjunction PIN diode with single 12um epilayer by novel high energy implantation system at Brookhaven National Laboratory (BNL) [1, 2]. Implantation employing high energy Al ions, can create lattice strain in the wafer by displacing the Si and C atoms. To characterize the nature of lattice strains in 4H-SiC wafer implanted with Al ions at energy range of 13 MeV to 65MeV, synchrotron X-ray rocking curve topography (SXRCT) [3] has been employed. With utilization of Si (331) beam conditioner in tandem with Si(111) double-crystal monochromator, the angular resolution of synchrotron X-ray topography (XRT) is increased by an order of magnitude. Using this setup, the recorded rocking curves reveal multiple diffraction peaks with an angular separation of only 2 arcseconds are observed on the topographs, indicating inhomogeneous strain distribution across the implanted layer. Using Rocking-curve Analysis by Dynamical Simulation (RADS), the strain profile of the implanted layer is obtained, showing a relatively lower strain near the surface and bottom of the implanted layer, while center of the layer has relatively uniform strain. This result shows a strong correlation with the results from SIMS analysis of the doping profile.

Reference:

1. R. Ghandi, C. Hitchcock, S. Kennerly, Medium-voltage sic devices for next generation of power conversion. ECS Transactions 104, 67 (2021)
2. P. Thieberger, C. Carlson, D. Steski, R. Ghandi, A. Bolotnikov, D. Lilienfeld, P. Losee, Novel high-energy ion implantation facility using a 15 mv tandem van de graaff accelerator. Nuclear Instruments and Methods in Physics Research Section B: Beam Interactions with Materials and Atoms 442, 36-40 (2019)
3. J. Guo, Y. Yang, B. Raghothamachar, M. Dudley, S. Stoupin, Mapping of lattice strain in 4h-sic crystals by synchrotron double-crystal x-ray topography. Journal of Electronic Materials 47, 903-909 (2018)

2:30 PM I04

Analysis of Dislocations in 4H-SiC Wafers Using Synchrotron X-Ray Topography Hongyu Peng, Zeyu Chen, Yafei Liu, Qianyu Cheng, Shanshan Hu, Balaji Raghothamachar and Michael Dudley; Stony Brook University, The State University of New York, United States

SiC is a promising material in power devices due to its superior physical properties. However, the defects in the material may harmfully influence the performance of the devices. Therefore, it is essential to investigate the defects such as dislocations in SiC. Threading screw/mixed dislocations (TSD/TMD) in 4H-SiC usually show elliptical white contrast in synchrotron X-ray grazing incidence topography [1,2] while they show circular white contrast in back reflection topography [3]. However, in synchrotron X-ray rocking curve topography (RCT), the contrast of TSD/TMD is dramatically changed since the rocking curve width of the SiC sample is narrowed by an order of magnitude to 2.5 arecseconds. Therefore, the minute lattice distortion (at the scale of 1 arcsecond) further away from the dislocation core will significantly reduce the diffracted intensity. Consequently, additional white contrast outside the enclosed ‘ellipse’ arises, indicative of the sign of the Burgers vector. Moreover, the contrast of the dislocations changes as the diffraction angle deviates from the perfect Bragg angle in all these three experiments (grazing incidence, back reflection and RCT). By carrying out ray-tracing simulations with modified diffraction intensity that track the rocking curve of the sample, the contrast of the dislocations under any diffraction conditions can be calculated. This indicates that the contrast of the dislocation in grazing incidence, back reflection and rocking cure topography either under strong diffraction condition or weak diffraction conditions can be described by the orientation contrast model [4].

References:

[1] W. M. Vetter, H. Tsuchida, I. Kamata and M. Dudley, J. Appl. Cryst. (2005). 38, 442–447
[2] J. Guo, Y. Yang, F. Wu, J. Sumakeris, R. Leonard, O. Goue, B. Raghothamachar, M. Dudley, J. Cryst. Growth, 452 (2016) 39–4340
[3] X. R. Huang, D. R. Black, A. T. Macrander, J. Maj, Y. Chen and M. Dudley, High-geometrical-resolution imaging of dislocations in SiC using monochromatic synchrotron topography, Appl. Phys. Lett. 91, 231903 (2007)
[4] M. Dudley, X. R. Huang & W. Huang, Assessment of orientation and extinction contrast contributions to the direct dislocation image, J. Phys. D: Appl. Phys. 32, A139 (1999)

2:50 PM I05

(Student) Determination of Effective Penetration Depths on Synchrotron X-Ray Topographic Images of Dislocations Lying on the Basal Plane in 4H-SiC Crystals Qianyu Cheng, Hongyu Peng, Shanshan Hu, Zeyu Chen, Yafei Liu, Balaji Raghothamachar and Michael Dudley; Stony Brook University, The State University of New York, United States

The demand for power electronic devices fabricated from silicon carbide (SiC) has increased rapidly in recent years for a diverse range of existing and emerging applications. The development of device technology highly depends on the quality of substrate and epitaxial material and the number of deleterious defects within, as those are critical factors that impact the device performance and long-term reliability [1, 2]. Therefore, understanding the nature of defects is of great importance for preventing the degradation or premature breakdown of devices. Synchrotron X-ray topography (XRT) is a well-known non-destructive approach for detailed analysis of dislocation configurations and density calculations in SiC wafers [3]. The grazing incident geometry which is commonly employed to record X-ray topographs reveals defect information from within the effective penetration depth of the X-rays. Several approaches to estimate the penetration depth were discussed in earlier studies [4, 5]. However, a universal method to determine the effective penetration depth for all dislocation types remain unclear.

In this study, a procedure to define this effective penetration depth is demonstrated by investigating physical vapor transport (PVT) grown off-axis 4H-SiC crystals through preforming systematic analysis of topographic and ray-tracing simulated contrast of dislocations with different Burgers vector and line direction combinations lying on the basal plane. The topographic images are recorded through synchrotron monochromatic beam in grazing incidence geometry. The simulation model is based on the principle of orientation contrast mechanism [6, 7] and developed by considering both the effects of surface relaxation [8] and X-ray absorption [9, 10] for evaluating the contributed factors of dislocation contrast formation. Analysis of the results indicates the observable dislocation contrast depends on the effective misorientation associated with the dislocation modulated by the photoelectric absorption effect. The dislocations with larger effective misorientation are associated with longer projected lengths and corresponding deeper effective penetration depths. A

more simplified factor based on an approximate expression for the misorientation is also introduced in this study as an alternative to the full ray-tracing simulation approach. The effective penetration depth determination method presented in this study enables three-dimensional dislocation configuration analysis and accurate density calculations.

Reference:
1. Das, H., et al., Materials Science Forum, 2019. 963: p. 284-287.
2. Kimoto, T., et al., Understanding and reduction of degradation phenomena in SiC power devices. in 2017 IEEE International Reliability Physics Symposium (IRPS). 2017.
3. Raghothamachar, B., et al., X-ray topography techniques for defect characterization of crystals, in Springer Handbook of Crystal Growth, G. Dhanaraj, et al., Editors. 2010, Springer: Berlin, Heidelberg. p. 1425-1451.
4. Dudley, M., et al., Nuclear Instruments and Methods in Physics Research Section B: Beam Interactions with Materials and Atoms, 1989. 40-41: p. 388-392.
5. Ishiji, K., et al., Japanese Journal of Applied Physics, 2017. 56(10): p. 106601.
6. Dudley, M., et al., Journal of Physics D: Applied Physics, 1999. 32(10A): p. A139-A144.
7. Huang, X.R., et al., Journal of Applied Crystallography, 1999. 32(3): p. 516-524.
8. Peng, H., et al., Journal of Applied Crystallography, 2021. 54(2): p. 439-443.
9. Fujie, F., et al., Acta Materialia, 2021. 208: p. 116746.
10. Ailihumaer, T., et al., Materials Science and Engineering: B, 2021. 271: p. 115281.

3:10 PM Refreshment Break

SESSION J: Nanoscale Characterization

Session Chairs: Lincoln Lauhon and Luis Miaja Avila
Wednesday Afternoon, June 29, 2022
Archie M. Griffin West Ballroom

3:30 PM J01
EUV Pulsed Atom Probe Tomography of β-Ga_2O_3 Semiconductor Materials Luis Miaja Avila[1], Benjamin Caplins[1], Ann Chiaramonti[1], Ming-Hsun Lee[2], Kris Bertness[1], Rebecca L. Peterson[2] and Norman Sanford[1]; [1]National Institute of Standards and Technology, United States; [2]University of Michigan, United States

Ga_2O_3 is an attractive ultra-wide bandgap semiconductor material due to its applications in optoelectronics and high-power devices [1]. Accurate measurements of the composition, dopants, and impurities in Ga_2O_3-based devices is of critical importance. Atom probe tomography (APT) is one of the analytical tools used to measure the composition of materials; however, recent APT measurements of III-nitride semiconductor materials have revealed compositional biases on such systems [2,3].
In this work we perform compositional APT studies on unintentionally doped β-Ga_2O_3 using a commercial APT instrument and a custom-built extreme ultraviolet (EUV) APT. While the commercial near-UV (NUV) APT system utilizes a 355-nm laser to induce field ion evaporation, in the custom system we replaced the near-ultraviolet laser in a straight flight-path atom probe tomograph with a coherent EUV light source and a vacuum beamline. With these modifications, we were able to illuminate the specimen's tip with 30-45 eV energy photons [4].
In our EUV APT measurements we maintain a constant ion detection rate while varying the EUV pulse energy by approximately two orders of magnitude (x120) and sample standing voltage. Our results show an underestimation of the oxygen composition when performing APT experiments under high EUV pulse energy or low E-field conditions. Compositional values closer to stoichiometric are obtained when performing experiments under high E-field conditions. These results are similar to recently published results with a NUV APT instrument [5]. These NUV experiments were performed at 100 kHz laser repetition rate, for this reason we performed additional studies with a commercial NUV APT instrument at 25 kHz. A careful compositional analysis comparison between the NUV and EUV systems will be discussed.
Our EUV APT data also shows the existence of unintentionally doped Si in the β-Ga_2O_3 sample. This is of importance as technologically-relevant devices with Si implantation are under development [6]. Further studies will focus on EUV APT reconstructions of Si-implanted β-Ga_2O_3.

References
[1] M. Higashiwaki et al., Semicond. Sci. Technol. 31, 034001 (2016)
[2] L. Mancini, N. Amirifar, D. Shinde, I. Blum, et al., J. Phys. Chem. C. 118, 24136 (2014)
[3] R.J.H. Morris, R. Cuduvally, D. Melkonyan, et al., Ultramicroscopy 206, 112813 (2019)
[4] A.N. Chiaramonti, L. Miaja-Avila, P.T. Blanchard, et al., MRS Advances 4, 44-45 2367 (2019)
[5] F. Chabanais, E. Di Russo, A. Karg, et al., Microscopy and Microanalysis 27, 687 (2021)
[6] M. Higashiwaki, Phys. Status Solidi RRL 15, 2100357 (2021)

3:50 PM J02
(Student) STM Simulation of High Aspect Ratio Tunneling Behavior on the Example of *In Situ* Harvested GaAs Nanowire Moritz Hansemann, Dorothee S. Rosenzweig and Holger Eisele; Technische Universität Berlin, Germany

In general, for scanning tunneling microscopy (STM) investigations the actual tip shape is negligible beyond the assumption of being reasonable sharp and the investigated topological differences are small in comparison with the tip. This assumption does no longer hold true, as soon as the size of the investigated structures get into the regime of the tip apex diameter. In this presentation, we show how through simulation of the physics of the tip- sample-system, we can explain the non trivial influence of the tip shape on a STM single scan line. Thus, we were able to reproduce STM measurements taken on GaAs nanowires (NW) with a diameter of 90 nm using this simulation. The simulation uses Monte-Carlo integration to approximate the tunneling current and simulates the resulting scanning process accordingly. The code is written in Python 3.8 using the numpy library. The program is not tailored to this explicit example, but rather simulates a specific tip geometry scanning a defined surface. It accepts the tip geometry and surface topology as a list of points respectively. Each point is then treated as an individual atom. An additional parameter can be added to each atom, which is used in the tunneling current calculation. Thus it is possible to create electrical differences for specific atoms, which could be used to represent chemical contrast. Although there is no individual calculation of an actual tunnel current. The calculated tunnel current is simply based on a precalculated function, which only depends on the distance
between a tip atom and a surface atom and the respective chemical parameters. This is sufficient for a first order approximation for the scanning behavior, although a sophisticated poison-solver could be added at this step, to increase the accuracy of the simulation in specific situations One major insight gained by the simulation is that in cases, in which the tip diameter exceeds the NW diameter, the resulting scan line images the tip geometry in the sidewall regions of the NW instead of the NW topology. This results in an image, in which the NW appears to be much broader than its actual size/width, but with the height roughly in the right size. This

simulation can be generalized to other scanning probe techniques by exchanging the electron tunneling with the actual interaction of the respective technique.

4:10 PM J03
(Student) Atomic Resolution Scanning Tunneling Microscopy Studies of Oxidized Cu(100) Surfaces Seth Shields and Jay Gupta; The Ohio State University, United States

Copper oxide based catalysts have the promising capability to selectively reduce CO_2 into useful products, however the details of the mechanism are not well understood. Scanning tunneling microscopy (STM) studies performed on oxidized Cu(100) single crystal surfaces allow for the investigation of the fundamentals of this process on an atomic scale. The well understood Cu(100)-O $(2\sqrt{2}\times2)$R45° missing row reconstruction is an initial oxidation step and acts as a starting point for our investigation of more highly oxidized surfaces. These surfaces were prepared by annealing a Cu(100) single crystal in 10^{-6} mbar O_2 between 80-275 °C, and then further UHV annealing at 150 °C. In addition to flat terraces, the surface also became more highly faceted, with grains 10s to 100s of nm high. Atomic-resolution STM imaging revealed a new hexagonal surface lattice, qualitatively consistent with Cu_2O(111), but with significant uniaxial strain.Tunneling spectroscopy of the new oxide surface indicates a gap-like feature of roughly 1.5 V, somewhat less than the bulk Cu_2O gap of ~ 2.2 eV. These studies emphasize the sensitivity of copper oxidation to initial conditions and sample history. After STM structural and electronic characterization of the surfaces, CO_2 was dosed in situ under cryogenic (77 K) conditions. Individual CO_2 molecules were not observed, however scratchiness in the imaging following deposition indicates physiosorbed CO_2 , likely being perturbed by the apex of the tip during scanning.

4:30 PM J04
(Student) GaAs(110) Surface Modifications by Adsorption Hydrogen at Room Temperature and Above Dorothee S. Rosenzweig[1], Moritz Hansemann[1], Michael Schnedler[2], Philipp Ebert[2] and Holger Eisele[1]; [1]Technische Universität Berlin, Germany; [2]Forschungszentrum Jülich GmbH, Germany

Zincblende III/V nanowires typically exhibit non-polar (110) surfaces as side facets [1]. For the nanoscopic analysis of such facets, hydrogen cleaning is a common procedure to achieve examinable surfaces. While this is reported to be destruction free [2] and achieving clean, atomically flat surfaces, as they are present directly after MBE growth, the actual process and dynamics during the cleaning procedure are rarely examined. From surface investigations without real space resolution in the 1980es [3] it is well known, that the introduction of hydrogen to such surfaces is rather destructive.

Therefore, we studied the GaAs(110) surface and its modifications as model system introduced by hydrogen at room temperature and under commonly used cleaning conditions by STM and STS.For depiction and measurement at the atomic scale, we used scanning tunneling microscopy and spectroscopy under UHV conditions. Using these methods we study the geometric arrangement of the adsorbed atoms as well as adsorbation induced additional electronic states, band bending, defect states and Fermi level pinning. For the experiments, we used *n*-type and *p*-type highly doped GaAs single crystals with carrier concentration of $2x10^{18}$ cm^{-3} and $1.6x10^{18}$ cm^{-3}, respectively.

Atomically resolved STM images of both clean surfaces are presented. Both cleavage surfaces are planar without noticeable steps. Defects on the *n*-type surface are identified as adatoms, those on the *p*-type surface are identified as As vacancies. At room temperature, at the *n*-type surface, Ga vacancies develop from the replacing of one Ga atom from the surface lattice to an adatom on top of the surface. Both defects are negatively charged, therefore they cannot recombine. At higher temperatures, defect formation rate is increased. Hydrogen cleaning treatment at 400°C leads to etching off the surfaces; especially adatoms are removed rapidly. Only thermally stable defects remain. As a result, there are only the Ga vacancies left on the *n*-type surfaces. *p*-type surfaces form As vacancies with increasing density over time. Therefore, the removed As atoms desorb quickly. Hydorgen exposure of 1 L (langmuir) at room temperature to both surfaces introduce an increase of defect density as well as a diversity of defect appearances. At cleaning temperatures, we find the surface of *n*-type GaAs with a distinctly different appearance: The defect density is severely reduced, some monoatomic steps are left to the surface and the defects have a much more uniform appearance.

Scanning tunneling spectra of the clean GaAs(110) surface and the GaAs(110) surface with adsorbed hydrogen are shown. For *n*-type material the apparent band gap is reduced to only 0.9 eV due to an additional accumulation current covering the band onset on the valence band side. In the hydrogen adsorbed and hydrogen cleaned surfaces' spectra, this covering is lifted by an additionally introduced state. This state also introduces a shift in the pinning level but does not change the fundamental bandgap of the material. Therefore, the state can only be related to the defects shown in the images. For the *p*-type material there is no accumulation current shown in the spectra of the clean surface. While additional hydrogen does not change the fundamental band gap or the onsets of the bands in general, there is an additional state visible on the conduction band side reaching into the band gap. These finding have severe consequences on the hydrogen cleaning procedure of III/V semiconductor surfaces.

[1] Motohisa et al., Phys. E **23**, 298 (2004)
[2] Webb et al., Nano Lett. **15**, 8, 4865–4875 (2015)
[3] MHamedi et al., Semicond Sci Technol **2** 418 (1987)

4:50 PM J05
(Student) A Near-Adiabatic Rapid-Sweep (NARS) Approach to Electrically Detected Magnetic Resonance (EDMR) and Near-Zero-Field Magnetoresistance (NZFMR) Fedor V. Sharov[1], Brian R. Manning[2] and Patrick M. Lenahan[1]; [1]The Pennsylvania State University, United States; [2]Keysight Inc., United States

Although magnetic resonance has unrivaled analytical power for the identification of atomic scale defects in semiconductors and insulators, its application in nanoscale device structures has been limited. The resonance technique called electrically detected magnetic resonance (EDMR) has been of substantial utility in investigation of very small devices. However, its potential could be increased with further improvements in sensitivity and time resolution.
In this presentation, we demonstrate: (1) a new method for improved EDMR data acquisition, using near-adiabatic rapid-sweep (NARS) [1] methodology, and (2) near-zero-field magnetoresistance (NZFMR) [2] spectroscopy, as well as how this detection scheme could be used to further investigate non-steady state effects. The NARS methodology significantly improves the sensitivity and data acquisition rate of EDMR in small device structures. The NZFMR technique additionally allows measurements to be made in structures with significant metallization.
In NARS EDMR, the central magnetic field is held constant at or around resonance, as the modulation coils provide triangular sweeps through resonance at high frequency. We accomplished this via the implementation of a digital feedback linearization scheme, into a custom-built rapid-scan software, allowing for such measurements to be performed at high-frequencies on commercially available resonators with only minor electrical modification to a typical electron paramagnetic resonance (EPR) system. This results in scan-averaging rates on the order of the

measurement frequency.
We present X-band data showing NARS EDMR spectra on a-Si:H capacitors and 4:H-SiC/SiO_2 MOSFETs that are undistorted and identical to both spin-dependent recombination (SDR) [3] and spin-dependent trap-assisted tunneling (SDTAT) [4] continuous wave (CW) EDMR spectra that are less sensitive to noise. This experimental set-up preserves the CW-EDMR line shape and chemical information, while providing the potential for a boost in sensitivity and time-resolution, with few changes to the experimental apparatus.
We utilize essentially the same data acquisition system to detect NZFMR. In our NZFMR measurements, we utilize the mixing of singlet and triplet states at near-zero fields. NZFMR utilizes the mixing of states at near-zero fields due to local magnetic field interactions. NZFMR has been modeled using Wagemen's two-site hopping model [5] and the stochastic quantum Liouville equation (SQLE) in the past define a steady-state solution for traditional slow-sweep NZFMR experiments. This approach has been used to identify important chemical devices in semiconductor devices, such as nuclear hyperfine constants and kinetic rates [2,6]. We demonstrate a comparison of both continuous-wave and NARS NZFMR measurements in a-Si:H capacitors.
A great advantage of NZFMR is that there is no radio-frequency microwave radiation and only very small magnetic fields are required. The NZFMR response can be interpreted to provide much of the analytical power present and far more expensive and complex EDMR and conventional EPR measurements in systems in which such measurements would be essentially impossible. In combination, NARS and NZFMR could be used as a tool to observe changes in defect concentrations of packaged device systems at high time resolution, such as integrated circuits.
Citations
[1] A. W. Kittell *et al., J. Magn. Reason.*, **211**, 228-233 (2011).
[2] Harmon *et al.*, *IEEE Trans. Nucl. Sci*., **67**, 1669-1673 (2020).
[3] T. Aichinger *et al.*, *Appl. Phys. Lett.*, **101**, 083504 (2012).
[4] M. A. Anders *et al.*, *J. Appl. Phys.*, **124**, 215105 (2018).
[5] W. Wagemans *et al.*, *J. Appl. Phys.* **103**, 07F303 (2008).
[6] E. B. Frantz *et al.*, *J. Appl. Phys.* **130**, 065701 (2021).

SESSION K: Metasurfaces and Structured Photonics

Session Chairs: Joshua Caldwell and Aaron Muhowski
Wednesday Afternoon, June 29, 2022
Ohio Staters Inc. Founders Room

1:30 PM K01
(Student) Meta-Optic Accelerators for Object Classifiers
Hanyu Zheng[1], Quan Liu[1], You Zhou[1], Ivan Kravchenko[2], Yuankai Huo[1] and Jason Valentine[1]; [1]Vanderbilt University, United States; [2]Oak Ridge National Laboratory, United States

Digital neural networks (NNs) and the availability of large training datasets have allowed for rapid progress in the performance of machine-based tasks for a wide range of applications including image analysis, sound recognition, and natural language translation. The enhanced capability has, however, come at a computational cost as increased complexity and accuracy have necessitated the need for ever larger deep neural networks (DNNs). One alternative to DNNs is the use of optical processors that have the advantages of ultra-fast processing times and low energy costs. These systems can be employed as stand-alone processors or as front-end accelerators for digital systems. In either case, optical systems are most impactful when used for the linear matrix-vector multiplications that comprise the convolution operations in DNNs as these are often the most computationally burdensome components typically comprising more than 90% of the required floating-point operations (FLOPs) in popular CNNs. In the case of image analysis, free-space approaches are attractive as spatial multiplexing can be readily achieved as well as the fact that an optical front-end can potentially be integrated directly with an imaging system.
The most traditional approach to free-space based optical image processing is the use of 4*f* optical correlators where spatial filters, either passive or dynamic, are placed in the Fourier plane of a 2-lens optical system. Recorded spatial features are then fed to a lightweight digital NN back-end for classification. An alternative approach is the use of diffractive neural networks which utilize cascaded diffractive elements as convolutional layers. Image classification is realized through redistribution of optical energy on the detector plane requiring minimal digital processing. The tradeoff is the need for several diffractive layers as well as coherent illumination, precluding use with ambient lighting. While these approaches have shown benefits in terms of processing speed and energy consumption, they necessitate enlarged imaging systems. Furthermore, none of these approaches utilize the additional information channels, such as polarization, that are available when utilizing an optical front-end.
Here, we demonstrate the use of meta-optic based optical accelerators that serve as the convolutional front-end for a hybrid image classification system. Spatial multiplexing is achieved by using a multi-channel metalens for image duplication and a metasurface-based convolutional layer. This system has the advantage of being compact while the use of metasurfaces allows for additional information channels, in this case, polarization, to be accessed enabling both image and polarization-based classification. The hybrid network utilizes end-to-end design such that the optical and digital components are co-optimized while also incorporating statistical noise resulting in a robust classification network. We experimentally demonstrate the classification of the MNIST dataset with an accuracy of 92% as well as 94% accurate classification of polarized MNIST digits. Due to the compact footprint, ease of integration with conventional imaging systems, and ability to access additional information channels, this type of system could find uses in high-dimensional imaging, information security, and machine vision.

1:50 PM K02
Probing Long-Range Coupling in Plasmonic Metasurfaces via Far-Field Diffraction Milan Palei, John Haug and Anthony Hoffman; University of Notre Dame, United States

The optical properties of metamaterials and metasurfaces result from engineered sub-wavelength structures rather than the constituent materials. For these designer materials, the permittivity and permeability can be tailored to realize hyperbolic dispersion, negative refraction, non-trivial topological photonic states, and more. For most metamaterial and metasurface designs, optical coupling between neighboring meta-atoms is weak. For designs that do leverage coupling, the interactions are often localized to the nearest neighbor meta-atoms. Increasing this range of this coupling provides an additional degree of freedom in the design of the metasurface and could enable new non-trivial topological photonic states that rely upon long range coupling.
In this work, we present a plasmonic metasurface that couples as many as 18 meta-atoms via traveling surface waves. The metasurface is the result of dual-scale engineering, where coupled sub-wavelength ridges are designed to support propagating surface modes with hyperbolic dispersion and coupling between the ridges of finite length is controlled via wavelength-scale engineering, Fig. 1(a). The finite length ridges that support multi-plasmon modes correspond to the meta-atoms in our metasurface.
We fabricate large arrays ($5{\times}5$ mm^2) of Ag metasurfaces on Si substrate using electron beam lithography and standard metal lift-off. In total, we fabricate 20 samples, each compromising Ag ridges of different lengths, L, ranging from 160 nm to 800 nm. For all the samples presented here, the lateral spacing is 90 nm. The

lateral spacing controls the dispersion of a propagating surface mode. The separation in longitudinal direction of the ridges, which controls coupling between the meta-atoms, is varied from 50 nm to 2.5 um

To determine the range of the coupling between meta-atoms, we measure the far-field diffraction pattern of the fabricated metasurfaces using continuous-wave lasers that emit at 473, 532, and 633 nm, a curved projection screen, and a camera, Fig. 1(b). For l = 532 and 633 nm, bright far-field peaks corresponding to primary order diffraction peaks (i.e., m = +1, 0, -1) are observed at angles predicted by diffraction theory. In addition to these primary peaks, we also observe dimmer secondary diffraction peaks for all three wavelengths. The number and angular position of these secondary diffraction peaks is related to long-range coupling between meta-atoms, and the number of coupled meta-atoms can be determined using Laue diffraction theory for a finite crystal. The recovered coupling range is shown by the blue diamonds in Fig. 1(c). To further understand the observed phenomena, we develop an analytical model that incorporates a decaying propagating surface mode that couples the meta-atoms, solid line in Fig. 1(c). The model incorporates loss in the propagating mode due to absorption and non-unity coupling between meta-atoms, Fig. 1(d). We incorporate realistic parameters into the model obtained using COMSOL Multiphysics (there are no free parameters) and observe good agreement with our measurements. This approach to long-range coupling in metasurfaces could be leveraged as an additional degree of freedom in metasurface design, enabling applications in ultra-flat beam steering, structured illumination imaging, and topological photonics. Additionally, our approach to determining the coupling range offers a new approach to metasurface characterization.

2:10 PM K03

Electromagnetics and Photonics in the Age of Digital Manufacturing Raymond C. Rumpf; The University of Texas at El Paso, United States

Digital manufacturing is revolutionizing the manufacturing industry. Recent breakthroughs in hybrid 3D printing by the EM Lab at the University of Texas at El Paso have made it possible to build three-dimensional parts composed of any distribution of metals, dielectrics, and other materials. This talk will cover some of the new and exciting applications in circuits, electromagnetics, photonics, and metamaterials that are being enabled by digital manufacturing.

Electrical circuits can be made three-dimensional where components are placed at any position xyz and oriented at any angle theta-phi. Interconnects can meaner along smooth paths throughout all three dimensions. This creates new degrees of freedom for layout and routing that can make circuits more compact, smaller, and lighter. Shorter trace lengths reduce parasitic impedance to improve power efficiency and increase bandwidth. 3D circuits can be manufactured into unconventional form factors and exploit physics, such as dielectric anisotropy, not easily accessed by planar circuits.

Another breakthrough by the EM Lab allows periodic structures to be bent, twisted, conformed, and otherwise spatially varied without deforming the size, shape and spacing of unit cells. Such deformations would weaken or erase the electromagnetic and optical properties of the lattices. The technology was first applied to photonic crystals where discoveries were made that led to the tightest bend of unguided optical beam, refractionless lenses, and photon funneling. The technology was next applied to metamaterials to develop a tool to generate metamaterial lattices for devices designed by transformation optics. The technology is now being used to generate periodic structures across doubly-curved surfaces.

2:30 PM K04

Electroplated Helical Slow-Wave Structures for Millimeter-Through-THz Vacuum Electronic Devices Anjali Chaudhary[1], Divya J. Prakash[2], R B Jacobson[1], Donald Savage[1], Shiva Hajitabarmarznaki[3], Daniel Weide[3], Max Lagally[1] and Francesca Cavallo[2,2]; [1]University of Wisconsin–Madison, United States; [2]The University of New Mexico, United States; [3]University of Wisconsin-Madison, United States

We report our recent results on scalable fabrication of helical slow wave structures (SWSs) applicable in millimeter-through-THz traveling wave tube amplifiers (TWTAs) [1]. The structure is unique in that it has microscale diameter dimensions, a helical geometry, and potentially higher electrical/thermal conductivity than other previously reported self-assembled helices. We fabricate the SWSs by self-assembly of a metal nanomembrane (NM) and electroplating of the helical film, thereby overcoming the inherent trade-off between NM thickness and helix diameter/pitch. Here we focus on our recent efforts on understanding and controlling electrodeposition on freestanding and curved NMs. In particular, we investigate the effect of varying current and temperature on the thickness of the deposited film and its uniformity. In addition, we characterize and justify any changes occurring in the geometry of the helix due to electrodeposition.

Fabrication of microscale SWSs started with defining NMs strips by optical lithography, metal evaporation, and lift-off. In our work we used Cr/Au/Cr NMs that have an inherent stress gradient across their thickness. We defined the metal strips onto a bulk Si substrate coated with a sacrificial or release layer such as Ge or GeO_x. The released NMs self-assembled into helices with a diameter between 100 and 200 mm upon selective etching of the sacrificial layer by a XeF_2 plasma. Helix diameter and pitch are controlled by varying the thickness, the elastic modulus, the residual stress, and the in plane geometry of the NMs. The electroplating procedure employs a two-electrode electrochemical setup with the self-assembled helix and a platinized mesh serving as cathode and anode, respectively. A sulphate-based gold solution is used for the process. We use pulsed current source with variable frequencies to obtain uniform electrodeposition of an Au film with a thickness of 1-2 mm depending on the electrodeposition parameters. In all investigated electroplating conditions, we observed uniformly deposited gold with lower roughness than the skin depth of the metal at THz frequencies, which are crucial attributes to minimize losses and heating in a TWTA based on the helical SWS.

Reference

[1] Prakash, Divya J., Matthew M. Dwyer, Marcos Martinez Argudo, Mengistie L. Debasu, Hassan Dibaji, Max G. Lagally, Daniel W. van der Weide, and Francesca Cavallo. 2020. "Self-Winding Helices as Slow-Wave Structures for Sub-Millimeter Traveling-Wave Tubes." ACS Nano, 2021, 15, 1229-1239. doi:10.1021/acsnano.0c08296.

Work supported by U.S. AFOSR-Award No. FA9550-19-1-0086

SESSION L: Gallium Oxide Growth

Session Chairs: Lisa Porter and Hongping Zhao
Wednesday Afternoon, June 29, 2022
Ohio Staters Inc. Traditions Room

1:30 PM L01

(Student) Epitaxial Growth on β-Ga2O3 (110) Substrate by Plasma-Assisted Molecular Beam Epitaxy Takeki Itoh, Akhil Mauze, Yuewei Zhang and James S. Speck; University of California, Santa Barbara, United States

Epitaxial growth of β-Ga_2O_3 with outstanding crystal quality has been performed on different crystal orientations such as (100),

(010), and (-201) via plasma-assisted molecular beam epitaxy (PAMBE) [1]. So far, most of the research on crystal growth and device fabrication has been performed on (010) substrates. However, investigation of surface morphologies on (010) substrates has revealed that (110) facets are revealed the chevron consistent features in reflection high-energy electron diffraction (RHEED) studies, which indicates (110) is a natural plane in β-Ga_2O_3 [2]. Figure 1 shows atomic models of (110) and (010) planes projected along [001] direction [3].

UID β-Ga_2O_3 epitaxial films were grown on Sn-doped ([Sn] = ~5×10^{18} cm^{-3}) (110) substrates via PAMBE while (010) substrates were co-loaded as growth reference. The temperatures of the substrates were kept at 600 °C and 700 °C. To optimize the growth condition, the Ga flux was changed from 3×10^{-6} Torr to 2.5×10^{-7} Torr which was measured by beam equivalent pressure (BEP). Prior to the growth, O polishing and Ga polishing were performed to remove the residual impurities from the surfaces. For characterizations, the film thickness was determined by measuring high-resolution X-ray diffraction (HRXRD). The surface morphology of the epitaxial films was measured by atomic force microscopy (AFM).

Figure 2 shows the RHEED pattern of (110) and (010) substrates after Ga polishing. Streaky patterns were observed from the surface of (110) substrates, which indicates atomically flat surface. Conversely, crossed lines (red guideline) corresponds to (110) and equivalent (-110) facets were observed from [001] azimuth on (010) substrate. Figure 3 shows the HRXRD result of the epitaxial film grown on (110) substrates. Clear thickness fringes indicate abrupt interface between β-Ga_2O_3 and β-$(Al_{1-x}Ga_x)_2O_3$ spacer layers. Figure 4 shows the growth rate dependence on Ga flux (010) and (110) substrates at 600 °C and 700 °C. In the O-rich regime, growth rates increase linearly with Ga flux. In the plateau regime, there was still too low excess Ga flux to have reduced growth rate. We expect higher Ga flux to yield reduced growth rates. The growth rates of β-Ga_2O_3 epitaxial films grown on (110) and (010) substrates are approximately the same in the O-rich regime. However, in the plateau regime, the growth rates of (110) are 10% lower than those of (010). Because the (110) facets are exposed in (010) growth, the crystal plane through which Ga and O are incorporated is the (110) plane for both orientations of growth. However, because of the geometry of the inclined (110) facets in (010) growth, the exposed (110) surface area is 10% more than that of (110) growth. Figure 5 shows the surface morphology of β-Ga_2O_3 films grown at 700 °C on (110) and (010) substrates. At Ga fluxes from 3.0×10^{-8} Torr to 1.5×10^{-7} Torr, in the O-rich regime, there are pits on the surface of both β-Ga_2O_3 epitaxial films grown on (110) and (010) substrates. At higher Ga flux in the plateau regime, smoother surfaces without pits are achieved and the crystal size of β-Ga_2O_3 becomes larger. The surface morphology of β-Ga_2O_3 epitaxial films is smooth on both (110) and (010) substrates with RMS roughness around 1.0 nm. Additionally, elongated features oriented along the [001] direction are exhibited in the plateau regime on both (110) and (010) substrates, while this feature is not expected on the β-Ga_2O_3 epitaxial films grown on the (110) substrates due to the absence of clear faceting. Despite the appearance of (110) facets in growth of (010) β-Ga_2O_3, the (110) plane does not have tendency to show a well-defined step-terrace structure. This may be attributed to the absence of step features on the as-received (110) substrates potentially due to the negligible miscut.

[1] F. Alema *et al*., APL Mater. **7**, 121110 (2019).
[2] P. Mazzolini *et al*., APL Mater. **7**, 022511 (2019).
[3] T. Itoh *et al*., Appl. Phys. Lett. **117**, 152105 (2020).

1:50 PM L02

Source Material Oxidation Challenges in Ge-Doped β-Ga_2O_3 Grown via Plasma-Assisted Molecular Beam Epitaxy Thaddeus J. Asel[1], Erich Steinbrunner[1,2], Jessica Hendricks[1,3], Adam T. Neal[1] and Shin Mou[1]; [1]Air Force Research Laboratory, United States; [2]Wright State University, United States; [3]Air Force Institute of Technology, United States

We utilized secondary ion mass spectroscopy (SIMS) and capacitance-voltage measurements to observe the behavior of Ge incorporation in *β*-Ga_2O_3 and utilized it for effective delta-doping. *β*-Ga_2O_3 has been of interest due to its large, predicted critical breakdown field (8 MV/cm)[1] and its ability to be grown from the melt for easy manufacturability. With the availability of native substrates being prevalent, studying the growth and doping of *β*-Ga_2O_3 thin films has been of great interest. Early Si delta doping studies showed promise with a Si background of 1×10^{17} cm^{-3} with good sheet carrier concentrations of 1.2×10^{13} cm^{-2}. [2] However, silicon has been identified to leave a significant background when the cell is left closed but hot in the chamber, based on shutter design and MBE geometry, so these results are not consistent from system to system.[3] This prevents Si from being used as a dopant for delta-doping applications in some PAMBE systems. However, investigating the control of Ge in PAMBE yields interesting results. The incorporation of Ge is seen to decrease in the film as the substrate temperature increases in PAMBE as measured by SIMS. The Ge incorporation also decreases as the Ga beam flux is increased as measured by SIMS. Site competition between the Ga and Ge atoms plays a significant role in their incorporation. As the Ge cell temperature is increased, SIMS revealed that the Ge incorporation decreased but at an exponential rate that is consistent with the oxidation of the Ge source material. This slow decrease in Ge incorporation is explained by the oxidation of the source material. The Ge oxidation still allows for the formation of GeO which we believe is the active species when doping *β*-Ga_2O_3. These results suggest that Ge may not be suitable for uniform doping applications. However, the background doping caused by Ge is in the range of 1-7 $\times 10^{16}$ cm^{-3} as seen in SIMS as opposed to 1×10^{18} cm^{-3} for Si in our chamber.[2] It suggests Ge is a good candidate for delta doping applications. Using a Ge cell temperature of 700 °C, a substrate temperature of 550 °C, a delta-doped structure that was capped with 50 nm of unintentionally doped *β*-Ga_2O_3 was grown and then measured by CV. The CV profile revealed a sharp peak at 58 nm into the sample with an integrated sheet concentration of 1×10^{13} cm^{-2} and a peak width of 12 nm at 10% of the maximum volume concentration. In summary, we have demonstrated that Ge source material oxidizes in PAMBE, reducing incorporation as a function of time. However, Ge can still be utilized for delta-doping applications with no oxidation issues such as is seen with Si.

[1] M. Higashiwaki, K. Sasaki, T. Kamimura, M.H. Wong, D. Krishnamurthy, A. Kuramata, T. Masui, and S. Yamakoshi, Appl. Phys. Lett. **103**, 123511 (2013).
[2] Z. Xia, C. Joishi, S. Krishnamoorthy, S. Bajaj, Y. Zhang, M. Brenner, S. Lodha, and S. Rajan, IEEE Electron Device Letters **39**, (4) 568-571 (2018).
[3] T.J. Asel, E. Stein Brunner, J. Hendricks, A.T. Neal, and S. Mou, J. Vac. Sci. Technol. A **38**, 043403 (2020).

2:10 PM L03

(Student) Characterization of *β*-Phase MgGaO Thin Films Grown by Molecular Beam Epitaxy Tianchen Yang, Chengyun Shou, Yuan Li and Jianlin Liu; University of California, Riverside, United States

β-phase MgGaO ternary alloy thin films of different Mg compositions were grown by using oxygen plasma assisted molecule beam epitaxy (MBE). The atomic ratios of Mg and Ga in sample A, B, and C were recorded as 11.15 at.%/88.85 at.%, 23.29 at.%/76.71 at.%, and 36.35 at.%/63.65 at.%, respectively, which

were measured by energy-dispersive X-ray (EDX) spectroscopy. The samples were characterized by a scanning electron microscope (SEM), showing that the surface becomes rougher in samples with higher Mg contents. Three typical monoclinic structure diffraction peaks located at 19.12°, 38.50°, and 59.14°, which correspond to the β phases of (-201),(-402), and (-603) were investigated by X-ray diffraction (XRD), and all these diffraction peaks exhibit an obvious blue shift compared with that of reference β-Ga_2O_3. Raman spectra were investigated by a confocal Raman microscope equipped with a high-resolution laser centered at 532 nm with a power of 60 mW. Four out of ten A_g and four out of five B_g Raman-active optical phonon modes were observed. The reduced peak intensity of $A_g^{(2)-(3)}$, $A_g^{(10)}$, $B_g^{(2)-(3)}$, and $B_g^{(5)}$ indicates that Mg^{2+} atoms have replaced the position of Ga^{3+} ions in both octahedral and tetrahedral chains. The ultra-wide bandgap absorption and transmittance spectra were measured using a UV-Vis-NIR spectrophotometer. Ultra-wide bandgaps of 4.98, 5.05, 5.20, and 5.30 eV were measured for pure Ga_2O_3, sample A, B, and C, respectively with all transmittances of light over 80% in the visible spectrum region. Temperature-dependent photoluminescence (PL) spectra were investigated by a 325-nm laser with temperatures ranging from 13 to 300 K, revealing only intermediate level transitions, which decrease with the increase of temperature. A MSM solar-blind ultraviolet photodetector (PD) was fabricated based on MgGaO films with Pt/Au electrodes. Photoresponse has been studied by typical dark and irradiated wavelength dependent I-V curves.

2:30 PM L04

(Student) MOCVD Growth of Si Doped (010) β-$(Al_xGa_{1-x})_2O_3$ Films—Structural and Electrical Properties A F M Anhar Uddin Bhuiyan[1], Zixuan Feng[1], Lingyu Meng[1], Andreas Fiedler[1], Hsien-Lien Huang[1], Adam T. Neal[2], Erich Steinbrunner[2], Shin Mou[2], Jinwoo Hwang[1], Siddharth Rajan[1,1] and Hongping Zhao[1,1]; [1]The Ohio State University, United States; [2]Air Force Research Laboratory, United States

β-$(Al_xGa_{1-x})_2O_3$ alloy with its tunable bandgap energy (4.87-7.51 eV) and high predicted breakdown field (~16 MV/cm with x ~ 0.8), is considered as a promising UWBG semiconductor material for next generation high power and radio frequency electronics. Metalorganic chemical vapor deposited (MOCVD) β-AlGaO films on (010), (100) and (-201) oriented β-Ga_2O_3 substrates have been demonstrated with great crystalline quality, alloy homogeneity and high Al incorporation. Si doped (010) β-AlGaO films (Al=0.06-0.33) grown on top of UID β-Ga_2O_3 buffer layer have shown promising mobilities (42-108 cm^2/V.s) at carrier concentrations of 10^{17}-10^{18} cm^{-3} [1]. While density functional theory (DFT) calculations predicted Si as the most efficient shallow donor in β-AlGaO films (Al ≤ 0.85) [2], the experimental investigation of the n-type doping of β-AlGaO alloy is still limited. In this work, we investigate the structural and electrical properties of MOCVD growth of Si doped (010) β-AlGaO films as a function of Al composition. In addition, the effects of MOCVD growth parameters including chamber pressure, temperature, and VI/III ratio on the physical and electrical properties of β-AlGaO films are also investigated in terms of growth rates, Al incorporations, strain properties and surface morphologies [3].
Phase pure Si doped ~400 nm thick β-AlGaO thin films with Al = 0.06, 0.11 and 0.18 were grown on Mg-doped semi-insulating β-Ga_2O_3 buffer layer on top of (010) β-Ga_2O_3 substrates using TEGa, TMAl, Cp_2Mg, SiH_4 and pure O_2 as Ga, Al, Mg, Si and O precursors, respectively. The RT mobility of 101 cm^2/V.s (n=6.56x10^{17} cm^{-3}) and low temperature (65K) peak mobility of 1157 cm^2/V.s (n=2.30x10^{17} cm^{-3}) with the donor activation energy (E_d) of 9 meV are measured from β-AlGaO film with Al = 0.06 (Figure 1). The Si donor activation energy of β-$(Al_{0.06}Ga_{0.94})_2O_3$ increases from 9 to 15 meV as the carrier concentration reduces from 6.56x10^{17} to 1.98x10^{17} cm^{-3}. With the same silane flow rate of 14.35 nmole/min, the Hall carrier density reduces from 1.54x10^{19} to 2.11x10^{17} cm^{-3} as the Al composition increases from 6% to 18%. The quantitative SIMS depth profile reveals reduced incorporation efficiency of Si in β-AlGaO films with higher Al compositions, whereas C and H impurities which may act as compensating acceptors in β-AlGaO are found to increase with the increase of Al compositions (Table 1), resulting in a significantly lower net Hall carrier concentration for samples with higher Al compositions. Lowering the chamber pressure leads to higher Al incorporation but with reduced Si doping level. Surface RMS roughness increases with the increase of both carrier concentration (for the same Al composition) and Al composition (for the same SiH_4 flow). The XRD RSM mapping reveals the growth of pseudomorphic coherent β-AlGaO films (Al ≤ 0.10) with much higher thicknesses on (010) β-Ga_2O_3 substrate than the theoretically predicted critical thickness, indicating strong influence of MOCVD growth conditions on film relaxation process. The cross-sectional STEM and optical macroscopic surface images reveal the formation of cracks along [001] direction for higher Al compositions due to the increased lattice mismatch. The (100) cleavage plane with the lowest surface energy is identified as the major cracking plane, which leads to highly anisotropic and inhomogeneous resistivity in high-Al β-AlGaO films (Figure 2).
In summary, MOCVD growth and fundamental characteristics of Si doped (010) β-AlGaO films were systematically investigated. Results from this study will provide fundamental understanding of Si doping in β-AlGaO, cirtical for future device designs and fabrications.
Acknowledgment: AFOSR (FA9550-18-1-0479) and NSF (1810041, 2019753).
References:
1. Bhuiyan et al., Appl. Phys. Lett. 115, 120602 (2019).
2. Varley et al., Appl. Phys. Lett. 116, 172104 (2020).
3. Bhuiyan et al., J. Mater. Res. 36, 4804 (2021).

2:50 PM L05

(Student) MOCVD Epitaxy of β-Ga_2O_3 Thin Films on (100) β-Ga_2O_3 Substrate Lingyu Meng, Zixuan Feng, A F M Anhar Uddin Bhuiyan, Hsien-Lien Huang, Jinwoo Hwang and Hongping Zhao; The Ohio State University, United States

Ultrawide bandgap (UWBG) gallium oxide (Ga_2O_3) represents an emerging semiconductor material promising for high power high frequency electronics, considering its associated advantages of wide energy bandgap (~ 4.8 eV), high predicted breakdown field strength (~ 8 MV/cm), and the availability of high quality native substrate. For the most thermally stable monoclinic β-Ga_2O_3 crystal, the available surface planes of native substrates include (-201), (010), (100) and (001). Epitaxy of high crystalline quality β-Ga_2O_3 thin films with high purity and high mobilities on (010) crystal orientation has been demonstrated via metalorganic chemical vapor deposition (MOCVD) [1, 2]. However, understanding of growth mechanisms and material properties on other orientations are still limited.

Previously, MOCVD growth of β-Ga_2O_3 on (100) Ga_2O_3 substrates revealed the importance of using miscut angles towards [001] to promote step-flow growth mode and improve crystalline quality of the (100) epi-films [3]. However, a systematic mapping of the MOCVD growth on (100) β-Ga_2O_3 is still lacking. In this work, we studied the correlation between the MOCVD growth parameters and the (100) β-Ga_2O_3 thin films properties. Specifically, key growth parameters including growth temperature, growth pressure, VI/III molar flow rate ratio and carrier gas (shroud gas) flow rate were tuned. Comprehensive material characterization was performed on the grown materials to probe the surface morphology (AFM, SEM), charge transport (Hall measurement), and growth rate (cross-sectional SEM).
Experimental results showed that decrease of shroud gas (Ar) flow rate leads to the increase of surface smoothness of the epi-films. As

the VI/III molar flow rate ratio increases, the growth rate of the film decreases but with an enhancement of the electron Hall mobility. Although there is no significant impact on the surface morphologies under different growth temperature, the general trend shows that the electron Hall mobility increases as growth temperature increases. A higher chamber pressure leads to a decrease of growth rate, mainly due to the more severe gas phase reaction. The carrier concentration of (100) β-Ga_2O_3 thin films was tuned between low-10^{17} cm^{-3} to low-10^{18} cm^{-3} via the control of silane flow rate. Under an optimized growth condition, a (100) β-Ga_2O_3 thin film with RMS roughness value of 1.64 nm was achieved. However, its room temperature mobility is still limited at 24 cm^2/Vs with a carrier concentration of 7.0×10^{17} cm^{-3}. High resolution STEM imaging is performed to investigate the defects in the epi-films.

In summary, MOCVD growth of on-axis (100) β-Ga_2O_3 thin films was systematically investigated. Results indicate that the MOCVD growth condition has a significant impact on the film surface morphology, growth rate and electron transport. However, the electron Hall mobility is limited below 25 cm^2/Vs mainly due to the formation of twin lamellae and stacking faults for films grown along on-axis (100) crystal orientation.

Acknowledgment: AFOSR (FA9550-18-1-0479) and NSF (1810041, 2019753).

References:

[1] Z. Feng, A F M A. U. Bhuiyan, M. R. Karim, H. Zhao, Appl. Phys. Lett., 114, 250601 (2019).

[2] Z. Feng, A. F. M. A. U. Bhuiyan, Z. Xia, W. Moore, Z. Chen, J. F. McGlone, D. R. Daughton, A. R. Arehart, S. A. Ringel, S. Rajan, and H. Zhao, Phys. Status Solidi RRL 14, 2000145 (2020).

[3] S. Bin Anooz, R. Grüneberg, C. Wouters, R. Schewski, M. Albrecht, A. Fiedler, K. Irmscher, Z. Galazka, W. Miller, G. Wagner, J. Schwarzkopf, and A. Popp, Appl. Phys. Lett. 116, 182106 (2020).

3:10 PM Refreshment Break

3:30 PM L06

(Student) Phase Composition and Microstructure of κ-Ga_2O_3 Heteroepitaxial Films Grown by MOCVD Kunyao Jiang, Jingyu Tang, Matthew Cabral, Anna Park, Liuxin Gu, Robert Davis and Lisa Porter; Carnegie Mellon University, United States

Gallium oxide (Ga_2O_3) is an ultra-wide bandgap semiconductor (4.85-5.3 eV) with emerging applications in power electronics because of its high thermal stability, large breakdown voltage and high dielectric constant. Ga_2O_3 occurs in the α, β, γ and κ(ε) polymorphs having trigonal, monoclinic, cubic normal spinel and orthorhombic structures, respectively. β-Ga_2O_3 is thermodynamically stable and produced in melt-grown substrates. Recently, k-Ga_2O_3 has accrued increased interest because it has demonstrated stability at temperatures ≧ 700°C[1-4] and its large spontaneous polarization could be exploited in heterostructures[5] for high electron mobility transistors. In this study, metal organic chemical vapor deposition (MOCVD) was used to grow epitaxial Ga_2O_3 films under different growth conditions including temperature, growth rate, and diluent gas flow rate. The growth experiments were conducted in a vertical, low-pressure, cold-wall MOCVD reactor using triethylgallium (TEGa) and O_2 precursors and commercially available 0.15 off-axis (toward m-plane) c-plane sapphire.[6] N_2 was used as both the carrier gas for TEGa and the diluent gas. The chamber pressure was held at 20 Torr. The growth rate was controlled by the TEGa flow rate which ranged from 0.29 sccm to 2.1 sccm. The diluent gas flow rate was varied from 4 slm to 8 slm. The O_2 flow rate was maintained at 500 sccm. The temperature was constant for each growth but varied from 470°C to 570 °C. Phase composition and microstructural evolution of the films were investigated using different analytical tools including the X-ray diffraction (XRD), scanning electron microscopy (SEM), high-resolution transmission electron microscopy (HRTEM) and scanning transmission electron microscopy (STEM). XRD and SEM revealed that the top layer varied in phase composition between ~100% κ-Ga_2O_3 and ~100% β-Ga_2O_3; the surface microstructure ranged from poorly coalesced to completely coalesced grains as a function of growth temperature, growth rate, or diluent gas flow rate. In general, it was found that the κ-phase tends to grow at lower temperatures and higher growth rates (higher TEGa flow rates). The growth of nominally single-phase κ-Ga_2O_3 within the top layer was observed in a temperature range between 500°C and 530°C. Below 470°C, only amorphous $Ga_2O_3$was obtained; above 570°C only the β-phase was deposited. HRTEM and STEM of a film grown at 530°C revealed the initial pseudomorphic growth of 3-4 monolayers of α-Ga_2O_3, a 20–60 nm transition layer that contained both β- and γ-Ga_2O_3, and a top ~700 nm thick layer of phase-pure κ-Ga_2O_3.

[1] H.Y. Playford, A.C. Hannon, E.R. Barney, and R.I. Walton, Chem. Eur. J. **19**, 2803 (2013).

[2] R. Roy, V.G. Hill, and E.F. Osborn, J. Am. Chem. Soc. **74**, 719 (1952).

[3] Y. Oshima, E.G. Víllora, Y. Matsushita, S. Yamamoto, and K. Shimamura, J. Appl. Phys. **118**, 085301 (2015).

[4] J. Lee, H. Kim, L. Gautam, K. He, X. Hu, V. Dravid, and M. Razeghi, Photonics **8**, 17 (2021).

[5] P. Ranga, S.B. Cho, R. Mishra, and S. Krishnamoorthy, Appl. Phys. Express **13**, 061009 (2020).

[6] K. Jiang, J. Tang, M. J. Cabral, A. Park, L. Gu, R. F. Davis and L. M. Porter, J. Appl. Phys. (2022)

3:50 PM L07

(Student) Inhomogeneous Aluminum Incorporation in (-201) β-$(Al_xGa_{1-x})_2O_3$ Films Grown on c-Plane and Miscut Sapphire Substrates Kenny Huynh[1], Yekan Wang[1], Michael E. Liao[1], Megan Klein[1], Praneeth Ranga[2], Sriram Krishnamoorthy[3] and Mark Goorsky[1]; [1]University of California, Los Angeles, United States; [2]The University of Utah, United States; [3]University of California - Santa Barbara, United States

High aluminum content striations were observed in (-201) β-$(Al_xGa_{1-x})_2O_3$ thin films (~500 nm) grown on (0001) and 6° miscut (0001) sapphire substrates. A modulated Al composition structure was observed whose orientation depended on the substrate miscut. High resolution x-ray diffraction (XRD) and transmission electron microscopy (TEM) were used to investigate the structural and chemical properties of the β-$(Al_xGa_{1-x})_2O_3$ films (with $0 < x < 0.1$) and the in-plane relationship with the underlying sapphire substrate. (-201) β-$(Al_xGa_{1-x})_2O_3$ films were grown by metalorganic vapor phase epitaxy and the Al composition was controlled by tuning the ratio of trimethylaluminum to triethylgallium flow. The growth was carried out at a substrate temperature of 810 °C and a reduced growth pressure of 15 Torr to minimize Al precursor prereactions.

Scanning transmission electron microscopy measurements (sensitive to Z-contrast) reveal alternating layers of high and low contrasting features throughout the β-$(Al_xGa_{1-x})_2O_3$ film. In conjunction with energy dispersive spectroscopy, the striations are identified as regions of high Al content. In the films that were grown on c-plane sapphire, the high Al content striations run parallel to the (-201) surface. However, in the case of the 6° miscut sapphire substrates, the high Al content striations are oriented about 8-10° from the surface. Recent studies of β-$(Al_xGa_{1-x})_2O_3$ film growth on common orientations including (010), (001), (-201) found that a lower surface energy found in (-201) surface planes lead to higher Al adatom incorporation.[1-3] We speculate that the anisotropy of the monoclinic structures, the surface energy differences associated with the miscut substrate, and step edge features impact the formation of the composition striations throughout the film.

X-ray phi scans revealed six-fold symmetry of the (-201) β-$(Al_xGa_{1-x})_2O_3$ films, which corresponds to three sets of twinning and an in-plane orientation where β-$(Al_xGa_{1-x})_2O_3$ [010] ∥ Al_2O_3 [10-10]. Uniform intensity of the peaks in the phi scan indicates an even distribution of the different twin orientations. Plan view atomic models are used to illustrate the different 60° rotational configurations possible for these sets of twins. XRD 2θ-ω scans for the (-603) β-$(Al_xGa_{1-x})_2O_3$ reflection were taken to estimate the aluminum composition in the deposited films. In general, the (-603) peak shifts towards higher angles for higher Al concentration as expected, although the broadness and asymmetry of the peaks suggest non-uniform or concentration gradients of the Al content that exist in the samples, which supports the observations made under TEM. In addition, the β-Ga_2O_3 layers as well as all of the β-$(Al_xGa_{1-x})_2O_3$ layers exhibited a different strain state (different a, b, c, and β lattice parameters) than bulk material as determined through multiple reflection reciprocal space maps.

References

1. Bhuiyan, A.A.U., Feng, Z., Johnson, J.M., Huang, H.L., Hwang, J. and Zhao, H., *Applied Physics Letters*, *117*(14), p.142107 (2020)
2. Bhuiyan, A.A.U., Feng, Z., Johnson, J.M., Huang, H.L., Sarker, J., Zhu, M., Karim, M.R., Mazumder, B., Hwang, J. and Zhao, H., *APL Materials*, *8*(3), p.031104 (2020)
3. Mu, S., Wang, M., Peelaers, H. and Van de Walle, C.G., *APL Materials*, *8*(9), p.091105 (2020)

4:10 PM L08

(Student) MOCVD Development and Bandoffsets of ε-Ga_2O_3 on GaN, AlN, YSZ and c-sapphire Substrates A F M Anhar Uddin Bhuiyan, Zixuan Feng, Hsien-Lien Huang, Lingyu Meng, Jinwoo Hwang and Hongping Zhao; The Ohio State University, United States

Ga_2O_3 represents an ultrawide bandgap (4.5-5.3 eV) transparent semiconducting oxide promising for next generation high power electronics. Among the five different polymorphs (α, β, γ, δ and ε) of Ga_2O_3, monoclinic β-Ga_2O_3 is the thermodynamically most stable structure. Only recently, orthorhombic ε-phase Ga_2O_3 (also refer to as κ-Ga_2O_3) with a bandgap energy similar to β-Ga_2O_3 has attracted substantial interests owing to its existence of strong spontaneous polarization (0.31 Cm^{-2}) as compared to those of polar semiconductors such as GaN (-0.034 Cm^{-2}) and AlN (-0.09 Cm^{-2}) [1]. The spontaneous polarization of ε-Ga_2O_3 is predicted to generate two orders of magnitude higher 2DEGs density (10^{14} cm^{-2}) at ε-Ga_2O_3/AlN (GaN) interfaces than the traditional AlGaN/GaN heterojunctions, potentially allowing the fabrication of high-electron-mobility transistors for high-power and radio frequency electronic applications. Although ε-Ga_2O_3 growths have been demonstrated by different growth techniques, investigation on the phase stabilization of ε-Ga_2O_3 on various substrates is still limited. In this work, a systematic growth mapping of ε-Ga_2O_3 films is performed via MOCVD on different substrates including c-sapphire, GaN-on-sapphire, AlN-on-sapphire, and yttria stabilized zirconia (YSZ). Moreover, the band offsets at the heterointerfaces of ε-Ga_2O_3/AlN (/GaN, /Sapphire, and /YSZ) are measured via XPS for the first time.

ε-Ga_2O_3 thin films were grown in Agnitron Agilis MOCVD reactor using TEGa and pure O_2 as Ga, and O precursors, respectively. The growth temperature and pressure were varied between 510-650 °C and 4-15 torr, respectively. The growth of phase pure ε-Ga_2O_3 films is achieved on YSZ, GaN- and AlN-on-sapphire substrates as shown in the XRD ω-2θ scans in Figure 1, whereas Ga_2O_3 film grown on sapphire substrate is found to be composed of both β- and ε- phases. Both lower pressure (3-5 torr) and temperature (620-650 °C) facilitate the growth of pure ε-Ga_2O_3 films. Owing to its large lattice mismatch with the substrates, ε-Ga_2O_3 films exhibit in-plane rotational domains as observed from XRD φ-scans and STEM nano diffractions. The compositional homogeneity and abrupt interfaces between ε-Ga_2O_3 and different substrates are observed from atomic resolution STEM imaging.

The asymmetrical reciprocal space mapping (RSM) indicates the growth of fully relaxed ε-Ga_2O_3 films on all investigated substrates. While relatively smooth surface morphologies with RMS roughness of ~1.6-3 nm are measured for the films grown on sapphire, GaN and YSZ substates, ε-Ga_2O_3 films grown on AlN-on-sapphire show rougher surface morphologies which can be attributed to the strong oxidation of Al adatoms on the growth surface. The chemical compositions, surface stoichiometry, band gaps and the band offsets at ε-Ga_2O_3/substrate interfaces are evaluated by XPS measurements. The O/Ga ratios are determined to range between 1.47-1.51, indicating that the surface stoichiometries of the films are well maintained. The bandgaps of ε-Ga_2O_3 films vary between 5.06-5.10 eV on different substrates. A type-II (staggered) band alignment is observed at ε-Ga_2O_3/c-sapphire (/AlN and /YSZ) interfaces, whereas ε-Ga_2O_3/GaN interface exhibits a type-I (straddling) band offset (Figure 2). Larger conduction band offsets of 3.92, 1.26, 1.40 and 1.07 eV are determined at the ε-Ga_2O_3/c-sapphire (/GaN, /AlN and /YSZ) interfaces, respectively, indicating great potential for excellent carrier confinement at the heterointerfaces between ε-Ga_2O_3 and various investigated substrates.

In summary, MOCVD growths of ε-Ga_2O_3 films on various substrates were systematically investigated. Results from this study will provide guidance for future epitaxial growths, device design and fabrication based on ε-Ga_2O_3 films.

Acknowledgment: AFOSR (FA9550-18-1-0479) and NSF (1810041, 2019753).

Reference:

1. J. Wang et al., Electron Device Lett. 41 (7), 1052 (2020).

4:30 PM L09

(Student) Electronic and Optical Properties of Rare-Earth Doped β-Ga_2O_3 Crystals Jani Jesenovec, Benjamin L. Dutton, Brooke Downing and John S. McCloy; Washington State University, United States

β-Ga_2O_3 is an emerging ultrawide bandgap material which can be alloyed with Al_2O_3 to increase the electronic bandgap. In this work, we explore analogous Sc_2O_3 alloying, producing bulk Czochralski single crystals of 10 mol.% Sc_2O_3 (β-$(Sc_{0.1}Ga_{0.9})_2O_3$, i.e., monoclinic 10 mol.% SGO). These materials show a +0.15 eV increase in the bandgap compared to β-Ga_2O_3. 10 mol.% SGO was characterized for structure (X-ray diffraction, rocking curve, Raman microscopy), purity (glow discharge mass spectroscopy, X-ray fluorescence), optical transmission (200 nm – 20 µm wavelengths), resistivity, and rare earth luminescence (laser induced fluorescence microscopy). Structural measurements indicate successful incorporation of Sc, although overall lower quality than β-Ga_2O_3 and β-$(Al_{0.1}Ga_{0.9})_2O_3$ crystals. Bulk crystals of β-$(Sc_{0.1}Ga_{0.9})_2O_3$ demonstrate intense Stark luminescence characteristic of Nd^{3+}, which are concentrated in certain areas of the crystal. SGO is not the best candidate substrate for thin film growth due to lower quality single crystals and numerous microscale defects related to ubiquitous rare earth impurities.

4:50 PM L10

(Student, Late News) Si-Doping in MBE-Grown Beta-Ga_2O_3 with Room Temperature Mobility > 125 cm^2/Vs Jonathan McCandless[1], Vladimir Protasenko[1], Brad Morrell[1], Erich Steinbrunner[2], Adam T. Neal[2], YongJin Cho[1], Nick Tanen[1], Huili Grace Xing[1] and Debdeep Jena[1]; [1]Cornell University, United States; [2]Air Force Research Laboratory, United States

Since 2012, the semiconductor β-Ga_2O_3 has gained significant attention due its large bandgap (~4.7eV), corresponding large critical electric field strength, and the availability of large-area, semi-insulating substrates. [1, 2] To make high-power diodes and high-frequency switches, devices that take advantage of these properties, it is critical that reliable doping control and low doping

densities be achieved [3]. Epitaxial layers of this material have been grown by many techniques such as halide vapor phase epitaxy, [4] pulsed laser deposition, [5] metalorganic vapor phase epitaxy, [6] and molecular beam epitaxy (MBE). [7, 8]

While MBE is a useful growth technique for forming atomically sharp interfaces, to-date, low doping of Ga_2O_3 by MBE has been challenging due to the n-type doping sources (e.g. silicon) oxidizing during the growth. As a result, doping densities tend to be high and uncontrolled, and the mobilities tend to be low due to ionized impurity scattering.

We report on an innovative approach to doping – which allowed us to have a high-degree of Si donor density control, and to achieve uniform doping densities of ~$1x10^{17}/cm^3$ over a thickness > 200 nm. We report temperature-dependent Hall effect measurements and secondary ion mass spectrometry data demonstrating doping control from low-$10^{17}/cm^3$ to $10^{20}/cm^3$. With these low densities, we are able to achieve room temperature mobilities > 125 cm^2/V which increase to over 390 cm^2/V at 97K, as the polar opitcal phonon scattering rate is reduced. The doped samples reported here, have among the highest mobilities of all growth techniques where ionized impurity scattering dominates. To further boost electron mobilities, modulation doped transistors (MODFETs) can be used. MODFETs rely on the formation of a 2DEG with carriers from a doped layer which is at a distance from the quantum well. This enhances the mobility due to a reduction in Coulomb scattering effects, an analysis of which will be discussed along with work

[1] M. Higashiwaki, *et al.*, Appl. Phys. Lett., 100, (2012); [2] H. Peelaers and C. G. Van de Walle, Phys. Status Solidi B 252 (2015); [3] N. Moser, *et al.*, Appl. Phys. Lett., 117, (2020); [4] K. Nomura, *et al.,* J. Cryst. Growth 405, 19 (2014); [5] K. D. Leedy, et al. Appl. Phys. Lett., 111, (2017); [6] G. Wagner, et al., Phys. Status Solidi (a), 211 (2013); [7] N. K. Kalarickal, *et al.,* Appl. Phys. Lett., 115, (2019); [8] T. J. Asel, *et al.,* JVST A, 38, 043403 (2020)

SESSION M: Solar Cell Materials and Devices

Session Chairs: Deidra Hodges and Mark Wistey
Wednesday Afternoon, June 29, 2022
Senate Chamber

1:30 PM M01
(Student, Late News) GaAs Laser Power Converters for Cryogenic Applications Bora Kim, Minjoo L. Lee, Mijung Kim and Brian Li; University of Illinois at Urbana-Champaign, United States

In power-over-fiber (PoF) technology, a continuous-wave laser mode is guided through optical fiber to a photovoltaic cell to provide power in applications where electrical isolation is critical. PoF is widely deployed for electronics and sensors in demanding environments that are sensitive to electromagnetic noise from wires or that are prone to failures by electrical arcing. An emerging application for PoF is in cryogenic environments, e.g. quantum computers, particle physics experiments, deep-space satellite missions. In this project, we are investigating the use of GaAs laser power converters (LPCs) to provide power for both analog and digital electronics in cryogenic neutrino sensors to be used in Fermilab's Deep Underground Neutrino Experiment. In this talk, we show that majority carrier blocking at heterojunctions can severely hamper fill factor FF at -190°C, leading to low power conversion efficiencies under moderate laser power densities (e.g. < 1 W/cm^2); in contrast, homojunction GaAs LPCs where majority carrier blocking is negligible give high FF values across all temperatures. We have recently grown new GaAs LPCs with redesigned heterojunctions that cause minimal majority carrier blocking at cryogenic temperatures, opening the potential for efficiency exceeding 60%.

All samples were grown by solid-source molecular beam epitaxy (SSMBE) and processed using standard photolithography, e-beam deposition, and wet etching methods. Cells were tested under illumination from an 808 nm laser over a range of temperatures. Sample A was a conventional cell design consisting of a 2 µm GaAs absorber surrounded by a lattice-matched n-InAlP window on the front and a lattice-matched p-InGaP back surface field (BSF) layer on the back. While these cells exhibit good characteristics at room-temperature, we noticed anomalously high series resistance values as temperature decreased to -190°C, accompanied by low FFs of 60-70%. Some degree of carrier freezeout was found to occur in layers used in the cells by Hall effect measurements of calibration samples, but all samples remained conductive. In contrast, a GaAs homojunction solar cell (sample B) that only uses n+GaAs as the window and p+GaAs as the BSF showed higher FF values > 80% at all temperature values tested, confirming the role of heterojunctions in increased series resistance. Heterojunctions are still important at cryogenic temperatures for ensuring high open-circuit voltage and external quantum efficiency (EQE), and we therefore designed and grew a new cell (sample C) with an n+InGaP window and p+GaAs BSF. While testing is still in progress, this cell shows very high FF of 88-89% at -100°C at laser power densities up to 7W/cm^2. Despite the differences in FF, cells A and B showed high open-circuit voltage values (~1.37-1.41V) at -190°C thanks to the expected reductions in dark current at such low temperatures. All cells show a reduction in EQE at 808 nm at cryogenic temperature, which may result from the combined effects of reduced optical absorption coefficient and reduced carrier diffusion length at low temperature. Overall, this work shows that GaAs solar cells cannot be simply repurposed for use as LPCs at cryogenic temperatures. Despite the benefit of strongly reduced dark current, GaAs LPCs must be carefully designed to minimize majority carrier blocking to ensure efficient operation at cryogenic temperatures.

1:50 PM M02
(Student) Time-Resolved Photoluminescence Studies of Perovskite Chalcogenides Kevin Ye[1], Boyang Zhao[2], Benjamin Diroll[3], Jayakanth Ravichandran[2] and Rafael Jaramillo[1]; [1]Massachusetts Institute of Technology, United States; [2]University of Southern California, United States; [3]Argonne National Laboratory, United States

Chalcogenides in the perovskite and related crystal structures may be useful for future optoelectronic and energy conversion technologies in as much as they have good excited-state, ambipolar transport properties [1]. In recent years, several studies have suggested that semiconductors in the Ba-Zr-S system have slow non-radiative recombination rates [2,3]. Here we present a more detailed time-resolved photoluminescence (TRPL) study of excited-state carrier mobility and recombination rates in the perovskite-structured material $BaZrS_3$, and the related Ruddlesden-Popper phase $Ba_3Zr_2S_7$. $BaZrS_3$ is a semiconductor with direct band gap of energy E_g = 1.8 eV; $Ba_3Zr_2S_7$ is an indirect-gap semiconductor with fundamental gap E_g = 1.25 eV, and has strong near-infrared absorption due to a direct transition near 1.3 eV. We measure state-of-the-art single crystal and epitaxial film samples, to identify intrinsic properties free from the influence of secondary phases and random grain boundaries [4,5]. We model and fit the data using a semiconductor physics simulation, to enable more direct determination of key material parameters than is possible with empirical data modeling. We model the data using a simulation of generation-diffusion-drift- recombination processes, implemented using software PC-1D [6]. We perform nonlinear

least-squares model refinement using a MATLAB script that runs using PC-1D as the kernel and can perform global refinement of few parameters over multiple data sets. We find that both materials have Shockley-Read-Hall recombination lifetime on the order of 100 ns and excited-state diffusion lengths on the order of 5 μm, which bode well for ambipolar device performance in optoelectronic technologies including thin-film solar cells.

1. R. Jaramillo and J. Ravichandran, "In praise and in search of highly-polarizable semiconductors: Technological promise and discovery strategies," APL Materials **7**(10), 100902 (2019).
2. S. Niu, D. Sarkar, K. Williams, Y. Zhou, Y. Li, E. Bianco, H. Huyan, S. B. Cronin, M. E. McConney, R. Haiges, R. Jaramillo, D. J. Singh, W. A. Tisdale, R. Kapadia, and J. Ravichandran, "Optimal Bandgap in a 2D Ruddlesden–Popper Perovskite Chalcogenide for Single-Junction Solar Cells," Chem. Mater. **30**(15), 4882–4886 (2018).
3. X. Wei, H. Hui, C. Zhao, C. Deng, M. Han, Z. Yu, A. Sheng, P. Roy, A. Chen, J. Lin, D. F. Watson, Y.-Y. Sun, T. Thomay, S. Yang, Q. Jia, S. Zhang, and H. Zeng, "Realization of BaZrS3 chalcogenide perovskite thin films for optoelectronics," Nano Energy **68**, 104317 (2020).
4. S. Niu, B. Zhao, K. Ye, E. Bianco, J. Zhou, M. E. McConney, C. Settens, R. Haiges, R. Jaramillo, and J. Ravichandran, "Crystal growth and structural analysis of perovskite chalcogenide BaZrS3 and Ruddlesden–Popper phase Ba3Zr2S7," Journal of Materials Research **34**(22), 3819–3826 (2019).
5. I. Sadeghi, K. Ye, M. Xu, Y. Li, J. M. Lebeau, and R. Jaramillo, “Making $BaZrS_3$ Chalcogenide Thin Films by Molecular Beam Epitaxy,” Advanced Functional Materials **31**(45), 2105563 (2021).
6. D. A. Clugston and P. A. Basore, "PC1D version 5: 32-bit solar cell modeling on personal computers," in *Conference Record of the Twenty Sixth IEEE Photovoltaic Specialists Conference - 1997* (1997), pp. 207–210.

2:10 PM M03
(Student) An Optical Response Analysis of Cadmium Telluride-Based Solar Cell Structures Incorporating High Resistivity Transparent Layers of Magnesium-Zinc Oxide

Mohammed Alaani[1], Prakash Koirala[1], Balaji Ramanujam[1], Ambalanath Shan[1], Adam Phillips[1], Michael Heben[1], Stephen O’Leary[2], Nikolas Podraza[1] and Robert Collins[1]; [1]Wright Center for Photovoltaics Innovation & Commercialization and Department of Physics & Astronomy, University of Toledo, United States; [2]The University of British Columbia, Canada

Parametric expressions that describe the complex dielectric function of polycrystalline $Mg_xZn_{1-x}O$ thin films as a function of the bandgap E_g have been applied in the metrology of cadmium telluride-based solar cell structures. Valid over the range $3.264 \leq E_g \leq 3.826$ eV, these parametric expressions are applied to facilitate mapping spectroscopic ellipsometry of device structures consisting of $Mg_xZn_{1-x}O$ deposited on TEC™-15 glass. Mapping spectroscopic ellipsometry is shown to provide maps for the $Mg_xZn_{1-x}O$ effective thickness, or volume per planar substrate area, and $Mg_xZn_{1-x}O$ bandgap within confidence limits of ± 1 nm and ± 0.003 eV, respectively. As a second application of the parametric expressions, an as-deposited cadmium telluride-based device structure has been analyzed by through-the-glass spectroscopic ellipsometry. Such an analysis is also shown to provide the $Mg_xZn_{1-x}O$ effective thickness and bandgap. The outcome of the through-the-glass spectroscopic ellipsometry analysis for this device structure enables simulations of the external quantum efficiency spectra of the resulting solar cell assuming different recombination losses within the individual layers of the structure. A comparison of these simulations with corresponding experimental spectra reveals high current collection from the front of the device with the almost complete collection from the cadmium sulfide components of the $Mg_xZn_{1-x}O$/cadmium sulfide and cadmium sulfide/cadmium telluride interface layers of the structure.

2:30 PM M04
(Student) Group-V Acceptors and Their AX Centers in CdTe

Intuon Chatratin, Shagorika Mukherjee and Anderson Janotti; University of Delaware, United States

CdTe solar cells are leading and commercially available thin-film technology. Several factors such as low cost, simple and rapid production, high photo absorption coefficient and a direct band gap of 1.5 eV have been driving the research to improve the efficiency of CdTe solar cells. The record efficiency of CdTe solar cells of 22.1% is still far below the theoretical limit of 29% mainly due to the low open-circuit voltage. Further improvement can be obtained by increasing the *p*-type carrier concentration in CdTe absorbers. Group-V impurities, P, As and Sb were shown to be promising for *p*-type doping in CdTe as seen in a recent Hall measurements where high *p*-type doping efficiencies were reported. However, early theoretical studies indicate rather high ionization energy for Sb and the formation of self-compensation AX centers, limiting the hole concentrations. From these calculated results, high *p*-type doping efficiency could not be achieved using group-V doping. To understand this contradiction between experiment and DFT calculations, we revisit the behavior of group-V acceptors and their AX centers in CdTe by using hybrid density functional. We pay special attention to the inclusion of spin-orbit coupling and the finite size effect of supercell to deal with the shallow acceptor levels. We find that the AX center is unstable for P and As, and barely stable in the case of Sb, suggesting that the formation of AX center is unlikely to play important roles as compensation center. The calculated acceptor transition levels of ~100 meV can explain the observed hole concentrations from temperature-dependent Hall measurements when a relatively low level of compensation from yet unknown donor defects is assumed.

2:50 PM M05
(Student) Investigation of Spin-Based Photovoltaic Effect in a Magnetic Tunnel Junction-Based Molecular Spintronic Devices (MTJMSDs) Marzieh Savadkoohi[1,2], Daniel Gopman[2] and Pawan Tyagi[1]; [1]University of the District of Columbia, United States; [2]National Institute of Standards and Technology, United States

The electronic charge-based photovoltaic effect is a familiar phenomenon in solar cell technology. Displacement of photon-excited electrons produces a potential difference and electricity. The spin-based photovoltaic effect [1] is a relatively newer phenomenon that is additionally sensitive to the spin of current-carrying electrons and the underlying magnetic properties of their host electrodes. This spin-based effect can similarly be used to generate electricity and perhaps more economically due to the usage of earth-abundant elements such as Nickel (Ni), Cobalt (Co), and Iron (Fe). Identifying systems that demonstrate this behavior is vital to the development of this phenomena as a viable approach for efficient photovoltaic technologies. This research investigates the charge transport properties and spin photovoltaic (P-V) effect in a spintronic device that exhibits a measurable spin P-V effect - a molecular-based spintronic device at room temperature. We observed a photovoltaic effect on a magnetic tunnel junction which was treated with organometallic molecules (OMC) at the exposed edges. Paramagnetic molecules, with a non-vanishing net spin state, can tailor magnetic exchange coupling between two ferromagnetic electrodes (FMEs) in magnetic tunnel junction-based molecular spintronics devices (MTJMSD) and correspondingly modify the magnetic electrodes transport and optical properties [1-3]. We previously observed spin-photovoltaic effects on MTJs comprising Co/NiFe bottom and NiFe top electrodes separated by an AlOx insulator. This study reveals that the photovoltaic effect seen previously is also evident in MgO-based MTJs, which is of much closer technological relevance to MgO-based MTJs used in commercial magnetic tunnel junction sensors and magnetic random-access memories. The MTJs were

deposited on a 300 nm thermally oxidized Si wafer with the stacking structure: Ta(5nm)/ Ru(8nm)/ Ta(5nm)/ Mo(10nm)/ CoFeB(6nm)/ MgO(2nm)/ CoFeB(4nm)/ Mo(10nm)/ Ta(5nm)/ Ru(8nm). Cross-junctions were produced by a 2-step photolithography and lift-off procedure. The OMCs are attached to the exposed edges of the MTJs as conductive bridges after the cross-junctions were fabricated.The compatibility of FMEs with molecules was tested before making MTJMSD using Vibrating Sample Magnetometry (VSM) and Ferromagnetic Resonance (FMR) characterization. The MTJ remained intact after molecule incorporation. To characterize the molecule-induced effect on electronic properties we performed a Kelvin force probe microscopy (KPFM) scans. Our preliminary results showed a noticeable voltage difference (V=100mV) between the top and bottom electrodes after molecular treatment during KPFM scans. We also observed an intriguing spin-based photovoltaic (P-V) effect under regular white light (=400-700mm) while performing charge transport studies. To test the observed phenomenon, we repeated the charge transport study of MTJMSD at different light intensities using a solar simulator. Our results showed that the observed photovoltaic phenomenon is due to the MTJMSD's light absorption and thus it is susceptible to light intensity. The electrodes' robustness to oxidation was tested via reflectance spectra study. The reflectance behavior of MTJMSD at a variety of temperatures (RT to 120 °C) showed stability until 100 °C. It is noteworthy that our sample preparation steps were designed not to exceed 90 °C to keep FME stable. The intriguing P-V effect that was observed in the current MTJMSD agrees with our previous studies in which OMC transformed a NiFe-based ferromagnetic film into photoresponsive material [4].

3:10 PM Refreshment Break

3:30 PM M06

(Student) A New Family of Hybrid Thiocyanate-Halide Compounds—A2Cd(SCN)2X2 Alexander A. Milder and Patrick Woodward; The Ohio State University, United States

Perovskites, a class of compounds that share the structure type of $CaTiO_3$, are notable for their massive structural and chemical adaptability, making ideal functional materials in for a variety of device applications. Perovskite oxides have long been explored for their ferroelectric and magnetic properties and halide perovskites have achieved widespread recognition as solar cell and LED materials. However, to meet the demand for materials in dielectric, multiferroic, and optoelectronic applications new modifications to the perovskite structure must be developed to allow for targeted synthesis of materials with these properties.

In one such modification perovskites can include a thiocyanate (SCN^-) molecular linker instead of an oxide or halide anion. These thiocyanate compounds gain increased flexibility due to the thiocyanate's multiple bonding modes and interactions with an organic cation, which stabilize structures and incorporate elements not seen in traditional perovskites. Previous work has demonstrated that these characteristics make them well suited to be dielectrics, multiferroics, optoelectronics, or magnets. However, the dearth of realized compounds in this family makes the targeted synthesis of materials for specific device applications difficult. Therefore, to move forward in developing application centered materials based on this hybrid structure it is necessary to first expand the existing chemical space of realized thiocyanate-linked organic-inorganic compounds.

To this end, we have synthesized a new family of hybrid organic-inorganic materials with the general formula $A_2Cd(SCN)_2X_2$ (A= $CH_3NH_3^+$, $(CH_3)_2NH_2^+$, $CH_3CH_2NH_3^+$, $CH_3(CH_2)_2NH_3^+$, X= Cl^-, Br^-). The new mixed thiocyanate-halide compounds demonstrate a novel bonding motif and represent an entirely new structure type not previously seen (Figures 1 and 2). The materials have been prepared via facile solid-state techniques and single crystals can be grown using solution-based methods. These hybrid materials incorporate mixed halide and thiocyanate anions to overcome problems with stability and demonstrate the validity of the proposed structural and chemical variations available. The new structure type also demonstrates the importance of hydrogen bonding in controlling the structure of molecular-linked compounds, an important structure directing effect that has not been previously explored in similar materials. The dielectric and optical properties of these hybrid compounds have been investigated to better understand the role of structure in determining material properties. By understanding the structure and properties of this family of thiocyanate perovskites, new compounds can now be targeted for synthesis that would be ideal functional materials for dielectric, multiferroic, and optoelectronic applications.

3:50 PM M07

Designing New Sustainable Semiconductor Materials with Cu-Chalcogenide Nanocrystals Soubantika Palchoudhury, Zeyad Al Abri, Madison Jones and Nicholas Saunders; University of Dayton, United States

Transition metal multinary chalcogenides are a unique class of material for photovoltaic (PV) and quantum dot light emitting (QLED) applications. They offer a higher level of flexibility from a materials perspective to achieve tunable band gaps through structural and compositional control. We aim to realize new and more sustainable direct band-gap semiconductor materials from multinary compositions of earth-abundant elements. To this end, detailed *ab initio* calculations are first performed for the parent binary Cu-chalcogenide composition. A series of new p-doped, n-doped, and degenerate semiconductors based on multinary Cu-chalcogenide nanocrystals are predicted using the theoretical investigations of the band gap and density of states. We experimentally realized the new multinary Cu-chalcogenide compositions via novel solution chemistry approaches. A detailed material characterization based on x-ray diffraction, electron microscopy, and ultraviolet-visible spectroscopy is reported for the new Cu-chalcogenide nanocrystals and thin films. These new results will provide key theoretical and experimental insights for achieving more sustainable absorber layer materials for inorganic solar cells.

4:10 PM M08

(Student, Late News) Solar Cell Effect with Magnetic Metamaterials Produced by Combining Magnetic Tunnel Junction and Magnetic Molecules Samba Gaye, Marzieh Savadkoohi, Eva Mutunga, Andrew C. Grizzle, Rodneycia Taylor, Pius Suh and Pawan Tyagi; University of the District of Columbia, United States

A new class of magnetic metamaterials can be produced by placing magnetic molecules between two ferromagnetic electrodes. Magnetic molecules can be designed to create strong exchange coupling between two ferromagnetic electrodes. Magnetic molecule-induced strong exchange coupling that can be harnessed as the means to initiate an automatic spin filtering process to shuffle the spin density of states in the two ferromagnetic electrodes. Our recent preliminary experimental studies showed that iron and nickel atom-based organometallic molecules (FeNi-OMC) produced a strong spin filtering effect between NiFe and Co/NiFe ferromagnetic electrodes (Tyagi, P.; Riso, C., Molecular spintronics devices exhibiting properties of a solar cell. Nanotechnology 2019, 30 (49), 49540).
Fe-Ni-OMC dramatically modified the magnetic properties of ferromagnetic electrodes present in the magnetic tunnel junction testbed at room temperature. This paper talks about the resulting Fe-NiOMC and magnetic tunnel junction-based magnetic metamaterial. This metamaterial showed an intriguing solar cell

effect. Further experimental studies are conducted to design several other forms of novel magnetic metamaterials by combining a wide range of Single-molecule magnetic (SMM) and porphyrin-like magnetic molecules with various permutations of magnetic electrodes. To produce a magnetic tunnel junction testbed that is to be used to test various molecules, we made extensive experimental optimization efforts at each stage of device fabrication to address device fabrication challenges associated with molecule-ferromagnet interactions. In this study, we have systematically optimized several factors using multiple Taguchi Design of Experiment approaches to improve the fabrication of the bottom electrode of the magnetic metamaterial. We systematically varied photolithography parameters and plasma treatment process to yield a bottom ferromagnetic electrode with <0.4 nm Ra roughness and oval-shaped edges. For this optimization work, we mainly focused on the plasma etching duration and the different aspects of the photolithography process, which included: the spin-coating speed, the baking temperature, the soaking time, and the exposure time. After lithography and plasma treatment, RF sputtering was performed to create a seed layer and NiFe ferromagnetic electrode, followed by the lift-off step. Atomic force microscopy was performed to study the roughness of the electrode and edge profile. We observed that only a few parameter combinations in Taguchi Design of experiments were successful in producing oval edge ultrasmooth bottom electrodes for advancing magnetic metamaterial experimental research. This foundation work is critical for making robust tunnel junction testbeds for harnessing magnetic molecule strengths and attributes of producing magnetic metamaterials.

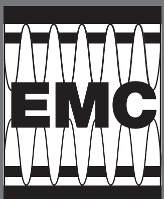

64TH ELECTRONIC MATERIALS CONFERENCE

June 29-July 1, 2022 // The Ohio State University // Columbus, Ohio

WEDNESDAY POSTER PRESENTATIONS

SESSION PS: Poster Session

Wednesday Afternoon, June 29, 2022
6:00 PM - 8:00 PM
Performance Hall & Potter Plaza

PS01

(Student) Growth and Characterization of High-Temperature Nitrogen-Polar InAlN Films and HEMTs Using Plasma Assisted Molecular Beam Epitaxy Majid Aalizadeh, Kamruzzaman Khan and Elaheh Ahmadi; University of Michigan–Ann Arbor, United States

Commercially available GaN-based electronic and optoelectronic devices are mainly fabricated on Gallium-polar GaN substrates. However, recent research has shown superior performance of the Nitrogen-polar GaN high electron mobility transistors (HEMTs) in the W-band in comparison with the Ga-polar GaN HEMTs. Meanwhile, the research and progress on N-polar films have been limited due to the fact that it is very challenging to grow films of high quality, unlike the metal-polar case.

Although AlGaN has been commonly used as the barrier in GaN HEMTs, InAlN can potentially be a great candidate to enable high charge in HEMTs with scaled channel. In particular, $In_{0.18}Al_{0.82}N$ which is lattice matched to GaN, has a wide bandgap, large spontaneous polarization, and high refractive index contrast with GaN. Therefore, it is attractive as the barrier material in HEMTs and UV light emitting diodes (LEDs).

Regardless, the growth of InAlN is challenging due to a large difference in the thermal stability of InN and AlN. Therefore, InAlN has been traditionally grown at temperatures much lower than optimized growth temperature for GaN using both metal-organic chemical vapor deposition (MOCVD) and molecular beam epitaxy (MBE) [1-3]. Lower growth temperature leads to higher incorporation of impurities such as oxygen and carbon. Moreover, lower growth temperature of InAlN would require several growth interruptions to change the substrate temperature for the growth of the other (Al,Ga)N layers in the epi-structure.

In this work, we present high temperature growth of InAlN on N-polar GaN substrate using plasma assisted molecular beam epitaxy (PAMBE). Next, we implement our findings in high temperature InAlN growth on growing and characterizing N-polar HEMTs using $In_{0.18}Al_{0.82}N$ (lattice matched to GaN) as the back barrier. The effects of different growth parameters are investigated on the mobility and 2DEG sheet charge density of the N-polar InAlN based HEMTs.

First, the quality and the composition of the $In_xAl_{1-x}N$ were explored at various high growth temperatures (600 to 800 °C). For this purpose, a Veeco GenXplor MBE system was used for epitaxial growth of the samples. First, a 200 nm-thick GaN layer was grown on top of a solvent-cleaned commercial bulk N-polar GaN substrate at 750 °C to ensure a smooth surface morphology. The growth was then interrupted to change the substrate temperature for the growth of a 50 nm InAlN film. The surface quality of the films were then characterized using Atomic Forced Microscopy (AFM) and the composition was calculated using the X-ray Diffraction (XRD) ω-2θ profile, assuming Vegard's law. Two series of InAlN films were grown by using the same Al flux of 4×10^{-8} torr but different In fluxes of 4×10^{-8} torr and 4×10^{-7} torr. For the first series with the In flux of 4×10^{-8}, the temperature was varied between 600 °C and 725 °C which resulted in the composition range of 37% to 8%. For the second series with the In flux of 4×10^{-7}, the temperature was varied between 700 °C and 800 °C which resulted in the composition range of 33% to 9%. Keeping fluxes the same in both series, by increasing the growth temperature, it was expected and observed that the In contribution was decreased due to higher In evaporation. Another series were grown all with InAlN at 750 °C (same as GaN growth temperature), with varying In flux and the Al flux of 4×10^{-8} torr. $In_{0.18}Al_{0.82}N$ film with smooth surface morphology and high structural quality was achieved at 750 °C (the optimum temperature for growth of N-polar GaN). It was observed that the film quality is enhanced by increasing the growth temperature.

Finally, different series of HEMTs were grown using InAlN as the back barrier, and GaN as the channel. The effects of different growth parameters, including the growth temperature of InAlN were investigated. Mobility values as high as 1320 (cm^2/Vs) with a 2DEG sheet charge density of 2.51×10^{13} (1/ cm^2) were measured.

PS02

(Student) Ni/Au and Co/Au Schottky Contacts on β-Ga_2O_3 and Effects of Annealing Elizabeth Favela[1], Kun Zhang[1], Alice Ho[1], Sun Ho Kim[1], Kalyan Das[2] and Lisa Porter[1]; [1]Carnegie Mellon University, United States; [2]North Carolina State University, United States

Beta-gallium oxide (β-Ga_2O_3) is a wide band gap (E_G ~ 4.8 eV) material that has attracted much interest and development due to its superior properties, such as Baliga's figure of merit and the availability of melt-grown bulk crystals. The development of thermally stable contacts capable of high temperature operation is necessary for Ga_2O_3 high power rectifiers. Currently, commercial high temperature electronics are based on Si, GaN, and SiC. Yet, for conventional Si electronics the temperature limit is typically below 150–200 °C. In this work we investigated the thermal stability of Co/Au and Ni/Au Schottky contacts to Sn-doped (N_D =10^{18} cm^{-3}) (-201) β-Ga_2O_3 substrates. Current-voltage and capacitance-voltage measurements were conducted after sequential annealing treatments totaling >400 h at 300 °C and >150 h at 500 °C in air. Co and Ni were chosen because of their high work functions and previous work by our group that showed near-ideal Schottky diode characteristics for these metals on (100) β-Ga_2O_3.[1] In addition, positive free energies of reaction were calculated for NiO, Co_3O_4, and CoO, indicating that Ni or Co should not reduce Ga_2O_3 to form Ni-oxide or Co-oxide at the interface, although they do not preclude the possibility of other reactions.

The average Schottky barrier heights calculated from I-V measurements displayed no significant change and remained within a narrow range (F_B = 1.02 – 1.07 eV for Co/Au and F_B = 1.09 – 1.17 eV for Ni/Au) throughout the anneals at 300 °C. The SBHs calculated from C-V measurements appeared relatively constant through ~350 h but increased by ~0.1 eV for anneals >350 h. The C-V determined barrier heights were higher (~0.2–0.3 eV) than the respective SBH values calculated from I-V measurements, a result attributed to the relatively high doping concentration and potentially associated with the presence of an inhomogeneous barrier. For 500 °C anneals the I-V characteristics for Ni-Au contacts displayed continual changes beginning with early anneals, whereas Co/Au contacts were relatively stable. These results indicate thermal stability for both contacts annealed for more than 400 h at 300°C, whereas 500°C anneals resulted in changes in the rectifying characteristics, particularly for Ni/Au contacts. To understand chemical and microstructural changes that may occur during annealing, samples are being investigated using transmission electron microscopy (TEM). Cross-section TEM images of as-deposited Co/Au and Ni/Au contacts show sharp interfaces and will be compared with TEM images of annealed interfaces.

[1] L.A.M. Lyle, K. Jiang, E.V. Favela, K. Das, A. Popp, Z. Galazka, G. Wagner, and L.M. Porter, J. Vac. Sci. Technol. A 39, 033202 (2021).

PS03

(Student) Comparison of Electrical Behavior in Ga-Polar and N-Polar GaN n-Type Schottky Diodes After Fast and Thermal Neutron Irradiation

Farnood Mirkhosravi[1], Arman Rashidi[1], Joshua Gallagher[2], Andrew A. Aragon[1], Kyle Ahn[3], Emily Mace[4], Azaree Lintereur[2], Michael Scarpulla[3] and Daniel Feezell[1]; [1]University of New Mexico, United States; [2]The Pennsylvania State University, United States; [3]The University of Utah, United States; [4]Pacific Northwest National Laboratory, United States

Studies of the radiation tolerance and electrical behavior of gallium nitride (GaN) based devices are important for the next generation of high-power and high-frequency electronics for use in harsh environments such as nuclear reactors, particle accelerators, and aerospace applications. In this work, we study the behavior of Ga-polar and N-polar GaN *n*-type Schottky diodes before and after exposure to fast (550 fast:1 thermal) and fast+thermal (1 fast:2 thermal) neutrons. Samples were irradiated to three different Fast Neutron Irradiator (FNI) fluences (10^{10}, 10^{14}, and 10^{16} n/cm^2), and to 10^{16} n/cm^2 thermal neutron in the Dry Tube, which provided a higher ratio of thermal to fast neutrons.
Temperature-dependent current-voltage (I-V) and circular transmission line method (CTLM) measurements were used to study the electrical characteristics. A strong reduction in reverse leakage current and an increase in differential resistance in forward bias were observed after neutron irradiation. A hysteresis effect depending on sweep direction was also observed after neutron irradiation on both Ga-polar and N-polar diodes. Thermionic emission (TE), Frenkel-Poole emission (FP), and Fowler-Nordheim tunneling (FN) models were used to explain the I-V characteristics pre- and post-irradiation. The effective barrier height for electron emission from trap sites extracted from the FP model shows a slight decrease for Ga-polar diodes after fast and fast+thermal neutron irradiation, while for N-polar diodes the effective barrier height increased after fast neutrons and disappeared altogether for the fast+thermal neutron irradiation. The FN tunneling model shows that tunneling at higher reverse bias becomes less dominant after neutron irradiation on Ga-polar diodes, while the effective tunneling barrier height is increase after fast neutron exposure and decreased after fast+thermal neutron irradiation on N-polar diodes.
The study shows that Ga-polar and N-polar GaN Schottky diodes exhibit significant and different changes in electrical behavior after fast and thermal neutron irradiation. The reverse bias characteristics of N-polar appear to be more tolerant after both fast and fast+thermal neutron irradiation compared to Ga-polar. On the other hand, for the case of fast neutron irradiation, N-polar diodes show slightly higher degradation in bulk resistivity. For the fast+thermal neutron irradiation, while the Ga-polar shows only degradation in contact properties, the N-polar shows degradation in both bulk resistivity and contact properties, suggesting that fast neutrons have more impact on N-polar diodes even at lower fast to thermal ratios. The Schottky barrier height (SBH) and ideality factor extracted from C-V measurements are also in agreement with the above changes in these diodes. The origin of the different behaviors is attributed to the fundamental differences between the Ga-polar and N-polar orientations, such as their opposite polarization and differences in impurity incorporation, defect types, and surface reactivity.

PS04

(Student) Leveraging Thermoelectric Anisotropy in Single Crystal Antimony for Novel Heat Flux Sensing Devices

Kenneth McAfee, Peter Sunderland and Oded Rabin; University of Maryland, United States

Certain crystallographic configurations of anisotropic single-crystal materials yield electrical signals both parallel and perpendicular to an applied steady-state heat flux. This effect is known as the Transverse Seebeck Effect and has the potential to significantly progress the state of the art in heat flux measurement technologies. We report on the use of single crystal Antimony prismatic structures to demonstrate the efficacy of the Transverse Seebeck Effect in unconventional heat flux sensor arrangements. A prototype heat flux sensor was constructed using a single Antimony sensing element and revealed a linear relationship between the applied temperature gradient and the measured perpendicular voltage. Measurements of the principal Seebeck coefficient tensor components in single crystal Antimony specimens accompanied with computational simulations reinforced the validity of the prototype sensor configuration. Integration of multiple Antimony transducers into a single package demonstrated the scalability of Transverse Seebeck Effect-based devices, as multiple sensing elements can be connected in series to amplify the measured electrical signal for a given heat flux. This work is supported by the Department of Energy Award Number DE-FE0031902.

PS05

Growth of Iron Selenide Thin Films on *c*-Al_2O_3(0001) via Molecular Beam Epitaxy

Ryan Schalip[1], Anupam Roy[1,2] and Sanjay Banerjee[1]; [1]The University of Texas at Austin, United States; [2]Birla Institute of Technology Mesra, India

Two-dimensional (2D) superconductors have been of interest to the research community ever since the discovery of high critical temperatures (T_c > ~2K) in some of these materials. In particular, Fe-based superconductors such as iron selenide (FeSe) have some of the higher reported T_c's among these materials (T_c = ~8K for a bulk single crystal)[1]. Further interest in FeSe was found when it was discovered that the critical temperature of this material could be drastically increased by being grown on certain substrates (of which Nb-doped strontium titanate has the highest reported, with T_c > 100K) [2]. This implies that superconductivity in FeSe is largely mediated and carried by those layers nearest the interface and therefore the critical temperature might be further improved through proper choice of substrate and control of factors (e.g. dopants) that can affect interface phenomena. Herein, *c*-Al_2O_3 was chosen for its differences in electrical and structural properties from previously reported substrates as well as its growth and characterization-friendly properties (chemically inert, insulating, etc.).

In this work, we demonstrate the epitaxial growth of FeSe thin films directly on Al_2O_3(0001) surfaces using molecular beam epitaxy (MBE), and probe their structural and spectroscopic properties *via* various *in situ* and *ex situ* characterization techniques, including reflection high-energy electron diffraction (RHEED), X-ray diffraction (XRD), and Raman spectroscopy. Growth at elevated temperatures with an accompanying annealing step yields well-structured FeSe films with high crystalline quality and atomically flat surface morphologies, as evidenced by the sharp, streaky features seen in RHEED patterns of film surfaces. XRD analysis shows characteristic peaks corresponding to the (0 0 *l*) family of planes in FeSe, along with those peaks originating from the Al_2O_3 substrate. This confirms the growth to be epitaxial in nature, as no peaks other than the aforementioned (0 0 *l*) peaks are seen to be present. From the XRD, the c-axis lattice constant was extracted and found to be 5.53 Å, which matches well with that of tetragonal β-FeSe[3]. Raman spectroscopy of the films yields two primary peaks at 183.9 cm^{-1} and 193.8 cm^{-1}, each matching well to one of the characteristic vibrational modes of FeSe (the A_{1g} mode of Se and the B_{1g} mode of Fe respectively)[4]. The absence of other peaks, namely those linked to $FeSe_2$ (180 cm^{-1}, 217 cm^{-1}, and 254 cm^{-1}) and oxidation (250 cm^{-1} and 300 cm^{-1}) respectively, which further indicates the quality of our films[5-6].

We hope these results could later prove useful in understanding the role of substrate properties, such asdielectric and lattice constant, in the modulation of the film-substrate interface physics and

subsequently lead to discovery of even higher critical temperatures in this material on other yet to be tested substrates.

This work was supported by the Army Research Office (ARO) Grant # W911NF-17-1-0312 (MURI).

References

[1] F.-C. Hsu, *et al.*, Proc. Natl. Acad. Sci. USA 105, 14262 (2008).
[2] Ge, JF., *et al.*, Nature Mater.14, 285–289 (2015).
[3] T. M. McQueen, *et al.*, Phys. Rev. B 79, 014522 (2009).
[4] Marko Opačić and Nenad Lazarević. J. Serb. Chem. Soc. 82(9) 957–983 (2017)
[5]B. Yuan, *et al*. Dalton Trans., 2012, 41, 772
[6]R. Yang, *et al*., IEEE Trans. On Nano., Volume 18, 2019

PS06

(Student) A Machine Learning Attack Resilient True Random Number Generator Based on Stochastic Programmability in Two-Dimensional Transistors Akshay Wali and Saptarshi Das; The Pennsylvania State University, United States

Information exchange forms the heart of modern-day communications technology such as the Internet of Things (IoTs) that requires transmission of humongous volumes of data over increasingly complex networks. To guarantee security of encryption and decryption schemes for exchanging sensitive information, high quality random numbers are required. A true random number generator (TRNG) is a critical hardware component that guarantees such protection. Random numbers are widely used for information security, cryptography, stochastic modelling and banking and financing. In this article, we demonstrate a machine learning resilient TRNG by exploiting stochastic nature of carrier trapping and de-trapping phenomenon in a two-dimensional (2D) transistor with layered transition metal dichalcogenides (TMDs) such as tungsten diselenide (WSe_2) and tungsten disulfide (WS_2) as the channel material and a programmable gate stack consisting of a 50 nm alumina (Al_2O_3) as the gate dielectric and a Pt/TiN/p^{++}-Si as the gate electrode. Our TRNG offers advantages in terms of circuit complexity and size since the randomness is derived from a single device. Furthermore, the generated bits pass the specified NIST Sp 800-22 rev. 1a randomness tests without any post-processing highlighting the potential of 2D-based hardware security primitives.

PS07

(Student) *In Situ* Chemical Analysis of Complex Oxide Interfaces via Auger Electron Spectroscopy Harish Kumarasubramanian, Thomas Orvis and Jayakanth Ravichandran; University of Southern California, United States

Complex Oxides [1-3] have been investigated for their unconventional physical and chemical properties and ensuing broad technological applications, especially in the epitaxial thin film form. The key to controlling the properties of complex oxides is sensitively tied to their structure, composition, and chemical state of the transition metal ions in these materials. For ultra-high vacuum epitaxial growth methods such as molecular beam epitaxy, *in situ* structural characterization methods such as reflection high energy electron diffraction (RHEED) and low energy electron diffraction (LEED) have revolutionized our ability to control the structure of thin films, heterostructures and superlattices of complex oxides down to a single unit cell. These methods, RHEED in particular, have been adopted to high-pressure epitaxial growth methods such as Pulsed Laser Deposition (PLD). Nevertheless, the studying of the chemical state and composition of the materials *in situ*, especially in high-pressure environments, remains challenging due to the need to develop facile, accurate and versatile chemical and compositional analysis probes.
Recent developments in probe design for surface sensitive chemical analysis techniques such as Auger Electron Spectroscopy (AES) have expanded their use in harsh oxygen-rich atmosphere required for oxide thin film growth using PLD. This has been achieved by using a differential pumping system that uses a retarding field analyser (RFA), coupled with a collimator lens. This has led to increased sensitivity and much improved signal-to-background and signal-to-noise. This has further enabled us to measure and understand subtle changes in composition of the films *vis-à-vis* laser fluence and pressure [4]. Quantitative, real-time measurements of the composition during the growth have also led us to monitor and deliberately switch the surface termination of different oxide films [5].
Oxide heterostructures exhibit novel interfacial phenomena such as two-dimensional electron gases (2-DEGs), emergent ferromagnetism, tunable spin-charge interconversion and topological states. These interfacial phenomena are sensitive to surface reconstructions and charge transfer across the interfaces. To probe and manipulate these interfacial phenomena, it is imperative to study the chemical state of transition metals and oxygen at the single unit cell level. Considering that auger electrons are particularly sensitive to chemical state due to their outer-shell origins, real-time, *in situ* measurements of oxidation state during growth would help us understand the interplay of charge transfer with lattice, spin, and orbital degrees of freedom. In this work, we simultaneously measure the oxidation state, surface composition and in essence the surface termination of complex oxides by monitoring the relative intensity ratios and shifts of satellite peaks in Auger fine spectra of both the transition metal cations and oxygen. Structural characterization using methods such as *in situ* RHEED and High-Resolution X-Ray Diffraction have been used to corroborate these findings.
REFERENCES :

1. Huang, Z.; Renshaw Wang, X.; Rusydi, A.; Chen, J.; Yang, H.; Venkatesan, T.; Ariando, X. Interface engineering and emergent phenomena in oxide heterostructures. Adv. Mater. 2018, 30, No. 1802439.
2. Ramesh, R. Emerging routes to multiferroics. Nature 2009, 461, 1218−1219.
3. Schlom, D. G.; Chen, L. Q.; Pan, X.; Schmehl, A.; Zurbuchen, M. A. A thin film approach to engineering functionality into oxides. J. Am. Ceram. Soc. 2008, 91, 2429−2454.
4. Orvis, T.; Kumarasubramanian, H.; Surendran, M.; Kutagulla, S.; Cunniff, A.; Ravichandran, J.; *ACS Appl. Electron. Mater.* 2021, 3, 3, 1422–1428
5. Orvis, T.; Cao, T.; Surendran, M.; Kumarasubramanian, H.; Thind, A.S.; Cunniff, A.; Mishra, R.; Ravichandran, J.; *Nano Lett.* 2021, 21, 10, 4160–4166

PS08

(Student) Design and Fabrication of ITO Based Transparent and Flexible Electrode Array for Simultaneous 2-Photon Imaging and Electrophysiology Vikrant Kumar[1], Connor McCullough[2], Caroline Yu[1], Emily Gibson[2], Diego Restrepo[2] and Ioannis Kymissis[1]; [1]Columbia University, United States; [2]University of Colorado Denver, United States

Neural electrodes with good electrical conductivity and optical transparency from visible to near-infrared could potentially allow for simultaneous 2-photon imaging and electrophysiology of brain tissues. Additionally, ultra-miniaturization of the microelectrode arrays is needed to achieve a higher spatial resolution of the neural recordings which requires simple fabrication techniques. Here we present a design and fabrication of an ITO-based transparent, flexible electrode array for simultaneous neurophysiological recording and 2-photon imaging. Finding correlation of imaging data and electrical recordings can provide additional insights towards understanding neural circuits. This is often limited by opaque metal electrodes used for recording electrical signals which don't allow optogenetic activation of neural cells directly underneath the electrodes. Transparent conductive electrodes from

visible to near-infrared (NIR) spectrum are needed to enable simultaneous 2-photon imaging and electrical recording. Along with transparency, it is also important to have individual electrode sizes of the same order as the neural cells for improved spatial resolution of the recorded signals while maintaining the signal-to-noise ratio (SNR) of the system. The presented system addresses the above-mentioned issues. The size of the individual electrodes is 12 µm x 12 µm and the array has 34 channels arranged in a circle with a total area of 250 µm x 250 µm to fit at the bottom of a GRIN lens. The ITO electrodes showed optical transmittance of more than 80% in visible to NIR range in spectrophotometry. Electrical characterization (electrochemical impedance spectroscopy) showed an average impedance magnitude of around 325 kΩ for 10 different channels of the array when interfacing with physiological saline as electrolyte. Two-photon imaging with a 920 nm laser light source through the electrode array showed no significant loss in the IR loss signal demonstrating its transparency at the desired wavelength. The electrode array is connected to a custom PCB using a heat seal connector for data acquisition. The integrated array can further be mounted on a head-bar which can be used as a head-mounted device on a freely moving rat for simultaneous 2-photon imaging and electrical recording in the future.

PS09

(Student) Impact of Biquadratic Exchange Coupling via Molecule on Magnetic Tunnel Junction Based Molecular Spintronics Devices with Competing Molecule Induced Inter-Electrode Coupling Hayden Brown, Andoniaina M. Randriambololona, Eva Mutunga, Andrew C. Grizzle, Christopher D'Angelo and Pawan Tyagi; University of the District of Columbia, United States

Molecular spintronics self-assembled on magnetic tunnel junction (MTJ) testbeds are a promising method to attain functioning nanoscale devices[1]. To fabricate a magnetic tunnel junction molecular spintronics device (MTJMSD), the desired geometry is created using photolithography, then the thin film MTJ material is deposited via physical vapor deposition. Magnetic molecules self-assemble – under an applied electric potential – across the MTJ dielectric gap and covalently bond to the MTJ ferromagnet creating a complete MTJMSD[2]. There is much to comprehend about competing couplings between the ferromagnetic metal electrodes when fabricating MTJMSDs. The attachment of molecule allows for Biquadratic exchange coupling (BC) and Heisenberg coupling (HC) between the ferromagnetic electrodes. Prior studies have focused on direct exchange coupling and Heisenberg exchange coupling, whereas this paper will explore the effects of BC with no direct exchange coupling and competing HC[3]. Scaling up production of robust devices requires a detailed understanding of how the interaction between BC and HC affects the magnetic properties of the device, the device's response to applied magnetic fields, and hence its performance.[HB1] . BC favors the perpendicular orientation, an effect which competes with Heisenberg exchange coupling[4].
In this study, Monte Carlo simulations (MCS) focused on molecule-induced BC are used to understand how this exchange coupling affects overall device behavior. Our MCS utilizes the 3D Heisenberg model to simulate the MTJMSD design. This simulation study looks at the effects of increasing BC when molecules spanning 4 edges connect ferromagnetic electrodes of a cross junction MTJ configuration. Simulated devices stabilized after 200 million iterations sampled with a frequency of 25000. Our results showed that BC in the absence of HC had no effect on the magnetic susceptibility of the ferromagnetic electrodes of the device but induced a high and localized magnetic susceptibility at the molecular region. However, in the presence of antiparallel HC and BC, the magnetic susceptibility increased in the ferromagnetic electrodes and diminished at the molecular region. Here, we will also discuss how BC and HC exchange couplings influence the heat capacity of MTJMSDs to elucidate their response to applied thermal energy. This study provides insights for designing and understanding futuristic molecular spintronics devices.
This research is supported by National Science Foundation-CREST Award (Contract # HRD- 1914751), Department of Energy/ National Nuclear Security Agency (DE-FOA-0003945).
[1] P. Tyagi: Multilayer edge molecular electronics devices: a review. *Journal of Materials Chemistry* **21**, 4733 (2011).
[2] P. Tyagi, Nanotechnology, vol. 26 no.30, 305602 (2015).
[3] H. Brown, A. Grizzle, C. D'Angelo, B.R. Dahal, and P. Tyagi, AIP Advances **11**, 015228 (2021).
[4] A. Kartsev, M. Augustin, R.F.L. Evans, K.S. Novoselov, and E.J.G. Santos, Npj Computational Materials **6**, (2020)

PS10

(Student) Spin Fluctuations in Molecule-Electrode Magnetic Tunnel Junction-Based Spintronics Devices Andrew C. Grizzle, Christopher D'Angelo and Pawan Tyagi; University of The District of Columbia, United States

Understanding the charge transport of paramagnetic single-molecular magnets (SMM) sandwiched between optimized magnetic tunnel junction (MTJ) electrodes is essential for designing innovative molecular electronics. As a result, magnetic tunnel junction-based molecular spintronic devices (MTJMSDs) with increased optical, electrical, and magnetic properties are developed. Previous computational and experimental studies show that when molecules with fluctuating spin states are placed at room temperature between ferromagnetic electrodes, they display substantial antiferromagnetic coupling. On the other hand, quantifying the SMM's spin state when attached to the MTJMSD remains challenging. In turn, we conduct a Monte Carlo Simulation (MCS) analysis to investigate the spatial and temporal influence of the SMM spin state and spin fluctuation on the cross junction-shaped MTJMSD. Using a Markov process lead MCS and a Heisenberg model of the MTJMSD, we investigated the temporal and spatial distribution of the molecule-ferromagnet correlated phases. We also looked at the magnetic moments of the MTJMSD as a function of the SMM spin fluctuation, device thermal energy, and molecular coupling strengths. We also looked into the MTJMSD's heat capacity and magnetic susceptibility. To generate highly correlated phases and the overall MTJMSD antiparallel state, the normalized molecular spin state must be greater than 0.2. Furthermore, the MTJMSD moment varied non-linearly with molecular coupling intensity. Our findings imply that while developing MTJMSDs, it is critical to quantify the SMM spin state.

PS11

(Student) A Comparison Between Heisenberg and Biquadratic Exchange Coupling Effects on Magnetic Tunnel Junction Molecular Spintronics Devices (MTJMSDs) Andoniaina M. Randriambololona, Hayden Brown, Eva Mutunga, Andrew C. Grizzle, Christopher D'Angelo and Pawan Tyagi; University of the District of Columbia, United States

The MTJMSD nanostructure consists of two adjacent ferromagnetic (FM) electrodes separated by an insulator with molecules bridged across the tunnel barrier. The molecules enable communication via electron flow between the FM electrodes[1, 2]. Heisenberg Exchange Coupling (HC) and Biquadratic Exchange Coupling (BQC) are present in this phenomenon and affect the device's magnetic behavior[3]. Strong HC is exhibited between the FM electrodes and the molecules that bridge the two electrodes of the MTJMSD. BQC – perpendicular alignment of the spin vectors of the adjacent FM electrodes – also occurs via the insulator or molecular nanostructures. Little is known about the competing effects between these two types of interlayer exchange couplings on MTJMSDs. We studied this effect using Monte Carlo simulations (MCS) based on a 3D Heisenberg model. We varied

the BQC strength for a device with strong parallel and antiparallel molecular HC and examined the physical and magnetic properties of the MTJMSD. We found that as we increased the BQC strength in an MTJMSD with antiparallel molecular HC, the range of the antiparallel molecular coupling effect increased in both FM electrodes. However, only slight changes in the overall magnetization of the device were observed, and the antiparallel state was maintained. HC still ultimately dominated the magnetization of MTJMSD. We also studied the effect of BQC on the device's magnetic equilibrium state by examining the temporal evolutions of the device. Here, we will present our results that indicate BQC plays a lesser role in overall device magnetization as it cannot overcome the more substantial magnetization effect produced by the HC. We will also discuss our results from several other HC versus BQC possibilities under which BQC promoted the development of magnetic phases at 90-degree alignment. The presence of BQC provides a plausible explanation for the experimentally observed difference in magnetic phase orientations other than parallel and antiparallel states around MTJMSD.

This research is supported by National Science Foundation-CREST Award (Contract # HRD- 1914751), Department of Energy/ National Nuclear Security Agency (DE-FOA-0003945).

References

1. P. Tyagi, C. Baker and C. D'Angelo: Paramagnetic molecule induced strong antiferromagnetic exchange coupling on a magnetic tunnel junction based molecular spintronics device. *Nanotechnology* **26**, 305602 (2015).
2. R. Gareev, D. Bürgler, R. Schreiber, H. Braak, M. Buchmeier and P. Grünberg: Antiferromagnetic interlayer exchange coupling across epitaxial, Ge-containing spacers. *Applied Physics Letters* **83** (2003).
3. A. Kartsev, M. Augustin, R.F.L. Evans, K.S. Novoselov and E.J.G. Santos: Biquadratic exchange interactions in two-dimensional magnets. *npj Computational Materials* **6**, 150 (2020).

PS12

(Student) A Monte Carlo Study of Paramagnetic Nanostructure Coupled with Two Ferromagnetic Electrodes of a Cross-Junction Shaped Spintronics Device at Different Thermal Energies Pranshu Tyagi[1], Andrew C. Grizzle[2], Christopher D'Angelo[2] and Eva Mutunga[2]; [1]Springbrook High School, United States; [2]University of the District of Columbia, United States

Nanoscale spintronics devices can revolutionize computer logic and memory units. Interestingly, paramagnetic nanostructures strongly exchange coupled with two ferromagnetic electrodes can yield novel forms of magnetic materials. However, there is a knowledge gap about the role of the number of paramagnetic nanostructures on the various properties of whole spintronics devices. To make this study relevant to the experimentally attainable device structure, we focus on the magnetic tunnel junction (MTJ) based spintronics device architecture. Under this approach, paramagnetic nanostructures are placed along the MTJ perimeter. We assume that the tunnel barrier of the MTJ does not allow any leakage current or exchange coupling, and paramagnetic nanostructures dictate the exchange coupling between the ferromagnetic electrodes. Also, the width of the ferromagnetic electrodes is governed by the number of paramagnetic nanostructures. This study systematically varied the number of nanostructures from 1 to 625 (25 x 25). The overall device was represented by a Heisenberg 3D model containing five atomic layer thick ferromagnetic electrodes. The number of paramagnetic nanostructures governed the width of the ferromagnetic electrodes. For instance, the device with a single nanostructure and 5 x 5 nanostructure possessed FM electrodes with one atom and five atom width, respectively. The paramagnetic nanostructures – sandwiched between the two FM electrodes – were placed on the perimeter of the 5 x 5 square with an empty space inside the square. The empty space shows the presence of an insulating spacer needed to provide the physical separation to enable paramagnetic nanostructures to control the spin dynamics of the device[1]. The strength of exchange coupling between the paramagnetic nanostructure and ferromagnetic electrodes was fixed to be antiferromagnetic, consistent with experimental observations with analogous devices[2]. We observed that thermal energy strongly influenced the temporal evolution of the equilibrium state of devices. The device with a single paramagnetic nanostructure struggled to align the left ferromagnet (Left-FM) and right ferromagnetic electrode (Right -FM) at low thermal energy of kT = 0.01. At higher thermal energy, devices with a single paramagnetic nanostructure underwent significant fluctuations. The device with a 5 x 5 paramagnetic structure also had difficulty attaining the fully antiparallel state at low thermal energy of kT = 0.01. However, at higher thermal energy of kT = 0.1, 5 x 5 paramagnetic nanostructure started producing conclusive antiparallel ferromagnetic electrodes. This paper will discuss the full range of paramagnetic nanostructures up to 25 x 25 sizes over the thermal energy range from 0.01 to 0.1. To estimate the spatial impact range of the nanostructures, we also investigated the spatial correlation factor for each case. In addition, we also compute the spatial magnetic susceptibility and heat capacity of the device.

References:

1. Tyagi, P.; Riso, C.; Friebe, E., Magnetic Tunnel Junction Based Molecular Spintronics Devices Exhibiting Current Suppression At Room Temperature. *Organic Electronics* **2019,** *64*, 188-194.
2. Savadkoohi, M.; Dahal, B. R.; Grizzle, A.; D'Angelo, C.; Tyagi, P., Interaction between magnetic molecules and two ferromagnetic electrodes of a magnetic tunnel junction (MTJ). *Journal of Magnetism and Magnetic Materials* **2021,** *529*, 167902.

PS13

(Student) Influence of Crystallographic Orientation on the Asymmetric Emission of Calcite Katja S. Diaz-Granados[1], Weiliang Ma[2], Guanyu Lu[1], Peining Li[2] and Joshua Caldwell[1]; [1]Vanderbilt University, United States; [2]Huazhong University of Science and Technology, China

Calcite is a naturally occurring crystal that has a high level of anisotropy, and as such, exhibits thermal properties that are asymmetric. The orientation of the optic (or anisotropy) axis of the crystal with respect to its surface is experimentally shown to modify its thermal emission pattern. As the optic axis is tilted away from the surface, the emissivity peaks associated with the primary IR vibrational modes of calcite are seen to change in both shape and magnitude, indicating that tilting the optic axis effectively changes the contributions of each mode to the measured emissivity. Further varying the optic axis orientation by changing the altitude, azimuth and polarization angle for each tilt angle suggests that the emissivity signature is sensitive to changes in both the in-plane and out-of-plane optic axis orientation, and that, consistent with polarization selection rules, changes in the optic axis alignment with respect to the detector and the polarizer orientation modify the sampled vibrational modes. The observed asymmetries suggest that changing the orientation of the optic axis offers a way to tune the material dictated Reststrahlen bands in naturally anisotropic crystals.

PS14

Magnetic Anisotropy Effect on the Magnetic Tunnel Junction-Based Molecular Spintronics Devices Bishnu R. Dahal, Marzieh Savadkoohi, Eva Mutunga, Christopher D'Angelo and Pawan Tyagi; University of the District of Columbia, United States

Molecular spintronics is gaining attraction because molecules possess a weak scattering mechanism. As a result, molecules retain spin information over time. Molecular Spintronics devices (MSD) are also considered crucial for futuristic quantum computing

technology [1]. However, the fabrication of robust and mass-producible MSD at the nanoscale is a major concern. To overcome this issue, we have designed a magnetic tunnel junction-based molecular spintronics device (MTJMSD). MTJMSD is fabricated by bridging paramagnetic molecules across the edges of the ferromagnetic electrodes. These molecules form conducting channels over tunneling conduction between two ferromagnetic electrodes of an MTJ. MTJMSD enables the utilization of ferromagnetic electrodes with a wide range of magnetic anisotropies. Here, we are analyzing the magnetic switching mechanism, hysteresis loop (M-H Curve), and the overall magnetic properties of MTJMD as a function of anisotropies along with constant Heisenberg couplings.
In this paper, we report a theoretical Monte Carlo Simulation (MCS) study to explain the impact of anisotropies on the MTJMSD equilibrium properties. We also investigate theoretically how the nature of magnetic hysteresis changes as we apply the in-plane, out-of-plane, and in-plane and out-of-plane at the same time on the same ferromagnetic electrode. The application of in-plane anisotropy creates multiple magnetic phases of opposite magnetic spins on the same ferromagnetic electrode. The application of out-of-plane anisotropy created a dominant magnetic phase on the electrode. When in-plane and out-of-plane anisotropies are applied on an electrode simultaneously, the magnetic moment of the electrodes possessed its maximum value. The MTJMSD possessed its maximum value since the competing effect of anisotropies wiped out the multiple magnetic phases.
In this study, we also investigated the effect of anisotropies on the nature of the hysteresis curves generated computationally using MCS. We applied the in-plane and out-of-plane magnetic anisotropies on the same ferromagnetic electrode of an MTJ. The effect of the in-plane anisotropy transformed the regular magnetic hysteresis of MTJMSD into a "wasp-waisted" -like hysteresis curve[2]. The "wasp-waisted" -like hysteresis curve is hypothesized due to the presence of multiple magnetic phases present on the ferromagnetic electrodes caused by strong magnetic anisotropy. The application of equal magnitude of in-plane and out-of-plane anisotropies brings back the M-H curve into a regular hysteresis curve but with nearly zero coercivity. The zero coercive hysteresis closely agrees with the experimentally measured hysteresis under the same situations. In this paper, we will also present the overall properties of MTJMSD when the spin fluctuations option is incorporated in the MCS code.
This research is supported by National Science Foundation-CREST Award (Contract # HRD- 1914751), Department of Energy/ National Nuclear Security Agency (DE-FOA-0003945).
References
[1] A. R. Rocha, V. M. García-suárez, S. W. Bailey, C. J. Lambert, J. Ferrer, and S. Sanvito, "Towards molecular spintronics," *Nature Materials,* vol. 4, no. 4, pp. 335-339, 2005/04/01 2005, doi: 10.1038/nmat1349.
[2] T. M. de Lima Alves *et al.*, "Wasp-waisted behavior in magnetic hysteresis curves of CoFe 2 O 4 nanopowder at a low temperature: Experimental evidence and theoretical approach," *RSC advances,* vol. 7, no. 36, pp. 22187-22196, 2017.

PS15
Control of the Color Centers in Diamond Through Surface Encapsulation Summayya Kouser and Peter V. Sushko; Pacific Northwest National Laboratory, United States

Color or vacancy centers in the diamond lattice have found applications in novel fields like quantum computation and single spin magnetometry due to the possibility to prepare and read out their corresponding spin state optically and their long spin coherence times [1-2]. For example, Nitrogen vacancy (NV) centers can act as single photon emitters in the visible range with absolute photo stability at room temperature. These vacancy centers occur in several charged states. Behavior of these optically addressable spin defects (OSD) is affected by surface termination, roughness, proximity of the spin defects to the surface, polar & charged surface adsorbents and interfaces with other materials. Optically favorable NV^- is the prevailing state for centers buried deep in high-purity material. However, it has been observed to become unstable and turn into NV^0 close to the surface of diamonds as well as in nano diamonds [3]. For applications such as magnetometry, the control of the NV charge state is a crucial point, as defects with reliable spin properties in close vicinity to the surface are required. Surface termination can evolve due to interactions with environmental species, thus affecting properties of the defects [4]. We propose that surface encapsulation with 2D materials can be used to preserve the ordered H-termination and the Fermi level can be tuned by simultaneous adsorption of appropriate electron scavengers on the capping layer by tuning surface dipole. To this end, we use ab initio simulations to examine binding energies of species that saturate dangling bond on diamond surfaces, their interaction with encapsulating 2D materials, and the effect of electron charge redistribution on the band bending in the vicinity of the surface. We also consider the barriers for the diffusion of the adsorbed species across encapsulating layer to identify environmental conditions that allow for surface protection.
[1] Neumann, P. et al.; Quantum register based on coupled electron spins in a room-temperature solid, *Nature Physics* **6**, 249–253 (2010).
[2] Maze, J. R. et al.; Nanoscale magnetic sensing with an individual electronic spin in diamond, *Nature* **455**, 655 (2008).
[3] Fu, K.-M.C. et al.; Conversion of neutral nitrogen-vacancy centers to negatively charged nitrogen-vacancy centers through selective oxidation, *Appl. Phys. Lett*. **96**, 121907 (2010).
[4] Kouser, S.; Gupta, S.; Yakobson, B. I.; Dual role of adsorbent and non-monotonic transfer p-doping of diamond, *ACS Appl. Mater. Interfaces* **13**, 4676-468 (2021).

PS16
(Student) Spatial and Thermal Properties of Magnetic Tunnel Junction Based Molecular Spintronics Device (MTJMSD) Due To Magnetic Anisotropy Rodneycia Taylor, Bishnu R. Dahal, Eva Mutunga, Andrew C. Grizzle, Christopher D'Angelo and Pawan Tyagi; University of the District of Columbia, United States

Magnetic tunnel junction molecular-based spintronics devices (MTJMSDs) make the miniaturization of spintronics devices possible. MTJMSDs are durable and mass-producible[1]. Here, a Monte Carlo Simulation (MCS) study is designed to study the MTJMSD properties. The MTJMSD nanostructure consists of covalently bonded paramagnetic molecules bridged across the edges of ferromagnetic electrodes of a cross-junction magnetic tunnel junction (MTJ)[2]. We have studied the magnetic and thermal properties of MTJMSDs based on various parameters such as anisotropy, FM electrodes' coupling strengths, molecule type, insulator thickness, spin state, device dimension, and thermal energy (kT).
In this paper, we looked at the anisotropy effect of the ferromagnetic electrodes on the MTJMSD's properties at various thermal energies. Magnetic anisotropy is important for molecular spintronics because applying the logic of controlled anisotropy is crucial to improving the performance of MTJMSD. The MTJMSD used in this study is represented by a 11 x 50 x 50 Ising model, with 11 being the thickness of the MTJMSD and 5 x 5 x 50 being the size of each electrode. These two electrodes are connected by 5 molecules on each edge at the cross-junction. We ran the Markov process for 500 million iterations to reach the equilibrium state. Our study shows that the multiple domains of opposite spins start to appear on a FM electrode as the anisotropy strength increases. These domains impact the overall magnetic properties of the device. Symmetric magnetic properties of MTJMSD were observed in the spatial spin states as the out-of-plane anisotropy was switched across the left and right FM electrodes. In the strong molecular coupling regime, the effect of variation in anisotropy was stable at a relatively high thermal energy. We observed that

anisotropy maintains the higher magnetic moment of the device close to the levels observed at Curie temperature, even when all the coupling effects get nullified due to thermal agitation. These studies are expected to impact the electrical and magnetic-transport properties of MTJMSD and may help in designing MTJMSDs for logic and memory operation. Heat capacity and magnetic susceptibility, essential quantities that are commonly used to measure anisotropy, will be part of this discussion.

1. P. Tyagi, Journal of Materials Chemistry **21** (13), 4733-4742 (2011).
2. P. Tyagi, C. Baker and C. D'Angelo, Nanotechnology **26** (30), 305602 (2015).

PS17

(Student) The Design and Synthesis of Lead-Free Layered Hybrid Perovskites as Room-Temperature Ferroelectrics

Joseph T. Race and Patrick Woodward; The Ohio State University, United States

A promising crystal structure type for ferroelectricity is the layered hybrid organic-inorganic perovskite (HOIP) due to their tendency for polar structural distortions, a requirement of ferroelectricity. The most prominent layered HOIPs reported to be ferroelectric have the Ruddlesden-Popper (RP) structure consisting of inorganic slabs *n*-octahedra thick separated by organic cation bilayers and often contain a water-soluble form of toxic lead (Pb^{2+}). We aim to synthesize hybrid RP double perovskite ferroelectrics that replace Pb^{2+} with non-toxic M^+/M^{3+} cation pairs (i.e. Ag^+/Bi^{3+} or Ag^+/In^{3+}) and to better understand the structural distortions that lead to these polar structures.

One of the common structural distortions in hybrid RP perovskites is an octahedral tilt/rotation of the corner-connected octahedra to optimize the hydrogen bonding interactions between inorganic perovskite slabs and organic cations. We aim to understand the octahedral tilting patterns that allow the dipole moments of the polar organic molecules to align, creating a spontaneous electrical polarization within the crystal. We also seek to probe the contribution of the inorganic layer to the electrical polarization and if it aligns cooperatively with the organic layer. X-ray diffraction will be used to study the phase transitions of these compounds.

PS18

(Student) Characterization of Aqueous Lead Sensing Performance of Bismuth Functionalized 3D Inkjet Printed Electrochemical Electrodes Annatoma Arif and Robert C Roberts; The University of Texas at El Paso, United States

This research represents the design, fabrication, and characterization of bismuth (Bi (III)) functionalized 3D inkjet printed (IP) thin film metal electrodes on shape memory polymer (SMP) towards improved electrochemical sensing performance of lead (Pb(II)). The fabricated Bi (III) coated electrodes are characterized with the sample analyte prepared with 10 µg/L lead (Pb (II)) added to drinking water (El Paso, TX). The electrochemical cell fabricated in this research consists of a three electrodes cell: a counter electrode (CE), a working electrode (WE), and a reference electrode (RE). The WE is modified with Bi (III) by two different procedures: (a) ex situ - under potential deposition (UPD) of Bi (III) with a full cycle of cyclic voltammetry (CV) electrochemical analysis and (b) in situ - addition of 400 µg/L Bi (III) to a sample analyte of alkaline based drinking water contaminated with Pb (II).

Bi (III) is an environment friendly material. It plays an important role for heavy metal ion detection. The advantages of Bi (III) coated electrodes in case of heavy metal ion detection are less toxicity, high capacity for fused-alloy formation, less interference of the dissolved oxygen in the test medium, and wide negative potential window. One major disadvantage of Bi (III) is that it requires specific test medium such as an alkaline solution to activate its behavior. In this research, the disadvantage is overcome by preparing sample analyte by adding a very small amount of 50% sodium hydroxide (NaOH) directly to Pb (II) contaminated drinking water. The achieved pH of the sample analyte is 14.

The electrodes are initially IP (Fujifilm, DMP-2831) on SMP substrate using silver (Ag) nanoparticle conductive ink (ANP DGP-40-LT-15-C). The electrochemical cell containing one CE, WE, and RE are cured, sintered, and shrunk simultaneously at 180 °C for 3 min. The final lateral dimension of the electrochemical cell is $13\times10\times1.52$ mm^3 and the lateral working electrode surface area is 4 mm^2. The CE and WE are then gold (Au) plated with 24K brushed gold solution. The RE is chlorinated with dilute sodium hypochlorite solution for 60 seconds for silver chloride (AgCl) formation. Finally, the Au working electrode is Bi (III) coated by electroplating a film of Bi (III) on the surface of the electrode. This process can be performed in two different ways such as ex situ and in situ. This research has focused on both procedures to understand their effectivity towards improved electrochemical sensing performance.

In the ex situ procedure, the electroplating is conducted prior to the electrochemical sensing analysis. In this research, the ex situ Bi (III) plating is performed in two steps. In the first step, the solution of bismuth (III) chloride ($BiCl_3$) and water (H_2O) was prepared. $BiCl_3$ is soluble in H_2O due to hydrolyses and produces BiOCl and HCl. In the next step, a full cycle of CV analysis is performed on the Au based IP SMP incorporated electrodes to deposit Bi (III) film on the electrodes based on UPD. After Bi (III) coating the electrodes are applied to electrochemical sensing such as Pb (II) detection in the drinking water (alkaline). It is observed from the CV analysis that the Pb (II) stripping is sharper and appeared at more negative potential compared to Au plated electrodes.

In the in situ procedure, the electroplating is conducted simultaneously with the electrochemical sensing process. 400 µg/L Bi (III) was added with the sample analyte of Pb (II) contaminated tap drinking water optimized with NaOH. It is observed from the CV analysis that in situ Bi (III) electroplated electrodes perform significantly better in terms of stripping peaks (sharpness and appearance at the potential) for electrochemical sensing performance of Pb (II) detection in the optimized drinking water.

PS19

(Student) Spin Fluctuation Effect on Magnetic Tunnel Junction-Based Molecular Spintronics Devices (MTJMSD)

Arush Guliani[1], Michal Tefera[2], Patricia Reese[3], Andrew C. Grizzle[3], Christopher D'Angelo[3], Eva Mutunga[3] and Pawan Tyagi[3]; [1]Dublin High School, United States; [2]Virginia Tech, United States; [3]University of the District of Columbia, United States

When paramagnetic molecules covalently bond to a ferromagnet (FM), they undergo extensive hybridization with the surface and result in a spin-polarized molecule-ferromagnet interface. The resulting ferromagnet-molecule hybridization leads to a wide range of active functionalities, such as energy-level control and spin filtering capabilities[1]. Magnetic tunnel junction-based molecular spintronics devices (MTJMSDs) are fabricated by bridging monolayers of molecules across the MTJ's tunnel barrier, where they chemically bond with the FM electrodes. Thus, MTJMSDs become a highly promising testbed for controlled spintronics at room temperature [2, 3]. MTJMSD testbed also allows the molecule-ferromagnet interface to become a significant spin pathway enabling new equilibrium density of states over long range[2, 3]. Understanding the role of spin fluctuations in MTJMSD with various types of metallic electrodes is exceptionally challenging. We conducted theoretical studies to understand the free electrons spin effect on MTJMSD magnetization using 3D Heisenberg-based Monte Carlo simulations. For this study, we varied the electron spin in 1) ferromagnet-ferromagnet, 2) ferromagnet-paramagnet, and 3) ferromagnet-antiferromagnet electrode pairs. In general, we found that as the magnitude of free electrons spin in the electrodes

and molecules increased, the device magnetization increased when the free electron had parallel coupling with its host atom. Conversely, the total device magnetization decreased for antiparallel electron-atom coupling. Interestingly, long-range ordering in antiferromagnetic electrodes diminished with antiparallel electron-atom coupling and was enhanced with parallel coupling for a free-electron spin of equal magnitude at room temperature. In this study, we also recorded the correlated distribution of the devices' magnetic moment to elucidate the spatial impact range of molecules as a function of free electron spin. We also explored the electron spin effect on magnetic susceptibility and heat capacity. This research may inform the designing of novel molecular spintronics devices by providing a knowledge base about the impact of free electron spin for varying electrode materials.

This research is supported by National Science Foundation-CREST Award (Contract # HRD- 1914751), Department of Energy/ National Nuclear Security Agency (DE-FOA-0003945).

1. A. Cornia and P. Seneor, Nature Materials **16** (5), 505-506 (2017).
2. P. Tyagi, C. Riso, U. Amir, C. Rojas-Dotti and J. Martínez-Lillo, RSC Advances **10** (22), 13006-13015 (2020).
3. P. Tyagi, C. Riso and E. Friebe, Organic Electronics **64**, 188-194 (2019).

PS20
(Student) Phase Equilibria in the Metal-Sc-N Systems and Their Relevance for Contacts to ScN, ScGaN and ScAlN Yao Li and Suzanne Mohney; The Pennsylvania State University, United States

The properties of neighboring layers in thin-film structures are critical for the reliability and lifetime of electronic devices, and the reactivity of metals on semiconductors can markedly affect contact resistance. Wurtzite alloys of GaN or AlN with ScN are emerging thin-film piezoelectric materials.[1] Some researchers have also suggested that ScN might be used to advantage for in situ ohmic contacts in nitride devices, [2] although there is limited work on contacts to ScN. [3] Little work has been performed to examine the reactivity of ScN with other transition metals. This study calculates ternary phase diagrams for the Sc-M-N systems (M=transition metal) using reported experimental and estimated values of thermodynamic data. The calculated phase diagrams allow the identification of the dominant phase(s) for each Sc-M-N system. Systems are classified as ScN dominant (in which ScN is unreactive with the metal), metal-scandide dominant, metal-nitride dominant, or no phase dominant. It appears that ScN is stable against reaction with more transition metals than is GaN [4] and perhaps even AlN. [5] Among the metal nitride-dominant systems, we predict Ti, Zr, and Hf to be reactive should kinetics permit. Palladium, Pt, and Au are also predicted to be reactive due to the stability of their metal scandides. Future work will consider the mutual solubility of ScN and other transition metal nitrides, and we will present the results of annealing studies of metals on ScN.

[1] M. A. Moram and S. Zhang, J. Mater. Chem. A 2, 6042 (2014).
[2] J. Casamento et al., Appl. Phys. Lett. 115, 172101 (2019).
[3] M.I. Ortiz-Libreros et al., Appl. Surf. Sci. 175–176, 512 (2001).
[4] S. E. Mohney and X. Lin, J. Electron. Mater. 25, 811 (1996).
[5] K.O. Schweitz and S.E. Mohney, J. Electron. Mater. 30, 175 (2001)

PS21
Effect of Distributed Bragg Reflectors on the Optical Crosstalk in InGaN-Based Flip-Chip Micro-LED Arrays A B M Hamidul Islam[1], Tae Kyoung Kim[1], Yu-Jung Cha[1], Jae Won Seo[1], Dong-Soo Shin[2], Jong-In Shim[2] and Joon Seop Kwak[1]; [1]Korea Institute of Energy Technology, Korea (the Republic of); [2]Hanyang University, Korea (the Republic of)

Nitride-based micro-light-emitting diodes (μ-LEDs) have received significant attention for various applications such as optogenetic sources, neuron stimulations, visible light communications (VLCs), and micro-displays. μ-LEDs are considered more suitable for micro-displays in augmented reality (AR), virtual reality (VR), projectors, and wearable devices than liquid-crystal displays (LCDs) and organic light-emitting diodes (OLEDs) since μ-LEDs are self-emissive devices with higher efficiency, low power consumption, and longer lifetime. While the OLEDs are also self-emissive, they still suffer from lifetime and brightness issues at high driving currents. Moreover, the InGaN/GaN inorganic semiconductor material has a longer lifespan under extreme conditions with higher brightness at high driving currents than the organic counterparts. It is expected that the next-generation micro-displays require arrays of highly efficient red-green-blue (RGB) pixels with lateral dimensions less than 100×100 μm^2, which are not possible with the existing LCD and OLED-based displays. Currently, the μ-LED displays fabricated on plain sapphire substrates are known to suffer from severe optical crosstalk. Both the patterned sapphire substrate (PSS) and the costly laser lift-off process can be utilized to reduce the sapphire-substrate-induced crosstalk. Additional optical crosstalk is caused by mesa sidewalls, which can be suppressed by fabricating highly-reflective distributed Bragg reflector (DBR) on the mesa sidewalls. However, aspects of the DBR fabricated on the mesa sidewalls have rarely been discussed in the literature for improving the performances of μ-LED displays.
In this study, we have fabricated InGaN/GaN multiple-quantum-well blue flip-chip μ-LED arrays with > 20,000 pixels to investigate the various effects of the DBR on the optoelectronic performances. The size of each pixel is 12×12 μm^2 and the pitch are 15 μm. Three similar-epitaxial-structure μ-LED arrays fabricated on the plain sapphire and the PSS are tested. The DBRs fabricated on the p-GaN layer and sidewalls for the highly-reflective p-type electrode and the decrease in sidewall optical crosstalk, respectively, are carefully examined.
Various optoelectronic performances such as the forward voltage, the reverse leakage current, the light output power (LOP), the external quantum efficiency (EQE), the light emission distribution at low and high currents, and the electroluminescence spectrum are systematically studied. It is found that the DBR-based μ-LED shows better optoelectronic performances than the samples without the DBR. Since the DBR suppresses the optical leakage from the sidewalls, the light-extraction efficiency (LEE) increases, which causes the EQE to increase, and also the spot size becomes smaller than the μ-LEDs without the DBR. On the other hand, the non-PSS-based μ-LED arrays suffer from severe optical crosstalk. In addition, the effect of the DBR on junction temperature is also interactively explained. During the presentation, we will discuss both theoretical and experimental backgrounds of this work in more detail.

PS22
Zinc Multi-Pnictogens Semiconductors—Cu Doping and Thermoelectric Characteristics Jeyanthinath Mayandi and Terje G. Finstad; University of Oslo, Norway

We explore possibilities in combining zinc pnictogens. For III_B-V_B semiconductors band gap engineering by creating solid solutions of different binary III_B-V_B or II_B-VI_B compound is a very successful method for obtaining band gaps for specific optical applications. For example, the compounds GaP, GaAs and GaSb have the same

zinc blende crystal structure and are mutually soluble. GaBi has also recently been reported to grow epitaxially 1D or 2D on GaAs nanowires with wurtzite structure[1]. For the IIB-V_B compounds, ZnSb is a well-known thermoelectric semiconductor[2] It has the orthorhombic Pbca #61 structure referred to as 'electron poor'[3]. The same structure is reported for ZnAs. [4] However it requires growth under high pressure. The compound ZnBi with Pbca structure has been reported but is also unstable.[5] The compounds ZnP and ZnN don't exist with the same crystal structure but containing similar short order consisting of polyhedra. The mono pnictogens could hypothetically intermix and stabilize in a common crystal structure stabilized by entropy of mixing, like high entropy alloys. We have made mixtures of these elements and given melting and heat treatments followed by phase characterization and compaction of samples followed by electrical characterization. Mixtures of Zn, As, and Sb, resulted in phase structures with phase separation between arsenide and antimonide dependent upon the mixing ratio. Here we report on some interesting results for a parameter space winding yielding composite of the semiconductors ZnSb and $ZnAs_2$ from X-ray analysis and analytical electron microscopy inspection. $ZnAs_2$ is a semiconductor[6]. We doped the composite by Cu. The temperature dependence of the is metallic like or like that of a degenerate semiconductor while the Seebeck coefficient is very high for the undoped material. The Hall coefficient and the sign of the Seebeck coefficient both show p-type behavior. The doping of the composite with Cu lowers the resistivity and the Zebeck coefficient but the latter is still interestingly high and the thermal conductivity low.

References

1. Y. Liu, J. V. Knutsson, N. Wilson, E. Young, S. Lehmann, K. A. Dick, C. J. Palmstrom, A. Mikkelsen, and R. Timm, Nat Commun **12,** 5990 (2021).
2. X. Song and T. G. Finstad, in *Thermoelectrics for Power Generation - A Look at Trends in the Technology*(IntechOpen, 2016).
Ch. 6, Review of research on the thermoelectric material ZnSb," in Thermoelectrics for Power Generation: A Look at Trends in the Technology (InTech, Rijeka, 2016).
3. U. Haussermann and A. S. Mikhaylushkin, Dalton Transactions 39, 1036 (2010)
4. A. Fischer, D. Eklof, D. E. Benson, Y. Wu, E. W. Scheidt, W. Scherer, and U. Haussermann, Inorg Chem **53,** 8691 (2014).
5. The Materials Project. *Materials Data on ZnBi by Materials Project*. United States: N. p., 2020. Web. doi:10.17188/1316712.
6. I.G. Stamov, N.N. Syrbu, V.V. Ursaki, A.V. Dorogan, Optics Communications **285**, 3104 (2012)

PS23

Epitaxial GaAs/GaAsSb Separate Absorption Multiplication (SAM) Avalanche Nanowire Photodetector Rabin Pokharel, Mehul Parakh, Kendall Dawkin and Shanthi Iyer; North Carolina A&T State University, United States

Nanowire (NW) avalanche photodetectors (APDs) have the advantage of increased gain and sensitivity by shrinking the multiplication region thickness and having strong nanophotonic resonances compared to traditional thin-film APDs. Epitaxially grown nanowire (NW) based GaAs/GaAsSb core-shell avalanche photodetector (APD) device with separate absorption multiplication regions is presented in this work. A tunable absorption region of GaAsSb with varying Sb composition is used as an absorber material and a higher bandgap material of GaAs as a multiplication layer. GaAsSb material has a superior absorption property covering a large portion of the near infrared (NIR) region, a cost-effective alternative over competing Indium-containing III-V material system and allows less stringent control tuning in realizing nanoscale devices. The NW heterostructure is tailored to achieve an avalanche breakdown exceeding a gain of 100 (at 200K) at the technologically relevant wavelength of 1064 nm. The avalanche characteristics of the device are studied using low-temperature I-V, CV, and noise measurements. This work aims towards a potential realization of a tunable NW-based APD covering a large portion of the NIR region with low multiplication noise and high quantum efficiency.

PS24

(Student) Flexible Electrochemically Reduced Graphene Oxide Sensors for Lead and Cadmium Detection Rebekah De Penning and Sonal Padalkar; Iowa State University of Science and Technology, United States

Electrochemically reduced graphene oxide (ERGO) is an excellent sensor material for toxic heavy metal ion detection due to its unique properties. The ERGO combines the conductivity of pristine graphene with oxygen-containing defects that provide active binding sites for ions such as Pb^{2+} and Cd^{2+}. Sensors can be fabricated directly via electrochemical reduction from graphene oxide (GO) solution. This GO solution can be prepared in bulk by the Hummers method. The ERGO layer thickness can easily be controlled by changing the process parameters during the electrochemical deposition cycle. It can be easily deposited on substrates with varying degree of conductivity including glassy carbon, indium tin oxide on glass, carbon paper, carbon cloth etc. The carbon cloth substrate is particularly interesting in that it is flexible, three-dimensional, conductive and inexpensive. The combination of carbon cloth and ERGO forms a sensitive and disposable solution to the simultaneous electrochemical detection of Pb^{2+} and $Cd^{2+.}$ By using differential pulse anodic stripping voltammetry, ERGO on glassy carbon can detect down to 50 nM of Pb^{2+} and 100 nM of Cd^{2+}, and could resolve simultaneous oxidation peaks for both ion species. Furthermore, the ERGO-carbon cloth sensor shows vastly improved current response compared to the glassy carbon substrate due to the cloth's 3D nature and high surface area combined with ERGO's affinity for heavy metal ions. Therefore, electrochemically reduced graphene oxide and carbon cloth form a promising material combination for heavy metal sensing in water and food products.

PS25

Superconducting Properties of Fe (Te, Se) Thin Film on YSZ Substrate Using Pulsed Laser Deposition (PLD) Technique Himanshu Chauhan and Ghanshyam D. Varma; Indian Institute of Technology Roorkee, India

More than a decade after the discovery, the Fe-based superconductors (FeSCs) continue to fascinate the material science and condensed matter physics communities, not only due to their high transition temperature, strong irreversibility field, and excellent crystallographic symmetry, but also as a platform to investigate the correlated quantum matter. Recently, topological states have also been reported in the iron-based superconductor which suggests a promising direction to realize topological superconductivity. In recent years, several groups have been trying to understand the origin of topological states in thin films, but so far there is not much experimental agreement on these issues, and further studies are needed. Here, we have studied structural, superconducting, and topological properties of $FeTe_{0.55}Se_{0.45}$ thin film on Yttria-stabilized zirconia (YSZ) single-crystalline substrates using pulsed laser deposition (PLD) technique. The superconductivity in the grown thin film at $T_C \sim 14$ K has been affirmed by the temperature-dependent resistivity measurements. Superconducting parameters such as upper critical field $H_{C2}(0)$ and corresponding coherence lengths (ξ) and activation energy (U_0) have been estimated using magnetotransport measurements. In addition, A non-saturating linear magnetoresistance (LMR) is also observed, suggesting the presence of a possible topological superconducting state in the grown thin film. Furthermore, I-V measurement data has been used to calculate transport J_C (~10^5 A/cm^2) of grown thin film and the high J_C value demonstrates its

potential for high current applications. Our work will be helpful in developing thin films of Fe (Te, Se) superconductors with good superconducting properties that are important for various superconducting electronic devices. The study of the presence of the topological phase in the grown film is very relevant to the current focus of developing quantum devices.

PS26

(Student) Phase-Control Enabled Tunable Optical Properties of Nanostructured GeO2 Wide Band Gap Semiconductor Thin Films Paul Gaurav G. Nalam, Debabrata Das and Chintalapalle Ramana; The Center for Advanced Materials Research, UTEP, United States

Germanium dioxide (GeO_2), which an ultra-wide band gap material, has been explored in depth due to its promising thermal, optical, and electrical properties. While GeO_2 films exhibit quite interesting electronic properties, such as a high dielectric constant and refractive index, understanding the process-property correlation is the key to tailor their device performance. In this work, GeO_2 films (100 nm) were deposited onto Si(100) and sapphire substrates using sputtering in an oxidizing environment. The post-deposition annealing was performed at 800-1100°C in order to study the temperature-induced effects on the structure, morphology, and optical properties of GeO_2 films. While the as-deposited GeO_2 films were amorphous, increasing temperature induces amorphous-to-crystalline transformation. At 800°C, GeO_2 films exhibit hexagonal phase and then a clear phase transition to tetragonal structure at 1000°C. Correspondingly, the optical quality and band gap variation is noted in annealed GeO_2 films. The results will be presented and discussed to establish the structure-property correlation.

PS27

(Student) Optimized Light Absorption in GaAsSb(N) Nanowires for Photodetector Application Kendall D. Dawkins and Shanthi Iyer; North Carolina A&T State University, United States

Nanowires (NWs) offer the ability to fabricate 3rd generation devices with unique properties such as enhanced optical absorption, quantum confinement, low footprint, and high surface-to-volume ratios. The nanowire architecture also allows for a high tolerance for lattice mismatch, which results in the ability for nanowires to be grown on a multitude of surfaces. Since the diameter of nanowires is constrained to usually tens of nanometers with the length varying up to several micrometers, this confines the carries in two dimensions and allows for free propagation in the 3rd dimension. This correlates to the high density of electronic states leading to electrical, optical, and magnetic properties that are different than bulk and thin-film devices. By changing certain physical features of the nanowires, one can potentially design nanowires to exhibit distinct features for specific devices. GaAsSb is an important material system covering the telecom wavelength range of 870 nm (GaAs) to 1700 nm (GaSb). Incorporation of small amounts of nitrogen, usually less than 2%, leads to the reduction in the bandgap as well as lattice constant which is unique for the dilute nitride system. In this study, Lumerical Finite-Difference Time-Domain (FDTD) modeling has been used to simulate the absorption characteristics of GaAsSb(N) nanowires. The optimal absorbance spectra for GaAsSb/(N) nanowires for arrays were determined by varying nanowire diameter (D), pitch (P), length (L), and array configuration. From our results, we show that particular D/P ratios of 0.5 offer optimized light absorption for GaAsSb(N) nanowires. We show that GaAsSb/(N) nanowires are excellent material choices for absorption in the telecom wavelength spectra reaching 1.55 µm in a first-of-its-kind study for the GaAsSb(N) material system.

Acknowledgment: This material is based upon research supported by the Air Force Office of Scientific Research (AFOSR) under grant number W911NF1910002 and National Science Foundation Award #ECCS-1832117.

PS28

Impact of Double Donor In and Ga Doping on Self-Compensating Process in ZnO Nanocrystal Films Tetyana V. Torchynska, Brahim El Filali, Jorge Luis Ramirez Garcia and Georgiy Polupan; Instituto Politecnico Nacional, Mexico

Zinc oxide has attracted attention for decades due to its important optical, electrical, chemical and microstructural properties, interesting for optoelectronic applications in light emitting devices, transparent conduction oxide (TCO) in solar cells, gas sensors, flat screens and touch panel displays, in vacuum fluorescent displays, in photovoltaics or thermal mirrors. But the n-type conductivity of non-doped ZnO films is not high enough to be used in devices. Group–III atoms (Al, Ga, In) are very important donors for ZnO film–based technology. However, the free electron density in doped ZnO films was revealed to be limited to 10^{19} - 10^{21} $cm^{-3.}$ due to the self-compensating effect, related to generation of the acceptor-type defects to counteract of donor doping. The nature of these acceptor type defects and the factors that stimulate the self-compensating effect still remain to be investigated.
It was supposed that one reason for the self – compensating effect can be connected with a high level of elastic stresses in the doped ZnO films with high donor contents. In the present work, the variation of the optical, structural and electrical parameters of the ZnO nanocrystal (NC) films doped with Ga and In atoms has been investigated. ZnO films of 2 groups were grown by ultrasonic spray pyrolysis with the In contents 1.0 at% (1) or 2.0 at% (2) and the different concentrations of Ga from the range 0.5-3.0 at %. Using co-doping by Ga and In atoms with lower (Ga) and higher (In) ionic radii compared to the Zn ions, it is expected to lower the stresses in the films and gain insight into the factors favored to the self-compensating effect.
The ZnO films have been studied using scanning electron microscopy (SEM), energy dispersive X ray spectroscopy (EDS), X ray diffraction (XRD), photoluminescence (PL) and X-ray photo electronic spectroscopy (XPS). Non-monotonic changes in the morphology of films were revealed that correlates with non-monotonic changes of oxygen and indium contents in ZnO films with variation of Ga contents. Compressive stresses arising due to In doping prevent effective oxidation at the film crystallization. The Ga doping up to 1.5 at% allows to compensate the compressive stresses in the films that is favored to the effective ZnO oxidation and the dissolution of In ions in the thermal annealing. High donor doping was shown to be accompanied by the appearance of a new near band edge (NBE) emission band, related to carrier recombination in the shallow donor-acceptor pairs (DAPs), which is a “fingerprint” of a beginning of the self-compensating process. Simultaneously, the effective charges of the Ga (In) ions decrease and the rate of electrical resistivity reduction slows down. The nature of shallow donors and acceptors in DAPs, as well as the impact of co-doping by Ga and In atoms on the self-compensating effect have been discussed.

PS29

(Student) Structure, Emission and Resistivity Variation with AL and In Co-Doping of ZnO Films Grown by Spray Pyrolysis Brahim El Filali[1], Isis C. Ballardo Rodriguez[1], Tetyana V. Torchynska[1], Georgiy Polupan[1] and Lyudmula Shcherbyna[2]; [1]Instituto Politécnico Nacional, Mexico; [2]V. Lashkaryov Institute of Semiconductor Physics at the NASU, Ukraine

One of the best candidate to be used as a transparent semiconductor oxide in solar cells is ZnO films. However, un-doped ZnO has a high resistivity. The aluminum, gallium or indium atoms are excellent candidates to be used as dopants to low the resistivity of ZnO films. Doping with only In atoms greatly

limits the resistivity between 44 (Ω cm) (ZnO 0%In) and 0.017 (Ω cm) (ZnO 3.5%In).The radius of In^{3+} ions (0.81Å) larger than the radius of Zn^{2+} ions (0.74Å) that causes the stresses in the doped ZnO:In films, which influence on their structure and optical properties. To minimizing the doping stimulated stresses in ZnO films, the ZnO films with Al and In co - doping are investigated in this work. Note that the radius of Al^{3-} ions (0.53Å) smaller than those of Zn^{2+} ions.
The variation of the optical, structural and electrical parameters of ZnO nanocrystal films co-doped with In and Al atoms has been studied. The ZnO:In:Al films were deposited by spray pyrolysis with constant In content of 1at% in all ZnO films, but the different Al concentrations in the range of 1.0-3.5 at%.
ZnO films have been studied using scanning electron microscopy (SEM), energy dispersive X-ray spectroscopy (EDS) and X-ray diffraction (XRD) for the analysis of the composition and structural parameters. Furthermore, the photoluminescence, absorption and transmittance spectra were measured for monitoring optical parameters, as well as electrical resistivity has been controlled for all films. Two doping stages of the variation of all studied parameters were analysis and discuss. The optimal concentration of In and Al co-doping is estimated.

PS30
(Student) Growth and Characterization of (BaxCa1-x)TiO3 Single Crystals in Ir, Pt and Mo Crucibles Benjamin L. Dutton, Jani Jesenovec, Brooke Downing, Matt D. McCluskey and John S. McCloy; Washington State University, United States

Selecting a crucible material for crystal growth of high melting temperature oxides is often limited due to atmospheric and chemical conditions. In the case of Barium Titanate ((Ba_xCa_{1-x})TiO_3, BCTO), iridium, platinum and molybdenum crucibles were explored for Czochralski (CZ) and Vertical Gradient Freeze growths. Compositions of $x = 0.185$ and $x = 0.227$ were utilized to avoid the hexagonal-cubic phase transition upon cooling which typically destroys a pulled $BaTiO_3$ crystal and achieve congruent melting in the case of the latter composition. Growth in an Ir crucible was found to produce the largest single crystals (~1 × 1 × 1 cm), although cost of growth in Ir in the current market is prohibitively expensive. Platinum crucibles were found to be difficult for CZ growth due to vertical temperature gradients inherent to induction heating, as well as a melting temperature near that of BCTO. Molybdenum was economic in comparison and was explored with various (ZrO_2, graphite) insulation materials in order to minimize oxidation and melt interaction of the crucible at T_m. As-grown and oxygen annealed single crystals were analyzed via Raman microscopy, X-Ray Diffraction and Scanning Electronic Microscopy, including Energy Dispersive Spectroscopy to determine dopant content, structure and analyze heterogeneous secondary phases. Fourier Transform Infrared Spectroscopy and Ultraviolet-Visible-Near Infrared spectroscopy were used to study the optical properties of the crystals.

PS31
Fabrication of a Roll-to-Roll Printed Cantilever Type Touch Sensing and Actuating Device Sang Hoon Lee[1], Jaehak Shin[2] and Sangyoon Lee[2]; [1]University of California, Irvine, United States; [2]Konkuk University, Korea (the Republic of)

Devices that serve touch sensing and actuating are particularly applicable for Haptic technology. In the MEMS technology, there is an air-gap under the cantilever type capacitive touch sensor, and the cantilever beam is deformed when a touch is applied. The sensor detects the change in capacitance depending on the distance between the electrode above the cantilever beam and at the bottom. In addition, in the case of the MEMS actuator, there is an air-gap under the cantilever, so it is easily actuated by applied external input. Compared to the MEMS technology, printed electronics has significantly high productivity. However, only 2D structures can be fabricated with printed electronics technology, and it is difficult to fabricate 3D structures with air-gaps. In this study, a cantilever type capacitive touch sensing and actuating device was fabricated. An air-gap was made by printing and removing a water-soluble polyvinyl pyrrolidone (PVP). (Figure 1) This method is similar to the wet etching in MEMS fabrication. In particular, productivity was further improved by using a roll-to-roll gravure printing (Figure 2) which has a high throughput capability. First, the bottom electrode was made on a flexible polyethylene terephthalate (PET) substrate by roll-to-roll gravure printing a silver paste, and the dielectric layer was made by roll-to-roll gravure printing a barium sulfate ($BaSO_4$). Then, a water-soluble PVP was roll-to-roll gravure printed to make the sacrificial layer. And the top electrode was made by spin-coating a stretchable silver paste. On the top electrode, magnetic actuating layer having the same shape and size with the top electrode was made by spin coating an iron oxide (Fe_3O_4) and SU-8 mixture. Finally, the sacrificial layer was removed with water to make an air-gap. As a result of actuating and sensing tests, the magnetic actuating layer of the device was deformed up to 2 mm by the applied electromagnetic fields, and touch sensing sensitivity was 0.153 %/kPa.

PS32
Force Spun PVDF-TPU/Au Nanofiber Based TENG for Flexible Energy Harvesting and Bio Mechanical Motion Sensor
Sk Shamim Hasan Abir and M. Jasim Uddin; University of Texas Rio Grande Valley, United States

Over the last few years nanofiber based triboelectric nanogenerator (TENG) has caught great attention to the researchers all over the world for its inherent capability of converting mechanical energy to usable electrical energy. In this study, poly(vinylidene fluoride) (PVDF) and thermoplastic polyurethane (TPU) nanofiber prepared by Forcespinning (FS) technique were used to fabricate TENG for self-charging energy storage and bio mechanical body motion sensor. The surface of the TPU nanofiber was modified by uniform deposition of thin gold film to enhance the frictional properties; yielded 254 V open circuit voltage (*V*oc) and 86 μA short circuit current (*I*sc), an increase of 112% *V*oc and 87% *I*sc in contrast to bare PVDF-TPU TENG. Moreover, the as fabricated PVDF-TPU/Au TENG was tested against variable capacitors and resistive load and showed that with a 3.2 x 2.5 cm^2 active contact area, it can quick charge up to 7.64 V within 30s using a 1.0 μF capacitor and generate significant 2.54 mW power enough able to light 75 commercial LEDs (1.5 V each) by the hand tapping motion at 4 Hz (240 beats per minutes (bpm)) load frequency. Furthermore, the TENG was attached to different body parts to capture distinctive electrical signals for various body movement elucidated the prospective usability of our prepared nanofiber based TENG in self-powered flexible body motion sensor application.

PS33
Effect of Radical on Morphology and Charge Generation in Polymer Non-Fullerene Solar Cells Bhoj Gautam[1], Sheenamelia Jones[1], Tia Wright[1], Daria Thomas[1], Shubo Han[1] and Evgney Danilov[2]; [1]Fayetteville State University, United States; [2]North Carolina State University, United States

Conjugated polymers and small molecules have been intensively studied due to their unique electronic and optical properties, and studies have shown the potential for optoelectronic applications including solar cells Here, we studied the effect of galvinoxyl radical on the morphology and charge generation dynamics in polymer non fullerene blends. We employed photoluminescence and transient absorption spectroscopy, and atomic force microscopy to study the charge carrier dynamics and morphology in these systems. We observed the morphological changes when 3% radical is added to PBDB-T:ITIC blend. The changes include the increased surface roughness and the aggregation. The change in aggregation is also reflected in photoluminescence spectra of these

blends. Transient absorption dynamics indicates that the ITIC exciton splitting is more efficient in radical added PBDB-T:ITIC blend compared to the pristine blend. Our results provide important guidelines for the design of efficient polymer non fullerene solar cells.

PS34
(Student) Micro-Sized Si-Based Anodes Characterization and Optimization Using *In Situ* Atomic Force Microscopy Jian Liu, Hanna Cho and Jung Hyun Kim; The Ohio State University, United States

Recently, extensive research efforts have been devoted to developing high-energy anodes for lithium-ion batteries (LIBs) by using Si-based materials due to their superior energy densities compared with conventional graphite anodes. Compared to Si nano powders, micro-sized Si-based anodes have unique advantages of high tap-density, low manufacturing cost, and good manufacturing safety. However, the practical implementation of the micro-Si anode requires understanding its electro-chemo-mechanical behaviors and its optimal operational conditions at the cell level. Otherwise, the large volume expansion of Si (c.a., 310 %) will lead to the mechanical pulverization of particles and consequent loss of electrical contact. In addition, the cracking of Si particles will produce new SEI layers, which not only consume active Li-ions but increase cell impedance.
To optimize the electrochemical performance of micro-Si anode, we developed approaches to mitigate the Si mechanical degradation during battery cycling. We characterized the real-time morphological changes using in-situ Atomic Force Microscopy (AFM) and a designed AFM unit cell. We successfully tracked the volumetric variations of a micro-Si particle with respect to the cell state-of-charge (SOC) change and revealed its morphology-performance relationship.
From the in-situ AFM measurement, we successfully characterized multiple important electro-chemo-mechanical behaviors of the micro-Si such as volume-expansion behavior, particle crack generation, and SEI growth. We found these mechanical behaviors were closed related to electrochemical voltage windows and would directly affect the cycling performance of micro-Si anodes. Micro-Si particles underwent initial particle pulverization and subsequent large volume expansion (180%) during lithiation, then Si surface fractures were generated when excessively removing Li from Si. The Si surface fracture and resultant SEI growth significantly increased the cell impedance and degraded the cell performance. Our observations provide direct evidence that micro-Si degradation was triggered by reaching critical electrochemical cycling conditions. Then, we demonstrate a proof-of-concept that micro-Si anode can deliver an improved cycle life and lower cell resistance by applying the optimal cell cycling conditions. The results propose that micro-Si anode can offer a stable performance after further optimization of the cell materials and systems for next-generation high-energy Li-ion batteries.

PS35
(Student) Magnetic Modification of Boron Nitride Nanotubes for Alignment in Thermal Interface Composite Adesewa O. Maselugbo and Jeffrey Alston; North Carolina A&T State University, United States

Boron nitride (BN) nanotube is an anisotropic nanomaterial that possess unique intrinsic properties like high thermal conductivity, electrically insulating, high oxidation resistance, superior mechanical strength, and piezoelectric property. The incorporation of the BN nanotubes in polymer has created opportunities to produce composites with a wide range of possible applications like aerospace applications, thermal interface material. However, the improved properties of these composite like thermal transport ability are still far from expected and theoretical stipulations due to the random orientation of these nanotubes with excellent in-plane properties and poor out-of-plane properties. Therefore, controlling the orientation of the nanotubes in the composite is important for optimizing its performance. This paper focused on the magnetic modification of boron nitride nanotubes for their alignment in polymer composite.
The magnetic modification of the BN nanotube is carried out by functionalizing nanotubes with iron oxide nanoparticles (magnetite) which produces paramagnetic BN nanotubes. These functionalized BN nanotubes exhibit magnetic responses that can enable control over their orientation and position under low external magnetic fields in low viscous fluids. The BN nanotubes are modified through electrostatic interaction with the iron oxide nanoparticles, therefore, preserving their intrinsic properties and structure. The paramagnetic nanotubes are to be dispersed in polymer fluid, controlled with magnets, and cured to maintain nanotubes' position and alignment.
The magnetic functionalization of BN nanotubes can provide the ability to spatially manipulate these nanotubes into more complex networks crucial for applications in nanoelectronics, sensors, spintronics, and thermoelectric devices. It can also enable the fabrication of anisotropic composite materials with improved directional property and high thermal transport ability.

PS36
A Universal Expression for Transport in Nanostructured Materials and Devices Andres Vercik; University of São Paulo, Brazil

The Space-Charge-Limited-Current (SCLC) spectroscopy technique in solids is an extension of the one-dimensional Child-Langmuir law for vacuum gaps leading to the well-known Mott-Gurney law. Beyond that, the trap filling process leads to the Mark-Helfrich law. More recently, quantum and relativistic effects, as well as higher dimensions were incorporated. All these models can be expressed as a single scaling law, relating the current, J_{SCLC} with voltage, V, and gap or sample thickness, D, as $J_{SCLC} \approx V^{\beta}/D^{\gamma}$, with different values for the exponents. Other mechanisms are expected to occur in nanoscale solids and devices, such as field emission (FE) and Fowler-Nordheim (FN) tunneling, which might lead to different dependencies of the current on voltage. However, some aspects of this technique remain obscure, especially when dealing with very thin (sub-10nm) gaps and solids. Beyond, the abrupt transitions between regimes, unusual SCLC characteristics, such as the transition from collisional to quantum tunneling regimes expected in out of 2D plane of 2D-material-based heterostructures, still remain unexplored. Therefore, there is a need for a universal model to describe SCL currents to include different conduction mechanisms as well as smooth transitions between them. This goal, pursued for decades without substantial success, might be not achievable based on the mentioned simple scaling laws, requiring a new approach. In this work we present a proposal for such universal model by writing the scaling laws in a slightly different way, with the same underlying physics, except for the treatment of transport through localized states, such as traps. A function h(V) which contains the relevant information for transport an accounts for most of the fingerprints observed in experimental I-V curves of the most diverse set of physical systems, form materials to devices, is proposed. This approach leads to the usual scaling laws for constant values of h(V), whereas it is abandoned for the trap filing regime, although the same familiar higher slopes can be recovered. In contrast to the usual interpretation, the proposed model relates slopes of the log I- log V plot to trap (or localized states) density instead of trap energy. In order to show its applicability and accuracy, the proposed model is used to fit the I-V curves of different materials and device, namely, nanostructure organic composites, ultra-thin Metal-Oxide-Semiconductor devices and GaAs/AlGaAs/ double barrier resonant tunneling diodes.

PS37
(Student) Intra-Molecular Coupling on the Magnetic Properties of Magnetic Tunnel Junction-Based Molecular Spintronics Devices Pius Suh, Marzieh Savadkoohi, Andrew C. Grizzle, Bishnu R. Dahal, Christopher D'Angelo and Pawan Tyagi; University of the District of Columbia, United States

With a net spin state, paramagnetic molecules can cause magnetic exchange coupling between two ferromagnetic (FM) electrodes in the magnetic tunnel junction-based molecular spintronics devices (MTJMSD). Magnetic coupling between paramagnetic molecules and two FM electrodes in MTJ-based devices is dependent on a net molecular spin state. However, there exists a missing piece of information regarding the role of the coupling between molecule to molecule on the magnetic properties of the MTJMSD. In this research, we tested the hypothesis that variation in the strength and nature of intra-molecular coupling among multiple segments of a molecule can produce a novel testbed to observe the novel phenomenon.
This paper investigates the effect of intra-molecular coupling (Jm) on the MTJMSD magnetic properties using Monte Carlo Simulation (MCS). The strength of Jm was varied from different molecular positions, and its subsequent impact on the MTJMSD magnetic properties at different thermal energies studied. The total Device magnetization was recorded as a function of time for various simulation counts to achieve device stabilization and to capture its temporal evolution. Our MCS results showed that low Jm yielded an impact localized around the junction area. These studies, creates a platform and serve as an appetizer for subsequent investigations on the effect of intra-molecular coupling on the magnetic properties of the MTJMSD.

PS38
Modified $ZnSnO_3$ Structure in the Smart Helmet as a Promising Human Motion Sensor Sk Md Ali Zaker Shawon and M. Jasim Uddin; University of Texas Rio Grande Valley, United States

Lead-free perovskite oxides in Piezoelectric nanogenerators (PENGs) as a prospective sustainable energy source have drawn the attention of the scientific community owing to their non-toxic tradeoff for piezoelectric output, as well as chemical and structural stability. Herein, we have proposed a novel method for the fabrication of a high-output PENG that comprised a composite of Al-doped $ZnSnO_3$ nanocube, encapsulated in PDMS. The high piezopotential of this PENG is attributed to the novel crystalline $ZnSnO_3$ round-cornered nanocubical structure (average side length 30nm-55nm). In addition to that doping with mesoporous Al nanoparticles, provides the shift in this $ZnSnO_3$ non-centrosymmetric structure, which resulted in higher piezoelectric output (open circuit voltage ranging from 80V to 175 V) in comparison to the current $ZnSnO_3$ based PENGs. With the presented high output-to-size ratio taken into consideration, the device was mounted in a helmet and tested as an energy harvester and wireless human motion sensor, which can generate electric charge as well as to detect human movements and transmit the corresponding signals wirelessly. Our work is indicative of a promising smart helmet using organic-inorganic hybrid materials.

PS39
Tunable Optical Response by Anion Engineering in Crystalline Gallium Oxynitride Thin Film Debabrata Das, Paul Gaurav G. Nalam and Chintalapalle Ramana; The University of Texas at El Paso, United States

Gallium oxide has received significant attention in recent years because of its various multifunctional capabilities, such as ultra-wide band gap, sustainability in extreme environments, higher breakdown voltage, and electrochemical energy storage capability. In situ anion engineering is an important strategy to tailor the structural and optical behavior of this metal oxide semiconductor. In this work, we have grown gallium oxynitride on sapphire substrates using magnetron sputtering. Nitrogen incorporation was controlled by tailoring the percentage of nitrogen plasma during deposition. Substrate temperature was kept at a preoptimized value to demonstrate crystalline gallium oxynitride thin film with lowest possible defect density. Optical transmission measurement showed a gradual band gap shifting, which is because of nitrogen incorporated elevation of valence band maxima. The structure-chemistry-property correlation will be discussed to optimize the gallium oxynitride thin films for optoelectronic applications.

PS40
(Student) A Numerical Study of Perovskite Solar Cells by Bandgap Tuning of Active Materials and Operating Temperature Variances Mahir Abrar, Srabanti Datta, Matty Sey and Deidra Hodges; Florida International University, United States

Perovskite solar cells have shown potential for high performance and low production costs and are considered as one of the most emerging solar cells technologies. In single-junction topologies, the solar cell efficiency of laboratory-scale devices using these materials improved from 3.8% in 2009 to 25.7% in 2021. Compositional differences in perovskites (ABX_3) can produce a wide variety of crystal formations, phases, and stabilities. In this work, the mixed halide perovskite configuration of ABX_3 (A = $CH_3NH_3^+$, $HC(NH_2)_2^+$, Cs^+; B = Pb^{+2}; X = I^{-1}, Br^{-1}) integrated with Spiro OMeTAD as the HTL layer, SnO2 as the ETL, FTO as the transparent front contact on a glass substrate, and Ag as the back contact studied theoretically. The solar cell simulation program wxAMPS had been used, which was an improvement of the prominent solar cell simulation platform AMPS. The research provided a thorough understanding of the effects of each layer throughout the solar cell as well as its impact on the overall photovoltaic parameters. The bandgap of the active materials and operating temperature of the simulated solar cell were found to have a strong impact on solar cell performance. Furthermore, the simulation results show that photovoltaic parameters are strongly dependent on the thickness and defect density of the light-absorbing layers.

PS41
(Student) Towards a High-Modulation Reconfigurable Filter for Photodetectors via an Electrochromic Device Mauro C. Victorio, Vladimir Pozdin and Pulak Bhushan; Florida International University, United States

Portable systems have received significant attention owing to their widespread applicability in personal health monitoring and environmental sensing applications. Among the various sensing modalities implemented in a flexible and small form factor, optical detection remains the most attractive method. However, flexible implementation of optical sensing is limited to fixed wavelength due to hardware limitation and optical filtering for low power operation. Detection of multi analytes with multimodal sensing allows one to obtain more fine-grained and personalized understanding of an individual's health condition or environmental changes. Multimodal sensing in portable systems requires duplicate hardware, which increase system footprint and cost. Thus, taking advantage of materials with tunable wavelengths to measure multiple signals can benefit multimodal optical biosensing applications. This work demonstrates a flexible reconfigurable filter via an electrochromic mechanism. An electrochromic longpass filter based on Prussian Blue electrodeposited on indium tin oxide/polyethylene naphthalate (ITO/PEN) electrodes is presented here. The multi-color electrochromism of the deposited film is achieved through tuning of the electrolyte composition and the film structure. In addition, functionalization of multi-walled carbon nanotubes (MWCNTs) on the electrode surface are utilized to further enhance the electrochromic performance of the device.

The presented device structure serves as a proof-of-concept to achieve reconfigurable filters for multiwavelength optical detection in wearable and environmental applications.

PS42

Simulation and Modeling of Perovskite Solar Cells for Renewable Energy Application Luis F. Hernandez Camas; The University of the District of Columbia, United States

The importance of renewable energy in our current time merits for further research. Solar energy has the capability to harness the energy required to power space satellites, homes, cars, etc. The conversion of sunlight into electricity therefore has become essential and promising. Perovskite Solar Cells (PSCs) are low cost, environmentally friendly and a new emerging technology that provides a solution. We have studied inorganic n-i-p planar structure to achieve a higher efficient solar cell. With the use of SCAPS simulation we simulate the deficient conditions of each layer of the PSCS such as thickness, defects, metal work function, shallow uniform acceptor density and the impact of different elements within the structure. In our model, we have different layers that consist of TiO2, SnO2, perovskite and a HTM layer. The highest efficiency is 23.09% and is found within CuSCN. The reason is high bandgap and high mobility which reduce back contact barrier and increase hole collection. The thickness of the perovskite also plays a role since it impacts photocurrent but slightly impacts open circuit voltage.

PS43

2D Material Based Ag-ZnO-CeO2 Heterostructure for Solar-Driven CO_2 Reduction Mohammed M. Al-Ghorbani[1,2]; [1]King Abdullah University of Science and Technology, Saudi Arabia; [2]Taibah University, Saudi Arabia

CO_2 emission is the main contributor to global warming that severely threatens life on the earth. Thus, there is an urgent need to reduce atmospheric CO_2 concentration. Solar-driven photocatalytic CO_2 reduction to produce useful fuels is a promising green approach to address the CO_2 emission and energy crisis simultaneously. An efficient photocatalyst should have full solar spectrum harvesting ability, negligible charge recombination rate, efficient charge transfer and separation, high concentration of photocatalytic active sites, and enough redox potential.
Due to their ultrathin morphology, 2D semiconductor materials exhibit high surface area, more catalytic exposed active sites, and high capacity of light absorption which made them promising materials for photocatalytic CO_2 reduction. Photocatalyst designing with negligible electron-hole recombination, and maximized redox potential is an essential prerequisite for achieving commercial-scale photocatalytic CO_2 reduction. This contribution combines surface plasmon resonance and Z-scheme charge transport in a single photocatalyst (Ag-ZnO-CeO2 heterostructure) aiming to improve its performance for photocatalytic CO2 reduction. The AgZnO-CeO_2 heterostructure is fabricated via sunlight-driven combustion and deposition approaches. Ag plays dual rules as an electron mediator to facilitate the Z-scheme charge transport and plasmonic material to maximize the light absorption in the visible region. The designed photocatalyst exhibits significantly enhanced photocatalytic activity for CO_2 reduction under simulated sunlight irradiation. This work offers the opportunity of constructing an efficient Z-scheme photocatalyst from wide bandgap semiconductors with the full-visible light response, suppressed electron-hole recombination and optimized redox potential.

PS44

(Late News) Depth-Dependent Photoluminescence Analysis of the Inhomogeneities in Perovskite Solar Cell Eulises Regalado-Perez[1,2], Evelyin Diaz-Cruz[1,3], Julieta Landa-Bautista[1], Nini Rose Mathews[1] and Xavier Mathew[1]; [1]Universidad Nacional Autónoma de México, Mexico; [2]Instituto de Física “Luis Rivera Terrazas”, Benemérita Universidad Autónoma de Puebla, Mexico; [3]Universidad del Istmo, Mexico

In this work, we report depth-dependent photoluminescence to investigate the impact of vertical inhomogeneity on carrier extraction in perovskite devices. The vertical inhomogeneities which include uneven grains, voids, and grain boundaries are closely linked to the underlying charge transport layer which controls the nucleation and grain growth in the perovskite film. In the present work, we studied devices based on mesoporous TiO_2 and planar SnO_2. By exploring the morphological properties and the PL emission from different depths across the device structures, we show that the lower vertical inhomogeneity leads to more efficient charge carrier extraction in planar SnO_2-based devices. A red shift and line broadening of PL emission was observed when grain size changes in the direction of the incident probe laser. The perovskite deposited over planar SnO_2 electron transport layer (ETL) showed least red shift and broadening compared to that on mesoporous TiO_2, as a consequence of higher vertical homogeneity and structural order. Overall, the devices fabricated with SnO_2 ETL demonstrated least trap-assisted recombination and higher charge extraction leading to better device performance. Our studies reveal that the choice of SnO_2 over TiO_2 is not only because of the higher electron affinity leading to more favorable band alignment but also due to the vertical homogeneity resulting in a more propitious charge extraction-recombination balance in the device structure. This work provides a broader understanding of the impact of vertical inhomogeneity on the charge extraction efficiency, and presents a methodology to study quantitatively the inhomogeneity of perovskite films in device structures.
Acknowledgements: This work was partially supported by the projects PAPIIT-UNAM IT100221 and Texas A&M-CONACyT collaborative grant 19-20-027.

PS45

(Late News) Wurtzite Crystalline Structure Enhances Second-Harmonic Generation in GaAs Nanowires Bin Zhang[1], Jan Stehr[1], Ping-Ping Chen[2], Xingjun Wang[2], Fumitaro Ishikawa[3], Weimin Chen[1] and Irina Buyanova[1]; [1]Linköping University, Sweden; [2]Shanghai Institute of Technical Physics, China; [3]Ehime University, Japan

Nonlinear optical processes, including second harmonic generation (SHG), can be utilized in a wide range of classical and quantum applications, including on-chip integrated nano-photonic systems, non-linear optical microscopy, IR light visualisation and sensing. Using nanowires (NWs) for such applications is advantageous for efficient miniaturization and provides freedom in tailoring their non-linear response. An additional degree of freedom in the engineering of the SHG response is provided by the ability to grow NWs with different lattice structures and, therefore, to explore non-linearity of crystallographic polytypes that cannot be fabricated in bulk under conventional growth conditions. This makes it possible to tailor a polarimetric response of SHG determined by crystal symmetry. The (Al)GaAs material system is especially appealing as non-linear media, as GaAs exhibits large bulk second-order nonlinear optical susceptibility, rendering GaAs NWs highly attractive for diverse nonlinear photonic devices. Though essential for optimization, ascertaining the origin of SHG in thin NWs, including GaAs-based NWs, is not trivial due to sensitivity of non-linear properties to surfaces, interfaces, defects, as well as lattice polymorphism. Until now, however, impacts of these effects on non-linear properties of GaAs NWs are still largely unexplored and are investigated in this work.

The investigated GaAs NWs were grown by molecular beam epitaxy. Both zinc blende (ZB) and wurtzite (WZ) NWs with diameters of around 80 - 100 nm were studied. Their crystallographic structure was ascertained by using transmission electron microscopy (TEM). It is found [1] that the SHG intensity is significantly stronger in WZ NWs as compared with ZB NWs (by about 7 times), reaching the value of 2.5×10^{-5} W^{-1}. This value is among the highest reported in the literature, including complex waveguide and nanoresonator structures, as well as hybrid plasmonic structures. Such enhancement was directly verified by correlative SHG intensity mapping and TEM characterization performed on the same polymorphic NWs. Polarization-resolved measurements shows that the increase of the orthogonal SHG component is chiefly controlled by the surface-induced SHG caused by structural and electric field discontinuity at the NW surface. This component, however, remains weaker than the parallel SHG output by about two orders of magnitude, due to weak out-coupling of the generated light from thin NWs. The dominant parallel SHG is proven to be enhanced in WZ via electric-field induced SHG, which is activated by the axial built-in electric field related to spontaneous polarization in WZ NWs, and can be controlled optically and potentially electrically. This SHG enhancement is found to be robust and does not require high structural quality of the NWs as the presence of structural defects in fact facilitates SHG by enhancing the internal electric field. Our results, therefore, demonstrate great potential of thin GaAs NWs for nonlinear nanophotonics and show that their non-linear properties can be manipulated via lattice engineering.

[1] B. Zhang et al., Adv. Funct. Mater. 31, 2104671 (2021).

PS46

(Student, Late News, Student) Revealing the Electronic Heterogeneity and Inhomogeneity in Perovskite $CsPbBr_3$ Nanowires Using Contactless Dielectric Force Microscopy

Rahayana Ruth Bautista[1], Shuang Liang[2], Tuong Trieu[1], Zhiqun Lin[2] and Yize Stephanie Li[1]; [1]California State University, Bakersfield, United States; [2]Georgia Institute of Technology, United States

Dielectric force microscopy (DFM) is a scanning force microscopy (SFM)-based technique that utilizes a double-pass imaging method to probe the electronic properties of low-dimensional materials, such as nanowires, nanorods, and nanotubes. In this work, we employ the DFM technique to identify majority charge carriers in all-inorganic metal halide perovskite $CsPbBr_3$ nanowires (NWs) synthesized using a hot-injection approach. Ambipolar, n-type, and p-type responses have been observed in different $CsPbBr_3$ NWs, revealing the electronic heterogeneities of the as-synthesized $CsPbBr_3$ NWs. Moreover, longitudinal and transverse electronic inhomogeneities have been unveiled in $CsPbBr_3$ NWs with diameters of 10-20 nm and 30-40 nm diameter, respectively. Such findings suggest the potential of further DFM studies on the electronic properties of other perovskites nanostructures.

PS47

(Late News) Thickness Dependence of Electronic Properties of GaN Slabs—A Density Functional Study

Narges Masoumi[1], Rasoul Khaledialidusti[2] and Reza Vatan Meidanshahi[1]; [1]Arizona State University, United States; [2]Norwegian University of Science and Technology, Norway

GaN with a wurtzite structure is of great interest due to its wide direct bandgap, high breakdown voltage, spontaneous polarization, high electron mobility, and high thermochemical stability. Such distinct properties make GaN a promising material for a broad range of applications in electronic and optoelectronic devices e.g., blue light-emitting diodes (LEDs) and lasers, high power transistors, piezodevices, high electron mobility transistor (HEMT), pyroelectric sensors, etc. As individual devices are continuously scaled-down, the thickness of the GaN layer reaches the nanometer level where the surface-to-volume ratio is significantly higher than its bulk counterpart. In this regime, the thickness and structural details of the surface play critical roles in determining the electronic properties of GaN and affect the GaN-based device fabrication and functionality.

Here we use ab initio density functional theory (DFT) to systematically investigate the effect of thickness on the electronic properties of wurtzite-structure Ga-terminated GaN (0001) slabs with 2x2 surface reconstruction which is the most frequently used surface orientation for the epitaxial growth of GaN in the fabrication of GaN-based devices. Therefore, the band structures, band bending, and surface charges of up to 9 bilayer GaN slabs are studied. Moreover, to study the polarity of the slabs, the work function of various slabs has been calculated. We found that after 6 Ga-N bilayers thickness, the electronic bulk properties of GaN are recovered in the middle of the slabs and the surface reconstruction remains unchanged. The bandgap is decreased from 3.4 eV for the slab with 2 Ga-N bilayers to 2.2 eV for the slabs with > 6 Ga-N bilayers. This larger bandgap in thinner slabs could lead to higher breakdown voltage in GaN power electronic devices. Our study reveals that the distortion of atoms from their equilibrium positions at lower thicknesses induces an additional polarization to the spontaneous polarization which consequently creates higher carrier concentration in the channel layer of HEMT devices. We also observed that in GaN slabs, surface charge density and band bending are highly correlated with the thickness such that both quantities increase when the slab thickness decreases. This behavior could potentially affect the fabrication of the low dimension GaN-based devices. Moreover, the obtained work function (electron affinity) for various slabs shows a linear dependency on the thickness with a positive slope.

PS48

(Late News) Effects of Ge Doping on the Properties of Cu_2ZnSnS_4 Thin Film Solar Cells

T.G Sanchez and Nini Rose Mathews; Instituto de Energías Renovables, Mexico

Effects of Ge doping on the properties of Cu_2ZnSnS_4 thin film solar cells

T.G. Sanchez[1], N.R. Mathews[1, *]
[1] Instituto de Energías Renovables, Universidad nacional Autónoma de México, Temixco, Morelos, 62580, México

Cu_2ZnSnS_4 is a p-type semiconductor with earth abundant and low toxicity constituent elements. It has a band gap of 1.5 eV and an absorption coefficient greater than 10^4 cm^{-1} and is considered as a potential candidate to replace other chalcogenides like CdTe, CIGS. Herein, we report the incorporation of Ge into Cu_2ZnSnS_4 (CZTS) films and its effect on the structural, morphological, and solar cell properties. CZTS thin films were developed from sputtered Cu/Sn/Cu/Zn metallic stacks followed by annealing under S atmosphere. Solar cells with the glass/Mo/CZTGS/CdS/i-ZnO/ITO architecture were fabricated and the role of Ge thickness on the devices parameters was studied. The Ge thickness investigated were 5, 10 and 15 nm. Devices made with the stack Mo/Cu/Sn/Cu/Zn/Ge with 5 nm thick Ge resulted in best performance and a 27 % efficiency improvement over the reference cell was obtained (from 5.5% up to 7%). The EQE curve showed an improvement in the collection of photo generated carriers. The carrier concentration was determined to be in the range of 1×10^{16} - 1×10^{17} cm^{-3} for CZTGS films, which is in the range of the values reported for CZTS.

Acknowledgements: This work was supported by the project PAPIIT: IN102921.

PS49
(Student, Late News, Student) Realizing an aTomically Flat Surface of Ge (111) Thin Film At Low Temperature (220°C) by Gold-Induced Layer Exchange Narin Sunthornpan and Kentaro Kyuno; Shibaura Institute of Technology, Japan

Germanium (Ge) thin film is one of the most promising semiconductor materials for next generation electronic devices. Ge offers several potential features, including higher electron and hole mobilities and a smaller energy bandgap compared with conventional silicon material, which makes it ideal for high-speed thin-film transistors and next-generation MOSFETs. Additionally, Ge has good lattice matching with group III-V semiconductor, which can be applied as a bottom layer for high efficiency GaAs solar cell. Especially, fabricating Ge thin film on plastic substrate could realize the high efficiency flexible solar cell. The metal-induced crystallization (MIC) method using gold (Au) catalyst is one of the most promising crystallization methods for crystallizing Ge thin films on plastic substrates like polyimide at low temperature. Nevertheless, the formation of excess Ge islands on the crystalline Ge films are generally found in the MIC method which roughens the surface. Additional processes are required to remove these Ge islands, which is usually done by wet etching processes by H_2O_2 or peeling off with tape which could damage the sample. In this study, it is found that the four growth conditions including (1) Au/Ge thickness ratio, (2) annealing temperature, (3) heating rate and (4) initial Au layer thickness, are very important factors to obtain a high-quality Ge thin film. The flat and continuous crystalline layer can be obtained by controlling these growth parameters, and no additional process is required. In this work, we successfully obtained a smooth and continuous layer of crystalline Ge thin films with mainly (111) orientation at low temperature crystallization by controlling these growth parameters. This achievement will open up the possibility to fabricate a high-quality Ge thin film on plastic substrate as a buffer layer instead of an expensive single crystalline Ge for the epitaxial growth of GaAs film for the next-generation flexible solar cell application.

The Au/Ge bilayer films were fabricated by RF magnetron sputtering process on Si wafer with 100nm thermally grown oxide (SiO_2) layer. The thickness of Au/Ge layer is Au(29nm)/Ge(46nm), which is the optimized value found in the previous study. The bilayer films were crystallized by using the MIC method at 220 and 250°C under N_2 ambient for 1hr at different heating rate conditions. Structural properties were examined by X-ray diffraction (XRD), Raman spectroscopy, scanning electron microscope (SEM) and electron backscattered diffraction (EBSD). The results show that Ge thin films are successfully crystallized even at an annealing temperature as low as 220°C, which is low enough to be fabricated on a plastic substrate. Surface coverage of as high as ~99% is achieved for sample annealed at 220°C with a low heating rate of 0.5°C/min. The film surface is very smooth and continuous coverage without excess Ge islands on crystalline Ge. From the Hall effect measurement, hole mobility of as high as 145 cm^2/Vs is achieved. Moreover, a smooth and continuous layer of crystalline Ge thin film with mainly (111) orientation is achieved when a thinner Au layer and low heating rate at low annealing temperature are adopted.

PS50
(Late News, Student) Aerosol Printed Asymmetric Coupled Stripline (ACS) fed Microstrip Antenna for Biomedical Applications Sanjee Lamsal[1], Joao Garretto[1], Srikanth Itapu[2], Frank X. Li[1], Pedro Cortes[1] and Vamsi Borra[1]; [1]Youngstown State University, United States; [2]Alliance University, India

Implantable antennas have gained significant interest owing to their applications in medical implant technologies such as wireless sensors, stimulators, and others. However, the design is constrained by miniaturization, transmission path loss via the human body, regulatory requirements, and biocompatibility. For identifying small items of concern in biomedical applications, sufficient resolution across the thickness is required. The initial focus of implantable antenna research was on linear polarized antennas. Because of the antenna's invisibility within the human body, it proved impossible to properly detect the orientation of the implanted antenna. As a result, circular polarization (CP) is preferred for implantable antennas to establish effective and efficient communication [1]. The proposed antenna is printed using an aerosol jet printing technology, and offers advantages such as compact size, simplicity of manufacturing, a larger impedance spectrum, simple design, and high performance. On a flexible FR4 substrate, an asymmetric-fed Coupled Stripline (ACS) antenna with an impedance bandwidth of 2 GHz to 20 GHz is 3D-printed using aerosol jet printing technology. To ensure optimal antenna performance, the printing process precisely controls the placement, geometry, and thickness of the deposit. The simulations were carried out with Ansys high frequency structural simulator (HFSS) Electronics Desktop v.20, and the results were confirmed with the help of Keysight Vector Network Analyzer (VNA).
References
[1] L.-J. Xu, X. Jin, D. Hua, W.-J. Lu, and Z. Duan, “Realization of Circular Polarization and Gain Enhancement for Implantable Antenna”, doi: 10.1109/ACCESS.2019.2963744.

PS51
(Student, Late News) Design and Development of Additively Manufacture Passive Heat Sink for Electronics Cooling
Wondwosen F. Demisse and Pawan Tyagi; University of the District of Columbia, United States

The increasing demand for data use in our community results in a massive data processing and computational hours. The state of art electronics uses significant power, and a part of it is converted into heat. This enormous amount of heat may result in overheating and compromise the electronics performance. Overheating can affect the device functions, speed and lead to random shutdowns, unusual sounds, crashes, or blue screen errors. Therefore, it is vital to find an excellent and efficient solution for heat generation due to the kinetic energy of electrons motion. As Additive manufacture opened novel avenues for creating innovative components, there is a great interest in the electronics industry for developing additively manufactured heatsinks. Additively manufactured heat sinks could be active, passive, or hybrid in nature. Passive heat sinks rely on natural convection, which utilizes buoyancy of hot air to produce airflow across the heat sink system. Active heat sinks use forced air to increase fluid flow across the hot area. Forced air is commonly generated by a fan, blower, or forward motion of hot object. Hybrid heat sinks blend some aspects of passive and active heat sinks.
We design an additive manufactured passive heat sink, which works on the principle of natural convection. The design is inspired by the natural movement of heat waves (gradient) from the hot surface. In passive heat exchangers the temperature will decrease from bottom to top. That means the heat transfer at the lower part of the heat sink is high. So it is appropriate to add more material to facilitate maximum absorption of heat from the source. We use L9 Taguchi design of experiments (TDOE) to optimize our heat sink design. In TDOE we varied parameters such as the

channel's material, shape, size, and pattern.
Heat sink fins receive heat from an electronic device and dissipate it into the surrounding coolant fluid. It is common to see vertical fins on most conventional heat sinks. Our heat sink design incorporates a horizontal fin in addition to the vertical fin. The horizontal fins will increase the surface area of additively manufactured heat sink. Hence, horizontal fins are increasing the convective heat transfer between the environment (air) and heat sink. Also, increasing the surface contact between the medium helps to maximize the overall efficiency of heat sink. The performance analysis for the heat sink is performed using COMSOL multiphysics. Results show new heatsink designs, which can be manufactured using additive manufacturing, are highly efficient as compared to conventional heat exchanger in the present day computers.

PS52

(Late News) Rhodium Nanoparticles Incorporated Mesoporous Silica as an Active Catalyst for Cyclohexene Hydrogenation Under Ambient Conditions Nabil AlZaqri; King Saud University, Saudi Arabia

Rhodium (Rh) nanoparticles were embedded in the mesopores of TUD-1 siliceous material and denoted as Rh-TUD-1. Five samples of Rh-TUD-1 were prepared with various loadings of Rh that ranged from 0.1 to 2 wt% using the sol-gel technique. The prepared samples were characterized by means of several chemical and physical techniques. The obtained characterization results show the formation of highly distributed Rh^0 nanoparticles with an average size ranging from 3 to 5 nm throughout the three-dimensional silica matrix of TUD-1. The catalytic activity of the prepared catalysts was evaluated in the solvent-free hydrogenation of cyclohexene to cyclohexane at room temperature using 1atm of hydrogen gas. The obtained catalytic results prove the high activity of Rh-TUD-1, in which aturn over frequency (TOF) ranging from 4.94 to 0.54 s^{-1} was obtained. Moreover, the change in reaction temperature during the reaction was monitored, and it showed an obvious increase in the reaction temperature as an indication of the spontaneous and exothermic nature of the reactions. Other optimization parameters, such as the substrate/catalyst ratio, and performing the reaction under non-ambient conditions (temperature = 60 C and hydrogen pressure = 5 atm) were also investigated. Rh-TUD-1 exhibited a high stability in a consecutive reaction of 5 runs under either ambient or non-ambient conditions.

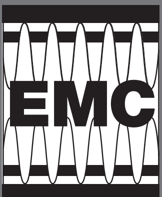

64TH ELECTRONIC MATERIALS CONFERENCE

June 29-July 1, 2022 // The Ohio State University // Columbus, Ohio

THURSDAY ORAL PRESENTATIONS

SESSION N: 2D Materials Growth and Surfaces

Session Chairs: Soaram Kim and Siddharth Rajan
Thursday Morning, June 30, 2022
Great Hall Meeting Room 1 & 2

8:20 AM N01
(Student) Molecular Beam Epitaxy Synthesis of In2Se3 Thin Films on Graphite in the Temperature Range 150 ºC - 250 ºC and 500 ºC – 700 ºC Cooper A. Voigt[1,2], Matthew Reingold[1], Lawrence Early[2], Alexander Dube[1], Brent Wagner[2] and Eric Vogel[1]; [1]Georgia Institute of Technology, United States; [2]Georgia Tech Research Institute, United States

α-In_2Se_3 is a two-dimensional (2D), semiconducting material in which ferroelectricity was discovered in 2018[1]. This combination of properties makes α-In_2Se_3 a promising material for emerging, low-power computing devices, such as ferroelectric field-effect transistors[2] and ferroelectric Schottky diodes for neuromorphic circuits[3]. Synthesis of large area (> 1 cm^2) α-In_2Se_3 thin-films with precise control of thickness and defect density is necessary for fabrication of neuromorphic circuits and industrial adoption; however, most reports in the literature of α-In_2Se_3's superlative performance in these applications are from studies conducted on a relatively small number of devices fabricated from isolated flakes. These flakes are obtained either from mechanical exfoliation of bulk material or from vapor deposition at temperatures far above the thermodynamic stability range of α-In_2Se_3 , resulting in uncoalesced, mixed phase films[1,4].

α-In_2Se_3 is thermodynamically stable below 200 ºC and transitions to the 2D, centrosymmetric β-In_2Se_3 phase upon heating above 200 ºC[5]. While the β to α-In_2Se_3 phase transition is achievable in bulk synthesis via slow cooling[6], the β to α-In_2Se_3 phase transition does not occur as readily in thin-films. Two reports from the last two years demonstrate large-area synthesis of β-In_2Se_3 thin-films metal-organic chemical vapor deposition and molecular beam epitaxy (MBE) at substrate temperatures greater than 300 ºC, but no β to α-In_2Se_3 phase transition is reported upon cooling[7,8]. Another study reported MBE synthesis of metastable, strained, mixed phase β/γ-In_2Se_3 films on Si(111) substrates at 180 ºC[9]. One study from 2018 claims deposition of large-area α-In_2Se_3 thin-films on graphene at a substrate temperature of 250 ºC via molecular beam epitaxy; however, it is difficult to distinguish the α from β phase by the Raman spectra and TEM micrograph along the c-axis. Development of direct synthesis of α-In_2Se_3 thin-films at substrate temperatures below 200 ºC would be advantageous to avoid the β to α-In_2Se_3 phase transition and reduce the thermal budget for CMOS integration.

In this work, In_2Se_3 films were synthesized on highly oriented pyrolytic graphite (HOPG) in the temperature range 150 - 250 ºC and the crystal structures then carefully characterized. HOPG provides a low defect density surface of van der Waals bonds that minimizes heterogeneous nucleation and maximizes adatom surface diffusion to promote layer-by-layer crystal growth. Furthermore, bulk α-In_2Se_3 powder and exfoliated flakes were annealed and characterized to study the α-β phase transition and correlate with results from thin films. Finally, In_2Se_3 films were synthesized at high substrate temperature (500 – 700 ºC) and the effect of cooling rate on film phase was measured. In summary, a detailed study of the impact of MBE synthesis conditions on the structure and properties of In_2Se_3 is presented and compared to the structure and phase transitions associated with exfoliated flakes. This material is based upon the work supported by the Georgia Tech Quantum Alliance and Georgia Tech Research Institute and conducted in part at the Georgia Tech Institute for Electronics and Nanotechnology, a member of the NNCI, which is supported by the NSF (ECCS-2025462).

References: 1. Xiao, J. *et al. Phys. Rev. Lett.* **120**, 227601 (2018).
2. Si, M. *et al. Nat. Electron.* **2**, 580–586 (2019).
3. Wang, L. *et al. Adv. Funct. Mater.* **30**, 1–9 (2020).
4. Liu, L. *et al. Chem. Mater.* **31**, 10143–10149 (2019).
5. Okamoto, H. *J. Phase Equilibria* **25**, (2004).
6. Küpers, M. *et al. Inorg. Chem.* **57**, 11775–11781 (2018).
7. Zhang, X. *et al. J. Cryst. Growth* **533**, 125471 (2020).
8. Claro, M. S. *et al. Adv. Opt. Mater.* **2001034**, 1–9 (2020).
9. Shen, Y. F. *et al. Chinese Phys. B* **29**, (2020).

8:40 AM N02
(Student) Molecular Beam Epitaxy Growth of Monolayer Hexagonal Boron Nitride on Nickel Substrates Incorporated with Oxygen Atoms Yuan Li; University of California, Riverside, United States

Reliable and controllable growth of two dimensional hexagonal boron nitride (h-BN) is essential for its wide range of applications. Here, we carried out molecular beam epitaxy (MBE) growth of monolayer h-BN on nickel (Ni) substrates by using ammonia (NH_3) and boron oxide (B_2O_3) as the sources. It was found that compared with normal growth of h-BN by introducing the NH_3 and B_2O_3 source at the same time, the pretreatment with B_2O_3 greatly inhibited the following epitaxial growth of h-BN. With the increase of B_2O_3 pretreatment time and then followed by 15 min h-BN growth, the coverage of h-BN exhibited an exponential decay relationship with the treatment time. The samples were analyzed using depth-profiling X-ray photoelectron spectroscopy (XPS) and reflection high-energy electron diffraction (RHEED). The oxygen/Ni peak intensity ratios derived from the XPS showed that the oxygen concentration increased with the increase of B_2O_3 pretreatment time from the surface while decreased gradually with the increase of XPS sputtering depth. Meanwhile, boron incorporation was negligible regardless of treatment time. The epitaxial relationship was studied by using h-BN coverage-dependent RHEED analysis, obtained on samples including Ni substrate after annealing only, Ni substrate with B_2O_3 pretreatment, h-BN samples with the B_2O_3 pretreatment and subsequent 50%, and 100% film coverage. Only two sets of patterns were observed and separated by 30, confirming that there is no in-plane rotation between the h-BN and Ni (111) surface. The oxygen incorporated into the Ni substrate not only suppressed h-BN nucleation by passivating the Ni surface active sites, but also decreased the growth rate of single crystal h-BN domains, shifting from larger sizes to smaller shapes. Detailed structural, optical and electrical characterizations of these monolayer h-BN films will also be presented. Our work reveals the influence of oxygen on the catalytic effect of Ni in the MBE growth of monolayer h-BN and provides an efficient way to control the morphology and quality of the 2D h-BN films.

9:00 AM N03
Kinetics of Wafer-Scale Epitaxial Growth of MoS_2 on Sapphire Nicholas Trainor[1,1], Chen Chen[1], Myeongok Kim[2], Dorota Kowalczyk[3] and Joan M. Redwing[1,1]; [1]The Pennsylvania State University, United States; [2]The University of Tokyo, Japan; [3]University of Lodz, Poland

Two-dimensional transition metal dichalcogenides (TMDs) such as MoS_2 hold great promise in a wide variety of electronic, optoelectronic, spintronic and valleytronic applications. However, fundamental understanding of their growth kinetics is lacking. One useful tool to achieve this is metal organic chemical vapor deposition (MOCVD) as its use of gas phase precursors enables tight control over gas chemistry and growth time. Additionally, sapphire has proven itself as a reliable substate for MoS_2, producing epitaxial films with minimal strain.
In this work, we discuss the wafer-scale growth of MoS_2 monolayers on sapphire via MOCVD. The growths were conducted in a horizontal cold-wall reactor using H_2S and $Mo(CO)_6$ as precursors and H_2 as the carrier gas. 2" c-plane

sapphire wafers were heated using a graphite susceptor to 900-1000 °C, where they were exposed to the precursors at a nominal chalcogen to metal ratio of 20,000. After the growth, the samples were annealed for 10 minutes under H_2S before cooling down. Surface coverage and domain density were measured using atomic force microscopy and scanning electron microscopy. The evolution of the Raman, photoluminescence, and absorption spectra as well as the average domain size from X-ray diffraction will also be presented.

Wafer-scale, fully coalesced monolayer MoS_2 films were achieved within only 12 minutes of growth. High nucleation densities between 1-2*10^3 μm^{-2} were achieved within 30s of growth, after which the density remained relatively constant. Within the first 3 minutes of the growth, the film grew rapidly with domain size increasing linearly with time at a rate of about 150 nm^2/min, indicating that the deposition rate is limited by gas phase transport of the source material to the substrate. After that, the domains began to merge, and the growth rate drops due to reduced adsorption of precursors on the MoS_2 van der Waals surface. Overall, the film coverage was roughly logarithmic with time, with 65% of the coalesced monolayer being deposited within 3 minutes. Past the 12 minutes of growth time, small bilayer regions were observed that eventually developed into spirals and pyramids at longer growth times.

Additionally, the effect of temperature and sapphire surface chemistry (adjusted using pre-anneals) on nucleation density and growth rate will be also discussed.

Our results help probe the effects of surface chemistry and growth conditions on the MOCVD growth of MoS_2, thereby enabling a deeper understanding of the fundamental kinetics of the system. This knowledge will be applicable to other TMDs as well as other deposition techniques.

9:20 AM N04

(Student, Late News) Facile Integration of Giant Exchange Bias in 2D Magnet/Oxide Heterostructures Shanchuan Liang, Ti Xie and Cheng Gong; University of Maryland, United States

Exchange bias, a magnetic phenomenon emerging at the interface between a ferromagnet (FM) and an antiferromagnet (AFM), originates from the pinning of spins in the FM layer by the adjacent AFM layer, effectively stabilizing the FM against the environmental stray magnetic fields. This phenomenon has been implemented in a wide range of technological applications including magnetic memories, magnetic read heads, and sensors, and plays the foundational role for advanced spintronics. Here, we report an approach to establishing strong exchange bias in the 2D magnet/oxide heterostructure by a single-step process – atomic layer deposition (ALD). The exchange bias we created is controllable in the range of ~300 to 1500 Oe by replacing different oxides in the heterostructure. Hence, this systematic work elucidates the essential role of ALD-enabled oxidization of layered magnets in the formation of exchange bias and establishes ALD of oxides as a facile, controllable, and generally effective approach to creating giant exchange bias in vdW magnets, representing an integral advance towards practical vdW spintronic devices.

9:40 AM N05

Fast and Easy Optical Imaging and Epitaxial Growth Control of Rotational Domains in SnSe Thin Films Wouter Mortelmans[1], Maria Hilse[2], Qian Song[1], Seong Soon Jo[1], Kevin Ye[1], Derreck Liu[2], Nitin Samarth[2] and Rafael Jaramillo[1]; [1]MIT, United States; [2]The Pennsylvania State University, United States

Layered chalcogenides are promising materials for future (opto-)electronic applications.[1,2] The semiconductor tin selenide (SnSe) is a member of the monochalcogenide (MX) family, which feature functionality including domain-switching behavior, ferroelasticity, thermo-, piezo- and ferroelectricity.[3–5] Orthorhombic α-SnSe has strong in-plane anisotropy with implications for thermal, electronic, and optical properties.[6] It has been studied for next-generation microelectronics, photonics and energy-conversion technologies, and has been the focus of a theoretical proposal for ultra-fast, non-thermal optical domain switching.[7,8] Control of rotational domains (*i.e.*, twins) during SnSe thin-film synthesis is key to enable high-quality, single-crystalline SnSe for the proposed applications.[9] This work focusses on MBE of SnSe. We demonstrate (1) a fast and easy method to probe rotational domains in SnSe thin films and (2) a solution to overcome the formation of rotational domains by focusing on symmetry and lattice-matched vdW epitaxy of SnSe on a-plane sapphire surfaces.

When orthorhombic SnSe (in-plane lattice parameters; a = 4.15Å and b = 4.44Å) is epitaxially grown on cubic MgO (a = 4.21Å), various rotational domains are formed as a result of the various symmetry structure of both materials.[10] The 2-fold rotational symmetry of SnSe combined with the 4-fold symmetry of MgO results in the formation 90° SnSe twins, and a high density of grain boundaries upon closure of the epitaxial film. Characterizing rotational domains in ultra-thin films of 2D materials is generally challenging (in-plane HR-XRD, 'large-area' cs-TEM imaging, *etc*.). We show that, thanks to the optical anisotropy of α-SnSe in the visible ($\Delta n = 0.88$)[1,8], supported by an optical model based on the reflectivity of linearly-polarized light, 90° SnSe twins are easily distinguishable using polarized optical microscopy. When studied under cross-polarization at 45° with respect to the SnSe optical axis, slightly increasing or decreasing the angle of the polarizer with respect to the analyzer enables the color splitting of 0°-oriented and 90°-oriented domains into blue and yellow, respectively, when illuminated with white light. We first demonstrate this method on thicker SnSe epitaxial crystallites (~50nm), using polarized Raman spectroscopy for validation, and we then apply it to thinner (~5nm) epitaxial SnSe films. The distribution of blue and yellow pixels in the optical image enables the quantification of rotational domains and confirms the presence of a high density of 90° twins on MgO.

To overcome the formation of 90° twins, we grow epitaxially on a-plane sapphire [α-Al_2O_3(11-20)] substrates. Similarly as α-SnSe, the surface unit of α-Al_2O_3(11-20) can be constructed using dissimilar in-plane lattice parameters; a = 8.24Å and b = 12.99Å.[11] This favors single-oriented domain epitaxy of (2 x 3) units of SnSe on α-Al_2O_3(11-20), explained by the symmetry match and small lattice mismatch in both in-plane directions, and confirmed experimentally by our polarized reflectivity method.

The developed optical method and epitaxy on a-plane sapphire represent a very useful combination of film metrology and growth methodology to realize high-quality, single-crystalline epitaxial SnSe thin films free of rotational twin domains. We will also highlight our epitaxial growth techniques, especially a comparison between solid-source and plasma-assisted methods.

1) Singh A et al *ACS Photonics* **2020**, *7* (12)
2) Liu Y et al *Nat. Rev. Mater.* **2016**, *1* (9)
3) Zhou J et al *Nano Lett.* **2018**, *18* (12)
4) Gomes C et al *J. Appl. Phys.* **2020**, *128* (12).
5) Chang K et al *Nano Lett.* **2020**, *20* (9)
6) Chen G et al *Prog. Mater. Sci.* **2018**, *97*
7) Zhao D et al *Nature* **2014**, *508* (7496)
8) Jo S et al *Adv. Photonics Res.* **2021**, *2100176*.
9) Mortelmans W et al *Appl. Mater. Today* **2021**, 22
10) Nguyen Q et al *J. Alloys Compd.* **2020**, *840*
11) Venkataramani K et al *Phys. Chem. Chem. Phys.* **2012**, *14* (6)

10:00 AM Refreshment Break

10:20 AM N06
(Student) Electron Emission Sources from Quasi-Freestanding Epitaxial Graphene Planar Devices Daniel Lewis and Kevin Daniels; University of Maryland, United States

Freestanding graphene nano- and microstructures have been shown to exhibit controllable electron emission when carrying a current and immersed in an external accelerating electric field. Through the mechanism of Phonon-Assisted Electron Emission, these structures demonstrate electron emission at electric field intensities and lattice temperatures below what would be expected for carbon to demonstrate field emission or thermionic emission, respectively. Emission currents have been measured primarily out of the plane of the device surface, allowing some directional control before the accelerating field is even considered.
Thus far, such demonstrations have tended to involve structural dimensions on the order of only a handful of um, and have commonly been fabricated from CVD transferred graphene, flakes, or carbon nanotubes in various vertical and horizontal arrangements. Applied fields for such devices typically approach hundreds of kV/cm, and emission currents rarely leave the nA range. Herein are presented graphene structures with dimensions up to cm, in fields not exceeding 1 kV/cm, and producing emission currents of nearly 10 uA.
Quasi-freestanding epitaxial graphene, synthesized from a silicon carbide substrate, offers several advantages compared to transferred graphene or unzipped nanotubes, including greater structural integrity, lower defect density, ease of handling, and ready compatibility with conventional simple photolithographic fabrication techniques. The devices presented here were fabricated with a low-cost, wafer scalable, single-photomask process that does not require material transfer to a secondary substrate and is easily tailored to create variations in design parameters, which allowed multiple batches of devices to be rapidly manufactured with precise variations for the purpose of performance testing.
The devices exhibit recognizable patterns of emission current performance relative to device and substrate temperature, including an identifiable turn-on point and emission current maintenance. Device behavior relative to substrate heating identifies the electron-phonon interactions that enable function and current emission, both when device temperature is supplied internally and externally. Emission currents are also observed to follow a performance pattern derived from purposeful device morphology, even exhibiting emission currents in accelerating fields as low as 50 V/cm.
Graphene electron emission devices present an opportunity for electron emission in a planar 2D heterostructure environment, beyond even the dimensional capabilities of field emission devices, and below the high operating temperatures of thermionic sources. Through refinements in the design and packaging, such devices, which are arbitrarily scalable between the micron and wafer level, could provide the electron sources for novel applications in X-ray generation or electron microscopy.

10:40 AM N07
(Student) Hot Electron Laser Assisted Cathode using Electronically Tunable Negative Electron Affinity Silicon Surface Subrata Das, Hyun Uk Chae and Rehan Kapadia; University of Southern California, United States

High-brightness photoemitters can be employed as electron sources in ultrafast electron diffraction and X-ray free-electron lasers, energy recovery linacs, electron microscopes, electron beam lithography, space propulsion and high-power microwave devices. To yield high quantum efficiencies, high brightness beams require rapid response times and low mean transverse energies (MTE). Recently, negative electron affinity (NEA) photocathodes, consisting of a GaAs wafer and a Cs/O surface layer, have been reported to exhibit both reasonably low MTE and good external quantum efficiencies (EQE) of ~10^{-3}-10^{-2}. However, NEA cathodes are rarely used due to their significantly complex fabrication process which includes high temperature processing steps, entirely in-situ activation as well as ultra-high vacuum storage and operating pressures. Their stability is not also up to the mark.
In this investigation, we have fabricated a Hot Electron Laser Assisted Cathode (HELAC) using electronically tunable negative electron affinity silicon surface. Briefly, the device consists of a three-layer stack of (i) a semiconductor, which absorbs incident photons, (ii) a monolayer of graphene, which acts as the gate, and (iii) an insulator, which allows a voltage drop between the semiconductor and graphene. In this device, an electric field is generated by applying a bias voltage between the semiconductor and graphene which mimics the surface dipole field in an NEA photocathode. Electrons injected into the graphene do not require transport to the emitting surface due to the monolayer thickness of the graphene. This device is air stable with a simple ex-situ fabrication flow while preserving the advantages of NEA photocathodes. We have demonstrated an initial proof-of-concept HELAC device with a p-silicon substrate, silicon oxide insulator and monolayer graphene stack and evaluated its performance using a 405 nm CW laser at ~40 mW of incident power. Despite having a non-optimized structure, this device has exhibited a current of ~70 μA (~1.1 mA/cm^2), resulting in an EQE of ~0.5%. Semiconductor modeling indicated that EQEs of ~10% and response times in the 1-10 ps range are plausible for this device. Additionally, it is expected that low-MTE is achievable by optimizing the quality of the insulator, the barrier height, and the tunneling mechanism. This is analogous to Cs-based NEA devices, where low MTEs are attainable despite a large electric field which is developed due to the surface dipole.

11:00 AM N08
Additive Manufacturing of Interface Engineered Colloidal 2D-Crystals for Flexible Thermoelectric Energy Harvesting Tony Varghese[1,1], Ariel E. Briggs[1], Fereshteh Rajabi[1], Jacob Manzi[1], Harish Subbaraman[1,2] and David Estrada[1,2,3]; [1]Boise State University, United States; [2]Center for Advanced Energy Studies, United States; [3]Idaho National Laboratory, United States

Bi_2Te_3, a narrow gap layered semiconductor, and a topological insulator has been reported to have excellent room temperature thermoelectric performances. Alloying and nanostructuring of the material have been widely studied for reducing the lattice thermal conductivity (K_L) of the materials to enhance the thermoelectric figure of merit (ZT). But the performance of printed thermoelectric devices is significantly low compared to bulk counterparts due to low density and porosity, here we report interface engineering and Nano inclusion in the crystals as an effective way to increase the performance of thermoelectric materials. This work demonstrates the scalable solvothermal synthesis of crystalline nanomaterials with engineered defects and interface engineering to improve the thermoelectric performance of the colloidal nano-inks. The engineered nanomaterials are transformed into devices using multiple additive manufacturing methods including Screen printing, Aerosol Jet Printing, Plasma Jet Printing, and Direct Writing. The low-cost scalable additive manufacturing methods and interface engineering developed in this work demonstrate a significant advance in the field of high-performing low-cost thermoelectric generators, advancing the commercial viability of the technology for energy harvesting, sensing, and cooling applications.

11:20 AM N09
Scanning Tunneling Microscopy of Monolayer Hexagonal Boron Nitride Monolayer Nanoribbons on Graphene William H. Koll[1], Ping Wang[2], Joseph Corbett[1,3], Jay Gupta[1] and Zetian Mi[2]; [1]The Ohio State University, United States; [2]University of Michigan–Ann Arbor, United States; [3]UES, Inc., United States

Van der Waals heterostructures involving 2D materials such as graphene (Gr) and hexagonal boron nitride (hBN) exhibit a variety of interesting physics in prototype devices, but require improvements in large-area growth and control over defect densities for wafer-scale implementation. In this work, we use scanning tunneling microscopy (STM) to characterize monolayer ribbons of hBN grown on highly oriented pyrolytic graphite (HOPG) via high-temperature molecular beam epitaxy (MBE) [1]. STM images confirm that the hBN ribbons grow outward from graphene step edges and the morphology depends on the configuration of graphene termination (armchair or zig-zag). Fourier analysis indicates that the hBN and graphene lattices are aligned across the growth interface. Moreover, we observe large area single-periodicity moiré patterns due to the interference between the graphene and hBN lattices. Notably, the measured moiré periodicity exceeds the maximum period of 14.2nm, calculated using a bulk hBN lattice constant and rotational alignment with the HOPG. The larger observed period suggests that the hBN lattice is compressively strained to be more commensurate with the underlying HOPG. We can place bounds on the strain (> 0.2%) and twist angle (< 0.9^{o}) from these measurements of the moiré lattices. Atomic-resolution imaging reveals three distinct periodicities: in addition to the expected hBN honeycomb lattice, there are hexagonal and superstructure periodicities which may reflect variations in local strain and/or the presence of intercalated species. The MBE-grown single-domain hBN studied herein presents an ideal substrate for studies of spin qubit candidates deposited on atomically thin insulators.

We acknowledge funding support from the NSF TAQS QII program (award # 1936219) and Army Research Office.
1) Wang, P. et al., (submitted)

SESSION O: Group III-Nitrides—MOCVD Growth

Session Chair: Fatemeh (Shadi) Shahedipour-Sandvik
Thursday Morning, June 30, 2022
Great Hall Meeting Room 3

8:20 AM O01
(Student) Facet Control by Supersaturation in III-Nitrides Jack Almeter[1], Ke Wang[1], James Loveless[1], Will Mecouch[2], Pramod Reddy[2], Seiji Mita[2], Ronny Kirste[2], Ramón Collazo[1] and Zlatko Sitar[1,2]; [1]North Carolina State University, United States; [2]Adroit Materials, United States

Heteroepitaxy of AlGaN layers on native GaN and AlN requires strain management schemes to achieve relaxed layers. Facet-controlled epitaxial lateral overgrowth (FACELO) allows for growth on inclined semi-polar facets from a typical c-plane substrate, enabling the generation of misfit dislocations for relaxation. While FACELO processes have been achieved in nitrides, there is no generalized model for the relationship between facet formation and growth conditions. This study presents a framework for controlling facet formation via the control of the vapor supersaturation, which describes the driving force for crystal growth.
GaN/sapphire wafers were patterned via SiO_2 stripes along the direction, consisting of alternating 2 μm SiO_2 stripes and 2 μm openings. AlN samples were prepared analogously from native AlN substrates following a maskless procedure, consisting of 2 μm wide stripes separated by 2 μm trenches etched via RIE to a depth of about 1.5 μm. Subsequent GaN or AlN structures were grown by MOCVD on prepared templates under various metal supersaturation conditions. Facet formation was investigated via cross-sectional SEM.
The reference growth conditions for GaN were selected at 900 °C, 80 Torr, 132 μmol/min TEG, 1.5 slm NH_3, H_2 diluent, and total flow 7.5 slm. Supersaturation increases with decreasing growth temperatures and increasing NH_3 flow rate. Observations of the shape at similar supersaturations but at different temperatures and ammonia flows were used to decouple the influence of any particular growth condition and to demonstrate the functionality with supersaturation. At low supersaturations, vertical and *c*-plane facets are preferred, giving a rectangular profile. As supersaturation increased, inclined facets appear, first in a truncated shape and then a trapezoid at higher supersaturations, eventually forming a triangle. These results were consistent between the temperature and ammonia flow series, demonstrating that the shape is determined specifically by the supersaturation.
For AlN growth, the reference growth condition was selected at 20 Torr, 13.4 μmol/min TMA, 0.3 slm NH_3, and 10 slm H_2. The growth temperature was varied to investigate the role of Al supersaturation on facet formation, which also increases with decreasing temperature. Temperatures in the range of 1020-1400°C but with similar growth times were used in this study. At higher supersaturation, the and facets are observed, resulting in a trapezoidal morphology. An investigation of the role of supersaturation decoupled from temperature is presented for AlN.
Based on these observations on the two nitrides, the main hypothesis that facet formation is controlled by the vapor supersaturation is supported [1]. Furthermore, it is predicted that facet formation is a result of the minimization of the overall surface energy where formation of a specific facet is dependent on its surface energy which is dependent on vapor supersaturation. This proposed facet formation mechanism will be used to engineer templates in native substrates for the controlled relaxation of AlGaN layers and their applications in either optoelectronic or power devices.
[1] Wang *et al.*, Appl. Phys. Lett. 120, 032104 (2022).

8:40 AM O02
Growth Evolution in Non-Planar GaN Selective Area Epitaxy Bingjun Li, Sizhen Wang and Jung Hahn; Yale University, United States

Lateral p-n junction is an important and necessary building block to achieve high performance power devices. In GaN material system, selective area etching followed by selective area regrowth is the most promising approach. Most of the researches about selective area growth in GaN have been focusing on the epitaxial lateral overgrowth (ELO), nanowires, etc., which is mainly governed by the convex facets. However, in the case of non-planar growth, concave growth starts to dominate the evolution of growth fronts. As an outcome, severe doping non-uniformity has been reported by several groups and an inverse correlation between growth rate and local Mg concentration has been discovered.
In this study, we apply kinetic Wulff diagram and Wulff construction to explain and determine the growth evolution happened in the a GaN trench. The undoped GaN was grown in a TMAH treated trench with vertical a-plane sidewalls under two distinct conditions, shown in Fig. 1(a) and (d). As expected, at the bottom corner of the trench, a curved surface is observed as a result of concave growth under secondary electron microscope (SEM). On the other hand, convex growth and a well-defined (11-22) facet dominate the growth at the top corner of the sidewall. Based on the growth rates of various facets extracted from SEM, kinetic Wulff diagrams (v-plot) are plotted, shown in Fig.1 (b) and (e). After applying Wulff construction on the v-plot (Fig. 1(c)), the

predicted shape is identical to the one from SEM. This indicates kinetic Wulff diagram is a powerful tool to determine, for example the shape of interfaces, and the dopant/impurity distribution. In addition, comparing Wulff diagrams of two conditions, growth rate anisotropy could be modified and controlled. Lastly, the effects of non-uniform Mg doping, originated from the non-planar growth within the trench, on different device structures are also studied from the perspective of TCAD simulations. Demonstrated in Fig. 2, nonuniform Mg doping improves the breakdown voltage of devices with floating field ring termination by alleviating the field crowding at the corner of the trench. On the other hand, non-uniformity has little effect on the performance on JFET structures by comparing the barrier height in the conduction band, as shown in Fig. 3. However, for a more sophisticated structure, such as superjunction devices, a detailed charge balance between electrons and holes is important. Nonuniform doping within the trench will adversely affect the device performance.

Acknowledgements
This work is supported by the Advanced Research Projects Agency-Energy (ARPA-E), U.S. Department of Energy, under Award Number DE-AR0000871 as part of the PNDIODES program managed by Dr. Isik Kizilyalli.

9:00 AM O03

Crack Suppression in High Al-Mole-Fraction AlGaN Beyond the Critical Layer Thickness via Non-Planar Growth Approach on Patterned GaN Platforms Frank Mehnke[1], Zhiyu Xu[1], Yuto Ando[1], Alec Fischer[2], Fernando Ponce[2], Shyh-Chiang Shen[1], Theeradetch Detchprohm[1] and Russell Dupuis[1]; [1]Georgia Institute of Technology, United States; [2]Arizona State University, United States

Tensile strain limits the epitaxial growth of a wide range of heteroepitaxial films beyond the critical layer thickness for III-V compound semiconductor material systems. Induced by both lattice mismatch and thermal expansion coefficient mismatch in their heteroepitaxial structure, such strain poses a significant challenge for the highly mismatched AlInGaN alloy system. For instance, the strain limits the growth of adequately thick layers of high Al mole fraction AlGaN on commercially-available low-defect-density GaN substrates, which is essential for a variety of device structures such as ultraviolet (UV) heterostructure laser diodes, UV avalanche photodiodes, and wider-bandgap high-power rectifiers. For layers under tensile strain, growth thicknesses beyond the critical layer thickness result in cracking which significantly lowers yield in device fabrication.
Up to now various methods have been devised to allow the heteroepitaxial growth of AlInGaN heterostructures to accommodate this inherent strain [1-4]. In this work, we introduce a non-planar growth approach that enables the deposition of crack-free $Al_xGa_{1-x}N$ with high Al mole fraction on patterned GaN/sapphire templates with large-area rectangular mesas. We have studied the effects of the patterned mesa width, mesa etch depth, and the gap in between the mesas on the heteroepitaxy of $Al_xGa_{1-x}N$ superlattices with an average Al mole fraction of $0.11 < x < 0.21$ and growth thicknesses up to 3.5µm. For a large mesa of 2 mm x 1mm, we observed surface cracking when exceeding the critical layer thickness similar to that of a planar growth approach for the $Al_xGa_{1-x}N$ superlattices with high average Al mole fraction. However, limiting the mesa dimension in one direction enables strain mitigation and allows to drastically extend the critical layer thickness. Besides, larger etch depths of the mesas support crack-free heteroepitaxy, especially for large overgrowth thicknesses, whereas the gap in between the mesas exhibits much less crucial influence. We demonstrate that the Al mole fraction and layer thicknesses of such heterostructures can be increased far beyond that for planar growth, *e.g.* 1610 nm thick $Al_{0.216}Ga_{0.784}N$-SL on 0.2 mm wide × 2 mm long and 3 mm deep etched mesa stripes, and achieve the growth of crack-free non-planar $Al_xGa_{1-x}N$/GaN heterostructures designed for laser operation at ~370 nm.

[References]
[1] O. H. Nam, T. S. Zheleva, M. D. Bremser, D. B. Thomson, and R. F. Davis, MRS On-Line Proc. **482**, 301 (1997).
[2] H. Amano, M. Iwaya, N. Hayashi, T. Kashima, S. Nitta, C. Wetzel, and I. Akasaki, Phys. Stat. Sol. (b) **216**, 683 (1999).
[3] C. J. Collins, T. Li, D. J. H. Lambert, M. M. Wong, R. D. Dupuis, and J. C. Campbell, Appl. Phys. Lett. **77**, 2810 (2000).
[4] H. Miyake, M. Narukawa, K. Hiramatsu, H. Naoi, Y. Iyechika, and T. Maeda, Phys. Stat. Sol. (a) **188**, 725 (2001).

9:20 AM O04

(Student) Effect of Growth Parameters on Be Incorporation Efficiency in MOCVD GaN:Be Benjamin McEwen[1], Emma Rocco[1], Vincent E. Meyers[1], Oleksandr Andrieiev[2], Mykhailo Vorobiov[2], Denis Demchenko[2], Michael Reshchikov[2] and Fatemeh (Shadi) Shahedipour-Sandvik[1]; [1]SUNY Polytechnic Institute, United States; [2]Virginia Commonwealth University, United States

Recently, beryllium has regained attention as a potential alternative to magnesium as a *p*-type dopant in III-Nitrides due to its shallower acceptor level. We recently reported the first systematic investigation of GaN:Be grown using metal-organic chemical vapor deposition (MOCVD) [1]. Despite the successful incorporation of Be into GaN grown by MOCVD, doping GaN with [Be] greater than $\sim 10^{18}$ cm^{-3} negatively impacts the growth, causing increased roughness and step-bunching, and [Be] saturates around 5×10^{19} cm^{-3} with high Be precursor flow rate. Furthermore, at these high flow rates, Be incorporation appears to be inconsistent throughout the growth, with a high degree of variation in [Be] with depth, as measured by SIMS. Further development is thus necessary to improve Be incorporation and activation efficiency in III-Nitrides.

Because Be is electrically similar to Mg (both are divalent alkaline earth metals), it is expected that activation efficiency will follow similar trends to that of Mg. On the other hand, the structural effects of Be and Mg are not expected to be the same; while Mg has a larger atomic radius than Ga, Be has a smaller atomic radius, which induces opposite-signed strain when each is incorporated into GaN. It is well known that a high V/III ratio (N-rich growth conditions) improves Mg activation efficiency, but total [Mg] varies only weakly with V/III ratio.

In this work, we study the effects of varying V/III and Ga/Be precursor flow ratios on Be incorporation and activation efficiency in GaN. Be concentration and incorporation efficiency is determined using secondary ion mass spectroscopy (SIMS), and photoluminescence (PL) is used to determine the relative activation efficiency of the highly resistive GaN:Be.

[1] McEwen, B., *et al*. MOCVD Growth and Characterization of Be-Doped GaN, *submitted to ACS Applied Electronic Materials*.

9:40 AM O05

Chemical Potential Control in p-Type N-Polar GaN Shashwat Rathkanthiwar[1], Dennis E. Szymanski[1], Dolar Khachariya[2], Pegah Bagheri[1], Ji Hyun Kim[1], Ke Wang[1], Andrew Klump[1], Seiji Mita[2], Erhard Kohn[1], Spyridon Pavlidis[1], Ronny Kirste[2], Pramod Reddy[2], Ramón Collazo[1] and Zlatko Sitar[1,2]; [1]North Carolina State University, United States; [2]Adroit Materials Inc., United States

Here, we demonstrate chemical potential control as an effective tool to suppress compensation in Mg-doped nitrogen-polar (N-polar) gallium nitride (GaN) films grown by metalorganic chemical vapor deposition (MOCVD). An increase in nitrogen chemical potential obtained by increasing the process supersaturation is shown to systematically reduce the incorporation of compensating oxygen and nitrogen-vacancy point defects. This is confirmed by photoluminescence and temperature-dependent Hall effect measurements. The suppressed compensation led to an

order of magnitude improvement in p-type conductivity with the room-temperature hole concentration, mobility, and resistivity measuring $6x10^{17}$ cm^{-3}, 9 cm^2/Vs, and 1.1 ohm-cm, respectively. These results are paramount in the pathway towards N-polar GaN power and optoelectronic devices.

GaN with N-polar orientation has attracted growing interest toward the development of high-performance electronic and optoelectronic devices such as high-frequency high electron mobility transistors (HEMTs), solar cells, long-wavelength LEDs, and ultraviolet photocathodes. A reversal of polarization field direction in N-polar GaN from its metal-polar counterpart allows for device designs that lead to improved performance, for example, enhanced carrier extraction efficiency in InGaN solar cells, enhanced hole injection, suppressed electron overflow and decreased droop in LEDs, improved confinement in the two-dimensional electron gas channel in AlGaN/GaN HEMTs, and improved transistor performance in polarization-engineered tunnel field-effect transistors (T-FETs). These novel device applications based on N-polar GaN can be further improved and optimized with the realization of low-resistivity p-type material. For example, achieving a steep device turn-on in T-FETs necessitates low resistance p-GaN layers, whereas high hole and electron concentrations are required near the p-n junction for optimal band alignment in these devices. Achieving efficient p-type doping in GaN is understood to be challenging due to an interplay between large Mg acceptor ionization energy (150-220 meV), incorporation of compensating point defects and point defect complexes during epitaxial growth, and low mobility values of holes as compared to electrons. Moreover, N-polar GaN offers added material challenges that need to be addressed to achieve high p-type conductivity. For instance, if not controlled, N-polar GaN grows with a rough surface morphology characterized by hexagonal hillocks, and high unintentional defect incorporation, notably oxygen, which incorporates at concentrations $>10^{19}$ cm^{-3}. Oxygen on the nitrogen site (O_N) acts as a shallow donor in N-polar GaN with an activation energy of ~29 meV which leads to significant difficulties in achieving p-type conductivity. In addition, the incorporation of nitrogen-vacancy (V_N)-related compensating defects is favored in p-type GaN due to low formation energy. While much work has focused on p-doping of Ga-polar GaN, to date, comprehensive electrical characterization and compensation control in p-type N-polar GaN is lacking in the literature.

The chemical potential control (CPC) is a predictive approach wherein the dependence of the defect formation energy is theoretically estimated as a function of MOCVD growth parameters. These growth parameters are, for example, the V/III ratio, diluent gas, temperature, pressure, and input partial pressures of gas species. Instead of these individual MOCVD "knobs", supersaturation is employed as a representative thermodynamic parameter. Following the CPC framework, increasing the supersaturation can be shown to increase the formation energy of both compensating defects, O_N and V_N. In this work, we demonstrate the utility of the CPC scheme in reducing the compensation in p-type N-polar GaN to realize state-of-the-art hole concentration and resistivity.

10:00 AM Refreshment Break

10:20 AM O06

(Student) Characterization of Traps in High-Growth-Rate MOCVD GaN Wenbo Li, Yuxuan Zhang, Vijay G. Thirupakuzi Vangipuram, Hongping Zhao, Steven A. Ringel and Aaron Arehart; The Ohio State University, United States

Gallium nitride's high electron mobility, wide bandgap, and high breakdown field would be ideal for thick vertical devices if higher growth rates could be obtained to be more cost effective while maintaining low defect concentrations to minimize threshold voltage drift, minimize leakage current, and allow controllable n-type doping in the low- to mid-10^{15} cm^{-3} range. In metal-organic chemical vapor deposition (MOCVD) growth, ammonia cracking efficiency is one of the limiting factors of achieving higher growth rate. To facilitate this, a laser is introduced in the MOCVD reactor to improve the ammonia cracking efficiency enabling higher MOCVD growth rates.[1] Higher growth rates and the laser require many new growth optimizations for crystal quality and minimizing traps. In this study, deep level transient/optical spectroscopy (DLTS/DLOS) are used to characterize traps in MOCVD GaN films grown with growth rates up to 9.4 µm/h and with and without laser-assistance to understand the trap incorporation.

The MOCVD films were grown on 2 in. Nitride Specialty Supply GaN-on-sapphire templates. First, an n+ doped layer for lateral conduction and where the Ti/Al/Ni/Au Ohmic contact was formed. Second, a lightly-doped n-type layer was grown with a semitransparent Schottky Ni contact deposited on top. The DLTS and DLOS measurements proved the traps in the lightly-doped layer . The Si doping was targeted at 5×10^{16} cm^{-3} in the lightly doped layer. For samples grown without laser-assistance, the growth rates were 2.0 µm/h for the traditional/optimized low growth rate (LGR) sample and 9.2 µm/h for the high growth rate (HGR) sample. For the laser-assisted MOCVD growth, the growth rate was 9.4 µm/h using a CO_2 laser at 250 W parallel to the growth surface to more efficiently crack ammonia. More details on the growth conditions can be found in Ref. 1 and measurement details in Ref. 2.

The HGR and LA samples have traps from DLTS at E_C – 0.25, ~E_C – 0.4, E_C – 0.65, E_C – 0.72, and E_C – 0.9 eV with concentrations ranging from high-10^{12} cm^{-3} to mid-10^{14} cm^{-3} but are overall up to ~2X lower in the LA sample than the HGR sample. One exception is the Fe-related E_C-0.57 eV level[3] in the LA sample with a concentration of ~$3x10^{13}$ cm^{-3} that was not detected in the HGR sample. Although the E_C-0.4 and E_C-0.65 eV levels were not detected in the LGR sample, both high growth rate samples' total DLTS trap concentrations are overall 2-3X lower than the LGR sample. These concentrations are well below the target 10^{15} cm^{-3} for vertical GaN devices and are unlikely to cause significant compensation. Conversely, traps were detected via DLOS at E_C – 1.35, E_C – 2.6, and E_C – 3.28 eV in all samples. Here, the trap concentrations are in the mid- to high-10^{14} cm^{-3} in the LGR sample but were in the 10^{15}-10^{16} cm^{-3} range in the HGR and LA samples. Like the DLTS results, the LA sample trap concentrations were ~2X lower than the HGR sample, but the traps, related to C and V_{Ga}[4,5], remain well above the LGR concentrations. Further mitigation of these traps is required to enable controllable low doping and mitigate other trap-related issues that cause reduced performance and reliability while simultaneously achieving with high growth rates for economical vertical GaN devices.

Reference

[1] Y. Zhang *et al.*, Phys. Stat. Sol. RRL **15,** 2100202 (2021).
[2] A. Hierro *et al.*, Appl. Phys. Lett. **76**, 3064 (2000).
[3] K. Galiano *et al.*, J. Appl. Phys. **123**, 224504 (2018).
[4] Z. Zhang *et al.*, J. Appl. Phys. **118**, 155701 (2015).
[5] A. Armstrong *et al.*, J. Appl. Phys. **98**, 053704 (2005).

10:40 AM O07

High-Speed MOCVD Growth of GaN Assisted by TBCl

Bingjun Li and Jung Hahn; Yale University, United States

GaN is a perfect candidate for high-power applications due to its intrinsic material properties, such as large bandgap, high critical electrical field, and reasonable electron mobility. In order to achieve extremely high breakdown voltage, vertical power devices need a thick drift layer (30~100 um), which cannot be feasibly produced by MOCVD processes due to low growth rate. On the other hand, hydride vapor phase epitaxy (HVPE) is capable of growth GaN at a very fast rate (>100um/h), but it is not scalable (growing >50 wafers/run) for mass production. Therefore, turning MOCVD into HVPE-like reactor is of great significance.

During MOCVD growth of GaN, gas-phase parasitic reaction of TMGa to form $GaMe_2$ and followed by $(GaMe_2)_n$ nano-clusters or particles greatly limits the growth rate under high TMGa partial pressure. As a result, under a constant pressure and temperature, the measured growth rate increases linearly with TMGa flow rate at the beginning and then saturates if not decreasing. There have been reports of co-flowing HCl during the GaN growth, demonstrating a growth rate above 25 um/h. However, HCl is highly corrosive to the stainless-steel apparatus and a hot wall reactor is needed to prevent the depletion of HCl by NH_3.
In this study, we introduced tiertiarybutyl-chloride (TBCl) into our MOCVD reactor. It doesn't decompose to form either HCl or Cl_2 under room temperature (RT). Therefore, it is less corrosive and it doesn't get consumed by NH_3, forming white powers (NH_4Cl) at the upstream of the reactor. In order to identify whether TBCl is capable of suppressing parasitic reaction or not, two different experiments were conducted. As shown in Fig. 1 (a), under a constant TMGa flow rate without co-flowing TBCl, growth rate decreased by a factor of 5 when the reactor pressure was increased from 200 mbar to 500 mbar. However, a relatively pressure-independent growth rate was observed when co-flowing 2.5 sccm of TBCl. On the other hand, a saturation of growth rate was observed at around 7.5um/h when we continuously increased the TMGa flow rate to 100 sccm without TBCl, shown in Fig. 1(b). Instead, after co-flowing TBCl, growth rate increases linearly with TMGa flow rate, without showing any sign of saturation even above 22um/h. Both experiments indicate that TMGa has been replaced by GaCl, a same precursor of Ga in HVPE system having little parasitic reaction. An atomically smooth surface with step-flow patterns has been confirmed by AFM (Fig. 2) for a sample grown at 15 um/h.
Besides, TBCl is also capable of modifying the growth rate anisotropy. The kinetic Wulff diagram with or without TBCl has been plotted in Fig. 3. TBCl tends to decrease the relative growth rate of c-plane and (10-11), while it increases (11-22) and r-plane (10-1-2) dramatically. This modification of growth anisotropy is potentially related to a different surface kinetics of GaCl precursor.
Acknowledgements
This work is supported by the Advanced Research Projects Agency-Energy (ARPA-E), U.S. Department of Energy, under Award Number DE-AR0000871 as part of the PNDIODES program managed by Dr. Isik Kizilyalli.

11:00 AM O08
(Student) High to Ultrahigh Si-Doped GaN Grown by Metalorganic Chemical Vapor Deposition at 550 °C for Heterogeneous Integration Vineeta R. Muthuraj, Caroline E. Reilly, Shuji Nakamura, Steven DenBaars and Stacia Keller; University of California, Santa Barbara, United States

The heterogeneous integration of III-nitride materials with other semiconductor systems for electronic devices is attractive because it combines the excellent electrical properties of the III-nitrides with other device platforms. Pursuing integration through metalorganic chemical vapor deposition (MOCVD) is desirable because of the scalability of the technique, but the high temperatures required for the MOCVD growth of III-nitrides (>1000 °C) are incompatible with heteroepitaxy on some semiconductor systems and fabricated wafers. Thus it is critical to develop III-nitride films with good electrical properties at growth temperatures compatible with temperature sensitive substrates. High crystal quality GaN films with reduced impurity levels have been achieved at temperatures as low as 500 °C using pulsed growth methods such as atomic layer epitaxy and flow modulation epitaxy (FME). However, the electrical behavior of doped LT III-nitride films is relatively unexplored.

In this work, thin Si-doped LT GaN films were grown at 550 °C by atmospheric pressure MOCVD using an FME scheme. Triethylgallium and ammonia were used as the GaN precursors and disilane as the Si dopant. Because of the very low growth rate (0.006 Å/s), 1200 FME cycles resulted in approximately 16 nm-thick films. Two different FME Si-doping schemes were investigated. The first series varied the fraction of cycles in which disilane was injected into the growing film. Samples were grown with disilane injected every 20, 10, 5, 3, 2, and 1 cycle. The second series varied the disilane flow while using the standard frequency of disilane injection (1 in 5 cycles). Samples were characterized by Hall measurements and secondary ion mass spectrometry (SIMS).

For the disilane injection series films, electron concentrations up to 6.97×10^{18} cm^{-3} were achieved, with electron mobilities from 34 to 119 cm^2 V^{-1} s^{-1}. The peak electron concentration was achieved for the sample with disilane injected in 1/3 of FME cycles during growth. The charge dropped off for samples with higher frequencies of disilane injection, likely because of degraded morphology. The Si concentrations measured by SIMS were somewhat higher than the electron concentrations measured by Hall. The background atmospheric impurity concentrations averaged 2.1×10^{17} cm^{-3} for oxygen and 3.9×10^{17} cm^{-3} for carbon, with no apparent dependence on Si concentration.
The disilane flow series resulted in films with electron concentrations from 5.98×10^{18} cm^{-3} to 5.91×10^{19} cm^{-3} and electron mobilities from 52 to 115 cm^2 V^{-1} s^{-1}, with the highest charge achieved with the highest disilane flow. The sheet resistance of this sample was 1068 Ω/■, which is comparable to low resistance GaN films grown at high temperature, which range from 100-500 Ω/■. These results demonstrate the potential for LT III-nitrides in electronics applications.
This work supported in part by Intel Corporation and the Solid State Lighting and Energy Electronics Center.

11:20 AM O09
(Student) Demonstration of Single Crystal InN & GaN/InN Heterostructures by MOCVD Tianhai Wu, Po Chun Chen and Shadi Dayeh; University of California, San Diego, United States

III nitride semiconductors have recently disrupted several industries and have remarkable potential to address unmet needs in electronics and optoelectronics. While gallium nitride (GaN) is the champion nitride material in solid state lighting and high power and high frequency electronics, there is abundant untapped potential in other nitrides that are otherwise harder to grow and to gain control over their electronic properties. Among these, Indium nitride (InN) that promises the highest saturation velocity in the nitride group poses two difficult challenges to realize its potential: (1) The epitaxial growth of high-quality InN films or structures is very challenging due to the competitive decomposition of InN at the temperatures for which efficient cracking of nitrogen sources occur, and (2) the difficulty in growing a larger bandgap barrier layer at the surface which requires even higher temperatures than the InN decomposition temperature, and with the absence of such layer, surface Fermi energy pinning challenges the modulation of the electron charge density to make functional transistor devices from any grown InN layers. Yes, there has been outstanding progress in the growth of InN layers by molecular beam epitaxy or plasma assisted metal-organic chemical vapor deposition (MOCVD), but the growth of smooth InN surfaces and the growth of larger barrier layers on InN has not been accomplished before: This work demonstrates by standard pulsed MOCVD growth the ability to grow defect free InN structures with smooth surfaces and the ability to grow with control GaN barrier layers and to demonstrate excellent transport characteristics in these structures. We hypothesized that coalescence of InN islands in constrained geometries such as lateral Fins can accelerate the formation of void-free and defect free InN growth within the first few nanometers of grown InN. We further hypothesized that we can raise the effective V/III ratio by pulsing the tri-methyl-indium source to avoid droplet formation, ripening and segregation which otherwise leads to the growth of defective and porous InN layers.

We validated these hypotheses by studying growth parameters and Fin widths in the range of 60 nm to 2000 nm (and control planar samples) and demonstrated InN Fins with defect-free surfaces and single crystal structures. Unannealed Ti/Au metal contacts on packed InN Fin arrays resulted in effective (un-corrected) specific contact resistance of approximately **6Ω•µm**, which is much smaller than that obtained for current GaN ohmic contacts, with an extracted contact transfer length less than **1µm**. To leverage these structures for high electron mobility applications and un-pin their surface Fermi energy, we successfully grew in-situ GaN/InN heterostructure without compromising the smooth InN surface. Transmission electron Microscopy showed clear interface between GaN and InN and single crystal structure. We then demonstrated that GaN can be selectively etched in the source/drain regions of the heterostructure and that unannealed Ti/Au metal contacts retain their low specific contact resistance on these structures. We are now investigating the fabrication of GaN/InN and AlN/InN HEMTs and their DC/RF performance.

11:40 AM O10
(Student) Effects of Pre-Metallization on the MOCVD Growth and Properties of Ge-Doped AlGaN on AlN Templates Tim Mirabito and Joan M. Redwing; The Pennsylvania State University, United States

AlGaN is an important ultra-wide bandgap material of interest for UV optoelectronics and vacuum nanoelectronics. However, the growth and n-type doping of Al-rich AlGaN is challenging due to the limited availability of AlN single crystal substrates and the increased ionization energy and compensation of donors, making it challenging to achieve highly doped n-type layers. AlN templates on sapphire are commonly used as substrates for AlGaN epitaxy, however, the crystalline quality and surface morphology of AlGaN is highly dependent on both the growth conditions and the presence of interlayers used to mediate the AlGaN/AlN epitaxial mismatch stress. Prior studies have demonstrated that pre-metallization of the AlN surface prior to AlGaN growth can be used to promote growth under metal-rich conditions which are beneficial to reduce surface roughness and point defects in the layers. However, the impact of pre-metallization on film stress, dislocations, and surface pitting in the AlGaN layers has not been examined in detail, particularly for highly n-type doped layers.
In this study, we investigate the effects of pre-metallization on the structural and electrical properties of Ge-doped $Al_xGa_{1-x}N$ (x~0.5-0.6) epilayers grown by MOCVD on 500 nm thick HVPE AlN templates on sapphire (Nitride Solutions). Germanium was used as the n-type dopant to achieve high n-type doping while avoiding problems associated with tensile stress and film cracking observed in highly Si-doped AlGaN.
The epilayer growth was carried out in a vertical cold wall MOCVD reactor with a k-Space multibeam optical stress (MOS) sensor. Trimethylaluminum (TMAl), trimethylgallium (TMGa), ultrahigh purity ammonia gas (NH_3), and germane (GeH_4; 2% in H_2) were used as Al, Ga, N and Ge sources, with hydrogen (H_2) as the carrier gas. The pre-metallization step was performed by switching NH_3 out of the reactor following the AlN layer and initiating the TMAl and TMGa flow prior to reintroducing the NH_3 and growing the AlGaN layer. For the unintentionally doped AlGaN, the effect of a 10 second pre-metallization step was investigated against a normal non-metallization AlGaN with the same flow rates and V/III ratios. The effect of a 5 second pre-metallization step was investigated for Ge doped AlGaN, where the flow rate was altered while maintaining the same TMAl/TMGa fraction to study the effects of strain and growth rate at a constant Al-composition. Characterization of these samples through AFM, XRD, wafer curvature measurements, and dark-field TEM aid in the quantification and imaging of the threading dislocations and STEM/EDS was used to measure the composition changes as a function of thickness.
AlGaN typically grows under compressive stress, due to larger lattice parameters relative to AlN. Comparatively, our results show that a pre-metallization step will alter the AlGaN stress from a compressive to a tensile state under the same flow conditions. This tensile grown AlGaN is also shown to reduce surface roughness in the undoped case, and v-pitting in the Ge doped case. From XRD measurements, the tensile AlGaN shows an increase in screw type dislocations while maintaining similar edge type dislocations as the nominal growth condition. Cross sectional TEM imaging is used to analyze the evolution of increased screw-type dislocations when using pre-metallization steps.
Additionally, we show that the transition from compressive to tensile growth is not only dependent on the pre-metallization step but the growth rate of the AlGaN layer at the AlGaN/AlN interface. By utilizing a pre-metallization step and a lower growth rate, it is possible to maintain low surface v-pitting and threading dislocation densities in Ge doped AlGaN.
Our results explore the stress, strain, and defect evolution at the AlGaN/AlN pre-metallization interface. Ultimately, these experiments help us establish a better understanding of AlGaN heteroepitaxy, and an effective pathway towards material improvement.

SESSION P: Quantum, Strongly Correlated and Topological Materials

Session Chairs: Stephanie Law and Quang To
Thursday Morning, June 30, 2022
US Bank Conference Theater

8:40 AM P01
(Student) Nonlocal Measurement as a Probe of the Spin Hall Effect in Topological Insulators Jennifer E. DeMell[1], Gregory Stephen[1], Owen Vail[2], Aubrey Hanbicki[1], Patrick Taylor[2] and Adam Friedman[1]; [1]Laboratory for Physical Sciences, United States; [2]U.S. Army Research Laboratory, United States

Topological insulators (TIs) are promising candidates for alternative computing device designs. In particular, they have great potential for spintronic devices, where utilization of electron spin rather than charge would allow for lower-power and higher-performance computing in next-generation architectures. Efficient conversion between spin and charge signals is crucial to spintronic technology. TIs provide highly efficient spin-to-charge conversion as a result of their unique topological properties. One way to electrically quantify conversion efficiency is with the spin Hall effect (SHE). Here, we present SHE measurements of the topological insulator $Bi_2Te_{2.5}Se_{0.5}$. Because of the topological nature of this material, we can measure the SHE without the use of ferromagnetic injectors or detectors. Using the nonlocal resistance, we measure spin Hall angles up to 2.4 with spin lifetimes up to 9 ps. Furthermore, ferromagnet-free measurement allows for quick diagnostics of the spin properties without the need to fabricate multilevel devices.

9:00 AM P02
Magnon-Mediated Entanglement of Solid-State Spin Qubit
Denis R. Candido and Michael E. Flatté; University of Iowa, United States

In this work we propose a hybrid quantum system that allows the creation of entanglement between solid-state qubits through magnon modes of a magnetic material [1,2]. Our first hybrid quantum system is composed of a diamond nitrogen-vacancy (NV) center spin coupled to a magnon mode of the low-damping, low-moment organic ferrimagnet vanadium tetracyanoethylene [1,3]. Accordingly, we derive an analytical expression for the spin-magnon cooperativity as a function of NV position under a

perpendicularly magnetized disk. We predict that the spin-magnon-mode coupling strength is g~2π×10 kHz, yielding cooperativity C_λ = 15 for a wide range of NV spin locations within the diamond, well within the spatial precision of NV center implantation [1]. Thus our proposal describes a practical pathway for single-spin-state-to-single-magnon-occupancy transduction and for entangling NV centers over micronlength scales [1]. Secondly, we generalize the same finding for rectangular bars made of Yttrium Iron Garnet (YIG) [2]. Additionally, we compare on-resonant transduction and off-resonant virtual-magnon exchange protocols and discuss the generation of entanglement for different temperatures, and under realistic experimental conditions [2].

[1] D. R. Candido, G. D. Fuchs, E. Johnston-Halperin, M. E. Flatté, Mater. Quantum. Technol. **1** 011001 (2021)
[2] M. Fukami, D. R. Candido, D. D. Awschalom, and M. E. Flatté, PRX Quantum **2**, 040314 (2021)
[3] A. Franson et. al., APL Materials **7**, 121113 (2019).

9:20 AM P03

Entanglement of Circularly Polarized Light with the Quantum Zeno Effect Ian C. Nodurft[1,2], Brian T. Kirby[3,4], Ryan T. Glasser[4], Harry C. Shaw[5] and Thomas Searles[1]; [1]University of Illinois at Chicago, United States; [2]Peraton, United States; [3]US Army Research Laboratory, United States; [4]Tulane University, United States; [5]NASA Goddard Space Flight Center, United States

The quantum Zeno effect reveals that a continuously observed quantum system exhibits a natural suppression of its time-evolution. And, as a consequence, the system experiences a measurement-dependent restriction of accessible quantum states. Therefore, one should be able to force a group of particles into an entangled state with the quantum Zeno effect. Here, we present a scheme, supported by numerical simulations, where an unentangled photon pair enters each side of a coupled waveguide and evolves into a polarization entangled state. Additionally, we find that a very similar setup with three photons can generate W-states. Our findings present a robust avenue for photonic-based quantum applications without the need for distribution protocols.

9:40 AM P04

(Student) Visible Light Emission During Electrical Threshold Switching of NbO2 Mott Switches Mahnaz Islam[1], Stephanie M. Bohaichuk[1], John A. Roberts[1], Chengyang Zhang[2], Tae Joon Park[2], Victoria Chen[1], A. A. Talin[3], Shriram Ramanathan[2], Jonathan A. Fan[1], Suhas Kumar[3] and Eric Pop[1,1]; [1]Stanford University, United States; [2]Purdue University, United States; [3]Sandia National Laboratories, United States

Post-CMOS computing aims to integrate both electrical and optical components that offer high on-chip functional density. Here we demonstrate simultaneous electrical and optical functions in a single device based on NbO_2, a Mott insulator-metal-transition (IMT) material. On one hand, the device displays volatile electrical threshold switching, a key ingredient in building artificial neurons [1] and selector devices for non-volatile memory [2]. On the other hand, we discover that during threshold switching the device also emits visible and infrared light, which represents a physically new phenomenon (for NbO_2 switches) with potential applications for metrology, electro-optical transduction, and on-chip light sources [3].
We constructed lateral two-terminal NbO_2 devices using 100–200 nm of NbO_2 grown on *c*-plane sapphire, with L = 2–8 μm of separation between metallic electrodes. Above a threshold voltage, the devices display abrupt volatile switching in current, a known behavior due to a Joule-heating-driven IMT at a transition temperature of ~1100 K. Devices with L in the range 2–5 μm switched at quasi-static voltages of ~50–90 V, in vacuum at room temperature ambient.
Operando visible optical microscopy of these devices with a visible-range camera revealed light emission during electrical switching. The intensity of the emission was highest during the transient current overshoots upon IMT threshold switching. The light emission was also present when the device is held in the low-resistance metallic state, albeit at a lower intensity. In this state, the intensity of the emission increased with increasing current, while the color of the emission for a given device remained the same irrespective of intensity. No light emission was observed in the high-resistance insulating state of the NbO_2 devices.
To identify the physical origins of the light emission, we obtained its spectroscopic information in visible wavelengths, which revealed the tail of a peak that is likely in the infrared. While this observation indicates elevated local temperatures, fitting with a blackbody emission model (with variable emissivity) did not yield a reasonable agreement with the experimental data, suggesting an electronic origin of the light emission. Further, comparison of optical and atomic force micrographs (AFMs) of devices before and after electrical switching showed permanent changes, revealing apparent current path formation between the electrodes, indicating local temperatures that exceeded the known IMT temperature of NbO_2 (~1100 K).
We also performed *operando* visible optical microscopy on devices with different sizes and at different ambient temperatures. In general, when the switching voltage was significantly lower, which was the case with smaller channel lengths or operation at elevated ambient temperatures, light emission was not observed. In contrast, the observed emission was brighter for longer channel lengths with higher IMT voltages at any given ambient temperature. These observations indicate that a higher input power, and thereby increased local temperatures due to Joule heating, was required for light emission. At the same time, the inconsistency with a pure blackbody model and the color of the light remaining invariant, indicate possible electronic origins of the light. Interestingly, devices which were switched *only* at a higher ambient temperature did not show a permanent current path formation, and light emission was also absent.
In conclusion, we present the discovery of a light emission process which occurs during the electrical threshold instability in NbO_2 devices. The process is likely both thermal and electronic in origin, paving the way for new metrology approaches and electro-optical components based on the IMT material NbO_2.

[1] Kumar et al., *Nature* 585, 518 (2020)
[2] Zhou et al., *Proc. IEEE* 103, 1289 (2015)
[3] Zhou et al., *Light: Sci. & Appl.* 4, 358 (2015)

10:00 AM Refreshment Break

10:20 AM P05

MBE Growth of Bi_2Se_3 with Reduced Twin Defect Density Patrick Taylor, George de Coster, Wendy Sarney, Blair Connelly and Harry Hier; U.S. Army Research Laboratory, United States

Topological Insulator (TI) materials promise a wide variety of disruptive new spintronic and electronic device technologies by leveraging the attractive spin-momentum-locked surface currents. The family of $(Bi,Sb)_2(Te,Se)_3$ TI materials are an interesting platform because they are three-dimensional TIs with robust Dirac surface state dispersion. Generally, the epitaxial growth of these materials contain a high volumetric density of anti-phase and other unwanted rotational domain disorder such as twinning. That disorder causes issues such as a small-angle carrier scattering, reduced response to circularly polarized light, and persistently high background carrier density[1] which degrades the efficiency and operability of devices.

In this work, we present results from a novel approach to reduce the twinning and anti-phase disorder in epitaxially grown TIs. The strategy involves the choice of a vicinal substrate orientation that yields a 60 degree zig-zag-like morphology of atomic ledges on the surface. The 60 degree bends in the ledges accommodate and seed the trigonal growth symmetry of $(Bi,Sb)_2(Te,Se)_3$ TI materials. The

success of this approach is demonstrated by a 4X reduction in twins for Bi_2Se_3 grown on (111)B InP substrates with a 2 degree miscut toward (010). We will present measurement results including terahertz emission, RHEED, as well as x-ray diffraction pole scans that all are consistent with a reduction in twin density. To help explain the significantly (about 10X) larger terahertz response using circularly polarized light, we calculated the Bi_2Se_3 band structure including spin-sensitivity near the Γ-point along the M direction.

Reference:

K. Kim, J. Lee, B. Kim, W. Choi, H. Chang, S. Won, B. Kwon, S. Kim, D. Hyun, H. Kim, H. Koo, J. Choi, D. Kim, J. Kim, S. Baek, Nature Comm. vol. 7, Article number: 12449 (2016).

10:40 AM P06

(Student) Epitaxial Growth of Kagome Ferromagnet Fe3Sn2 and Sn-Modulated Heterostructures Shuyu Cheng, Binbin Wang, Igor Lyalin, Nuria Bagues Salguero, Alexander J. Bishop, David McComb and Roland Kawakami; The Ohio State University, United States

Kagome magnets are interesting due to the co-existence of Weyl points and spin frustration in these materials. The thin-film form of these materials is particularly desired for both fundamental research and practical application. Here we report the molecular beam epitaxy (MBE) growth of kagome magnet Fe_3Sn_2 on epitaxial Pt(111) buffer layer on Al_2O_3(0001) substrate. Using our unique atomic-layer MBE (AL-MBE) technique, we are able to grow these materials at a lower temperature, which reduces interdiffusion and generates a sharp interface. The structure of Fe_3Sn_2 is confirmed by a combination of reflection high-energy electron diffraction (RHEED), X-ray diffraction (XRD), and transmission electron microscopy (TEM), while the magnetic properties of Fe_3Sn_2 are demonstrated by magneto-optical Kerr effect (MOKE), SQUID magnetometry, and anomalous Nernst effect (ANE) imaging. Furthermore, AL-MBE technique allows us to grow Sn layer modulated [Fe_3Sn_2/Fe_3Sn] superlattices, whose structure is also confirmed by TEM and Energy-dispersive X-ray spectroscopy (EDX). These results demonstrate our ability to control the sample structure at the atomic level using AL-MBE.

11:00 AM P07

(Student) Fermi Level Tuning and Band Alignment in Mn Doped InAs/GaSb Logan Riney[1], Joaquin B. Ortiz[2], Gauthier Krizman[3], Seul-Ki Bac[1], Jiashu Wang[1], Maksym Zhukovskyi[4], Tatyana Orlova[4], Louis-Anne DeVaulchier[2], Yves Guldner[2], Roland Winkler[5], Jacek K. Furdyna[1], Xinyu Liu[1] and Badih Assaf[1]; [1]University of Notre Dame, United States; [2]Ecole Normale Supérieure, France; [3]Johannes Kepler Universität Linz, Austria; [4]Notre Dame Integrated Imaging Facility, United States; [5]Northern Illinois University, United States

InAs/GaSb hosts a broken gap band alignment that has been shown to generate helical topological edge states. Upon the introduction of Mn into the structure, it has been predicted to host a quantized anomalous Hall effect. Here, we show that dilute Mn doping on InAs in InAs/GaSb, allows a tuning of the Fermi level, the introduction of paramagnetism, but also has a non-trivial impact on the band alignment of the system. The measurement of Shubnikov-de-Haas oscillations, cyclotron resonance, and a non-linear Hall effect in Mn-doped samples indicate the coexistence of a high mobility two-dimensional electron gas and a hole gas. Conversely, in undoped InAs/GaSb, pure-n-type transport is observed. We hypothesize that Mn acceptor levels can pin the Fermi energy near the valence band edge of InAs, far from the interface, which introduces a strong band bending to preserve the band offset at the InAs/GaSb interface. The realization of the QAHE in this structure will thus require a careful control of the band alignment to preserve topological insulating character.

11:20 AM P08

(Student) Confinement-Induced Topological Phase Transition in Thin-Film Rare-Earth Pnictides Quoc Dai Ho[1], Ruiqi Hu[1], Quang To[1], Garnett Bryant[2] and Anderson Janotti[1]; [1]University of Delaware, United States; [2]National Institute of Standards and Technology, United States

Metal-insulator phase transition is a classic phenomenon induced by various reasons. The transition caused by quantization effect when going from bulk materials to a very thin film limit is rather well-known. In this work, by using first principles calculations, we investigate the phase transition when 3D bulk semimetallic rare-earth pnictides having simple rock salt structure become as thin as quasi 2D materials with growth direction chosen to be along [001]. The electronic structure of 3D rare-earth pnictides typically consists of three equivalent electron pockets at three X points and two hole pockets at Γ point in the Brillouin zone. These charge carriers are very sensitive to external stimuli such as strain or dimensional confinement. We find that due to its unique electronic structure, the electron pockets of these rare-earth pnictides show unique behavior upon quantum confinement in thin films. More specifically, the two in-plane electron pockets in reciprocal space moves up in energy, opeing a gap at the X_1 and X_2 points while the out-of-plane electron pocket at X_3, projected onto the Γ point, does not change, maintaining the system in a metallic state. This characteristic prevents a semi-metal to semiconductor transition. However, in the ultra-thin limit of few monolayer thick, we observe a topological phase transition from a trivial 3D semi-metal to a 2D spin Hall insulator with a sizeable band gap due to the spin-orbit coupling. This finding introduces a new member to the 2D spin Hall insulator family and offers a new platform to realize the 2D spin Hall insulator experimentally.

11:40 AM P09

(Student) Charge Transport in a Dirac Semimetal, Na3Bi Dhruv C. Desai[1], Jinsoo Park[1], Jin-Jian Zhou[2] and Marco Bernardi[1]; [1]California Institute of Technology, United States; [2]Beijing Institute of Technology, China

Dirac semimetals exhibit unconventional transport properties due to their topological band structure. Despite rapid experimental progress, microscopic understanding of electronic scattering mechanisms and (magneto)transport coefficients remains limited. In this talk, we present first-principles calculations of the resistivity, mobility and magnetoresistance in the Dirac semimetal Na_3Bi. We compute the electron-phonon interactions and solve the Boltzmann Transport equation (BTE), overcoming key challenges such as handling large unit cells and ultra-fine momentum grids, as well as taking into account the spin-orbit coupling, Berry curvature, and Zeeman splitting to study novel transport regimes. Taken together, our results shed light on the microscopic mechanisms governing the electronic properties of Na_3Bi.

SESSION Q: Oxide Semiconductor Devices, Defects and Transport

Session Chairs: Leonard Brillson and Sarah Swisher
Thursday Morning, June 30, 2022
Ohio Staters Inc. Traditions Room

8:20 AM Q01

Large-Area Photonic Lift-off Process for Flexible Thin-Film Transistors Adam Weidling[1], Vikram S. Turkani[2], Vahid Akhavan[2], Kurt A. Schroder[2] and Sarah L. Swisher[1]; [1]University of Minnesota, United States; [2]NovaCentrix, United States

As the complexity of flexible electronic devices such as displays and sensors has increased, new plastic-compatible manufacturing

methods are becoming necessary to produce high-yield, low-defect flexible circuits. While solution-processed methods such as printing can be used to fabricate circuits on low-temperature substrates, printing is not always a feasible option to realize complex, high-density circuits with small devices. In particular, high-resolution display applications typically require single-micron feature sizes and excellent uniformity over large-area substrates. For these applications, more precise fabrication techniques such as photolithography are required. However, due to the poor dimensional stability of polymers, even low-temperature processes such as soft bakes during lithography can alter the substrate dimensions. The problem of dimensional stability can be overcome by attaching the polymer film to a rigid carrier during device fabrication, then releasing the polymer substrate with the fully fabricated device layer on top. For this reason, the separation of polymer films from rigid carriers remains a crucial step in creating next-generation flexible electronics.

In this talk, we will discuss a large-area, high-throughput photonic lift-off (PLO) process to rapidly separate polymer films from rigid carriers. PLO uses broadband light (200 nm – 1100 nm) from a flashlamp to lift off a polymer film from a rigid carrier coated with a light-absorbing layer (LAL), where the polymer film may contain functional devices [1]. Compared to a raster process such as excimer laser lift-off, the PLO process is advantageous as it can enable large area lift-off (150 mm x 75 mm) in one flash of light lasting between 100- 200 μs, thus enabling higher throughput. Furthermore, the LAL prevents direct illumination of the polymer substrate during lift-off and facilitates cleaner lift-off without polymer ashing. The LAL also makes PLO a polymer-agnostic process, enabling lift-off of a wide range of polymers.

We will discuss our recent work fabricating flexible thin-film transistors (TFTs) using PLO [2]. Polyimide with a low coefficient of thermal expansion (CTE) was used to minimize residual film stress. Indium zinc oxide (IZO) TFTs were fabricated on the polyimide films and subsequently released from the carrier using PLO. The released devices demonstrated no significant changes after the PLO process, yielding a mobility of ~3 $cm^2V^{-1}s^{-1}$ before and after lift-off. The flexible TFTs were robust to bending stress, showing no notable decrease in mobility while bent with a 10 mm radius of curvature. When combined with the ability to successfully separate the PI from the carrier, the low-CTE PI creates a robust fabrication platform for flexible electronics that allows conventional patterning and deposition techniques to be used on a plastic substrate while maintaining dimensional stability with processing temperatures up to 380 °C. A 3D finite element model indicates that the polymer/LAL interface reaches above 800 °C during PLO, but the top surface of the PI remains below 120 °C. The model shows that the maximum temperature at the device layer during PLO is strongly impacted by the thickness and material properties of the polymer film, highlighting the value of the model to guide PLO device design. This work demonstrates the feasibility of PLO to successfully release polyimide substrates containing flexible electronic devices from glass carriers after withstanding conventional lithographic processing methods.

[1] R. Hendriks and K. A. Schroder, "Method for performing delamination of a polymer film. U.S. Patent 10,011,104.," U.S. Patent 10,011,104, Jul. 03, 2018
[2] A. M. Weidling, V. S. Turkani, V. Akhavan, K. A. Schroder, and S. L. Swisher, "Large-Area Photonic Lift-off Process for Flexible Thin-Film Transistors," *in press*.

8:40 AM Q02
(Student) Facile Processing and Properties of P-Type SnOx and Oxide-Based p-n Heterojunction Application with n-InGaZnO Dong Hun Lee[1], Sunghwan Lee[1], Han Wook Song[2], Molly Rothschild[1] and Junsoo Choi[1]; [1]Purdue University, United States; [2]Korea Research Institute of Standards and Science, Korea (the Republic of)

In recent years, oxide electronics has emerged as one of the most promising new technologies for a variety of electrical and optoelectronic applications, including next-generation displays, solar cells, batteries, and photodetectors. Oxide electronics have a lot of potential because of their high carrier mobilities and ability to be manufactured at low temperatures. However, the preponderance of oxide semiconductors is n-type oxides, limiting present applications to unipolar devices and stifling the development of oxide-based bipolar devices like p-n diodes and complementary metal-oxide–semiconductors.

We have contributed to oxide electronics, particularly on transition metal oxide semiconductors of which the cations include In, Zn, Sn and Ga. We have integrated these oxide semiconductors into thin film transistors (TFTs) as active channel layer in light of the unique combination of electronic and optical properties such as high carrier mobility (5-10 cm^2/Vs), optical transparency in the visible regime (>~90%) and mild thermal budget processing (200-400°C).
In this study, we achieved four different results. The first result is that unlike several previous reports on oxide p-n junctions fabricated exploiting a thin film epitaxial growth technique (known as molecular beam epitaxy, MBE) or a high-powered laser beam process (known as pulsed laser deposition, PLD) that requires ultra-high vacuum conditions, a large amount of power, and is limited for large-area processing, we demonstrate oxide-based heterojunction p-n diodes that consist of sputter-synthesized p-SnOx and n-IGZO of which the manufacturing routes are in-line with current manufacturing requirements. The second result is that the synthesized p-SnOx films are devoid of metallic Sn phases (i.e., Sn^0 state) with carrier density tuneability and high carrier mobility (> 2 cm2/Vs). The third result is that the charge blocking performance of the metallurgical junction is significantly enhanced by the engineering of trap/defect density of n-IGZO, which is identified using photoelectron microscopy and valence band measurements. The last result is that the resulting oxide-based p-n heterojunction exhibits a high rectification ratio greater than 10^3 at ±3 V (highest among the sputter-processed oxide junctions), a low saturation current of $\sim 2\times10^{-10}$ A, and a small turn-on voltage of ~0.5 V.
The outcomes of the current study are expected to contribute to the development of p-type oxides and their industrial device applications such as p-n diodes of which the manufacturing routes are in-line with the current processing requirements.
Reference:
1. Lee, S.; Paine, D. C., Metallization selection and the performance of amorphous In-Zn-O thin film transistors. Applied Physics Letters 2014, 104 (25), 252103.
2. Liu, M.; Kim, H.; Wang, X.; Song, H. W.; No, K.; Lee, S., Carrier Density-Tunable Work Function Buffer at the Channel/Metallization Interface for Amorphous Oxide Thin-Film Transistors. ACS Applied Electronic Materials 2021, 3 (6), 2703-2711.
3. Chu, X., Zhuang, S., Chi, C., Xu, H., Du, G., Dong, X., & Yin, J. (2017). Study on the electroluminescence properties of the P-nimgo:Li/mgo/n-zno nanowires/ito heterojunction. Journal of Luminescence, 187, 486–491.
4. Kawazoe, H.; Yanagi, H.; Ueda, K.; Hosono, H., Transparent p-Type Conducting Oxides: Design and Fabrication of p-n Heterojunctions. MRS Bull. 2000, 25 (08), 28-36.
5. Mo, X., Fang, G., Long, H., Li, S., Wang, H., Chen, Z., Huang, H., Zeng, W., Zhang, Y., & Pan, C. (2014). Unusual

electroluminescence from n-ZnO@i-MgO core–shell nanowire color-tunable light-emitting diode at reverse bias. Phys. Chem. Chem. Phys., 16(20), 9302–9308.
6. Nomura, K.; Ohta, H.; Takagi, A.; Kamiya, T.; Hirano, M.; Hosono, H., Room-temperature fabrication of transparent flexible thin-film transistors using amorphous oxide semiconductors. Nature 2004, 432 (7016), 488-492.

9:00 AM Q03
(Student) Separation of Defect States and Intrinsic Channel Mobility on the Electrical Operation of IGZO TFTs
Muhammad S. Kabir[1], Eli Powell[1], Robert Manley[2] and Karl D. Hirschman[1]; [1]Rochester Institute of Technology, United States; [2]Corning Incorporated, United States

The role of band-tail states (BTS) on the operation of IGZO TFTs is well established, however there is wide variation in the interpretation of the interaction and/or independence of channel mobility and charge trapping. In many reports the influence of BTS on the level of free charge is accounted for by an effective mobility which is dependent on the applied gate bias. While this may accurately match current-voltage characteristics, this treatment is lumping together the effects of charge trapping and carrier scattering which should remain distinct. When these effects are combined, a model which can accurately represent device behavior over a wide temperature range is not possible due to fundamental differences in temperature dependence.

Bottom-gate TFTs were fabricated with a 50 nm IGZO film sandwiched between a 50 nm gate oxide and a 50 nm passivation oxide layer. The working metal was molybdenum for the gate electrode and source/drain contacts. A passivation anneal was done and a capping layer was added to promote electrical stability; full process details are provided in a previous report. Devices were tested using a Lakeshore cryogenic probe station, with transfer characteristic measurements taken from room temperature to below 100 K.

Electrical measurements made on long-channel devices (L = 12 μm) has revealed temperature-dependent behavior that is not explained by existing TCAD models employed for defect states and carrier mobility. An IGZO TFT device model has been recently developed using Silvaco Atlas, which accounts for the role of donor-like oxygen vacancy defects, acceptor-like BTS, acceptor-like interface traps, and a temperature-dependent intrinsic channel mobility. The model demonstrates a remarkable match to transfer characteristics measured at T = 150 K to room temperature. The temperature-dependent mobility follows a power-law relationship, resembling behavior consistent with ionized defect scattering. The mobility model is independent of carrier concentration, without dependence on the applied gate bias. Details of the material and device model, and associated defect distribution parameters will be presented.

9:20 AM Q04
(Student) Investigation of p-Type SnO Sub-Bandgap Defects by Comparing Experimental Transistor Data to Numerical Device Simulations Kishwar Mashooq, Jaesung Jo and Rebecca L. Peterson; University of Michigan Ann Arbor, United States

Metal oxide semiconductors have gained a lot attention for applications in thin film transistor (TFT) technology, large-area displays and flexible electronics. Although *n*-type metal oxide semiconductors already have been commercialized, extensive research is being conducted to find a suitable *p*-type counterpart. Among the *p*-type oxide semiconductors available, *p*-type SnO has gained a lot of attention as its hybridization of O 2p and Sn 5s orbitals at the valence band maximum enables it to avoid charge localization, which limits hole mobility in other *p*-type oxides. Although there are many reports of SnO TFTs, most show a relatively low field effect mobility (μ_p) of ~1−2 $cm^2V^{-1}s^{-1}$ and a poor on-off current ratio (I_{on}/I_{off}) of ~10^2 −10^3. To understand and improve SnO TFT performance, it is necessary to have a quantitative study of sub-bandgap defect states in SnO and at its dielectric interface. In this work, we extracted the SnO sub-bandgap defect parameters by comparing experimental TFT data with 2D numerical device simulations using Silvaco TCAD ATLAS. We found that the accuracy of the defect state models can be improved significantly by concurrent fitting of I_{DS}-V_{GS} and μ_p-V_{GS} curves. To obtain experimental data, we RF sputtered polycrystalline SnO on SiO_2/*n*-Si, which acts as the gate stack. To form a TFT, we deposited 20 nm Ni/ 80 nm Au source/drain contacts by e-beam evaporation. For numerical simulation, the material properties of SnO were taken from literature [1,2]. To model the sub-bandgap defect states in *p*-type SnO, the Mott-CFO density of states model in ATLAS was used. We established a SnO defect state model by first fitting the experimentally-obtained I_{DS}-V_{GS} curves to simulation. Although the preliminary model showed a good fit between experimental and simulated transfer curves, a large discrepancy was observed between modeled and measured μ_p-V_{GS} curves. So, to improve the SnO defect state model accuracy, we performed concurrent fitting of I_{DS}-V_{GS} and μ_p-V_{GS} curves. Using our optimized SnO sub-bandgap defect state model, we identified the dominant factors limiting SnO TFT performance: the high density of interface donor-like tail states and high contact resistance limit μ_p, while the high density of shallow, bulk Gaussian acceptor-like defects leads to poor I_{on}/I_{off}. By addressing these specific defect states, SnO TFT performance can be improved significantly.
The authors thank Intel Components Research for helpful discussions and funding.
[1] Y. Ogo *et al.*, "Tin monoxide as an s-orbital-based p-type oxide semiconductor: Electronic structures and TFT application," *Phys Status Solidi A,* vol. 206, no. 9, pp. 2187–2191, Sep. 2009, doi: 10.1002/pssa.200881792.
[2] N. F. Quackenbush *et al.*, "Origin of the Bipolar Doping Behavior of SnO from X-ray Spectroscopy and Density Functional Theory," *Chem. Mater.*, vol. 25, no. 15, pp. 3114–3123, Aug. 2013, doi: 10.1021/cm401343a.

9:40 AM Q05
(Student) Materials Characterization of LaCoO3 Grown by Optimized Reactive DC Magnetron Sputtering and Evaluation of Contact Metal Resistivities by Transmission Line Measurement Technique Rajashree Bhattacharya[1,2]; [1]UCLA, United States; [2]Northrop Grumman Corporation, United States

In traditional band theory, a fermi level in a bandgap leads to insulating behavior, and a finite amount of energy is required to excite an electron to the next highest accessible orbital to carry electric current. Band theory fails to accurately predict when other effects such as electron-electron interactions within orbitals or disorder cause electron localization, especially in transition metal oxides. Emerging transition metal compounds that exhibit rapid, reversible changes in conductivity as a function of temperature (a.k.a Insulator to Metal Transition, IMT) offer high switching ratios suitable for electronic switches and high power thermal management.
The motivation behind this work is to further understand the IMT mechanism of Lanthanum Cobaltite (LaCoO3, LCO) and enable its fabrication into ultra-fast electronic switches. LaCoO3 demonstrates a large magnitude Co (III) two-stage spin-state transition to metallic state at 500K which can be leveraged towards for high temperature and high power operation. We developed a high temperature reactive metal co-sputtering process for wafer and fabrication scale synthesis of LCO. Reactive sputtering affords greater flexibility and larger area deposition than other deposition methods such as molecular beam epitaxy, which has previously been used to explore the feasibility of LCO for abrupt switches. We present firstly on the influence of growth temperature,

composition, and substrate choice on grain size, topology and crystallinity as studied by atomic force microscopy and x-ray diffraction. The Berg Model of reactive sputtering and voltage discharge hysteresis experiments are utilized to optimize for the reactive gas partial pressure in the vacuum chamber. Temperature-dependent resistivity for epitaxial versus polycrystalline films is evaluated by four-point probe method and correlated to the high temperature bandgap-collapse observed by near-IR optical absorption.
Two terminal switching devices are fabricated on SiC, sapphire, and Lanthanum Aluminate substrates. Voltage-triggered switching results could support the theory of a critical power density criteria for LCO devices, rather than the Mott criterion established in vanadium dioxide devices. Finally, we will briefly discuss evaluation of various e-beam evaporated metals and annealing procedures *via* the transmission line measurement method. These methods are used determine the most thermally stable and lowest contact resistivity materials to aid in integration of LCO into power devices.

10:00 AM Refreshment Break

10:20 AM Q06
Controlling the *p*-Type Conductivity of SnO (001) Films by Group-III Doping During Molecular Beam Epitaxy Kingsley Egbo[1], Georg Hoffman[1], Jonas Lähnemann[1], Andreas Falkenstein[2], Joel Varley[3] and Oliver Bierwagen[1]; [1]Paul Drude Institute for Solid State Electronics, Germany; [2]Institute of Physical Chemistry, RWTH Aachen University, Germany; [3]Lawrence Livermore National Laboratory, United States

Reliable bipolar carrier transport remains a challenge in most transparent semiconducting oxides and this limits the widespread device adoption of oxides for optoelectronic devices [1]. Most widely applied transparent semiconducting oxides can only be doped *n*-type, their *p*-type doping remains challenging. However, few oxides show *p*-type character, Tin (II) oxide (SnO) is among the few *p*-type oxide semiconductors. Its optical bandgap of ~2.7 eV and high hole mobility~3-5 cm2/V.s relative to other binary *p*-type semiconducting oxides makes it a candidate material for transparent oxide heterojunctions with *n*-type materials[2][3]. Unintentional (UID) *p*-type conductivity is believed to be controlled primarily by Sn-vacancies [4] or their complex with hydrogen [5]. Few theoretical studies have also suggested the possibility of bipolar doping in SnO [6]. However, experimental studies exploring the effect of intentional impurities in SnO are lacking. Solely, the doping of SnO with >8 cation % of Sb has been experimentally shown to produce 10^{17}cm-3 electrons [7]. Here we show an experimental and theoretical study on the effects of group III dopants on SnO. SnO (001) films doped with the group III In, Ga, and La species were grown on YSZ (100) substrates by molecular beam epitaxy (MBE). We explore two growth techniques for SnO; plasma-assisted MBE with a metallic Sn source [8] and suboxide MBE using a SnO_2+Sn mixture as pure SnO source without the use of additional oxyge[9]. In both growth techniques, the dopant elements were incorporated using the metal effusion cells and the dopant concentration, measured by energy-dispersive x-ray spectroscopy and secondary ion mass spectrometry, was varied by changing the dopant cell temperatures for different growths. The grown films were *in-situ* analyzed by reflection high-energy electron diffraction (RHEED), and *ex-situ* structurally investigated by x-ray diffraction (XRD), atomic force microscopy (AFM), and Raman spectroscopy. The structural characterization showed that the solubility limit of Ga, In and La in SnO are ~6.0 cation%, 2.0 cation %, and 3.3 cation % respectively. Detailed electrical properties of the doped films are obtained from Hall Effect measurements and Seebeck coefficient analysis. Hole concentration, p of ~1.2 x 10^{19} cm^{-3} and resistivity, ρ of 0.2 Ω-cm respectively is obtained for UID SnO (001) films grown using plasma-assisted MBE and we find that p increases to ~ 5.0 x 10^{19} cm^{-3} and ρ decreased to 0.063 Ω-cm for ~2.3at% Ga doped films. While SnO (001) films grown using a SnO_2+Sn mixed source show lower unintentional p ~1.2 x 10^{18} cm^{-3} and, ρ of 4.9 Ω-cm and p increases up to 2.0 x 10^{19} cm^{-3} and ρ decrease to 0.07 Ω-cm with Ga doping. In contrast, thin films doped with increasing concentrations of La show reduction in p and remarkable increase of ρ up to 680 Ω-cm without transition to an *n*-type conductivity. Computational results confirm that Ga acts as an acceptor defect in SnO while La acts as compensating donor. Our results reveal that *p*-type conductivity in SnO can be controlled by intentional Ga- and La-doping over four orders of magnitude, whereas the successful *n*-type doping remains challenging.
References:
1. M. Grundmann *et. al.*, J. Phys. D: Apply. Phys. **49**, 213001 (2016)
2. K. Zhang *et. al.,* J. Phys.: Condens. Matter 28, 383002 (2016)
3. M. Budde *et. al.,* Appl. Phys.Lett. **117**, 252106 (2020)
4. A. Togo *et. al.*, Phys. Rev. B, **74**, 195128 (2006)
5. J. Varley *et. al.*, Appl. Phys.Lett. **103**, 082118 (2013)
6. M. Grauzinyte *et. al.*, Phys. Rev. Materials, **2**, 104604(2018)
7. H. Hosono *et. al.*, Electrochem. Solid-State Lett, **14**, H13 (2010)
8. M. Budde *et. al.,* Phys. Rev. Materials, **4**, 124602 (2020)
9. G. Hoffman *et. al.*, APL Materials **8**, 031110 (2020)

10:40 AM Q07
(Student) Defects, Doping and Electronic Structure Correlations of Indium Tin Oxide (ITO) Thin Films Jade Cowsky[1], Oliver Bierwagen[2], Leonard J. Brillson[1], D.C. Look[3] and K.D. Leedy[4]; [1]The Ohio State University, United States; [2]Paul Drude Institut für Festkörperelektronik, Germany; [3]Wright State University, United States; [4]Air Force Research Laboratory, United States

Indium Tin Oxide (ITO) is a widely used transparent conducting oxide (TCO) with a 3.5 eV and higher band gap with high conductivity. Degenerately doped In_2O_3 with Sn enables ITO to serve as very thin conducting yet transparent films for touchscreens, solar cells, and light-emitting diodes. A challenge for ITO is to achieve the high conductivity of thicker crystalline films while maintaining the optical smoothness of ultrathin films. Central to the conductivity of such films are the density, spatial distribution, and physical nature of native point defects, which can scatter and trap free carriers in multiple ways to degrade mobility. We used depth-resolved cathodoluminescence spectroscopy (DRCLS) to measure the electronic band structure of ITO, the electronic states of dominant ITO native point defects, their nanoscale spatial distributions inside ultrathin and thicker films, and the dependence of In_2O_3 band structure and defects on Sn doping levels. Furthermore, these results can now be compared between films grown by molecular beam epitaxy (MBE) and pulsed laser deposition (PLD).
Optical spectroscopy of ITO band structure and defects can be challenging because of contributions from both direct and indirect band gaps as well as its degenerate doping, which produce Burstein-Moss (BM) Fermi level movements out of the band gap well into the conduction band. The presence of defect states within the band gap enables additional transitions into and out these states. In addition, the non-momentum-conserving nature of cathodoluminescence transitions allows observation of indirect transitions which might not be observed via photoluminescence spectroscopy. These multiple transitions are evident in Figs. 1 and 2, which exhibit peaks corresponding to all the aforementioned transition types and which correspond to the arrows between ITO conduction, valence, and defect gap levels in Fig. 3. Energies of the peaks assigned to direct and indirect transitions are in good agreement with those reported previously.[1] Furthermore, shifts in these energies due to doping, BM-induced Fermi level, and thereby effective band gap changes are consistent with changes in free carrier densities measured via Hall effect. Relative to the direct and indirect transition intensities, defect transition intensities increase

toward the free surface by >5x over tens of nm. (Fig. 4.) These defects and their spatial distributions (Fig. 5) appear to be similar for both MBE- and PLD-grown films, suggesting similar types of defects and depth-dependence even with different growth processes.
The DRCLS peak features lend themselves to interpretations of their physical nature. DFT theory of thermodynamic stability and charge state transition energies [2] in Fig. 6 provides support for identifying the 2.7-2.9 eV defect transition with oxygen vacancies V_O since it is the most thermodynamically stable point defect under O-poor conditions, and it has a charge state transition near the 2.7 eV indirect band gap edge. Other defects with transitions deeper within the band gap may be related to oxygen interstitials O_i or cation vacancies complexed with hydrogen, e.g. V_{In}-H.[3] Studies to further identify and control these defects are presently underway.

1. M. Feneberg *et al.*, Phys. Rev. B **93**, 045203 (2016).
2. I. Chatratin *et al,* Phys. Rev. Mater. **3**, 074604 (2019).
3. J.B. Varley *et al.,* J. Phys.: Condens. Matter **23,** 334212 (2011)

11:00 AM Q08
(Student) Study of Hole Scattering Mechanisms in P-Type Cu_2O Jaesung Jo, Zihao Deng, Nocona Sanders, Emmanouil Kioupakis and Rebecca L. Peterson; University of Michigan, United States

P-type oxide semiconductor development is a bottleneck that limits complementary metal oxide semiconductor thin film circuitry. One of the most famous p-type oxides is cuprous oxide, Cu_2O. This well-known p-type semiconductor has been widely explored for photovoltaic applications due to its high mobility and wide bandgap. The high hole mobility is also attractive for high-performance p-type oxide semiconductor electronics. In our previous work investigating RF sputtered Cu_2O thin film transistors (TFTs), we identified two main issues that limit device performance [1]. One is that the field effect mobility of the TFT is much lower than the material's Hall mobility due to device level problems such as contact resistance and interface traps. The other is that the Hall mobility is lower than the theoretically-estimated value or previously-reported mobility obtained under different thin film deposition conditions. To understand the scattering factors that fundamentally limit the Hall mobility of Cu_2O, in this work we investigated hole transport via experiments, analytical models, and density function theory (DFT). We compared an RF-sputtered polycrystalline Cu_2O thin film and a single-crystalline bulk substrate, which is a natural crystal. Temperature-dependent Hall measurements were performed from 200 K to 400 K. Temperature-dependent hole carrier concentration data was analyzed using a two-acceptor state model. The experimental results showed that both the Cu_2O thin film and the Cu_2O bulk substrate have relatively deep acceptors. The measured mobility data was analyzed using analytical models that incorporate scattering due to ionized impurities, neutral impurities, optical phonons, acoustic phonons, and grain boundaries. We found that neutral impurity and grain boundary scattering are the dominant scattering mechanisms for the Cu_2O thin film. On the other hand, phonon scattering is the dominant factor for the Cu_2O bulk substrate. Our DFT calculations, focusing on phonon scattering, indicate that the hole mobility of Cu_2O at 300 K should be > 100 $cm^2V^{-1}s^{-1}$. The two most dominant phonon modes were identified. This high mobility indicates that Cu_2O is a promising material compared to other p-type oxide semiconductors. Our results showed that, to achieve the high hole mobility in Cu_2O thin films, it is important to reduce the impurity concentrations and increase the grain size. This work provides insights toward high performance Cu_2O-based p-type devices. The authors thank Intel Components Research for helpful discussions and funding. [1] J. Jo, J. D. Lenef, K. Mashooq, O. Trejo, N. P. Dasgupta, and R. L. Peterson, *IEEE Trans. Electron Devices*, vol. 67, no. 12, pp. 5557–5563, Dec. 2020.

11:20 AM Q09
(Student) Electron Transport Mechanism and Mobility Prediction in Amorphous In_2O_3 for BEOL Transistors Yaoqiao Hu and Kyeongjae Cho; The University of Texas at Dallas, United States

Amorphous semiconducting metal oxides like In_2O_3, IGZO are now being investigated for back-end-of-line (BEOL) transistors due to their wide band gap, high electron mobility, and ease of synthesis at low temperature. In this work, we use density functional theory (DFT) based first principles calculations to investigate the electron conduction mechanism in a-In_2O_3, and compare the theory with experimental data. Useful insights and practical guidance are provided for device engineers to further optimize the performance of a-In_2O_3 based transistors.
Atomic structure of a-In_2O_3 was first generated by melt quench method with ab-initio molecular dynamic simulations. Local bonding distortion was observed in a-In_2O_3, which effectively elongates the In-O bonding distance and negatively impacts electron transport. The electronic density of states was calculated, showing that amorphous disorder and *n*-type W dopants can induce defect states in the band gap. These defect states could become electrically active and trap electrons, causing threshold voltage instability. Band structure calculation on crystalline phase In_2O_3 (c-In_2O_3) reveals that the In-In direct orbital overlap forms the electron conduction pathway (ECP) in c-In_2O_3. The local amorphous disorder in a-In_2O_3 effectively decreases the In-In medium range connectivity and therefore reduces the electron transport pathway. The electron mobility in a-In_2O_3 was further calculated based on the degree of electronic spatial localization, which determines the amorphous mobility at 30~50 cm^2/Vs. This value is well consistent with the experimental measured mobilities in W doped a-In_2O_3 devices. The effect of oxygen vacancy (V_O) is also investigated, which unveils that higher V_O reduces the In-In connection and impede electron transport in a-In_2O_3 films. Lastly, we studied the influence of film density on electron mobility, which shows that higher film density leads to compact atomic connectivity and enhanced electron mobility. These findings will contribute to the current general understanding of electron transport in amorphous solids. Our results provide useful guidance and predictive capability for device engineers on enhancing the electron transport in a-In_2O_3 to achieving better device performance.

SESSION R: Detectors and Narrow Bandgap Materials

Session Chairs: Ganesh Balakrishnan and Daniel Wasserman
Thursday Morning, June 30, 2022
Senate Chamber

8:20 AM R01
Undoing Band Anticrossing in Highly Mismatched Alloys Qian Meng[1], Tuhin Dey[2], Mohammad S. Reza[2], Augustus Arbogast[2], Seth R. Bank[1] and Mark Wistey[2,2]; [1]The University of Texas at Austin, United States; [2]Texas State University, United States

Highly mismatched alloys (HMAs) are mixtures of atoms of very different size and electronegativity, as in $Ge_{1-x}C_x$ or $GaAs_{1-y}N_y$. In conventional alloys, bandgap (E_g) and lattice constant follow an inverse trend. But small-atom HMAs often decrease E_g, giving device designers additional design freedom. The reduction in Eg is usually attributed to band anti-crossing (BAC): repulsion between the conduction band (CB) and a new state within the band introduced by the isoelectronic impurity, splitting the CB into E+ and E- bands. Anions (e.g. B), cations (e.g. N), and carbon (C) can all cause the effect.

However, past results from another HMA, GaInNAs, showed that nearest neighbor arrangements can also have a significant effect on bandgap, leading to a blueshift or increase in bandgap upon anneal. In this work, ab-initio modeling of different nearest neighbor arrangements of 54 and 128 atom supercells of $B_xIn_yGa_{1-x-y}As$ and $Ge_{1-x-y}Sn_xC_y$, respectively, was performed. HSE06 hybrid functionals were used to improve accuracy of bandgaps, and all supercells were fully relaxed in both configuration and volume, i.e. their native (computational) lattice constant.

The results show that band anticrossing effects in different HMAs, particularly bandgap, can be reduced and even eliminated by atomic arrangement in ternaries and quaternaries. A highly mismatched atom may not be sufficient in itself to cause band splitting if compensating atoms are within 2 bond lengths from it. Instead, distortion of the host lattice appears to be necessary. We also note that, as one might expect based on local strains, the lowest energy state is always the one in which Sn atoms are bonded directly to C rather than farther away.

The consistent results across three different HMAs suggests this is a general property applicable to many materials. Furthermore, this may explain the wide variation in properties reported by different groups, since nearest-neighbor arrangement can be highly sensitive to growth temperature, surface reconstruction, flux ratios, and the presence of surfactants such as Sn or Sb.

8:40 AM R02
(Student) Growth and Characterization of AlxIn1-xAsySb1-y Digital Alloys Grown on InP Ellie Y. Wang, Joshua A. McArthur, Ann K. Rockwell and Seth R. Bank; The University of Texas at Austin, United States

$Al_xIn_{1-x}As_ySb_{1-y}$ (referred to as AlInAsSb) grown as a digital alloy lattice-matched to GaSb substrates has been shown to have characteristics useful for avalanche photodetectors (APDs). In addition to a broadly tunable bandgap over a wide compositional range, the material system has favorable band offsets, with most of the bandgap change occurring in the conduction band, and it exhibits low excess noise due to impact ionization coefficient ratios as low as $k = 0.01$ [1]. The digital alloy method of growing thin binary layers to form extremely short-period superlattices enables the growth of high quality AlInAsSb within the miscibility gap. It also allows for more consistent parameters and finer control over compositional gradings in the growth of complex heterostructures when compared to analog alloy growth [2]. In some cases, the technique improves the noise characteristics of the material. For example, digitally grown $Al_{0.48}In_{0.52}As$ on InP exhibits a lower impact ionization ratio than the $Al_{0.48}In_{0.52}As$ random alloy, with $k \sim 0.05$ and $k \sim 0.2$, respectively [3]. Similarly, when grown as a digital alloy on InP, $AlAs_{0.56}Sb_{0.44}$ also exhibits reduced k as low as ~0.005 [4], compared to the random alloy with $k \sim 0.1$ [5].
Noteworthy, $Al_{0.48}In_{0.52}As$ and $AlAs_{0.56}Sb_{0.44}$ represent the lattice-matched extremes of the AlInAsSb quaternary on InP, with Al compositions of $x = 0.48$ and $x = 1.00$, respectively, suggesting the low-noise potential of the digital alloy system on InP across the full compositional range. Although $Al_{0.79}In_{0.21}As_{0.74}Sb_{0.26}$ random alloys on InP have shown low noise, growth at other Al compositions is challenged by phase separation that could potentially be overcome by digital alloying [6, 7]. The benefits of using InP substrates instead of GaSb for AlInAsSb growth are twofold: first, the maximum accessible bandgap would extend to ~1.8 eV, compared to ~1.25 eV on GaSb. Second, the more mature InP manufacturing infrastructure could be leveraged to produce high-quality APDs. The advances of AlInAsSb grown on GaSb substrates and the potential to enhance device performance using a mature InP platform motivated this study.
Here we present AlInAsSb grown as a lattice-matched digital alloy on InP substrates. AlInAsSb digital alloys of different aluminum compositions were grown using the molecular beam epitaxy (MBE) growth approach described in [8], where the aluminum composition is calculated as the sum of the number of AlAs and AlSb monolayers divided by the total number of monolayers. Lattice-matching to InP at each composition was achieved by adjusting the AlAs/AlSb thickness ratio while maintaining a constant InAs thickness. X-ray diffraction (XRD), photoluminescence (PL) and atomic force microscopy (AFM) measurements were performed on preliminary samples of AlInAs ($x = 0.48$) and AlAsSb ($x = 1.00$) to verify the structural, optical, and surface qualities at the compositional limits. XRD scans suggest high-quality crystal structures, as indicated by the sharp superlattice peaks and strain-balancing to the InP substrates. Room temperature PL was observed for both samples, showing optical emission at wavelengths of ~1.2 μm ($x = 0.48$) and ~0.9 μm ($x = 1.00$). AFM showed smooth surface morphology with RMS roughnesses of 0.3 nm ($x = 0.48$) and 1 nm ($x = 1.00$). In order to fully explore the compositional space of the material, the growth and characterization of additional AlInAsSb digital alloys with intermediate aluminum compositions are underway and will be reported at the conference.
References
[1] S. R. Bank, et al. *JSTQE* (2018). [2] A. J. Muhowski, et al. *JVST* (2021). [3] A. K. Rockwell, et al. *Appl. Phys. Lett.* (2018). [4] X. Yi, et al. *Nat. Pho.* (2019). [5] J. Xie, et al. *IEEE TED* (2012). [6] S. H. Kodati, et al. *Appl. Phys. Lett* (2021). [7] S. Tomasulo, et al. *J. Cryst. Growth* (2020). [8] S. J. Maddox, et al. *Cryst. Growth Des.* (2016).

9:00 AM R03
(Student) Exploring the Impact of Sn Alloying on Structure and Luminescence in PbSnSe Epitaxial Films on GaAs Jarod Meyer[1], Christian Martinez[1], Eamonn T. Hughes[2], Leland J. Nordin[1] and Kunal Mukherjee[1,2]; [1]Stanford University, United States; [2]University of California, Santa Barbara, United States

The narrow gap IV-VI semiconductor PbSe is an intriguing option for heterogeneously integrated mid-infrared light emitters in the 3 – 5 µm wavelength range. Thanks to its rare combination of ionic, covalent, and metallic bonding, PbSe has an anomalously low bulk Auger recombination coefficient, high tolerance of its minority carriers to crystal defects, and favorably low temperatures for epitaxy. The growth of PbSe and related IV-VI materials on substrates like GaAs is of great interest as these exciting optoelectronic properties of PbSe may be paired with the superior mechanical, chemical, and thermal properties of III-V materials and potentially even in functional heterostructures with III-V optoelectronic devices. Recently, we demonstrated epitaxial thin films of PbSe on 8%-lattice mismatched GaAs that nevertheless emit brightly, indicating high internal quantum efficiency for photoluminescence at room-temperature.[1]
Moving beyond the binary compound, we may tune the bandgap across the mid-IR and into the far-IR by substituting Pb with the isovalent element Sn as $Pb_{1-x}Sn_xSe$.[2] This alloy was also recently discovered to be a topological crystalline insulator past ~22% Sn following a complete band gap closure.[3] This motivates us to explore how alloying Sn alters the microstructure and otherwise excellent luminescence properties of PbSe films. Strain-induced structural distortions, stemming from lattice-constant and thermal-expansion mismatch with GaAs, are also an important parameter in understanding the electronic properties of these thin films. The lattice constant for $Pb_{1-x}Sn_xSe$ spans a range from 6.126 for PbSe to roughly 6.00 Å for cubic SnSe (a roughly 2% lattice mismatch between the two binaries).
We grew $Pb_{1-x}Sn_xSe$ epitaxial films on (001)-oriented GaAs substrates by molecular beam epitaxy at 280–300 °C using PbSe and SnSe compound source effusion cells, following a 400 °C surface pretreatment with PbSe flux that we find is essential for good photoluminescence, and a 330C PbSe buffer layer. Across a Sn composition range of x = 0–0.4, full-width-at-half-maximum of

(004) rocking curves increase from 350 to 515 arcseconds, suggesting a slight decrease in structural quality despite a decreased lattice mismatch to the GaAs substrate. We also find an increase in the in-plane residual tensile strain from 0.37–0.55% at room-temperature as the Sn content is increased, determined via high resolution x-ray diffraction reciprocal space maps. At growth temperatures, the nearly 8% lattice mismatch between PbSe and GaAs is fully relaxed. However, a tensile strain develops upon cooldown from growth temperature due to the large thermal-expansion mismatch between PbSe and GaAs.[4] The increased tensile strain in the higher Sn alloys is attributed to tensile strain with respect to the higher lattice constant PbSe buffer.
While higher Sn-content $Pb_{1-x}Sn_xSe$ ternaries suffer from a loss in structural quality, only less than 20% Sn is required to tune the emission wavelength from 4 – 10 µm.[2] Preliminary room-temperature photoluminescence show redshifted peak wavelengths out to 4.6 µm for a film of $Pb_{0.97}Sn_{0.03}Se$, but with decrease in emission intensity compared to PbSe. We will present results investigating and comparing loss mechanisms in PbSe and $Pb_{1-x}Sn_xSe$ to understand whether these are fundamental in nature or if they may be overcome by engineering.

[1] J. Meyer, A. J. Muhowski, L. J. Nordin, E. T. Hughes, B. B. Haidet, D. Wasserman, K. Mukherjee *APL Materials* **9** 111112 (2021).
[2] H. Preier, *Appl. Phys.* **20** 189 – 206 (1979).
[3] P. Dziawa, B. J. Kowalski, K. Dybko, R. Buczko, A. Szczerbakow, M. Szot, E. Lusakowska, T. Balasubramanian, B. M. Wojek, M. H. Bernsten, O. Tjernberg, T. Story, *Nat. Mater.* **11** 1023 – 1027 (2012)
[4] C. P. Li, P. J. McCann, X. M. Fang, *J. Cryst. Growth.* **208** 423 – 430 (2000).

9:20 AM R04

(Student) Growth of InAsSbBi on InSb Towards Lattice-Matched Longwave-Infrared Optoelectronics
Rachel C. White, Morgan Bergthold, Aaron J. Muhowski, Leland J. Nordin, Amberly Ricks, Daniel Wasserman and Seth R. Bank; The University of Texas at Austin, United States

While III-V-bismide alloys have received substantial attention due to the significant bandgap reduction induced by the incorporation of dilute concentrations of bismuth, the need for a highly optimized growth regime so disparate from the host alloy's ideal growth conditions has hindered their development relative to traditional III-V semiconductors.[1] In particular, low substrate temperatures are necessary to minimize bismuth desorption and promote substitutional incorporation, however, this parameter must be carefully balanced to minimize defects.[2] $InSb_{1-x}Bi_x$, while relatively underexplored, is a particularly promising candidate material system for accessing the longwave-infrared due to the similar growth temperatures that are ideal for InSb and III-Bi materials. We recently demonstrated the growth of high-quality $InSb_{1-x}Bi_x$ and, consequently, reported the first photoluminescence (PL) measurements from $InSb_{1-x}Bi_x$ alloys.[3] Alloying very small concentrations of arsenic to form the quaternary $InAs_ySb_{1-x-y}Bi_x$ can further reduce the bandgap energy and restore lattice-match to InSb substrates. Incorporating arsenic and bismuth in ~1:3 proportions enables lattice-matching to InSb while simultaneously further reducing the bandgap energy due to the band-bowing of $InAs_xSb_{1-x}$.[4] In this work, we report our progress towards optimizing the growth of $InAs_ySb_{1-x-y}Bi_x$ alloys and their structural and optical properties.
Epitaxial $InAs_ySb_{1-x-y}Bi_x$ films were grown by solid-source molecular beam epitaxy on n-type (100) InSb substrates under growth conditions targeting a kinetically-limited growth regime, such as that employed for the growth of high-quality $GaAs_{1-x}Bi_x$[5] and $InAs_{1-x}Bi_x$.[6] A low substrate temperature of approximately 300°C and an Sb/III flux ratio just below stoichiometry were employed to encourage bismuth incorporation. A relatively fast growth rate of approximately 1 µm/hr was utilized to further promote substitutional bismuth incorporation. Photoluminescence (PL) and atomic force microscopy (AFM) measurements were performed to quantify the optical quality and surface morphology of the films. X-ray diffraction (XRD) ω-2θ scans are in progress to confirm the bismuth and arsenic concentrations in the films and will be reported at the conference.
PL measurements of $InSb_{1-x}Bi_x$ and $InAs_ySb_{1-x-y}Bi_x$ films both targeting ~1 % Bi incorporation demonstrated an expected redshift in emission wavelength from the film with additional As incorporation. By targeting further increased As and Bi concentrations, wavelength extension out to approximately 6.6 µm was achieved from $InAs_ySb_{1-x-y}Bi_x$ alloys on InSb. While AFM measurements of the $InSb_{1-x}Bi_x$ film showed a relatively smooth surface, the $InAs_ySb_{1-x-y}Bi_x$ films exhibited some droplet formation. We expect this can be mitigated through careful optimization of the growth parameters. Current work includes optimizing the growth of $InAs_ySb_{1-x-y}Bi_x$ for enhanced structural and optical quality as well as investigating the limits of Bi incorporation in this material system. Progress towards these goals will be reported at the conference.
This work was supported by Lockheed Martin and NSF (ECCS-1933836). This work was performed in part at the University of Texas Microelectronics Research Center, a member of the National Nanotechnology Coordinated Infrastructure (NNCI), which is supported by the NSF (No. ECCS-1542159). This work was also supported by an NSF Graduate Fellowship (RCW).

[1]S. Francoeur et al., *Appl. Phys. Lett.* **82** (2003).
[2]S. Tixier et al., *Appl. Phys. Lett.* **82** (2003).
[3]R. C. White et al., *63rd Electronic Materials Conf.* (2021).
[4]S. Svensson et al., *Phys. Rev. B* **86** (2012).
[5]A. J. Ptak et al., *J. Cryst. Growth* **338** (2012).
[6]S. J. Maddox et al., *54th Electronic Materials Conf.* (2012).

9:40 AM R05

(Student) Growth and Characterization of AlInSbBi for Wide-Bandgap Barriers on InSb
Amberly Ricks[1], Rachel C. White[1], Qian Meng[1,2], Morgan Bergthold[1], Mark Wistey[2] and Seth R. Bank[1]; [1]The University of Texas at Austin, United States; [2]Texas State University, United States

Bi-containing III-V alloys have attracted attention over the past few decades due to their suitability for optoelectronic devices operating across a wide spectrum of the infrared region.[1] Integrating small amounts of Bi into III-V materials offers the flexibility to decrease the bandgap energy, which enables infrared emission, and increases spin orbit (SO) split band properties, which can suppress Auger recombination when larger than the bandgap energy.[2] Current approaches for photodetector operation in the mid-wave and long-wave infrared, such as HgCdTe and InSb-based devices, suffer from large dark currents.[3] While nBn structures can suppress many sources of dark current, the use of AlInSb barriers in InSb-based nBn detectors result in a difficult tradeoff between undesirable valence band offset and high barrier layer strain.[4] A flexible method to mitigate these challenges in InSb-based nBn detectors is to introduce small amounts of Bi and Al to InSb to tune the bandgap of InSbBi absorber regions and AlInSbBi barriers, while simultaneously minimizing strain. However, AlInSbBi remains largely underexplored, in part due to the difficulties of growing Bi-containing III-V alloys. Noteworthy are the tradeoffs in temperature and growth rate, which pose challenges in the ability to grow quality III-V-Bi materials.[5,6] In this work, material properties such as bandgap energy, lattice constant, surface morphology, and photoluminescence of AlInSbBi alloys were investigated to optimize material quality for barrier layer applications.
AlInSbBi was grown by solid-source molecular beam epitaxy on n-type InSb substrates. To promote Bi incorporation, the substrate temperature was maintained around 300ºC and a low V/III flux ratio of 0.975x was employed.[7] The growth rate was chosen to be

~1 µm/hr. Atomic force microscopy (AFM) and photoluminescence (PL) measurements were performed on an AlInSbBi thin film targeting ~1% Bi and ~5% Al incorporation. AFM measurements showed droplets on the film surface, however further optimization of the growth parameters may be able to mitigate droplet formation. PL measurements at 83K demonstrated that the AlInSbBi film emitted at roughly 5.1 µm, whereas the AlInSb and InSbBi control films emitted at 4.9 and 5.6 µm, respectively, suggesting ~0.5% Bi incorporation into AlInSb. To investigate the bandgap change with Bi incorporation, preliminary density functional theory (DFT) simulations with hybrid functionals (HSE) were performed using a 54-atom supercell with 1 Al and 1 Bi atom (corresponding to 3.7% Al and Bi). DFT predicts that the direct bandgap of $Al_{0.037}In_{0.963}Sb_{0.963}Bi_{0.037}$ is reduced by ~20 meV from that of InSb, in qualitative agreement with the observed reduction in PL emission energy. Further growths are underway for additional alloy compositions to fill out the AlInSbBi growth space and optimize the bandgap energy, lattice constant, surface morphology, and photoluminescence to act as a barrier layer.

[1]J. J. Lee et. al., Appl. Phys. Lett. **71**, (1997).
[2]L. Wang et al., Crystals **7**, (2017).
[3]A. V. Voitsekhovskii and D. I. Gorn, Journ. of Comm. Tech. and Elec. **62**, (2017).
[4]A. Evirgen et al., Elec. Lett. **50**, (2014).
[5]M. K. Rajpalke et al., Appl. Phys. Lett. **105**, (2014).
[6]S. Tixier et al., Appl. Phys. Lett. **82**, (2003).
[7]R. C. White et al., 21st International Conf. on MBE, (2021).

10:00 AM Refreshment Break

10:20 AM R06

Low Growth Temperature Epitaxial PbSe for Heterogeneous Mid-Infrared Emitters Leland J. Nordin, Jarod Meyer, Pooja D. Reddy and Kunal Mukherjee; Stanford University, United States

The mid-infrared (MIR) wavelength range is vital for an abundance of sensing, health/biological monitoring, security and defense, and fundamental science applications. For compact solid-state sources of MIR light, III-V semiconductor heterostructures, such as quantum cascade lasers (QCL), interband cascade lasers (ICL), or type-II superlattice light emitting diodes (SLED), are often used. However, QCL, ICL, and SLED structures all suffer from substantial growth complexity and, in addition, SLEDs struggle to achieve high performance at room temperature. Moreover, typical III-V growth temperatures (>450 °C) prevent III-V based MIR emitters to be heterogeneously integrated during the back-end-of-line (BEOL) portion of Si fabrication. Recently, thin films of PbSe grown epitaxially on III-V GaAs (001) substrates have shown remarkably high internal quantum efficiency (IQE) of nearly 30% at room temperature and comparatively low growth temperatures of 300 °C, compatible with BEOL [1]. However, the total film thickness is restricted (<200 nm) for growth on GaAs (001) due to thermal mismatch induced crack formation and thus the prospect of heterogeneous devices is narrow.

In this work, we show that the growth window for high optical-quality PbSe/III-V extends to substantially lower temperatures than previously demonstrated and investigate the recombination dynamics of the low growth temperature films. A high temperature (300 °C) PbSe film [Figure 1(a)] and a lower temperature (170 °C) PbSe film [Fig. 1(b)] were grown on oxide-desorbed and arsenic-capped GaAs (001) substrates in a Riber Compact 21 molecular beam epitaxy (MBE) system using a compound PbSe source. Both growths started with a PbSe dose procedure and nucleation layer [2]. Following the nucleation layer, the growth temperature was lowered to the either 300 °C or 170 °C, and 80 nm of PbSe was grown.

Following growth, room temperature MIR photoluminescence (PL) was measured on both films and is shown in Fig. 1(c). Notably, the magnitude of PL is nearly identical for both the high growth temperature and low growth temperature films, suggesting that SRH recombination rates, often associated with poor growth quality, are comparable in both films. We attribute the slight redshift of the PL-peak to a lower strain energy contribution. This strain energy is accumulated when cooling down from growth temperature to room temperature. To better understand the impact of growth temperature on luminescence efficiency we performed power dependent PL (PDPL) measurements and shown in Figure 2. is PL efficiency (PL magnitude divided by laser power, the optical analog of wall plug efficiency) versus laser power. Remarkably, we do not see a substantial deviation in PL magnitude for lower pump powers, further corroborating the similar SRH recombination rates. However, we do not observe a pump power independent PL magnitude, suggesting that we have not reached low injection in these measurements, so we cannot claim identical SRH recombination rates.

We have grown PbSe films on GaAs substrates at 300 °C and 170 °C and investigated their luminescence properties, both spectral and power dependent PL. PL magnitude is not dramatically impacted by the lower growth temperature, corroborated by both the magnitude of spectral dependent PL, which was performed at high injection, and power dependent PL. Most importantly, the low growth temperatures investigated are compatible with BEOL processes, likely extend the accessible crack-free film thicknesses, and possess bright PL. The confluence of these properties suggests that low growth temperature PbSe films are an ideal candidate for MIR heterogeneous emitters. Additionally, these low growth temperatures enable the investigation of more esoteric ternaries, such as PbGeSe, which require extremely low growth temperatures.

[1] J. Meyer et al. ... K. Mukherjee, *APL Mater.,* **9,** 111112 (2021).
[2] B. B. Haidet et al. ... K. Mukherjee, *Phys. Rev. Mater.*, **4,** 033402 (2020).

10:40 AM R07

(Student) Investigation of Polarity of Unintentionally Doped AlGaAsSb and AlInAsSb Avalanche Photodiodes on InP Substrates Mariah L. Schwartz[1], Sri Harsha Kodati[1], Seung Hyun Lee[1], Hyemin Jung[1], Dekang Chen[2], Christoph Grein[3], T.J. Ronningen[1], Joe Campbell[2] and Sanjay Krishna[1]; [1]The Ohio State University, United States; [2]University of Virginia, United States; [3]University of Illinois at Chicago, United States

Background doping polarity is a critical design parameter for the performance of many optoelectronic devices, including avalanche photodiodes (APDs). For a separate, absorption, charge and multiplication (SACM) APD, it is important to the know the background polarity of the absorber and the multiplier to properly adjust the applied electric field distribution in the device. The polarity of the layers can be affected by several factors including unintentional dopants, impurities, and defects. The background doping in a semiconductor material needs to be carefully optimized by changing the growth parameters including the substrate temperature, growth rate and V/III ratio. We have developed a technique using capacitance-voltage (CV) measurements on double mesa structures with p-i-n or n-i-p homojunctions to determine the background doping polarity type of unintentionally doped (UID) intrinsic regions[1]. The underlying physics of this approach is based on the fact that CV measurements scale with the mesa area, and the effective capacitance of a reverse biased PN junction in series with a PP or a NN junction is dominated by the PN junction capacitance. We have fabricated several double mesa diodes with systematically varied top diameter while keeping the bottom diameter constant. Similarly, we have a set of devices in which the bottom diameter is varied while keeping the top diameter fixed. By studying the variation of the capacitance as a function of the top or bottom diameter, we can determine the background doping polarity. In this work, we have grown, fabricated, and tested AlGaAsSb and AlInAsSb random alloy double mesa structures and

undertaken CV measurements at 295, 150 and 77 K (see Fig.1). We found that the capacitance varies with the top mesa diameter for both material systems, and not the bottom mesa diameter, indicating that the unintentionally doped intrinsic region is n-type in nature.

11:00 AM R08

(Student) Majority Carrier Concentration and Minority Carrier Lifetime in Mid-wave Infrared InGaAs/InAsSb and InAs/InAsSb Superlattice nBn Detectors Alexander T. Newell[1,2], Preston T. Webster[2,3], Chris P. Hains[2,3], Julie V. Logan[2], Rigo A. Carrasco[2], Perry C. Grant[2], Zinah M. Alsaad[2,3], Diana Maestas[2], Christian P. Morath[2] and Ganesh Balakrishnan[1]; [1]University of New Mexico, United States; [2]Air Force Research Laboratory, United States; [3]A-tech, LLC, a BlueHalo company (ATA BlueHalo), United States

Infrared unipolar barrier detectors based on III-V materials have progressed tremendously due to success in improving material quality and bandgap engineering. In the standard *n*B*n* detector, the single unipolar barrier extends into the conduction band, blocking the majority carrier dark current and significantly inhibiting the generation-recombination and surface contributions to the dark current. The barrier serves to make the detector a minority carrier, diffusion-limited device, however doping still has a dominant impact on device performance due to its relationship with the minority carrier lifetime and minority carrier concentration. Increasing doping degrades the minority carrier lifetime, and thus the quantum efficiency of the photodetector. Diffusion dark current in the *n*B*n* detector, which is proportional to the minority carrier concentration, is initially reduced by increased doping until it begins to have an adverse effect on the minority carrier lifetime. Ultimately, absorber doping density significantly affects *n*B*n* photocollection and noise characteristics and must be precisely controlled to optimize photodetector performance.

Recent advances leading to high minority carrier lifetime in strain balanced InGaAs/InAsSb superlattices have led to it being considered as a higher mobility drop-in replacement to the InAs/InAsSb superlattice *n*B*n*. Two InAs/InAsSb and three InGaAs/InAsSb *n*B*n* structures designed for maximum electron-hole wavefunction overlap with 5.1-5.3 μm wavelength cutoffs have been grown with different absorber doping profiles by molecular beam epitaxy. The material is examined by time-resolved and steady-state photoluminescence, X-ray diffraction, and Nomarski surface imaging. The samples are then processed into variable-area mesa arrays using standard lithography and contact metal deposition. The devices are packaged in and wire-bonded to 68-pin leadless-chip carriers, which are then mounted in a vacuum-sealed dewar for temperature-controlled measurements of the photocurrent, dark current, and capacitance-voltage to evaluate the doping concentration profile in each device. The undoped Ga-free *n*B*n*'s exhibited the lowest background n-type majority carrier concentration of 6×10^{14} cm^{-3} with a minority carrier lifetime of 3 μs. The undoped InGaAs/InAsSb superlattice exhibited a ~4× higher majority carrier concentration of 2×10^{15} cm^{-3} with a minority carrier lifetime of 2 μs. Si-doped samples with constant and graded doping profiles are also examined, and the minority carrier lifetime is observed to degrade with increased doping. An analysis of the minority carrier lifetime's dependance on doping, impact on detector performance and other characterization results will be presented.

Approved for public release: Distribution is unlimited. AFMC PA number xxx-xxxx

11:20 AM R09

(Student) Guided-Mode Resonance Enhanced Room-Temperature Infrared Detectors Abhilasha Kamboj[1], Leland J. Nordin[1], David Woolf[2] and Daniel Wasserman[1]; [1]University of Texas at Austin, United States; [2]Physical Sciences Inc., United States

The mid-infrared wavelength range (3 −30 μm, mid-IR) is a spectral range of significant importance. The mid-wave infrared (MWIR, 3 −5 μm) transmission window, specifically, is vital for applications such as gas sensing and free-space communication, as well as thermal imaging of mechanical objects (engines, turbines, etc) that have temperatures ∼580−970 K. For an infrared detector, efficient operation at high temperatures is typically the primary goal. While Mercury-Cadmium-Telluride (HgCdTe) detectors are the current state-of-art infrared detectors, the type-II superlattices (T2SLs) have shown to be a promising alternative material system. However, the comparatively lower absorption coefficient of the T2SL detectors presents a challenge, due to the trade-off (as a function of the absorber thickness) between large external quantum efficiency and higher collection efficiency/reduced dark current. This limitation can be addressed by incorporating thin detector absorber regions in resonant photonic architectures. One such architecture is the guided-mode resonance structure, comprising a high-refractive index grating layer sandwiched between two low-index layers[1]. Incident light diffracts into guided modes in the grating layer, which can then couple out to free space. When the outcoupled light interferes constructively/destructively with reflected/transmitted light, strong and narrow resonant peaks/dips can occur in the reflection/transmission spectra. We design a GMR structure where index-contrast required is achieved with highly doped (n^{++}) semiconductor layers, which can be modeled with the Drude formalism, allowing for a lattice matched material system with extremely low refractive index in the MWIR, which can serve as a waveguide cladding layer.

In this work, we build on our previous efforts[2], to demonstrate GMR-enhanced all-epitaxial uncooled (room-temperature) MWIR nBn InAs/InAsSb T2SL detectors. We have designed, grown, fabricated and characterized GMR detectors showing such enhancement in a T2SL absorber only 250 nm thick. GaSb serves as a high-index grating layer which, together with the nBn detector (serving as a waveguide core), is sandwiched between a low-index n^{++} virtual substrate and air. For grating periods Λ= 1.6 μm and 1.8 μm, resonances with enhancement of ≈ 8× & 14× are shown at wavelengths, λ= 4.4 μm & 4.7 μm respectively which is very close to the band-edge of the absorber (≈5 μm). Typically, due to the steep drop in absorption coefficient close to the band-edge, it is extremely difficult to obtain sufficient external quantum efficiency near the absorber band edge. Thus, detectors must be grown with lower energy cut-off, which will significantly increase dark current and degrade device detectivity. The ability to enhance EQE at the band edge of the absorber T2SL, allows us to use higher energy cut-off absorbers without degrading absorption efficiency. Moreover, the ultra-thin absorber, when compared to a typical MWIR detector, offers a significant reduction in dark current, when compared to traditional MWIR III-V detectors operating in same wavelength range, at similar temperatures. Significant improvement in both the optical and electrical performance of the GMR detectors results in superior specific detectivities. TE-polarized estimated specific detectivity $D^* = 1.2\times10^{10}$ & 1×10^{10} cm√Hz/W are reported for the Λ= 1.6 μm and 1.8 μm devices, respectively. Future work will investigate polarization-independent detectors with substrate-side illumination for potential incorporation into focal-plane array architectures.

The authors gratefully acknowledge United States Army under Prime Contract W909MY-20-P-0010 and National Science Foundation (ECCS-1926187 and ECCS-2025227).

References:

1. S. S. Wang and R. Magnusson, Appl. Opt., vol. 32, no. 14, pp. 2606–2613, May 1993.

2. A. Kamboj, L. Nordin, P. Petluru, A. J. Muhowski, D. N. Woolf, and D. Wasserman, Appl. Phys. Lett., vol. 118, no. 20, p. 201102, 2021.

11:40 AM R10
(Student) High-Speed Long-Wave Infrared Ultrathin nBn T2SL Detectors Yinan Wang[1], Leland J. Nordin[2], Sukrith Dev[3], Monica Allen[3], Jeffery Allen[3] and Daniel Wasserman[1]; [1]The University of Texas at Austin, United States; [2]Stanford University, United States; [3]Air Force Research Laboratory, United States

The primary focus of mid-wave (MWIR) and long-wave infrared (LWIR) detector research has been to optimize detector detectivity and operating temperature. However, emerging applications such as free-space optical communication, lidar sensing, and dual-comb spectroscopy require, in addition to high detectivity and operating temperature, detectors with fast time response (high bandwidth). Traditional high-speed device structures, such as p-i-n photodiodes, have been proven highly suitable for the shorter near-infrared telecommunication wavelengths, but are difficult to design and implement in the MWIR and especially LWIR due to the increasingly narrow material bandgap, which causes a number of undesirable effects that undermine device performance. In the LWIR spectral region (8-12 μm), high-speed detection is usually achieved with the intersubband quantum well infrared photodetectors (QWIP) or quantum cascade detectors (QCD), which generally have much lower responsivity than detectors leveraging bulk, narrow bandgap absorber materials.
Here, we demonstrate a LWIR detector using a plasmonically enhanced type-II superlattice (T2SL) material as the absorber. The detector has an nBn device architecture, where the barrier (B layer) blocks the flow of majority carriers (electrons) and thus reduces the dark current. Previous work has shown that by using a highly doped layer as a plasmonic backplane, optical absorption in the ~300 nm thick (~λ/33) absorber can be strongly enhanced, achieving an external quantum efficiency and detectivity similar to detectors that have much thicker absorber layers [1]. In addition to improvements in the magnitude of the response, the ultrathin absorber layer should also lead to a fast time response, enabling high-speed operations. To investigate the temporal response of these ultra-thin plasmonic detectors, we fabricate the material into mesa structures of varying areas, with coplanar waveguide metal contacts, and measure the time response of the detectors using an optical parametric amplifier (OPA) configured to output λ=5 μm ~200 fs pulsed light. The devices are biased using an external voltage source connected to a bias tee, and the DC-filtered time response signal is captured with a digital sampling oscilloscope and subsequently Fourier transformed to determine the 3dB cutoff bandwidth.
The time response measurements show that for a 50 μm diameter circular mesa device, at an operating voltage of -0.6 V and temperature of 180 K, the device exhibits a bandwidth of 530 MHz, equivalent to a 300 ps time constant. The detector bandwidth increases with increased bias voltage but not significantly, indicating that drift is unlikely the dominating transport mechanism in this detector. Although the carrier transport is expected to be diffusion-dominated, the bandwidth achieved in this ultrathin detector is comparable to other thick detectors that need to operate in a high bias, drift-dominated regime. These results show the promising potential of the ultrathin plasmonic LWIR detectors as a material platform for high-speed LWIR detectors.
[1] Nordin, L., Petluru, P., Kamboj, A., Muhowski, A. J., & Wasserman, D. (2021). Ultra-thin plasmonic detectors. *Optica*, *8*(12), 1545-1551.

SESSION S: Emerging Epitaxial Materials

Session Chairs Joshua Zide
Thursday Morning, June 30, 2022
Cartoon Room #1

8:20 AM S01
Wafer-Scale Ferromagnetic Fe_3GeTe_2 Thin Films by Molecular Beam Epitaxy Ke Zou; The University of British Columbia, Canada

Until now, two–dimensional ferromagnets still remain mostly limited to exfoliated micron–sized samples. Large–scale thin films are desirable for the fabrication of integrated devices for spintronic and memory storage applications. Among this group of materials, Fe_3GeTe_3 (FGT) can host ferromagnetic states at room temperature upon optimized gating. We achieve, by molecular beam epitaxy, the synthesis of high-quality monolayer and multilayer FGT films. Surface x–ray diffraction confirms its quintuple layer substructures with hexagonal symmetry. Thickness-dependent transport measurements are used to characterize and probe for magnetic order. Ferromagnetic states exist in 1–10 layer thick FGT, with Curie temperatures ranging from ~75 K in one layer samples to above 175 K in ten layer samples. A ferromagnetic phase with significant magnetic anisotropy is revealed for all layer numbers.

8:40 AM S02
(Student) MBE Growth of Cr:BixSb1-xTe for Enhancing Spin-Orbital-Torque Switching and Stabilizing Quantum Anomalous Hall Effect Yuxing Ren[1,1], Su-Kong Chong[2,1], Lixuan Tai[2,1], Peng Zhang[2,1], Ting-Hsun Yang[2], Xiang Dong[2,1] and Kang-Lung Wang[1,2,1]; [1]University of California, Los Angeles, United States; [2]University Of California, Los Angeles, United States

CrBiSbTe is a magnetic topological insulator which could achieve quantum anomalous Hall (QAH) effect and spin-orbit torque (SOT) switching in the same structure. This is promising for its future applications in memory or switching applications with its robust surface properties by topological protection. In this work we have grown CrBiSbTe on GaAs (111) substrate through modulation doping (of Cr) by MBE (Molecular Beam Epitaxy). The doping level and the thickness of each layer is examined to tune the bandgap and the Fermi level of the whole sample. In this way, we can tune the Fermi level into the bandgap and optimize the total resistivity of the sample to achieve quantization. The influence of electrical field is also examined. This will help us optimize materials properties and design the device structure to enhance the performance of future SOT switching applications.

9:00 AM S03
(Student) Epitaxial Thin Films of Chalcogenide Perovskites and Related Phases Mythili Surendran[1], Huandong Chen[1], Boyang Zhao[1], Arashdeep Thind[2], Shantanu Singh[1], Thomas Orvis[1], Huan Zhao[3], Han Htoon[3], Megumi Kawasaki[4], Rohan Mishra[2] and Jayakanth Ravichandran[1]; [1]University of Southern California, United States; [2]Washington University in St. Louis, United States; [3]Los Alamos National Laboratory, United States; [4]Oregon State University, United States

Chalcogenide perovskites have recently emerged as a new class of semiconductors composed of earth abundant, non-toxic elements with large chemical and structural bandgap tunability in the visible-infrared region and desirable opto-electronic properties. Past investigations on single crystals of perovskites such as BaZrS3 (BZS)[1] and the corresponding Ruddlesden-Popper phases such as Ba3Zr2S7, both with corner shared ZrS_6 octahedral connectivity, show that these materials are suitable for solar energy conversion due to their optimum band gaps and strong light absorption. On the other hand, Quasi-1D hexagonal chalcogenide perovskites with face shared octahedral connectivity such as

$BaTiS_3$ (BTS)[2] and $Sr_{1+x}TiS_3$[3] exhibit optical anisotropy resulting in large birefringence and linear dichroism in the mid-wave and long-wave infrared region. The demonstration of high-quality epitaxial thin film growth of these chalcogenide perovskites is a critical next step to improve our understanding of their physical properties and to realize heterostructures of these materials that host emergent physical phenomena. Recently, multiple groups have developed innovative but multi-step approaches[4, 5] to achieve thin films of the prototypical chalcogenide perovskite BZS. Nevertheless, the direct epitaxial growth of chalcogenide perovskites is challenging due to a large mismatch in the vapor pressure for the cations and chalcogens, and the corrosive and reactive nature of most chalcogen precursors.
Here we report single-step epitaxial growth of BZS thin films on perovskite oxide substrates by pulsed laser deposition[6] from stoichiometric polycrystalline targets. X-ray diffraction (XRD) shows that the films are strongly textured out of plane and have a clear in-plane epitaxial relationship with the substrate. Electron microscopy studies confirm the presence of epitaxy despite the polycrystalline nature, with a large number of extended defects away from interface, suggesting the potential for further improvement in growth. X-Ray reflectivity (XRR) and atomic force microscopy (AFM) show smooth film surfaces and interfaces between the substrate and the film. The films show strong light absorption and fast photo response.
Further, we used the same approach of growth to realize thin films of BTS. XRD shows that the films are polycrystalline with a strong out of plane texture and multiple in-plane domains. Extensive structural characterization was performed to understand the orientation of these domains. XRR and AFM show film surfaces and interfaces with relatively large roughness (~1-2 nm), which hinder the growth of large grains with low defect density. The role of processing parameters such as substrate temperature, background gas composition and pressure, laser fluence and the choice of single crystal substrates on controlling the structure and improving the quality of these films will also be discussed.
References:
[1] S. Niu, *et al.*, Adv Mater 2017, 29.
[2] S. Niu, *et al.*, Nature Photonics 2018, 12, 392.
[3] S. Niu, *et al.*, Chemistry of Materials 2018, 30, 4897.
[4] Z. Yu, *et al.*, Nano Energy 2021, 85.
[5] X. Wei, *et al.*, Nano Energy 2020, 68.
[6] M. Surendran, *et al.*, Chemistry of Materials 2021, 33, 7457.

9:20 AM S04
(Student) High-Quality van der Waals Material on a Semiconductor Substrate Yongchen Liu[1], Wilder Acuna[1], Huairuo Zhang[2,3], Quoc Dai Ho[1], Ruiqi Hu[1], Zhengtianye Wang[1], Anderson Janotti[1], Garnett Bryant[2], Albert Davydov[2], Joshua Zide[1] and Stephanie Law[1]; [1]University of Delaware, United States; [2]National Institute of Standards and Technology, United States; [3]Theiss Research,Inc., United States

Van der Waals (vdW) materials are promising candidates for future optoelectronic and quantum devices. They feature strong covalent bonding in the plane but weak vdW bonding between layers and can be grown by vdW epitaxy. Most research has focused on growing vdW materials on substrates such as sapphire which are inert and easy to grow on. However, growth on traditional semiconductor substrates is necessary if we want to integrate vdW materials with current semiconductor-based structures for optical, electronic, or optoelectronic applications. Bi_2Se_3 is a prototypical topological insulator and vdW material. In this paper, we will investigate the vdW material epitaxy of Bi_2Se_3 on a GaAs semiconductor substrate using a variety of substrate pretreatment conditions.
We started by synthesizing 50nm $(0001)_H$ Bi_2Se_3 on (001)-oriented GaAs substrates with different treatments: one substrate had the native oxide thermally desorbed under a Se-overpressure, one had the oxide desorbed under an As-overpressure, and the final had a 100nm GaAs/AlAs smoothing superlattice (SL) and a 50nm GaAs buffer layer grown on it. After growth, samples were characterized using scanning transmission electron microscopy (STEM), atomic force microscopy (AFM), x-ray diffraction (XRD), and room-temperature Hall effect measurements. In STEM images, the As-desorbed sample and the Se-desorbed sample show a rough interface with Bi_2Se_3 grains grown in two different orientations: the desired $(0001)_H$ and the undesired $(10\text{-}15)_H$. In contrast, a large-scale smooth Bi_2Se_3/GaAs interface was obtained in the SL sample. All three samples show the similar terraced surface morphology with triangular domains according to the AFM, however, the root mean square surface roughness of the SL sample was smaller than the other two samples. The XRD scans confirm the existence of $(10\text{-}15)_H$ -oriented grains in the Se-desorbed and As-desorbed samples only. From the AFM results, we could see two sets of triangular domains rotated 60° with respect to each other, called antiphase or twin domains. To quantify the percentage of the antiphase domains, we performed x-ray pole scans around the $(10\text{-}15)_H$ reflection. All three samples show a similar degree of antiphase defects although the SL sample is slightly better. In addition to the experiments above, we also performed density function theory (DFT) calculations to explore the termination of the Bi_2Se_3/GaAs interface and found that a Se-terminated substrate is the lowest interface energy which is consistent with previous experimental results. In summary, this work shows that substrate treatment and interface quality is critical for the growth of vdW materials despite the relatively weak interaction between the film and substrate. This procedure can be applied to the growth of other vdW materials on semiconductor substrates for next-generation electronic and optoelectronic devices.

9:40 AM S05
Making Chalcogenide Perovskite Semiconductor Thin Films by Gas-Source Molecular Beam Epitaxy Rafael Jaramillo; Massachusetts Institute of Technology, United States

Chemical intuition, first-principles calculations, and recent experimental results suggest that chalcogenide perovskites may be an outstanding class of semiconductors. Chalcogenide perovskites feature the large dielectric response familiar in oxide perovskites, but also have band gap in the VIS-IR and strong light absorption [1]. Preliminary results suggest that chalcogenide perovskites feature excellent excited-state charge transport properties familiar in halide perovskites, while also being thermally-stable and comprised of abundant and non-toxic elements. Nearly all experimental results on chalcogenide perovskites to-date were obtained on powder samples and microscopic single crystals; thin film synthesis is in its infancy. Further progress in fundamental understanding and development for applications will hinge on the availability of high-quality, controllable thin film synthesis, and that the best film quality and control is achieved by molecular beam epitaxy (MBE).

Here we report epitaxial synthesis of chalcogenide perovskite thin films: $BaZrS_3$ films on (001)-oriented $LaAlO_3$ substrates, made by single-step, gas-source MBE [2]. Films are stoichiometric and oxygen-free. The perovskite phase is confirmed by X-ray diffraction (XRD) and Raman spectroscopy. The films are atomically-smooth over large areas, as evidenced by reflection high-energy electron diffraction (RHEED) and atomic-force microscopy (AFM). Scanning transmission electron microscopy (STEM) shows an atomically-abrupt substrate/film (oxide/sulfide) interface with no chemical interdiffusion. RHEED, XRD, and STEM reveal competing epitaxial growth mechanisms: direct rotated-cube-on-cube growth, and strain-relaxed growth with a self-assembled buffer layer. The film color, spectroscopic ellipsometry, and photoluminescence spectroscopy demonstrate that the films have strong light absorption with direct band gap near 1.9 eV. We also present results of tuning the band gap in the $BaZr(S,Se)_3$ alloy series.

This work sets the stage for developing chalcogenide perovskites as a family of semiconductor alloys with properties that can be tuned with strain and composition in high-quality epitaxial thin films, as long-established for other semiconductor materials, while also displaying rich solid-state chemistry and physics familiar in complex oxides. Our methods also represent a revival of gas-source chalcogenide MBE, with potential for impact on research on chalcogenide perovskites and other sulfur- and selenium-containing compounds.

[1] R. Jaramillo and J. Ravichandran, *In Praise and in Search of Highly-Polarizable Semiconductors: Technological Promise and Discovery Strategies*, APL Mater. **7**, 100902 (2019).
[2] I. Sadeghi, K. Ye, M. Xu, Y. Li, J. M. LeBeau, and R. Jaramillo, *Making BaZrS3 Chalcogenide Perovskite Thin Films by Molecular Beam Epitaxy*, Adv. Funct. Mater. **31**, 2105563 (2021).

10:00 AM Refreshment Break

SESSION T: Epitaxial Growth of Highly Mismatched Alloys

Session Chair: Joshua Zide
Thursday Morning, June 30, 2022
Cartoon Room #1

10:20 AM T01
Critical Evaluation of Thermal and Compositional Dependences in a Finite Strain Model of Ge-Si-Sn Alloys on Ge(100) and GeSn Buffer Layers from DFT Narges Masoumi and Andrew Chizmeshya; Arizona State University, United States

Ge rich Si-Ge-Sn alloys typically adopt the a-phase (diamond) structure of Ge, while the b-phase is expected to prevail in the limit of large Sn concentration. Strain has an important influence on the stability of the a-phase (diamond) structure of Si-Ge-Sn alloys, but its role in the a-b non-isomorphism has to our knowledge not been studied or reported to date. Here we report the outcome of *ab initio* thermochemistry calculations based on DFT and special quasi-random supercell representations, which show that the a-phase exhibits a stability field spanning ~ 0-90% Sn in the $Si_{1-x}Sn_x$ and $Ge_{1-x}Sn_x$ systems for T between 300-500K. Another key aspect of epitaxial stability is the strain response of thermodynamically stable alloys grown on either pure Ge clad Si, or various GeSn buffers. In the small strain limit linear elasticity theory can be used to relate the perpendicular and parallel strains .In this paper we develop a thermodynamics model for fully relaxed hetero-epitaxial alloys over the entire 0-100% Sn composition range corresponding to 0-13% compressive biaxial strains on Ge (001), beyond linear elasticity estimates commonly used (Hooke's law). The numerical results are fitted to an analytic model which includes compositional and thermal bowing corrections to Vegard's law, and the elastic ratio, and reproduces known strained lattice parameters over the wide composition range. For $Ge_{1-x}Sn_x$ alloys we predict the existence of a "sweet spot" in the vicinity of strain values of 6%. Below this value the linear elasticity theory appears to overestimate the perpendicular strain, while above this value the converse behavior ensues.

10:40 AM T02
(Student) Molecular Beam Epitaxy Growth of Highly Tensile Strained GeSnC Alloys up to 4% Sn and 3% C Tuhin Dey[1], Mohammad S. Reza[1], Augustus Arbogast[1], Aaron J. Muhowski[2], Daniel Wasserman[2], Seth R. Bank[2], Mark W. Holtz[1,1] and Mark Wistey[1,1]; [1]Texas State University, United States; [2]The University of Texas at Austin, United States

Ge has a nearly direct bandgap because the direct Γ valley (k = 0 in momentum space) is only 140 meV above the indirect L valley. Tensile strain (>2%) and alloying ($Ge_{1-x}Sn_x$ or $Ge_{1-y}C_y$) are the two most common approaches to make Ge-based direct bandgap materials[1]. Although $Ge_{1-x}Sn_x$ becomes a direct bandgap material with x>10%, strained growth on Ge or GaAs adds undesirable compressive strain[2]. Worse, the very small electron effective mass ($m_e^* \approx 0.02m_0$) loses the direct bandgap when confined in a quantum well (QW) or dot[3].
Our group has previously demonstrated that $Ge_{1-y}C_y$ with $y \approx 1\%$ has a direct bandgap, and reported GeC using a special precursor (4GeMe) as a C source in molecular beam epitaxy (MBE), with no defects detected in transmission electron microscopy (TEM)[4,5]. In this work, we instead grew $Ge_{1-x-y}Sn_xC_y$ using a simpler C precursor. GeSnC adds additional control in epitaxial growth: Sn and C partially compensate local strain and distortion of the host Ge bonds. Ab-initio calculations predict that C-Sn-C bonding would be energetically favorable over C-C bonds in the Ge lattice. This is likely to increase both C and Sn substitutional incorporation and provides a more stable material, similar to InGaAs:N[6]. We saw no evidence of Sn segregation as surface droplets, nor C incorporation as undesirable C-C or C=C bonded nano-clusters. Therefore, adding Sn might reduce the carbon clustering at the surface which would be a great achievement compare with past growths by other groups. As an added benefit, GeC offers a larger electron effective mass (m_{eff}), which would preserve the direct bandgap in GeSnC even when confined in a QW.
Tensile strained $Ge_xSn_yC_{1-x-y}$ was grown on GaAs (004) substrate in hybrid MBE using thermal Ge, Sn sources and commercial carbon tetrabromide (CBr_4) as the carbon source. We believe sp2 C-C pairs are likely defects in the carbon containing alloys, so we also used hydrogen to preferentially remove sp2 carbon, as is done in growth of epitaxial diamond. High resolution x-ray diffraction (HRXRD) reveals good crystallinity in the epi-layer with maximum 3% of substitutional carbon and 4% tin. Raman observation of the C local mode at 530 cm^{-1} confirms substitutional incorporation into the crystal. Atomic Force Microscopy (AFM) shows mostly flat surfaces. Unlike most other carbon sources, no sp2 (graphitic) or amorphous carbon bonds were detected in Raman spectroscopy from 1200-1600 cm^{-1} (not shown). The successful incorporation of C into Ge substitutionally, without cluster carbon, is a major step toward efficient Group IV lasers for silicon photonics. We have also observed emissions in 0.50-0.60 eV range both from bulk and multiple quantum well (MQW) GeSnC samples. These peaks could be from different atomic arrangements, from defects, or from non-uniform QW compositions. The detailed origins of the emission spectrum are currently under investigation and will be reported at the conference.
Reference

1. Jifeng Liu, Photonics **1** (3), 162 (2014)
2. G. Grzybowski, R. T. Beeler, L. Jiang, D. J. Smith, J. Kouvetakis, and J. Menéndez, Applied Physics Letters **101** (7), 072105 (2012)
3. M. P. Polak, P. Scharoch, and R. Kudrawiec, Journal of Physics D: Applied Physics
50 (19) (2017)
4. C. A. Stephenson, W. A. O'Brien, M. W. Penninger, W. F. Schneider, M. GillettKunnath, J. Zajicek, K. M. Yu, R. Kudrawiec, R. A. Stillwell, and M. A. Wistey, Journal of Applied Physics **120** (5) (2016)
5. C. A. Stephenson, W. A. O'Brien, M. W. Penninger, W. F.

Schneider, M. Gillett-Kunnath, J. Zajicek, K. M. Yu, R. Kudrawiec, R. A. Stillwell, and M. A. Wistey, Journal of Applied Physics **120** (5) (2016).
6. Vincenzo Lordi, Homan B. Yuen, Seth R. Bank, Mark A. Wistey, James S. Harris, and Stephan Friedrich, Physical Review B **71** (12) (2005)

11:00 AM T03

(Student) MBE Growth and Characterization of GeSnC/Ge Multiple Quantum Well Structure Augustus Arbogast; Texas State University, United States

GeSnC offers a route to on-chip lasers, amplifiers, and compact modulators for dense silicon photonics. The addition of either C or Sn to Ge can modify the band structure to create a direct bandgap and adding both can improve growth quality of both C and Sn. More important for devices is the electron effective mass, m_e^*. In GeSn, m_e^* in the direct conduction band (CB) valley (Γ) can be as small as $0.015m_0$. When confined in a quantum well (QW), this light effective mass gets pushed up by quantum confinement to higher energies much faster than the indirect (L) CB valley, converting the quantum well back to an indirect bandgap. Therefore, quantum wells offer a stringent but necessary test of whether GeSn-based alloys can be made suitable for lasers and other direct bandgap photonic devices.
In this work, we grew stacks of 25 $Ge_{1-x-y}Sn_xC_y$ quantum wells separated by Ge barriers using hybrid solid+gas source molecular beam epitaxy to yield high quality GeSnC crystal growth over various temperature regimes based on previous bulk growths. The MQW structures were grown on GaAs substrates with a 300 nm Ge buffer layer. The quantum wells were 5 nm GeSnC with 18.6 nm Ge barriers, ending with a 20 nm Ge cap layer. Based on samples of bulk GeSnC grown under similar conditions, we estimate the QW composition to be at 4% Sn and 3% substitutional C. As reported in a separate talk (T. Dey), Raman observation of the C local mode at 530 cm^{-1} from these previous growths also confirmed substitutional carbon incorporation into the QW layers. Compared with its parent GeSnC bulk materials, we observed several new peaks in photoluminescence from the MQW samples, around 0.35 eV and 0.5 eV. Recent ab-initio results suggest that the mixture of C and Sn could lead to both increased and decreased bandgaps depending on nearest neighbor ordering, which may explain the multiple peaks. Further studies are underway to determine if some of the emission might also be due to defects or non-uniform QW compositions, and these will be reported at the conference.
In summary, this work presents the first growth and PL of GeSnC QWs. These samples showed emission at significantly smaller photon energies, as low as 0.35 eV, compared with bulk GeSnC and previous reports of Ge alloys. This emission range may be useful for LIDAR and other mid-IR light sources, as well as IR photodetectors.

11:20 AM T04

(Student) Mechanical and Electronic Effect of B on the Band Structure of BGaAs Alloys Qian Meng[1], Rasha El-Jaroudi[1], Rachel C. White[1], Tuhin Dey[2], Mohammad S. Reza[2], Seth R. Bank[1] and Mark Wistey[2,2]; [1]The University of Texas at Austin, United States; [2]Texas State University, United States

The addition of boron into conventional III-V alloys provides a method for strain engineering of near-infrared, direct-bandgap materials and to lattice-match with silicon[1] and other substrates.[2] However, the addition of boron into conventional III-V material forms a highly-mismatched alloy whose material properties are underexplored. In other highly-mismatched alloys, such as dilute-nitrides and dilute-bismides, small amount of nitrogen and bismuth can perturb the host band structure, resulting in a reduction in the bandgap while undesirably degrading material properties. In contrast, boron is predicted to have a higher solid solubility, and B-III-V is predicted to degrade material properties less severely than other highly mismatched alloys.[3] This suggests that higher B concentration with superior material quality is achievable.
A significant reduction in carrier mobility has been found in the dilute-nitrides and -bismides, which was attributed to alloy scattering in the band edges due to band anticrossing (BAC) and materials degradation due to growth.[4] In contrast, we observed a weaker reduction in carrier mobility in BGaAs compared with dilute nitrides, and the hole mobility of p-type doped $B_{0.05}Ga_{0.95}As$ can be at around 180 cm^2/V-s.[1] Here we investigate the effects of boron incorporation on the electronic band structure of III-V alloys to determine their fundamental properties and ultimate device potential.
Theoretical calculations of the electronic properties were performed using the density function theory (DFT) package Vienna Ab initio Simulation Package (VASP) using HSE06 hybrid functionals. The influences of mechanical structure change in lattice because of the small size of the B and the influences of electronic differences between B and Ga/As were separated by creating different configurations: substitutionally incorporated BGaAs; B_{Ga}: replace single B atom with Ga and keep the lattice constant and local distortion of substitutional BGaAs; pristine GaAs; Ga_B: replace single Ga atom with B and keep the perfect zincblende structure of GaAs. We found a splitting in conduction band minimum (CBM) created by the existence of B and the conduction band 1 (CB1) and conduction band 2 (CB2) states were changing between extended states and localized states according to the wavefunction and energy change with pressure. The band splitting and pressure-dependence are consistent with the hallmarks of band-anticrossing. The decreased lattice constant and local distortion had minimal influences on the band splitting, and changing the lattice constant proportionally changed the bandgap, clarifying that the presence of the highly-mismatched boron atom drives the anticrossing. Further analysis of the origin of CB1/CB2 states in BGa(In)As alloys is underway and will be reported at the conference. Experimental characterization of the band splitting in BGa(In)As alloys, grown by solid-source molecular beam epitaxy, will also be reported.
This work was performed in part at the University of Texas Microelectronics Research Center, a member of the National Nanotechnology Coordinated Infrastructure (NNCI), which is supported by the NSF (No. ECCS-1542159). This work was also supported by the National Science Foundation (Award Nos. ECCS-1933836, DMR-1508646, and CBET-1438608). The authors also acknowledge the Learning, Exploration, Analysis, and Processing (LEAP) cluster at Texas State University for computing resources.
1 McNicholas et al. 60th Electronic Materials Conference (2018)
2 El-Jaroudi et al. Appl. Phys. Lett. (2020)
3 Hart and Zunger. Phys. Rev. B. (2000)
4 Fahy and O'Reilly. Appl. Phys. Lett. (2003)

11:40 AM T05

(Student, Late News) Impact Ionization Coefficients and Excess Noise in $Al_{0.85}Ga_{0.15}As_{0.56}Sb_{0.44}$ Avalanche Photodiodes Harry Lewis[1], Xiao Jin[1], Bingtian Guo[2], Seung Hyun Lee[3], Hyemin Jung[3], Sri Harsha Kodati[3], Baolai Liang[4], Sanjay Krishna[3], Joe Campbell[2] and John David[1]; [1]The University of Sheffield, United Kingdom; [2]University of Virginia, United States; [3]The Ohio State University, United States; [4]California State University, Los Angeles, United States

$Al_{0.85}Ga_{0.15}As_{0.56}Sb_{0.44}$ (AlGaAsSb hereafter) has recently been identified as a promising material for the multiplication region of SACM APD structures for optical communications, as it is lattice matched to InP and can use InGaAs or GaAsSb as the absorber material. This follows work showing a very wide ratio between the electron and hole impact ionization coefficients (α and β respectively) of $AlAs_{0.56}Sb_{0.44}$ (AlAsSb) and the potential to achieve a device sensitivity of -33dBm at 10Gb/s, even with a

600nm thick multiplication region. AlGaAsSb provides advantages of reduced dark currents and increased device reliability over AlAsSb and recent research has indicated that it also exhibits very low excess noise. Unfortunately, there is currently a lack of data of the material's impact ionization behavior across a wide electric-field range, making it difficult to design APDs for different applications. This work presents the first comprehensive analysis of the electron and hole impact ionization coefficients for AlGaAsSb, calculated from avalanche multiplication data and the excess noise characteristics, on a wide range of structures with thicknesses from ~400-1020nm. Measurements have been performed under pure electron injection conditions, pure hole injection conditions (using 455nm light), and a range of mixed injection conditions on AlGaAsSb *p-i-n/n-i-p* structures grown on InP substrates using MBE. Mesa diodes were fabricated using standard wet etching and very low dark currents were obtained on unoptimized devices. Multiplication measurements were carried out using phase-sensitive detection to differentiate the photocurrent from the dark current. Excess noise measurements were performed using a transimpedance amplifier-based phase-sensitive detection system enabling measurements of multiplication >37. The ionization coefficients were extracted by fitting the multiplication data using a numerical model which takes any electric-field variations into account. These ionization coefficients are capable of replicating the multiplication data even in significantly thinner AlGaAsSb structures where the effect of the 'dead-space' can be observed at low multiplication values. The α/β ratio in AlGaAsSb is only slightly smaller than in AlAsSb and still much larger than other comparable semiconductors. There is a significant difference obtained in the excess noise from electron and hole-initiated multiplication, further confirming the presence of a large α/β ratio in this material system. The excess noise from pure electron injection (F_e) in *p-i-n* structures with 1020nm, 600nm and 400nm widths increases as the device width decreases. F_e=2 is obtained at multiplication values of 25, 12 and 10 in these structures as the avalanche width decreases. Note that the shape of the F_e vs M characteristic does not follow the classical McIntyre behaviour, suggesting that the ionization probability in these structures is not a simple exponential function. Based on the α/β ratio which changes with electric field, these multiplication regions would give a 3dB bandwidth (excluding the absorber) of 8.4GHz, 23GHz and 31.3GHz respectively for the multiplication values stated earlier. Despite the increasing F_e with decreasing structure thickness, these results are still significantly better than those for InAlAs or InP. The lowest excess noise, seen in the 890nm *p-i-n* structure under pure electron injection conditions, gives an F_e of 2.34 at a multiplication of 37. Our findings indicate that, in this alloy system, the benefit of the larger α/β ratio in thicker structures at lower electric fields will outweigh the improvement in noise performance which occurs in thin APD structures due to the effects of the carrier dead space. This offers the possibility of extremely high sensitivity 1550nm APDs for LiDAR and sensing applications as we shall show.

SESSION U: Nano-Magnetic, Magnetic Memory and Spintronic Materials

Session Chairs: Denis Candido and Pawan Tyagi
Thursday Afternoon, June 30, 2022
Great Hall Meeting Room 1 & 2

1:30 PM U01
Spin-Polarized Scanning Tunneling Microscopy of Epitaxial Fe_3GeTe_2 Alexander J. Bishop, Robert Walko, Wenyi Zhou, Jay Gupta and Roland Kawakami; The Ohio State University, United States

In recent years Fe_3GeTe_2 (FGT) has become an exciting material due to its perpendicular magnetic anisotropy and high curie temperature while maintaining a 2D van der Waals structure. These properties have led to the manifestation of skyrmions and room temperature ferromagnetism in exfoliated FGT heterostructures and thin films. Another mechanism for achieving precisely controlled thin films and heterostructures is molecular beam epitaxy (MBE) which is used here to achieve monolayer and multilayer FGT structures grown on Ge(111) substrates. These samples are then studied with spin-polarized scanning tunneling microscopy (SPSTM) which allows for structural analysis of sample surface with atomic resolution and can attest to the high quality of films grown with MBE. The spin polarized nature of SPSTM can resolve the magnetic structure of FGT and its dependence on the atomic stacking structure. The magnetic field dependent local density of states is also probed systematically to reveal domain structure switching on the sample surface.

1:50 PM U02
(Student) Kinetically-Controlled Epitaxial Growth of vdW Fe3GeTe2 Ferromagnets and Their Heterostructures with Topological Insulators Wenyi Zhou, Alexander J. Bishop, Menglin Zhu, Igor Lyalin, Shuyu Cheng, Jinwoo Hwang and Roland Kawakami; The Ohio State University, United States

As a 2D van der Waals material, Fe_3GeTe_2 (FGT) stands out because of its strong perpendicular magnetic anisotropy and high Curie temperature (T_C). A lot of interesting phenomena have been studied in FGT thin films and heterostructures, such as skyrmions and room temperature ferromagnetism. However, most studies are based on exfoliated FGT. Here, we ultilize molecular beam epitaxy (MBE) for high-quality epitaxial monolayer and multilayer FGT. Cross-sectional transmission electron microscopy (TEM) shows an atomically-sharp interface between the FGT film and Ge(111) substrate. Our study also demonstrates that kinetics play an important role in the epitaxial growth of FGT films by MBE. By varying the deposition rate, we observe control the formation or suppression of an initial tellurium-deficient non-van der Waals phase (Fe_3Ge_2) prior to realizing epitaxial growth of the vdW FGT phase. This demonstrates how the interplay of energetics and kinetics can help tune the re-evaporation rate of chalcogen atoms and interdiffusion from the underlayer, which paves the way for future studies of van der Waals epitaxy.
In addition, we developed heterostructures with topological insulators such as FGT/Bi_2Te_3 and FGT/SnTe which are very interesting for spin-orbit torque and magnetic topological states. Magneto-optic Kerr Effect (MOKE), magnetic circular dichroism (MCD) and Anomalous Hall Effect (AHE) were used to confirm square hysteresis loops and MOKE microscopy made it possible for us to catch a glimpse of its domain structure during magnetization switching.
This work is supported by AFOSR MURI 2D MAGIC (FA9550-19-1-0390), DOE (DE-SC0016379), NSF-MRSEC (DMR-2011876), DARPA (D18AP00008).

2:10 PM U03
(Student) Spin Polarized STM Imaging of Magnetic Skyrmions in Metallic Thin-Film Heterostructures Brad Goff, Jake Repicky, Shuyu Cheng, Roland Kawakami and Jay Gupta; The Ohio State University, United States

Magnetic skyrmions are ideal bits for next generation information storage due to their small size, low depinning current, and topological stability. Co/X/Pt heterostructures are a promising platform to host small skyrmions because of the system's tunability. In our work, we use spin polarized Scanning Tunneling Microscopy (STM) on Co/Cu/Pt heterostructures to detect and characterize individual skyrmions at cryogenic and room temperatures. We grow our heterostructures with molecular beam epitaxy and keep them under ultra-high vacuum to preserve the surface's quality. Topographic STM images of the surface show small granular domains with a typical diameter of 30 nm; the surface is atomically flat over 10-100's of μm with a variation of grain heights of less than 1 nm. Spin polarized STM, with a magnetic Ni tip, can detect skyrmions through differential conductance measurements. Our differential conductance scans reveal skyrmions as small as 30 nm in diameter. We have preliminary evidence of tip-induced motion of skyrmions. Future high resolution (~Å) images will allow us to identify pinning sites and study the energetics of skyrmion motion, creation, and annihilation.
We acknowledge funding support from the DARPA TEE program (award # D18AP00008)

2:30 PM U04
(Student) Tuning Magnetic Properties of [Pt/Co/Cu] Multilayers Shuyu Cheng[1], Nuria Bagues Salguero[2], Camelia Selcu[1], Binbin Wang[2], Ziling Li[1], Shekhar Das[1], David McComb[2], Chris Hammel[1] and Roland Kawakami[1]; [1]The Ohio State University, United States; [2]Ohio State University, United States

Skyrmions, which are nanometer-sized vortex-like magnetic textures, stand out as a strong candidate for next-generation information storage and processing. The main advantages of skyrmion-based devices are topological robustness, high energy efficiency, and small sizes. Using molecular beam epitaxy (MBE), we have successfully synthesized [Pt/Co/Cu] magnetic multilayers, a skyrmion-hosting material. The broken inversion symmetry in this type of material gives rise to non-zero Dzyaloshinskii-Moriya interaction (DMI), which plays a key role in skyrmion formation. We have established the connection between the sample structure (thickness of each layer and number of periods) and magnetic properties revealed by magneto-optical Kerr effect (MOKE) measurement. Based on these results, we are able to engineer the sample structure to tune various magnetic interactions (exchange interaction, interfacial magnetic anisotropy, magnetic shape anisotropy, DMI, etc.) and controllably generate skyrmions in our designed multilayer samples. The room-temperature skyrmions have been observed in these samples by magnetic force microscopy (MFM) and Lorentz transmission electron microscopy (LTEM). Furthermore, we have also successfully realized skyrmions nucleation/motion by applying current pulses.

2:50 PM U05
(Student, Late News) Electromagnetic Interference (EMI) Shielding Techniques for Simulated PVDF-TrFE/Fe_3O_4 Multiferroic Monopolar Antenna Richard I. Harry, Shaik Zainuddin and Shaik Jeelani; Tuskegee University, United States

Magneto-electric materials have widely been used as a conducting medium for monopolar, dipolar, and conical antennas based off of their interaction with electromagnetic fields and transverse wave absorption properties. Upon application, these antennas tend to perform extraordinary due to their tailorable properties at a nanoscale, and have opened doors for many applications in large scale sensor, detection, and radar systems. In this study, we investigated the potential of nanocomposite films made from P(VDF-TrFE) loaded with 5wt%, and 7wt% Fe_3O_4 nanoparticles as receiving microstrip patch antennas. Simulation of device was conducted using 2021 ANSYS HFSS software. Electronic properties such as electro-conductivity, magnetic permeability, dielectric constant, elastic modulus, and loss values of nanocomposites were incorporated to model storage/reflectance behavior under increasing electromagnetic frequencies up to 5GHz.

3:10 PM Refreshment Break

3:30 PM U06
(Student) The Effect of Spin Fluctuations on Temporal and Spatial Evolution of Magnetic Moment in A Magnetic Tunnel Junction-Based Molecular Spintronic Device (MTJMSD) Marzieh Savadkoohi, Bishnu R. Dahal, Christopher D'Angelo, Andrew C. Grizzle and Pawan Tyagi; University of the District of Columbia, United States

Spintronics in conjunction with molecular electronics can lead to the development of quantum computers and highly efficient logic and memory devices [1]. Spin is an intrinsic property of atoms that exist in infinite states compared to electric charges which are available only in a binary state. Superposition of spin-up and spin-down states enables computational devices to function much faster than today's computers. They can also increase hard drives' storage capacity significantly. Spintronic properties can be tailored with organic molecules. Controlling and manipulating electrons' spin of ferromagnetic (FM) materials via magnetic molecules can lead to novel magnetic phenomena and numerous computational applications.
Here, we report the preliminary result of our computational and experimental study on a magnetic tunnel junction-based molecular spintronic device (MTJMSD). Using Monte Carlo Simulations (MCS) we have simulated an MTJMSD composed of two ferromagnetic layers separated by a nano-scale insulator and magnetic molecules attached to the exposed edges of the device [2-4]. The interaction between magnetic molecules and FM electrodes, strengths and nature of couplings, molecules and electrodes' type, thermal energy, and several other factors play important role in defining MTJMSD ultimate properties. In our previous research, we have shown that the strength and nature of Heisenberg exchange coupling between magnetic molecules and FM layers dictate MTJMSD's magnetic properties [5]. Here, we are investigating the effect of spin fluctuations on MTJMSD's magnetic moment and other physical properties such as heat capacity.
Our MCS preliminary results showed that spin fluctuations impact temporal and spatial evolution of magnetic moment of MTJMSD at room temperature. The magnetic instability caused by spin fluctuation also increased MTJMSD's heat capacity when molecules made FM coupling with both electrodes, antiFM coupling with both electrodes and FM coupling with one electrode, and antiFM coupling with another electrode. Our computational work agrees with the experimental research in which MTJMSD was exposed to the external magnetic field. According to our observations, MTJMSD produces a symmetric hysteresis loop with saturated magnetic moment on both negative and positive range of applied field. The low magnetic coercivity represents a soft magnetic behavior in the presence of spin fluctuation. To gain a better insight we will use MCS to investigate MTJMSD magnetic behavior in the presence and absence of spin fluctuations for both parallel and antiparallel molecule-FM electrodes couplings.

3:50 PM U07

Design of Experiment Approach for Harnessing Robust Molecular Spintronic Devices Bishnu R. Dahal, Eva Mutunga, Hayden Brown, Joshua Dillard, Marzieh Savadkoohi and Pawan Tyagi; University of the District of Columbia, United States

Molecular spintronics is gaining attraction because molecules possess a weak spin-orbit coupling and longer relaxation time[1]. Therefore, molecular spintronics devices (MSD) are considered highly promising for the future of quantum computing technology. However, the fabrication of robust and mass-producible MSD at the nanoscale is a major concern[2]. To overcome this issue, we have designed a magnetic tunnel junction-based molecular spintronics device (MTJMSD). An MTJMSD utilizes a tunnel barrier to ensure a robust and mass-producible physical gap between two ferromagnetic electrodes. Molecular device channels are covalently bonded between two ferromagnets across the insulating barrier. MTJMSD approach may benefit from MTJ's industrial practices; however, the MTJMSD approach still needs to overcome additional challenges arising from defects of nearly 4 nm thin insulating layers[3]. An insulating barrier may possess a variety of potential defects arising during the fabrication or operational phase. This study describes the Taguchi Design of Experiment approach (DOE) to make ~4 nm of robust AlO_x insulator between two ferromagnetic layers. The DOE parameters for AlO_x insulator deposition were sample position, deposition rate, deposition power, the flow rate of Ar/O_2 inside the sputtering chamber, pressure of the chamber, and argon-etching rate and wait time after etching. Based on the DOE approach, we tailored the most appropriate parameters to fabricate the robust insulator. We successfully produced >95% yield of robust ~4 nm tunnel barrier with 20-40 nA tunneling current at 100 mV to serve as testbed for MTJMSD realization. In this paper, we will present the experimental data based on the electrical and magneto-transport properties of MTJ and its effect on the transport properties after creating the conducting molecular channel between two ferromagnetic electrodes.

This research is supported by National Science Foundation-CREST Award (Contract # HRD- 1914751), Department of Energy/ National Nuclear Security Agency (DE-FOA-0003945).

[1] A. R. Rocha, V. M. García-suárez, S. W. Bailey, C. J. Lambert, J. Ferrer, and S. Sanvito, "Towards molecular spintronics," *Nature Materials,* vol. 4, no. 4, pp. 335-339, 2005/04/01 2005, doi: 10.1038/nmat1349.
[2] S. Sanvito, "Molecular spintronics," *Chemical Society Reviews,* vol. 40, no. 6, pp. 3336-3355, 2011.
[3] P. Tyagi, H. Brown, A. Grizzle, C. D'Angelo, and B. R. Dahal, "Molecular coupling competing with defects within insulator of the magnetic tunnel junction-based molecular spintronics devices," *Scientific reports,* vol. 11, no. 1, pp. 1-13, 2021.

4:10 PM U08

(Student) Spin–Orbit Torque in Bilayers of Kagome Ferromagnet Fe3Sn2 and Pt Igor Lyalin, Shuyu Cheng and Roland Kawakami; The Ohio State University, United States

Spin–orbit torque phenomena enable efficient manipulation of the magnetization in ferromagnet/heavy metal bilayer systems for prospective magnetic memory and logic applications. Kagome magnets are of particular interest for spin–orbit torque due to the interplay of magnetic order and the nontrivial band topology (e.g., flat bands and Dirac and Weyl points). Here we demonstrate spin–orbit torque and quantify its efficiency in a bilayer system of topological kagome ferromagnet Fe_3Sn_2 and platinum. We use two different techniques, one based on the quasistatic magneto-optic Kerr effect (MOKE) and another based on time-resolved MOKE, to quantify spin–orbit torque. Both techniques give a consistent value of the effective spin Hall angle of the Fe_3Sn_2/Pt system. Our work may lead to further advances in spintronics based on topological kagome magnets.

4:30 PM U09

(Student) Magnetic Properties of Doped and Undoped Organic Magnetic Semiconductors—V(TCNE)2, Cr(TCNE)2 and Nb(TCNE)2 Yueguang Shi and Michael E. Flatté; The University of Iowa, United States

Vanadium tetracyanoethylene, $V(TCNE)_2$, is a room temperature ferrimagnetic semiconductor with a T_c ~ 600 K, which has very low loss ferromagnetic resonance and spin-wave propagation. [1,2,3] We explore the electronic structure, optical properties, magnetic dynamics, magnetic anisotropy, and magnetoelastic properties using a plane-wave code VASP and XC functional Heyd-Scuseria-Ernzerhof (HSE06).[4,5,6,7] We also present features of $Nb(TCNE)_2$ and $Cr(TCNE)_2$, which are analogs with different transition metal ions, as well as features of doped $V(TCNE)_2$.

We acknowledge funding from NSF Grant No. DMR-1808742, and for doped materials the Center for Molecular Quantum Transduction, an EFRC funded by the US DOE under Award DE-SC0021314.

[1] H. Yu, M. Harberts, R. Adur, Y. Lu, P. C. Hammel, E. Johnston-Halperin, and A. J. Epstein, Appl. Phys. Lett. 105, 012407 (2014).
[2] N. Zhu, X. Zhang, I. H. Froning, M. E. Flatté, E. Johnston-Halperin, and H. X. Tang, Appl. Phys. Lett. 109,082402 (2016).
[3] J. M. Manriquez, G. T. Yee, R. S. McLean, A. J. Epstein, and J. S. Miller, Science 252, 1415 (1991).
[4] G. Kresse and J. Hafner, Phys. Rev. B 47, 558 (1993); ibid. 49, 14 251(1994).
[5] G. Kresse and J. Furthmüller, Comput. Mat. Sci. 6, 15 (1996).
[6] G. Kresse and J. Furthmüller, Phys. Rev. B 54, 11 169 (1996).
[7] J. Heyd, G. E. Scuseria, M. Ernzerhof, J. Chem. Phys. 118, 18 8207(2003).

4:50 PM U10

(Late News) Generating Room-Temperature Electron Spin Polarization Exceeding 90% in an Opto-Spintronic Semiconductor Nanostructure Y.Q. Huang[1], V Polojärvi[2], S Hiura[3], P Hojer[1], A Aho[2], R Isoaho[2], T Hakkarainen[2], M Guina[2], S Sato[3], J Takayama[3], A Murayama[3], Irina Buyanova[1] and Weimin M. Chen[1]; [1]Linköping University, Sweden; [2]Tampere University, Finland; [3]Hokkaido University, Japan

Spintronics represents a new paradigm for future electronics, photonics and information technology, which explores the spin degree of freedom of the electron for information storage, processing and transfer. Since 1990s, we have witnessed great success of metal-based spintronics that has revolutionized the mass data storage industry. There has also been an enormous push for semiconductor spintronics during the past three decades, with the aim to capitalize the past and current success of charge-based semiconductor technology and to make its spin counterpart the backbone of future spintronics just like semiconductors have done in today's electronics/photonics. An exclusive advantage of semiconductor spintronics is its potential for opto-spintronics that will allow integration of spin-based information processing and storage with photon-based information transfer and communications on the same chip based on a single material/technology platform. Unfortunately, progresses of semiconductor spintronics have so far been severely hampered by the failure to generate nearly fully spin-polarized charge carriers in semiconductors at and above room temperature (RT) at which today's devices operate. To date, the highest achievable conduction electron spin polarization remains ≤60%.

In this work, we succeed to achieve conduction electron spin polarization exceeding 90% at RT in a semiconductor nanostructure, which remains steadily high even up to 110°C [1]. This represents the highest RT electron spin polarization ever reported in any semiconductor by any approach! This breakthrough

is accomplished by a conceptually new approach of defect-engineered remote spin filtering and amplification of InAs quantum-dot (QD) electrons via an adjacent tunneling-coupled GaNAs quantum well acting as a spin filter. The extraordinary spin filtering effect in GaNAs is enabled by spin-dependent recombination via spin-polarized defects, i.e. grown-in Ga self-interstitials, which selectively deplete conduction electrons with an opposite spin orientation to that of the defect electron. In sharp contrast to the general trend of deteriorating spin polarization with increasing temperature seen in all other approaches of spin generation, our approach is gifted with an opposite temperature dependence up to RT thanks to a thermally accelerated remote spin-filtering effect as a result of thermally activated recombination via the defects. We further show that the QD electron spin can be remotely manipulated by spin control in the adjacent spin filter, paving the way for remote spin encoding and writing of quantum memory as well as for remote spin control of spin-photon interfaces. The fact that the demonstrated spin functionality is implemented in a commonly used semiconductor optoelectronic nanostructure system (i.e. InAs/GaAs QDs) based on the mature GaAs technology can greatly facilitate the integration of spin functionalities with the existing electronic and photonic devices. It could also pave the way for a range of potential spintronic and opto-spintronic applications exploiting the state-of-the-art GaAs technology platform, such as spin-LEDs, spin lasers, spin-polarized single-photon sources, spin-photon interfaces, spin qubits, etc. This work demonstrates the feasibility to implement opto-spintronic functionality under practical device operation conditions in a semiconductor nanostructure system based on the mature III-V semiconductor technology commonly used for today's optoelectronics and photonics.

[1] Y. Huang, V. Polojärvi, S. Hiura, P. Höjer, A. Aho, R. Isoaho, T. Hakkarainen, M. Guina, S. Sato, J. Takayama, A. Murayama, I.A. Buyanova and W.M. Chen, ***Nature Photonics*** 15, 475 (2021).

SESSION V: Group III-Nitrides—Light Emitting Diodes

Session Chair: Theeradetch Detchprohm
Thursday Afternoon, June 30, 2022
Great Hall Meeting Room 3

1:30 PM V01

(Student) Enhancing the External Quantum Efficiency of Micro-LEDs via Optimized Dry Etching Condition

Jeong-Hwan Park[1], Heajeong Cheong[2], Yasuhisa Ushida[2], Wentao Cai[1], Yuta Furusawa[2], Tae-Yeon Seong[3] and Hiroshi Amano[2]; [1]Nagoya University, Japan; [2]Institute of Materials and Systems for Sustainability (IMaSS), Nagoya University, Nagoya, Japan; [3]Department of Materials Science and Engineering, Korea University, Korea (the Republic of)

Micro light-emitting diodes (μLEDs) based on iii–V compounds can realize next-generation displays with attractive properties, such as high resolution, long lifetime, and low power consumption. Even though μLEDs have better physical properties than organic LEDs, performance issues such as external quantum efficiency (EQE) remain as the LED chip size decreases due to plasma damage at the sidewall. To overcome this issue, chemical treatment or passivation layer deposition have been reported by many researchers; however, these methods require additional processes after dry etching.
In this study, we evaluated the influence of dry etching conditions on the performance of μLEDs. We found that the chemical reaction between Cl_2 (i.e., etching gas) and GaN dominated the etching process, rather than physical plasma etching, as the dry etching power (P_{bias}) decreased during the mesa fabrication process. The dominant effect of the chemical reaction led to low plasma damage on the etched GaN surface and created a rough sidewall morphology as shown in Figure1a. In addition, it was observed that the maximum external quantum efficiency (EQE) differed depending on etching bias and were 3.23%, 2.65%, 2.43%, and 2.25% for 2.5 W, 5 W, 15 W, and 30 W, respectively as shown in Figure 1b, which behavior enhancing maximum EQE could be attributed to the suppressed plasma induced sidewall damage on micro-LED; thus, the EQE improved without requiring an additional process. The effect of low P_{bias} was further investigated by cathodoluminescence using various substrates, demonstrating that low P_{bias} is related to the chemical reaction; that will be explained in the presentation in detail.

1:50 PM V02

(Student) Impact of Photon Recycling on Absorption Losses in Tunnel Junction-Based III-Nitride LEDs

Mohammad Awwad, Betty L. Anderson and Siddharth Rajan; The Ohio State University, United States

III-Nitride light emitting diodes have been successfully adopted in visible display and illumination applications, and are very promising for ultra-violet wavelength applications. Tunnel junctions can provide several significant advantages for operation of both visible (for multiple active region LEDs) and UV LEDs (to act as transparent spreading layers). Recent work on tunnel junctions have demonstrated excellent characteristics for both GaN, as well as ultra-wide bandgap AlGaN. Although tunnel junctions (TJs) have been demonstrated with excellent electrical efficiency, and low voltage drop, especially for GaN-based LEDs, the absorption introduced by them has not been well-understood. Design of tunnel junctions for low voltage drop often requires the use of ultra-thin layers of lower bandgap material (such as InGaN) which could have substantial absorption at emission wavelengths. Previously used methods to calculate tunnel junction absorption losses, such as ray tracing and finite-difference time-domain FDTD [1] do not take into account photon recycling in the TJ. In this work we propose a theoretical model that can provide an intuitive understanding of the impact of photon recycling on the optical absorption losses in tunnel junction-based LEDs.
The proposed model is derived using a 1-dimensional *N*-cascaded GaN LED structure. The top metal contact is considered as a perfect reflector, and the output optical power is collected at the bottom side. GaN layers are assumed to be transparent, while any power absorbed by the TJ is recycled by generating an electron-hole pair (EHP) that is injected back to the active region to recombine there. The efficiency, η , by which the generated EHPs produce new photons in the active region is assumed to be the mathematical product of the IQE and the injection efficiency. The proposed closed form model takes into account the infinitely repeated photon recycling process.
The model enables an estimate of the normalized light extraction efficiency, and can be compared with estimates from simple ray tracing model single and cascaded multiple active region TJ LEDs. It is shown that as the number of TJs increases and/or its absorption increases, the recycled power increases. Consequently, while ray tracing models would predict significant absorption losses, taking into account photon recycling shows that the effective loss is significantly lower. The model can also describe the impact of the internal quantum efficiency on the effective light extraction efficiency. For InGaN polarization engineered TJs, a comparison between the two models at various Indium compositions and thicknesses shows that for $In_{0.24}Ga_{0.76}N$ TJ LED, ray tracing model predicts absorption losses that are significantly higher. For example, for 3 nm 24% In-content tunnel junction, the ray tracing model predicts total absorption loss of 7.95%, whereas the loss including the photon recycling is only 2.94%.
In summary, our work shows that absorption effects in tunnel junctions can be significantly overestimated if photon recycling is not taken into account. The work presented enables rational design

of tunnel-junction based LEDs with accurate estimation of absorption losses.

References: [1] L. and C. M. and W. C. Lalau Keraly C. and Kuritzky, "Light Extraction Efficiency Part A. Ray Tracing for Light Extraction Efficiency (LEE) Modeling in Nitride LEDs," in III-Nitride Based Light Emitting Diodes and Applications, J. and A. H. and M. H. Seong Tae-Yeon and Han, Ed. Dordrecht: Springer Netherlands, 2013, pp. 231–269. doi: 10.1007/978-94-007-5863-6_9.

2:10 PM V03

(Student) High In-Content InGaN Platelets as Underlayer for Light-Emitting Diodes Toward Long Wavelength Application

Wentao Cai[1], Yuta Furusawa[2], Jeong-Hwan Park[1], Heajeong Cheong[1,3], Shugo Nitta[2], Yoshio Honda[2] and Hiroshi Amano[2,3,4]; [1]Nagoya University, Japan; [2]Institute of Materials and Systems for Sustainability (IMaSS), Nagoya University, Japan; [3]Venture Business Laboratory, Nagoya University, Japan; [4]Akasaki Research Center, Nagoya University, Japan

It was both theoretically and experimentally proved that the growth of $In_xGa_{1-x}N$ quantum wells (QWs) on $In_yGa_{1-y}N$ underlayer ($x > y$) would significantly improve the light emitting diodes (LEDs) performance, attributing to the reduction of non-radiative recombination centers, the decline of the internal electrostatic field, and the improvement of indium composition uniformity in QWs. Moreover, the reduced lattice mismatch between QWs and underlayer greatly suppresses composition pulling effect, which improves indium incorporation rate grown at the same temperature, resulting in In-rich InGaN with highly crystalline. However, to serve as templates for red emission QWs, a thicker InGaN pseudo-substrate with closer indium mole fraction to QWs grown beyond the critical layer thickness is desired.

In this work, we present an approach to achieve a sub-micron size InGaN underlayer with high to 30 % indium composition, while the thickness is around 90 nm, far exceeding the critical layer thickness of such In-rich InGaN layer on planar c-plane GaN (reported less than 5 nm). The InGaN platelet is demonstrated by selective area growth (SAG) on arrays of GaN seed from circle openings with a diameter of 400 nm in a SiN_x mask. To our best knowledge, SAG of InGaN results in random nucleation and uneven shape due to the low diffusion length of gallium precursor at relatively low growth temperature. It was reported that the selectivity of InGaN can be enhanced by introducing pyramid shaped GaN seed first, resulting in InGaN pyramid. However, the local indium composition fluctuation on the semipolar facet of the InGaN pyramid hinders pure red emission of QWs with small full width at half maximum (FWHM). In this work, planar hexagonal shape of GaN seed was introduced first before SAG of InGaN, leading to the formation of uniform InGaN platelets with c-plane domain morphology. The optical properties of the InGaN platelets were characterized by photoluminescence (PL, excited by a He-Cd laser of 325 nm, 15 mW, room-temperature), showing PL peaks around 530 nm with FWHM of 141 meV, suggesting around 30 % indium incorporated. AFM scan of the top c-plane surface of the InGaN platelet indicates an atomically flat surface without v-pits or trench defects while the thickness is over 90 nm. Cross-sectional TEM characterization of InGaN platelet suggests homogenous crystalline and shape interface between InGaN and GaN seed. According to localized EDX line measurements recorded with the same area, the InGaN platelet shows indium composition almost linearly increased from InGaN/GaN interface to c-plane surface. Detailed line profiles show indium composition of 25 % to 30 % at the top surface and 15 % to 20 % at InGaN/GaN interface.
Such high indium-content InGaN platelets are competitive candidates for the development of high-quality yellow-to-red emission InGaN micro-LED, by increasing the indium incorporation rate and reducing the lattice mismatch for later In-rich quantum wells.

2:30 PM V04

(Student) Significant Improvement in Quantum Efficiencies and Wall-Plug Efficiency of Flexible AlGaN-Based Deep-Ultraviolet Light-Emitting Diodes

Miad Yarali[1,1,1], Sara Pouladi[1,1,1], Shahab Shervin[1,1,1], Hanyoul Ryu[2], Ja Yeon Kim[3], Min-Ki Kwon[4] and Jae-Hyun Ryou[1,1,1]; [1]University of Houston, United States; [2]Inha University, Korea (the Republic of); [3]Korea Photonics Technology Institute (KOPTI), Korea (the Republic of); [4]Chosun University, Korea (the Republic of)

AlGaN-based deep ultraviolet light-emitting diodes (DUV LEDs) are considered as the foremost promising candidate for environment-friendly DUV light sources. III-N-based LEDs with the emission wavelength range of 400 – 200 nm (UVA, UVB, and UVC) can be produced only by adding aluminum nitride (AlN) to the GaN alloy system. As a result, emitted photon wavelength becomes as short as 210 nm. DUV-LEDs are potentially powerful, harmless to the ecosystem, and can display extremely long lifetimes. Its remarkable properties assign DUV-LEDs as a key enabling segment for various new applications that cannot be accessed by regular UV sources such as food and medical equipment sterilization, water and air purification, plant lighting, and non-line-of-sight communication. Nevertheless, the current status of DUV LEDs is not mature enough and they suffer from low efficiency and optical power therefore significant improvement is highly needed in the performance of these devices. The highest external quantum efficiency (EQE) of DUV LEDs reported so far is less than 10%. Spontaneous polarization and strain-induced or piezoelectric polarization charges exist in the active region leading to Quantum Confined Stark Effect (QCSE) in which the conduction and valence bands are tilted thus electron and hole wave functions are separated leads to less radiative recombination and poor internal quantum efficiency. On the other hand, a small barrier height exists as a consequence of QCSE and electrons leaking from the active region. Meanwhile, the tendency of photon emission mode changes from transverse-electric (TE) mode to transverse-magnetic (TM) mode when mole fraction of AlN is getting higher in ternary AlGaN heterostructure resulting in low light extraction efficiency (LEE). All these technical challenges hinder the progress to fully replace widely used toxic mercury UV lamps.
In this study, we report a new approach to fabricate and characterize flip-chip AlGaN based DUV LED by introducing flexibility to the device to mitigate QCSE, improve barrier height for electron leakage and enhance TE polarized mode of emission by external strain applied in the flexible structure. The device consists of n and p types AlGaN, active region, and p-GaN as a p-contact layer, all grown on a sapphire substrate. This rigid substrate is lifted off via laser lift-off process then the device is flipped and a thick layer of copper is electroplated as a flexible substrate. We investigate the effect of bending degree on the device performance and according to the simulation results, the device gets the highest IQE, LEE, and wall-plug efficiency when it is bent upward with a radius of 2.5 mm. Additionally, we report the ohmic contact configuration on N-face Al-rich n-AlGaN for the first time. This high efficiency flexible AlGaN-based DUV LED has great potential to replace conventional UV light sources since the performance is significantly improved.

SESSION W: Group III Nitrides—MBE, CVD and Sputtering

Session Chair: W. Alan Doolittle
Thursday Afternoon, June 30, 2022
Great Hall Meeting Room 3

3:30 PM W01
(Student) Observation of Compositional Modulation in AlGaN Self-Assembled Superlattices by Transmission Electron Microscopy Keisuke Motoki, Zachary Engel, Christopher M. Matthews and W. Alan Doolittle; Georgia Institute of Technology, United States

$Al_xGa_{1-x}N/Al_yGa_{1-y}N$ superlattices (SLs) have been studied with interest for strain relief layers, defect reduction buffers, high-performance ultra-violet (UV) light emitting diodes (LEDs) and distributed Bragg reflectors (DBRs). SLs typically require compromises in growth conditions such as changes in metal fluxes and substrate temperatures for each SL layer and these growth interrupts involve undesired accumulation of contaminants at the interfaces leading to a loss of optical emission and/or creating structural defects in the film. Furthermore, strain from lattice mismatch in the SLs can cause plastic deformation and is thought to be exaggerated by growth interrupts. Therefore, eliminating the interrupts is key for improving the film quality. Metal Modulated Epitaxy (MME) has demonstrated its ability to grow self-assembled SLs (SASLs) at multiple μms/hour, providing uninterrupted rapid growth of abrupt and coherent SLs by using a shuttered scheme on the metal effusion cells (Al and Ga) in a metal rich condition using surface segregation to achieve composition steps[1]. This method facilitates the design of the period, thickness, and compositions of the well and barriers in the SLs. However, structural information, detailed compositional distributions, and its mechanisms for the creation of SASLs are not well known up to now. Transmission electron microscopy (TEM) is used to provide detailed examination of the composition changes, coherency and unintentional composition modulation within the SASLs. Unintentionally doped (UID) MME SASL AlGaN films were grown on MME AlN on hydride vapor phase epitaxy (HVPE) AlN templates on c-plane sapphire substrates as described elsewhere[1], using plasma-assisted molecular-beam-epitaxy (PA-MBE). Well and cladding compositions, strain and crystal structure in the AlGaN SASLs have been investigated by TEM. The cross-sectioned sample is prepared by standard mechanical polishing methods, followed by argon ion milling. High resolution (HR) TEM images close to [1 1 -2 0] zone axis shows highly coherent SASLs of 910 nm total thickness consisting of 13 nm periods of $Al_{0.7}Ga_{0.3}N$ barriers and $Al_{0.18}Ga_{0.82}N$ wells for a film grown at 2.8 μm/hour. This period thickness corresponds with the amount of material grown per shutter cycle. TEM images with a two-beam condition g = 〈0 0 0 2〉 show large contrast between Al-rich (bright) and Ga-rich (dark) layers. The thickness of the Al-rich layer is 10 ±1.5 nm and the Ga-rich layer is 3.5 ±1.5 nm. A finer contrast modulation, on the order of ~2 nm within the Al-rich layer is also observed in the image and in the line intensity scan corresponding to unintentional compositional modulation along the growth direction during the MME cycle where both Ga and Al metal shutters are open. Such a compositional modulation has not been previously observed in MME grown films. A strain map calculated from 4D-STEM shows strain relaxation in both and direction in the SASLs especially near dislocations suggesting the SASL is effective in modifying defect structures. Further investigation quantifying the compositions and strain in the AlGaN SASLs are ongoing.

1. Engel, *et. al.*, Appl. Phys. Lett., 130, 165304, 2021.
2. Iliopoulos, *et. al.,* Mater. Sci. and Eng. B, 87, 227-236, 2001.

3:50 PM W02
(Student) Molecular Beam Epitaxial Growth of AlGaN Epilayers on Si Using a Nanowire Template Qihua Zhang, Xue Yin, Eli Martel, Heemal Parimoo and Songrui Zhao; McGill University, Canada

Aluminum gallium nitride (AlGaN) on silicon (Si) represents a technologically important platform, not only for the ultrawide, direct, and tunable bandgap energies of AlGaN alloys, but also for the advantages of Si substrate such as low cost, easy removal by chemical wet etching, and so on. However, owing to the large lattice mismatch between AlGaN alloys and Si, obtaining high quality AlGaN epilayers on Si remains to be a challenge in the field. This is in particular the case for the growth of AlN epilayers on Si. In this context, we present a new method of growing AlGaN epilayers on Si by molecular beam epitaxy. Such a method involves the usage of a thin nanowire template. The growth of AlN epilayers is described first. Such AlN epilayers are grown in nitrogen- (N-) rich conditions; and compared to the typical growth conditions of AlN nanowires on Si, the reduced AlN growth temperature promotes the coalescence of AlN [1]. This coalescence is reflected by the appearance of streaky pattern from the reflection high-energy electron diffraction (RHEED). Characterizations using electron microscopes and atomic force microscopy (AFM) further indicate a relatively smooth surface can be obtained within a small thickness (~200 nm), with a root-mean-square (rms) roughness of ~2 nm, within the range of typical III-nitride epilayers grown in N-rich conditions. RHEED 3 × 3 reconstruction and potassium hydroxide (KOH) etching experiments further indicate that the AlN epilayers are N-polar. Using such AlN epilayers as a buffer layer, the growth of AlGaN epilayers is further demonstrated. The AlGaN epilayers in this case are also grown in N-rich conditions and are found be to N-polar as well, following the polarity of the AlN epilayers underneath [2]. The rms roughness of such AlGaN epilayers is similar to that of AlN epilayers. Current progress on a more detailed growth investigation of AlGaN epilayers and recent deep ultraviolet (UV) light emitting devices development will be presented as well.

[1] X. Yin, Q. Zhang, and S. Zhao, "Molecular Beam Epitaxial Growth of AlN Thin Films on Si through Exploiting Low Al Adatom Migration and the Nitrogen-Rich Environment on a Nanowire Template," *Crystal Growth & Design* **21**, 3645 (2021).
[2] Q. Zhang, X. Yin, E. Martel, and S. Zhao, "Molecular beam epitaxy growth and characterization of AlGaN epilayers in nitrogen-rich condition on Si substrate," *Materials Science in Semiconductor Processing* **135**, 106099 (2021).

4:10 PM W03
(Student) Transition-Metal-Alloyed Group-III-Nitride Piezoelectric Thin Films Grown by Hybrid Chemical Vapor Deposition and Sputtering Deposition Techniques Mina Moradnia, Sara Pouladi, Nam-In Kim, Rebecca Forrest and Jae-Hyun Ryou; University of Houston, United States

Transition-metal-alloyed III-V nitride thin films have been considered because of their significant impact on the enhancement of the piezoelectric properties in Group-IIIa-N (III-N) films, such as wurtzite AlN, by group-IIIb transition metals. For example, Sc incorporation as an alloying element to substitute aluminum (Al) in wurtzite-structure AlN, forming $Sc_xAl_{1-x}N$, is a promising approach to improve the piezoelectric coefficients of AlN-based materials on the piezoelectric devices to enhance their performance, hence extending their applications in wireless communication, sensors, mechanical energy harvesting, and semiconductor-based ferroelectrics. Several deposition techniques have been employed to grow the transition-metal-alloyed III-N films. We are focusing on the DC reactive magnetron sputtering system and a new hybrid chemical vapor deposition (HybCVD) thin film growth method. The $Sc_xAl_{1-x}N$ deposited thin film by the physical vapor deposition of the sputtering technique relies on a

dual target sputtering method using an aluminum target and a scandium target, which are sputtered at the same time. The HybCVD is a CVD with a combination of different types of precursors. Hydride vapor phase epitaxy (HVPE) has been employed for the alloying of group-IIIa elements, such as AlGaN. However, this technique cannot be extended to III-N with transition metal alloys, due to the problems related to the chloride form of Sc. Therefore, the new HybCVD employs chloride, elemental source, and hydride for the precursors of the group-III element, transition-metal element, and nitrogen, respectively, for ScAlN thin films to address the issue regarding the HVPE growth method. The phase equilibria between transition-metal nitride (ScN) and III-N (AlN) to form ternary alloy system, such as ScAlN, show a phase separation with the formation of cubic rock-salt structure ScN in wurtzite III-N film with increasing alloy composition of transition-metal nitride, resulting in degradation and eventually the disappearance of its piezoelectric properties. HybCVD growth method provides accurate control of alloy composition along with the high crystalline quality required in designing highly functional piezoelectric materials. In this regard, we numerically investigate the thermodynamics of precursors and vapor-solid reactions on the alloy composition of $Sc_xAl_{1-x}N$ by HybVPE. The equilibrium partial pressures of the gaseous species and the driving force for AlN and ScN solid composition at various temperatures, reaction gases, and partial pressure of hydrogen in the carrier gas have been thermodynamically calculated in source and growth zones. Equilibrium partial pressures of gaseous species over Al metal in the Al source zone can be controlled at different values of temperature which suggests the temperature range of the source zone up to 620 °C to avoid any damage to the CVD furnace. The preferential reaction in the Al source zone happens below 620 °C to produce enough partial pressure of $AlCl_3$ as the desired group III input from the Al source zone for AlN deposition in the growth zone. Elemental Sc source precursor is capable to provide high precursor input and enough driving force for the ScN formation. According to the thermodynamic calculations, the Sc composition in the alloy can be accurately controlled by the mixture ratio of the cation precursors. Here, the combination of MOCVD and HVPE growth methods simultaneously provides well control on the uniformity and quality of piezoelectric films based on transition-metal-alloyed III-N materials.

4:30 PM W04

(Student) Use of a TiN Seed Layer to Enhance (0002) Epitaxy and Piezoelectric Coupling of AlN Thin Films Morton Greenslit, Mauricio P. da Cunha and Robert J. Lad; University of Maine, United States

Aluminum nitride remains piezoelectric up to at least 1000ºC and has higher phase velocity then other high temperature piezoelectrics such as langasite and potential for reduced acoustic loss. The ability to grow epitaxial (0002) oriented AlN thin films using PVD techniques makes them attractive materials for use in bulk acoustic wave (BAW) or surface acoustic wave (SAW) sensors that can operate in high temperature harsh environments. High quality epitaxy of AlN (0002) grain growth has been reported on single crystal sapphire and GaN substrates by several groups. In this work, we report on the use of an ultrathin TiN seed layer that targets the formation of AlN (0002) oriented grains independent of the underlying substrate.

TiN seed layers were grown on several different substrates including sapphire, silicon, Mo, steel and Inconel by using nitrogen plasma-assisted e-beam evaporation of Ti at a growth temperature of 930ºC. A highly textured TiN (111) seed layer was formed as confirmed by high-resolution x-ray diffraction and in situ RHEED. AlN (0002) oriented films were grown on the TiN seed layers using nitrogen plasma-assisted e-beam evaporation of Al also at a growth temperature of 930ºC.
The TiN seed layer on sapphire induced a larger population of (0002) grains and a reduction in the mosaic grain spread compared to growth of AlN on thermally nitride sapphire without the TiN layer. The enhancements in AlN (0002) epitaxy can be attributed to the highly textured growth of TiN (111) grains and the 1.8% lattice mismatch between (0002) AlN and (111) TiN. In situ RHEED and X-ray diffraction pole figures verify the highly oriented AlN (0002) grains as well as in-plane texture of the nucleated AlN grains.

The degree of piezoelectric coupling of AlN films grown on the TiN seed layers was evaluated by measuring the acoustic responses from surface acoustic wave resonator (SAWR) devices fabricated using the epitaxial AlN films. By measuring the reflection coefficient (S_{11}) frequency response from one-port SAWR devices, the admittance, conductance, susceptance, and electromechanical coupling coefficient (K^2) were determined. The addition of the TiN seed layer led to a doubling in K^2 value compared to AlN growth on c-sapphire alone. The TiN seed layer can be used to induce AlN (0002) epitaxy and piezoelectric coupling on other substrates as well.

4:50 PM W05

(Student) Sputter Deposition of III-N Thin Films Joshua Nordlander[1], Ramón Collazo[2], Zlatko Sitar[2] and Jon-Paul Maria[1]; [1]The Pennsylvania State University, United States; [2]North Carolina State University, United States

In this presentation, we demonstrate that reactive High-Power Impulse Magnetron Sputtering (HiPIMS) is an effective alternative for depositing high quality, epitaxial III-N thin films. In contrast to conventional direct current (DC) or radio frequency (RF) sputtering, HiPIMS provides the needed kinetic energy and ionization fraction to establish a sufficiently reactive environment to promote full nitridation. Specifically, the low duty cycle regime of HiPIMS provides access to kW/cm^2 peak power densities without target degradation and thus dramatically increased metal reactivity. In addition, adding an opposite polarity voltage pulse between the target bombarding events, known as a kick pulse, further allows one to tailor both the adatom landing energy on the substrate surface, and mitigate target poisoning.

This unique capability set enables us to prepare high crystal quality epitaxial InN thin films with low out-of-plane mosaicity and electron mobilities in excess of 400 cm^2/Vs with a step-and-terrace microstructure when deposited on AlN-nucleated sapphire substrates. InN grows epitaxially strained and the electron concentration decreases with increasing film thickness in films up to about 200nm until significant cracking is observed.

In addition, homoepitaxial GaN thin films can be deposited at temperatures below 600°C with smooth surface morphologies characterized by c/2 steps and terraces. The presentation will focus on the relationships between sputtering parameters and III-N thin film crystal quality, surface morphology, and growth rate.

SESSION X: Low-Dimensional Materials and Nanofabrication

Session Chairs: Kris Bertness and Paul Simmonds
Thursday Afternoon, June 30, 2022
US Bank Conference Theater

1:30 PM X01
(Student) Density Functional Theory Calculations of Rare-Earth Mono-Pnictides Embedded in III-Vs Ruiqi Hu[1], Quoc Dai Ho[1], Quang To[1], Anderson Janotti[1] and Garnett Bryant[2]; [1]University of Delaware, United States; [2]National Institute of Standards and Technology, United States

Embedding semi-metallic rare-earth mono-pnictide (RE-V) nanoparticles into III-V semiconductors enables nanocomposites with a wide range of optical, electrical, and thermoelectric properties. The inclusion of nanostructured components in a III-V increases the area of interfaces contributing to decreased carrier lifetime, increased phonon scattering, and reduced thermal conductivity, also providing enhanced electrical conduction through electron filtering mechanisms. Group-V continuing sublattice across the interface offers a good contact of rock salt semimetal RE-V (e.g. ErAs) and zinc-blende semiconductor III-V (e.g. GaAs, AlAs) matrices with similar lattice parameters. In this paper, first principles calculation based on density functional theory is used to simulate the electronic properties of ErAs nanoparticles embedded in GaAs and AlAs matrices. We investigate the stability of different nanoparticle shapes and sizes, from cubic to spherical, deriving formation energies are function of As chemical potential. We find a direct correlation between the electron density and atomic density associated with excess metal atoms at the interface and the formation energy. Spherical nanoparticles lead to the smallest density lowest formation enthalpies, and show good agreement with images obtained from transmission electron microscope in previous experiments. The results from atom-resolved density of states (DOS) suggest that the Fermi level in the ErAs:GaAs and ErAs:AlAs is pinned at the same energy with respect to the vacuum level, enabling us to extract a valence band offset between AlAs and GaAs in good agreement with experiments. Moreover, as the size of ErAs nanoparticles increases, the Fermi level moves towards the valence band of the III-V semiconductor.
This work was supported as part of the Center for Hybrid, Active, & Responsive Materials (MRSEC) funded by NSF DMR-2011824.

1:50 PM X02
Ga(As)Sb Nanostructures Formed by Arsenic-Induced Etching of III-Sb Surfaces Sadhvikas Addamane[1], Alexander T. Hendrickson[1], Thomas J. Rotter[2], Ashish Chanana[3], Paul Kotula[1], Julia Deitz[1], Marcelo Davanco[3], John F. Klem[1] and Ganesh Balakrishnan[2]; [1]Sandia National Laboratories, United States; [2]The University of New Mexico, United States; [3]National Institute of Standards and Technology, United States

Epitaxially-grown III-V semiconductor nanostructures — quantum dots (QDs) in particular — are considered nearly ideal single- and entangled-photon emitters for applications in quantum information technologies. They offer high efficiencies, ease of integration with existing photonic/electronic components and hold records for photon purity and indistinguishability[1]. State-of-the-art approaches for realizing III-V QDs include: (i)the Stranski-Krastanov (SK) growth mode where the strain between a substrate (e.g., GaAs) and QD material (InAs) leads to 3-dimensional island formation; and (ii) the droplet epitaxy (DE) method which uses the controlled crystallization of metal nanodroplets into nanostructures. While both techniques have their individual merits, epitaxial QDs are currently at a disadvantage in three areas: lack of control over size/shape, location; SK QDs need specific material combinations leading to a limited emission wavelength range; DE QDs suffer from low efficiencies. To that end, research into alternative methods of realizing epitaxial nanostructures is relevant and ongoing. In this work, we present an in-situ etching technique using arsenic (As_2) to form nanostructures on III-Sb surfaces.

As_2 is known to aggressively react with GaSb through both an anion exchange reaction and an isoelectronic AsSb compound formation[2]. In a previous study, prolonged exposure of GaSb surfaces to an As_2 flux was shown to form highly faceted nanoscale pits[3]. The original aim of our work was to use these nanoscale pits as seedling locations and to infill the voids to form QDs. However, on close examination of the pit-etching process, we found that the interaction of As_2 with the GaSb surface initially forms 3-dimensional nanostructures which evolve into nanoscale pits with higher exposure flux and/or longer exposure times. Since the As_2-induced etch itself yielded QD-like features, it eliminated the need to develop an etch + infill process. These nanostructures were found to be mainly GaAs and have dimensions similar to SK or DE QDs and their size/shape and areal density could be controlled using As_2 flux density, exposure temperature and duration.

Methods: The samples described in this study were grown on GaSb substrates in a molecular beam epitaxy (MBE) reactor equipped with valved cracker sources for both As and Sb. Following thermal oxide removal at 540 ^{0}C, a 200nm GaSb smoothing layer was grown. The substrate temperature was then adjusted for the As_2 etch process (if needed) and the GaSb surface was exposed to a controlled As_2 flux. The beam flux monitor equivalent pressures (BFM) for As_2 were in the range of 7E-7 to 1E-5 Torr and the exposure time was varied from 60s to 600s. The As_2 etch was followed by a 300s Sb soak to aid the formation of nanostructures. In samples for structural measurements, the growth was terminated at this point. For optical measurements, a 4 nm GaSb layer sandwiched in between $Al_{0.5}Ga_{0.5}Sb$ barrier layers was etched using As_2. Cross-sectional transmission electron microscopy (TEM) and energy dispersive x-ray analysis (EDX) were performed to analyze the dimensions and compositions of the nanostructures. Areal density and structural properties were measured using atomic force microscopy (AFM). Cryogenic photoluminescence (PL) measurement efforts are ongoing and will also be presented.
[1]Aharonovich et al., Nat. Photonics 10(10) – 2016.
[2]M. Losurdo et al., J. Appl. Phys. 100 (1) – 2006.
[3]S.H. Huang et al., J. Appl. Phys. 102(4) – 2007.
This work was performed, in part, at CINT, an Office of Science User Facility operated for the U.S. Department of Energy (DOE) Office of Science. Sandia National Labs is a multimission laboratory managed and operated by National Technology & Engineering Solutions of Sandia, LLC, a wholly owned subsidiary of Honeywell International, Inc., for the U.S. DOE's National Nuclear Security Administration under contract DE-NA-0003525. SJA acknowledges funding from Sandia's LDRD program

2:10 PM X03
(Student) Structural Analysis of Highly Luminescent and Narrow Bandwidth Cl-Doped InP/ZnSe/ZnS Quantum Dot Heterostructures Takafumi Moriyama[1,2], Akihito Kumamoto[1], Hirokazu Sasaki[2], Naoya Shibata[1,1,3] and Yuichi Ikuhara[1,1,3]; [1]The University of Tokyo, Japan; [2]Shoei Chemical Inc., Japan; [3]Japan Fine Ceramics Center, Japan

Semiconductor nanocrystals, also known as quantum dots, are attracting great attention as the future material for light-emitting diode, photodetectors, phototransistors, and photovoltaics because of their unique optical and electronic properties. InP quantum dots are the promising candidate as the heavy-metal free quantum dot emitter, however, their emission full-width at half-maximum (FWHM) and photoluminescence quantum yield (PLQY) are poorer than commonly used CdSe quantum dots. To improve the

quality of InP quantum dots, understanding the relationship between their structure and optical properties is quite important. In this work, we have prepared high performance InP/ZnSe/ZnS core/shell/shell quantum dot heterostructures using halogen atoms and evaluated their optical properties, morphology, and atomic structure. Various kinds of halogens were added to InP cores, and shell layers were formed in the presence of halogens. Among halogens, Cl and Br increased PLQY to >90 %, almost doubled from the halogen-free sample. In addition to that, Cl drastically reduced the FWHM from 37 nm to 31 nm. Cl is commonly used as a surface capping agent to increase PLQY [1]. However, because the addition of Cl after shell formation had little effect on FWHM, there should be the different mechanism. To understand the role of Cl, structural analysis was performed using Cs-corrected scanning transmission electron microscope (STEM). Compared with the non-Cl doped samples, the shape of the Cl added quantum dots was more spherical and their particle size distribution was narrower. This indicates that Cl influences the shell growth dynamics. Atomic-resolution high-angle annular dark field (HAADF)-STEM image revealed that Cl added quantum dots contained stacking faults. Until now, stacking faults were believed to degrade the emission efficiency [2]. However, these results suggested that stacking faults in Cl-added InP quantum dots may not deteriorate the optical properties.

[1] D. A. Taylor et al., *Chem. Mater.* **33**, 4399-4407 (2021).
[2] E. Jang et al., *ACS Energy Lett.* **5**, 1316-1327 (2020).

2:30 PM X04

Study of Al_2O_3 Dielectric on Ga-Assisted MBE Grown $GaAs_{1-x}Sb_x$ Nanowires Priyanka Ramaswamy, Mehul Parakh, Shisir Devkota, Hirandeep Reddy Kuchoor, Kendall D. Dawkins and Shanthi Iyer; North Carolina A&T State University, United States

III-V semiconductor nanowires (NWs) are being pursued as a potential candidate for next-generation electro-optical devices. They offer unique and superior properties stemming from their anisotropic geometry compared to their bulk counterparts. The self-catalyzed vapor-liquid-solid (VLS) growth mechanism of these nanowires enables high phase purity growth with excellent homogeneity amongst NW ensembles, thus eliminating foreign contamination and induced defects arising from metal-catalyzed growth that has been commonly used until recently. However, the presence of a high density of surface states arising due to the anisotropic NW geometry is detrimental to the efficiency, sensitivity, and speed of these self-catalyzed III-V NW devices. The severity of surface state formation depends on the un-passivated dangling bonds arising from the sharp termination of material growth radially and native oxide formation. These can act as non-radiative recombination centers or surface charge traps, thereby increasing surface scattering leading to decreased carrier mobility and increased density of electronic states within the bandgap, causing Fermi level pinning at the surface. It is known that the Fermi level pinning creates a depletion region on the surface, which can extend throughout the NW volume, rendering it entirely insulating or non-conducting, thereby hindering the use of NWs for practical applications. Hence, to reduce the effect of surface states, different passivation schemes have been investigated using atomic layer deposition technique (ALD). This work evaluates the passivation efficacy of the thermal ALD deposited Al_2O_3 dielectric layer on self-catalyzed $GaAs_{1-x}Sb_x$ NWs grown using molecular beam epitaxy (MBE). A detailed assessment of surface chemical composition and optical properties of Al_2O_3 passivated NWs with and without prior sulfur treatment were studied and compared to as-grown samples using x-ray photoelectron spectroscopy (XPS), Raman spectroscopy, and low-temperature photoluminescence (PL) measurements.
The effect of sulfur treatment and Al_2O_3 passivation using thermal ALD ex-situ deposition on self-catalyzed GaAsSb NWs using XPS, PL, and Raman were successfully studied. The 4K-PL spectra revealed a significant drop in PL intensity (~ 10 fold) for Al_2O_3 passivated NWs compared to as-grown irrespective of prior sulfur treatment. The XPS spectral analysis indicated that precleaning with sulfur treatment before Al_2O_3 ALD deposition effectively removed III-V native oxides formed on the NW surface, thus ruling out the effect of native oxides on optical degradation. Further, the Raman characterization observed significant redshifts, peak broadening, and asymmetry for Al_2O_3 passivated NWs when compared to as-grown NWs, suggesting the presence of point defects on Al_2O_3 ALD deposition. Hence, the 4K-PL optical degradation observed in both sulfur-treated and untreated Al_2O_3 passivated NWs samples suggests non-radiative recombination centers arising from complex NW/dielectric interface formation to be the main contributing factor. Reporting of similar PL degradation in GaAs NWs, while enhanced PL intensity in In-based NWs allows us to speculate that non-radiative recombination centers arising from the Al_2O_3/NW interface states are peculiar to Ga-based III-V NWs only, and surface faceting in GaAsSb NWs may also enhance this contribution. Thus, ALD deposited Al_2O_3 layer is not a good choice for the passivation layer for GaAsSb NWs.

Acknowledgments:
This work is primarily based upon research supported by the Air Force Office of Scientific Research (AFOSR) under grant number W911NF1910002. The National Science Foundation (NSF) also funded a part of this work under grant# 1832117. This work was performed at the JSNN, a member of the Southeastern Nanotechnology Infrastructure Corridor (SENIC) and National Nanotechnology Coordinated Infrastructure (NNCI), which is supported by the National Science Foundation (ECCS-1542174).

2:50 PM X05

(Student) Tuning Selective Narrowband Infrared Absorption Using Coaxial InAs-GaAs0.1Sb0.9 Nanowires with Partial Shell Segment Coverage Alireza Abrand[1,1], Nicklas Anttu[2] and Parsian Mohseni[1,1,1]; [1]Rochester Institute of Technology, United States; [2]Åbo Akademi University, Finland

Vertical III–V nanowire (NW) arrays with core-shell geometries are promising candidates for infrared (IR) photodetection applications due to their unique optoelectronic properties such as efficient carrier collection, strong light absorption, and high detectivity under room temperature operation. Due to their remarkable ability to accommodate strain relaxation, an unprecedented set of lattice-mismatched material combinations can be realized using coaxial NW geometries with tailored properties. Generally, NWs with large diameters are required for efficient absorption in the IR range. However, increasing the NW diameter results in a loss of spectral range selectivity and an enhancement in dark current due to increase in material volume. Therefore, novel methods for achieving spectrally-selective light absorption while minimizing the collection medium volume and array fill factor are highly desired for applications in NW-based IR photodetectors with low-size, weight, power, and cost (SWaP-C) metrics.
Based on simulations performed independently using finite element method (FEM) and rigorous coupled-wave analysis (RCWA) techniques, we demonstrate dramatic tunability of the IR absorption spectrum of coaxially heterostructured NW arrays consisting of InAs core segments that are partially encapsulated by $GaAs_{0.1}Sb_{0.9}$ shell layers. Embedding the bases of InAs NWs in Au backside contact layers results in periodic evanescent fields between adjacent NWs. The position, spatial extent, and separation of the evanescent modes depend mainly on the NW core segment diameter and wavelength of incident light. We show that otherwise decoupled light in the 2 to 3 µm wavelength range can be selectively absorbed in InAs NW core segments by adding partial $GaAs_{0.1}Sb_{0.9}$ shell layers with dimensions corresponding to the position and spatial extent of the evanescent field. The $GaAs_{0.1}Sb_{0.9}$ layers are transparent at this wavelength range and only act to enhance absorption of otherwise decoupled light. Wavelength-selective absorption is localized to positions along the InAs core

segments where they are partially encapsulated. The absorption wavelength can be manipulated as a function of the partial shell segment position, length, and diameter. Moreover, narrowband wavelength selectivity can be controlled by tuning the length of the InAs NW core segment. Such site-specific absorption in InAs NWs can be exploited for enhancement of carrier collection efficiency by positioning active p-n junctions at the predefined locations of $GaAs_{0.1}Sb_{0.9}$ shell layers. The design approaches highlighted in this work enable novel, low-SWaP-C, NW-based IR photodetector membranes with tunable narrowband selectivity along specific NW locations.

3:10 PM Refreshment Break

3:30 PM X06
(Student) Growth and Transformation of Mixed Valence Manganese Oxide Nanostructures on Epitaxial Graphene-Silicon Carbide Heterostructures Michael Pedowitz, Daniel Lewis, Soaram Kim and Kevin Daniels; University of Maryland, United States

Mixed valence manganese oxides (MnO_x) have attracted significant research interest in recent years due to the easily reversible redox reactions between manganese oxidation states[1] which enable applications in catalysis[2], energy storage[3], and gas sensing[4]. Of these mixed-valence manganese oxides, those containing high concentrations of Mn^{+3} atoms have been of particular interest due to the high reactivity of these sites[5]. However, the use of these MnO_x materials has been hampered by their low electrical conductivity (10^{-5}-10^{-6} S)[6], which significantly reduces the speed of surface redox reactions. To overcome this challenge, heterostructures have been formed between manganese oxide, and graphene, which seek to couple the high conductivity of graphene to the reactive properties of MnO_x compounds[1]. Currently, these methods are hampered by the use of graphene oxide and reduced graphene oxide, due to the use of harsh oxidizing chemicals, which significantly limits the conductivity enhancements of these heterostructures[7]. In this work, we demonstrate the growth electrochemical growth of layered δ-MnO2 on pristine epitaxial graphene, and its non-destructive transformation to Mn_2O_3 and Mn_3O_4 via a simple heat treatment. The electrodeposition was carried out in a three-electrode electrochemical cell with an Ag/AgCl reference electrode, a Pt counter electrode, EG/SiC as the working electrode, and a 100mM manganese acetate solution. The electrodeposition process contained three steps, a reduction step, oxidation step, and reduction step, with their potentials determined by cyclic voltammetry. The resulting δ-MnO2 thin films were then annealed in argon and air at 500°C to produce Mn_3O4 and Mn_2O_3 respectively. These films were then characterized through Raman spectroscopy, scanning electron microscopy (SEM), and atomic force microscopy (AFM) to determine their crystalline structure and surface morphology. Raman spectroscopy of the three films indicated the initial formation of δ-MnO2 due to the presence of peaks at 640-650 cm^{-1}[8], 575-585 cm^{-1}[8], and 490-510 cm^{-1}[8] (Fig 1.a). The transformation of these films to Mn_2O_3 and Mn_3O_4 was also confirmed by the Raman data, with the formation of strong peaks at 650 cm^{-1}[9], and 705 cm^{-1}[9] in the case of Mn_2O_3 and strong peaks at 650 cm^{-1}[5], 374 cm^{-1}[5], and 320 cm^{-1}[5] for Mn_3O_4 (Fig 1.b-c). The surface morphology of the films was also revealed through AFM and SEM. The SEM images indicated that the δ-MnO2 was of nanofibrous character, with nanofibers on the order of 10nm thick (Fig 2.a). After transformation to Mn_2O_3 these nanofibers were replaced with a large plane covered in nanopores, and with transformation to Mn_3O_4 these were further replaced with nanocubes connected by nanowalls (Fig 2.b-c). The AFM revealed similar information about the morphology of MnO_2, while also indicating that the transformation process had led to an increase in surface roughness of the films (Fig .4). In addition to our transformations of δ-MnO_2 we also attempted to intercalate various metal ions into the layered δ-MnO_2 structure (Li, K, Na). Raman analysis of these results (Fig. 4) indicated that we were successful in intercalating some of the ions, specifically Na, as indicated by the changes in the Raman spectra after the reaction. This demonstrates that we can successfully deposit films of δ-MnO_2 on conductive EG/SiC, and transform it to alternate birnessites as well as Mn2O3 and Mn3O4, providing a platform for enhanced performance from these materials.

[1]L. Spinelle et al. Sensors 17(7), 1520(2017)[2] F. Cheng et al. Chem. Mater 22(3), 898-905(2010)[3] Y.J. Huang et al. Electrochim Acta 99, 161-165(2013)[4]N. Joshi et al. Microchim. Acta 185, 213(2018) [5] Julien et al. Spectrochim Acta A 60, 3(2004) [6] F. K. Tan et al. Int. J. Eng. Sci. Technol. 19, 4, (2019) [7] Q. Zhang et al. J. Electroanal. Chem., 837(2019)) [8] Julien et al. Solid State Ionics 159, 4(2003) [9] S. H. Shim et al Phys. Chem. Min. 38, 9 (2011)

3:50 PM X07
(Student) Enhancement of Visible Photoluminescence Through Atomic Layer Deposition Surface Passivation of Porous Silicon Nanowire Arrays Fabricated by Metal-Assisted Chemical Etching Kyle G. Tezanos and Parsian Mohseni; Rochester Institute of Technology, United States

The unique optical response properties of porous silicon nanowires (SiNWs) in the visible range enables potential applications across a variety of energy conversion technologies. While crystalline silicon has an indirect band gap of 1.12 eV and provides only low photoluminescence (PL) quantum yield in the bulk form, porous silicon exhibits strong visible emission at room temperature, attributed to a combination of surface state and quantum confinement effects. In this work, dense arrays of porous SiNWs are fabricated via metal-assisted chemical etching (MacEtch) with Au-Pd alloy catalyst layers. Room-temperature PL spectra collected from as-prepared samples show a clear variability in the intensity of the characteristic broad visible emission peak, centered at ~650 nm, as a function of the porous SiNW array volume. The influence of metal oxide surface passivation by atomic layer deposition (ALD) on PL emission wavelength and intensity is investigated. Commonly used ALD materials, including alumina (Al_2O_3), hafnia (HfO_2), and titania (TiO_2), are deposited on MacEtch-fabricated samples varying in etch depth from 30 to 100 µm. The emission spectra of ALD-passivated SiNW samples are compared to those coated with indium tin oxide (ITO) by sputter deposition. A clear enhancement of PL emission is observed for all ALD-processed samples as the passivation layer thickness is increased from 10 to 50 nm, favoring those passivated with HfO_2. The passivation potential of each ALD material is tracked over a 6-month period from the time of deposition and compared. This work highlights the importance of conformal passivation of ultra-high aspect ratio porous SiNWs and tunability of their optical response properties toward applications in photoelectrocatalytic water splitting and photovoltaic energy conversion.

4:10 PM X08
Intraband Optical Gain in Colloidal Nanoplates Benjamin Diroll; Argonne National Laboratory, United States

Colloidal nanoplatelets show some of the most promising optical gain characteristics of any materials. Using a modified quantum fountain design, thresholdless intraband optical gain at near-infrared wavelengths is demonstrated in using colloidal nanoplatelets. This is the first demonstration of unipolar gain in a colloidal system, requiring only electrons in this case. Stimulated emission depends on the thickness of the samples and can be tuned to technologically important wavelengths such as 1.3 and 1.5 µm. The modal gain, gain bandwidth, and gain lifetime of this intraband gain may be manipulated using excitation energy and temperature. Unlike bipolar laser media which competes with non-radiative Auger recombination, intraband stimulated emission must

compete with intraband relaxation via longitudinal optical and surface phonons.

4:30 PM X09
Development of Granular Metals for High Voltage Applications Laura Biedermann, Simeon Gilbert, Michael Siegal, Peter Sharma, Jack Flicker, Samantha Rosenberg, Melissa Meyerson, Paul Kotula and Thomas Kmieciak; Sandia National Laboratories, United States

Granular metals comprise nanoscale metal islands embedded in an insulating matrix. These materials are of great interest both as a platform for studying fundamental electron transport mechanisms and for enabling unique applications. Electron transport studies often feature noble metals (Au, Ag) in silica or yttria-stabilized zirconia (YSZ) matrices. In such materials, the transition from tunneling and hopping transport for low-metal fraction granular metals (dielectric regime) to percolative transport at high metal fractions (metallic regime) has been well-studied. This change in conduction mechanisms manifests as a 10^6 to 10^{12} increase in DC conductivity as the metal fraction increases, 20% to 80%, for various granular metals [1]. Applications include strain sensors and memory storage with magnetic granular metals exhibiting giant magnetoresistance.

To expand the potential application space of granular metals into high voltage and high current applications, we developed granular metals with Co and Mo islands in silicon nitride and YSZ matrices. These materials were chosen to protect against joule heating causing island coalescence at high current densities. Mo and Co granular metal films with metal fractions 20% to 80% were prepared via rf co-sputtering of the metal and insulator. Electron microscopy images and DC conductivity measurements of these films showed the nanostructures and dielectric-to-metallic transitions characteristic of granular metals. Preliminary tests show breakdown strengths > 100 kV/m. These Co-SiN and Mo-SiN are the first known granular metals with a silicon nitride insulating matrix. This work complements prior development of Co-YSZ [2] and expands on limited prior studies of Mo-based granular metals [3].

The conductivity of our granular metal films was moderately sensitive to metal fraction, increasing 10^4 - 10^6 times as the metal fraction increased 20-80%. To understand these conductivity trends, we used x-ray photoelectron spectroscopy to evaluate metal/insulator interactions such as surface oxidation of the metal islands and band bending resulting from the work function differences between the metal islands and YSZ matrices. We found that metal/insulator interface interactions, including bonding, alloying, and band-bending, have a pronounced and previously unappreciated impact on granular metal conductivity. We posit that such interfacial interactions underlie conductivity trends in the broader family of granular metals [4].

This work was supported by the Laboratory Directed Research and Development program at
Sandia National Laboratories, a multimission laboratory managed and operated by National
Technology and Engineering Solutions of Sandia LLC, a wholly owned subsidiary of Honeywell
International Inc. for the U.S. Department of Energy's National Nuclear Security Administration
under contract DE-NA0003525.

[1] C. Grimaldi, PRB 89, 214201 (2014)
[2] B. Hattink et al., PRB 67, 033402 (2003).
[3] Y. Wu et al., PRB 82, 092202 (2010).
[4] S. Gilbert et al., under review (2022).

SESSION Y: Materials Processing and Integration

Session Chairs: Daniel Ewing and Patrick Shea
Thursday Afternoon, June 30, 2022
Ohio Staters Inc. Traditions Room

1:30 PM Y01
(Student) Chromium Segregation in Silicon Thin Films During Wide Area Sub-Millisecond Melting and Recrystallization
Glenn Packard[1], Matthew Hum[1], Karl D. Hirschman[1] and Robert Manley[2]; [1]Rochester Institute of Technology, United States; [2]Corning Incorporated, United States

The use of a chromium underlayer has been established as promoting adhesion in amorphous silicon thin films during crystallization by flash lamp annealing (FLA). This process has minimal adverse effects for the 3-5 μm-thick layers needed for photovoltaic applications; however, as silicon thickness is reduced to the < 100 nm films ideal for thin film transistors, the behavior and penetration of chromium, a known cause of deep-level trap states, within the silicon region becomes potentially significant. In this work, thin films of amorphous silicon between 20 and 100 nm in thickness are deposited on a thin chromium underlayer on glass substrates and crystallized FLA. The resulting textures and morphologies indicate an improved adhesion over samples without a Cr underlayer.
The micrometer-scale texture of long, edge-directed crystallographic ridges that is visible under optical microscopy overshadows a unique nanometer-scale texture which is revealed by atomic force microscopy and high-resolution scanning electron microscopy. The silicon surface is further broken by recessed parallel trenches containing regular rows of pits 10-30 nm in diameter as well as non-textured SEM "bright spots" representing localized chromium accumulation. Transmission electron microscopy further reveals the presence of chromium-rich particulates invading the silicon layer in discrete and discontinuous chunks. As the thickness of the silicon layer is reduced, trenches become wider and more dendritic, while discrete Cr agglomerations spread out into smaller and more numerous regions of Cr prevalence. Energy-dispersive x-ray spectroscopy confirms localized abundances of chromium within regions of dense bright specks.
Simple p-type field effect transistors are built using similarly varied thicknesses of flash lamp annealed polycrystalline silicon on a chromium underlayer. These devices will be tested electrically to compare hole carrier mobility and prevalence of trap states that impede current saturation. The trends visible in microscope metrology are compared with electrical trends with a view on the relation between silicon/chromium thickness ratio and device performance.

1:50 PM Y02
(Student) Interfacial Thermal Transport of Thinned and Chemical Mechanical Polished (-201) β-Ga_2O_3 Direct Wafer Bonded to (001) Si Michael E. Liao[1], Kenny Huynh[1], Tingyu Bai[2], Yekan Wang[1], Milena Milich[3], John Tomko[3], Patrick Hopkins[3,3,3], Quang Tu Thieu[4], Kohei Sasaki[4], Akito Kuramata[4], Marko Tadjer[5], Karl Hobart[5] and Mark Goorsky[1]; [1]University of California, Los Angeles, United States; [2]LAM Research, United States; [3]University of Virginia, United States; [4]Novel Crystal Technology, Inc., Japan; [5]U.S. Naval Research Laboratory, United States

Room temperature direct wafer bonding of ($\underline{2}01$) β-Ga_2O_3 and (001) Si substrates was performed, whose bonded interface consisted of thin ~2 nm SiO_2 and ~4 nm Ti interlayers. The thermal transport characteristics of the bonded interface were measured using steady-state thermoreflectance,[1] which showed a thermal boundary conductance of ~63 MW/(m^2K). However,

because the bonded β-Ga_2O_3 substrate was initially ~700 μm thick, the β-Ga_2O_3 was thinned prior to measuring the thermal boundary conductance of the bonded interface. Post-bonding β-Ga_2O_3 thinning and polishing recipes were developed in this study and triple-axis X-ray diffraction symmetric rocking curves were employed to examine the subsurface lattice damage induced or removed by each thinning and polishing step. For all thinning (grinding and lapping) and polishing steps, ~10 kPa downward pressure and 30 RPM pad rotation speed were used. After bonding to Si, the unbonded backside of the β-Ga_2O_3 was grinded with 30 μm diamond paste. This resulted in a ($\bar{6}$03) β-Ga_2O_3 XRD rocking curve FWHM of ~170" and FW(0.0001)M of ~19000" after removing ~600 μm of material. After grinding, 5 μm then 1 μm Al_2O_3 particles were used for lapping. After lapping with 5 μm Al_2O_3, the rocking curve FWHM and FW(0.0001)M decreased to ~40" and ~1300", respectively. 1 μm Al_2O_3 particles were then used as a finer lapping step, which further reduced the FWHM and FW(0.0001)M to ~30" and ~1000". The reduction in rocking curve peak widths (either changing to a softer particle material or smaller size) corresponds to the removal of subsurface lattice damage induced by each previous step. Lastly, 70-nm colloidal silica was used as the final polishing step, which reduced the rocking curve FWHM and FW(0.0001)M to 20" and ~400", respectively. The final polished surface roughness was 0.4 nm. During the lapping and polishing steps, a wedge in the β-Ga_2O_3 was intentionally induced such that the β-Ga_2O_3 layer had a thickness gradient ranging from ~2 to ~10 μm. The thickness gradient enables a more reliable extraction of the thermal boundary conductance of the bonded interface using steady-state thermoreflectance. The thermal boundary conductance measured for these bonded β-Ga_2O_3|Si structures is comparable to our previous work[2] bonding β-Ga_2O_3 to 4H-SiC (~65 MW/(m^2K)), and greater than other work reported in the literature that utilized mechanical tape exfoliation methods to bond (100) or ($\bar{2}$01) β-Ga_2O_3 to quartz or diamond (8-17 MW/(m^2K)).[3-5]

The authors would like to acknowledge the support from the Office of Naval Research through a MURI program, grant No. N00014-18-1-2429.

References
1. J.L. Braun, et al., Rev. Sci. Instrum. 90, 024905 (2019).
2. Z. Cheng, et al., ACS Appl. Mater. Interfaces, 12(40), 44943 (2020).
3. Y. Zhang, et al., Appl. Phys. Lett., 116, 202101 (2020).
4. Y. Zhang, et al., ECS J. Solid State and Technol., 9, 055007 (2020).
5. Z. Cheng, et al., APL Mater. 7, 031118 (2019).

2:10 PM Y03
Ionic Exchange in Perovskite Thin Films Using Solid-State Reactions Martin G. Reyes-Banda, Leunam Fernandez-Izquierdo, Jesus Alfonso Caraveo Frescas, Victor Fan and Manuel Quevedo Lopez; The University of Texas at Dallas, United States

One of the most appealing aspects of perovskite materials is that their composition can be tuned to dramatically to impact carrier mobility, carrier concentration, bad gap, etc. Their unique composition tuning can enable applications such as solar cells, LEDs, sensors, batteries, transistors, memories, lasers, photodetectors, X-ray, and radiation sensor, among many others. Besides directly impacting device performance, perovskite composition also plays a crucial in the resulting reliability and stability of any of these devices. In this work, a simple solvent-free, versatile, and flexible route for material properties modulation in halide perovskite thin films has been developed using $CsPbBr_3$ thin-films. The method enables composition, morphology and electrical properties control using a solid-state ion-exchange reaction in the presence of Pb$\mathbf{X}_2$ ($\mathbf{X}$= Cl^-, Br^-, I^-) or $\mathbf{B}Br_2$ ($\mathbf{B}$= Cd^{2+}, Mn^{2+}) vapor.
The original $CsPbBr_3$ thin films were grown using close-space sublimation (CSS), and $CsPbBr_3$ crystals obtained by grown by the antisolvent vapor crystallization (AVC) method as the precursor. The resulting $CsPb(Br_{1-x}\mathbf{X}_x)_3$ (PbX_2 treated) films maintained an orthorhombic structure with increased mobility and remarkable grain growth with grains as large as 25 μm in films as thick as 8 μm. This perovskite annealing process also tune their band gap in the range of 1.7 - 2.9 eV and tailor their transport electronic properties. Exposure to PbX_2 (X=Cl, Br) vapors for longer annealing durations resulted in higher mobility (~13 cm^2 (V s)$^{-1}$) and an increase in carrier concentration (5x10^{11} cm^{-3}).
Furthermore, the $CsPb(Br_{1-x}\mathbf{X}_x)_3$ films enabled diodes with very low leakage current (1x10^{-8} A/mm^2), likely due to the large crystalline grains. The diodes were used as radiation detectors, with superior alpha particle sensing from a ^{210}Po source.
In addition, preliminary results of B-site ion exchange show blue-shift emission and recrystallization opening a way to control both the composition, optoelectronic and electronic properties of inorganic perovskite thin films while enabling depositing films using a large area compatible methodology.

2:30 PM Y04
Planar and 3D Microstructured $CsPbBr_3$ Perovskite Devices for Neutron Detection Leunam Fernandez-Izquierdo, Martin G. Reyes-Banda, Jesus Alfonso Caraveo Frescas and Manuel Quevedo Lopez; The University of Texas at Dallas, United States

The need for high-efficiency radiation detectors with wide-area coverage is essential in applications such as nuclear medicine, industrial imagining, environmental radioactivity monitoring, spacecraft applications, homeland security, among others. For these applications, the detector material should interact strongly with high-energy particles or photons, must be able to operate at high electric fields with negligible leakage current, possess high resistivity, and be scalable. Cesium lead bromide ($CsPbBr_3$) possesses excellent electric, electronic and spectroscopic properties while showing endurance to humidity and good stability under extreme operating conditions. These properties make it an ideal material for high-energy radiation detectors. The use of $CsPbBr_3$ for heavily charged particle sensing is normally limited to single crystals due to the lack of deposition techniques for thick $CsPbBr_3$ films, which is necessary for efficient radiation and neutron sensing. To overcome this, thin films were deposited using the close space sublimation (CSS) process, which allows the deposition of stoichiometric and high-quality $CsPbBr_3$ films with reduced defects, large grains, and high deposition rates.
Here, we demonstrate the first evidence of neutron detection using a planar Ga_2O_3/$CsPbBr_3$ solid-state diode enabled by an innovative close space sublimation (CSS) method which allows deposition of thick $CsPbBr_3$ films. Furthermore, indirect neutron sensing is achieved using a ^{10}B layer for diodes biased at voltages as low as -5V, showing the potential for low power operation. The neutron response is enabled by the low leakage current (~10^{-8} A/mm^2), the rectification of ~10^4, capacitance as low as 15 pF, and fast response of the Ga_2O_3/$CsPbBr_3$ diode. The superior performance of the $CsPbBr_3$ is due to the phase-purity, stoichiometry control, and large single-grain columnar growth of the films obtained by the CSS method.
Furthermore, perovskite patterning and ^{10}B back-fill technique enabled the high neutron detection efficiency in a perovskite-based microstructured thermal neutron detector. High-efficiency cesium lead bromide ($CsPbBr_3$) perovskite-based micro-structured detectors are also demonstrated in this work. Trenches up to 10 μm deep were etched into the $CsPbBr_3$ thin films using a novel dry etching process involving a combination of HBr and argon plasma. The micro-structured diodes were then backfilled with isotopically enriched Boron as neutron conversion material via a sedimentation process to preserve the perovskite integrity. The fabricated micro-structured $CsPbBr_3$ thermal neutron detectors show efficiency of 4.3%. This represents >1.2x efficiency improvement over planar silicon (3.5%) and >2x efficiency improvement over planar $CsPbBr_3$ (2.1%) detectors, respectively. More importantly, gamma-

ray discrimination of 10^7 was measured in $CsPbBr_3$-based microstructured neutron detectors.

2:50 PM Y05
(Student) Predicting Premature Failure of Quantum Cascade Lasers Using Supervised Machine Learning Cagri Aydinkarahaliloglu[1], Shashank Jatar[2], Xiaojun Wang[2], Mary Fong[2], Vijay Gupta[1], Mariano Troccoli[3] and Anthony Hoffman[1]; [1]University of Notre Dame, United States; [2]Adtech Photonics, United States; [3]Evolution Photonics Inc, United States

Quantum cascade lasers (QCLs) are mid-infrared electrically injected lasers that generate photons via electronic transitions between bound levels of coupled quantum well heterostructures. Since the initial demonstration in 1994, QCLs have rapidly matured and are now available commercially. QCL lifetime is a significant consideration in the cost of ownership of one of these devices. Previous studies have predicted device lifetimes exceeding eight-hundred nine thousand hours; however, little attention has been given to predicting premature device failure where the device fails within several hundred hours of operation. Premature device failure presents a significant cost-threat to work where QCLs are integrated into complex systems, and a method to predict this failure would be able to help mitigate this threat. In this paper, we show how an accelerated burn-in process coupled with a support vector machine (SVM), a type of supervised learning algorithm, can be used to predict premature failure of QCLs. We report accurate prediction of premature device failure up to 201 hours prior to the catastrophic failure of a device.

In total, 9 QCLs undergo an accelerated burn-in process. The devices are operated in continuous-wave (CW) mode at 80% of their peak CW optical power at an elevated heat sink of 328K. All the QCLs are from different portions of the same semiconductor wafer that was grown by metal organic chemical vapor deposition. The devices are 5 mm long and have ridge widths that vary from 9 to 12 μm. During the burn-in process, light-current-voltage (LIV) measurements are measured approximately every 2.5 hours. For two of the devices that undergo longer burn-in testing, the interval between measurements varies from 10 to 4 hours. Across the nine devices, 473 LIV measurements are acquired.

The accelerated aging test consists of two stages. In the first stage, the LIV data from 5 QCLs are used to train the SVM model, and the LIV measurements from the remaining 2 devices are used to test the model. We use different combinations of the devices for training and testing to avoid overfitting to a particular combination of devices, and the parameters of the SVM are optimized over these 10 combinations. In the second stage, all 7 devices from the prior stage are used to train the same SVM model while test dataset consists of 2 new devices.

The model identifies healthy devices with 100% accuracy for every test combination, encompassing over 1300 hours of measurements for the operational devices. Across all measurements, an LIV from an operational device is never labeled as an LIV from a device that will fail prematurely. Additionally, every device that fails during the accelerated burn-in testing has at least one LIV labeled as belonging to a failed device. For many devices, LIV measurements very early in the testing are identified as problematic, which would allow an operator to cease testing well before the actual catastrophic failure of the device. This can be as much as 201 hours before failure. The proposed aging procedure can be integrated into a QCL production pipeline to decrease manufacturing costs and the time required before deployment.

3:10 PM Refreshment Break

SESSION Z: Heterogeneous Integration Technologies

Session Chairs: Mona Ebrish and Michael Hamilton
Thursday Afternoon, June 30, 2022
Ohio Staters Inc. Traditions Room

3:30 PM Z01
(Student) Heterogeneous Integration of Blue GaN Laser Diode Using Electrochemical Etching Chenziyi Mi[1], Rami Elafandy[1], Jung Hahn[1], Yubo Wang[1], Hong Tang[1], Brad Siskavich[2] and Josh Brown[2]; [1]Yale University, United States; [2]Bluglass Inc., Australia

Photonic integrated circuit (PIC) has found its applications in multiple fields such as signal processing and data transmission. However, the materials commonly used for PIC systems do not render efficient coherent light sources. Introducing efficient pumping light sources to the PICs has become a necessity. Even though heteroepitaxial integration of laser diodes has been demonstrated through selective area growth, the device lifetime and reliability remain a concern. Heterogeneous integration provides an alternative solution that has been found effective in InP systems.
Since its first demonstration in 1996, GaN edge emitting laser diodes (EELD) have seen steady improvement and have found applications in lighting and display. Heterogeneous integration of GaN EELDs will open up new opportunities for short-wavelength PIC applications. The goal of this study is to heterogeneously integrate GaN EELD to AlN-based PICs to explore nonlinear photonic signal processing in the visible wavelength range. To enable wafer-scale integration and bonding, we formed edge-emitting laser diodes using a combined dry (ICP) etching followed by a wet TMAH facet polishing. After facet etching and metallization, the laser diodes were first tested and the results are shown in Fig 1. Reasonably good performance with a threshold current density of 6kA/cm2 has been observed.
The bonding and liftoff processes are important steps to transfer the laser diode to foreign substrate. Our process utilizes transfer printing of fabricated laser diodes with SU8 as bonding layers. Detailed process flow is depicted in Fig 2. Based on our previous reported results, an undercut electrochemical (EC) etching was performed to selectively remove a highly doped sacrificial layer and to sever the EELDs from the original substrates (Step 8 in Fig 2). It is found that the mesa width is critical when performing the undercut EC etching with bonded wafers. Laser diode structures were successfully lifted-off and transferred to the handle wafer. The transfer yield is relatively high which makes our process promising. We will report the details of the transfer and bonding process and the performance of laser diodes before and after the transfer printing of GaN EELDs (Fig 3).

3:50 PM Z02
(Student) Electronic Packaging and Interconnect Technologies for Cryogenic and Superconducting Applications Sherman Peek, Bhargav Yelamanchili, Harshil Goyal, George Hughes, Archit Shah, John Sellers and Michael Hamilton; Auburn University, United States

Cryogenic applications such as quantum computation, space exploration, and medical instrumentation has become a significant field in today's electronics industry. As cryogenic systems become more complex, the need for optimized packaging and interconnect approaches becomes increasingly important. Variety in approaches with cryogenic interconnects and packaging techniques is important due to the number of materials used in a given cryogenic system. Additionally, the spatial constraints of these cryogenic systems (often times dilution refrigerators) are significant and are moving to the forefront of research challenges. In this work, we demonstrate a collection of solutions ranging from electronic

packaging techniques to examples of interconnect technologies, all proven reliable at cryogenic temperatures. Electronic packaging techniques demonstrated focus on low temperature flip-chip bonding, compatible with process-sensitive superconducting materials. Additionally, epoxy underfill processes are demonstrated and evaluated with confocal scanning acoustic microscopy. Unique cabling solutions that we have designed and developed that utilize these low temperature electronic packaging techniques are demonstrated. Fabrication processes performed to yield reliable cryogenic cables are detailed and significant material considerations are described. Cables designed are proven reliable at cryogenic temperatures and against multiple thermal cycles (from room temperature, to as low as 4.2 K, returning to room temperature) for DC and RF applications. Dielectrics used in the fabrication of cables were characterized by utilizing superconducting half-wavelength, series microstrip resonators. These resonators facilitated the extraction of parameters such as dielectric constant and loss tangent at GHz frequencies for cryogenic temperatures. Lastly as an extension to electronic packaging techniques, thru-hole processing on molybdenum (a robust low coefficient of thermal expansion material) is demonstrated, specifically comparing the use of nanosecond and femtosecond pulsed laser processing. Molybdenum thermal characterizations performed as low as 2.2 K with a physical property measurement system are described to augment future cryogenic electronic interconnect simulations. Techniques, processes, and characterizations detailed in this work provide excellent solutions for cryogenic interconnect challenges while creating a framework for forward-looking unique approaches.

4:10 PM Z03
Indium Microbump Interface Evolution with Varying Underbump Metallurgy Stack-Ups Rebecca A. Wheeling; Sandia National Laboratories, United States

Flip chip interconnections using indium have many advantages for high bandwidth applications with large strain between layers and/or cryogenic operation temperatures. Indium can form a cold weld at room temperature preventing undue stress during the flip chip bonding process. Furthermore, indium is highly ductile even at cryogenic temperatures and thus capable of accommodating strain between CTE mismatched substrates. Despite wide and diverse use, understanding of the reliability of indium microbumps is limited by the complex metallurgy occurring at the indium/under bump metal interface.
Due to the low melting point and high sputtering efficiency, it is difficult to obtain cross-sectional images of indium interconnects and thus determine the kinetics of intermetallic formation, qualities important to the reliability of the interconnect. We utilize cryogenic focus ion beam (cryo-FIB) and scanning electron microscopy to determine the kinetics of intermetallic formation. Three kinetic parameters: activation energy, time exponent, and pre-exponential constant are calculated through a multivariable linear analysis of intermetallic thickness as a function of time and temperature. The intermetallic stoichiometries are further validated with x-ray diffraction. Additionally, interfacial evolution will be modeled and correlated to mechanical performance via shear testing.
Three underbump metallurgy stack-ups have been evaluated: 1) Ti/Cu/Ni; 2) Ti/Ni; 3) Ti/Ni/Au. The addition of Au appears to significantly reduce the activation energy for intermetallic growth, compared to only Ti/Ni. The Ti/Ni stack-up is the most stable of these three. However, at elevated temperatures, complete consumption of the indium bump occurs by the Ni-In intermetallic, confirmed by diffraction data. Mechanical performance of the bumps for each stack-up will be reported.

4:30 PM Z04
(Student) UV Curable Ink Composition for Novel Direct Ink Writing Processes Yuri Piro[1], Chris Areias[1], Yibo Li[1], Andrew M. Luce[1], Emily Lamport[1], Oshadha Ranasingha[1], Susan Trulli[2], Craig Armiento[1] and Alkim Akyurtlu[1]; [1]University of Massachusetts Lowell, United States; [2]Raytheon, United States

A UV curable dielectric ink composition is presented which enables adaptable and high-resolution direct ink writing for printed electronic applications. The UV curable dielectric ink composition is designed using non-hazardous, commercially available ingredients. Specifically, the ink composition includes bisphenol-A type acrylate and epoxide monomers, a longwave ultraviolet light absorbing Type 1 radical photoinitiator, an ionic liquid to aid in epoxide monomer conversion post process, and high aspect ratio boron nitride nanoparticles. The ink manufacturing procedure is devised to require only fundamental lab equipment, without the need for complex reaction conditions or harmful processes. The UV dielectric ink composition is engineered to meet a range of direct ink writing application specific needs. These needs include a tailored rheology, cured film rigidity, dielectric performance, and adhesive ability onto substrates which are central to the printed electronics ecosystem. The versatility of this ink composition is demonstrated through the fabrication of dielectric bridges for printed coplanar waveguides, bare die chip integration, and interconnects between printed circuit board regions.

4:50 PM Z05
(Student) Additive Microfabrication of System in Package for Heterogenous Integration with Semiconductor Dies Bhushan Lohani and Robert C Roberts; University of Texas at El Paso, United States

This abstract explores the possibility of employing metal additive microfabrication of system in package (SiP) with inbuilt heat sinks and leadframe consisting of multiple pads for QFN packaging. The SiPs were fabricated using 17-4Ph stainless steel powder employing a relatively less expensive DMLS system. The use of affordable metal additive manufacturing systems is considered by the authors to encourage further research on its applicability towards heterogenous integration in the semiconductor industries. The International Technology Roadmap for Semiconductors (IRTD) 2012 emphasized on the importance of integration of system on chip (SoC) and SiP. DMLS is one possibility for such heterogenous integration due to the possibility of customization as the parts are directly fabricated from a CAD file. DMLS has been considered superior to its plastic or resin-based counterparts in applications where conductive parts with better accuracy and strength are required. All these features make DMLS parts, a possible option for the fabrication of SiP with few functionalities like heat sinks and connectivity. 3D packaging and heat extraction for die is one of the grand challenges of International Roadmap for Devices and Systems (IRDS).
In this abstract, different QFN leadframes with and without cooling systems are presented. The original leadframe design with only the pads forms a comparison reference for the remaining three systems. The three systems are: QFN leadframe with microchannel, inlet, and outlet for fluid flow, QFN leadframe with arrays of fins below the die location, and a QFN leadframe with fins along with additional inlet and outlet for optional fluid flow. Figure 1 shows the CAD top views of all four proposed package system. Each package system can hold a 1cm by 1cm semiconductor die for testing purposes. The microchannels are 500μm square channels whereas the fins are 1000μm in diameter. The affordability comes with the trade-off of resolution and the present DMLS system can faithfully produce the mentioned dimensions with compatible features for the channels and fins.

The first step towards the fabrication of the packages is the CAD design and simulation. The CAD design was then fed to the metal

3D printer, which then sliced the model and created 3D laser part. The fabrication proceeds by melting and fusing a 30μm layer of powder, repeating the process, creating layers on top of layers, and fusing them together until the final 3D part is built as per the CAD file. EDM wire cutting or grinding of previously created support structure could be used to separate the parts from the build plate. Figure 2 shows the steps involved in fabrication. On each separate parts, 1cm by 1cm semiconductor dies (all same) are carefully placed. Wire bonding will be used to connect the via to the leadframe pads and inlets/outlets will be extended. The whole system will then be covered with epoxy and left to cure. The final step will be to grind away the back end of the cured part to remove support metal plate on the bottom of the packaging parts as shown in Figure 3.
Figure 4 shows the separated parts with a spot for semiconductor die to be affixed and various other sub-parts. Figure 5 shows the water (colored for visibility) filled leadframe with microchannel, and the other one with fins, inlet, and outlet is shown in Figure 6. Figure 7 shows the preliminary infra-red image of all four devices heated to 40°C and left to cool down. The devices were in the same order as Figure 4. As per the theoretical idea, fins with channels performs the best followed by the one with microchannel, and the one with only fins based on the time required for them to cool down (a-f in Figure 4). The preliminary result appears promising and the material characterization along with testing is in process. Figure 8 and 9 shows the SEM characterization of build device compared to the design. The variation from the design is very small.

SESSION AA: Plasmon and Surface Phonon Polaritons

Session Chairs: Anthony Hoffman and Milan Palei
Thursday Afternoon, June 30, 2022
Senate Chamber

1:30 PM AA01
(Student) Lateral Permittivity Patterning by Ion Irradiation in CdO Thin Films for Mid-IR Plasmonics Angela Cleri[1], Mingze He[2], Katja S. Diaz-Granados[2], Joshua Caldwell[2] and Jon-Paul Maria[1]; [1]The Pennsylvania State University, United States; [2]Vanderbilt University, United States

Donor doped cadmium oxide (CdO) thin films demonstrate excellent optoelectronic properties, further enabled by advanced synthesis techniques such as high-power impulse magnetron sputtering (HiPIMS), which yields high quality crystals with easily controllable transport properties. Tunable carrier concentrations between 10^{19}-10^{21} cm^{-3} while maintaining mobilities between 300-500 cm^2/V-s facilitate low-loss plasmon modes spanning the mid-IR. Further, fabricating layered CdO structures with varying thickness and carrier density in each stack has given way to interesting nanophotonic phenomena such as multiple epsilon-near-zero (ENZ) resonances in a single structure, strong coupling between ENZ and surface plasmon polariton modes, and hyperbolic behavior in homoepitaxial structures. By controlling donor dopant levels in individual layers, one can engineer permittivity of a stack in the out-of-plane dimension. Here, we extend this principle to the in-plane dimensions by ion irradiation patterning to locally induce donor defects and achieve lateral permittivity control. Current methodsto achieve similar lateral control, e.g. nanopatterning, require lithographic approaches that almost always introduce physical boundaries, roughness, or interface defect densities that interfere with high fidelity plasmonic modes. Instead, this novel ion irradiation method creates lateral patterns which are free of physical interfaces but exhibit sharp contrast in permittivity. In this presentation, we will demonstrate lateral control of electronic and optical properties in thin film CdO by ion irradiation using patterned hard masks.

1:50 PM AA02
MBE Growth of Delta Doped Si:InAsSb/GaSb HMM and Their Hyperbolic Response Kurt Eyink, Heather Haugan, Krishnamurthy Mahalingam, Derek Bas and Augustine Urbas; Air Force Research Laboratory, United States

Hyperbolic metamaterials have been receiving considerable due to their large density of states, high spontaneous emission rates and tailorable properties. One way of forming these structures is through the combination of a degenerately doped semiconductor and undoped semiconductor to form stacks of these materials. Here the metallic component is the degenerately doped semiconductor and the metallic fraction is fixed from the ratio of the metallic region to the total thickness. We, as well as others, used a doped InAsSb in combination with undoped GaSb. The composition of the InAsSb was lattice matched to the GaSb to allow a wider range of topological structures. We have recently characterized Si:InAsSb/GaSb stacks and have found that the Si:InAsSb structures have the doped charge squeezed into the central region of the InAsSb. We had found that the amount of squeezing was relatively independent of the size of the InAsSb region being consistently in the 3nm range. In this study we first look at the delta doping an Si:InAsSb/GaSb stacks. The constant doped density was similar to the previous study (~$2x10^{19}/cm^3$). Delta doping was studies as a function of position and amount in the structures and was characterized using HRXRD and spectroscopic ellipsometry. Delta doping was achieve by interrupting the growth while continuing to expose the surface to Si. HRXRD showed that with interruption on the GaSb surface, a large degradation in the quality of the stack occurred. Whereas, interruption on the InAsSb retained a high quality stack. We further showed this layer could be as thin as a single monolayer thus effectively allowing the delta doping at each interface. Stacks of InAsSb/GaSb with Si delta doping at both edges of the InAsSb as well as constant doping throughout the structure were formed and subsequently characterized with spectroscopic ellipsometery. We found contrary to the constant doped structures which contained a single peak in the spectroscopic ellipsometry response these structures contained two peaks. This peaks presence of these peaks will be discussed in terms of doping as well as potential quantum transitions in the structure.

2:10 PM AA03
(Student) Understanding Organ Pipe Resonances in SPhP Trenches for Spectroscopic Sensing Seyedeh Maryam Vaghefi Esfidani and Thomas G Folland; The University of Iowa, United States

Surface plasmon polaritons (SPPs) and surface phonon polariton (SPhP) modes form when light interacts with the surface of materials with a negative dielectric function. They have attracted much attention due to their ability to confine light to deeply subwavelength dimensions which can enable significantly enhanced interaction with nanoscale systems. Understanding the design principles for excitation of SPhP modes in the mid infrared (MIR) will make them more relevant for applications including optical modulators, photodetectors, and sensor technologies. For instance, using surface enhancement infrared absorption (SERIA) one can create high sensitivity molecular sensors. In SERIA a SPhP is used to enhance the optical absorption of the molecule. However, to design an effective SEIRA sensor it is critical to carefully optimize the coupling between free space light, the SPhP mode, and the molecule, to get a large change in signal when operated. Given that SEIRA is a resonant process, which is dependent on the interaction between numerous geometric parameters of the SPhP resonator, designing an efficient and low-cost biosensor is very time consuming. Therefore, understanding

the design of resonant structures is crucial to improve the enhancement.
In our work, we investigate periodic trenches etched into a silicon carbide surface. Resonances in this structure form between the walls of the trenches, and form a vertical standing wave which, analogous to resonances in an organ pipe. We develop a model based on considering the structures as finite length metal-insulator-metal (MIM) waveguide to investigate the frequency of modes and optimize the height and pitch of the structure for the purpose of sensing. Attention will be focused on various heights and trench widths that are important for realizing a sensor. Numerical simulations are compared between using two different approaches-numerical solutions to maxwells equations computed using full wave simulations and a simplified analytical model implemented in MATLAB based on S-matrix formalism and cavity model. The measured SPhP modes of standing wave in different mode with various height and gaps of both methods are compared, and we find the simplified analytical model is well capable of calculating the reflection and quality factor for MIM waveguide. Our results are general, and can be applied to any types of rectangular MIM waveguides to achieve an optimal design, notably for the comparison of different sensor geometries and materials.

2:30 PM AA04
(Student) Physical Vapor Transport Growth of α-MoO_3 Sheets for Hypersonic Thermal Transport via Hyperbolic Phonon Polaritons Ryan Spangler[1], Angela Cleri[1], Joshua Nordlander[1], Katja S. Diaz-Granados[2], Daniel Hirt[3], John Tomko[3], Patrick Hopkins[3], Joshua Caldwell[2] and Jon-Paul Maria[1]; [1]The Pennsylvania State University, United States; [2]Vanderbilt University, United States; [3]University of Virginia, United States

For high-frequency and high-power electronics, especially those that rely on low-thermal conductivity semiconductors, advanced thermal management is critical in improving device performance and lifetime. In recent years, van der Waals materials such as h-BN and α-MoO_3 have been identified as natural platforms for hosting low loss, highly confined hyperbolic phonon polaritons (HPhPs). These quasiparticles of coupled oscillations of light and heat result from extreme anisotropy of the dielectric function, where the in-plane and out-of-plane dielectric permittivity have opposite signs. Furthermore, in α-MoO_3, the in-plane components also exhibit hyperbolic dispersion in some spectral regions; in this way, the propagation of HPhPs can be restricted to a single crystal direction. These rays may permit delocalized heating, where energy absorbed by a hyperbolic material may travel ballistically at hypersonic velocities, even against a thermal gradient, before thermalizing. In this work, single crystals of α-MoO_3 have been synthesized using a physical vapor transport technique, which has been identified as an effective approach for the growth of these materials. We have achieved α-MoO_3 growth oriented with the b-axis perpendicular to the substrate and with low out-of-plane mosaicity, eliminating the tendency of the crystals to grow in other orientations which would limit applicability in devices. We present structural, microscopic, and optical data characterizing the formation of α-MoO_3 crystals on various substrates for the purpose of investigating hyperbolic phonon polariton behavior.

2:50 PM AA05
(Student) Control of Thermal Transport at Ultrahigh Temperatures by Immiscible Oxide Heterostructures Sean McSherry[1], Matthew Webb[1], Jonathan Kaufman[2], Zihao Deng[1], Ali Davoodabadi[1], Tao Ma[3], Emmanouil Kioupakis[1,1], Keivan Esfarjani[2,2,2], John T. Heron[1] and Andrej Lenert[1]; [1]University of Michigan–Ann Arbor, United States; [2]University of Virginia, United States; [3]University of Michigan, United States

Degradation of materials under harsh, high-temperature conditions is one of the grand challenges of high-performance energy conversion. Current approaches make use of refractory materials that do not possess ideal properties but are resistant to decomposition by heat. To suppress undesired thermal transport, multiple refractory materials are shaped and arranged with varying degrees of complexity, ranging from multilayers to plasmonic arrays and 3D photonic crystals. Ultimately these structures progress toward more thermodynamically favorable configurations and result in intermixing, reaction or new phase formation, and coarsening. This severely limits their performance in extreme conditions. Here, we introduce the concept of using immiscible refractory oxides with high crystallinity as building blocks of functional ultrahigh-temperature materials. We demonstrate epitaxial oxide heterostructures made from perovskite $BaZr_{0.5}Hf_{0.5}O_3$ (BZHO) and rocksalt MgO as a photonic crystal (PhC) that can suppress undesired thermal emission at a desired cutoff wavelength. The PhC is implemented as surface filter to suppress mid-infrared thermal emission from the best intrinsic, spectrally selective emitter operating at 1350°C in air. The heterostructure exhibits coherent atomic registry that retains clearly separated refractive index mismatched layers without interface coarsening, interdiffusion, phase change, or decomposition up to at least 1100°C in dry air. The use of dissimilar crystal structures, with low lattice and thermal expansion mismatch, allows for high crystallinity superlattices with interlayer immiscibility at high temperatures. The understanding gained from this study can be used to develop thermal barrier coatings and selective emitters that are resistant to instabilities in air. Beyond BZHO/MgO, we computationally identify ~10^3 potential oxide pairings that fit our design criteria, demonstrating the vast potential of this approach.

3:10 PM Refreshment Break

3:30 PM AA06
Plasmon-Enhanced Distributed Bragg Reflectors Aaron J. Muhowski, Morgan Bergthold and Daniel Wasserman; The University of Texas at Austin, United States

Distributed Bragg reflectors (DBRs), comprising quarter wavelength pairs of low and high refractive index layers, are a key element of modern photonic architectures, with applications ranging from vertical-cavity surface emitting lasers, to resonant cavity photo- and light-emitting diodes, to Fabry-Perot reflection modulators, to high-Q cavities for single photon emission. While DBRs are commonplace in mature visible and near-infrared wavelength systems, the quarter-wavelength thickness of the constituent layers becomes increasingly problematic at the longer wavelengths of the mid-infrared spectral region. As a result, III-V resonant cavity photonic devices often employ AlAsSb/GaSb DBRs with mirror thicknesses approaching 10 μm, despite the comparatively high refractive index contrast of 0.6 between AlAsSb and GaSb [1]. Such thick mirrors significantly increase fabrication complexity and decrease the yield of the resulting devices, to the point where mid-infrared resonant cavity photonics are largely untenable. Critically, DBR thicknesses for a given reflectance can be reduced by increasing the refractive index contrast of the constituent layers. Various avenues towards increasing index contrast have been explored have been explored, including oxide [2] and air-gap DBRs [3] at shorter wavelengths, as well as heteroepitaxial integration of high-contrast materials [4]—each with their own additional degree of complexity over conventional epitaxial DBRs.
The free electron response of highly-doped semiconductors has long been known to reduce the refractive index. Indeed, this exact mechanism has been exploited as plasmon-enhanced waveguides for quantum cascade lasers [5]. Here, we explore the application of highly-doped semiconductors as low index layers within DBRs. Simulations for DBRs over a range of design wavelengths and achievable doping densities are used to illustrate the unique features of plasmon-enhanced DBRs and examine the interplay between free-carrier losses, stop band width, and maximum

reflectance. Finally, we realize a plasmon-enhanced DBR using highly-doped InAsSb lattice-matched to GaSb with a design wavelength of 4.2 μm that is 43 % thinner than an AlAsSb/GaSb DBR with equivalent reflectance. In contrast to other low-index epitaxial DBR technologies, this marked reduction in mirror thickness requires no additional *ex situ* fabrication or heteroepitaxy outside of a conventional material system.

References

[1] Bewley *et al.,* Appl. Phys. Lett. **109,** 151108 (2016)
[2] MacDougal *et al.,* Electron. Lett. **30**(14), 1147 (1994)
[3] Ho *et al.,* Appl. Phys. Lett. **57**(14), 1387 (1990)
[4] Fan *et al.,* Appl. Phys. Lett. **101**, 121909 (2012)
[5] Sirtori *et al.,* Appl. Phys. Lett. **66**(24), 3242 (1995)

3:50 PM AA07

(Student) All-Epitaxial Ultra-Thin Long-Wave Infrared Plasmonic Detectors Morgan Bergthold[1], Priyanka Petluru[1], Aaron J. Muhowski[1], Leland J. Nordin[2] and Daniel Wasserman[1]; [1]The University of Texas at Austin, United States; [2]Stanford University, United States

The desire to confine light into sub-diffractive volumes for optoelectronic device applications has long driven interest in the field of plasmonics. Strong subwavelength confinement can be achieved by leveraging modes, supported at metal/dielectric interfaces, such as the surface plasmon-polariton (SPP) or the localized surface plasmon (LSP). Devices using these modes often operate in the visible or near IR wavelength ranges where noble metals such as Au and Ag can function as the plasmonic material. Unfortunately, with rising wavelength these metals behave increasingly like perfect electrical conductors—precluding them from supporting highly confined plasmonic modes [1] at long wavelengths. Fortunately, other classes of plasmonic media, such as transparent conducting oxides [2] and highly doped semiconductors [3] can be used as tunable plasmonic media in the mid-infrared (mid-IR). Furthermore, highly doped semiconductors can be grown by molecular beam epitaxy (MBE), thus their optical properties can be tightly controlled and they can be monolithically integrated with mid-IR optoelectronic device architectures with relative ease.

One such device architecture is the nBn detectors, which is comprised of an (n-doped) absorber-conduction band barrier-(n-doped) thin epitaxial contact region, design. Ultra-thin plasmonic detectors [4] leveraging nBn device architectures, which exhibit markedly lower dark current than their conventional counterparts, use a commensurately thinner contact region. In this regime, metal diffusion becomes increasingly problematic and can effectively short out the device, particularly when the fabrication processes require high temperatures. Likewise, the metallic grating, which provides momentum matching of the SPP to free space, can serve as a problematic source of diffusion. One method to mitigate metal diffusion would be to replace the grating layer with a highly doped semiconductor, eliminating metal diffusion from the grating and providing additional space for the metal contact to diffuse without the associated risk of device failure.

In this work we demonstrate a type-II superlattice nBn detector with epitaxial gratings. A 750 nm thick silicon doped (n^{++}) InAs/InAsSb T2SL grown lattice matched to the GaSb substrate serves as a plasmonic semiconductor backplane. On top of this highly doped material is a 311 nm InAs/InAsSb long-wave infrared (LWIR) T2SL absorber followed by a 146 nm AlAsSb barrier then a 46 nm LWIR T2SL top contact layer. The top layer consists of 127 nm of the same highly doped InAs/InAsSb T2SL that forms the plasmonic backplane. After growth this layer is lithographically patterned and wet etched into square patch antennas with a 1.5 μm width and 3.0 μm period that allow coupling into the SPP modes at the n^{++}/absorber interfaces. A lithography and wet etch process is then used to fabricate electrically isolated mesas and top and bottom contacts are deposited. After fabrication the detectors are mounted in a cryostat where spectral response, responsivity, and IV measurements are performed. External quantum efficiency (EQE) is then calculated from the spectral response and responsivity. The detector EQE peaks at 9 μm with a magnitude of 34% in an active region with thickness $\lambda_0/29$.

[1] S Law, V Podolskiy, and D Wasserman, "Towards nano-scale photonics with micro-scale photons…," Nanophotonics 2 (2013).
[2] G.V. Naik, J. Kim, A. Boltasseva, Oxides and nitrides as alternative plasmonic materials in the optical range. Opt Mater Exp 2011;1:1090–9.
[3] S. Law, D. C. Adams, A. M. Taylor, and D. Wasserman, "Mid-infrared designer metals," Opt. Express 20, 12155 (2012).
[4] L. Nordin, P. Petluru, A. Kamboj, A. J. Muhowski, and D. Wasserman, "Ultra-thin plasmonic detectors," Optica 8, 1545-1551 (2021)
[5] From V. A. Podolskiy's research group, see http://viktor-podolskiy-research.wiki.uml.edu/RCWA.

4:10 PM AA08

(Student) ErAs:InGaAlBiAs for 1.55 μm-pumped Terahertz Photoconductive Switches Wilder Acuna, Joseph P. Avenoso, James Bork, Lars Gundlach and Joshua Zide; University of Delaware, United States

We present our latest work on the molecular beam epitaxy growth of ErAs nanoparticles embedded within an InP-based $(InGaBiAs)_x$ $(InAlBiAs)_{1-x}$ digital alloy for use in photoconductive (PC) switches for terahertz (THz) sources and detectors. A high-performance PC switch requires specific properties in the active layer; specifically, ErAs:$(InGaBiAs)_x$ $(InAlBiAs)_{1-x}$ (hereinafter: ErAs:InGaAlBiAs) must have a short carrier lifetime, high dark resistivity, and high carrier mobility. In addition, a semiconductor working at a 1550 nm pumping wavelength is highly desirable due to the many advantages of compact, fiber-based components in the setup. For these desired properties, ErAs:InGaAlBiAs offers some advantages; ErAs nanoparticles pin the Fermi level and act as efficient carrier capture traps, decreasing the carrier lifetime to sub-picosecond values [1]. On the other hand, the InGaAlBiAs matrix gives enough degrees of freedom to engineer the band alignment to the pinned Fermi level, thereby increasing the dark resistance while having a bandgap below 0.8 eV. To quantify these properties, we characterized the materials with several techniques. High-resolution X-ray diffraction (HR-XRD) is used to determine material quality and an approximation of the bismuth incorporation. Spectrophotometry allows the measurement of the bandgap in the material. Hall effect measurements can be used to determine dark resistance, carrier concentration, and mobility. In the same way, optical-pump THz-probe spectroscopy provides the carrier dynamics in the structure. Finally, we present our progress on both measurement of material quality and also direct testing of PC switches properties in fabricated devices. [1] Appl. Phys. Lett. 75, 3548 (1999).

4:30 PM AA09

Plasmon-Phonon-Intersubband Transition Interactions at THz Frequency in Bi_2Se_3 -GaAs Heterostructures Quang To[1], Zhengtianye Wang[1], Quoc Dai Ho[1], Ruiqi Hu[1], Garnett Bryant[2], Anderson Janotti[1], Joshua Zide[1], Stephanie Law[1] and Matthew Doty[1]; [1]University of Delaware, United States; [2]National Institute of Standards and Technology, United States

In this work we probe theoretically strong coupling at THz frequency in a system consisting of Bi_2Se_3 and AlGaAs/GaAs quantum wells, focusing on the creation of new hybrid excitation modes, namely Dirac plasmon phonon intersubband transition (ISBT) polaritons. Rabi splitting arising from the interactions among the THz excitations in the system shows features of strong coupling which can be experimentally observable. Our calculations based on scattering matrix method reveal that the Rabi splitting

depends strongly on doping level and scattering rate in the quantum wells, as well as on the thickness of the GaAs spacer layer which separates the quantum well structures from the topological insulator (TI) layer. Our model also addresses contributions from an extra two-dimensional electron gas (2DEG) occurring at the Bi_2Se_3/GaAs interface as predicted by density functional theory calculations. This massive two-dimensional electron gas gives rise to a shift in the dispersion of the Dirac plasmon-ISBT polaritons to higher frequencies. This work lays the foundation and serves as a guide for setting up future experimental explorations into the coupling between a TI and a III-V heterostructure.
This work was supported as part of the Center for Hybrid, Active, & Responsive Materials (MRSEC) funded by NSF DMR-2011824.

4:50 PM AA10
(Student) In-Plane Plasmon Coupling in Topological Insulator Bi2Se3 Thin Films Saadia Nasir, Zhengtianye Wang, Sivakumar V. Mambakkam and Stephanie Law; University of Delaware, United States

Topological insulators (TIs) are materials whose bulk band gap is crossed by conducting surface states. The electrons that reside in these surface states are massless and obey time-reversal symmetry due to the large spin-orbit coupling in the system that prohibits their backscattering. Bi_2Se_3 is a widely-studied 3D TI with a single Dirac cone at the Γ point. Plasmons are the collective oscillation of the free electrons in a system. Plasmons excited on the surface states of a TI are called Dirac plasmon polaritons (DPPs) and their resonance frequencies lie in the terahertz (THz) range of the optical spectrum. The THz is an important frequency range for many practical applications as many molecules have absorption resonances in this range which can be used for gas sensing and monitoring, pharmaceutical testing, and so on. In this paper, we will explore in-plane plasmon coupling between TI nanostructures for future applications in THz plasmonic or metasurface devices. In TI films where the film thickness is much smaller than the wavelength of the light, DPPs are excited on both top and bottom surfaces simultaneously. They then couple to each other through their evanescent electric fields. This results in the two coupled DPP modes: the acoustic and the optical mode. Due to the momentum mismatch between the photon and the plasmon, it is not possible to excite plasmons by directly shining light on the sample. Patterning the film into stripes of width (W) adds the momentum of π/W to the incoming photons to overcome the momentum mismatch required for the excitation of plasmons. Researchers have mapped the DPP dispersion by changing the stripe width and thickness of samples. Although it helped us to understand the basic physics of DPPs, a clear idea of how these plasmons couple to each other in the plane was still missing. We started by growing eight 50 nm Bi_2Se_3 thin films on sapphire (0001) substrates using molecular beam epitaxy. From room temperature hall measurement, we get the sheet density of $(-2.46\pm0.01) \times 10^{13}$ cm^{-2}. As mentioned earlier, plasmons cannot be excited directly in the TI films, therefore we etched all films into stripes of width 2.5 μm with variable gap lengths ranging from 0.3 μm to 7.5 μm using electron beam lithography. Then we measured the transmission through the samples both in transverse electric (TE) mode and transverse magnetic (TM) mode using the room temperature Fourier transform infrared spectroscopy. Plasmons can be excited only in TM mode as a standing wave. The extinction spectra for all samples were calculated using $E=1- T(\omega)/T_0(\omega)$, where E is extinction, T_0 is the transmission through bare sapphire and T is the transmission through the sample. The TE extinction spectra of all samples looked similar with two distinct phonon modes α and β around 2 THz and 3.9 THz. For TM extinction curves instead of distinct phonon peaks, we observed a broader asymmetric peak around 3 THz that blue shifted with the increase in gap size. It indicates the excitation of plasmons and that couple to the phonons. We therefore modeled our data using a double Fano-type interaction model to extract the plasmon frequency. We observed an increase in the plasmon frequency with increasing gap size indicating in-plane coupling between the plasmons. We were able to fit the data with an exponential decay curve which is consistent with dipole-dipole coupling. We demonstrated that the in-plane coupling becomes negligible when the lattice constant exceeds 2.8 times the stripe width. This result is comparable to the studies on the in-plane plasmon coupling of metallic nanoparticles. In summary, this work helped to explore and understand the nature of in-plane plasmon coupling in TIs and can be useful in designing TI-based metasurfaces to manipulate THz light.

SESSION BB: Electrochemical Energy Storage and Conversion

Session Chairs: Jung-Hyun Kim and Edward Yu
Thursday Afternoon, June 30, 2022
Cartoon Room #1

1:30 PM BB01
(Student) High Performance Wafer-Scale Metal-Insulator-Semiconductor Photoanodes for Solar-Driven Water Splitting Soonil Lee and Edward T. Yu; The University of Texas at Austin, United States

Solar-driven water splitting offers a promising and environmentally friendly route for conversion of renewable solar energy to hydrogen gas that can serve as a transportable fuel, chemical feedstock, or energy storage medium. Various semiconductor materials have been studied for use as the light absorption layer in photoelectrochemical (PEC) cells designed to execute reduction and/or oxidation of water to create hydrogen and oxygen molecules, respectively. Among those materials, Si as the light absorber in PEC cells is especially attractive due to its moderate bandgap, high charge mobility, diffusion length, cost efficiency, and scalability in manufacturing. To improve the stability of Si-based PEC cells in operation, metal-insulator-semiconductor (MIS) structures have been widely used for high-performance Si-based photoanodes and photocathodes. For photoanodes, a metal catalyst improves the oxygen evolution reaction (OER) kinetics and the insulating layer protects the Si surface from corrosion. Typically in such structures, the photogenerated charges must be extracted through the insulating layer via tunneling so that a very thin insulating layer is required for efficient operation. However, a thick insulating layer is desirable for long-term stability. Therefore, optimizing the insulating layer thickness is important for both stable and efficient Si-based MIS photoanodes. In this work, we employ a simple and highly scalable method to fabricate high performance Si-based MIS photoanodes with localized conduction paths through the thick SiO_2 insulating layers and demonstrate its application to the fabrication of wafer-scale photoanodes. The localized conduction path enables low-resistance charge extraction even through thick insulating layers, and this approach has been shown in our previous work to yield photoanodes with excellent stability. In addition, we demonstrate a two-step Ni/NiFe electrodeposition process to create efficient OER catalysts. The Ni/NiFe catalyst layers increase Schottky barriers between Si and metal catalyst and lower the photoanode onset potential, improving applied bias photon conversion efficiency (ABPE) by a factor of more than two compared to a Ni catalyst, to 2.5%. The fabricated wafer-scale photoanodes show low onset potential 0.9 V vs. RHE and saturation current density over 25 mA/cm2 under outdoor solar illumination. Excellent device stability is also achieved. Similar approaches are also under development for wafer-scale fabrication of Si-based MIS photocathodes for the hydrogen evolution reaction (HER) in solar water splitting.

1:50 PM BB02
Highly Robust Solid Oxide Fuel Cells—Prevention of Chemical Inter-Diffusion by Introducing a Buffer Layer Amjad Hussain[1,2], Rak-Hyun Song[1,2], Tae-Hun Kim[1,2], Muhammad Measam Ali[1,2], Beom-Su Kwon[1,2], Dong Woo Joh[1,2], Jong-Eun Hong[1,2], Seung-Bok Lee[1,2] and Tak-Hyoung Lim[1,2]; [1]Korea Institute of Energy Research, Korea (the Republic of); [2]Department of Advanced Energy and System Engineering, University of Science and Technology (UST), Korea (the Republic of)

A major challenge in the field of solid oxide fuel cell development is the long-term durability of system and cell components. Last decades, a huge number of long-term durability tests have been carried out on SOFC materials and complete systems, aiming at extreme low degradation rate over the required life expectancy of at least 5 years. Even though an extensive degradation mechanism resulting in the severe failure of the cell components has been revealed. Herein, we introduced a highly robust GDC buffer layer that completely overwhelms the interdiffusion of cell components during high-temperature operation. This buffer layer is fabricated via a multi-layer green film lamination approach, in which the NiO-YSZ, NiO-ScCeSZ, ScCeSZ, and GDC green films were co-laminated by warm iso-static pressing and co-sintered. This green film lamination process improved the interfacial connectivity and packing density of both ScCeSZ and GDC layers. Thus, the inter-diffusion between the cathode to the electrolyte is efficiently suppressed during high-temperature operation. The multi-layer anode supported cell exhibited a very low degradation rate of 0.1%/kh, which fulfills the critical life expectancy benchmark for the commercialization of technology. This work presents a facile, cost-effective, scalable, and reproducible technique for mass production of highly reliable and robust anode-supported SOFC.

2:10 PM BB03
PiFM (Photo Induced Force Microscopy) Based Nanoscale IR Spectroscopy and Imaging in Energy Research Song Xu and Derek Nowak; Molecular Vista, United States

Correlating spatial chemical information with the morphology of closely packed nanostructures remains a challenge for the scientific community. For example, supramolecular self-assembly, which provides a powerful and low-cost way to create nanoscale patterns and engineered nanostructures, is not easily interrogated in real space via existing nondestructive techniques based on optics or electrons. A novel scanning probe technique called infrared photoinduced force microscopy (IR PiFM) directly measures the photoinduced polarizability of the sample in the near field by detecting the time-integrated force between the tip and the sample. By imaging at multiple IR wavelengths corresponding to absorption peaks of different chemical species, PiFM has demonstrated the ability to spatially map nm-scale patterns of the individual chemical components of two different types of self-assembled block copolymer films. With chemical-specific nanometer-scale imaging, PiFM provides a powerful new analytical method for deepening our understanding of nanomaterials.
We will discuss three topics that demonstrate the application potential of PiFM application in energy research:
1. nanometer resolution chemical analysis of a solar cell material, the ternary cation halide $Cs_{0.05}FA_{0.81}MA_{0.14}PbI_{2.55}Br_{0.45}$ (CsFAMA)-based perovskite visual sensor.
2. PiFM chemical imaging of a low cost high performance polymer solar cells with donor poly[(thiophene)-alt-(6,7-difluoro-2-(2-hexyldecyloxy) quinoxaline)] (PTQ10).
3. PiFM chemical imaging of lithium-ion migration during the charging process. We observed the high resolution mapping of delithiation process

2:30 PM BB04
(Student) Porous Current Collector Network Materials for High-Loading Li-Ion Battery Cathodes Michael Lee[1], Navni Verma[1], Lalith Rao[1], Christopher Brooks[2], Jay Sayre[1], Hanna Cho[1] and Jung Hyun Kim[1]; [1]The Ohio State University, United States; [2]Honda R&D Americas, LLC, United States

The demand for Lithium Ion Batteries (LIBs) in the energy, transportation, and consumer sectors has led to widespread investigation of approaches for increasing the energy density and rate performance of batteries. In order to overcome the rate limitations of ionic diffusion, production batteries are limited to relatively thin layers of active material in both electrodes (100um). This structure, when layered, results in a high volume and mass of passive material in the battery cell and offers the potential for energy density and performance increases if the electrode porosity and ionic resistivity can be adequately reduced. To this end, many groups have proposed 3D electrode materials structured by a variety of methods, from laser ablation to freeze casting, but none have proven economical and scalable enough for widespread implementation. To this end, we have investigated the performance of a porous aluminum current collector material which enables new 3D electrode geometries to be fabricated without these specialized methods.
We began with the hypothesis that the use of a porous aluminum material could improve electrode performance in two ways. First, the experimental current collector would create an unbroken electrically conductive network of aluminum strands spanning the full thickness of the electrode, improving the electrical conductivity to a degree impossible in traditional electrodes of the same thickness. Second, we hypothesized that cracking and delamination behaviors which were found to hurt the performance of traditional thick electrodes would align with the strands of current collectors in the porous electrodes, enhancing the ionic conductivity. We informed these hypotheses with parameters based on physics-based computational modelling, allowing us to select behavior-optimized electrode characteristics.
We fabricated a series of electrodes using Lithium Iron Phosphate (LFP) as an active material and 95% porous aluminum from the Sumitomo Electric Industries “Celmet” line as a current collector, and measured the effects of composition, mass loading, degree of calendaring, and other key parameters on cell performance at variable rates of both charge and discharge. We found that, controlling for other electrode parameters, our electrodes could achieve up to 6 times the active material loading of traditional thin electrodes while performing comparatively well when discharged at C-rates beyond 1C. We also observed favorable electrode cycle life. To support this understanding, we comprehensively characterized the material structure and compositional heterogeneity before and after testing via SEM, XRD, and other methods. Our findings indicate that, based on electrode performance and manufacturing accessibility, 3D thick electrodes manufactured by this method have the potential to significantly improve battery energy density.

2:50 PM BB05
(Student) Strategy to Passivate High-Voltage Spinel Cathode-Electrolyte Interfaces (CEI) Lalith Rao[1], Tianyang Wang[1], Xinwei Jiao[1], Meghan Stout[2], Cody Lockhart[2], Neil Kidner[2], Jay Sayre[1] and Jung-Hyun Kim[1]; [1]The Ohio State University, United States; [2]Nexceris, United States

The $LiNi_{0.5}Mn_{1.5}O_4$ (LNMO) spinel cathode has been extensively researched as a promising candidate for next-generation Li-ion batteries owing to its high operating voltage (~ 4.7 $V_{vs.Li}$) and high

specific energy (650 Wh/kg). In addition to this, its cobalt-free composition and excellent rate capability due to three-dimensional Li^+ diffusion makes it particularly attractive for a wide range of applications. However, the high operating voltage in full-cells (LNMO/Graphite) triggers unwanted parasitic reactions at the electrode/electrolyte interface which lead to active Li^+ consumption and consequent capacity fading.
Elemental substitution of Ni/Mn is a very actively pursued strategy to alleviate the capacity fading. In particular, Ti-substitution for Mn in $LiNi_{0.5}Mn_{1.5-x}Ti_xO_4$ (LNMTO) has improved the full-cell performances as evidenced by (i) higher capacity retention and Coulombic efficiency and (ii) lower oxidative reaction and self-discharge rates. The primary improvement mechanism of the Ti-substitution in LNMTO is a formation of Ti-enriched passivation layer at the expense of initial Mn-dissolution at the cathode-electrolyte interface (CEI). Once generating the passivation layer, further Mn-dissolution became suppressed. Despite these results, carbon conductor (Super P) inside cathode still actively oxidizes the electrolyte due to its good electrical conductivity and large surface areas.
In this regard, we adopted advanced binders to passivate the carbon conductors for the LNMTO cathodes. Polyvinylidene fluoride (PVdF) has been used as the binder in cathodes due to its electrochemical stability. However, PVdF does not offer the effective passivation of carbon conductors, while suffering from mediocre adhesion strength and raising environmental concerns by using N-Methyl-2-pyrrolidone (NMP), a toxic organic solvent. Studies have shown that advanced aqueous binder chemistries can be used to create an effective passivating layer at the cathode-electrolyte interface, improve adhesion strength and eliminate the use of toxic organic solvents. Among them, lithium polyacrylate (LiPAA) has demonstrated positive multifunctions such as proton scavenging, donating Li^+ and effective passivation of both carbon and active material particles. Our full-cell testing data showed that the LiPAA binder in LNMTO cathodes delivered an improved cycle life and a lower cell impedance compared to those of PVdF binder in LNMTO cathodes. To better understand the characteristics of the CEI passivation on the LiPAA and LNMTO cathodes, we will discuss about the various surface analyses of the fresh and aged electrodes using XPS, Raman, and HR-TEM.

3:10 PM Refreshment Break

3:30 PM BB06
(Student) Study of V2O5/LiPON Interface Using Depth-Resolved Cathodoluminescence Spectroscopy Pablo Rosas Martinez[1], Zachary Levy[1], Victoria Ferrari[2], Mitchell Walker[3], David Stewart[2] and Leonard J. Brillson[1]; [1]The Ohio State University, United States; [2]University of Maryland, United States; [3]Northwestern University, United States

Lithiated V2O5 has shown great potential as a candidate cathode material for solid-state batteries. Usually, LiPON is a common choice of a solid electrolyte due to its stability in a large voltage window and it can be manufactured using different systems such as ALD and rf-sputtering. In order to improve the applications of solid-state batteries, it is important to understand the process of lithiation that occurs when the battery is cycled. While cycling the battery system, the V2O5/LiPON battery system lithiates. With enough lithiation, the battery may undergo to an irreversible phase change and can degrade over time. Pure V2O5 has been shown to have several characteristic emissions, such as 1.8eV/2.0eV, 2.7, 3.0, 3.3, 3.7, and 4.0 eV[1]. The 1.8eV/2.0 eV is called the split-off band, which corresponds to the V3dzy -Oc2px/2py states. The "split-off" part signifies a gap in the density of states between the two peaks (1.8/2 eV) and the V3d t2g conduction bands [1]. As V2O5 is lithiated, the split-off band decreases, most likely due to lattice distortion as V2O5 undergoes a phase change.
In order to conduct this experiment, multiple thin films of V2O5/LiPON were sent to us by Dr. David Stewart and his graduate student Victoria Ferrari. These thin films were made by both co-sputtering V2O5 and Li2O, and then sputtering LiPON on top, and by electrochemically cycling V2O5 under LiPON, in order to achieve different levels of lithiated V2O5/LiPON. X-ray Photoemission Spectroscopy (XPS) was also conducted on pure lithiated V2O5 versus depth to track the lithiation throughout V2O5. We then proceeded to use Depth-Resolved Cathodoluminescence Spectroscopy (DRCLS) to study the band structure of various amounts of cycled V2O5/LiPON. Using Monte Carlo simulations to extract the maximum penetration depth of secondary electrons at a particular beam energy, we can precisely observe different characteristic emissions of V2O5/LiPON at various depths. Using the analytical technique known as Differential-Depth Resolved Cathodoluminescence Spectroscopy (DDRCLS), we can isolate the interface of V2O5/LiPON. In correlating the CL data with the XPS data, we can see that lithium tends to migrate to the bottom of the V2O5 layer and observe the decrease of the split-off bands as V2O5 becomes more lithiated. In isolating the interface, we see that the interface is very sensitive to both the presence of LiPON and how much the V2O5 layer is cycled. This work was supported by NSF grant DMR-18-00130 (P.R., Z.L., M. J. W., and L. J. B.) and also supported by the U.S. Department of Energy, Office of Science, Office of Basic Energy Sciences, under Grant DE-SC0021070. (D.S. and V.F.).
[1] M. Walker et al., J. Mater. Chem. A, 2020, 8, 11800-11810

3:50 PM BB07
(Student) Comparing Performance Enhancement by Different Carbon Additives for Si Anodes in Lithium-Ion Batteries Jun Wei Yap, Jung Hyun Kim and Hanna Cho; The Ohio State University, United States

In recent years, following the increasing demand for Lithium-ion (Li-ion) batteries with higher energy density, interest in Si-based anodes has soared. Si-based anode holds superior theoretical capacity (4200mAh/g) when compared to conventional graphite anodes (372 mAh/g). However, Si-based anode suffers from large volume change and poor electronic conductivity. To resolve the former issue, Si nanopowder has been used because nano-sized Si experiences faster relaxation of mechanical stress caused by the volume expansion. To address the latter issue, we investigated the effect of carbon conducting additives on the electrochemical performance of Si anodes.

The baseline Si-anode is made using conductive carbon black (Super P Li^{TM}) which consists of ~ 50 nm scale carbon particles. To enhance carbon network and improve the electron transport within the anode microstructure, we employed carbon nanotubes (CNT) from Aldrich and carbon nanofibers (CNF) from Aldrich. CNF's specification is 100 nm in diameter and 20-200 micro m in length, while CNT's specification is 6 - 13 nm in diameter and 2.5 – 20 micro m in length. Although adopting the CNF or CNT in Si anode would not be a new approach, there is lack of systematic work to compare and understand the mechanisms in which CNF and CNT improve the performance of Si anodes.
In this work, different percentages of CNT and CNF (calculated based on total weight of conductive carbon content) were added to Si-anodes. Understanding of the performance difference is done by examining electrochemical performances and microstructure. Surface morphology of the anodes before and after cycle aging is

studied with the help of scanning electron microscopy (SEM). The results revealed significantly different quality of coated anode surfaces; 5wt% of CNT and above suffers from the poor surface coating, whereas CNF maintained good quality coating throughout.

For electrochemical characterization, galvanostatic cycling, electrochemical impedance spectroscopy (EIS), and fast charging/discharge capability tests were performed. Data analysis showed that CNT and CNF both, helped improved the capacity retention and fast charge/discharge capability, albeit to different extend. Linking this to EIS results, reveals that the improvement seen are from lower early cycle charge transfer impedance and lower late cycle loss of contact impedance. When comparing between anodes with CNT and CNF, it is revealed that performance of anode with CNT is sporadic, which could stem from the inconsistency in surface coating seen in SEM images. However, anodes with CNF followed a predictable trend of higher CNF content equaling better performance. Overall, this work proofs that both materials provide different level of improvement to the cell performance, with CNF showing larger improvement in performance. Future work can be aimed investigating origin of the bad surface coating seen in Si anode with CNT and experimenting on different types of CNT, such as single walled, multi walled and double walled to further understand the contribution of conductive additive on the performance of Si anode.

4:10 PM BB08

(Student) Enabling High-Rate Long-Lifespan Lithium-Sulfur Batteries via Stereolithography Technique and Oxidative Chemical Vapor Deposition Yuxuan Zhang[1], Han Wook Song[2] and Sunghwan Lee[1]; [1]Purdue University, United States; [2]Korea Research Institute of Standards and Science, Korea (the Republic of)

Enhancing battery energy storage capability and reducing the cost per average energy capacity is urgent to satisfy the increasing energy demand in modern society. The lithium-sulfur (Li-S) battery is especially attractive because of its high theoretical specific energy (around 2600 W h kg^{-1}), low cost, and low toxicity.[1]
Despite these advantages, the practical utilization of lithium-sulfur (Li-S) batteries to date has been hindered by a series of obstacles, including low active material loading, shuttle effects, and sluggish sulfur conversion kinetics.[2] The traditional 2D planer thick electrode is considered as a general approach to enhance the mass loading of the Li-S battery.[3] However, the longer diffusion length of lithium ions, which resulted in high tortuosity in the compact stacking thick electrode, decreases the penetration ability of the electrolyte into the entire cathode.[4] Although an effort to induce catalysts in the cathode was made to promote sulfur conversion kinetic conditions, catalysts based on transition metals suffered from the low electronic conductivity and some elements (i.e.: Co, Mn) may even absorb and restrict polysulfides for further reaction.[5]
To mitigate the issues listed above, herein we propose a novel sulfur cathode design strategy enabled by additive manufacturing and oxidative chemical vapor deposition (oCVD). [6,7] Specifically, the cathode is designed to have a hierarchal hollow structure via a stereolithography technique to increase sulfur usage. Microchannels are constructed on the tailored sulfur cathode to further fortify the wettability of the electrolyte. The as-printed cathode is then sintered at 700 °C in a N_2 atmosphere in order to generate a carbon skeleton (i.e.: carbonization of resin) with intrinsic carbon defects. The intrinsic carbon defects are expected to create favorable sulfur conversion conditions with sufficient electronic conductivity. In this study, the oCVD technique is leveraged to produce a conformal coating layer to eliminate shuttle effects. Identified by scanning electron microscopy and energy-dispersive X-ray spectroscopy mapping characterizations, the oCVD PEDOT is not only covered on the surface of the cathode but also the inner surface of the microchannels. High resolution x-ray photoelectron spectroscopy analyses (C 1s and S 2p orbitals) between pristine and modified sample demonstrate that the high concentration of the defects have been produced on the sulfur matrix after sintering and posttreatment. In-operando XRD diffractograms show that the Li_2S is generated in the oCVD PEDOT-coated sample during the charge and discharge process even with a high current density, confirming an eminent sulfur conversion kinetic condition. In addition, ICP-OES results of lithium metal anode at different states of charge (SoC) verify that the shuttle effects are excellently restricted by oCVD PEDOT. Overall, the high mass loading (> 5 mg cm^{-2}) with an elevated sulfur utilization ratio, accelerated reaction kinetics, and stabilized electrochemical process have been achieved on the sulfur cathode by implementing this innovative cathode design strategy. The results of this study demonstrate significant promises of employing pure sulfur powder with high electrochemical performance and suggest a pathway to the higher energy and power density battery.
1 Chen, Y. *Adv Mater* **33**, e2003666.
2 Bhargav, A. *Joule* **4**, 285-291.
3 Liu, S. *Nano Energy* **63**, 103894.
4 Chu, T. *Carbon Energy* **3**.
5 Li, Y. *Matter* **4**, 1142-1188.
6 John P. Lock. *Macromolecules* **39**, 4 (2006).
7 Zekoll, S. *Energy & Environmental Science* **11**, 185-201.

4:30 PM BB09

(Student) Optimization of Li_3BO_3 Interlayer for Garnet-Based All-Solid-State Lithium Metal Batteries Zhenghuan Tang; The Ohio State University, United States

Recently Solid-State Battery has received increased attention as the next generation energy storage device due to its high energy density, improved safety, and thermal stability. Among various types of solid electrolytes (SE), lithium (Li)-stuffed garnet-type $Li_{6.75}La_3Zr_{1.75}Ta_{0.25}O_{12}$ (LLZT) delivered high ionic conductivity (~10^{-4} S/cm) and wide electrochemical stability window. Despite such promising ionic conductivity, there are few technical challenges that prevent the implementation of LLZT in practical battery cells. First, LLZT suffers from a high interfacial resistance due to its poor wettability in contact with Li metal anode. Second, LLZT suffers from Li- dendrite penetration through grain boundaries during cycling. It was reported that grain boundaries have high electrical and low ionic conductivities which favors Li-ions and electrons to nucleate and form Li metal. Additionally, poor wetting between Li-anode and LLZT causes partial contacting at the Li/SE interface. In result, contacting area at the interface are limited to several small hot spots. Therefore, current is focused on those small spots and more Li nucleate and deposit at these hot spots during cycling, which eventually aggravates Li penetration into SE. Many strategies such as element doping, in-situ Solid Electrolyte Interface formation, and interlayer engineering have been proposed to improve the issues. In our study, we chose to apply an amorphous glass coating layer between Li-anode and LLZT because of its simple processibility, and potentials towards industrial manufacturing. Preparation of the amorphous glass layer coating onto the LLZT pellet requires melting the glass by heating above its melting temperature followed by fast cooling. Therefore, melting temperature of the coating layer(< 1000ºC) is be one of the important criteria because we want to avoid unwanted reactions at

the interface and maintain mechanical integrity of the cell at heat treatment temperature. In addition, the coating layer should have a moderate ionic conductivity (>10^{-6}S/cm) which does not sacrifice the overall conductivity. Various materials have been proposed, and we down selected the materials to Li_3BO_3 (LBO)due to its low melting point(~700ºC), good stability between Li metal and LLZT, and moderate ionic conductivity(~10^{-6}S/cm),. In the study, we systematically controlled the critical parameters such as heating rate, cooling rate, slurry composition, heat treatment temperature, and heat treatment duration to improve coating quality. During optimization process, we found that good coating quality required: slow heating rate, low binder content in the slurry, moderate cooling rate, heat treatment temperature and duration. Using the optimized coating condition, we managed to obtain an 8-μm LBO coating layer without cracks or pinholes. After coating the interlayer, we fabricated Li symmetric Swagelok cells using the LBO-coated LLZT for electrochemical characterization and uncoated LLZT for reference. Based on our Electrochemical Impedance Spectroscopy (EIS) results, LBO coated symmetric cell managed to reduce the interfacial resistance from 6000 to 400 Ω cm^2. Secondly, we conducted a Critical Current Density (CCD) test to study the tolerance against Li-dendrite penetration. LBO-coated LLZT reached 0.4mA/cm^2 while bare LLZT only reached 0.1 mA/cm^2. Finally, we performed a cycling test which we plate/strip the symmetric cells under 0.1 mA/cm^2 with a capacity of 0.05 mAh/cm^2. The bare LLZT cell failed after 10 cycles, but the LBO-coated cell managed to stay operating without shortage for 93 cycles. Our optimization steps could be a useful guideline for future researchers if they plan to apply coating using similar method even with other materials. Furthermore, our results showed a proof of concept that our optimized LBO amorphous glass interlayer significantly improves LLZT performance by suppressing Li dendrite growth and improving interfacial wetting.

4:50 PM BB10
(Late News) Rapid Thermochemical Solvent-Free Synthesis of Crystalline Metal Borides and Their Investigation as Water Splitting Electrocatalysts Edward Gillan; University of Iowa, United States

Metal borides are often refractory solids that are produced from higher energy process such as arc melting and high temperature sustained heating. Elemental boron is itself a refractory solid and is often used as a starting material. Solution precipitation routes can form amorphous, structurally ill-defined metal borides that require annealing to crystallize them. Transition-metal borides have very long history as refractory materials and often are electrically conducting. In recent years, metal non-oxides have been extensively investigated as electroactive heterogeneous catalysts and metal borides are beginning to find interest as water splitting electrochemistry (hydrogen evolution and oxygen evolution reactions, HER and OER). To better investigate the possible value of refractory metal borides in electrocatalysis, it is useful to develop facile and rapid synthetic strategies that can produce well-defined crystalline metal borides and composite structures. This Late News presentation will describe our recent success using reactive MgB_2 and Mg/B powder mixtures to rapidly reduce and react with a series of anhydrous early and late metal halides to produce crystalline metal borides in seconds (e.g., TiB_2, ZrB_2, CoB, and NiB). Notably, these syntheses are oxygen and hydrogen free and produces several hundred milligrams of product for analysis and electrocatalysis investigations. The tunability and thermochemistry of these exothermic and solvent-free solid-state metathesis (SSM) reactions will be described. In some cases, it is possible to mix multiple precursors together to form composite structures such as TiB_2/TiN and TiB_2/CoB materials. Several crystalline metal borides were investigated as HER and OER electrocatalysts in acidic and basic solutions. In some cases, earth abundant metal borides show appreciable HER and OER activities in pure form and in composite structures.

5:10 PM BB11
(Late News) Atomistic Simulations of Reaction Kinetics at Electrochemical Interface Yuanyue Liu; University of Texas at Austin, United States

Electrochemistry at solid-water interface lies at the center of many technologies to address energy and environment challenges. However, there is a general lack of kinetic information (e.g. activation energy) at atomic scale, especially for electrochemical steps. One of the major challenges is the lack of computational methods to effectively simulate the electrochemical kinetics at solid-water interface. Here we present an effective first-principles model, and use it to elucidate the atomistic mechanisms of single metal atom in graphene for carbon dioxide reduction and oxygen reduction reactions [1,2,3]. This method enables us to explain the puzzling experiments that cannot be explained by conventional models focusing on thermodynamics.
[1] X. Zhao, Y. Liu*, 2021, J. Am. Chem. Soc. DOI: 10.1021/jacs.1c02186
[2] X. Zhao, Y. Liu*, J. Am. Chem. Soc. 2020, DOI: 10.1021/jacs.9b13872
[3] D. Kim, J. Shi, Y. Liu*, J. Am. Chem. Soc. 2018, DOI: 10.1021/jacs.8b03002

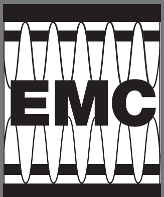

64TH ELECTRONIC MATERIALS CONFERENCE

June 29-July 1, 2022 // The Ohio State University // Columbus, Ohio

FRIDAY ORAL PRESENTATIONS

SESSION CC: Neuromorphic + Late News

Session Chair: Angel Yanguas-Gil
Friday Morning, July 1, 2022
Great Hall Meeting Room 1 & 2

8:20 AM CC01
Nonvolatile Analog Electrochemical Random Access Memory for In-Memory Computing Yiyang Li; University of Michigan, United States

In-memory computing using analog resistive memory can significantly reduce energy and latency in data-intensive tasks like machine learning. Resistive random access memory (RRAM) stores resistance states through the motion of oxygen vacancies in mixed ionic and electronic conductors (MIEC), whereby the oxygen vacancies act as electron donors. Existing resistive memory suffers from nonlinear & stochastic switching due to the creation of a nanosized 1D conducting filament. As a result, filament-based RRAM has struggled with reliable analog switching.
To create a more predictable analog resistive memory, we incorporated an yttria-stabilized zirconia (YSZ) solid electrolyte sandwiched between the two MIECs like TiO_{2-x} and WO_{3-x}. During writing, the solid electrolyte blocks direct electronic current and joule heating; instead, only electrochemical currents are allowed to move oxygen vacancies between the MIECs. The oxygen vacancy concentration in the MIEC is used to store analog resistance states. Our electrochemical random access memory (ECRAM cells show highly linear and symmetric switching with very low read and write currents (<100 nA), and endurance of 300 million read/write cycles. Moreover, our ECRAM cells show long term nonvolatile analog state retention at elevated temperatures. ECRAM is highly promising as an analog resistive synapse for future in-memory and neuromorphic computing applications.

8:40 AM CC02
(Student, Late News) Effects of Small Molecule Dopants in Piezoresistive Sensing PAAMPSA/PANI/PA Polymer Complex Colton Duprey[1], Hadi Rouhi[1], Elham Ghalavand[1], Nicole Penners[2,1], Katherine Webb[3,1], Sarah Veres[1], Gina Lusvardi[1], Sofia Luna[1], George Chen[1] and Evan Wujcik[1]; [1]The University of Alabama, United States; [2]New Mexico Institute of Mining and Technology, United States; [3]University of Florida, United States

As wearable electronics increase in popularity, it becomes evident that a sensitive, flexible, comfortable, and biologically compatible material is required to make an optimal wearable biosensor. As a result, polymeric piezoresistive sensors show great promise in movement monitoring and biosensing. Their polymer composition provides flexibility and stretchability which allows for unique sensor applications where traditional metallic sensors are too brittle and rigid. The polymer complex to be used as a strain sensor is composed of a templating poly(2-acrylamido-2-methyl-1-propanesiulfonic acid), polyaniline, and a small molecule dopant, originally phytic acid. By substituting the small molecule dopant for various other small molecule acids, the impacts the various dopants have on the strain sensor's conductivity, mechanical properties, and piezoresistive sensitivity can be studied. Typically, small molecule dopants that increase conductivity decrease stretchability and mechanical stability, which stems from more acidic dopants being able to protonate and facilitate ion transport throughout the sensor. On the opposite hand, functional groups with increased hydrogen bonding tend to increase mechanical properties, as well as allow for autonomous self-healing. By increasing our understanding of the impact these various dopants have on the properties of the strain sensor, we can tailor the usage of these small molecule dopants as we try to increase the sensitivity and conductivity of our sensor for usage in biosensing and kinesiological monitoring applications.

9:00 AM CC03
(Student) Influence of Oxygen Vacancy and Top Electrode on Switching Behavior of InGaZnO Based Resistive Random Access Memory Fei Qin[1], Han Wook Song[2] and Sunghwan Lee[1]; [1]Purdue University, United States; [2]Korea Research Institute of Standards and Science, Korea (the Republic of)

Biomimetic synaptic processes, which are imitated by functional memory devices in the computer industry, are a key focus of artificial intelligence (AI) research. It is critical to develop a memory technology that is compatible with Brain-Inspired Computing in order to eliminate the von Neumann bottleneck that restricts the efficiency of traditional computer designs. Due to restrictions such as high operation voltage, poor retention capacity, and high power consumption, silicon-based flash memory, which presently dominates the data storage devices market, is having difficulty meeting the requirements of future data storage device development. The developing resistive random-access memory (RRAM) has sparked intense investigation because of its simple two-terminal structure: two electrodes and a switching layer. RRAM has a resistive switching phenomenon which is a cycling behavior between the high resistance state and the low resistance state. This developing device type is projected to outperform traditional memory devices. Indium gallium zinc oxide (IGZO) has attracted great attention for the RRAM switching layer because of its high transparency and high atomic diffusion property of oxygen atoms. More importantly, by controlling the oxygen ratio in the sputter gas, its electrical properties can be easily tuned. The IGZO has been applied to the thin-film transistor (TFT), thus, it is very promising to integrate RRAM with TFT.
In this work, we proposed IGZO-based RRAMs. ITO was chosen as the bottom electrode towards achieving a fully transparent memristor. And for the IGZO switching layer, we varied the O_2/Ar ratio during the deposition to modify the oxygen vacancy of IGZO. Through the XPS measurement, we confirmed that the higher O_2/Ar ratio can lower the oxygen vacancy concentration and lower the ratio. We also chose ITO as the top electrode, and also, for the comparison, two active metals copper and silver were tested for the top electrode materials. For our IGZO layer, the best ratio of O_2/Ar is the middle value. And copper top electrode device has the most stable cycling switching and the silver one is perfect for large memory window, however, it encounters a stability issue. The optical transmission examination was performed using a UV-Vis spectrometer, and the average transmittance of the complete devices in the visible-light wavelength range was greater than 90%, indicating good transparency. 50nm, 100nm, and 150nm RS layers of IGZO RRAM were produced to explore the thickness dependency on the characteristics of the RS layer. Also, because the oxygen vacancy concentration influences the RS and RRAM performance, the oxygen partial pressure during IGZO sputtering was modified to maximize the property. Electrode selection is critical and can have a significant influence on the device's overall performance. As a result, Cu TE was chosen for our second type of device because Cu ion diffusion can aid in the development of conductive filaments (CF). Finally, between the TE and RS layers, a 5 nm SiO2 barrier layer was used to limit Cu penetration into the RS layer. Simultaneously, this SiO2 inserting layer can offer extra interfacial series resistance in the device, lowering the off current and, as a result, improving the on/off ratio and overall performance.
In conclusion, transparent IGZO-based RRAMs have been created. The thickness of the RS layer and the sputtering conditions of the RS layer were modified to tailor the property of the RS layer. A series of TE materials and a barrier layer were incorporated into an IGZO-based RRAM and the performance was evaluated in order to design the TE material's diffusion capabilities to the RS layer and the BE. Our positive findings show that IGZO is a potential material for RRAM applications and overcoming the existing memory technology limitation.

9:20 AM CC04
(Student) SiOx Nanorod Memristive Neuron for Probabilistic Inference Applications Sanghyeon Choi[1], Gwang Su Kim[1,2], Jehyeon Yang[1], Haein Cho[1], Chong-Yun Kang[1,2] and Gunuk Wang[1]; [1]Korea University, Korea (the Republic of); [2]Korea Institute of Science and Technology (KIST), Korea (the Republic of)

Memristor, which simply consists of a switching layer inserted between two electrodes, is one of the most strong candidates to become a device-platform for imitating the principal characteristics of the biological neural network due to its nonlinear and dynamic electrical characteristics depending on the history of applied electrical programming [1-3]. In this study, we fabricated a SiO_x nanorod memristor using E-beam evaporator with glancing angle deposition at the wafer-scale and utilized the device as an artificial neuron for probabilistic computing applications [4]. Notably, the SiO_x nanorod structure provides the random distribution of multiple nanopores all across the active area, capable of forming a multitude of Si filaments at many SiO_x nanorod edges after the electromigration process. This can facilitate probabilistic switching that can mimic integrate-and-fire signaling and the stochastic dynamics of biological neurons with very high dynamic range ($\sim 5.15 \times 10^{10}$) and low energy (~4.06 pJ). Different probabilistic activation (*ProbAct*) functions in a sigmoid form are implemented, showing its controllability with low variation by manufacturing and electrical programming schemes. Then, as a proof of concept, based on the suggested memristive neuron, we demonstrated the self-resting neural operation with local circuit configuration and revealed the probabilistic Bayesian inferences for genetic regulatory networks with low errors ($< \sim 2.41 \times 10^{-2}$) with its robustness to the *ProbAct* variation. Taken all together, our study shows the availability of the designed SiO_x nanorod memristive neuron for probabilistic neural networks that can be efficiently used for a variety of uncertainty quantification problems.

References [1] S. Choi, J.-W. Choi, J. C. Kim, H. Y. Jeong, J. Shin, S. Jang, S. Ham, N.-D. Kim, and G. Wang, *Nano Energy*, 84, 105947 (2021)
[2] S. Choi, J. Yang, G. Wang, *Adv. Mater.*, 32, 2004659 (2020)
[3] S. Choi, S. Jang, J.-H. Moon, J. C. Kim, H. Y. Jeong, P. Jang, K.-J. Lee, and G. Wang. *NPG Asia Mater.* 10, 1097–1106 (2018)
[4] S. Choi G. S. Kim, J. Yang, H. Cho, C. –Y. Kang and G. Wang, *Adv. Mater.,* 34, 2104598 (2022)

9:40 AM CC05
(Late News) Silicon Carbide Growth Reaction Engineering for Quantum Sensing—Impact of Thermodynamic Model Uncertainty on Product Distributions Joshua Gabriel and Angel Yanguas-Gil; Argonne National Laboratory, United States

Finding optimal growth conditions for the step-flow growth of silicon carbide, using the economical silane-alkane-hydrogen process towards quantum sensing applications, with minimal deleterious by-products such as silicon droplet formation, requires understanding the thermodynamic properties of key intermediate mixtures formed along the reaction sequence. Owing to the complexities of the high-temperature process, there is a lack of direct observation of whether silicon droplets are formed or not for a given reaction precursor mixture and temperature. Reaction kinetics simulations are hence used to predict the formation of droplets using available thermodynamic and kinetic property predictions for the reactants, intermediates, and products, sourced from thermodynamic function tables such as the NASA9 heat capacity polynomial. However, the coefficients for the NASA9 polynomial are derived from room temperature experimental heat capacity measurements and high-temperature heat capacity computations/estimations using calculated vibrational spectra [1]. While the current models predict product distributions for targeting silicon carbide growth from a mixture of alkanes and silanes, they lack in quantifying the reliability of predictions at temperatures where there are no experimental measurements. In this work, Bayesian inference is used to estimate the posterior distributions for the parameters of the Gibbs free energy of reaction that can be derived from the NASA9 polynomial parameters for the heat capacity, and hence through uncertainty propagation, provide the uncertainty associated with the Gibbs free energy of reaction for each reaction in a reaction network for silicon carbide growth. Finally, the uncertainty or range of equilibrium concentration of the species are estimated through reaction kinetics simulations with Cantera and compared with the indicators of silicon droplet formation observed via *in situ* X-ray diffraction studies.
[1] Burcat and Goos, https://doi.org/10.1002/kin.21188

10:00 AM Refreshment Break

10:20 AM CC06
(Student) A Low-Power, Bio-inspired, Adaptive Machine Vision Based on Atomically Thin Memtransistors Akhil Dodda, Darsith Jayachandran, Andrew L. Pannone, Yikai Zheng, Abu M. M Abdullah, Shiva S. Radhakrishnan, Nicholas Trainor, Joan M. Redwing and Saptarshi Das; The Pennsylvania State University, United States

With the rapid advancements of information technology, the internet of things (IoT), and their integration; machine vision systems have become a crucial component in autonomous driving, robotics, security, autonomous production, and other domains. However, with the increase in the volume of data, new requirements are put-forward on the traditional hardware vision systems. Conventional hardware vision platforms rely on von Neumann architectures and consume an enormous amount of energy while transmitting the data between processing and memory units, thereby, necessitating the need for innovation in device design, material discovery, and novel hardware architectures to bridge the physical gap between the sensor, processor, and memory units. Acknowledging these limitations and deriving inspiration from the human visual system, we here propose and experimentally demonstrate a low-power, bio-inspired hardware vision platform based on a monolayer MoS_2 memtransistor array. We have fabricated a 30×30 fully integrated memtransistor crossbar array to dynamically sense, store, and forget the input optical information. The memtransistors are locally back-gated using a gate-dielectric stack comprising of atomic layer deposition (ALD) grown 50 nm Al_2O_3 on sputter-deposited 50/20 nm Pt/TiN. All the back-gate islands were placed on a commercially purchased SiO_2/p^{++}-si substrate. Our entire hardware platform utilizes a total of 900 MoS_2 FETs, where each transistor carries individual pixel information. We exploit the phenomenon of gate-tunable persistent photoconductivity or optical memory in MoS_2 phototransistors to sense and store visual information. We demonstrate the reliability of our monolayer MoS_2 memtransistors by showing little-to-no variation in the photoresponse across 100 devices. Leveraging the merits of gate-tunable persistent photoconductivity we also demonstrate a record-high responsivity of $\sim 3.6\times 10^7$ A/W and a record-high detectivity of $\sim 5.6\times 10^{13}$ Jones. Furthermore, we demonstrate analog level learning to different illumination wavelengths and learning adaptation to different illumination intensities and illumination wavelengths in the visible spectrum. In addition to persistent photoconductivity, we exploit the gate-voltage induced analog and non-volatile threshold voltage shift in MoS_2 memtransistors for gradual or immediate forgetting of the stored information. By combining optical learning and electrical forgetting we demonstrate dynamic learning and relearning of the input patterns sensed from external visual stimuli. Finally, we show the efficacy of our learning and forgetting mechanism under the high signal-to-noise ratio condition. Overall, in performing the learning, relearning, and forgetting mechanisms the amount of energy consumed was found to be a few tens of nano Joules highlighting the benefits of our

hardware vision platform for designing next-generation machine intelligent systems.

10:40 AM CC07
(Student) Spike-Timing Based Adaptive Photo Encoder Considering Monolayer MoS_2 Based Memtransistors Dipanjan Sen, Shiva S. Radhakrishnan, Shakya Chakrabarti, Mayukh Das, Thomas Schranghamer, Amritanand Sebastian and Saptarshi Das; The Pennsylvania State University, United States

Bio-inspired devices and systems have effectively showed its potential in the current era of neuromorphic chips. Moreover, it has also depicted the capability to bridge the gap between natural and artificial intelligence. It must be highlighted that imitating the functionalities of a brain paves the way for smart computing with an intent to solve complex problems. In this context, the spiking neural networks (SNNs) have captured a lot of attention as it mimics the processing of information with minimum energy consumption and faster inference. Note that, the SNNs tend to convert the external stimuli into corresponding spike trains by exploiting some afferent neurons. Here, we have designed and fabricated an optoelectronic integrated circuit comprising of 21 memtransistors based on monolayer MoS_2 for spike-timing dependent photo encoding. In addition to this, we have demonstrated that the different illumination intensities can be efficiently encoded into spike trains, where the time to the first spike determines the strength of the visual stimuli, i.e., higher illumination intensity generates earlier spikes and vice versa. Furthermore, the non-volatile storage and electrical programming capability of the photo sensitive memtransistors enables the encoder for photo encoding with controlled adaptivity that allows accelerated spike trains under low light condition and delayed spike trains under higher illumination intensities, respectively. Therefore, it can be inferred that our demonstration of the spike-timing based photo encoder exploiting the 2D memtransistors can be transformative for cutting-edge neuromorphic applications.

11:00 AM CC08
(Student) Ultralow-Power Photoactivated Spiking Silicon Neurons Ragib Ahsan, Hyun Uk Chae and Rehan Kapadia; University of Southern California, United States

Human brains can perform complex computations with an unparalleled power efficiency that exceeds state-of-the-art digital computers by ~100,000 times. The spiking neurons in the brain are instrumental to achieving such extraordinary efficiency. There has been a great amount of effort put into emulating the spiking behavior of spiking neurons recently thanks to the emergence of memristors. Relaxation oscillators closely mimic the spiking action potentials. There are 3 different approaches to making these relaxation oscillators: (1) using metal-insulator transition (MIT) memristors, (2) using ferroelectric field-effect transistors (FeFET), and (3) using CMOS based circuit techniques. Here, we have fabricated and characterized a silicon-graphene photodiode that shows a photoactivated voltage-controlled negative differential resistance (NDR) behavior that can generate spiking oscillations when connected to an active inductor. This oscillator marks a new fourth approach to generating spiking neural behavior and the first approach ever that shows photoactivated neural oscillations emulating the behavior of retinal neurons that also with an unprecedented power efficiency that exceeds that of biological neurons and other artificial ones. The core of our neuron is made of a silicon-graphene photodiode. We have taken a moderately doped (5e15 cm^{-3}) p-Si wafer, photolithographically defined and deposited a 65 nm thick Au-Ti metal mesh on top of the silicon. Monolayer graphene is then transferred on top of the mesh using the wet transfer method. Then we have sputtered a 100 nm Al film on the backside of silicon. The top Au-Ti mesh and bottom Al film act as the two contacts to the device. The active area of this device is 0.25 cm^2. This silicon-graphene photodiode shows a light-activated NDR behavior. In order to generate oscillating behavior, a voltage-controlled NDR device needs to be connected to an inductive circuit element. This is analogous to the relaxation oscillation behavior observed in a current-controlled NDR device when connected to a capacitor. However, fabrication of inductors in CMOS processes is area inefficient and presents further scaling issues. Therefore, we have adopted an active inductor topology called Hara active inductor. A Hara inductor consists of a resistor and a MOSFET. The photodiode is then connected to a Hara inductor and generates a spiking oscillation with an amplitude of 0.32V and frequency of 558 Hz only under optical illumination. The only source of electrical power dissipation in this circuit is the resistor R connected in series to the gate of the MOSFET. We have simultaneously measured the current through this resistor and calculated the electrical power consumption to be ~50 nW which translates into an electrical power density of ~2 fW/ μm^2 which is ~1400 times smaller than the current state-of-the-art spiking neuron made in CMOS technology. We have fabricated devices with an active area from 600 μm^2 to 1 cm^2 covering almost 6 orders of device sizes. Our measurements have shown that all of them show spiking behavior under optical illumination. Our modeling approaches have further shown that it is possible to scale this neuron down to 1 μm^2 and generate 100 Hz oscillations under 1.3 pW light illumination with an electrical power cost of ~10 aW. While our measurements show already an extraordinarily small power cost for these neurons, the potential to make photoactivated spiking neurons with attowatts of power cost makes our approach one of the most promising ones yet discovered.

11:20 AM CC09
Atomic Layer Deposition of Antimony(III) Telluride James C. Carter, Ian Campbell, Ama Agyapong and Suzanne E. Mohney; The Pennsylvania State University, United States

Antimony(III) telluride has a layered structure with van der Waals bonds between Te atoms in adjacent quintuple layers. It is interesting as a topological insulator and because it is a component of phase-change alloys. We have performed atomic layer deposition of Sb_2Te_3 using bis(trimethylsilyl)tellurium and antimony(III) ethoxide, which are previously reported complementary precursors.[1] Bis(triethylsilyl)tellurium was also used in some experiments. In this work, we studied growth on a variety of substrates using different surface preparations. Growth of a continuous layer with few cycles is highly dependent on the starting surface. On SiO_2, incompletely coalesced islands were observed by scanning electron microscopy even after 500 cycles, and the samples remained insulating when four-point probe measurements were performed. Conversely, continuous Sb_2Te_3 film growth was observed after 500 cycles on amorphous GeTe, single-crystal Bi_2Te_3, and polycrystalline TiN films, only when subjected *in situ* to a remote Ar plasma before growth. X-ray photoelectron spectroscopy confirmed the presence of Sb and Te with $3d_{5/2}$ core levels near 527 eV and 572 eV, respectively. Compared to Sb_2Te_3 reference spectra, the ratio of intensities also matches the expected stoichiometry. Moreover, the sheet resistance of amorphous GeTe and polycrystalline TiN samples also dropped noticeably. We will further consider atomic layer epitaxy of Sb2Te3 in upcoming experiments. The authors are grateful to ONR N0014-18-12511 for support and Penn State's 2DCC through DMR-1539916 for epitaxial substrates.
1. Eom et al., Chem. Mater. 24, 2099, 2012

11:40 AM CC10
(Student, Late News) Electrochemical Additive Manufacturing Producing Composite Materials for Electronics Wondwosen F. Demisse, Pawan Tyagi and Eva Mutunga; University of the District of Columbia, United States

Due to tremendous potential to deliver unique features, not attainable by traditional manufacturing methods, 3D printed

electronics have caught the interest of industry and researchers in recent years. This new technology has the potential to revolutionize electronics device design and manufacturing methods. 3D printing involving porous conducting materials, composite materials with metal and polymer components, and microscopic particles encapsulated in copper like thin films can lead to new set of materials. Although multi-material additive manufacturing has advanced significantly in recent years, little progress has been made in the additive manufacturing of hybrid components. Here we discuss a low temperature 3D hybrid material printing method that can yield novel composite materials for futuristic computer hardware. We investigated electrochemical additive manufacturing(ECAM) method. The basic working principle of the ECAM machine we are developing is based on the transport of metal particles from ionic solution to the substrate covered with microscopic metallic powder. Metallic powder is dispersed on the substrate by a custom designed nozzle that serves two purposes: (a) control the metal particle dispersion rate on to the substrate, and (b) serve as the counter electrode to provide bonding between metal powders via electrodeposition. For example, ECAM can disperse ~10-50 µm nickel powder and produce copper thin film coating among particles. This approach creates a multi material composite at fast rate. A vast range of materials are possible via ECAM that can be tested for variety of computer heat control systems and other applications. These materials can also produce radiation and electro-magnetic protection casings for the application of computer hardware in challenging environments.

SESSION DD: Group III-Nitrides—Contacts and Novel Devices

Session Chair: Christian Wetzel
Friday Morning, July 1, 2022
Great Hall Meeting Room 3

8:20 AM DD01
(Student) Role of Point Defects and Compensation in the Formation of Ohmic Contacts to Mg-Doped GaN Cristyan E. Quiñones García[1], Pegah Bagheri[1], Ji Hyun Kim[1], Dolar Khachariya[2], Ronny Kirste[2], Pramod Reddy[2], Seiji Mita[2], Erhard Kohn[1], Ramón Collazo[1] and Zlatko Sitar[1,2]; [1]North Carolina State University, United States; [2]Adroit Materials, United States

In order to obtain low resistance ohmic contacts to p-type semiconductors, large ionized acceptor densities are required. This is difficult to achieve in GaN, as increasing the acceptor Mg concentration past a certain point (called the “knee behavior”) induces the formation of compensating point defects which reduce the net ionized charge, N_A-N_D. This is known as self-compensation and is usually attributed to the formation of charged nitrogen vacancies (V_N), which act as donor-like defects. Therefore, in order to understand the formation of and achieve ohmic contacts to p-type GaN, a thorough understanding and control over the formation of compensating point defects in the high doping regime is necessary.
In this work we demonstrate that improved ohmic contacts to p-type GaN can be achieved by suppressing the formation of V_N via systematic chemical potential control (CPC) based point defect control. Accordingly, Mg-doped GaN samples were grown with V/III ratios varying from 200 to 8000 by increasing ammonia flow. By growing with higher V/III ratios through higher ammonia partial pressures, we provide nitrogen-richer conditions and consequently increase the chemical potential of nitrogen, and the formation energy of V_N. This reduces V_N incorporation and shifts the onset of the self-compensation towards higher Mg concentrations as evidenced via photoluminescence (PL) measurements.
Transmission line model (TLM) was used to analyze Ni/Au contacts to p-type GaN grown under these high V/III ratios. The specific contact resistance and threshold voltages were accordingly extracted using a method for analyzing non-ohmic contacts described by Sarkar et al[1]. The alloyed contacts to samples grown at high V/III consistently showed lower contact resistance and threshold voltages with increasing Mg concentration. In fact, contacts with a threshold voltage of ~0 V were only obtained for samples grown with large V/III ratios, suggesting that the suppression of V_N formation is necessary.
Finally, we demonstrate that by growing a thin, heavily doped ([Mg] > $8x10^{19}$ cm^{-3}) GaN layer with V_N control on a more lightly doped ([Mg]~$2x10^{19}$ cm^{-3}) p-GaN layer, better ohmic contacts are achieved. Using reactive-ion etching (RIE) to expose the lower layer, TLM measurements were performed on both as grown and etched surfaces. The extracted threshold voltages and specific contact resistances on each of the individual layers clearly demonstrate that improved ohmic contacts are achieved by incorporating the heavily Mg-doped, V_N controlled GaN layer. Potential application of these contacts to UV optoelectronics devices will be discussed.
References
1. Sarkar, B. *et al.* On Ni/Au Alloyed Contacts to Mg-Doped GaN. *J. Electron. Mater.* **47**, 305–311 (2018).

8:40 AM DD02
Effect of Rhenium Layer Thickness and Annealing Temperature on the Surface Microstructure of Re-Al-Ni-Au Based Ohmic Contacts on n-Type GaN Amit P. Shah, Bhagyashri Chalke, Vilas Mhatre and Arnab Bhattacharya; Tata Institute of Fundamental Research, India

Low specific contact resistivity ohmic contacts (ρ_c~10^{-6} Ω-cm^2) with thermal and chemical stability play an important role in III-nitrides based optoelectronic, high temperature and high frequency devices. A Ti/Al/Ni/Au based multilayer metallization is the most commonly used scheme and requires high temperatures (>800ºC) to form reliable ohmic contacts. High temperature annealing can result in intermixing in the multi-quantum-well layers and introduce additional defects. There are very few reports on the microstructure analysis of the ohmic contacts formed on n-GaN substrates[1].
Low specific contact resistivity ohmic contacts (ρ_c<10^{-7} Ω-cm^2) were formed on n-GaN using Re-Al-Ni-Au based multilayer metallization [2]. In this work, we report the effect of rhenium (Re) layer thickness and annealing temperature on the microstructure of such Re-Al-Ni-Au based contacts. Several samples with Re thicknesses (10, 30, 60 nm) were prepared and annealed at 550ºC, 650ºC and 750ºC temperatures. The resistivity was estimated using C-TLM measurements while AFM, GIXRD and SEM equipped with EDS were used to analyze the chemical composition and microstructure characteristics of the ohmic contacts.
For the sample with Re~30 nm thickness annealed at 650ºC, 40 µm x 40 µm AFM scans show numerous islands with sizes up to 3 µm and average height of ~400-450 nm, much higher than the original metal stack thickness of 290 nm (Re, Al, Ni and Au~30, 100, 60 and 100 nm respectively). The RMS roughness is ~90 nm. We surmise that the islands are formed due to segregation of the metals.
For the sample with Re~30 nm thickness annealed at 650ºC, the GIXRD profile shows several diffraction peaks corresponding to known inter-metallic phases of alloys of the Re-Al, Re-Ni-Al and Al-Au systems, indicating that there is a considerable intermixing of the metal layers. The diffraction peaks observed are mainly from different phases such as $ReNi_2Al_{7.967}$, Al_6Re, $AlAu_2$ and Al_2Au_5. We observe the same phases in other samples with different rhenium thickness and annealed at different temperatures. We believe that these inter-metallic phases are responsible for the lowering of the barrier height Φ_B, and hence the reduction of

contact resistance. We have not observed any peak related to the phase $AlAu_4$, which seems to be responsible for the lateral flow of the metal.
Energy dispersive spectroscopy (EDS) maps of the elements – rhenium, aluminum, nickel and gold – present in the metal stack were obtained to evaluate the spatial elemental distribution over the contact area. For the sample with Re~30 nm thickness annealed at 650°C, the SEM image of the annealed metal contact shows three distinct regions; region-A: dark isolated rectangular agglomerates, region-B: white layer surrounding the agglomerates and region-C: grey colored background. From the corresponding EDX chemical analysis for Re, Al, Ni and Au respectively, we observe that during annealing near the temperature where Al becomes liquid (660°C), the Al starts forming droplets which dissolves Ni to form crystalline Ni-Al alloy agglomerates (region-A). Due to migration of the agglomerates on the surface and coalescence, we get various sizes of isolated agglomerates distributed over the surface. The top Au layer cracks and accumulate around these agglomerates to from Al-Au alloy (region-B). The background consists of all the four metals (region-C). The contrast seen in the Re signal is likely to be influenced by the uneven thickness of the overlying agglomerates and the Al-Au alloy. The RMS roughness increase with temperature can be attributed to the formation, migration and coalescence of Al-Ni agglomerates.

References:

[1] W. Macherzynski et al., *Optica Applicata*, **XLIII**, 67 (2013).
[2] A. P. Shah, A. Bhattacharya, 3562012 - 63rd Electronic Materials Conference (Virtual), June 2021.

9:00 AM DD03

Development of Low Resistance Ohmic Contacts with Bilayer Ni/Al-Doped ZnO Thin Films to *p*-Type GaN Taoufik Slimani Tlemcani[1], Clément Mauduit[1], Matthew Charles[2], Romain Gwoziecki[2], Arnaud Yvon[3] and Daniel Alquier[1]; [1]GREMAN Laboratory, Tours University, France; [2]Univ. Grenoble Alpes, CEA, LETI, France; [3]STMicroelectronics, France, France

The fabrication of low-resistance and thermally stable Ohmic contacts is essential for the fabrication of reliable GaN power devices. In the particular case of the *p*-type GaN, a thin Ni/Au bilayer is commonly used for Ohmic contacts. However, Au metal contacts are quite expensive, incompatible with the complementary metal-oxide-semiconductor (CMOS) foundries and also have poor thermal stability. Thus, seeking an alternative that is affordable and thermally stable is crucial. In the present study, we investigate Au-free Ohmic contact formation on *p*-type GaN using a bilayer Ni/Al-doped ZnO (AZO) thin film. The Ni/AZO thin films were prepared by thermal evaporation and radio frequency (RF) magnetron sputtering, respectively. Careful studies were focused on identifying the role of process parameters such as layer thicknesses and annealing parameters: time, temperature and atmosphere in order to obtain an excellent Ohmic contact on *p*-GaN. Interestingly, structural, morphological and electrical properties of the Ni/AZO contacts deposited on the *p*-type GaN layer were analyzed in detail using X-ray diffraction (XRD), transmission electron microscopy (TEM) as well as circular transfer length model (c-TLM) techniques, respectively. Our results show that the contact resistance can be significantly reduced using an AZO/Ni bilayer with a suitable rapid thermal process. We demonstrate that specific contact resistance for AZO/Ni on *p*-GaN can reach a lowest value of 1.85×10^{-4} Ω.cm^2 for a sample annealed at 500°C in air ambient for 5 min with a 5 nm Ni layer. These results present also methods for improving the electrical properties of the contacts to *p*-GaN. Our work demonstrate that the bilayer Ni/AZO contact could be a suitable scheme for efficient GaN power diodes.

9:20 AM DD04

(Student, Late News) HTOL Reliability of Novel Re-GaN Schottky Diodes Nathaniel O'Neal[1], Alex Molina[2], Guillermo Passrobles[3], Alexander Mund[1], Burnell Clemmer[1], Matthew A. Porter[1], Christopher Martino[3], Todd R. Weatherford[1] and Suzanne Mohney[2]; [1]Naval Postgraduate School, United States; [2]The Pennsylvania State University, United States; [3]U.S. Naval Academy, United States

Vertical power devices fabricated on native bulk GaN substrates have demonstrated performance comparable to SiC power devices in recent research. While continuing improvements have been achieved in substrate quality and device performance characteristics, little research has been carried out on the reliability of metal-semiconductor interfaces under the levels of high current stress expected in power device operation. This work examines the reliability of Re-GaN Schottky interfaces under high current stress. Research on thermal stability of Re-GaN Schottky contacts through thermal annealing studies has shown that the barrier height of the contact is not reduced by annealing conditions up to 600 C, in contrast to more commonly used Pd-GaN contacts which degrade significantly in barrier height after similar thermal conditions. This stability makes Re-GaN a prime candidate for a Schottky contact with high stability under high current stress conditions, under which self-heating at the junction is expected to be significant. To carry out experimental studies, n-type GaN epitaxial layers were grown via MOCVD to a doping level of 2×10^{16} cm^{-3} and a thickness of 11 um atop a n+ doped bulk GaN substrate. Re Schottky diodes were fabricated via e-beam deposition of Re followed by electroplating with 1 um of Au. Die were singulated and packaged on DBC Al_2O_3 ceramic substrates for testing. Testing under high temperature operating life (HTOL) conditions was performed using a novel automated stress-measure-stress system enabling time dependent measurements of the diode characteristics via IVT characterization. Devices were initially stressed under a time-dependent step-stress regime, in which the stress current density was stepped from 950 A/cm^2 to 2000 A/cm^2 in 150 A/cm^2 steps, and held at the stress current at each step for 6 hours and a package temperature of 30 °C. Step-stress testing showed that the barrier height of the Schottky contacts remained stable with less than 1% degradation up to a stress current density of 1600 A/cm^2, after which the barrier height degraded quickly by over 10% from a maximum of 0.8 eV. The ideality factor of the diode also degraded by 13% to a maximum of 1.3 above this stress current. Constant stress-measure-stress HTOL testing was also performed at current densities of 1500 A/cm^2, 1600 A/cm^2, 1700 A/cm^2, 1800 A/cm^2 and 2000 A/cm^2 at fixed package temperatures for a stress period of over 90 hours. The contact barrier height was found to remain stable for 1500-1700 A/cm^2 tests, while degrading by 16% and 11% for the 1800 A/cm^2 test. It was found that the degradation rate was not constant but changed rapidly at a time dependent upon the magnitude of the current density. There is also a degree of variation among the devices leading to these rates nonuniformly increasing. Subsequent tests will include HTOL testing on similarly fabricated Pd-GaN diodes as a basis for comparison. Based upon these results, Re-GaN Schottky contacts show promising stability under high current density stress conditions and are a prime candidate for Schottky contacts in large area vertical GaN power devices.

9:40 AM DD05

(Student, Late News) N-Polar GaN HEMTs with ALD HfO_2 as Gate Dielectric Subhajit Mohanty[1], Zhe Ashley Jian[1], Kamruzzaman Khan[2] and Elaheh Ahmadi[1]; [1]University of Michigan, Ann Arbor, United States; [2]University of Michigan–Ann Arbor, United States

High power efficiency over wide range of frequency range has established GaN-based high electron mobility transistors (HEMTs) de-facto standard for RF power amplifiers in radars and high

frequency applications [1]. N-polar GaN has a natural back-barrier which offers several advantages over Ga-polar counterpart such as better 2DEG confinement, improved ohmic contact, output resistance and pinch-off characteristics [2]. Moreover, the frequency of operation can be increased by reducing gate length which requires reducing GaN channel thickness proportionately to maintain aspect ratio to suppress short-channel effects [2]. This scaling down typically leads to higher gate leakage current which can be suppressed by inserting a thick insulator layer between channel and gate metal. High-k dielectrics such as HfO_2 with thick dielectric can be deposited without altering the gate capacitance. In this work, we demonstrate an N-polar HEMT with regrown contacts and implanted mesa isolation which exhibits low leakage and DC-RF dispersion.
MOCVD-grown N-polar GaN HEMT structure commercially available from Transphorm Inc., was used for this study [3]. SiO_2 and Al_2O_3 were used as the hard mask and etch stop to define the regrown area and a UID-GaN/n^+ GaN was regrown in source/drain regions to minimize ohmic contact resistance. Device isolation was achieved by ion implantation with Aluminum to form high-resistive region between devices. Then, the sample underwent a sequence of wet cleaning, UV-ozone conditioning and in-situ ALD plasma treatment prior to deposition of thermal ALD HfO_2. HfO_2 was removed under the contact area using a BCl_3-based dry etch and a hydrochloric acid wet etch was performed immediately before 30/200 nm of Ti/Au deposition by electron-beam evaporation. A very low Metal-to-GaN contact resistance of 0.1 Ω-mm was measured from un-passivated Transfer Length Method (TLM) with sheet resistance (R_{sh}) of 282 Ω/sq. Finally, 30/420 nm of Ti/Au optical gate and contact pads were patterned via liftoff followed by 120 nm PECVD SiN passivation.
A combination of a capacitance-voltage (C-V) measurement and gated TLMs (GTLMs) on passivated structure exhibited a 2DEG density of 1.38×10^{13} cm^{-2} with R_{sh} of 320 Ω/sq, and mobility (μ) of 1416 cm^2/V-s at $V_G = 0$ V. DC measurements were performed on device with $W_G = 2 \times 50$ μm, $L_G = 500$ nm, $L_{GS} = 400$ nm, $L_{GD} = 2.4$ μm. The output characteristics demonstrated a maximum I_{DS} of 1.02 A/mm and an ON-resistance (R_{ON}) of 1.28 Ω-mm at $V_{GS} = 0$ V. The transfer characteristics showed a peak trans-conductance (g_m) of 254 mS/mm, pinch-off voltage (V_P) of -7.3 V and a subthreshold swing of 135.7 mV/dec at $V_{DS} = 3$ V. The device revealed an OFF-state current of 1.5×10^{-7} A/mm at $V_{DS} = 3$V with $I_{ON}/I_{OFF} = 7.6 \times 10^6$. The gate leakage current was very low (~10 nA/mm) which increases to 200 nA/mm with an increase in $V_{GD} = 13$V. The device exhibited decent DC-RF dispersion indicating presence of surface traps between gate-drain region. The small-signal RF results were obtained using a Keysight N5247B network analyzer calibrated to the probe tips via a Short-Open-Load-Thru (SOLT) calibration method from an off-wafer impedance substrate standard. The device demonstrated a peak $f_T = 19.1$ GHz (f_T*L_G = 9.55 GHz-μm) at V_{DS}= 10V and V_{GS} = -3V and a peak f_{max} = 69.5 GHz at V_{DS} = 11V and V_{GS} = -4V. HfO_2 gate insulator is effective in suppressing the gate leakage which shows promises for ultra-thin channel high-aspect ratio HEMT devices for high frequency applications.

[1] U. K. Mishra et al., *Proc. IEEE*, vol. 96, no. 2, pp. 287–305, Feb. 2008.
[2] M. H. Wong *et al.*, *Semicond. Sci. Technol.*, vol. 28, no. 7, p. 074009, Jul. 2013.
[3] D. Bisi *et al.*, *2021 IEEE 8th Workshop on Wide Bandgap Power Devices and Applications (WiPDA)*, 2021, pp. 250–254.

10:00 AM Refreshment Break

10:20 AM DD06
(Student) N-Polar GaN Photocathodes Stabilized with h-BN

Emma Rocco[1], Vincent E. Meyers[1], Benjamin McEwen[1], L. D. Bell[2] and Fatemeh (Shadi) Shahedipour-Sandvik[1]; [1]SUNY Polytechnic Institute, United States; [2]California Institute of Technology, United States

III-nitride photocathode detectors provide picosecond response, low noise, single photon detection across a broad spectrum spanning from IR to UV wavelengths. N-polar III-nitride photocathodes have shown particular promise in simulation as well as experiment due to positive surface charge produced by the structure depletion and polarization. However, the N-polar surface is challenged by a thicker native oxide, and N-polar photocathodes must be etched using HCl to remove this oxide prior to measurement or packaging.
Surface encapsulation with 2D materials have previously been proposed for alkali photocathodes. 2D materials are advantageous as they are molecularly impermeable, allowing surface stabilization without detrimental widening of the surface potential well. Simulations of Cs_3Sb photocathodes with BN suggest improved quantum efficiency due to the smaller work function of BN compared to the Cs_3Sb bulk. Surface stabilization with 2D materials have also been shown experimentally with graphene coatings on K_2CsSb and Cu photocathodes.
Monolayer hexagonal (h-)BN surface stabilization of N-polar GaN photocathodes is reported here for the first time.
N-polar GaN photocathodes consisting of 450 nm p-GaN/10 nm u-GaN cap were grown via metal organic chemical vapor deposition (MOCVD). The photocathode was cleaned in HCl to remove surface oxide and contaminants immediately prior to placement of monolayer h-BN on the surface through a wet transfer process. A control sample of N-polar GaN photocathode without h-BN stabilizing layer was studied, also utilizing HCl cleaning prior to photoemission measurement. The control sample exhibited a quantum efficiency of 1.9% at 6 eV incident photon energy. For similar N-polar GaN photocathodes, QE decays in efficiency due to air exposure almost immediately following HCl cleaning, with a percent change of -96% after 10 days to ~0.15%. The photocathode terminated with h-BN exhibited a maximum QE of 0.4% at 6 eV photon energy, due to the addition of the h-BN layer. While the initial maximum QE is lower the QE decay is markedly slower, with a percent change of -50% after 10 days in air—an improvement in the degradation rate by a factor of x12.5. The decreased QE of h-BN capped photocathode after air exposure may be the result of incomplete coverage or damage to the h-BN layer. X-ray photoelectron spectroscopy shows lower coverage of oxygen and carbon on the h-BN sample after air exposure, compared to the bare GaN photocathode sample. This result shows proof of concept for stabilizing N-polar III-nitride photocathodes with 2D h-BN. Development of the wet transfer process of h-BN to N-polar GaN photocathodes will also be discussed.

10:40 AM DD07
(Student) Pulsed-Mode MOCVD Growth of ZnSn(Ga)N2 and Determination of the Valence Band Offset with GaN

Kaitian Zhang[1], Chenxi Hu[2], A F M Anhar Uddin Bhuiyan[1], Menglin Zhu[1], Vijay G. Thirupakuzi Vangipuram[1], Md Rezaul Karim[1], Benthara H. Jayatunga[2], Jinwoo Hwang[1], Kathleen Kash[2] and Hongping Zhao[1,1]; [1]The Ohio State University, United States; [2]Case Western Reserve University, United States

Orthorhombic $ZnSnN_2$ is analogous to wurtzite GaN, with a doubled unit cell and cation sites replaced by Zn and Sn. Cation-disordered $ZnSnN_2$ exhibits wurtzitic symmetry. Both phases can in principle be integrated with III-nitride heterostructures. The concept of type-II InGaN-$ZnSnN_2$ quantum wells (QWs) was proposed as an active region for high-efficiency amber light emitting diodes (LEDs) [1]. To achieve the predicted performance, high quality $ZnSnN_2$ and $ZnSnN_2$/InGaN heterostructures must be

developed. However, efforts on the growth of $ZnSnN_2$ by MOCVD are still very limited. Our previous studies have shown that the MOCVD growth window of $ZnSnN_2$, particularly temperature, is limited, and Sn droplets form readily at the higher growth temperatures.

In this work, pulsed-mode MOCVD growth of $ZnSn(Ga)N_2$ on GaN-on-sapphire templates was investigated. DEZn, TMSn, TMGa and ammonia were used as the precursors for Zn, Sn, Ga and N, respectively. Unintentionally doped GaN (uGaN) regrowth at 975 °C and a chamber pressure of 200 Torr was done prior to the $ZnSn(Ga)N_2$ growth. For the $ZnSn(Ga)N_2$ growth, the TMGa and NH_3 molar flow rates were 90.6 µmol/min and 178 µmol/min, respectively, the reactor pressure was 500 Torr, and growth temperature varied from 560 °C to 580 °C. The DEZn, TMSn and NH_3 molar flow rates were 36.6 µmol/min, 36.5 µmol/min and 201 µmol/min, respectively. It was found that GaN was unintentionally incorporated into the films, which were intended to be pure $ZnSnN_2$.

For the TMSn pulsed-mode growth, the TMSn flow was pulsed periodically while the flow rates of DEZn and NH_3 were kept constant, as shown in Figure 1. While the DEZn and NH_3 were kept at constant flow rates, the TMSn flow rate was controlled with t_{ON} (flowing to chamber) and t_{OFF} (bypass) for each pulsing cycle (1 min). Experimental results revealed that the pulsed-growth mode allowed the expansion of the MOCVD growth window of $ZnSn(Ga)N_2$ towards higher temperatures while avoiding the formation of Sn droplets. It was also found that a GaN regrowth layer inserted prior to the pulsed-mode growth had substantial impact on improving the $ZnSn(Ga)N_2$ crystalline quality. The pulsed-mode growth was optimized by tuning the TMSn pulsing rate to 15 sec on, 45 sec off (Fig. 2). At 580 °C, a $ZnSnGa_2N_4$ film with a stoichiometric Zn/Sn ratio and a 50% alloy with GaN was grown. X-ray photoemission spectroscopy (XPS) measurements show a valence band offset of 0.97 eV at the $ZnSnGa_2N_4$/GaN heterointerface, in line with the theoretical prediction (Fig. 3) [2].

In summary, pulsed-mode MOCVD growth of $ZnSn(Ga)N_2$ on a GaN template was investigated. Results from this study will motivate applications of $ZnSn(Ga)N_2$ and III-N heterostructures for device designs, with the potential to address some of the key challenges facing III-nitride-based electronic and optoelectronic devices today.

Acknowledgment: The authors acknowledge funding support from the U.S. Department of Energy (DE-EE0008718).

References:

1. Karim, M. R et al.; Zhao, H. Design of InGaN-$ZnSnN_2$ Quantum Wells for High-Efficiency Amber Light Emitting Diodes. *Journal of Applied Physics* **2018**, *124* (3), 034303.
2. Punya, A.; Lambrecht, W. R. Band Offsets between $ZnGeN_2$, GaN, ZnO, and $ZnSnN_2$ and Their Potential Impact for Solar Cells. *Physical Review B* **2013**, *88* (7), 075302.

11:00 AM DD08

Novel Treatment of Raman and Photoluminescence Spectroscopy Analysis for Assessment of Electrical Characteristics of Mg Implanted-Annealed GaN

Elaheh Kheirandish[1], Vincent E. Meyers[1], Emma Rocco[1], Benjamin McEwen[1], Mike Shevelev[2], Vlad Sklyar[2] and Fatemeh (Shadi) Shahedipour-Sandvik[1]; [1]SUNY Polytechnic Institute, United States; [2]Gyrotron Technology Inc, United States

For its advanced electronic and optical characteristics including a direct tunable bandgap, high critical electric field and high electron mobility, GaN has proven to be a promising material for advanced high power electronics, optoelectronics, sensors and RF technologies. Development and characterization of uniform, high conductivity p-type GaN either by Mg implantation or selective area growth are essential to the advancement of next generation high power electronics and optoelectronics. [1-2]

In polar semiconductors, the coupling between the Raman active longitudinal optical (LO) phonon modes and plasma oscillations of the free carrier gas results in the emergence of the Raman active coupled phonon-Plasmon LPP modes. [3] The energy exchange between the carrier relaxation and transport is related to the LPP. [8] Therefore, the shift and change in the width of LPP permits interrogation of some electrical parameters of the material. [4-9,8] Prior analysis of the upper LPP mode, LPP^+ mode, for n-type GaSb, ZnO and GaN have provided reasonable estimations of carrier concentration and mobility close to experimental values using Hall measurement. However, evaluation of the electronic properties of p-GaN through examination of LPP^+ mode has been unsuccessful due to the highly damped Plasmon in the material. [8-10]

In this study, photoluminescence (PL) and Raman spectroscopy were used to evaluate the carrier concentration and Plasmon damping constant, and correlation of these with optical properties of Mg+N co-implanted GaN, before and after high temperature annealing, using various techniques including gyrotron microwave annealing. Metal organic chemical vapor deposition (MOCVD) grown unintentionally doped GaN (u-GaN) was grown on n^+-HVPE GaN and is co-implanted with 10^{19} cm^{-3} Mg+N ions to 250 nm depth, capped with AlN, and annealed in N_2 at 1000 °C for 30 minutes. Annealing was performed at temperatures roughly at 1350, 1400 and 1450 °C peak temperatures. The AlN cap layer was etched away after the annealing process prior to PL and Raman spectroscopy. A quality assessment parameter ΔLPP^+ ranging from 10^{-3}–10^{-1} cm^2 was defined for quantitive study. ΔLPP^+ is defined by the relative shift of the LPP^+ frequency and by its FWHM. Using this parameter, we demonstrate that there is a correlation between this parameter and the PL intensity ratio of UVL to GL2 defect bands. This parameter qualitatively relates to the Mg dopant activation efficiency, reduction of the optically active V_N, and the presence of p-type doped or semi-insulating implanted regions on the u-GaN/n^+-HVPE templates. The hole concentration estimation of the p-GaN layers is assessed to be in the range of 10^{16}-10^{18} cm^{-3} for different annealing conditions. This study could offer a nondestructive, contactless, optical method for evaluation of the electronic and optoelectronic quality of p-type GaN in the p-n structure.

Acknowledgement

This work was funded by a grant from ARPA-E PNDIODES program, Grant No. DE-FOA-001691 under the direction of Dr. Isik C. Kizilyalli.

References

1. V. Meyers et al., J. Appl. Phys. **128**, 085701 (2020)
2. V. Meyers et al., J. Appl. Phys. **130**, 085704 (2021)
3. L.H. Robins et al., Journal of Applied Physics **120**, 124313 (2016)
4. T.Stoica et al., IEEE J. Sel. Top. Quantum Electron. **17**, 859 (2011)
5. T. Kozawa et al., J. Appl. Phys. **75**, 1098 (1994)
6. P. J. Colwell et al., Physical Review B, Vol.**6**, No.2 (1972)
7. H. Harima et al., Applied Physics Letters, **73** (14), 2000 (1998)
8. A-J Cheng et al., J. Appl. Phys. 105, 073104 (2009)
9. J. E. Maslar et al., Journal of Applied Physics, 104, 103521 (2008)
10. H.J. Park et al., Journal of Crystal Growth, 350, 85-88 (2012)

SESSION EE: Flexible, Printed, and Organic Electronic Materials and Devices

Session Chairs: Gerd Grau and William Scheideler
Friday Morning, July 1, 2022
US Bank Conference Theater

8:20 AM EE01
Liquid Metal Printing of High Mobility 2D In_2O_3 for Flexible Electronics William J. Scheideler, Andrew B. Hamlin and Youxiong Ye; Dartmouth College, United States

Transparent conducting oxides' exceptional optoelectronic properties make them promising materials for driving emerging sensing, neuromorphic computing, and virtual reality applications. The high performance of oxide semiconductors can unlocked by utilizing ultrathin two-dimensional (2D) layers offering electrostatic control. Here we present a new class of two-dimensional (2D) TCOs synthesized by liquid metal printing. Liquid metal (LM) printing utilizes rapid and spontaneous Cabrera-Mott surface oxidation to generate 2D oxide films at the interface of molten metals such as In, Ga, and Sn. We exploit this LM process to print large area continuous films (> 30 cm^2) as thin as 2 nm using a precursor consisting only of molten In (M.P. = 157 °C). These LM printed 2D oxides exhibit high mobility, extreme transparency, and crystallinity comparable to that of vacuum-deposited films.

This talk investigates the origins of the remarkable electronic performance of 2D In_2O_3. Compared with solution-processed oxides, LM printed 2D oxides fortuitously do not require pyrolysis or precursor decomposition. XPS reveals this advantage relative to sol-gels by illustrating the elimination of M-OH bonding and a lack of C and N impurities. The LM printed In_2O_3 also exhibits higher crystallinity at low process temperatures (< 180 °C) than sol-gels, with XRD showing the bixbyite c-In_2O_3 phase as-deposited. HRTEM shows 10-30 nm crystallites of In_2O_3 despite their 2 nm thickness. Multilayers exhibit Moire fringes indicating a unique morphology of overlapping plate-like grains.

Studies of electronic transport in single and multilayer 2D In_2O_3 suggest the unique grain morphology results in significant enhancements to electron mobility when implemented in thin film transistors (TFTs). TFTs with LM printed In_2O_3 channels demonstrate linear mobility of > 30 cm^2/Vs at 175 °C and > 65 cm^2/Vs with 250 °C post annealing, with minimal hysteresis and $I_{on}/I_{off} > 10^7$. Extraction of the density of states (DOS) and carrier concentration by Hall measurements reveal how the combination of high mobility and electrostatic control is achieved due to the ultrathin nature, which induces bandgap widening to control the degeneracy. Finally, we will discuss opportunities to control the electronic properties through LM printed 2D heterostructures (InO_x / GaO_x, InO_x / AlO_x) and benchmark these materials against oxide semiconductors formed from sol-gels and nanoparticles.

8:40 AM EE02
(Student) Surface Morphology Effects of Inkjet-Printed Silver Electrodes on the Contact Resistance of Printed Organic Thin-Film Transistors Hyunwoo Choi, Roksana T. Rashid, Wontae Park and William Wong; University of Waterloo, Canada

Silver nanoparticles (Ag NPs) have been successfully utilized in the development of printed metal electrodes for thin-film transistors (TFTs). Unlike vacuum-deposited bulk Ag films, solution-processed Ag NPs may be deposited and patterned simultaneously through various printing methods where a final sintering process converts the ink into a conductive film. This process depends on the processing temperature that affects the film morphology and electrical properties. Since the Ag ink consists of spherical nanoparticles, the thin-film density and structure can be altered in terms of its porosity and surface roughness. These properties may affect the electrical contact between the Ag electrode and the semiconductor, changing the overall electrical behavior of the TFT.
In this work, a Ag NP ink (DGP 40LT-15C, ANP) was inkjet-printed (using a Ceradrop Printer with a Fujifilm Dimatix inkjet print cartridges) on 100 nm thick thermal SiO_2 on a Si wafer. The printed ink was sintered with different temperatures (T_{Ag}) from 90 °C to 240 °C in 30 °C steps. Using these conditions, a bottom-gate bottom-contact TFT structure was fabricated by inkjet-printing of regioregular poly(3-hexylthiophene-2,5-diyl) (P3HT, Ossila) as the active layer with printed Ag source and drain (S/D) electrodes (using a MicroFab printhead on the Ceradrop printer) The devices had a 30 µm and 850 µm channel length and width, respectively. Current-voltage (I-V) measurements of the fabricated TFTs showed good switching behavior. The transfer characteristic in the saturation regime (V_D = 30 V) shows that the on-current level increased with increasing Ag NP T_{Ag}. The extracted saturation field-effect mobility (μ_{sat}) increased from 8 10^{-4} cm^2/Vs for the device with T_{Ag} = 150 °C to 2.3 10^{-3} cm^2/Vs with T_{Ag} = 210 °C. It was observed that while the sheet resistance of the printed Ag NP decreased with increasing annealing temperature, at T_{Ag} > 180 °C, the sheet resistance did not change significantly, but the TFT μ_{sat} increased by about a factor of two. To investigate the origin of this effect, scanning electron microscopy (SEM) was used to characterize the structure and morphology of the sintered Ag. From the SEM characterization, the diameter of Ag NPs was ~30 nm prior to annealing. After a T_{Ag} = 150 °C, the printed Ag nanoparticles were observed to form a porous film with a high density of void structures. At T_{Ag} = 180 °C, most of the Ag NPs merged together with neighboring NPs forming a more continuous film. At T_{Ag} = 210 °C, the structure transformed into large clusters of a few hundred nanometers, but with noticeably larger vacancies between the clusters. Based on four-point probe measurements, the sheet resistance remained constant between T_{Ag} = 180 and 210 °C. Further investigation of the P3HT formation on the Ag electrodes showed the P3HT structure improved on the Ag electrodes annealed at higher T_{Ag}. Atomic force microscopy (AFM) revealed the polymer film surface morphology and structure were dependent on the annealed Ag NP electrodes. The surface morphology of the P3HT film was found to change with the Ag surface roughness where large continuous Ag clusters resulted in smoother P3HT films. The smoother P3HT morphology on these S/D regions correlated to T_{Ag} between 150 °C to 210°C. The change in the structural characteristics of the polymer matrix may provide the thin-film semiconductor with better crystallinity, enhancing the electrical contact between the semiconductor and Ag electrode. Verification of this hypothesis was examined by extracting the contact resistance for the different annealing conditions using the Y-function method and the I-V data in a linear regime. The calculated contact resistance (R_C) values were 1.83, 0.75, and 0.38 MΩ-cm for devices annealed at T_{Ag} = 150, 180, and 210 °C, respectively. Finally, we will describe approaches to further minimize the R_C of the inkjet-printed OTFT and optimize the printed Ag film to enhance device performance.

9:00 AM EE03
Semiconductor Nanomembranes for Electromagnetic Interference Shielding Applications Emma J. Renteria[1], Grant Heileman[2], Arnab Majee[1], Thomas J. Rotter[1], Ganesh Balakrishnan[1,2], Christos Christodoulou[2] and Francesca Cavallo[1,2]; [1]University of New Mexico, United States; [2]The University of New Mexico, United States

The increasing use of radio-frequency (RF) devices saturates the environment with electromagnetic radiation capable of disrupting the operation of electronic components, including sources and detectors of infrared (IR) radiation that are widely used in communication systems and night-vision cameras. Therefore, IR

devices must be enclosed by a material that blocks RF waves while allowing the transmission of IR radiation. Transparent conducting oxides (TCOs), metal meshes, and 2D materials have been proposed and investigated to implement IR-transparent shields of electromagnetic interference (EMI). However, a material with minimum trade-off between shielding effectiveness, optical transmittance, scalability, and durability is elusive. Here, we show that single-crystalline semiconductor nanomembranes (NMs) are viable candidates for shielding IR devices from EMI as they provide sufficiently high shielding effectiveness, high optical transmittance, and bending durability. Our experimental work encompasses fabrication of large-area, degenerately doped semiconductor NMs, characterization of the conductivity and IR transmittance of the NM, and measurements of the NM shield effectiveness at radio frequencies. Thickness, doping level, chemical and physical structure of the surface can be varied with a high degree of control. We have grown a 200 nm-thick GaAs NM onto an undoped AlGaAs sacrificial layer/semi-insulating (001) GaAs substrate. Silicon impurities were introduced in the NM during epitaxial growth to achieve a nominal doping level of 1×10^{19} cm^{-3}. We have fabricated van der Pauw test devices and measured a conductivity of 1.15×10^5 S/m for the as-grown NM. The calculated shield effectiveness of the GaAs NMs based on the measured conductivity is as high as 42 dB at 8 GHz. Next, GaAs NMs are released from the substrate surface via selective removal of the AlGaAs sacrificial layer. Freestanding NMs are transferred to optically transparent substrates (e.g., flexible Kapton films) to characterize IR transmittance and shielding effectiveness. Measurements are ongoing.
This research was supported by an appointment to the Intelligence Community Postdoctoral Research Fellowship Program at University of New Mexico *administered by Oak Ridge Institute for Science and Education (ORISE) through an interagency agreement between the U.S. Department of Energy and the Office of the Director of National Intelligence (ODNI). This work was performed, in part, at the Center for Integrated Nanotechnologies, an Office of Science User Facility operated for the U.S. Department of Energy (DOE) Office of Science by Los Alamos National Laboratory (Contract 89233218CNA000001) and Sandia National Laboratories (Contract DE-NA-0003525).*

9:20 AM EE04
(Student) Substrate-Free Organic Electrochemical Transistors Based on Ionic Liquid Crystal Elastomer Pushpa R. Paudel[1], Chathuranga Prageeth Hemantha Rajapaksha[1], Panambara Mudiyanselage Sineth G. Kodikara[1], Drona Dahal[1], Thiloka Madhumanie D. Dassanayake Mudiyanselage[1], Vikash Kaphle[1], Bjorn Lussem[1,2] and Antal Jakli[1,1]; [1]Kent State University, United States; [2]University of Bremen, Germany

Organic electrochemical transistors (OECTs) have attracted great attention since their discovery in 1984 due to their flexibility and biocompatibility. Although an intense focus has been put on the design of new organic semiconductors, fewer efforts are directed towards the development of optimized electrolytes. However, the electrolyte is an integral part of OECTs and strongly influences the transient responses of these devices. Also, best performing OECTs currently use liquid electrolytes, but there is a growing need for solid electrolytes, as they can be easily integrated into wearable devices. Here, we demonstrate that ionic liquid crystal elastomers can be used as solid electrolytes of flexible, substrate-free organic electrochemical transistors. We introduce the alignment of the director of the liquid crystal elastomers as a new parameter to tune and improve both steady state and transient responses. The normalized maximum transconductance g_m/w of the most sensitive iLCE, was found to be the highest (7 S m^{-1}) among all solid state-based OECTs. [1]
Acknowledgements: This research was supported by the National Science Foundation under grant DMR-1904167 and ECCS 1750011.

References:
[1] C. P. H. Rajapaksha, P. R. Paudel et al., *Applied Physics Reviews*, **In press** (2022).

9:40 AM EE05
Exploration of New Classes of Solution-Processed High-*K* Dielectric Materials for Low-Power Electronics Sheida Faraji[1,2], Navid Mohammadian[2], Mane Seck[3], Karim Diallo[3], Kamel Khirouni[4] and Leszek A. Majewski[2]; [1]Istanbul Technical University, Turkey; [2]The University of Manchester, United Kingdom; [3]Gaston Berger University, Senegal; [4]University of Gabès, Tunisia

Organic thin-film transistors (OTFTs) have gained significant attention due to their attractive features, such as low process temperatures, mechanical flexibility, light weight, large-area production and compatibility with all kinds (rigid and flexible) of substrates. For several decades, remarkable advances in development of new semiconducting materials and novel fabrication techniques have resulted in charge carrier mobility of OTFTs to drastically surpass 1 $cm^2V^{-1}s^{-1}$. Inevitable scaling down of electronic components to few nanometres and growing demand for low-cost flexible electronic circuits have made development of new classes of high dielectric constant (so-called high-*k*) materials processable from solution in ambient conditions with good mechanical strength highly desirable. Now with the promising emerge of green electronics to reduce e-waste, environmentally friendly, biodegradable and biocompatible materials and processes have attracted significant attention to realise ecological and recyclable electronic devices. Green electronics aims to manufacture devices in an environmentally friendly and sustainable way. The involved electronic materials are naturally occurring and non-toxic and can be processed using simple, low energy deposition processes and fabrication techniques.

Traditional solution-processed polymers used in the semiconductor industry are generally low-*k* dielectrics which hinders integration of OTFTs in practical applications, for instance in wearable/portable sensors for health monitoring, due to their relatively high operating voltages (≥ 3 V). To enable operation of OTFTs at substantially low voltage (1 to 3 V), while maintaining high output current, thin but robust layer(s) of high capacitance gate dielectric is required. For the past decade, we have progressively explored and developed new classes of solution-processed, high-*k* naturally occurring or 'man-made' organic, inorganic and inorganic-organic hybrid dielectric materials for applications in low-power and recyclable electronic devices and circuitries. We successfully fabricated low voltage (< 3 V) OTFTs in high yields using novel, solution processed high-*k* nanocomposite/low-*k* polymer bilayer gate dielectric. Different nanocomposite suspensions of barium strontium titanate (BST) and barium zirconate (BZ) nanoparticles dispersed separately in poly (vinylidene fluoride-co-hexafluoropropylene) P(VDF-HFP) and cyanoethyl cellulose (CEC) polymer matrices were prepared to form high-*k* nanocomposite layers. Following successful demonstration of solution-processed OTFTs operating at 1 V using ultra-thin (~4 nm), self-assembled monolayer (SAM) modified aluminium oxide (Al_2O_3) layers as the gate dielectric, we also reported fabrication of ultralow voltage OTFTs with SAM-modified ultra-thin (~7 nm) tantalum pentoxide (Ta_2O_5) as the gate dielectric. Most recently, our work was focused on using natural occurring water-processed materials such as almond gum, gum Arabic and Aloe Vera as the gate dielectric in low-voltage OTFTs. Almond gum and Arabic gum are both natural, biodegradable insulator materials that can be directly collected from almond trees and used without any further purification. Moreover, the compelling properties of these gums, such as water solubility, ease of processing, good insulation, low leakage current and good film quality. Such dielectric layers displayed a high capacitance per unit area and low leakage current density below. The corresponding

almond and Arabic gum OTFTs showed relatively large carrier mobilities at low voltages (< 3 V). Using such naturally occurring materials paves the way towards green manufacturing of the next generation of electronic devices. This work is aimed at reviewing various high-k dielectric materials, focusing on green materials, for low power electronics.

10:00 AM Refreshment Break

10:20 AM EE06
(Student) Bandlike and Polaronic Charge Transport in Organic Crystals from First-Principles Benjamin K. Chang, Jin-Jian Zhou, Nien-En Lee and Marco Bernardi; California Institute of Technology, United States

Predicting charge transport in organic molecular crystals (OMCs) is challenging due to their complex crystal structures and electron-phonon (e-ph) interactions. In this talk, we will present two first-principles frameworks to accurately predict the charge carrier mobilities in OMCs. The first is the Boltzmann transport equation (BTE) with ab initio e-ph interactions, which describes the bandlike transport regime in OMCs [1]. We will show BTE calculations of hole mobilities in various molecular systems, and examine the effect of strain on charge transport. The second method is the cumulant plus Green-Kubo (CK) [2,3], which addresses the regime where the e-ph interactions are of intermediate strength and the charge carriers form polarons. We will present our recent CK calculations of electron mobilities and electron spectral functions in OMCs. Both our BTE and CK approaches provide mobilities in very good agreement with experiments over a wide temperature range. These broadly applicable methods advance the understanding of charge transport in organic semiconductors.
[1] Lee *et al.*, Phys. Rev. B, **97**, 115203 (2018)
[2] Zhou *et al.*, Phys. Rev. Research, **1**, 033138 (2019)
[3] Chang *et al.*, arXiv:2106.09810

10:40 AM EE07
PiFM—Nanoscale Chemical Mapping and Spectroscopy via AFM-IR for Ultrathin Organic Films Padraic O'Reilly, Derek Nowak and Song Xu; Molecular Vista, United States

Real-space imaging and identification of chemical components in multi-component systems with nanometer scale spatial resolution remains a challenge for the nano and molecular electronics community. In this talk, we introduce a new nanoscale and non-destructive chemical imaging technique called photo-induced force microscopy (PiFM) where the dipole-dipole force due to optical response of the sample is measured by an atomic force microscope (AFM) along with the standard AFM topography [1]. PiFM can be coupled with a tunable infrared (IR) light sources to probe the IR absorption of various organic and inorganic materials for identification of molecular materials and their relationship to local topography. PiFM is surface sensitive due to the short interaction range of the measured dipole-dipole force and achieves single-molecule-level of chemical sensitivity and ~ 5 nm spatial resolution, making it an ideal tool for characterizing thin films and devices of organic and inorganic materials; monolayer of organic/inorganic constituents, contaminants, and residues can be clearly and uniquely visualized for failure analysis and process development of biosensors and organic/molecular devices. The capabilities of PiFM will be highlighted by presenting data on area selective deposition, which features self-assembled monolayer (SAM) of organic materials as well as ultrathin dielectrics grown via atomic layer deposition (ALD). PiFM provides a powerful new analytical method for deepening our understanding of nanomaterials and facilitating technological applications of such materials.
[1]. Nowak, D., et al., Sci. Adv. 2 (2016), e1501571.

11:00 AM EE08
(Student) Assessing the Contribution to OPV Efficiency of Energy Transfer in Charge Transfer Coupled H-Aggregates
Tyler J. Wiegand[1], Steven A. Diaz[2], David W. McCamant[2], Kristen M. Burson[3], Tonya Coffey[4] and Christopher J. Collison[1,1]; [1]Rochester Institute of Technology, United States; [2]University of Rochester, United States; [3]Hamilton College, United States; [4]Appalachian State University, United States

Organic photovoltaics (OPVs) utilizing easily synthesized Squaraine (SQ) molecules are a promising candidate for commercialization. However, small molecule OPVs suffer from declining device efficiency over operational lifetime. A primary cause of efficiency deterioration is molecular phase separation in the bulk heterojunction. Specific to SQs, phase separation leads to formation of dimer H-aggregates (DHA) and intermolecular charge transfer coupled H-aggregates (CT-HA) as molecules phase separate to form pure, tightly packed SQ crystal structures. Theoretically these aggregates should have poor energy transfer capabilities through their excited states, detrimental to device efficiency. Control of aggregate populations can be achieved through changing blend ratios, annealing, and adding a second SQ surfactant in a ternary blend. Once controlled, measurement of relative populations of monomer, DHA, and CT-HA in a $DBSQ(OH)_2$ squaraine is accomplished spectroscopically. This work correlates the relative population of these species with device efficiency and, unexpectedly, device efficiency increases with an increase to CT-HA fractions, despite predicted low energy transfer rates. Energy transfer rates for aggregates must therefore be reexamined. This is realized using intensity dependent sub-picosecond transient absorption measurements. For the first time, we demonstrate accurate measurement of a complex array of excited state species and how they influence device performance. In parallel, this work establishes an improved understanding of energy transfer rates in CT-HAs, which dominate after long term device use in the field. These conclusions therefore connect morphology, device mechanism and long-term device efficiency for an all-small molecule OPV.

11:20 AM EE09
(Student) Impact of Surfactant Choice on Polymer Emulsions, Thin-Film Morphology and LED Performance Buang Zhang[1], Sabila Pinky[2], Albert Kwansa[2], Yaroslava Yingling[2] and Adrienne Stiff-Roberts[1,1]; [1]Duke University, United States; [2]North Carolina State University, United States

Poly(9,9-di-n-octylfluorenyl-2,7-diyl), also known as PFO, has been considered a promising material for blue light-emitting diodes (LEDs). [1] The crystalline beta-phase of PFO exhibits a more planar backbone configuration compared to its amorphous phase, and it greatly enhances the luminance efficiency of LEDs, even with minimal content in thin films. It has been proven previously that PFO deposition by emulsion-based, resonant infrared, matrix-assisted pulsed laser evaporation (RIR-MAPLE) can promote the crystalline beta-phase. [2] RIR-MAPLE uses a frozen "oil-in-water" emulsion target featuring primary solvent (trichlorobenzene), secondary solvent (phenol), polymer (PFO), water, and surfactant. Polymer is first dissolved in nonpolar primary solvent, and then water with surfactant is added to form the complex emulsion. A secondary solvent is included to lower the emulsion vapor pressure. The target is then cooled using liquid nitrogen and kept at -196°C during the deposition. RIR-MAPLE takes advantage of an Er:YAG laser (peak wavelength of 2.94 microns) that is resonantly absorbed by the hydroxyl bond vibrational mode, thereby sublimating the water ice matrix within the frozen emulsion target to form a plume. This plume transfers emulsified solvent particles, containing the polymer, from the target to the substrate without any degradation; therefore, the morphology of the emulsion directly impacts the final film morphology.

Because the complex emulsion target consists of multiple components, the existing two-phase emulsion theory cannot predict the resultant emulsion morphology. Even though the amount of surfactant within the emulsion is too low to be detected by X-ray diffraction, surfactant plays an important role in facilitating the emulsion micelle formation, thereby impacting the film morphology and resulting device performance. In this study, we used different surfactants to find out the effect on emulsion morphology, PFO beta-phase content, and LED device performance. We chose two groups of surfactants in this study. The first group featured sodium dodecyl sulfate (SDS), didodecyldimethylammonium bromide (DDMABr), and tridodecylmethylammonium iodide (TDMAI) with one, two, and three hydrophobic carbon tails, respectively. The second group featured sodium benzylsulfate (SBS) with one aromatic ring and sodium dodecylbenzenesulfate (SDBS) with one aromatic ring and one hydrophobic carbon tail. Given the complexity of the system, for this study, molecular dynamics (MD) simulations were used to study the emulsification behavior.
The hypothesis of this work was that the surfactant that induces the smoothest film would also have the highest beta-phase content and the best device performance in terms of color purity and luminance efficiency. The MD simulation predicted emulsion formation, non-bonded interaction energy, and micelle mass density. The morphology parameters of the film, including thickness and roughness, were determined using atomic force microscopy. The optical properties were characterized using photoluminescence and UV-Vis spectroscopy. The beta-phase content was determined using Beer-Lambert law. [3] LEDs were fabricated with the device stack of ITO/PEDOT:PSS/PFO+MEH-PPV/LiF/Al. LED performance was characterized in the following aspects: current density vs. voltage curves, electroluminescence spectra, brightness measurements, LED emission spectra, and CIE color coordinates. In this study, a pinhole-free PFO thin film with significant beta-phase content (21%) was achieved via RIR-MAPLE with deep blue color purity.
This material is based upon work supported by the National Science Foundation under Grant No. NSF CMMI-1727572.
References:
[1] Peet. J, et al., Adv. Mat., 20(10), p 3938 (2008)
[2] Ferguson, S; et. al., J. Electron. Mat, vol. 48(5)(2019)
[3] Liu Y; et. al., Chinese J. Polym. Sci., (37), 664–673 (2019)

11:40 AM EE10
(Late News) Microwave-Facilitated Few-Layer COF/Monolayer TMD Heterostructures Lucas K. Beagle[1,2], David Moore[1,2], Ly Tran[1,2], Luke Baldwin[2] and Nicholas R. Glavin[2]; [1]UES, Inc., United States; [2]AFRL, United States

Chemical and biological sensing using 2D nanomaterials has been an area of intense investigation including inorganic materials that exhibit high sensitivity, however it has been limited as a field due to the lack of selectivity among analytes. While 2D inorganic materials, such as transition metal dichalcogenides (TMD), can readily decipher between donor/acceptor groups, strategies to incorporate selectivity in these devices is often challenging. Organic 2D materials such as covalent organic frameworks (COFs), known for their highly crystalline repeated organic moieties, have been shown to act as selectivity agents due to their functionalization and porosity. This research focuses on the association of COFs with 2D nanomaterials using top-down microwave-assisted activation of TMDs and deposition of COF nanoparticles creating coupled heterostructures. Several known TMD and COF species have been examined to understand the fundamental surface interactions between 2D nanomaterials and few layer COFs, this unique methodology allows the study of mono- to few layer properties of both the organic and inorganic materials simultaneously. Kinetics and mechanistic studies were used to determine the manner of association of the inorganic and organic substrates. Photoluminescence and electronic measurement studies demonstrate a microwave power dependent electronic coupling of the inorganic and organic materials in these highly tunable hybrid materials.

SESSION FF: Gallium Oxide—Material Processing, Characterization and Defects

Session Chairs: Rebecca Peterson and Marko Tadjer
Friday Morning, July 1, 2022
Ohio Staters Inc. Traditions Room

8:20 AM FF01
(Student) High Breakdown Field Strength in Molecular Beam Epitaxy-Grown Al_2O_3/β-Ga_2O_3 Structures Sushovan Dhara, Nidhin Kurian Kalarickal, Chandan Joishi, Andreas Fiedler, Joe F. McGlone, Ashok V. Dheenan, Steven A. Ringel and Siddharth Rajan; The Ohio State University, United States

β-Ga_2O_3 is a promising material for high power devices due to its high theoretical breakdown field of 8MV/cm and availability of bulk substrates. In order to take full advantage of the potential of this material, synthesis and properties of dielectric-semiconductor interfaces is critical. Dielectric-semiconductor interfaces are needed to sustain electric fields that are significantly higher than previous Si or GaN devices, while maintaining low leakage current and controlled interface traps and charge. For this purpose, Al_2O_3 grown by different methods such as ALD [1], MOCVD [2] have been explored. In this work, we discuss the synthesis and electronic properties of Al_2O_3 deposited using plasma-assisted molecular beam epitaxy on n-type (001)-oriented Ga_2O_3 layers. Al_2O_3/β-Ga_2O_3 metal-oxide-semiconductor capacitors with high reverse breakdown voltage up to 1843V (breakdown field strength of 5.1 MV/cm).
Devices were fabricated on commercially available (001) n-type doped halide vapor phase epitaxy (HVPE) grown gallium oxide epitaxial layer ($n=4x10^{16}/cm^3$). The substrates were first cleaned in Acetone/IPA/DI water followed by a 20 min dip in 49% HF for removing surface contaminants. The dielectric growth was carried out in a Riber M7 Oxide system equipped with an O_2 plasma source. 50 nm of Al_2O_3 was deposited at temperatures 300°C, 400°C and 500°C. Al flux of $2x10^{-8}$ Torr and oxygen flow and plasma power of 2.5 sccm and 250 W were used for the growth. Top contacts were then patterned using optical lithography followed by e-beam evaporation of Pt/Au (30/70nm) contacts, and blanket deposition of the bottom Ti/Au (30/70nm) ohmic contact. Capacitance-voltage (CV) measurements for all three temperatures investigated here showed low hysteresis and frequency dispersion. When compared with the ideal CV curve, the measured CV curves were found to be shifted towards positive biases in all cases with a shift of 0.6V, 2.7V, and 5.4V for 500°C, 400°C, and 300°C Al_2O_3 MOS capacitors, respectively. This confirms the presence of negative charges in the Al_2O_3 bulk or at the Al_2O_3/β-Ga_2O_3 interface. Assuming the charge was at the oxide-semiconductor interface, we estimated negative sheet charge of $5.97x10^{11}/cm^2$, $1.69x10^{12}/cm^2$, and $4.38x10^{12}/cm^2$ for 500°C , 400°C , and 300°C samples, respectively. All three samples showed low reverse leakage current <$100nA/cm^2$, suggesting their promise for gate or field plate dielectric applications.
The MOSCAPs were further stressed to high reverse bias till they breakdown. The 300°C MOS capacitor showed the lowest average breakdown voltage (< 1453V), whereas the 400°C and 500°C had higher breakdown voltage of 1843 V and 1720 V respectively. The corresponding parallel plate electric field in gallium oxide found to be 4.54MV/cm 5.12 MV/cm, and 4.95 MV/cm for 300°C, 400°C, and 500°C samples respectively. The hard irreversible breakdown occurred at the edge of the MOSCAP pads, suggesting that edge termination could help to achieve better performance. The forward

stress also displayed irreversible breakdown, with the 300°C sample showing the highest forward breakdown voltage of 21.7 V, corresponding to a maximum electric field of 4.2 MV/cm.
In summary we have demonstrated MBE-grown Al_2O_3/β-Ga_2O_3 MOS capacitors with low forward and reverse leakage current. A maximum electric field of 4.95 MV/cm is sustained in the Gallium Oxide layer. The in situ deposition technique demonstrated could enable novel dielectric integration schemes for future Gallium Oxide devices. This work was supported by funding from Department of Energy / National Nuclear Security Administration under Award Number(s) DE-NA000392, and AFOSR GAME MURI (Award No. FA9550-18-1-0479, project manager Dr. Ali Sayir).
Reference: [1] Hung, T., et al. Appl. Phys. Lett. 104, 162106 (2014) [2] Roy, S., et al. Adv. Electron. Mater. 2021, 7, 2100333

8:40 AM FF02
Ion Implantation Doping for β-$Al_xGa_{2-x}O_3$ and the Application for Ohmic Contact Formation Ming-Hsun Lee[1], Alan G. Jacobs[2], Marko Tadjer[2] and Rebecca L. Peterson[1,1]; [1]University of Michigan, United States; [2]U.S. Naval Research Laboratory, United States

The system of gallium oxide has attracted worldwide attention for its potential for next-generation power electronics. Beyond the intrinsic limit of β-Ga_2O_3, alloying the material with Al can effectively widen its bandgap and opens the possibility for high-performance heterostructure device applications.[1] Although common extrinsic dopant elements (e.g. Si and Sn) in gallium oxide are predicted to be shallow donors in Al-alloyed gallium oxide,[2] studies have shown degraded film quality and/or poor dopant incorporation in as-grown Si-doped β-$Al_xGa_{2-x}O_3$ film.[3,4] To resolve this problem, here we report a method for doping $Al_xGa_{2-x}O_3$ via Si-ion implantation and demonstrate its application for forming ohmic contacts on β-$Al_xGa_{2-x}O_3$.
Device fabrication started with multiple Si-implantations which were carried out at room temperature to form a ~80-nm-deep box-profile in $Al_{0.4}Ga_{1.6}O_3$ epitaxial film followed by a post-implant anneal process in a non-oxidizing environment. The projected Si box-concentration ranges from 3.0×10^{19} cm^{-3} to 9.0×10^{19} cm^{-3}. Circular transmission line method (CTLM) device structures were then defined with evaporated 20-nm Ti/ 80-nm Au metal stack and lift-off process. To ensure the metallization is in direct contact with the heavily doped implanted $Al_{0.4}Ga_{1.6}O_3$ region, a BCl_3-based reactive-ion-etch recess was applied prior to metallization. Post-metallization rapid-thermal-anneal (RTA) was performed at 470°C for 1-min in N_2 to improve ohmic contact performance. Electrical testing and material characterizations (XRD, AFM, SIMS, and S/TEM) were carried out afterward to examine the fabricated devices.
Compared with the highly-resistive un-implanted sample, the ion-implanted samples showed much-improved current-voltage (*I-V)* characteristics, suggesting that the implanted species were successfully activated in the $Al_{0.4}Ga_{1.6}O_3$ epitaxial film. Linear *I-V* characteristics were obtained from implanted samples and low specific contact resistivity were extracted from the CTLM devices. The process windows for implant dosage and post-implant anneal were investigated and identified. Coupled with the improved electrical properties, evidence from materials characterization suggests the necessity of post-implant anneals to annihilate defects and second-phase formation that can occur during ion beam modification. The electrical and material properties are tightly linked for Ti/Au ohmic contacts to ion-implanted β-$Al_xGa_{2-x}O_3$.
[1] H. Peelaers, J.B. Varley, J.S. Speck, and C.G. Van de Walle, Appl. Phys. Lett. **112**, 242101 (2018).
[2] J.B. Varley, A. Perron, V. Lordi, D. Wickramaratne, and J.L. Lyons, Appl. Phys. Lett. **116**, 172104 (2020).
[3] P. Ranga, A. Rishinaramangalam, J. Varley, A. Bhattacharyya, D. Feezell, and S. Krishnamoorthy, Appl. Phys. Express **12**, 111004 (2019).
[4] A.F.M. Anhar Uddin Bhuiyan, Z. Feng, J.M. Johnson, Z. Chen, H.-L. Huang, J. Hwang, and H. Zhao, Appl. Phys. Lett. **115**, 120602 (2019).

9:00 AM FF03
(Student) Activation of Si, Sn and Ge Donors in High-Resistivity Halide Vapor Phase Epitaxial β-Ga_2O_3:N Joseph Spencer[1,2], Marko Tadjer[2], Alan G. Jacobs[2], James C. Gallagher[2], Jaime Freitas[2], Kohei Sasaki[3], Akito Kuramata[3], Quang Tu Thieu[3], Yuhao Zhang[1], Travis Anderson[2] and Karl Hobart[2]; [1]Virginia Tech, United States; [2]U.S. Naval Research Laboratory, United States; [3]Novel Crystal Technology, Japan

Gallium oxide (GO) has seen a large rise in research interest from both the electronic device and material growth communities due to its ultra-wide band gap (4.8 eV), high critical field (6-8 MV/cm) and melt-growth technology similar to Silicon. The control of dopants in a material with such a large bandgap is crucial for device fabrication. Despite the large bandgap, donors in GO have exhibited a very low activation energy, 30 meV for Si and 60 meV for Sn [1,2]. At low doping levels (10^{15} cm^{-3}) mobility of GO:Si has been demonstrated at 196 cm^2/Vs. With the inclusion of nitrogen acceptors into GO, the unintentional donor doping level can be decreased further; as low as 10^{14} cm^{-3}, extending the donor doping window of GO from $<10^{14}$ cm^{-3} to as high as 10^{20} cm^{-3} [3,4]. The addition of N acceptors serves to make GO very resistive and act as a current blocking layer (CBL) while the addition of donors serves to increase conductivity. Here we demonstrate selective ion implant of Si, Ge, and Sn donors into highly resistive GO:N, overcompensating the N acceptors and generating highly conductive films.

The halide vapor phase epitaxial (HVPE) films were grown on semi-insulating (001) GO:Fe substrates and characterized in previous works [5]. Secondary ion mass spectroscopy (SIMS) verified the 9.2 μm film thickness with nitrogen as the compensating acceptor. Capacitance-voltage measurements showed a net free carrier concentration (N_D-N_A) less than 10^{14} cm^{-3}. Lateral Schottky barrier diode structures on the HVPE films resulted in breakdown voltages exceeding 2 kV [5].
Samples were patterned for linear and circular transfer length method (LTLM/CTLM) structures as well as van der Pauw (VdP) testing structures for selective ion implantation. Si, Ge, and Sn ions were selectively implanted in order to achieve an approximately 100 nm implant box profile at 3e19 cm^{-3} dopant concentration for a total dose of 3.33e14 cm^{-2}. Rapid thermal annealing (RTA) at 925 °C for 30 min in N_2 was performed to activate the implanted ions and remove implant damage. The LTLM/CTLM and VdP structures were further isolated by a 150 nm BCl_3 reactive ion etch at 800 W. Evaporated Ti/Au ohmic contacts were deposited and an\ standard ohmic contact anneal was performed.
LTLM and CTLM measurements demonstrated ohmic contacts between the Ti/Au metal stack and GO with a contact resistance (R_c) of 1.2 Ωmm and 2.3 Ωmm for the Si and Sn implanted samples, respectively. Room temperature (RT) and temperature dependent Hall effect measurements were performed to extract the sheet carrier concentration (n_s), sheet resistance (R_{sh}), and mobility (μ). VdP structures received ion implants at various locations within the structure to confirm if the implanted donors could overcompensate for the N-doped CBL. Hall structures that did not receive implantation of the active region between the ohmic contacts could not be measured due to excessive resistance demonstrating retention of N doped film resistivity. At ambient, the Si, Ge, and Sn doped samples achieved measured mobilities, sheet resistances, and sheet electron densities of 86, 71, and 59 cm2/Vs, 324, 941, and 1750 Ω/sq, and 2.25e14, 9.3e13, and 6.0e13 cm^{-2} respectively. The implant activation efficiency was found to be 66%, 28%, and 18% for Si, Ge, and Sn, respectively. Temperature dependent Hall effect measurements from 15 K to 300 K showed little variation in the sheet carrier concentration.

Photocurrent measurements of the highly resistive non-implanted VdP structures were performed using an above bandgap UV light with a power of 217 μW. A low dark current was measured ranging from 1-100 pA and photocurrent ranging from 1-100 nA.

[1] Neal, A.T., et al. *Appl. Phys. Let.* 113, 062101 (2018).
[2] Higashiwaki, M, et al. *Appl. Phys. Let.* 103, 123511 (2013).
[3] Kamimura, T. et al., IEEE Elec. Dev. Let. 40, 1064 (2019).
[4] Leedy, K.D. et al., *Appl. Phys. Let.* 111, 012103 (2017).
[5] Tadjer, M.J., et al. *Appl. Phys. Let.* 113, 192102 (2018).

9:20 AM FF04

Formation of Deep Acceptors by Nitrogen Implantation in HVPE Grown β-Ga_2O_3 Hemant J. Ghadi[1], Joe F. McGlone[1], Evan M. Cornuelle[1], Alexander Senckowski[2], Shivam Sharma[3], Uttam Singisetti[3], Man Hoi Wong[2], Aaron Arehart[1] and Steven A. Ringel[1]; [1]The Ohio State University, United States; [2]University of Massachusetts, Lowell, United States; [3]University of Buffalo, United States

Beta phase gallium oxide (β-Ga_2O_3) is a strong contender for applications in next-generation high power and RF devices. Investigating the presence and properties of crystalline defects and their manifestation as bandgap states within the ~ 4.8 eV β-Ga_2O_3 bandgap has been vital in improving the material quality. Exploring deep-level defects has helped optimize the crystal growth and provided a means for intentional incorporation of deep compensating acceptors for achieving semi-insulating layers needed in some device applications. Iron as an impurity has been thoroughly investigated and primarily used for creating semi-insulating (SI) β-Ga_2O_3 substrates. There is also great interest in alternative, nitrogen (N) doping to create SI layers and isolation regions, especially via implantation, however, much less is experimentally known regarding the specific electronic properties of N doping needed for this to develop. Here, we discuss results from a systematic study of N-implanted halide vapor phase epitaxy (HVPE)-grown β-Ga_2O_3 material, with a primary focus on the properties and analysis of defect states created by N, and by implantation damage, using a combination of deep-level thermal transient and optical spectroscopy (DLTS/DLOS) along with CV analysis to connect traps with carrier compensation.
Two Si-doped HVPE grown β-Ga_2O_3 epilayers with net doping concentrations of 1.9×10^{16} and 1.2×10^{17} cm^{-3} on a 5×10^{18} cm^{-3} Sn-doped n-type β-Ga_2O_3 substrates were used for N-implantation studies. Three uniform N-implantation profiles of 1×10^{15}, $2\times10^{16,}$ and 5×10^{16} cm^{-3} up to 700 nm from the surface were created using SRIM, and the implantations were performed at a commercial implanter using multiple energies (10–680 keV) and doses. Singly ionized N species (N^+) were used for energies at or below 120 keV, while doubly ionized species (N^{++}) were used above 120 keV. The as-implanted samples were fully depleted, and subsequent annealing at 1100°C in N_2 ambient for 10 minutes enabled dopant activation and carrier recovery. Unimplanted samples were also subjected to the same annealing conditions to compare the defect arising from thermal effects. All test devices were fabricated with Ni Schottky contact of 300 × 300 μm^2 on top of the HVPE grown layer and ohmic stack (Ti/Al/Ni/Au) on the backside substrate. Before implantation and annealing, DLTS detected deep levels at E_C-0.7 eV and E_C-0.8 eV, whereas DLOS revealed deeper states at E_C-2.0 eV and E_C-4.4 eV. The as-implanted samples displayed states at E_C-0.34, E_C-0.6, E_C-0.7, E_C-0.8, and E_C-1.36 eV from DLTS. The DLOS spectra of as-implanted samples exhibited an increase in the concentration of E_C-2.0 and E_C-4.4 eV levels. After annealing, concentrations of the E_C-0.34, E_C-0.6, E_C-0.7, and the E_C-1.36 eV traps were reduced, with the latter going below the detection limit. Another level at E_C-0.25 eV was newly introduced after annealing. Each of these states closely resembles the energy levels and cross-sections (Arrhenius behavior) of previously reported defects due to proton-radiated damage[1], implying that these defect states are due to implantation damage. In contrast, one state detected by DLOS at E_C- 2.88 eV tracks the N-implantation concentration and is not diminished by annealing. DFT calculations have predicted that nitrogen occupying oxygen site III will have the lowest formation energy, with an energy state close to the measured DLOS energy, and would act as a compensator[2]. The results of a deep analysis of each defect state, particularly the E_C-2.88 eV defect, including thermal stability, will be presented. Additionally, SIMS measurements are underway to reveal better correlations between the N-implant concentration and the evolution of defect states.

References:

[1] J McGlone, H. Ghadi, and S.Ringel. Manuscript submitted.
[2] H. Peelaers, J.L. Lyons, J.B. Varley, and C.G. Van de Walle, APL Materials **7**, 022519 (2019).
[3] R. Passler, J. Appl. Phys. **96**, 715 (2004).

9:40 AM FF05

(Student) Chemical Mechanical Polishing of (010) β-Ga_2O_3 Substrates Michael E. Liao, Lezli Matto, Kenny Huynh and Mark Goorsky; University of California, Los Angeles, United States

(010) β-Ga_2O_3 substrates were chemical mechanical polished and the effect of applied polishing pressure was addressed. We find that an applied pressure of 1 kPa is necessary for achieving both smooth (0.6 nm r.m.s. roughness) surfaces and subsurface-damage-free material simultaneously using an alkaline colloidal silica slurry. Triple-axis X-ray diffraction rocking curves of the symmetric (020) reflection were employed to assess the subsurface lattice damage by measuring diffuse scatter intensity (e.g. lattice mosaicity). Diffuse scatter intensity was measured by the FWXM (e.g. X = 0.001) of rocking curves. Pristine (010) β-Ga_2O_3 substrates were used as a benchmark for unequivocally determining if certain polishing parameters induced any subsurface lattice damage. All samples were carefully mounted on the X-ray diffractometer such that no strain to the substrate was introduced. Large instrumental broadening, poor sample mounting, and/or poor crystalline quality material can obscure polish-induced damage when measuring X-ray rocking curves. The (020) rocking curve widths of the pristine substrates were narrow: ~10" and 120" for the FWHM and FW(0.001)M, respectively.
An alkaline 70-nm colloidal silica slurry was used, with an applied pressure of only 1 kPa in order to produce a smooth (r.m.s. roughness less than 0.6 nm) and subsurface damage-free substrate. This technique was also employed to remove the subsurface damage for substrates that were initially polished using > 1 kPa pressures. For example, the rocking curves of the substrates that were initially polished using ~3 kPa of pressure reduced from ~30" and ~760" to ~20" and ~470" for the FWHM and FW(0.001)M, respectively after the 1 kPa process. Typical reports of CMP of β-Ga_2O_3 describe much higher polishing pressure and have produced smooth surfaces. We have also demonstrated smooth surfaces under such conditions but with significant levels of subsurface damage. The removal rate for the 1 kPa process is ~0.4 μm/hr which is also suitable for CMP for wafer bonding β-Ga_2O_3 and for assessing the thermal transport characteristics of damaged vs pristine β-Ga_2O_3 surfaces. Compared to our previous work that used diluted bleach and citric acid to chemical mechanical polish various III-V materials,[1,2] we show that this chemistry combination is ineffective on β-Ga_2O_3. Also, reduction of Si on the substrate surfaces can be achieved with utilizing alumina or ceria based slurries instead of silica.

The authors would like to acknowledge the support from the Office of Naval Research through a MURI program, grant No. N00014-18-1-2429.

References

1. S. Hayashi, et al., ECS Trans., 16(8), 295 (2008).
2. S. Hayashi, et al., J. Electrochem. Soc., 155(2), H113 (2008).
3. C. Huang, et al., Precision Engineering, 56, 184 (2019).
4. C. Huang, et al., RSC Adv., 8, 6544 (2018).

10:00 AM Refreshment Break

10:20 AM FF06

(Student) Observation of Hyperbolic Shear Polaritons in Monoclinic Crystals Giulia Carini[1], Nikolai C. Passler[1], Xiang Ni[2], Guangwei Hu[2,3], Joseph R. Matson[4], Martin Wolf[1], Joshua Caldwell[4], Mathias Schubert[5], Andrea Alù[2], Thomas G. Folland[6] and Alexander Paarmann[1]; [1]Fritz Haber Institute of the Max Planck Society, Germany; [2]City University of New York, United States; [3]National University of Singapore, Singapore; [4]Vanderbilt University, United States; [5]University of Nebraska, United States; [6]The University of Iowa, United States

Surface phonon polaritons, light-matter coupled waves at the interface between a dielectric and a polar crystal, have recently attracted much attention as a versatile tool for low-loss nanophotonic applications in a range spanning from mid- to far-infrared. These modes can exist inside the *Reststrahlendband*, i.e. the region included between the two resonance frequencies of optical phonons (LO and TO) with a negative dielectric permittivity. In particular, materials featuring high optical anisotropy have been shown to support a hyperbolic response that results in hyperbolic polaritons with highly directional propagation and extremely large momenta, enabling the compression of light to deeply sub-wavelength scales. Typically, volume-confined hyperbolic modes in thin films of hexagonal[1] or orthorhombic[2] crystals have been observed, with only few demonstrations of inplane-hyperbolic surface waves on anisotropic bulk crystal surfaces.[3]

In our contribution, we demonstrate the emergence of a new type of hyperbolic surface waves with broken symmetry of the inplane-hyperbolic propagation that exist at surface of the even lower symmetry monoclinic crystal beta-gallium oxide (bGO).[4] We directly compare our observations with the higher symmetry hyperbolic surface phonon polaritons on alpha-quartz (aQ). We show that shear phenomena in the dielectric response of the monoclinic system are directly linked to the symmetry breaking, leading to a new polariton class which we call hyperbolic shear polaritons (HShPs). These modes emerge in low-symmetry monoclinic (and triclinic) crystals whose dielectric permittivity tensor cannot be diagonalized, due to the presence of multiple oscillators with non-orthogonal relative orientations contributing to the optical response.

We experimentally demonstrate HShPs in bGO using the Otto-type prism coupling experiments, by mapping out the azimuthal polariton dispersion. Further, we extract the in-plane hyperbolic dispersion at several wavenumbers, by following the frequency momentum dispersion at many azimuth angles. This allows us to reveal the main novel features of HShPs, that is, the continuous evolution of its propagation direction with frequency and asymmetric responses.

Hyperbolic shear polaritons complement previous observations of hyperbolic phonon polaritons in higher symmetry systems. The shear phenomena observed here may provide new opportunities for topological photonics. We anticipate that our results on HShPs will not only offer additional design options for nanophotonic applications, but will additionally greatly expand on the material base for such devices.

References

1. J. D. Caldwell, et al., Nat. Commun. 5, 5221 (2014).
2. W. Ma, et al., Nature 562, 557-562 (2018).
3. W. Ma, et al., Nature 596(7872), 362-366 (2021).
4. N. C. Passler, et al., in print (2022).

10:40 AM FF07

High Temperature Annealing Effects and Defect Populations of β-Ga_2O_3 Alan G. Jacobs[1], Boris N. Feigelson[1], Marko Tadjer[1], Marc H. Weber[2], Karen N. Heinselman[3], Robert T. Bell[3], Karl Hobart[1], Travis Anderson[1], Kohei Sasaki[4] and Akito Kuramata[4]; [1]US Naval Research Lab, United States; [2]Washington State University, United States; [3]National Renewable Energy Laboratory, United States; [4]Novel Crystal Technology, Japan

Beta gallium oxide (bGO) presents great potential for next generation power and RF devices in no small part due to the large area, high quality, melt grown, bulk substrates available, something lacking in alternatives such as gallium nitride, aluminum nitride, and diamond. While bulk crystal growth is essential, so too is growth of high quality and exceedingly phase-pure single crystal epitaxial structures. Among growth techniques, molecular beam epitaxy (MBE) and metalorganic chemical vapor deposition (MOCVD) are common with differing tradeoffs in purity, crystal structure, and defect populations. MBE films are typically grown at more moderate temperatures which can benefit purity at the expense of a greatly reduced growth rate as well as reduced atomic mobility for crystal refinement. Here, we focus on the effects of high temperature annealing on the quality and defect structure of a 500nm thick MBE bGO film grown on an 010 bulk substrate. Specifically, we target annealing near typical MOCVD growth regimes at 1000°C by both RTA and moderate pressure (~30 bar) annealing in nitrogen, as well as rapid heating and cooling pulses (max ~300 K/s) at moderate pressures via multicycle rapid thermal annealing (MRTA) to access intermediate (~1450°C) and high temperature (1600°C) states near the melting point (~1725°C) with rapid quenching to assess the high temperature state. Samples were probed by Nomarski imaging, Raman scattering, X-ray diffraction, positron annihilation spectroscopy (PAS), and Rutherford backscattering spectroscopy with channeling (RBS/c).

Macroscopically, bare films annealed at low and moderate temperatures were unchanged while annealing near the melting point yielded surface reconstruction and features parallel to [001]. Suppression of surface reconstruction was achieved using a 100nm PECVD SiO2 cap during annealing. Phononic behavior was not greatly affected as measured by Raman shift and peak width, and only minor deviations in intensity ratios were notable which could be attributed to spatial anisotropy or slight deviations in substrate rotation during acquisition. High-resolution X-ray diffraction indicates consistent quality of films and substrates with no deleterious effects after quenching from any anneal condition.

At the atomic scale, PAS measures defect populations by the annihilation lifetime of injected positrons. Energy dependent PAS was obtained for all conditions yielding S and W parameters as a function of depth. This data was fit to a three layer model to capture surface mediated artifacts, a true film population (~500nm), and the bulk substrate population. Measurements on virgin material shows a greater S parameter of the MBE film and surface relative to the substrate indicating the expected greater defect concentration from the low film growth temperature. Upon annealing, the MBE film defect populations are significantly affected by both the sample temperature and presence of the cap while the bulk material defect population was relatively unaffected by any anneal condition. Film defect populations were indeed even improved upon beyond the population of the bulk substrate as indicated by the reduced S-parameter. Furthermore, plots of S vs W show a linear trend for both the MBE film and substrate for all samples indicating a similar defect or defect complex dominating the PAS signal for all films and substrates.

11:00 AM FF08

(Student) Effect of Extended Defects on Photoluminescence of Gallium Oxide and Aluminum Gallium Oxide Epitaxial Films

Jacqueline Cooke[1], Praneeth Ranga[1], Jani Jesenovec[2], John S. McCloy[2], Sriram Krishnamoorthy[3], Michael Scarpulla[1] and Berardi Sensale Rodriguez[1]; [1]The University of Utah, United States; [2]Washington State University, United States; [3]University of California, United States

Photoluminescence (PL) has been under intense scrutiny in an attempt to define the mechanisms that generate the emissions in gallium oxide (Ga_2O_3). In general, PL spectra is used to characterize the defects leading to radiative recombination processes within a specific material. In this regard, the PL spectra for β-Ga_2O_3 has generally been deconvoluted in three emission peaks: UV, blue, and green. However, peak shapes from any point defect are expected to require more than a single Gaussian for a complex crystal structure like β-Ga_2O_3, possibly having an asymmetric shape and requiring a more complex model, which takes into consideration the vibrational broadening of the PL spectrum due to electron-phonon coupling. The sum of many phonon replicas makes it challenging to fit the spectra uniquely. Adding energy level broadening from disorder or extended defects makes deconvolution of the β-Ga_2O_3 PL spectra even more difficult. As such, there is little chance of being able to spectroscopically discern different types of defects in β-Ga_2O_3 from luminescence as any defect considered can result in a very wide luminescence band, even near 0 Kelvin.

This has resulted in an intense debate in defining the defects and phenomenological explanations of electronic processes that cause these particular emissions. In these debates, point defects have been the only explored and discussed potential source for the visible PL emission in β-Ga_2O_3. But, as far as can be determined, no previous works in the literature have discussed whether extended defects affect PL.

Here, a systematic PL study on three series of β-Ga_2O_3 /aluminum gallium oxide films and bulk single crystals is performed. The first series includes three film samples with varying Si-doping: UID (~10^{16} cm^{-3}), ~10^{17} cm^{-3}, and ~10^{18} cm^{-3}. All samples in the series are (010) oriented Si-doped β-Ga_2O_3 film grown on Fe-doped β-Ga_2O_3. The second series contains three samples and compares (-201) β-Ga_2O_3. This series includes a bulk crystal of (-201) UID β-Ga_2O_3, a (-201) UID β-Ga_2O_3 film grown on Fe-doped β-Ga_2O_3, and a (-201) UID β-Ga_2O_3 film grown on sapphire. The last series compares (010) oriented $(Al_xGa_{1-x})_2O_3$ films, i.e., AGO of varying Al concentrations (0%, 10%, and 25%), grown on Fe-doped β-Ga_2O_3. These are compared to a (100) oriented bulk 10% AGO (β-$Al_{0.2}Ga_{1.8}O_3$) crystal. A second part of the series compares (-201) oriented 0%, 2%, 10%, and 28% AGO films grown on sapphire. The Si-doped series yields homogeneous crystalline films with a low density of extended defects [1] and a dominant UV emission in PL. In the (-201) series, the bulk (-201) β-Ga_2O_3 sample also shows a dominant UV emission. On the other hand, Heteroepitaxial and homoepitaxial (-201) β-Ga_2O_3 films show consistent PL features with dominant blue emission. The (-201) films' poor quality [2, 3] is likely the reason for this shift in the dominant emission, as observed when comparing UID films grown on (010) and (-201) bulk β-Ga_2O_3 crystals with comparable growth conditions. The AGO series shows consistent blue centered PL with no UV emission for both homoepitaxial and heteroepitaxial AGO samples. The AGO films show extended defects throughout a poor-quality film revealed using transmission electron microscopy (TEM) on the 25% AGO grown on (010) bulk β-Ga_2O_3 crystal.

Lastly, representative samples chosen from all three series were compared and it is shown that extended defects have an essential role in the PL emission of β-Ga_2O_3 and AGO films. Homogeneous films with no extended defects or stacking faults and bulk crystals will yield a UV dominant PL emission. Samples of poor film quality that have stacking faults and extended defects will have a dominant blue PL emission.

References: [1] Rafique, S., *et al.*, *Appl. Phys. Lett.* **108**, 182105 (2016).

[2] Ghadbeigi, L., *et al.*, *Journal of Elec Materi.* **50**, 2990-2998 (2021).

[3] Eisner, B. A., *et al.*, *J. Appl. Phys.* **128**, 195703 (2020).

11:20 AM FF09

(Student) Ultrafast Laser Induced Deep Level Defects and Correlations with Crystallinity in β-Ga2O3 Daram N. Ramdin, Micah Haseman, Emma DeAngelis, Mohamed Yaseen Noor, Enam Chowdhury and Leonard J. Brillson; The Ohio State University, United States

β -Ga2O3 has received widespread attention due to its ultrawide bandgap, which potentially permits applications in extreme conditions. Ultrafast laser irradiation of β -Ga2O3 provides a means for exploring the response of the material under such conditions, which could result in the generation of point defects as well as a localized modification of structural features that could yield properties that differ from the pristine surface. An understanding and control of the effects of laser irradiation thus constitutes an important scientific as well as technological venture. Previous works [1-2] focus on the nature of morphological changes and their relationship with surface and electrical properties. The nature of defects

created by laser irradiation and their correlation with morphologically distinct regions created by laser irradiation remains a relatively unexplored and important problem. We report depth-resolved cathodoluminescence (DRCLS) measurements that describe the nanoscale spatial evolution of both native defects and crystallinity in Ga2O3 across different morphological regions generated by a p-polarized 1064 nm pulsed laser with a duration of 100 fs and fluence of 2.1 J/cm2. DRCLS reveals an emergent ~2.4 eV emission that becomes more prominent towards the surface in regions that have distinct morphological changes. Since disassociated Frenkel pairs are expected to form upon ultrafast laser irradiation [2], and that anionic Frenkel pairs are predicted to dominate the defect structure of Ga2O3 [3], potential sources of the ~2.4 eV emission are oxygen interstitials [4] or divacancy complexes [5]. Mapping the crystallinity reveals that a higher density of the ~2.4 eV emission corresponds to regions of low crystallinity. The defect of density decreases as a function of distance from the least crystalline region, while the crystallinity increases as distance from that region increases. Depth profiling reveals that in the most damaged region, the ~2.4 eV emission extends for over 100 nm; in less damaged

regions the emission is more surface localized (<50 nm). These measurements suggest that defect formation and crystallinity reduction in laser-damaged

regions have a distinct correlation with the morphology of the region and consequently with mechanical breakdown. The emergence of a deep level near damaged regions points to a strong relationship between morphological damage and optical/electronic properties that can potentially have implications on device fabrication and processing in extreme conditions. However, DRCLS reveals new defects extending even into flat morphology regions. Research efforts are underway to identify the impact of ultrafast laser irradiation for fluences where damage is invisible.

[1] Ahn. et al., Journal of Applied Physics 125, 223104 (2019)

[2] Ahn. et al., Oxide-Based Material and Devices XI (2020)

[3] M.A. Blanco et al., Phys. Rev. B 72, 184103 (2005)

[4] M.E. Ingebrigtsen et al., APL Materials 7, 022510 (2019)

[5] Y.K. Frodason et al., Phys. Rev. Materials 5, 025402 (2021)

11:40 AM FF10
(Student) Photoluminescence Spectroscopy of Cr^{3+} in β-Ga_2O_3 and $(Al_{0.1}Ga_{0.9})_2O_3$ Cassandra Remple, Jani Jesenovec, Benjamin L. Dutton, John S. McCloy and Matt D. McCluskey; Washington State University, United States

Alloying β-Ga_2O_3 with Al_2O_3 to create $(Al_xGa_{1-x})_2O_3$ enables ultra-wide band gap material deep into the UV. Here, photoluminescence (PL) spectra of Cr^{3+} dopant is compared between monoclinic single crystals β-Ga_2O_3 and 10 mol.% Al_2O_3 alloyed with β-Ga_2O_3, denoted β-$(Al_{0.1}Ga_{0.9})_2O_3$ or AGO. Temperature dependent PL properties were studied for Cr^{3+} in AGO and β-Ga_2O_3 from 285 to 16 K. For β-Ga_2O_3 at room temperature, the red-line emission doublet R_1 and R_2 occurs at 696 nm (1.78 eV) and 690 nm (1.80 eV) respectively along with a broad emission band at 709 nm (1.75 eV). The R_1 line is approximately 1 nm higher for AGO compared to that of β-Ga_2O_3. For both AGO and β-Ga_2O_3 the R_1 line increases in intensity with decreasing temperature. This can be explained by the thermal depopulation effect of the R_1 state, which occurs with increasing temperature. The R_1 and R_2 lines of both materials were observed to blue-shift with decreasing temperature. Additional emission lines emerge at lower temperatures, with β-Ga_2O_3 showing more peaks than AGO. R_1 and R_2 peak parameters such as energy, intensity, width, and splitting were studied as a function of temperature, with significant differences between the two materials.

SESSION GG: Epitaxial Growth on Patterned Substrates

Session Chairs: Minjoo Lee and Kyle McNicholas
Friday Morning, July 1, 2022
Cartoon Room #1

8:20 AM GG01
(Student) Selective Area Epitaxy by MBE for Self-Aligned III-V Devices Alec M. Skipper[1], Andrew Jones[2], Morgan Bergthold[1], Aaron J. Muhowski[1], Ashlee Garcia[1], Daniel J. Ironside[1], Daniel Wasserman[1], Joe Campbell[2] and Seth R. Bank[1]; [1]University of Texas at Austin, United States; [2]University of Virginia, United States

Semiconductor devices have historically been processed with growth first, followed by metal and dielectric deposition, patterning, and etching. However, careful process control is required to reduce undesirable recombination and dark current at device surfaces. Commonly used III-V materials experience Fermi level pinning at the semiconductor/air interface [1], leading to undesirable device characteristics such as elevated dark currents arising from etch residue, sidewall damage, and oxidation [2-4]. As a result, great care must be taken to choose the correct etch chemistry and surface passivation must be performed quickly before harmful oxides form on the etched sidewalls. Additional process steps are required to mitigate these effects, complicating the manufacturing process and reducing device yield/performance. By contrast, devices created by selective area growth present a possible solution to these issues by bypassing the need for challenging alignment and surface treatment steps [5]. Selective area growth utilizes a template on the surface of the sample to define the device regions. Unlike self-assembled quantum dots and nanowires, selective area growth allows complete control over the size, placement, and distribution of the grown nanostructures by simple photolithography. Furthermore, since the device structure is created *in situ* during growth under ultra-high vacuum, there is no risk of oxidation and the sidewalls can be nearly atomically smooth. We present self-aligned devices passivated *in vacuo* by selective area molecular beam epitaxy growth. Silicon dioxide was deposited on III-V wafers and windows were etched to the substrate in the shape of the desired devices. Periodic supply epitaxy (PSE) was then used to selectively grow the device layer structures in the windows. PSE utilizes interruptions in the group-III flux and high growth temperatures to enhance desorption and diffusion on the silicon dioxide surface, ensuring growth only occurs in regions seeded from the substrate [6]. This results in the device structure growing within the window that naturally conforms to the dielectric sidewall. Furthermore, this semiconductor-dielectric interface is formed *in vacuo*, meaning there is no risk of creating unstable III-V oxides. As a prototype, an InAs tunnel diode was grown by selective area epitaxy and compared to a conventionally fabricated diode with the same layer structure. Comparable current-voltage characteristics were observed from the two devices, suggesting that the PSE growth process does not negatively impact electrical characteristics. Investigation of dark current and photoluminescence are underway and will be reported at the conference.
This research was partially supported by Lockheed Martin and the National Science Foundation through the Center for Dynamics and Control of Materials: an NSF MRSEC under Cooperative Agreement No. DMR-1720595, as well as DMR-1839175, CCF-1838435, and ECCS-1926187.
[1] C. Mead and W. Spitzer, "Fermi Level Position at Semiconductor Interfaces," Phys. Rev. Lett. (1963)
[2] Y. B. Hahn et al., "High-density plasma-induced etch damage of InGaN/GaN multiple quantum well light-emitting diodes," J. Appl. Phys. (2002)
[3] O. Demichel et al., "Impact of surfaces on the optical properties of GaAs nanowires," Appl. Phys. Letters (2010)
[4] E. Pils et al., "Passivation techniues for InAs/GaSb strained layer superlattice detectors," Laser Photonics (2013)
[5] J. Bai et al., "A Direct Epitaxial Approach to Achieving Ultrasmall and Ultrabright InGaN Micro Light-Emitting Diodes (μLEDs)," ACS Photonics (2020)
[6] D. Ironside et al., "High-Quality GaAs Planar Coalescence over Embedded Dielectric Microstructures Using an All-MBE Approach," ACS Cryst. Growth Des. (2019)

8:40 AM GG02
(Student) Molecular Beam Epitaxy for Photonic Crystal Surface Emitting Lasers (PCSELs) Subhashree Seth[1], Kevin J. Reilly[1], Fatih F. Ince[1], Akhil Kalapala[2], Thomas J. Rotter[1], Zhongue Liu[2], Emma J. Renteria[1], Weidong Zhou[2] and Ganesh Balakrishnan[1]; [1]The University of New Mexico, United States; [2]The University of Texas at Arlington, United States

Photonic crystal surface emitting lasers (PCSELs) are fabricated by molecular beam epitaxy (MBE). Electrically injected devices are demonstrated using epitaxial regrowth. Non-regrowth fabrication is explored and compared to regrowth.
Traditional semiconductor lasers struggle to realize both high-power high-quality beams from a monolithic form-factor. PCSELs incorporate a photonic crystal (PC) laser cavity to isolate a single lasing mode; thereby enabling PCSELs to power scale with area whilst maintaining coherent emission.
Early PCSELs were fabricated by wafer fusion in which a PC is bonded to a second wafer containing a laser active region [1]. This technique creates a high density of defects at the bonded interface. Modern PCSELs instead employ epitaxial regrowth [2]. By this method, an initial epitaxy constructs the bulk of the laser structure including a lower cladding layer, active region, and a PC region. In a second step, the top PC layer is patterned by electron-beam lithography and ICP etch to create a series of periodically spaced voids at the surface. This surface is then regrown with top cladding and contact layers. In recent years, there have been attempts to simplify PCSEL fabrication by using non-regrowth methods described as a "PC slab-on-substrate" structure [3]. Avoiding regrowth simplifies PCSEL construction and is more time

efficient. However, optical output is limited compared to regrown devices.
While epitaxial regrowth is optimal for device performance, it introduces new complexity due to infilling of the PC and because obtaining a clean regrowth surface is challenging. We optimize pre-regrowth chemical treatment and identify the maximum tolerable temperatures for in-situ thermal cleaning. Secondly, for PCSEL design, it is important to match the resonance of the PC cavity to the photoluminescence of the active region. Relevant parameters include PC lattice structure, lattice period, void shape, PC fill factor, and the relative indices of refraction of PC materials. To control PC resonance, the influence of regrowth to void morphology is investigated and reported. In this study, a PC region is patterned over a range of 8 exposure doses to vary printed void radii. The voids are then measured by SEM before and after regrowth and compared. This study demonstrates that pre-regrowth void radius influences growth direction, i.e. growth at the sidewalls or at the bottom of the void, and allows us to engineer pre-regrowth voids to produce the desired post-regrowth morphology. Regrown PCSEL devices are demonstrated by optical pumping and electrical injection.
In addition to PCSEL fabrication by regrowth methods, non-regrowth methods are explored. Non-regrowth is advantageous because it significantly reduces fabrication time, enabling researchers to make quick empirical studies of photonic crystal designs. Additionally, it bypasses the complicated regrowth step and the high temperature exposure associated with it. This can be particularly important for quantum dot devices as high temperatures can blue shift their emission. However, relative to regrowth, the optical output of these devices is limited. Non regrowth fabrication consists of a single epitaxial growth with a bottom contact layer, bottom cladding, active region, top cladding, and top contact layer. The epitaxial structure is patterned by electron beam lithography and ICP etch. A SiN aperture is formed by liftoff and chemical vapor deposition (CVD). Indium tin oxide (ITO) is deposited by sputtering as a transparent conductive material to make electrical contact with the PCSEL surface. Non-regrowth PCSELs are fabricated for electrical injection and compared to edge-emitters from the same epitaxial structure.
1. M. Imada et al, IEEE Journal of Quantum Electronics. 35, 1277-83 (1999)
2. M. Yoshida et al, Nature Material. 18, 121-128 (2018)
3. MY Hsu et al, Optics Express. 25, 32697-704 (2017)
4. K. Reilly et al, Journal of Crystal Growth. 535, 125531 (2020)

9:00 AM GG03
(Student) Orientation-Aligned InP on Si by Templated Liquid Phase Growth Jun Tao, Juan S. Vazquez, Amir Avishai and Rehan Kapadia; University of Southern California, United States

III-V semiconductors have many merits that make them ideal for use in electronics and optoelectronics. But heterogeneous integration of single-crystalline III-V on Si is highly challenging. The low-temperature templated liquid phase (LT-TLP) growth approach was developed to solve the problem of lattice mismatch and satisfy the thermal requirement. However, the randomly distributed crystalline orientation of each mesa blocked the pathway for the technique to be commercialized. Here, we demonstrate the orientation-aligned InP on Si by TLP growth, providing a new platform for scalable and cost-effective III-V on Si integration.
Starting from the n-type silicon wafer with <100> orientation, GaAs nucleation layer and InP layer were deposited through MOCVD. The GaAs nucleation layer works as a buffer layer to ease the lattice mismatch at InP/Si (~8%) interface. Then ~800 nm InP was grown with three phases, but a large number of defects is still expected at the interface. Then, templated In (20x20x1 μm^3) and SiO_2 capping layer were deposited, followed by InP growth in a single-zone furnace at 550°C with PH3 ambient. III-V dry etch and HF wet etch were implemented after the growth to remove the lateral growth and SiO_2 capping layer, respectively.
The representative SEM image of the fully grown InP mesa and the map of photoluminescence (PL) peak intensity are shown in Figure 2 (a) and (b). The contrast from two orders of peak intensity difference clearly depicted the mesa boundary, indicating weaker non-radiative carrier recombination in TLP grown InP mesa. The normalized PL of InP wafer and InP by TLP showed a slight peak shift (10meV) caused by phosphorus vacancies, and identical FWHM (50 meV), indicating good quality of the grown material. Additionally, the Urbach parameters were extracted from the curves (8.01 meV for InP wafer, 8.3 meV for TLP InP), suggesting the high electronic quality. The total recombination can be described by $R = An+Bn^2+Cn^3$, where A is the SRH recombination rate, B is the radiative recombination rate, and C is the Auger recombination rate. Given the unintentionally doped carrier concentration (~10^{17} cm^{-3}) and low Auger recombination coefficient, the contribution from Auger recombination can be neglected. The TLP grown InP on MOCVD InP showed 10 to 100 folds higher peak intensity than that from the MOCVD grown InP on Si and TLP grown InP on SiO_2. It indicates the much lower contribution of trap-assisted non-radiation recombination and lower defect density.
At the GaAs/InP and Si interface, various thread defects and stacking faults can be observed from the TEM image, some of which propagate to the surface of the GaAs/InP layer, but are terminated at the interface. However, InP by TLP strictly followed the MOCVD grown InP lattice structure, and none of the point defects, stacking fault, or twinning boundaries were observed in this region.
Crystalline orientation was determined by electron backscatter diffraction (EBSD) and Transmission Kikuchi diffraction (TKD). As demonstrated in Figure 4 (a) and (b), a representative area of TLP mesas showed identical <100> out-of-plane orientation with the MOCVD GaAs/InP substrate across the whole sample. A much lower number of twinning boundaries were observed from the raw crystal orientation map compared with the map from InP on SiO_2. The inverse pole figure by TKD from the cross-section lamella of the sample allowed the detailed orientation and texture study with higher resolution (~40 nm in this measurement). The three-directional crystal orientation map in Figure 4 (d) to (f) confirmed the ideal orientation-alignment of InP by TLP growth in this new approach.
In conclusion, orientation-aligned InP mesas were integrated on Si wafer with TLP growth technique and demonstrated superior structural and optoelectronic properties. It paved the pathway toward scalable 3D high-quality III-V semiconductor-based devices on Si.

9:20 AM GG04
(Student) Molecular Beam Epitaxy Selective Area Regrowth of High Aspect Ratio Microstructures Ashlee Garcia, Alec M. Skipper, Daniel J. Ironside and Seth R. Bank; The University of Texas at Austin, United States

A molecular beam epitaxy (MBE) approach to selective area epitaxy (SAE) of III-V semiconductors could enable the seamless integration of metals, dielectrics, and high-quality crystalline semiconductors. This technique has the potential to advance novel optoelectronic structures, such as high-contrast photonics, site-controlled quantum emitters, stacked pixel detectors, and photonic integrated circuits. Utilizing patterned dielectrics and metals to define crystal seeding regions, SAE can be used to embed microstructures into crystalline semiconductors[1]. While SAE by metal organic chemical vapor deposition has been widely successful due to its high material deposition selectivity, an SAE MBE method could enable further advances through its high layer precision and access to non-equilibrium growth conditions[1,2]. SAE is difficult to achieve with conventional MBE due to III-V nucleation on the amorphous mask even at temperatures as high as 700°C. As a result, Allegretti et al. developed periodic supply

epitaxy (PSE), a method to inhibit polycrystal deposition by cycling group III deposition under a constant group V flux[2,3]. Combined with high growth temperatures and low growth rates, PSE enables SAE by mitigating the nucleation of poly-GaAs through increased Ga adatom diffusion to seeding windows and desorption off the mask[3-4]. While an all-MBE approach has been demonstrated to achieve selective growth of features ~2µm wide and ~300nm tall, applications requiring larger features such as mid- and long-wave infrared high-contrast photonics[5] and aspect ratio trapping of threading dislocations for metamorphic growth[6], are limited by nucleation of polycrystalline semiconductor on the amorphous surface due to low adatom surface diffusion[1,3].
To expand the accessible applications, a numerical 1D model was developed to describe PSE selectivity by fitting adsorption, desorption, and diffusion constants to GaAs growth on SiO_2 films at 600°C with a growth rate of 0.7A/s and a 65x As_4/Ga ratio[7-10]. The model (1) identifies selective growth regimes to clarify their underlying mechanisms and (2) allows optimized growth conditions to be determined for a given SiO_2 pattern. Two growth regimes were identified: desorption- and diffusion-limited. The desorption-limited regime relies only on thermal desorption off the mask to achieve selectivity and therefore is feature-independent. The remainder of the space is diffusion-limited in which sufficient III adatom diffusion off the mask is required to achieve selectivity. Desorption-based selectivity can be achieved with a PSE cycle, the fraction of time the group III shutter is open, under 18% based on the model. This regime was verified experimentally with scanning electron microscopy. No polycrystal formation on the mask surface after 100nm of GaAs growth with a 10% cycle on a SiO_2 film and SiO_2 gratings spaced 1µm apart with varied widths from 1 to 10µm indicates the ability to achieve selective growth over any arbitrary set of features. Experiments to further extend achievable mask height using a feature-independent growth regime and investigate the physical limit of diffusion-based growth for high aspect ratio features are underway and will be reported at the conference.
[1] D.J. Ironside et al., *J. Cryst. Growth* (2019). [2] A.M. Skipper et al., 2019 MRS EMC. [3] F.E. Allegretti et al., *J. Cryst. Growth* (1995). [4] S.C. Lee et al. *J. of Appl. Phys.* (2002). [5] Jun Wang *et al.* 2017 *Laser Phys. Lett.* 14 125801. [6] J.Z. Li et al. Appl. Phys. Lett. 91 (2) (2007). [7] S. Shankar. Diffusion in 1D and 2D, MATLAB. Retrieved Apr. 2020. [8] Aseev et al. *Nano. Lett*. (2019). [9] S.C. Lee et al. *Cryst. Growth Des.* 2016. [10] E.M. Gibson et al. *Appl. Phys. Lett.* (1990).
This research was partly done at the Texas Nanofabrication Facility (NSF grant NNCI-2025227) and was supported by Lockheed Martin and NSF via the UT CDCM: an NSF MRSEC under Cooperative Agreement DMR-1720595, as well as CCF-1838435 and DMR-1839175.

9:40 AM GG05
(Student) Monolithic Integration of III-Vs with Silicon Nitride Integrated Photonics by MBE Yiteng Wang[1,2], Pankul Dhingra[1,2], Cheryl Sorace-Agaskar[3], Christopher Heidelberger[3] and Minjoo L. Lee[1,2]; [1]University of Illinois Urbana-Champaign, United States; [2]University of Illinois at Urbana-Champaign, United States; [3]Massachusetts Institute of Technology, United States

Integration of visible III-V lasers with silicon nitride (SiN_x) photonics is a promising route towards low-cost, on-chip photonic platforms for applications such as quantum computing [1], biosensing [2], and displays [3]. Wafer- and chip-scale bonding is utilized commercially for integration of III-V lasers with Si photonic integrated circuits (PICs), but improved economies of scale and higher integration densities can be realized via direct epitaxial growth. Our group recently reported visible quantum well and quantum dot lasers epitaxially grown on Si substrates using molecular beam epitaxy (MBE), attaining low threshold current densities despite a threading dislocation density (TDD) of 1×10^7 cm^{-2} [4]. Heidelberger *et al.* recently demonstrated a SiN_x PIC designed for in-plane butt-coupling of epitaxial III-V lasers, modulators, and detectors grown in pockets etched into the dielectric layers [5]. In this work, we demonstrate MBE regrowth of GaAs in prefabricated SiN_x PICs as an essential step towards integration of on-chip visible and near-infrared lasers and optical amplifiers.
The PIC structure consists of SiN_x waveguides cladded with SiO_2, fabricated on a 1 µm blanket Ge film on offcut Si (001) (see [5] for further details). Metal organic chemical vapor deposition (MOCVD) is used for selective growth of GaAs (~3 µm thick) in etched pockets that expose the surface of the Ge layer. The samples are then transferred to our solid-source MBE system for non-selective growth of subsequent III-V layers. No wet cleaning steps were performed, and standard de-oxidation conditions under As_2 flux were used prior to growth. We grew 1 µm GaAs films on PIC templates at substrate temperatures (T_{sub}) of 400-650°C at a rate of 1 µm/hr and V/III ratio of 15-23.
While the MBE growth conditions used in this work do not lead to selective epitaxy, the sample grown at T_{sub} = 650°C shows no deposition of polycrystalline GaAs on the vertical dielectric sidewalls due to reduced flux and enhanced migration of Ga adatoms. In contrast, the samples grown at T_{sub} = 400 and 580°C exhibited ~180-200 nm of polycrystalline GaAs on the vertical sidewalls. While all samples exhibited faceting near the interface between the III-V epi-layer and dielectric sidewall, the use of lower T_{sub} led to steeper facets (~44°) due to inhibited adatom migration. We observed smooth surface morphologies for GaAs grown at T_{sub} = 400 and 650°C, though the roughness increased for samples grown at 580°C.
The TDD within the GaAs epitaxial pockets was ~2.5×10^7 cm^{-2} for the sample grown at T_{sub} = 650°C, which is similar to the typical value for relaxed Ge on Si [6]. Our group and others have shown that such TDD values are acceptable for quantum dot lasers due to their improved dislocation tolerance, making these results promising for future device integration. Additional study on the growth of quantum well and quantum dot-based phosphide active regions in PICs will be presented at the conference.
References
[1] J. Wang, F. Sciarrino, A. Laing, and M. G. Thompson, Nat. Photonics **14**, 273–284 (2020).
[2] K. D. Vos, I. Bartolozzi, E. Schacht, P. Bienstman, and R. Baets, Opt. Express **15**, 7610–7615 (2007).
[3] H. Hamada, Fiber Integrated Opt. **34**, 259-281 (2015)
[4] P. Dhingra, P. Su, B. D. Li, R. D. Hool, A. J. Muhowski, M. Kim, D. Wasserman, J. Dallesasse, and M. L. Lee, Optica **8**, 1495-1500 (2021)
[5] C. Heidelberger, C. S. Agaskar, J. J. Plant, D. Kharas, R. B. Swint, P. Dhingra, M. L. Lee, P. W. Juodawlkis, IEEE Photonics Conference, 1-2 (2021)
[6] K. H. Lee, A. Jandl, Y. H. Tan, E. A. Fitzgerald, and C. S. Tan, AIP Adv. **3**, 092123 (2013)

10:00 AM Refreshment Break

SESSION HH: Lattice Mismatched Epitaxial Growth

Session Chairs: Minjoo Lee and Kyle McNicholas
Friday Morning, July 1, 2022
Cartoon Room #1

10:20 AM HH01
(Student) Growth of GaP on Silicon-on-Insulator Mijung Kim, Ryan D. Hool and Minjoo L. Lee; University of Illinois at Urbana-Champaign, United States

Nanophotonic devices based on GaP have recently attracted significant interest due to (1) lattice constant close to Si, (2) low

two-photon absorption for wavelengths >1.1 µm, (3) large refractive index (~3.1-3.4), (4) relatively wide bandgap of 2.26 eV for visible wavelengths > 0.55 µm, and (5) non-centrosymmetric crystal structure. GaP-on-Insulator (GaPOI) fabricated by wafer bonding and etch-back has recently been proposed as a novel platform for integrated nonlinear photonics. An alternative integration method would be to grow GaP directly on the silicon-on-insulator (SOI) wafers that are commonly used in Si photonics foundries, followed by selective Si removal using XeF_2 to form suspended GaP structures. In this work, we describe the effects of molecular beam epitaxy (MBE) growth parameters on the structural properties of GaP on SOI. By studying the impact of V/III ratio on Ga-induced pitting, surface roughness, and anti-phase boundary (APB) formation, we achieved epitaxial GaP on SOI films with root-mean-square (RMS) surface roughness of ~1 nm.

GaP was grown by MBE on SOI wafer pieces (SEH America) over substrate temperatures (T_{sub}) of 535-580°C and V/III of 5-10. We consider formation of anti-phase boundaries (APBs) to be unavoidable in these layers, since commercially available SOI wafers are manufactured with an exact (001) surface orientation. While APBs are unacceptable in minority carrier optoelectronic devices, their effect may be less severe in the passive photonic structures targeted here. Before growth, SOI substrates were precleaned with piranha and diluted HF to remove organic residues and oxides. After deoxidation in the growth chamber at T_{sub} = 800°C for 20 min, 220 nm of GaP was directly grown at 0.5 µm/hr. Symmetric (004) omega-2theta high-resolution XRD scans confirmed the epitaxial relationship between GaP and SOI, with the appearance of Pendellösung fringes indicating a smooth interface. The surface morphology and roughness of samples were investigated by Nomarski microscopy, SEM, and AFM.

All GaP on SOI samples exhibit pits with a density of 10^7-10^8 cm^{-2}. Tilted-view SEM image showed that pits at the GaP surface originated from damage at the Si surface, most likely due to Ga-induced melt-back etching at the beginning of growth. Accordingly, the sample grown with the lowest V/III ratio (5) exhibits the highest pit density of 8.7×10^7 cm^{-2}. Lower substrate temperature or higher V/III ratio decreased the pit density by ~7×, presumably due to reduced Ga clustering.

V/III ratio is also a critical factor to obtain a smooth surface in the regions away from pits, and samples grown with V/III=6.0-7.5 showed ~1.5-2.0× higher RMS surface roughness than one with V/III=5. To balance the contradictory effects of V/III ratio on pit density and surface smoothness, we employed a two-step growth using a high V/III ratio (10) for the first 20 nm of growth and a low V/III ratio (5) for the remaining 200 nm. The sample grown using this two-step growth process exhibited RMS roughness of 1.29 nm; for context, high-quality, relaxed GaP grown on GaP/Si templates from NAsP GmbH typically exhibit roughness of 0.6-2.1 nm. Interestingly, the low RMS roughness of the two-step growth sample was also accompanied by a lower APB density. In conclusion, by understanding the strong effect of V/III ratio on surface morphology, we showed epitaxial GaP on SOI with ~1 nm RMS roughness. SOI wafers are widespread in Si photonics foundries, and the addition of GaP to the palette of available materials could enable new applications such as integrated visible and non-linear photonics.

10:40 AM HH02

(Student) Monolithic III-V Growth Directly on Metal for Device Application Hyun Uk Chae and Rehan Kapadia; USC, United States

Direct growth of III-V crystalline on top of metal has been desired to design electrically tunable photonics devices to utilize the metal layer as an electrical contact and bottom reflector. Devices such as metal-insulator-metal (MIM) resonator can be achieved by using this approach. Here in this work, we have demonstrated indium arsenide (InAs) directly grown on metal to build a platform for the device application. Indium arsenide was selected among other III-V semiconductors for growth demonstration thanks to their low bandgap and high electron mobility, which has high potential to achieve the fast dynamic change in refractive index for the photonics devices. The growth was carried at growth temperature of 300°C by low temperature templated liquid phase (LT-TLP) growth. Unlike our previous grown templates on top of amorphous substrates, it is noteworthy that the size of the grown InAs area is over > 80 µm domain size with various InAs thickness (from ~100 nm up to µm scale) by tuning the initial indium template thickness. Thickness of the InAs was verified by using Fourier Transform Infrared Spectroscopy (FT-IR) and focused ion beam (FIB). This approach enables us to control the size and thickness of the grown crystalline, potentially can be used to grow single crystalline size up to *mm* scale by optimizing the growth conditions and processes, opening the new door to realize the large scale III-V growth on metal for device applications.

11:00 AM HH03

(Student) Integrating GaSb-Based Infrared Detectors with Si Substrates via Interfacial Misfit Arrays Trent Garrett[1], Madison Drake[1], Pooja D. Reddy[2], Kunal Mukherjee[2], Shimon Maimon[3] and Paul Simmonds[1,1]; [1]Boise State University, United States; [2]Stanford University, United States; [3]NetZVision LLC, United States

With applications from night vision and aerial target acquisition, to space telescope operation, infrared (IR) detectors are of great interest to the defense and scientific communities alike. The functionality of these detectors hinges on achieving a high signal-to-noise ratio so that weak signals can still be resolved. Of the many designs for IR detectors, the nBn device has emerged as a leading choice. As the name suggests, nBn detectors comprise an *n*-type absorber layer, an electron-blocking barrier, and an *n*-type contact layer. This simple, yet effective, design prevents the collection of majority carriers (electrons), while allowing minority carriers (holes) to flow freely to the collector [1].

nBn-based IR detectors are typically grown on GaSb, which marks perhaps their biggest disadvantage. GaSb substrates are expensive and only widely available up to 4” diameter formats, placing a limit on high volume manufacturing. Successfully integrating III-V based nBn detectors with Si substrates would overcome these wafer cost and size constraints. However, this approach comes with its own set of challenges, primarily due to the large lattice mismatch between GaSb and Si. Direct deposition of GaSb onto Si typically results in the formation of large 3D islands that prevent planar growth, as well as the formation of a high density of threading dislocations and other defects that help to relieve the strain [2]. These threading dislocations mean that an nBn detector grown above this interface will suffer from poor performance.

We are therefore adopting the use of interfacial misfit (IMF) arrays to manage the heterointerface between the III-V epilayers grown by molecular beam epitaxy (MBE) on Si substrates. IMFs consist

of the spontaneous formation of a 2D array of 90° dislocations that lie in the plane of the heterointerface. Unlike 60° threading dislocations, 90° dislocations do not migrate vertically to affect layers grown above. IMFs have been shown to relieve close to 100% of the strain right at the interface, enabling the growth of smooth, high-quality material above [3].

For the specific case of III-Sb materials grown on Si substrates, previous studies have shown that thin layers of AlSb are critical for producing the aforementioned IMF arrays. Compared with the growth of GaSb directly on Si, GaSb deposited onto an AlSb/Si IMF heterostructure has dramatically improved material quality and lower threading dislocation density (TDD) [4]. To ensure the growth of GaSb-on-Si virtual substrates with the highest possible quality for subsequent nBn growth, perfecting the growth of this AlSb/Si IMF layer is fundamentally important.
We will discuss how choices regarding AlSb growth initiation, Si substrate temperature, annealing strategies, AlSb thickness, and AlSb growth rate affect the quality of GaSb overlayers. By optimizing these MBE growth conditions, initial results suggest that we can grow GaSb layers with quality comparable to the current state-of-the-art, which provides us with a valuable reference point from which to make further improvements. Next steps to further enhance material quality will include the use of dopant species, such as Be, to reduce dislocation mobility via solid solution strengthening. We will also investigate the use of dislocation filtering superlattices above the IMF to induce dislocation annihilation and further reduce TDD in nBn devices grown on these GaSb-on-Si templates.

This work is supported by the Office of Naval Research through grant ##N00014-21-1-2445.
[1] S. Maimon and G.W. Wicks, Applied Physics Letters **89**, (2006).
[2] S.H. Vajargah, S. Ghanad-Tavakoli, J.S. Preston, R.N. Kleiman, and G.A. Botton, Journal of Applied Physics **114**, 113101 (2013).
[3] S.H. Huang, G. Balakrishnan, A. Khoshakhlagh, L.R. Dawson, and D.L. Huffaker, Applied Physics Letters **93**, 071102 (2008).
[4] K. Akahane, N. Yamamoto, S.-ichiro Gozu, and N. Ohtani, Journal of Crystal Growth **264**, 21 (2004).

11:20 AM HH04
(Student) Heteroepitaxy of GaSb on GaAs (111)A Substrates for Electron Transport Studies Madison D. Drake, Trent Garrett and Paul Simmonds; Boise State University, United States

III-V semiconductors grown by molecular beam epitaxy (MBE) on (111) surfaces have some interesting electronic properties. For certain materials with a (111)-orientation, the Γ- and L-valleys are reasonably close in energy. This means that it may be possible to take advantage of electron conduction in the L- and Γ-valleys at the same time, allowing us to overcome the so-called “density-of-states bottleneck,” and enable transistors with large drive currents [1]. We are eager to investigate this phenomenon in GaSb- and InAs-based 2D electron gases for which the electron effective masses are low.

However, growth of materials with a (111) orientation is typically more challenging than on traditional (001) surfaces. The MBE conditions needed to grow high quality material are often poorly understood [2]. We began by exploring InAs/GaSb quantum well (QW) structures, [3] grown directly on GaSb(111)A substrates. We will show that low growth rates under very high group V overpressures produce good GaSb homoepitaxy and InAs heteroepitaxy, as characterized by XRD and AFM. However, although we have been able to identify MBE conditions that lead to the growth of smooth, high-quality material, GaSb(111)A substrates are extremely expensive, as well as being intrinsically n-type, which complicates the carrier transport measurements in which we are interested. If we could instead grow our GaSb-based QW structures on cheaper, non-conductive GaAs(111)A substrates, we could overcome these issues. The challenge is the large lattice mismatch between GaSb and GaAs, which typically results in strain-driven crystallographic disorder at the heterointerface and poor material quality.

One technique that has shown promise in circumventing these problems on (001) surfaces is the use of interfacial misfit arrays (IMFs). Under specific molecular beam epitaxy (MBE) conditions it is possible to produce an array of 90° dislocations that lie in the GaSb/GaAs(001) heterointerface. These dislocations efficiently relieve the strain between the two materials without generating the high density of threading dislocations that one would ordinarily expect. As a result, it is possible to grow high quality materials and active device structures above these IMF-based heterointerfaces.

We will discuss our attempts to extend a modified version of this IMF technique to (111) surfaces in order to grow our InAs/GaSb QW structures on GaAs(111)A substrates. So far, this work has produced GaSb grown on GaAs (111)A with a full-width-half-maximum (FWHM) XRD peak value of 270’’. For GaSb/GaAs(001) grown via an IMF approach, other groups have reported FWHM values of 240’’ [4]. We hope to reach similar values after further optimization. We will show how various MBE parameters such as growth temperature, Sb overpressure, GaSb growth initiation and GaSb growth rate affect IMF formation. As a result, we hope to report initial electron transport measurements from InAs/GaSb QWs grown on GaAs(001) and (111) substrates via this IMF technique.

References:
Mehrotra, et.al., IEEE Electron Device Letters, 34, 9 (2013)
Yerino, et.al., Journal of Vacuum Science & Technology, B 35, 010801 (2017)
Eyink, et.al., Journal of Applied Physics, 104, 1074901 (2008)
Reyner, et.al., Applied Physics Letters, 99, 231906 (2011)

11:40 AM HH05
(Student) High Mobility n and p Pseudomorphic Channels Grown on Interfacial Misfit Dislocation Assisted Growth on GaSb/GaAs Fatih F. Ince[1], Alexander T. Newell[1,2], Kevin J. Reilly[1], Subhashree Seth[1], Thomas J. Rotter[1], Ahmad Mansoori[1], Darryl Shima[1], Preston T. Webster[2], Erin Vaughan[2] and Ganesh Balakrishnan[1]; [1]The University of New Mexico, United States; [2]Air Force Research Laboratory, United States

The majority of the antimonide devices are grown on GaSb substrates. These include detectors, lasers, thermophotovoltaic devices and transistors. However, the ability to grow such devices on a GaAs substrate could have significant benefits, including larger substrate sizes, semi-insulating substrates and reduced surface defect density. An added factor is the economics of growing on GaAs which is a much more established substrate technology and costs considerably less when compared to GaSb. The interfacial misfit dislocation growth mode allows us to realize high quality metamorphic GaSb on GaAs.[1] This growth mode is superior to other metamorphic approaches such as step graded buffers due to the spontaneous relaxation of the GaSb layer on the GaAs substrate thus resulting in significant reduction in buffer

thickness. It has resulted in ~ 10^8 dislocations/cm^2 with instantaneous relaxation for 0.5 µm of GaSb grown on GaAs. This is achieved by the formation of a highly periodic misfit dislocation array between the GaSb and GaAs layers that almost fully accommodates the mismatch.[1] Several publications by various authors have shown cross-section transmission electron micrograph (X-TEM) analysis and selective area diffraction analysis of the growth, showing complete and spontaneous relaxation of the GaSb epilayers.[1, 2]

Despite over a decade of work on such IMF growths of GaSb on GaAs, there is the issue of residual threading dislocations. The residual dislocations are formed during the coalescence of fully relaxed GaSb islands during the initial stages of GaSb growth on GaAs. The islands themselves are formed with a periodic misfit dislocation network, however when individual islands coalesce, these networks merge but are not in registry with each other. This leads to the formation of 60º misfit dislocations at the points of coalescence which subsequently threads into the GaSb epilayer and results in the aforementioned residual threading dislocations. With thicker growths, the dislocation density can be reduced to the high 10^7 dislocations/cm^2 range, however any further progress is difficult.

In this work we include AlSb based defect filter layers immediately after the GaSb/GaAs interface to bend residual dislocations. The mismatch between AlSb ($a_{o\ AlSb}$ = 6.13 Å) and GaSb ($a_{o\ GaSb}$ = 6.09 Å) results in compressive strain at the growth interface which causes the dislocations to bend at this interface. The bent dislocations at the AlSb/GaSb interface form a secondary network that appear as a mesh in plan view transmission electron micrographs. The dislocations interact with each other, resulting in significant annihilation and a much reduced threading dislocation density of ~ 10^7 dislocations/cm^2. The presentation will provide an extensive TEM based analysis of the GaSb/GaAs misfit dislocation interface and the plan view analysis of dislocation annihilation in AlSb/GaSb defect filter layers.

Finally, we will demonstrate the growth of InAs n-channels and InGaSb p-channels on these GaSb/GaAs growths. The purpose of the study is to investigate the mobility of these channels with varied threading dislocation density. A baseline for the study is established by growing the structures on an AlSb buffer on GaSb. While this is not lattice matched, the mismatch is minimum and should result in ~ 5 x 10^5 dislocations/cm^2. We then demonstrate similar channels on GaSb on GaAs grown using the IMF layer with ~ 5 x 10^8 dislocations/cm^2. Finally, with different defect layer designs, we will also be able to show the channels on GaSb with dislocation densities ranging from 5 x 10^6 to 5 x 10^7 dislocations/cm^2. This allows us to study the effect of dislocation densities on n and p channel mobility across four orders of magnitude. The MBE growth of the structures is completed and the hall measurements on the samples is completed for most of the structures at this point.

A

Aalizadeh, Majid, **PS01**
Abate, Vincent, A03
Abir, Sk Shamim Hasan, PS32
Abrand, Alireza, **X05**
Abrar, Mahir, **PS40**
Abuzaid, Hattan, G03
Acuna, Wilder, S04, **AA08**
Addamane, Sadhvikas, F04, **X02**
Agapiou, Daphne, D06
Agarwal, Anant, B02, B04, B05
Agyapong, Ama, CC09
Ahmad, Habib, A05
Ahmadi, Elaheh, D06, DD05, PS01
Ahn, Kyle, PS03
Aho, A, U10
Ahsan, Ragib, **CC08**
Ahyi, Ayayi, B03
Ai, Yuehan, C02
Akhavan, Vahid, Q01
Akyurtlu, Alkim, Z04
Alaani, Mohammed, **M03**
Al Abri, Zeyad, M07
Alam, Md Didarul, **H08**
Al-Ghorbani, Mohammed, **PS43**
Ali, Muhammad Measam, BB02
Al-Jassim, Mowafak, B01
Allen, Jeffery, R10
Allen, Monica, R10
Allerman, Andrew, A03, H06
Almeter, Jack, **O01**
Alqatari, Feras, C03
Alquier, Daniel, DD03
Alsaad, Zinah, R08
Alston, Jeffrey, PS35
Alù, Andrea, FF06
AlZaqri, Nabil, **PS52**
Amano, Hiroshi, V01, V03
Anderson, Betty, V02
Anderson, Travis, A04, D02, H01, H03, H08, FF03, FF07
Ando, Yuto, **O03**
Andrieiev, Oleksandr, O04
Anttu, Nicklas, X05
Aqib, Muhammad, C03
Aragon, Andrew, PS03
Arbogast, Augustus, R01, T02, **T03**
Arehart, Aaron, O06, FF04
Areias, Chris, Z04
Arif, Annatoma, **PS18**
Armiento, Craig, Z04
Armstrong, Andrew, **A03**, H
Asel, Thaddeus, E04, **L02**
Assaf, Badih, P07
Avenoso, Joseph, AA08
Avishai, Amir, GG03
Awwad, Mohammad, **V02**
Aydinkarahaliloglu, Cagri, **Y05**

B

Babcock, Susan, E02
Bac, Seul-Ki, P07
Bagheri, Pegah, O05, DD01
Bagues Salguero, Nuria, P06, U04
Bai, Tingyu, Y02
Bakhtiary-Noodeh, Marzieh, A02
Balakrishnan, Ganesh, F04, R, R08, X02, EE03, GG02, HH05
Baldwin, Luke, EE10
Ballardo Rodriguez, Isis, PS29
Banerjee, Sanjay, PS05
Bank, Seth, R01, R02, R04, R05, T02, T04, GG01, GG04
Bas, Derek, AA02
Bautista, Rahayana Ruth, **PS46**
Beagle, Lucas, **EE10**
Bégin, Théophile, E01
Bell, L. D., DD06
Bell, Robert, FF07
Ber, Emanuel, **G10**
Bergthold, Morgan, R04, R05, AA06, **AA07**, GG01
Bernardi, Marco, P09, EE06
Bertani, Paul, C02
Bertness, Kris, M01, X
Bhattacharya, Arnab, DD02
Bhattacharya, Rajashree, **Q05**
Bhuiyan, A F M Anhar Uddin, **L04**, L05, **L08**, DD07
Bhushan, Pulak, PS41
Biedermann, Laura, **X09**
Bierwagen, Oliver, Q06, Q07
Biju, Jacob, B06
Binder, Andrew, H06
Bishop, Alexander, P06, **U01**, U02
Bockowski, Michael, F03
Bohaichuk, Stephanie, P04
Bonef, Bastien, F02
Booske, John, E02
Bork, James, AA08
Borra, Vamsi, PS50
Bowers, John, F02
Brady, Lauren, **C05**
Breckenridge, Mathew, F03
Brenner, Mark, D01, D03
Briggs, Ariel, N08
Brillson, Leonard, E03, E04, Q, Q07, BB06, FF09
Brooks, Christopher, BB04
Brown, Hayden, U07, **PS09**, PS11
Brown, Josh, Z01
Bryant, Garnett, P08, S04, X01, AA09
Burson, Kristen, EE08
Buyanova, Irina, U10, **PS45**

C

Cabral, Matthew, L06
Cai, Wentao, V01, **V03**
Caldwell, Joshua, K, AA01, AA04, FF06, PS13
Campbell, Ian, CC09
Campbell, Joe, R07, T05, GG01
Candido, Denis, **P02**, U
Cao, Linyou, G03
Caplins, Benjamin, M01
Caraveo Frescas, Jesus Alfonso, Y03, Y04
Carini, Giulia, **FF06**
Carrasco, Rigo, R08
Carter, James, **CC09**
Cavallo, Francesca, K04, EE03
Centrone, Andrea, D02
Cha, Yu-Jung, PS21
Chae, Hyun Uk, N07, CC08, **HH02**
Chaker, Mohamed, E01
Chakrabarti, Shakya, CC07
Chalke, Bhagyashri, DD02
Chanana, Ashish, X02
Chandrashekhar, MVS, H08
Chang, Alexander, A01
Chang, Benjamin, **EE06**
Charles, Matthew, DD03
Chatratin, Intuon, **M04**
Chaudhary, Anjali, **K04**
Chauhan, Himanshu, PS25
Chen, Chen, N03
Chen, Dekang, R07
Chen, George, CC02
Chen, Huandong, S03
Chen, Jie, C01, C03, C06
Chen, Lei, D02
Chen, Ping-Ping, PS45
Chen, Po Chun, O09
Chen, Victoria, P04
Chen, Weimin, **U10**, PS45
Chen, Zeyu, H02, **L03**, L04, L05
Chen, Zhaoying, H04
Cheng, Qianyu, H02, L03, L04, **L05**
Cheng, Shuyu, **P06**, U02, U03, **U04**, U08
Cheng, Zhihui, **G03**
Cheong, Heajeong, V01, V03
Chiaramonti, Ann, M01
Chizmeshya, Andrew, T01
Cho, Haein, CC04
Cho, Hanna, BB04, BB07, PS34
Cho, Kyeongjae, Q09
Cho, Minkyu, A02
Cho, YongJin, H10, L10
Choi, Hyunwoo, **EE02**
Choi, Junsoo, Q02
Choi, Sanghyeon, **CC04**
Chong, Su-Kong, S02
Chowdhury, Enam, FF09
Christodoulou, Christos, EE03
Clemmer, Burnell, DD04
Cleri, Angela, **AA01**, AA04
Clymore, Christopher, D06
Coffey, Tonya, EE08
Collazo, Ramón, F03, O01, O05, W05, DD01
Collins, Robert, M03
Collison, Christopher, EE08
Connelly, Blair, P05
Cooke, Jacqueline, **FF08**
Corbett, Joseph, N09
Cornuelle, Evan, FF04
Cortes, Pedro, PS50
Cowsky, Jade, **Q07**
Crawford, Mary, A03

D

da Cunha, Mauricio, W04
Daeumer, Matthias, H04
Dahal, Bishnu, U06, U07, **PS14**, PS16, PS37
Dahal, Drona, EE04
Daniels, Kevin, G, G07, N06, X06
Danilov, Evgney, PS33
Das, Debabrata, PS26, **PS39**
Das, Kalyan, PS02
Das, Mayukh, CC07
Das, Saptarshi, G01, G02, CC06, CC07, PS06
Das, Sarbashis, **G01**
Das, Shekhar, U04
Das, Subrata, **N07**
Das, Suman, **B03**
Das, Suprem, C
Dassanayake Mudiyanselage, Thiloka Madhumanie D., EE04
Datta, Srabanti, PS40
Davanco, Marcelo, X02
David, John, T05
Davis, Robert, L06
Davoodabadi, Ali, AA05
Davydov, Albert, G03, S04
Dawkin, Kendall, PS23
Dawkins, Kendall, X04, **PS27**
Dayeh, Shadi, O09
Dean, Scott, G06
DeAngelis, Emma, FF09
de Coster, George, P05
Dede, Didem, F05
Deitz, Julia, X02
Demchenko, Denis, O04
DeMell, Jennifer, **P01**
Demisse, Wondwosen, **CC10**, **PS51**
DenBaars, Steven, O08
Deng, Zihao, Q08, AA05
De Penning, Rebekah, **PS24**

Desai, Dhruv, **P09**
Detchprohm, Theeradetch, A, A02, O03, V
Dev, Sukrith, R10
DeVaulchier, Louis-Anne, P07
Devkota, Shisir, X04
Dey, Tuhin, R01, **T02**, T04
Dhar, Sarit, B03
Dhara, Sushovan, D01, **FF01**
Dheenan, Ashok, D01, **D03**, FF01
Dhingra, Pankul, GG05
Diallo, Karim, EE05
Diaz, Steven, EE08
Diaz-Cruz, Evelyin, PS44
Diaz-Granados, Katja, AA01, AA04, **PS13**
Dillard, Joshua, U07
Diroll, Benjamin, M02, **X08**
Dodda, Akhil, **G02**, **CC06**
Dong, Xiang, S02
Doolittle, W. Alan, A05, W, W01
Doty, Matthew, AA09
Downing, Brooke, L09, PS30
Drake, Madison, HH03, **HH04**
Du, Dongxue, E02
Dube, Alexander, N01
Dudley, Michael, H02, L03, L04, L05
Duprey, Colton, **CC02**
Dupuis, Russell, A, **A02**, O03
Dutton, Benjamin, L09, FF10, **PS30**
D'Angelo, Christopher, U06, PS09, PS10, PS11, PS12, PS14, PS16, PS19, PS37

E
Early, Lawrence, N01
Ebert, Philipp, M04
Ebrish, Mona, A04, H03, Z
Egbo, Kingsley, **Q06**
Eisele, Holger, M02, M04
Elafandy, Rami, Z01
El Filali, Brahim, PS28, **PS29**
El Hageali, Sami, **B01**
El-Jaroudi, Rasha, T04
Émond, Nicolas, E01
Encomendero, Jimy, H10
Engel, Zachary, A05, W01
Eom, Chang-Beom, E04
Erickson, Jeffrey, G06
Esfarjani, Keivan, AA05
Estrada, David, N08
Evans, Paul, E02
Ewing, Daniel, B, I, Y
Eyink, Kurt, **AA02**

F
Falkenstein, Andreas, Q06
Fan, Jonathan, P04
Fan, Victor, Y03
Faraji, Sheida, **EE05**
Favela, Elizabeth, **PS02**
Feezell, Daniel, H06, PS03
Feigelson, Boris, H08, FF07
Feng, Zixuan, L04, L05, L08
Fernandez-Izquierdo, Leunam, Y03, **Y04**
Ferrari, Victoria, BB06
Ferrigno, Joshua, **F06**
Fiedler, Andreas, D01, L04, FF01
Finstad, Terje, **PS22**
Fischer, Alec, O03
Flatté, Michael, P02, U09
Flicker, Jack, X09
Folland, Thomas, FF06
Folland, Thomas G, AA03
Fong, Mary, Y05
Fontcuberta i Morral, Anna, F05
Forrest, Rebecca, W03
Franklin, Aaron, G03
Freitas, Jaime, FF03
Friedl, Martin, F05
Friedman, Adam, P01
Frisone, Sam, A01
Furdyna, Jacek, P07
Furusawa, Yuta, V01, V03

G
Gabriel, Joshua, **CC05**
Gallagher, James, A04, D05, H01, **H03**, FF03
Gallagher, Joshua, PS03
Ganguly, Swaroop, B04
Garcia, Ashlee, GG01, **GG04**
Garcia Andrade, Manuel Alejandro, E06
Garrett, Trent, **HH03**, HH04
Garretto, Joao, PS50
Gautam, Bhoj, **PS33**
Gaye, Samba, **M08**
Ghadi, Hemant, **FF04**
Ghalavand, Elham, CC02
Ghandi, Reza, L03
Gibson, Emily, PS08
Gilbert, Simeon, X09
Gillan, Edward, **BB10**
Glaser, Caleb, A03, **H06**
Glasser, Ryan, P03
Glavin, Nicholas, EE10
Goff, Brad, **U03**
Goggin, David, G09
Golden, Joel, G06
Goldman, Rachel, A01
Gong, Cheng, N04
Goorsky, Mark, F, F03, H01, L07, Y02, FF05
Gopman, Daniel, M05
Gorman, Brian, B01
Gourbilleau, Fabrice, E06
Goyal, Harshil, Z02
Grady, Ryan, G10
Grant, Perry, R08
Grau, Gerd, EE
Greenslit, Morton, **W04**
Grein, Christoph, R07
Grizzle, Andrew, M08, U06, PS09, **PS10**, PS11, PS12, PS16, PS19, PS37
Gu, Liuxin, L06
Guina, M, U10
Guldner, Yves, P07
Guliani, Arush, **PS19**
Gundlach, Lars, AA08
Gunning, Brendan, H03
Guo, Bingtian, T05
Gupta, Jay, M03, N09, U01, U03
Gupta, Vijay, Y05
Guthrey, Harvey, B01
Gwoziecki, Romain, DD03

H
Hahn, Jung, A01, O02, O07, Z01
Hains, Chris, R08
Hajitabarmarznaki, Shiva, K04
Hajzus, Jenifer, **G06**, G07, L01
Hakkarainen, T, U10
Hall, Doug, E
Hamilton, Michael, Z, Z02
Hamlin, Andrew, EE01
Hammel, Chris, U04
Han, Sang, F04
Han, Shubo, PS33
Hanbicki, Aubrey, P01
Hansemann, Moritz, **M02**, M04
Harry, Richard, **U05**
Haseman, Micah, E03, FF09
Haug, John, K02
Haugan, Heather, AA02
He, Mingze, AA01
Heben, Michael, M03
Heidelberger, Christopher, GG05
Heileman, Grant, EE03
Heinselman, Karen, FF07
Hendricks, Jessica, L02
Hendrickson, Alexander, X02
Hernandez Camas, Luis, **PS42**
Heron, John, AA05
Hier, Harry, P05
Higashiwaki, Masataka, D04
Hilse, Maria, N05
Hirschman, Karl, Q03, Y01
Hirt, Daniel, AA04
Hite, Jennifer, H08
Hiura, S, U10
Ho, Alice, PS02
Ho, Quoc Dai, **P08**, S04, X01, AA09
Hobart, Karl, A04, D02, D05, H03, H08, Y02, FF03, FF07
Hodges, Deidra, M, PS40
Hoffman, Anthony, K02, Y05, AA
Hoffman, Georg, Q06
Hojer, P, U10
Holtz, Mark, T02
Honda, Yoshio, V03
Hong, Jong-Eun, BB02
Hool, Ryan, HH01
Hopkins, Patrick, Y02, AA04
Htoon, Han, S03
Hu, Chenxi, DD07
Hu, Guangwei, FF06
Hu, Ruiqi, P08, S04, **X01**, AA09
Hu, Shanshan, H02, L03, L04, L05
Hu, Yaoqiao, **Q09**
Huang, Chunyi, **F05**
Huang, Hsien-Lien, D03, L04, L05, L08
Huang, Xianrong, H01
Huang, Y.Q., U10
Hughes, Eamonn, **F02**, R03
Hughes, George, Z02
Hum, Matthew, Y01
Huo, Yuankai, K01
Hussain, Amjad, **BB02**
Hussain, Kamal, H08
Huynh, Kenny, F03, H01, **L07**, Y02, FF05
Hwang, Jinwoo, D03, L04, L05, L08, U02, DD07

I
Ikuhara, Yuichi, X03
Ince, Fatih, **F04**, GG02, **HH05**
Ironside, Daniel, GG01, GG04
Ishikawa, Fumitaro, PS45
Islam, A B M Hamidul, **PS21**
Islam, Mahnaz, **P04**
Isoaho, R, U10
Itapu, Srikanth, PS50
Itoh, Takeki, **L01**
Iyer, Shanthi, G08, X04, PS23, PS27

J
Jacobs, Alan, A04, D02, D05, H03, **H08**, FF02, FF03, **FF07**
Jacobs, Ryan, E02
Jacobson, R B, K04
Jakli, Antal, EE04
Janotti, Anderson, M04, P08, S04, X01, AA09
Jaramillo, Rafael, **F01**, **G04**, M02, N05, **S05**
Jatar, Shashank, Y05
Jayachandran, Darsith, CC06
Jayatunga, Benthara, DD07
Jeelani, Shaik, E05, U05

Jena, Debdeep, H10, L10
Jesenovec, Jani, **L09**, FF08, FF10, PS30
Jian, Zhe Ashley, **D06**, DD05
Jiang, Kunyao, **L06**
Jiao, Xinwei, BB05
Jin, Xiao, T05
Jo, Jaesung, Q04, **Q08**
Jo, Seong Soon, N05
Joh, Dong Woo, BB02
Johnston, Steven, B01
Joishi, Chandan, FF01
Jones, Andrew, GG01
Jones, Madison, M07
Jones, Sheenamelia, PS33
Jung, Hyemin, R07, T05

K

Kabir, Muhammad, Q03
Kalapala, Akhil, GG02
Kalarickal, Nidhin Kurian, **D01**, D03, FF01
Kamboj, Abhilasha, **R09**
Kang, Chong-Yun, CC04
Kapadia, Rehan, N07, CC08, GG03, HH02
Kaphle, Vikash, EE04
Kaplar, Robert, H03, H06
Karim, Md Rezaul, DD07
Kash, Kathleen, DD07
Kaufman, Jonathan, AA05
Kawakami, Roland, P06, U01, U02, U03, U04, U08
Kawasaki, Jason, E02
Kawasaki, Megumi, S03
Keller, Robert, G09
Keller, Stacia, O08
Kennerly, Stacey, L03
Khachariya, Dolar, O05, DD01
Khafizov, Marat, F06
Khaledialidusti, Rasoul, PS47
Khan, Asif, H08
Khan, Kamruzzaman, DD05, PS01
Kheirandish, Elaheh, **DD08**
Khirouni, Kamel, EE05
Khomenkova, Larysa, E06
Kidner, Neil, BB05
Kim, Bora, **M01**
Kim, Gwang Su, CC04
Kim, Ja Yeon, V04
Kim, Ji Hyun, O05, DD01
Kim, Jung Hyun, BB04, BB07, PS34
Kim, Jung-Hyun, BB, BB05
Kim, Mijung, M01, **HH01**
Kim, Myeongok, N03
Kim, Nam-In, **C01**, **C03**, **C06**, W03
Kim, Soaram, **G07**, N, X06
Kim, Sun Ho, PS02
Kim, Tae-Hun, BB02
Kim, Tae Kyoung, PS21
Kioupakis, Emmanouil, H06, Q08, AA05
Kirby, Brian, P03
Kirste, Ronny, O01, O05, DD01
Kitada, Takahiro, D04
Klein, Megan, L07
Klem, John, X02
Klump, Andrew, O05
Kmieciak, Thomas, X09
Kodati, Sri Harsha, R07, T05
Kodikara, Panambara Mudiyanselage Sineth G., EE04
Kohn, Erhard, O05, DD01
Koirala, Prakash, M03
Koll, William, **N09**
Konishi, Keita, D02
Korsunska, Nadiia, E06
Kotula, Paul, X02, X09
Kouser, Summayya, **PS15**
Kowalczyk, Dorota, N03
Kravchenko, Ivan, K01
Krishna, Sanjay, R07, T05
Krishnamoorthy, Sriram, D, L07, FF08
Krizman, Gauthier, P07
Kuchoor, Hirandeep Reddy, **G08**, X04
Kumamoto, Akihito, X03
Kumar, Suhas, P04
Kumar, Vikrant, **PS08**
Kumarasubramanian, Harish, **PS07**
Kuramata, Akito, D02, D05, Y02, FF03, FF07
Kuroda, Marcelo, B03
Kusch, Gunnar, F02
Kwak, Joon Seop, PS21
Kwansa, Albert, EE09
Kwon, Beom-Su, BB02
Kwon, Min-Ki, V04
Kymissis, Ioannis, PS08
Kyuno, Kentaro, PS49

L

Lad, Robert, W04
Lagally, Max, K04
Lähnemann, Jonas, Q06
Lamport, Emily, Z04
Lamsal, Sanjee, **PS50**
Landa-Bautista, Julieta, PS44
Lang, Andrew, L01
Lange, Andrew, H04
Lauhon, Lincoln, **A01**, F05, J
Laurence, Ted, H04
Law, Stephanie, P, S04, AA09, AA10
Le, Son, G03
Le Drogoff, Boris, E01
Lee, Daesu, E04
Lee, Dong Hun, **Q02**
Lee, Dongseop, **C02**
Lee, Jiyoung, C02
Lee, Jung-woo, E04
Lee, Michael, **BB04**
Lee, Ming-Hsun, M01, **FF02**
Lee, Minjoo, M01, GG, GG05, HH, HH01
Lee, Nien-En, EE06
Lee, Sangho, A05
Lee, Sang Hoon, **PS31**
Lee, Sangyoon, PS31
Lee, Seung-Bok, BB02
Lee, Seung Hyun, R07, T05
Lee, Seungjun, C02
Lee, Soonil, **BB01**
Lee, Sunghwan, Q02, BB08, CC03
Leedy, K.D., Q07
Lenahan, Patrick, B06, E, M05
Lenert, Andrej, AA05
Levy, Zachary, BB06
Lewis, Daniel, **N06**, X06
Lewis, Harry, **T05**
Li, Andrew, F04
Li, Bingjun, A01, **O02**, **O07**
Li, Brian, M01
Li, Frank, PS50
Li, Guoqing, G03
Li, Jia, G08
Li, Peining, PS13
Li, Wenbo, **O06**
Li, Xiaohang, C03
Li, Yao, **PS20**
Li, Yibo, Z04
Li, Yiyang, **CC01**
Li, Yize Stephanie, PS46
Li, Yuan, L03, **N02**
Li, Ziling, U04
Liang, Baolai, T05
Liang, Jianbo, D04
Liang, Shanchuan, **N04**
Liang, Shuang, PS46
Liao, Che-Hao, C03
Liao, Michael, F03, H01, L07, **Y02**, **FF05**
Lim, Tak-Hyoung, BB02
Lin, Lin, E02
Lin, Zhiqun, PS46
Lintereur, Azaree, PS03
Liu, Derreck, N05
Liu, Jian, **PS34**
Liu, Jianlin, L03
Liu, Quan, K01
Liu, Tianshi, B02
Liu, Xinyu, P07
Liu, Yafei, **H02**, L03, L04, L05
Liu, Yongchen, **S04**
Liu, Yuanyue, **G05**, **BB11**
Liu, Zhongue, GG02
Lockhart, Cody, BB05
Logan, Julie, R08
Lohani, Bhushan, **Z05**
Look, D.C., Q07
Loveless, James, O01
Lozano, Karen, C04
Lu, Guanyu, PS13
Lu, Wu, B05, C02, H04
Luce, Andrew, Z04
Luna, Sofia, CC02
Lussem, Bjorn, EE04
Lusvardi, Gina, CC02
Lyalin, Igor, P06, U02, **U08**

M

Ma, Tao, AA05
Ma, Weiliang, PS13
M Abdullah, Abu, CC06
Mace, Emily, PS03
Maddi, Hema Lata Rao, B04, **B05**
Maestas, Diana, R08
Mahadik, Nadeemullah, B, B01, I, **L02**
Mahalingam, Krishnamurthy, AA02
Maimon, Shimon, HH03
Majee, Arnab, EE03
Majewski, Leszek, EE05
Mambakkam, Sivakumar, AA10
Manley, Robert, Q03, Y01
Manning, Brian, M05
Mansfield, Elisabeth, **G09**
Mansoori, Ahmad, F04, HH05
Mansouri, Sabeur, E01
Manzi, Jacob, N08
Margot, Joëlle, E01
Maria, Jon-Paul, W05, AA01, AA04
Marks, Samuel, **E02**
Martel, Eli, W02
Martinez, Christian, R03
Martino, Christopher, DD04
Maselugbo, Adesewa, **PS35**
Mashooq, Kishwar, **Q04**
Masoumi, Narges, **T01**, **PS47**
Mastro, Michael, D02, H03
Mathew, Xavier, **PS44**
Mathews, Nini Rose, PS44, **PS48**
Matson, Joseph, FF06
Matthews, Christopher, **A05**, W01
Matto, Lezli, FF05
Mauduit, Clément, DD03
Mauze, Akhil, L01
Mayandi, Jeyanthinath, PS22
McAfee, Kenneth, **PS04**
McArthur, Joshua, R02
McCamant, David, EE08
McCandless, Jonathan, **L10**
McCloy, John, L09, FF08, FF10, PS30
McCluskey, Matt, FF10, PS30
McComb, David, P06, U04

McCullough, Connor, PS08
McEwen, Benjamin, A06, **O04**, DD06, DD08
McGlone, Joe, D01, D03, FF01, FF04
McNicholas, Kyle, GG, HH
McSherry, Sean, **AA05**
Mecouch, Will, O01
Mehnke, Frank, O03
Meng, Lingyu, L04, **L05**, L08
Meng, Qian, R01, R05, **T04**
Meyer, Jarod, **R03**, R06
Meyers, Vincent, **A06**, O04, DD06, DD08
Meyerson, Melissa, X09
Mhatre, Vilas, DD02
Mi, Chenziyi, **Z01**
Mi, Zetian, N09
Miaja Avila, Luis, J, **M01**
Milder, Alexander, **M06**
Milich, Milena, Y02
Milton, Donald, G07
Mirabito, Tim, **O10**
Mirkhosravi, Farnood, **PS03**
Miroshnik, Leonid, F04
Mishra, Rohan, S03
Mishra, Umesh, D06
Mita, Seiji, O01, O05, DD01
Mock, Alyssa, D05
Mohammadian, Navid, EE05
Mohanty, Subhajit, **DD05**
Mohney, Suzanne, CC09, DD04, PS20
Mohseni, Parsian, X05, X07
Molina, Alex, DD04
Molla, Mahlet, **H06**
Moore, David, EE10
Moradnia, Mina, C06, **W03**
Morath, Christian, R08
Moriyama, Takafumi, **X03**
Morrell, Brad, L10
Mortelmans, Wouter, **N05**
Motoki, Keisuke, A05, **W01**
Mou, Shin, L02, L04
Muhowski, Aaron, K, R04, T02, **AA06**, AA07, GG01
Mukherjee, Kunal, F, F02, R03, R06, HH03
Mukherjee, Shagorika, M04
Mund, Alexander, DD04
Murayama, A, U10
Muthuraj, Vineeta, **O08**
Mutunga, Eva, M08, **U07**, CC10, PS09, PS11, PS12, PS14, PS16, PS19
Myers-Ward, Rachael, G06, G07, L01

N

Nakamura, Shuji, O08
Nalam, Paul Gaurav, **PS26**, PS39
Nalamati, Surya Ratna Kiran, G08
Nasir, Saadia, **AA10**
Nayak, Suvendu, **B04**, B05
Neal, Adam T., L02, L04, L10
Newell, Alexander, F04, **R08**, HH05
Ni, Xiang, FF06
Nitta, Shugo, V03
Nodurft, Ian, **P03**
Noesges, Brenton, **E04**
Nomoto, Kazuki, H10
Nong, Mongtao, C03
Noor, Mohamed Yaseen, FF09
Nordin, Leland, R03, R04, **R06**, R09, R10, AA07
Nordlander, Joshua, **W05**, AA04
Norman, Andrew, B01
Norman, Justin, F02
Nowak, Derek, BB03, EE07

O

O'Neal, Nathaniel, **DD04**
O'Reilly, Padraic, EE07
Odekirk, Bruce, B01, L02
Oliver, Rachel, F02
Olsen, William, H01
Orlova, Tatyana, P07
Ortiz, Joaquin, P07
Orvis, Thomas, S03, PS07
O'Leary, Stephen, M03

P

Paarmann, Alexander, FF06
Packard, Glenn, **Y01**
Padalkar, Sonal, PS24
Palchoudhury, Soubantika, **M07**
Palei, Milan, **K02**, AA
Pan, Jinbo, E04
Pannone, Andrew, CC06
Parakh, Mehul, X04, PS23
Parimoo, Heemal, W02
Park, Anna, L06
Park, Jeong-Hwan, **V01**, V03
Park, Jinsoo, P09
Park, Tae Joon, P04
Park, Wontae, EE02
Passler, Nikolai, FF06
Passrobles, Guillermo, DD04
Paudel, Pushpa, **EE04**
Pavlidis, Georges, D02
Pavlidis, Spyridon, O05
Pedowitz, Michael, G07, **X06**
Peek, Sherman, **Z02**
Peng, Hongyu, H02, L03, **L04**, L05
Pennachio, Daniel, G, G06, G07, **L01**
Penners, Nicole, CC02
Peterson, Rebecca, M01, Q04, Q08, FF, FF02
Petluru, Priyanka, AA07
Phillips, Adam, M03
Pickrell, Greg, A03
Pinky, Sabila, EE09
Piro, Yuri, **Z04**
Podraza, Nikolas, M03
Pokharel, Rabin, **PS23**
Polojärvi, V, U10
Polupan, Georgiy, E06, PS28, PS29
Ponce, Fernando, O03
Pop, Eric, G10, P04
Porter, Lisa, L, L06, PL, PS02
Porter, Matthew, **A04**, DD04
Portier, Xavier, E06
Pouladi, Sara, C06, V04, W03
Powell, Eli, **Q03**
Pozdin, Vladimir, PS41
Prakash, Divya, K04
Protasenko, Vladimir, L10
Purcell, Ashton, **B06**

Q

Qian, Jiashu, B05
Qin, Fei, **CC03**
Quevedo Lopez, Manuel, Y03, Y04
Quiñones García, Cristyan, **DD01**

R

Rabin, Oded, PS04
Race, Joseph, **PS17**
Radhakrishnan, Shiva, CC06, CC07
Raghothamachar, Balaji, H02, L03, L04, L05
Rajabi, Fereshteh, N08
Rajan, Siddharth, D, D01, D03, L04, N, V02, FF01
Rajapaksha, Chathuranga Prageeth Hemantha, EE04
Ramana, Chintalapalle, PS26, PS39
Ramanathan, Shriram, P04
Ramanujam, Balaji, M03
Ramaswamy, Priyanka, **X04**
Ramdin, Daram, **FF09**
Ramirez Garcia, Jorge Luis, PS28
Ranasingha, Oshadha, Z04
Randriambololona, Andoniaina, PS09, **PS11**
Ranga, Praneeth, L07, FF08
Rangari, Vijaya, E05
Rao, Lalith, BB04, **BB05**
Rashid, Roksana, EE02
Rashidi, Arman, PS03
Rathkanthiwar, Shashwat, **O05**
Ravichandran, Jayakanth, M02, S03, PS07
Reddy, Pooja, R06, HH03
Reddy, Pramod, F03, O01, O05, DD01
Redwing, Joan, G02, N03, O10, CC06
Rees, James Dylan, C05
Reese, Patricia, PS19
Regalado-Perez, Eulises, PS44
Reilly, Caroline, O08
Reilly, Kevin, F04, GG02, HH05
Reingold, Matthew, N01
Remple, Cassandra, **FF10**
Ren, Yuxing, **S02**
Renteria, Emma, **EE03**, GG02
Repicky, Jake, U03
Reshchikov, Michael, O04
Restrepo, Diego, PS08
Reyes-Banda, Martin, **Y03**, Y04
Reza, Mohammad, R01, T02, T04
Richter, Curt, G03
Ricks, Amberly, R04, **R05**
Riney, Logan, **P07**
Ringel, Steven, D01, D03, O06, FF01, FF04
Roberts, John, P04
Roberts, Robert C, Z05, PS18
Robertson, John, G07
Rocco, Emma, A06, O04, **DD06**, DD08
Rockwell, Ann, R02
Ronningen, T.J., R07
Rosas Martinez, Pablo, **BB06**
Rosenberg, Samantha, X09
Rosenzweig, Dorothee, M02, **M04**
Rothschild, Molly, Q02
Rotter, Thomas, F04, X02, EE03, GG02, HH05
Rouhi, Hadi, CC02
Roy, Anupam, PS05
Rummel, Brian, F04
Rumpf, Raymond, **K03**
Ryou, Jae-Hyun, C01, C03, C06, V04, W03
Ryu, Hanyoul, V04
Ryu, Heeju, G07

S

Salas Toledo, Julia, **C04**
Salemi, Arash, B02
Samarth, Nitin, N05
Sanchez, T.G, PS48
Sanders, Nocona, Q08
Sanford, Norman, M01
Sarney, Wendy, P05
Sasaki, Hirokazu, X03
Sasaki, Kohei, D02, D05, Y02, FF03, FF07
Sato, S, U10
Saunders, Nicholas, M07
Savadkoohi, Marzieh, **M05**, M08, **U06**, U07, PS14, PS37
Savage, Donald, E02, K04
Sawyer, Shayla, C, C05
Sayre, Jay, BB04, BB05
Scarpulla, Michael, FF08, PS03

Schalip, Ryan, **PS05**
Scheideler, William, EE, **EE01**
Schnedler, Michael, M04
Schranghamer, Thomas, CC07
Schroder, Kurt, Q01
Schubert, Mathias, FF06
Schwartz, Mariah, **R07**
Searles, Thomas, P03
Sebastian, Amritanand, CC07
Seck, Mane, EE05
Selcu, Camelia, U04
Sellers, John, Z02
Selvidge, Jennifer, F02
Sen, Dipanjan, **CC07**
Senckowski, Alexander, FF04
Sensale Rodriguez, Berardi, FF08
Seo, Jae Won, PS21
Seong, Tae-Yeon, V01
Seth, Subhashree, F04, **GG02**, HH05
Sey, Matty, PS40
Shah, Amit, **DD02**
Shah, Archit, Z02
Shahedipour-Sandvik, Fatemeh (Shadi), A06, O, O04, DD06, DD08
Shan, Ambalanath, M03
Shao, Qinghui, H04
Sharma, Peter, X09
Sharma, Shivam, FF04
Sharov, Fedor, B06, **M05**
Shaw, Harry, P03
Shawon, Sk Md Ali Zaker, **PS38**
Shcherbyna, Lyudmula, PS29
Shea, Patrick, Y
Shen, Shyh-Chiang, A02, O03
Sheridan, David, B02
Shervin, Shahab, V04
Shevelev, Mike, A06, DD08
Shi, Yueguang, **U09**
Shibata, Naoya, X03
Shields, Seth, **M03**
Shigekawa, Naoteru, D04
Shim, Jong-In, PS21
Shima, Darryl, F04, HH05
Shin, Dong-Soo, PS21
Shin, Jaehak, PS31
Shou, Chengyun, L03
Shriver-Lake, Lisa, G06
Siegal, Michael, X09
Simin, Grigory, H08
Simmonds, Paul, X, HH03, HH04
Singh, Shantanu, S03
Singhal, Jashan, H10
Singisetti, Uttam, FF04
Sinno, Talid, F04
Siskavich, Brad, Z01
Sitar, Zlatko, F03, O01, O05, W05, DD01
Skipper, Alec, **GG01**, GG04
Sklyar, Vlad, A06, DD08
Slimani Tlemcani, Taoufik, **DD03**
Smith, Lyndon, **E05**
Smith, Trevor, A03
Song, Han Wook, Q02, BB08, CC03
Song, Qian, N05
Song, Rak-Hyun, BB02
Sorace-Agaskar, Cheryl, GG05
Soto, Jake, B01, L02
Spangler, Ryan, **AA04**
Speck, James, L01
Spencer, Joseph, D02, **D05**, H08, **FF03**
Stahlbush, Robert, B01, L02
Stehr, Jan, PS45
Steinbrunner, Erich, L02, L04, L10
Stephen, Gregory, P01
Stewart, David, BB06
Stiff-Roberts, Adrienne, EE09
Stout, Meghan, BB05
Strohbeen, Patrick, E02
Stroud, Rhonda, L01
Subbaraman, Harish, N08
Suh, Pius, M08, **PS37**
Suleiman, Aminat Oyiza, **E01**
Sunderland, Peter, PS04
Sunthornpan, Narin, **PS49**
Surendran, Mythili, **S03**
Sushko, Peter, PS15
Swisher, Sarah, Q, **Q01**
Szymanski, Dennis, O05

T

Tadjer, Marko, **D02**, D05, H08, Y02, FF, FF02, FF03, FF07
Tai, Lixuan, S02
Tai, Sheldon, G07
Takatsuki, Daiki, D04
Takayama, J, U10
Talesara, Vishank, B05, H04
Talin, A., P04
Tanen, Nick, L10
Tang, Hong, Z01
Tang, Jingyu, L06
Tang, Zhenghuan, **BB09**
Tao, Jun, **GG03**
Taylor, Patrick, P01, **P05**
Taylor, Rodneycia, M08, **PS16**
Tefera, Michal, PS19
Tezanos, Kyle, **X07**
Thieberger, Peter, L03
Thieu, Quang Tu, Y02, FF03
Thind, Arashdeep, S03
Thirupakuzi Vangipuram, Vijay, O06, DD07
Thomas, Daria, PS33
Thompson, Kamila, **E03**
To, Quang, P, P08, X01, **AA09**
Toita, Masato, H10
Tomko, John, Y02, AA04
Torchynska, Tetyana, **E06**, **PS28**, PS29
Trainor, Nicholas, G02, **N03**, CC06
Trammell, Scott, G06
Tran, Ly, EE10
Trieu, Tuong, PS46
Troccoli, Mariano, Y05
Trolier-McKinstry, Susan, ***PL01**
Trulli, Susan, Z04
Turkani, Vikram, Q01
Tweedie, James, F03
Tyagi, Pawan, M05, M08, U, U06, U07, CC10, PS09, PS10, PS11, PS14, PS16, PS19, PS37, PS51
Tyagi, Pranshu, **PS12**

U

Uddin, M. Jasim, C04, **PS32**, PS38
Urbas, Augustine, AA02
Ushida, Yasuhisa, V01

V

Vaghefi Esfidani, Seyedeh Maryam, **AA03**
Vail, Owen, P01
Valentine, Jason, K01
Varghese, Tony, **N08**
Varley, Joel, Q06
Varma, Ghanshyam, **PS25**
Vatan Meidanshahi, Reza, PS47
Vaughan, Erin, HH05
Vazquez, Juan, GG03
Vega Macotela, Leonardo, E06
Vercik, Andres, **PS36**
Veres, Sarah, CC02
Verma, Navni, BB04
Victorio, Mauro, **PS41**
Villagran, Martha, C01
Vogel, Eric, N01
Voigt, Cooper, **N01**
Vorobiov, Mykhailo, O04

W

Wagner, Brent, N01
Waldvogel, Jason, E02
Wali, Akshay, **PS06**
Walker, Mitchell, BB06
Walko, Robert, U01
Wang, Binbin, P06, U04
Wang, Boyan, D05
Wang, Ellie, **R02**
Wang, Gunuk, CC04
Wang, Hongwei, E04
Wang, Jiashu, P07
Wang, Kang-Lung, S02
Wang, Ke, O01, O05
Wang, Ping, N09
Wang, Sizhen, A01, O02
Wang, Tianyang, BB05
Wang, Xiaojun, Y05
Wang, Xingjun, PS45
Wang, Yekan, **F03**, **H01**, L07, Y02
Wang, Yinan, **R10**
Wang, Yiteng, **GG05**
Wang, Yubo, Z01
Wang, Zhengtianye, S04, AA09, AA10
Wang, Zhenwei, **D04**
Wasserman, Daniel, R, R04, R09, R10, T02, AA06, AA07, GG01, PL
Weatherford, Todd, DD04
Webb, Katherine, CC02
Webb, Matthew, AA05
Weber, Marc, FF07
Webster, Preston, R08, HH05
Weide, Daniel, K04
Weidling, Adam, Q01
Wetzel, Christian, DD
Wheeling, Rebecca, **Z03**
White, Marvin, B02, B05
White, Rachel, **R04**, R05, T04
Wiegand, Tyler, **EE08**
Winkler, Roland, P07
Wistey, Mark, M, **R01**, R05, T02, T04
Wojcik, Michael, H01
Wolf, Martin, FF06
Wong, Man Hoi, FF04
Wong, William, EE02
Woodward, Patrick, M06, PS17
Woolf, David, R09
Wosik, Jarek, C01
Wright, Tia, PS33
Wu, Tianhai, **O09**
Wu, Xifan, E04
Wujcik, Evan, CC02

X

Xiao, Ming, D05
Xie, Ti, N04
Xing, Huili Grace, H10, L10
Xu, Song, **BB03**, **EE07**
Xu, Yibo, B05
Xu, Zhiyu, A02, O03

Y

Yalon, Eilam, G10
Yan, Qimin, E04
Yang, Jehyeon, CC04
Yang, Tianchen, **L03**
Yang, Ting-Hsun, S02
Yanguas-Gil, Angel, CC, CC05
Yap, Jun Wei, **BB07**
Yarali, Miad, **V04**
Yates, Luke, H06
Ye, Kevin, **M02**, N05
Ye, Youxiong, EE01
Yelamanchili, Bhargav, Z02

Yin, Xue, W02
Yingling, Yaroslava, EE09
Yoo, Jae Hyuck, H04
Yu, Caroline, PS08
Yu, Edward, BB, BB01
Yvon, Arnaud, DD03

Z

Zabetakis, Daniel, G06
Zainuddin, Shaik, U05
Zhang, Bin, PS45
Zhang, Buang, **EE09**
Zhang, Chengyang, P04
Zhang, Huairuo, G03, S04
Zhang, Kaitian, **DD07**
Zhang, Kun, PS02
Zhang, Peng, S02
Zhang, Qihua, **W02**
Zhang, Yuewei, L01
Zhang, Yuhao, D05, FF03
Zhang, Yuxuan, **H04**, O06, **BB08**
Zhang, Zexuan, **H10**
Zhao, Boyang, M02, S03
Zhao, Hongping, H04, L, L04, L05, L08,
O06, DD07
Zhao, Huan, S03
Zhao, Songrui, W02
Zheng, Hanyu, **K01**
Zheng, Yikai, CC06
Zhou, Jin-Jian, P09, EE06
Zhou, Weidong, GG02
Zhou, Wenyi, U01, **U02**
Zhou, You, K01
Zhu, Menglin, U02, DD07
Zhu, Shengnan, **B02**
Zhukovskyi, Maksym, P07
Zide, Joshua, S, S04, T, AA08, AA09
Zou, Ke, **S01**
Zuo, Peng, E02

EMC 2022 Program Grid

Registration is located First Floor, Great Hall Foyer

Rooms	Wednesday AM	Wednesday PM	Thursday AM	Thursday PM	Friday AM
Great Hall Foyer, 1st floor	**EMC Registration:** 7:30 am - 5:00 pm		**EMC Registration:** 8:00 am - 5:00 pm		**EMC Registration:** 8:00 am - 12:00 pm
Performance Hall 1st floor	**AM Break:** 9:20 am - 10:00 am **Exhibit Hours:** 9:00 am - 12:00 pm 1:30 pm - 4:00 pm 6:00 pm - 8:00 pm **PM Break:** 3:10 pm - 3:30 pm **Poster Reception:** 6:00 pm - 8:00 pm		**AM Break:** 10:00 am - 10:20 am **Exhibit Hours:** 9:00 am - 12:00 pm 1:30 pm - 4:00 pm **PM Break:** 3:10 pm - 3:30 pm		**AM Break:** 10:00 am - 10:20 am
Great Hall Meeting Room 1 &2 1st floor		G: 2D Material Devices and Sensors	N: 2D Materials Growth and Surfaces	U: Nano-Magnetic, Magnetic Memory and Spintronic Materials	CC: Neuromorphic + Late News
Great Hall Meeting Room 3 1st floor	A: Group III-Nitrides—Power Diodes	H: Group III-Nitrides—Power Diodes and HEMTs	O: Group III-Nitrides—MOCVD Growth	V: Group III-Nitrides—Light Emitting Diodes W: Group III-Nitrides—MBE, CVD and Sputtering	DD: Group III-Nitrides—Contacts and Novel Devices
U.S. Bank Conference Theater 1st floor	DRC: Session 11: Heterogeneous Integration	DRC: Session 12: Wide Bandgap III - III-N HEMTs	P: Quantum, Strongly Correlated and Topological Materials	X: Low-Dimensional Materials and Nanofabrication	EE: Flexible, Printed, and Organic Electronic Materials and Devices
Archie M. Griffin West Ballroom 2nd floor	Plenary Session 8:20 - 9:20 am B: Silicon Carbide—Devices and Reliability	I: Silicon Carbide Materials and Characterization J: Nanoscale Characterization			
Ohio Staters Inc. Founders Room 2nd floor	C: Wearable Electronics and Biosensors	K: Metasurfaces and Structured Photonics			
Ohio Staters Inc. Traditions Room 2nd floor	D: Gallium Oxide Devices	L: Gallium Oxide Growth	Q: Oxide Semiconductor Devices, Defects and Transport	Y: Materials Processing and Integration Z: Heterogeneous Integration Technologies	FF: Gallium Oxide—Material Processing, Characterization and Defects
Senate Chamber 2nd floor	E: Dielectrics and Multifunctional Oxides	M: Solar Cell Materials and Devices	R: Detectors and Narrow Bandgap Materials	AA: Plasmon and Surface Phonon Polaritons	
Cartoon Room 1 3rd floor			S: Emerging Epitaxial Materials T: Epitaxial Growth of Highly Mismatched Alloys	BB: Electrochemical Energy Storage and Conversion	GG: Epitaxial Growth on Patterned Substrates HH: Lattice Mismatched Epitaxial Growth
Rosa M. Ailabouni Room 3rd floor	F: Point Defects, Doping, and Extended Defects				
Archie M. Griffin East Ballroom 2nd floor				Conference Dinner Reception 6:00 pm - 8:00 pm	